



**HAL**  
open science

# Crack Initiation Mechanisms in Very High Cycle Fatigue at High Temperatures of Ni-based Single Crystal Superalloys: Transition from Internal Sites to the Surface

Luciana Maria Bortoluci Ormastroni

► **To cite this version:**

Luciana Maria Bortoluci Ormastroni. Crack Initiation Mechanisms in Very High Cycle Fatigue at High Temperatures of Ni-based Single Crystal Superalloys: Transition from Internal Sites to the Surface. Other. ISAE-ENSMA Ecole Nationale Supérieure de Mécanique et d'Aérotechnique - Poitiers, 2022. English. NNT: 2022ESMA0005 . tel-04042436

**HAL Id: tel-04042436**

**<https://theses.hal.science/tel-04042436v1>**

Submitted on 23 Mar 2023

**HAL** is a multi-disciplinary open access archive for the deposit and dissemination of scientific research documents, whether they are published or not. The documents may come from teaching and research institutions in France or abroad, or from public or private research centers.

L'archive ouverte pluridisciplinaire **HAL**, est destinée au dépôt et à la diffusion de documents scientifiques de niveau recherche, publiés ou non, émanant des établissements d'enseignement et de recherche français ou étrangers, des laboratoires publics ou privés.

# THÈSE

Pour l'obtention du Grade de

## DOCTEUR DE L'ÉCOLE NATIONALE SUPÉRIEURE DE MÉCANIQUE ET D'AÉROTECHNIQUE

*(Diplôme National – Arrêté du 25 mai 2016)*

École Doctorale Sciences et Ingénierie en Matériaux, Mécanique, Énergétique

Secteur de Recherche : Mécanique des solides, des matériaux, des structures et des surfaces

Présentée par :

**Luciana Maria BORTOLUCI ORMASTRONI**

\*\*\*\*\*

**Crack initiation mechanisms in Very High Cycle Fatigue at high temperatures of Ni-based single crystal superalloys: transition from internal sites to the surface**

\*\*\*\*\*

Directeur de thèse : Patrick VILLECHAISE

Co-encadrant de thèse : Jonathan CORMIER

\*\*\*\*\*

Soutenue le 23 Mars 2022

devant la Commission d'Examen

\*\*\*\*\*

**JURY**

### **Rapporteurs :**

Marion BARTSCH, Professeure, German Aerospace Center (DLR), Allemagne

Vincent MAUREL, Maître de recherche, MINES Paris-Tech, Paris

### **Examineurs :**

Fernando PEDRAZA, Professeur, Université de La Rochelle, La Rochelle

Véronique FAVIER, Professeure, Arts et Métiers Paris-Tech, Paris

Jonathan CORMIER, Maître de conférences, Institut P<sup>2</sup>, ISAE-ENSMA, Poitiers

Patrick VILLECHAISE, Directeur de recherche CNRS, Institut P<sup>2</sup>, Poitiers

### **Invité.e.s :**

Alice CERVELLON, Ingénieur Mécanique et Métallurgie, Safran Aircraft Engines, Châtellerault

Jérémy RAME, Ingénieur Matériaux et Procédés, Safran Aircraft Engines, Gennevilliers



---

*Há um ditado que ensina "o gênio é uma grande paciência"; sem pretender ser gênio, teimei em ser um grande paciente. As invenções são, sobretudo, o resultado de um trabalho teimoso, em que não deve haver lugar para o esmorecimento.*

*There is a saying that teaches: "the genius is of great patience"; without pretending to be a genius, I insisted on being a great patient. Inventions are, above all, the result of stubborn work, in which there should be no room for discouragement.*

*Il y a un proverbe qui enseigne que « le génie est une grande patience » ; sans prétendre être un génie, j'ai tenu à être un grand patient. Les inventions sont avant tout le résultat d'un travail acharné, dans lequel il ne doit y avoir aucune place pour le découragement.*

***Alberto Santos-Dumont***

Le pionnier franco-brésilien de l'aviation. Il a construit des nombreux ballons qu'il a piloté ; il a également conçu et piloté un des premiers dirigeables. Attiré par le « plus lourd que l'air », il effectue les premiers vols de son avion 14 Bis, à Bagatelle près de Paris, ce qui lui permit d'établir le premier record du monde officiel d'aviation le 23 octobre 1906.



# **Acknowledgements**



This thesis research is a combination of great partnerships. I would like to show my gratitude to the “Contrat de Plan Etat - Région Nouvelle-Aquitaine (CPER)” as well as the “Fonds Européen de Développement Régional (FEDER)” for their financial support to the reported work. Part of this study was supported by the Nouvelle-Aquitaine French region through the ECOREVE project (project number 2018–1R10122). This study is also part of the "Self- Heating" ANR-Safran-Naval group research chair (Grant # ANR-20-CHIN-0002) involving the Safran Companies, Naval group, ENSTA Bretagne (IRDL) and Institut Pprime. In addition, I would like to acknowledge the Institut Pprime for the financial support since my internship.

This research work was a material-rich project due to the superalloys provided by different institutions in the world. Thus, I would like to express my gratitude to the National Institute for Materials Science (NIMS) and to Hiroshi Harada and Kyoko Kawagishi for the TMS-238 superalloy and our Superalloys 2020 contribution; to the Institute of Metal Research (IMR) and to Jian Zhang for the DD33 superalloy (Bridgman, LMC and HIP) and for our great scientific discussion; to the Ruhr-Universität Bochum & Friedrich-Alexander-Universität Erlangen-Nürnberg – Germany for the ERBO/1 superalloy and the PBF-E CMSX-4 bars and HIP treatments and to Benjamin Rutttert, Carolin Körner, Inmaculada Lopez-Galilea, Julian Pistor and Werner Theisen for our great (and my sweetheart) scientific contribution at the Additive Manufacturing Journal. A special thanks to the great and hard work of Inmaculada and Benjamin during these last years, I am really looking forward to meet both of you; to Safran Aircraft Engines for the AM1 and Rene N5 superalloys, and for the APVS coating, also to André Malié, Jérémy Rame, Luc Bianchi, Noureddine Bourhila, Romain Lavaud, Sandrine Charles, Sarah Hamadi, Vincent Ezan and Virginie Jacquet for the great exchanges during the last four years, it was essential to my professional development; to the Université de La Rochelle and LaSIE for the Slurry coating, also to Fernando Pedraza and Thomas Kepa for the great adventure that is ECOREVE project, the friendship and the good moments. It was an honor to me to work with all of you.

I would like to acknowledge the excellent work of my jury members and to thank all of them to have accepted this mission. Thank you, Marion Bartsch and Vincent Maurel, for the corrections and suggestions through my thesis report. Véronique Favier thanks to have conducted so well the defense and to have accepted to be the president of the jury. Fernando Pedraza, Alice Cervellon and Jérémy Rame thanks for the well-prepared questions. All of you enriched the scientific discussion of my defense.

An especial mention to my thesis directors:

Patrick Villechaise merci pour nous donner la liberté de donner vie au laboratoire. Si on a une ambiance magnifique à l'Institut Pprime c'est surtout parce que la direction le permet. Merci pour tous les conseils, les histoires, les bons moments au-delà du laboratoire... ça été un plaisir que tu aies fait partie de mon encadrement.

Jonathan Cormier un gros merci pour tous que tu as fait pour moi depuis 2018. Surtout, merci pour avoir cru que j'étais capable de vivre le monde des superalliages. Merci de m'avoir motivé et de m'avoir donné tous les outils pour grandir dans ce domaine. Sache que je suis super fière d'avoir eu l'opportunité de t'avoir comme mon encadrent de thèse et que je suis reconnaissante de tout ce que tu as donné pour ce projet. Tu es le génie des superalliages, mais pas seulement, tu es aussi un grand ami.

Une institution ne peut pas bien marcher sans que l'équipe travaille en harmonie. Donc, si j'ai réussi à finir ce projet de thèse c'est surtout grâce au travail fait derrière. Merci à Brigitte, Valérie, Karine et Francine pour être toujours ouverte à nous recevoir avec un gros sourire. Merci à l'équipe de l'atelier Jacques, Laurent et Loïc pour le travail parfait d'usinage et de réparation de la machine VHCF quand j'en avais besoin. Merci à l'ensemble de l'équipe du laboratoire pour l'effort de nous préparer, nous aider et nous accompagner pendant des années pour qu'on puisse réussir. Denis, merci pour les bons moments d'échange, ta bonne humeur est un reflet de ta bonne âme. Amélie et David merci pour les analyses au tomo, ça été un moment clé de ma thèse. Amélie, merci pour la photo blague ;) Florence, merci pour être une grande inspiration pour moi. Tu es une des meilleures personnes et la meilleure ingénieure que je connais. Florent, merci pour faire exister la team VHCF, sans toi rien ne pourrait être possible. Enfin, merci à l'ensemble de l'équipe de l'Institut Pprime, à tous les doctorants et post-doctorants que j'ai eu le plaisir de connaître. Vous me manquez tous les jours.

Je ne peux pas finir sans quelques remerciements spéciaux :

Merci à notre showman Nico qui organise les meilleures soirées en France. Nico être avec toi ce n'est jamais ennuyeux, au contraire, ce sont des meilleurs moments que j'ai eu à Poitiers. Merci pour avoir m'invité à connaître l'Eurovision, d'une façon tu as changé ma vie avec cette invitation. Merci à Lucille pour m'avoir influencé à tomber amoureuse des jeux des sociétés, des soirées Disney, des plantes et aussi de Cyril xD. Un gros merci à mes petits Guillaume, Maxime, Florent, Julie, Théotime et Jérémy pour les bières, les jeux de sociétés, les barbecs, les soirées, les apéros-visios... enfin merci pour tous les bons moments partagés. J'ai une pensée aussi pour Mélanie, Happy et Salvador qu'ont été toujours des bonnes compagnies et des bons amis. Pour finir, à mon petit Antonio, le nouveau père de la machine VHCF, je te souhaite une période fantastique au laboratoire plein des bonnes vibrations ;)

My dear friend Satoshi Utada, thank you to have been so kind and so generous with me. You have no idea how much I enjoyed our exchanges (scientifically and personally) and how much I missed you when you choose the English beer over the French one. Thank you to have travelled to Poitiers the day of my defense. I was really touched by your presence. You have a friend that cheers for your success (and deep inside hope that you come back). Miss you... as always.

Merci à Coline, Sarah et Samuel pour tous les moments partagés depuis 2018, de la folie de l'ATEM à la fin de la soutenance. C'est incroyable comme je suis toujours entouré par des gens magnifiques et vous êtes trois des plus gentil que je connais. Je me suis beaucoup amusé avec vous et je n'aurais pas pu choisir une meilleure promo. Coline, malgré les difficultés c'est fini xD Sarah, finalement, la thèse n'était pas si mal ;). Samuel, notre projet baleine n'est pas encore fini ;P. On se voit en Tunisie :\*\*\*\*\*

Alice et Samuel merci pour ouvrir la porte de chez vous à nous. Samuel, merci pour tous les barbecues que tu m'as invités, ça m'a fait me sentir au Brésil xD. Merci surtout pour les innombrables moments qu'on a partagé les dernières années. Alice, merci pour être ma source d'inspiration, je voudrais être moitié de l'ingénieure que tu es. Mais plus que ça, merci pour avoir m'a accueilli quand je suis arrivée et d'être revenu en France, tu nous as beaucoup manqué.

Merci à mon "toujours là" ami Clément que n'importe l'heure ou le jour il était toujours dispo pour nous aider (ou à boire une bière). Mais surtout, merci pour les moments légers pendant l'interminable rédaction de ce manuscrit. Ta présence m'a donné une énorme force pour y arriver. Merci pour tous les vidéos de chiens mignons que tu m'envoie presque tous les jours depuis cette période, ce sont des moments que j'apprécie énormément. J'espère que toi et Océane reviennent vite de l'aventure en Asie pour qu'on puisse passer des beaux moments ensemble. Tu nous vas beaucoup manquer ;)

Merci à mes collègues du meilleur bureau (B008 of course), un gros merci pour la patience, oui je sais ce n'était pas facile pour vous, mais c'est fini. Merci Paul et Caroline pour m'avoir reçu et accueilli. Paul merci pour ton amitié et pour avoir partagé (avec Pauline) des moments magnifiques avec moi et Cyril. Prasad, thanks to be such good and kind friend. I am so proud to have shared with you the last four years and so happy that you choose to be in B008. Always remember my good friend: Life is a bit@@! Aux petits, Quentin, quelle bonne surprise quand on a su que tu avais choisi le B008. Tu as amené des bonnes rigolades au B008 et a changé nos mood de désespoir xD. Benoît et Thomas, quel plaisir partager ma dernière année avec vous, vous êtes des personnes magnifiques et je ne pouvais pas demander des meilleurs co-bureau.

Merci à mon chéri Cyril pour la patience, pour la compréhension, pour le support émotionnel et pour tous les sacrifices que tu as fait (et que tu fais encore) pour que je puisse continuer cette bataille. Tu as été une des plus belles surprises de la thèse. J'apprends tous les jours avec ta façon de voir la vie et d'aimer intensément. J'ai que à remercier toi tous les jours pour m'avoir choisi pour partager ces dernières années. Je t'aime mon ange ;) Un gros merci à ta famille qui m'a accueilli à bras ouverts, me surprenant toujours avec les gestes d'amour. Vous êtes des jolis cadeaux de la vie auquel je suis éternellement reconnaissante.

Eu tenho e sempre terei muito orgulho de carregar comigo o nome da Unifei. E muito mais que um grande amor pela instituição, eu sou eternamente grata a todos os professores que foram essenciais nessa minha caminhada. Gostaria de agradecer também à AD-UNIFEI Europa que é um suporte essencial para nós imigrantes e que me trouxe momentos maravilhosos. É um pedacinho da nossa vida universitária que me faz muito feliz. Agradeço às minhas companheiras de vida Thalita, Ana Paula e Jaqueline pela amizade, companheirismo e inspiração nesses últimos dez anos. E por fim, URUBU, URUBU, AU, AU... ENGENHARIA ENGENHARIA FEDERAL ;)

Como todo bom brasileiro que encontra brasileiro em todo cantinho do mundo, eu tive a chance de encontrar algumas peças raras em Poitiers. Fábio, Ladeira e Ramon obrigada por não me deixarem enlouquecer nesse último ano ;). Bárbara, Babi, miga... obrigada, nem no melhor dos meus sonhos eu imaginei encontrar uma amiga como você em uma cidade no interior da França. Você é a pessoa mais generosa que eu conheço e essa generosidade era tudo o que eu precisava para sobreviver esses últimos anos. Como eu te disse, eu espero poder fazer por você tudo o que você fez por mim, e mais, espero poder te carregar comigo para sempre. Te amo fofinha.

A vida é feita de equilíbrio e desequilíbrio, de bons e complicados momentos, mas se você tiver as pessoas certas ao seu lado, tudo se transforma. Eu agradeço às minhas eternas e amadas amigas Corina, Lara, Lígia, Lívia e Juliana, obrigada por transformarem a minha vida desde 2010. Eu sou eternamente grata ao destino por ter cruzado o meu caminho com o seus, eu não poderia pedir por mais nada nessa vida porque eu gastei toda sorte do mundo em ter encontrado vocês. Obrigada por esses quase 15 anos de amizade do qual eu tenho um orgulho eterno. Saibam que eu sou apaixonada por vocês, que a felicidade de vocês é a minha e nada disso tem sentido se vocês não estivessem sempre ao meu lado (mesmo que do outro lado do Oceano). Eu amo vocês e morro de saudades todos os dias.

Um agradecimento especial aos grandes responsáveis dessa conquista que são meus pais. Obrigada por me impulsionar a ser tudo o que eu gostaria de ser nessa vida. Por terem me dado todas as oportunidades que

vocês não tiveram, pelos conselhos, pela educação, pelos sacrifícios e pelo companheirismo. Se eu pude voar, é porque vocês me deram asas. Amo vocês, tudo o que eu faço é por vocês.

Agradeço também à minha alma gêmea, minha irmã Luhana de quem eu tenho muito orgulho. Obrigada por ser essa mulher forte, sensível e engraçada que me defende de tudo e de todos. Eu queria ter metade da sua sabedoria milenar. Você é a melhor parte de mim. Te amo vaquinha!

E por fim, parafraseando a pensadora contemporânea Larissa de Macedo Machado xD “hoje eu gostaria de agradecer à mim mesma por não ter desistido desse sonho”.



# **Table of contents**



<b>ACRONYMS AND ABBREVIATIONS .....</b>	<b>19</b>
<b>GENERAL INTRODUCTION .....</b>	<b>23</b>
<b><u>CHAPTER I. LITERATURE REVIEW .....</u></b>	<b><u>29</u></b>
<b>REVUE DE LA LITTÉRATURE ET CONTEXTE DES TRAVAUX DE RECHERCHE .....</b>	<b>31</b>
<b>1. NICKEL BASED SX SUPERALLOYS: SOLIDIFICATION METHODS, CHEMICAL COMPOSITION, AND METALLURGICAL DEFECTS .....</b>	<b>35</b>
1.1. Investment casting: High-rate-solidification (HRS) or Bridgman method, and Liquid melting cooling (LMC) method .....	36
1.2. Mechanism of shrinkage, influence of solidification variables on the dendrite arm spacings, and casting pore size .....	40
1.3. Chemical composition of nickel-based single crystalline superalloys .....	42
1.3.1. Chemical composition and microstructure of Ni-based superalloys .....	42
1.3.2. Chemical evolution .....	43
1.4. Topologically closed-packed phases .....	47
1.5. Additive manufacturing: future of solidification and refurbishment of SX turbine components? ...	47
1.5.1. CMSX-4 SX superalloy PBF-E processing .....	48
1.5.2. Dislocation density .....	50
1.5.3. CMSX-4 additive manufactured microstructure .....	51
<b>2. SOLUTION AND AGING HEAT TREATMENTS .....</b>	<b>52</b>
2.1. Microsegregation, chemical homogenization and dissolution of eutectics .....	52
2.2. Hot isostatic pressing treatment .....	55
2.2.1. HIPed pore's morphology .....	55
2.2.2. HIP treatment of AM Ni-based SX .....	57
<b>3. HIGH TEMPERATURE MECHANICAL PROPERTIES OF NI-BASED SUPERALLOYS AND THE IMPACT OF A BOND COAT .....</b>	<b>58</b>
3.1. Microstructure and mechanical behavior .....	58
3.1.1. Precipitates influence on tensile and creep properties .....	58
3.1.2. Fundamentals of high temperature deformation mechanisms .....	60
3.2. High temperature oxidation of Ni-based superalloys: bare substrate .....	62
3.3. Bond coat .....	64
3.3.1. Slurry aluminide bond coat .....	64
3.3.2. Aluminide BC elements diffusion, interdiffusion zone (IDZ), and second reaction zone (SRZ) .	65
<b>4. FATIGUE OF NICKEL-BASED SINGLE-CRYSTAL SUPERALLOYS AT HIGH TEMPERATURES .....</b>	<b>67</b>
4.1. Fatigue fundamentals .....	69
4.2. Internal or sub-surface crack initiation without the influence of oxidation .....	71
4.2.1. Fatigue at low frequencies .....	71
4.2.2. Fatigue at very high frequencies .....	73
4.2.3. Fatigue indicator parameter .....	79
4.3. Microstructure and its effect on the fatigue life .....	82
4.4. Surface crack initiation due to oxidation .....	86
4.5. Crack initiation in fatigue in coated specimens .....	92
4.5.1. Fatigue at low frequencies .....	92
4.5.2. Fatigue at (very) high frequencies .....	95

4.5.3. Summary .....	96
<b>5. SUMMARY AND OBJECTIVES.....</b>	<b>97</b>

**CHAPTER II. MATERIALS AND EXPERIMENTAL PROCEDURES..... 99**

**MATERIAUX ETUDIES ET LES PROCEDURES EXPERIMENTALES ..... 101**

<b>1. INTRODUCTION.....</b>	<b>105</b>
<b>2. SUPERALLOYS AND BOND COAT DETAILS .....</b>	<b>106</b>
2.1. Ni-based SX superalloys chemical composition, solidification, and microstructure details.....	106
2.2. Bond coat characteristics .....	117
2.3. Summary .....	120
<b>3. MECHANICAL TESTING PROCEDURES.....</b>	<b>121</b>
3.1. Ultrasonic fatigue bench .....	121
3.1.1. Induction heating system .....	121
3.1.2. Ultrasonic fatigue tests challenges.....	122
3.1.3. Experimental procedure.....	123
3.1.4. Neglected points .....	125
3.1.5. Summary.....	125
3.2. Instron 8562 .....	126
<b>4. CHARACTERIZATION METHODS.....</b>	<b>128</b>
4.1. Non-destructive characterization .....	128
4.1.1. Microscopy .....	128
4.2. Destructive characterizations .....	129
4.2.1. Longitudinal analysis.....	129
4.2.2. Microscopy .....	130
<b>5. MECHANICAL TESTS SUMMARY .....</b>	<b>131</b>

**CHAPTER III. VERY HIGH CYCLE FATIGUE DURABILITY OF UNCOATED SUBSTRATES 133**

**DUREE DE VIE EN FATIGUE GIGACYCLIQUE DE SUBSTRATS NON-REJETES..... 135**

<b>1. INTRODUCTION.....</b>	<b>137</b>
<b>2. CASTING PORE SIZE AND THE SOLIDIFICATION PROCESS IMPACT .....</b>	<b>138</b>
2.1. Bridgman processed Ni-based SX superalloys: pore's size effect .....	139
2.2. LMC processed Ni-based SX superalloy: cooling rate effect.....	144
2.3. Fatigue indicator parameter .....	147
2.4. Summary .....	150
<b>3. HIP TREATMENT AND COMPACTED CASTING PORES .....</b>	<b>150</b>
3.1. Impact of the HIP process on the VHCF life.....	151
3.2. VHCF endurance and crack initiation after HIP treatment.....	153
3.3. Compacted pores morphology .....	158
3.4. Solidification pores vs. compacted pores .....	162
3.5. Impact of incipient melting during the HIP treatment on VHCF life.....	164
3.6. Summary .....	168
<b>4. PBF-E PROCESSED NI-BASED SX SUPERALLOY: TOWARD DEFECT-FREE SINGLE-CRYSTALS? .....</b>	<b>168</b>
4.1. VHCF performance of PBF-E SX .....	169

4.2. Crack initiation from an internal site: AM/HIP/REC specimen .....	171
4.3. Summary .....	175
<b>5. PROCESSING DEFECTS: STRAY GRAINS .....</b>	<b>175</b>
5.1. Summary .....	180
<b>6. CRACK INITIATION FROM THE SURFACE .....</b>	<b>180</b>
6.1. VHCF endurance and surface crack initiation .....	181
6.2. Role of oxidation in VHCF and high temperatures .....	184
6.3. Surface damage mechanism.....	197
6.4. Summary .....	202
<b>7. CONCLUSIONS.....</b>	<b>203</b>
<b><u>CHAPTER IV. FATIGUE LIFE OF COATED NI-BASED SINGLE CRYSTAL SUPERALLOYS .....</u></b>	<b><u>205</u></b>
<b>DUREE DE VIE EN FATIGUE DE SUPERALLIAGES BASE-NI MONOCRISTALLINS REVETUS .....</b>	<b>207</b>
<b>1. INTRODUCTION.....</b>	<b>209</b>
<b>2. IMPACT OF THE BOND-COAT ON THE LCF DURABILITY .....</b>	<b>210</b>
2.1. Tensile strength of bond-coated specimens .....	210
2.2. Microstructure, polishing, and bond coat: which parameter primarily controls the LCF life? .....	215
2.3. Impact of a slurry-type bond coat on MAR-M200 +Hf SX LCF life.....	229
2.4. NiAl bond coat behavior at high temperatures .....	234
2.4.1. Bond coat deposition via the APVS method .....	234
2.4.2. Slurry-type bond coat.....	238
2.5. Damage mechanism and durability of NiAl bond coated samples in LCF at high temperatures...	241
2.6. Summary .....	242
<b>3. IMPACT OF THE BOND COAT IN VERY HIGH CYCLE FATIGUE.....</b>	<b>243</b>
3.1. VHCF endurance and crack initiation .....	244
3.2. Coating damage under VHCF conditions.....	247
3.3. Casting pore vs. recrystallized layer .....	252
3.4. Casting pore/IDZ interaction in VHCF .....	258
3.5. Summary.....	261
<b>4. CONCLUSIONS.....</b>	<b>262</b>
<b><u>CHAPTER V. ANALYSIS OF CRACK INITIATION MECHANISM TRANSITION FROM INTERNAL SITES TO THE SURFACE IN THE VERY HIGH CYCLE FATIGUE REGIME..</u></b>	<b><u>263</u></b>
<b>ANALYSE DE LA TRANSITION DE L'AMORÇAGE DES FISSURES DES SITES INTERNES VERS LA SURFACE EN REGIME DE FATIGUE GIGACYCLIQUE.....</b>	<b>265</b>
<b>GENERAL CONCLUSIONS AND FUTURE PROSPECTS .....</b>	<b>277</b>
<b>APPENDICES.....</b>	<b>283</b>
<b>REFERENCES.....</b>	<b>323</b>



## **Acronyms and abbreviations**



AG – Aging  
 AM – Additive Manufacturing  
 APB – Anti-Phase Boundary  
 APVS – Alumination en Phase Vapeur Snecma  
 BC – Bond Coat  
 BSE – Back-Scattered Electron  
 DS – Directionally Solidified  
 DZ – Dendrite Zone  
 EBSD – Electron Backscatter Diffraction  
 EDS – Energy Dispersive X-ray Spectrometry  
 FCC – Face Centered Cubic  
 FEG-SEM - Field Emission Gun Scanning Electron Microscope  
 FIP – Fatigue Indicator Parameter  
 GROD – Grain Reference Orientation Deviation  
 HAGB – High Angle Grain Boundary  
 HCF – High Cycle Fatigue  
 HIP – Hot Isostatic Pressing  
 HT – Heat Treatment  
 IDZ – Inter Diffusion zone  
 IM – Incipient Melting  
 IPF MAP – Inverse Pole Figure  
 IQ – Image Quality  
 IZ – Interdendrite Zone  
 KAM – Kernel Average Misorientation  
 LAGB – Low Angle Grain Boundary  
 LCF – Low Cycle Fatigue  
 LMC – Liquid Melting Cooling  
 N-rafts – Rafting normal to the loading axis  
 P-rafts – Rafting parallel to the loading axis  
 PDAS – Primary Dendrite Arm Spacing  
 PFZ – Precipitate Free Zones  
 RX – Recrystallization  
 S-EBM/PBF-E – Selective Electron Beam Melting  
 SDAS – Secondary Dendrite Arm Spacings  
 SEI – Secondary Electron Imaging  
 SEM – Scanning Electron Microscope  
 SFE – Stacking Fault Energy  
 SHT – Solution Heat Treatment  
 SRZ – Secondary Reaction Zone  
 SX – Single crystalline  
 TBC – Thermal Barrier Coating  
 TCP – Topologically Closed Packed phase  
 TGO – Thermally Grown Oxide  
 UTS – Ultimate Tensile Strength  
 VHCF – Very High Cycle Fatigue  
 YS – Yield Strength



# General introduction



Among the harshest environments that materials can withstand, the turbine section of an aircraft engine is one of the most severe. To provide aircraft propulsion and the efficiency of the gas turbine operations, specific mechanical properties are requested to cope with the combination of high temperature and high pressure/volume of gas passing from the combustion chamber to the external environment (McLean et al., 1995). Up to now, only superalloys can supply the mechanical properties and oxidation resistance required in these conditions. Indeed, the superalloys are defined to be capable of maintaining structural, surface, and property stability at elevated temperatures, under high stresses, and in severe environments (i. e., room temperature ductility, intermediate temperature strength, and fatigue resistance, coupled with good environmental properties such as resistance to oxidation and hot corrosion) (Boesch, 1989). Extending this definition, physical properties such as a density as low as possible and production characteristics such as fabricability or/and castability are equally important (Nicholson, 1976).

This class of material and its casting techniques improvements in the last 50 years have enabled superalloys to be used first as equiaxed castings in the 1940s, then as directionally solidified (DS) in the 1970s, and the single crystalline (SX) form in the 1980s (Harris et al., 1999). During the past years, nickel based SX cast alloys have been successfully used as blade and vanes material, especially in the hottest sections of gas turbines. Also, the improvement of superalloys chemistry, and the more efficient design for air cooling systems increased these components operational temperature (McLean et al., 1995). It results in reduced fuel consumption, reduced pollution, and lower operating costs.

**Figure 1** shows an example of a gas turbine and its sections' temperature/pressure details, and examples of high-pressure turbine blades and high-pressure turbine vanes are presented.

Components made of superalloys may experience small, localized plastic strain (i.e., low frequency cyclic loading), or vibrations and airflow between the stages of the turbine (i.e., very high frequency cyclic loading) (Pollock and Tin, 2008; Reed, 2006). Up to now, fatigue is responsible for most of the crack initiation events/failure cases of internally cooled blades of aero-engines (Zhang, 2016). Therefore, it is essential to investigate the fatigue properties of new generations of Ni-based superalloys. The very high cycle fatigue regime has a particular importance because it leads to a certifying criterion of airfoils according to airworthiness authorities (e.g., EASA and

FAA), as the loading by vibratory stresses turns out to be a matter of safety requirement of aero-engines (Cervellon et al., 2020b, 2018, 2017).

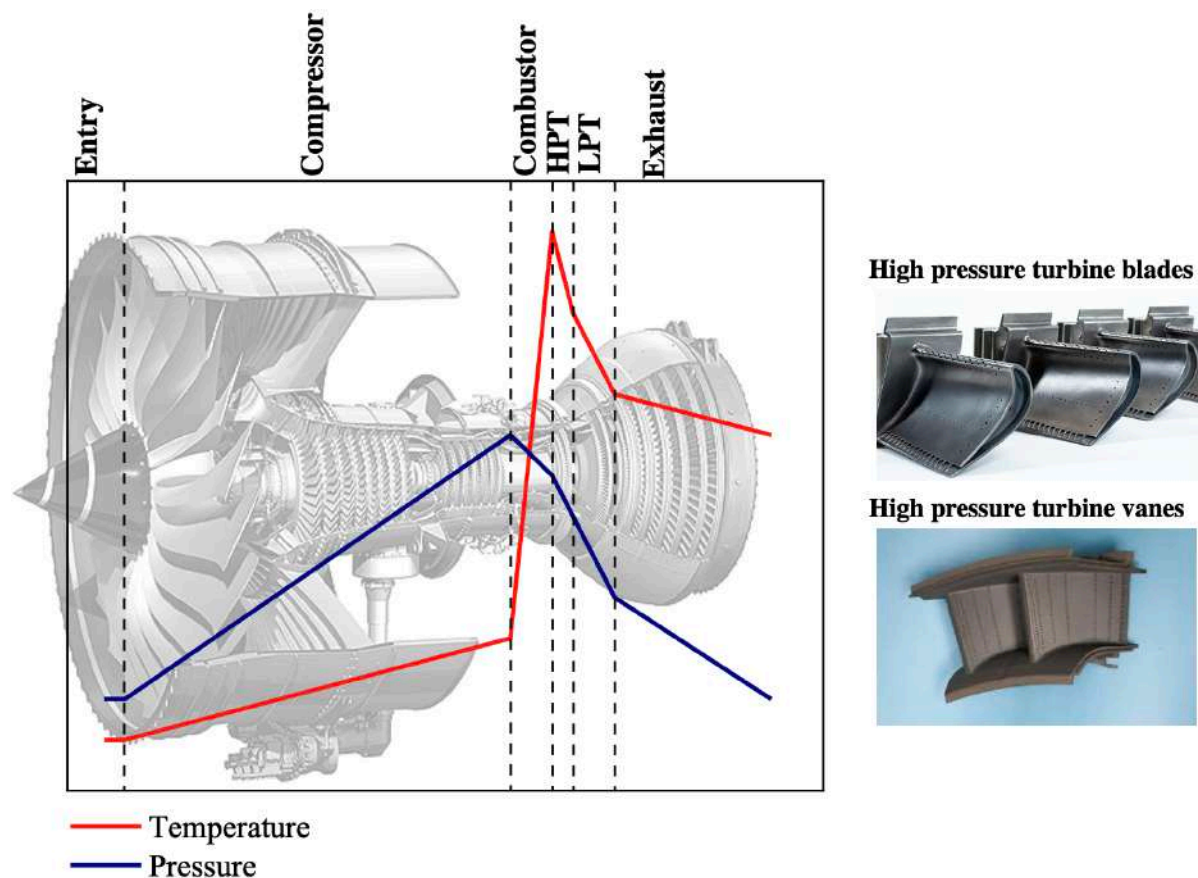


**Figure 1** Large civil aero-engine schematic illustration indicating the main turbine sections temperature and pressure variation. An example of high-pressure turbine blades and the high-pressure turbine vanes is detailed, adapted from (Darolia, 2018; Greatrix, 2012).

With the increase of the operating temperatures, the role of environmental degradation on the mechanical performance of an aero-engine component becomes substantial, mainly because the formation of oxides promotes early crack initiation that may (or may not) overcome the internal crack initiation mechanism and reduce the component lives (Coffin, 1974). Decreasing the amount (or suppressing) and size of internal casting defects to improve the component’s durability may be counterbalanced by a worse environmental resistance.

While modern cooling systems enable gas temperatures above the superalloy melting point, the development of bond coat (BC) and thermal barrier coatings (TBC) allowed an additional increase

in operational temperatures. The higher temperature demands in the last 10/15 years (Reed, 2006) exposes the superalloy/BC/TBC system to more severe conditions. Thus, repairing, recoating, and refurbishing gas turbine hot section components operating in service in highly severe conditions is essential to maintain airfoil structure integrity.

Due to the industrial request to increase the operational temperature and component's life, more complex solidification methods were developed to process the Ni-based SX airfoils avoiding or annihilating the casting pores. Moreover, new chemical compositions are constantly in development with the aim to improve the superalloy's properties to resist to oxidation. Finally, with the objective to faster turbine blades' refurbishment, adapted BC deposition methods are necessary. New questions are raised considering the impact of these new technological processes in the fatigue life of Ni-based SX superalloys, and consequently, fracture mode and the transition of the fatigue crack initiation from internal sites to the surface.

Several remaining questions from the literature will be discussed in this work. It is divided into five main sections:

**Chapter I** is a literature review on nickel based SX superalloys solidification methods, chemical composition, heat treatments, and casting defects. The first sections of this chapter summarize the state-of-the-art and newer studies about Ni-based SX superalloys and their main microstructure characteristics. Further, the last sections are dedicated to the mechanical properties of Ni-based SX superalloys at high temperatures, bare or coated substrate, with a particular focus on the role of oxidation on the fatigue properties. This last one is divided into low and very high frequencies.

**Chapter II** describes the investigated superalloys (chemical composition and specificities such as solidification methods), solution heat treatments and aging, HIP treatments (if any), and coating composition and deposition methods. Furthermore, a description of the mechanical tests and the microscopic observations is also performed.

**Chapter III** is dedicated to the influence of the solidification methods of Ni-based SX superalloys and the HIP treatment on the crack initiation transition from the internal features to the surface at very high frequencies (20kHz), fully reversed loading, and a temperature of 1,000 °C (i.e., in high temperatures VHCF regime).

**Chapter IV** is dedicated to the impact of a bond-coat on the fatigue crack initiation mechanisms at different frequencies (0.5 Hz and 20 kHz), stress-ratio (0.05 and -1, respectively), and high temperatures 900 °C/950 °C and 1,000 °C. The results presented in this sub-section are part of an industrial project named ECOREVE aiming to decrease the time and the costs of the turbine blades' refurbishment.

**Chapter V** is dedicated to a discussion on the crack's initiation conditions, elucidating the different parameters contributing to a crack initiation transition from internal sites to the surface in the VHCF regime. Moreover, the author discusses the fatigue limit and the external life-limiting factors.

Conclusions and (possible) future prospects are finally proposed.

# **Chapter I. Literature review**



# Revue de la littérature et contexte des travaux de recherche

Le premier chapitre de ce manuscrit de thèse est dédié à la revue de littérature des problématiques étudiées dans ce travail de thèse. Il sera divisé en 4 axes principaux qui sont essentiels pour une bonne compréhension de cette étude :

- Développements, chimie, procédés de solidification des monocristaux, microstructure et défauts dans les superalliages base nickel (Ni) monocristallins.
- Les traitements thermiques et le traitement de compaction isostatique à chaud (CIC).
- Mode d'endommagement des superalliages monocristallins base Ni à chaud (plus particulièrement le rôle d'oxydation).
- Mode d'endommagement en fatigue oligocyclique et gigacyclique à chaud des superalliages monocristallins base Ni.

Ce chapitre présente dans un premier temps le développement des superalliages base-nickel et les améliorations de ses techniques de fonderie au cours des dernières années, avec une attention particulière à la fabrication de superalliages monocristallins par fabrication additive. Ensuite il aborde la microstructure de ces superalliages à différentes échelles.

La chimie est un aspect mis en valeur par la suite, avec un bref descriptif des différentes compositions chimiques des générations successives des superalliages base Ni. La composition chimique des superalliages des différentes générations est présentée dans cette première partie parce que ce manuscrit évalue les propriétés en fatigue de onze superalliages différents de la première à la sixième (et dernière) génération.

Dans la présente étude, les pores de fonderie joueront un rôle critique dans les mécanismes d'endommagement des superalliages monocristallin base nickel, plus particulièrement en fatigue gigacyclique à chaud. Pour cela, ce chapitre détaille les études antérieures menées afin de comprendre les mécanismes d'amorçages à cœur.

En raison de l'augmentation de la température de fonctionnement des moteurs aéronautiques, le rôle de la dégradation liée à l'environnement dans les performances mécaniques d'un composant de moteur d'avion devient important. Ainsi, la diminution ou la suppression des défauts de

fonderie internes peut ne pas augmenter la durabilité du composant si les superalliages ne résistent pas à l'environnement sévère. Par conséquent, les propriétés mécaniques typiques des revêtements (plus particulièrement NiAl) en fatigue oligocyclique et gigacycliques sont présentées et positionnées par rapport aux études de l'endommagement des matériaux nus.

En raison des nouvelles demandes industrielles, les profils aérodynamiques superalliages base Ni monogranulaires exigent des méthodes de solidification de plus en plus complexes, des propriétés accrues de résistance à l'oxydation/corrosion à chaud et une composition chimique adaptée au dépôt des revêtements de liaison. Par conséquent, il est essentiel de clarifier les paramètres critiques qui conduisent à la rupture par fatigue dans des conditions sévères. Ainsi, les nombreuses questions restantes dans la littérature seront discutées plus en détail dans ce manuscrit.

La question principale guidant les résultats et la discussion du présent manuscrit est la transition d'amorçage de fissure du cœur vers la surface des superalliages base Ni monogranulaires sous chargement cyclique et haute température. Même si la principale conclusion de la revue de la littérature reste que le pore de fonderie est le principal site d'amorçage en fatigue des superalliages base Ni monogranulaires nus, l'amorçage de la fissure en surface semble être déclenchée dans des conditions spécifiques :

- Pour un même rapport de charge/une même amplitude de sollicitation, la température contrôle le site d'amorçage des fissures dans des conditions de basses et hautes fréquences. Plus la température est élevée, plus la contribution de l'oxydation est élevée, augmentant le risque d'amorçage en surface.
- Pour les échantillons revêtus, la température et l'interaction des propriétés mécaniques du système superalliage/revêtement déterminent le mécanisme d'amorçage et de propagation des fissures. Plus la température est élevée, moins l'influence du revêtement sur le comportement mécanique du substrat aux basses fréquences est élevée. De plus, la zone d'interdiffusion contrôlera la durée de vie en fatigue à hautes températures et hautes fréquences.

Ainsi, de nombreux paramètres comme la vitesse de solidification, le traitement thermique, le revêtement (chimie et procédé de dépôt), la température, le rapport de charge, l'amplitude du chargement, l'environnement et les fréquences impactent le passage de l'amorçage des défauts internes vers l'amorçage de fissure en surface. Étant donné que les propriétés de fatigue et le mécanisme d'amorçage des fissures des superalliages base Ni monogranulaires testés à basses

fréquences sont mieux connus qu'à très hautes fréquences à hautes températures, et que la caractérisation de la fatigue gigacyclique est essentielle à la conception des profils aérodynamiques, ce manuscrit est principalement centré sur les mécanismes d'amorçage des fissures de fatigue sous de très hautes fréquences.



## **1. Nickel based SX superalloys: Solidification methods, chemical composition, and metallurgical defects**

Cast Ni-based superalloys were first developed to respond to wrought alloys' lack of development potential (Nicholson, 1976). Thus, better creep and thermal fatigue resistance requirements led to new superalloys processing techniques (McLean et al., 1995). As a result, Ni-based SX superalloy produced by investment casting, resulting from a variant of the directional solidification (DS) process, are nowadays considered as "state-of-the-art" for advanced aerospace applications such as blades and vanes of the hottest sections (Reed, 2006).

Simultaneously to the evolution of solidification methods, cast superalloys' chemical composition has been continuously improved and refined. Regularly, the industry/laboratories have been creating new superalloys generation to supply the engineering needs of turbines in terms of maximum operating temperature and service life to increase power and reduce the specific consumption of gas turbines. The first Ni-based single crystalline (SX) superalloy developed in the 1970s was produced with the same chemical elements as the polycrystalline alloys. Progressively, refractory elements content of Tantalum (Ta), Tungsten (W), and Molybdenum (Mo) was increased, featuring the 1<sup>st</sup> generation of SX Ni-based superalloys. Subsequently, the introduction of Rhenium (Re) in the 1980s remodeled the market. It led to the development of the 2<sup>nd</sup> generation ( $\approx 3$  wt. pct. of Re), and then the 3<sup>rd</sup> generation ( $\approx 6$  wt. pct. of Re), increasing the temperature capability and the high-temperature  $\gamma/\gamma'$  stability (Caron, 2016, 2000; Donachie and Donachie, 2002).

The latest superalloys' chemical evolution (Kawagishi et al., 2012; Koizumi et al., 2004) aims to develop material with high oxidation resistance and excellent microstructure stability. Moreover, the superalloys' processes recent progress turns out toward the use of additive manufacturing (AM) technique to avoid solidification defects and to develop the complex geometrical design of components (Körner et al., 2018; Pistor and Körner, 2021; Reed, 2006; Shao et al., 2019; Tucho et al., 2017).

### 1.1. Investment casting: High-rate-solidification (HRS) or Bridgman method, and Liquid melting cooling (LMC) method

**Figure I-1a** shows a schematic illustration of a typical set-up of a Bridgman directional solidification process, by far the most widely used process to produce nickel-based superalloys SX components. It consists of a (top) hot zone and a (bottom) cold zone separated by a baffle, in addition to a chill plate on which the mold is located. The mold is dynamically moved downward into the cold zone by withdrawing the chill plate at a rigorously controlled velocity and, in most cases, at constant velocity (Kounitzky et al., 1991).

Among the investment casting challenges, the velocity of withdrawal turns out to be a very sensitive parameter, because it controls the cooling rate. Increasing the cooling rate decreases the tendency for grain defect formation, for example freckles, spurious grains, and low angle grain boundaries (LAGB) and is enhanced for components of larger size (Reed, 2006). Therefore, enhanced cooling methods like the liquid metal cooling (LMC) technique are desirable to limit the nucleation of such defects.

**Figure I-1b** depicts the LMC process. The cold zone is made of a low melting and low vapor pressure liquid metal (e.g., Sn). It is maintained at a temperature always much lower than the solidus temperature of the Ni-based superalloy. The ceramic mold filled with the superalloys is thus progressively immersed into the liquid metal (usually, a tin bath). Both heat flow through the liquid metal and baffle floating above it ensures a temperature gradient at the solidification front of 2 to 3 times higher than the standard Bridgman process in the 1,500 – 900 °C interval (Reed, 2006). On the one hand, the finer dendritic microstructure, and the influence on the non-metallic defects (i.e., smaller casting pores) are advantages of the LMC method over a classical Bridgman process. On the other hand, the interaction between the Ni-based superalloy and liquid metal could be an issue in case of mold cracking at the lowest temperatures at the end of the solidification process (Brundidge et al., 2012; Giamei and Tschinkel, 1976).

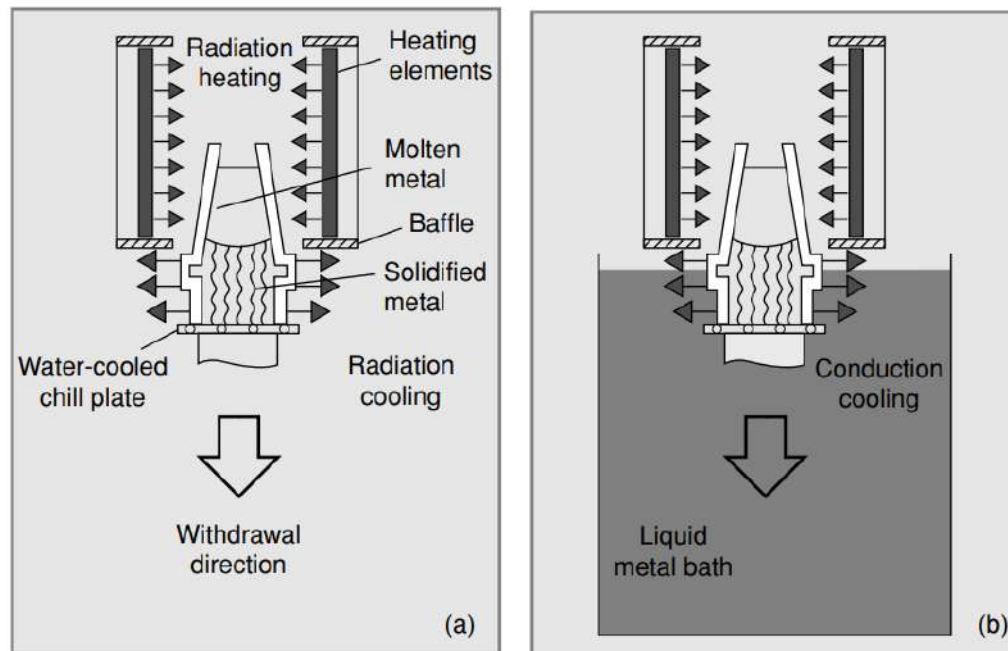


**Figure I-1** Schematic illustration of two directional solidification processes. Bridgman method (a). Liquid metal cooling method (b), (Reed, 2006).

The industry usually employs two different methods to achieve a single-crystalline form: (i) a “grain selector” placed at the very base of the wax mold. The grain selector is adapted to select only one grain that will enter the cavity of the casting and/or (ii) a seed is introduced at the casting basis and the solidification will occur with an orientation consistent with that of the seed (Reed, 2006).

SX casting solidification is dendritic (i.e., a complex three-dimensional structure morphologically influenced by the orientation of the grain) by nature. An example of a Cu-10Co (at. pct.) alloy casting dendrite is shown in **Figure I-2**. The cooling rate influences the primary and secondary dendrite arm spacing (PDAS and SDAS). It thus determines the dendrite and interdendrite zone (DZ and IZ) chemical homogenization, the orientation, the casting pore size, and the further heat treatments (HT) necessary to homogenize the superalloys microstructure. *The final microstructure and the superalloy mechanical properties depend entirely on the thermal conditions present during the casting and subsequent heat treatment operations* (Pollock and Tin, 2008; Rezaei et al., 2018).

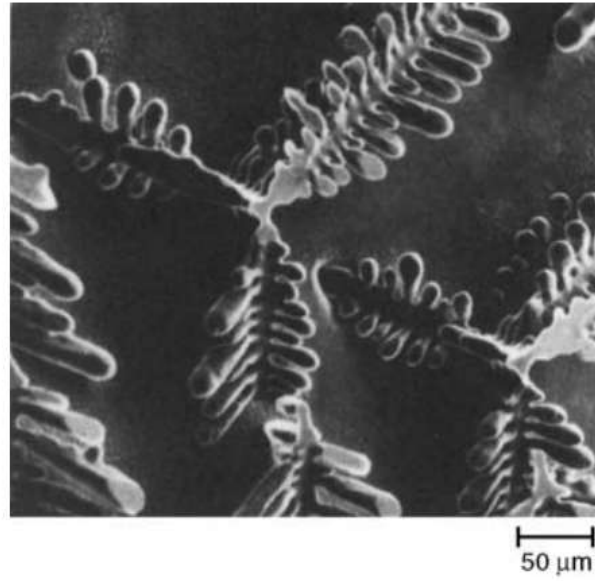


**Figure I-2** Secondary electron micrograph of Cu-10Co (at. pct.) alloy casting. Magnification:  $\times 150$ , (Boettinger W.J., 1974).

The preferred dendritic growth direction for nickel and its alloys, in common with all known face-centered cubic (FCC) alloys, is the [001] direction. To understand the influence of the crystallographic orientation on creep life performance, Mackay and Maier (Mackay and Maier, 1982) investigated the MAR-M247 SX superalloy creep properties at 760 °C and different orientations. Based on the results obtained, they have built a creep resistance map in the standard triangle of the stereographic projection, see **Figure I-3**. A primary misorientation of only 10 ° from the perfect [001] orientation was found to greatly affect the creep life at 760 °C/high applied stresses. Consequently, to avoid mechanical deterioration, the crystallographic orientation must be the [001] direction. This direction is closely aligned to the casting axis and main mechanical loading direction. *Hence, during this project, a primary misorientation of a maximum of 10 ° was accepted to perform fatigue tests and a maximum of 5 ° for creep and tensile tests.*

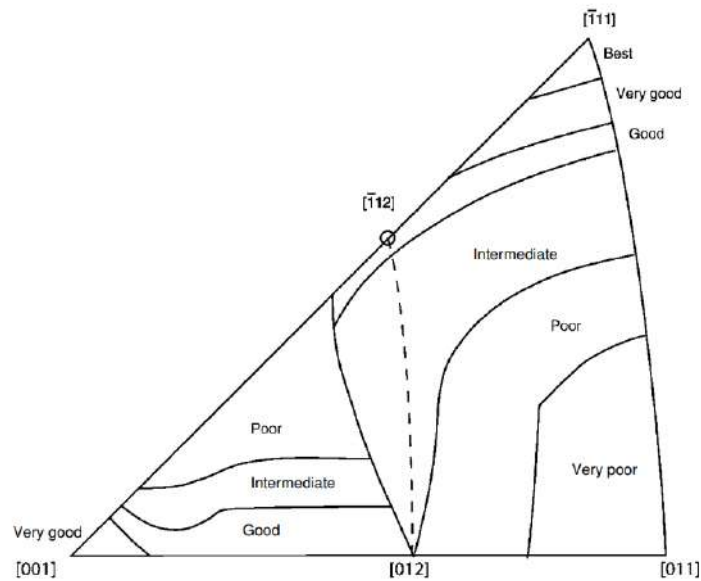


**Figure I-3** Variation of creep performance of Mar-M247 SX superalloy deformed at  $760\text{ }^{\circ}\text{C}/\sigma_o=689-724\text{ MPa}$ . Orientations near the  $[011]$  pole have the shortest rupture lives, while orientations near the  $[111]$  pole perform the best, (Mackay and Maier, 1982).

The casting process is also known to leave defects. As a result of the differences in volume contraction during solidification between dendritic and interdendritic spacings, the most common casting defects are the shrinkage pores, detailed in **sub-section 1.2** (Kurz and Fisher, 1986). The second most common defect is the globular  $\gamma/\gamma'$  eutectic precipitates formed in the IZ due to the microsegregation process. These last features will be detailed in **sub-section 2.1**. In addition, another possible defect is the formation of subgrains. High-angle grain boundary (HAGB, misorientation  $> 15^{\circ}$ ) and low-angle grain boundary (LAGB misorientation  $< 15^{\circ}$ ) arise when the grain selector fails to work correctly, and more than one grain survive to the growing competition. The HAGB is also a consequence of spurious grains nucleation around re-entrant features like the platforms and shrouds (Cormier and Gandin, 2021; Pettinari-Sturmel and Nazé, 2021; Reed, 2006; Siredey et al., 1993)

## 1.2. Mechanism of shrinkage, influence of solidification variables on the dendrite arm spacings, and casting pore size

The PDAS and SDAS are characteristics of the microstructural structure of cast superalloys (Whitesell et al., 1999). Among other features influenced by the solidification parameters, the pores are the most critical ones. Three groups of pores are defined in the literature. The first group includes casting/solidification pores (S-pores), corresponding to, shrinkage and gas porosity. The second group includes homogenization pores (H-pores). These pores form during technological operations (Bokstein et al., 2007; McCartney and Hunt, 1981). They are related to homogenizing treatments and the application of environmental protective coatings. The third is called deformation pores (D-pore). They form during high temperature slow creep straining due to the vacancies' condensation (Link et al., 2006; Utada et al., 2020). Below, the S-pores formation is described. *The H-pores will be presented in sub-section 2.1, and the D-pores will not be further detailed since proved to have no impact on the fatigue life previously* (Cervellon et al., 2017; Epishin et al., 2014).

The complex mechanism of shrinkage was discovered by Plancher et al. (Plancher et al., 2019) from the analysis of pore formation during the directional solidification of a Ni-based SX superalloy using a time-resolved synchrotron microtomography. They have visualized the evolution of dendritic structures, identifying two mechanisms leading to shrinkage pores formation. Both mechanisms are illustrated in **Figure I-4**.

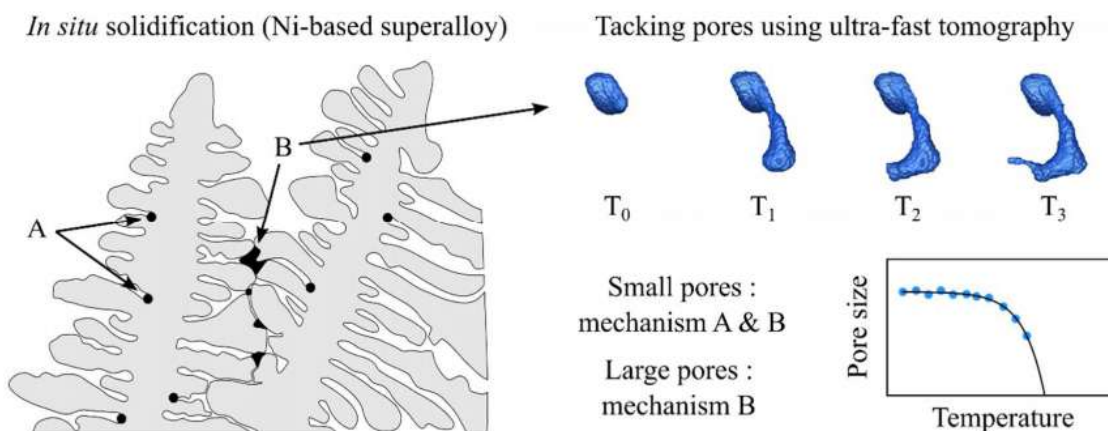


**Figure I-4** Illustrations of shrinkage solidification pore mechanism A, associated with the coalescence of secondary dendrite arms, and mechanism B, related to insufficient liquid feeding in the IZ during the last stages of solidification, adapted from (Plancher et al., 2019).

Following the pioneering work of Flood and Hunt (Flood and Hunt, 1987), these results show that the magnitude and direction of the thermal gradient and the solidification rate are the key parameters controlling the cast microstructure. The evolution of the PDAS and the SDAS of the Bridgman and LMC processed specimens has been investigated by Brundidge et al. (Brundidge et al., 2012). Some optical observations of the dendritic structures are shown in **Figure I-5**. The PDAS and SDAS values were reduced by approximately 50 - 60 pct., respectively, using LMC (compare **Figure I-5a** and **c, b**, and **d**). The LMC solidification method resulted in a reduction of 65 pct. in the maximum pore size while the pores volume fraction is hardly affected. As introduced above, the finer microstructure produced by faster withdrawal rates can lead to better mechanical properties (especially fatigue ones, further detailed in **sub-section 4.2**) and higher solidus and liquidus temperatures (Wilson et al., 2008).

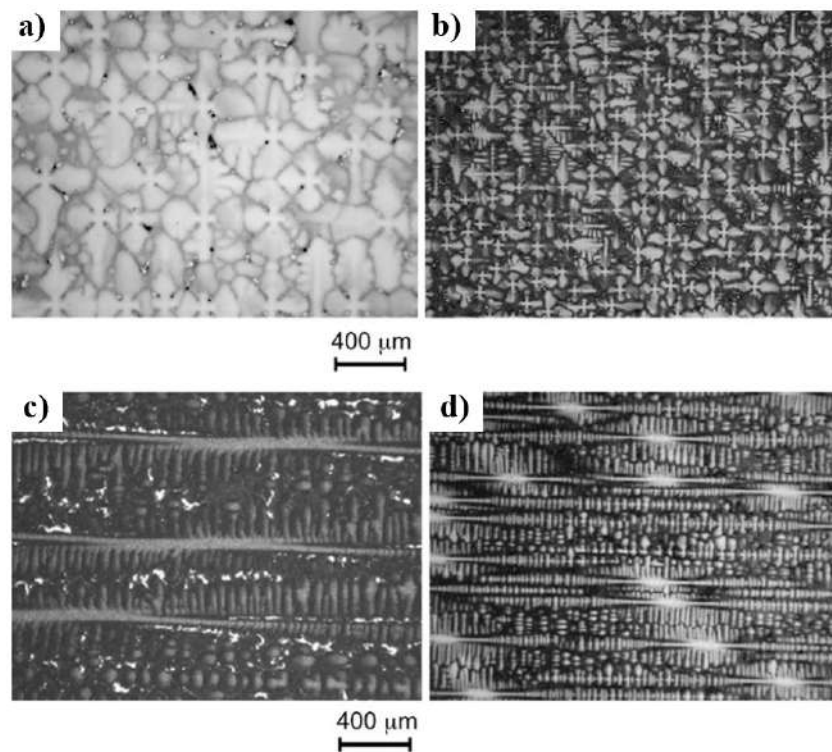


**Figure I-5** As-cast dendritic structures of Rene N5 alloy solidified by Bridgman process at 3.2 mm/min (a) and (c), and by LMC at 12.7 mm/min (b) and (d). Optical micrographs in (a) and (b) are shown normal to the [001] growth direction. (c) and (d) along [001] growth direction, adapted from (Brundidge et al., 2012).

### 1.3. Chemical composition of nickel-based single crystalline superalloys

In the opening of this chapter, a brief introduction of superalloys' chemical evolution was given. In this sub-section, a more detailed background will be presented.

#### 1.3.1. Chemical composition and microstructure of Ni-based superalloys

The Nickel-Aluminum (Ni-Al) system is an example of  $\gamma'$ -strengthened superalloys. As the aluminum level added to the austenite phase ( $\gamma$ ) increases, a second phase forms. This phase has a nominal composition of  $\text{Ni}_3\text{Al}$ , designated as the  $\gamma'$  phase, and has an ordered intermetallic  $\text{L1}_2$  crystal structure illustrated in **Figure I-6a** (Pollock and Tin, 2008).

While microstructurally simple, superalloys are chemically complex by nature (Pineau and Antolovich, 2009). In general, refractory alloying elements with large differences in an electronic structure and atomic radii compared to Ni, like Mo, W, Niobium (Nb), and Re, are added to provide higher solid solution strengthening of the  $\gamma$  phase and a lower stacking fault energy (SFE). Additions of Titanium (Ti), Ta, and Nb also contribute to the formation and strengthening of the  $\text{Ni}_3(\text{Al}, \text{Ti}, \text{Ta}, \text{Nb})$   $\gamma'$  phase (Durand-Charre, 1997; King, 1987; Sims et al., 1986). The  $\gamma'$  volume fraction is directly proportional to the amounts of these refractory elements in the superalloy (King, 1987). Besides, elements Al and Chromium (Cr) ensure oxidation and corrosion resistance, and ruthenium (Ru) ensures long-term alloy stability (Long et al., 2018).

$\gamma'$  precipitates exist as spherical particles with lattice misfit (i.e., differences in lattice constants of both phases,  $\gamma/\gamma'$ ) up to about 0 – 2.0 % or as cubes between 0.5 and 1.0 % in absolute value (Betteridge and Shaw, 1987; Geddes et al., 2010; Miracle, 1993).  $\gamma'$  cuboidal precipitates have their edges parallel to the (001) planes of the  $\gamma$  matrix, meaning that their edges are aligned with [001] directions of the SX. The DD22 superalloy as-cast microstructure (**Figure I-6b**) and after HTs (**Figure I-6c**) is shown hereafter (Long et al., 2018).

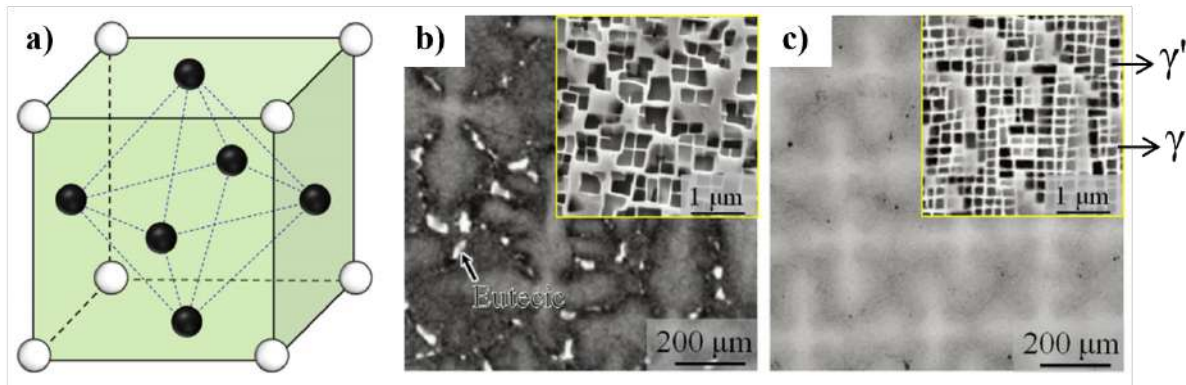


**Figure I-6** Schematic of the  $L1_2$  structure of the  $\gamma'$  phase, the white spheres exemplify the Ni atoms' position, and the black spheres exemplify the Al atoms' position (a). Microstructure of single crystalline DD22 superalloy in the as-cast showing an eutectic (see arrows) (b). DD22 superalloy's microstructure after full heat treatment sequence (c). The insets in (b) and (c) are the  $\gamma/\gamma'$  microstructure at higher magnifications, adapted from (Long et al., 2018).

### 1.3.2. Chemical evolution

Since the first Ni-based SX superalloy used for blades developed in the 1980s, (i.e., PWA 1480 (Milligan and Antolovich, 1987)), different chemical compositions were developed to improve the mechanical and chemical properties of this class of alloys. The SX Ni-based superalloys can be classified into six different generations, as illustrated in **Figure I-7** and **Table I-1**.

The so-called 1<sup>st</sup> generation SX superalloys such as PWA1480, CMSX-2 (Harris et al., 1984), AM1 (Davidson et al., 1983), and Rene N4 (Gabb et al., 1986) were developed in the early 1980s. They contain the same major elements, Cobalt (Co), Cr, Mo, W, Al, Ti, and Ta, as in the previous cast Ni-based superalloys, although with elements enhancing the formation of  $\gamma'$  precipitates.

The 2<sup>nd</sup> generation PWA1484 (Cetel and Duhl, 1988), CMSX-4 (Frasier et al., 1990), and Rene N5 (Wukusick and Buchakjian Jr., 1991), benefited from the addition of Re refractory element with a content of  $\approx 3$  wt. pct.. The Re content has been increased to about 6 wt. pct. for the 3<sup>rd</sup> generation SX superalloys CMSX-10 (Erickson, 1996), Rene N6 (W. S. Walston et al., 1996), (Perrut et al., 2018; Pollock and Tin, 2008; Reed, 2006), and TMS-75 (Wang et al., 2004).

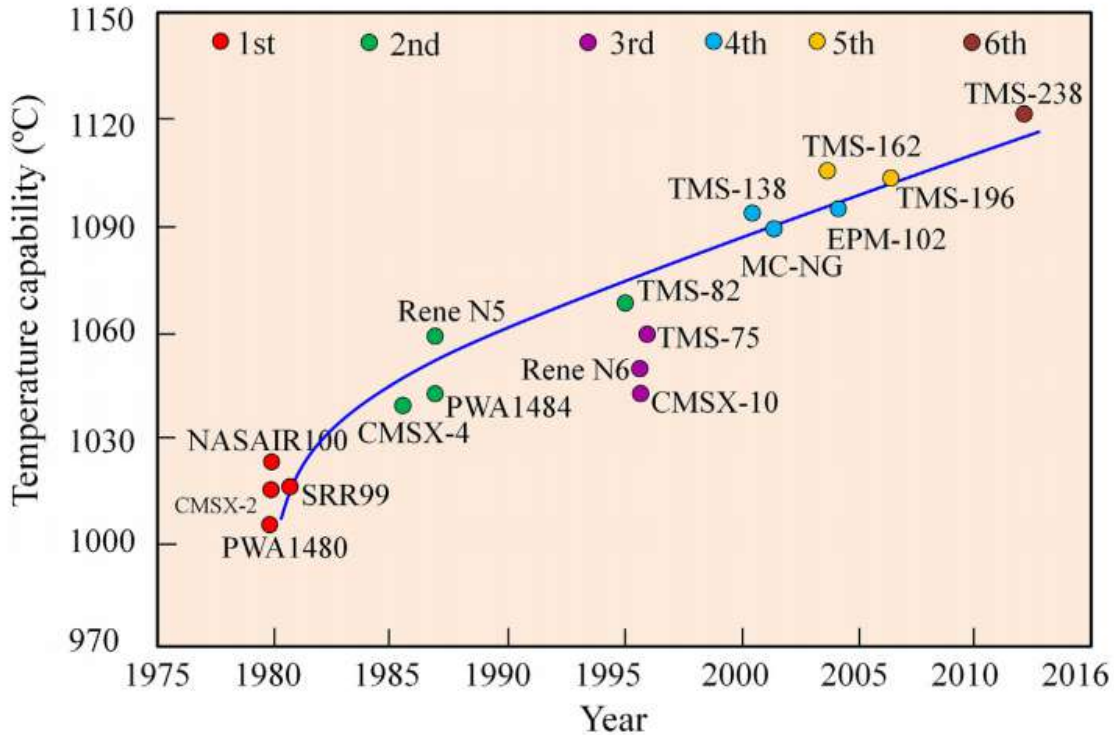


**Figure I-7** High temperature capability of some typical Ni-based single crystalline superalloys. The high temperature capability is evaluated by the highest temperature an alloy can withstand for 1,000 h of creep testing under a 137 MPa tensile stress without fracture, (Long et al., 2018; Reed, 2006).

Re acts as a very efficient solid solution strengthener of the  $\gamma$  matrix where this element is partitioning preferentially (Volek et al., 2005). As a low diffusion rate characterizes Re, it strongly reduces the kinetics of  $\gamma'$  precipitate coarsening at high temperatures, which is beneficial to the mechanical properties. The diffusion-controlled dislocation climb mechanisms active during creep at high temperature are also strongly slowed down due to Re addition, improving creep, and fatigue properties (Mottura et al., 2012). The main drawbacks of rhenium are its material costs, as it is a relatively rare and expensive element, and its density that directly affects the overall superalloy density (Perrut et al., 2018). The 2<sup>nd</sup> and 3<sup>rd</sup> generations are characterized by significantly lower concentrations of Cr and higher concentrations of Al. Concentrations of Ti and Mo are now at modest levels (Reed, 2006). The CMSX-4 Plus (Harris and Wahl, 2016) alloy was developed with a Re content between the one of 2<sup>nd</sup> and 3<sup>rd</sup> generations alloys.

The 4<sup>th</sup> generation, developed in the 2000s, is characterized by the addition of Ru and is represented by MC-NG (Caron, 2000), MX-4 (EPM-102) (Walston et al., 2004), PWA 1497 (Zitara et al., 2011), and TMS-138 (Zhang et al., 2002), (Perrut et al., 2018; Pollock and Tin, 2008; Reed, 2006). The addition of Ru was an alternative to the addition of Re. Alloys containing both elements are less prone to precipitation of topologically close-packed phases (TCP) (**sub-section 1.4**) (Matuszewski et al., 2015) and lighter than alloys from the 3<sup>rd</sup> generation.

The 5<sup>th</sup> and 6<sup>th</sup> generations consisted in the adjustment of the Re and Ru elements. The 5<sup>th</sup> generation TMS-196 (Sato et al., 2007) is based on the TMS-138A 4<sup>th</sup> generation superalloy composition with Ru and Cr adjustments. The 6<sup>th</sup> generation TMS-238 (Kawagishi et al., 2012) presents an excellent resistance against high-temperature creep, oxidation, and corrosion.

The evolution in chemical composition for future generations is to incorporate platinum (Pt) group materials (PGMs) as solid solution strengtheners. They are mainly employed to simplify a Ni-based superalloy coating process and directly influence the bond coat/substrate compatibility. However, it is known that the Pt element is not as much effective as Ta or Mo to strengthen the material at temperatures below 750 °C (Van Sluytman, 2010; Vattré et al., 2009). Therefore, the influence of the Pt element on the tensile or fatigue properties in Ni-based SX superalloys is not entirely understood.

TROPEA (Rame et al., 2020; Rame and Cormier, 2019) alloy has been investigated as a potential candidate alloy for future aeroengines airfoils. The specificity of this alloy is a remarkably high Ta content to increase the resistance to  $\gamma'$  shearing, a reduced Re content to preserve density, and 1.95 wt. pct. Pt. The main idea behind the development of this alloy was to increase the environmental resistance to have a low  $\gamma/\gamma'$  lattice misfit (in magnitude) by increasing the  $\gamma'$  lattice parameter. Moreover, to maximize the strength and the stability of the  $\gamma'$  phase by forming a (Ni, Pt)<sub>3</sub> (Al, Ti, Ta) L1<sub>2</sub> structure at very high temperature (Cormier, 2016; Rame et al., 2020; Rame and Cormier, 2019; Tin et al., 2007). TROPEA is an experimental superalloy that still presents impurities in its composition. *This work will present some tests performed using this superalloy under VHCF conditions and tensile and LCF tests are presented elsewhere* (Bortolucci Ormastroni et al., 2020b).

**Table I-1** Chemical composition (wt. pct.) of different nickel based SX superalloys from different generations. The balance to 100 % is Ni. D accounts for density.

<b>Gen.</b>	<b>Alloy</b>	<b>Co</b>	<b>Cr</b>	<b>Mo</b>	<b>W</b>	<b>Al</b>	<b>Ti</b>	<b>Ta</b>	<b>Hf</b>	<b>Re</b>	<b>Others</b>	<b>d (g/cm<sup>3</sup>)</b>
	<b>MAR-M200 + Hf</b>	9.5	8.6	11.8	4.9	1.9	1.6				0.6 Nb 0.1 C	8.62
	<b>AMI</b>	6.6	7.5	2.0	5.5	1.2	7.9	0.1				8.59
<b>1<sup>st</sup></b>	<b>PWA1480</b>	5.3	10.4	4.1	4.8	1.3	11.9				42 ppm C	8.70
	<b>CMSX-2</b>	4.6	8.0	0.6	8.0	5.6	1.0	6.0				8.60
	<b>Rene N4</b>	8.0	9.0	2.0	6.0	3.7	4.2	4.0			0.5 Nb	8.56
	<b>CMSX-4</b>	9.6	6.5	0.6	6.4	5.6	1.0	6.5	0.1	3.0		8.70
<b>2<sup>nd</sup></b>	<b>PWA1484</b>	10.0	5.0	2.0	6.0	5.6	9.0	0.1	0.1	3.0		8.95
	<b>Rene N5</b>	8.0	7.0	2.0	5.0	6.2	7.0	0.2	0.2	3.0		8.70
<b>2<sup>nd</sup>/3<sup>rd</sup></b>	<b>CMSX-4 Plus</b>	10.0	3.5	0.6	6.0	5.7	0.9	8.0	0.1	4.8		8.93
	<b>CMSX-10K</b>	3.0	2.0	0.4	5.0	5.7	0.2	8.0	0.03	6.0		9.05
<b>3<sup>rd</sup></b>	<b>Rene N6</b>	12.5	4.2	1.4	6.0	5.75	7.2	0.15	5.4		0.05 C 0.004 B	8.97
	<b>MC-NG</b>	<0.2	4.0	1.0	5.0	6.0	0.5	5.0	0.1	4.0	4.0 Ru	8.75
	<b>TMS-138A</b>	5.8	3.2	2.8	5.6	5.7	5.6	0.1	5.8		3.6 Ru	9.02
<b>5<sup>th</sup></b>	<b>TMS-196</b>	5.6	4.6	2.4	5.0	5.6	5.6	0.1	6.4		5.0 Ru	9.01
<b>6<sup>th</sup></b>	<b>TMS-238</b>	6.5	4.6	1.1	4.0	5.9	7.6	0.1	6.4		5.0 Ru	8.95
	<b>TROPEA</b>	8.9	6.4	0.6	6.1	5.4	1.0	9.1	0.08	1.0	1.95 Pt	8.83

#### **1.4. Topologically closed-packed phases**

The significant additions of refractory elements in newer generations of Ni-based superalloys resulted in the precipitation of TCP phases during exposure to high temperature and stress (Pessah et al., 1992; Simonetti and Caron, 1998). The typical TCP phases P (orthorhombic), R (rhombohedral),  $\mu$  (rhombohedral), and  $\sigma$  (tetragonal) have complex structures (Sinha, 1969), and complex chemistry, being composed of the elements of Ni, Cr, Mo, Co, W, and Re (creep strengtheners elements). In addition, the precipitation of TCPs at high temperatures is frequently associated with a more brittle fracture mode (Simonetti and Caron, 1998). These phases have been shown to reduce the creep life in case of excessive precipitation (le Graverend et al., 2012; Simonetti and Caron, 1998). Their precipitation is also assisted by local stresses (Meid et al., 2019b).

#### **1.5. Additive manufacturing: future of solidification and refurbishment of SX turbine components?**

Ni-based superalloys are typically produced using wrought, cast, and powder metallurgy processing technologies (Pollock and Tin, 2008; Reed, 2006). However, these techniques are limited with respect to the production of parts with very complex geometry or shapes. The additive manufacturing (AM) methods could offer a cost-effective solution. It enables the near-net-shaping of parts by a bottom-up, layer-by-layer fabrication strategy (Johnson et al., 2017). Further, the technique enables refurbishment of damaged components that experienced service conditions. Not only is remanufacturing financially rewarding, but also it is faster in maintenance (Anand Kumar et al., 2021).

Thanks to tight control of processing parameters, crack-free bulk single crystals of an SX Ni-based superalloy were processed by electron beam based powder bed fusion (PBF-E) without requiring a crystal selector or a seed (Körner et al., 2018; Lopez-Galilea et al., 2019).

*The following sub-sections will be focused on the technique used to manufacture the AM specimens further tested and analyzed in this work.*

### 1.5.1. CMSX-4 SX superalloy PBF-E processing

Ramsperger et al. (Ramsperger et al., 2016) fabricated CMSX-4 superalloy using PBF-E, namely selective electron beam melting (S-EBM) technique. First, they have atomized CMSX-4 bars provided by Cannon Muskegon, obtaining powder with a chemical composition within the specifications of the Cannon Muskegon Group. They have used powder with a particle size distribution in the 45 - 105  $\mu\text{m}$  range. Then, the powder was processed in an ARCAM A2 EBM system operating at 60 kV accelerating voltage in a controlled  $10^{-3}$  mbar helium atmosphere. They have used a target operating temperature above 950 °C as the base plate was pre-heated, and a constant layer thickness of 50  $\mu\text{m}$  was used (Ramsperger et al., 2016).

The S-EBM cycle can be divided into four steps: (i) a new powder layer is applied with a rake system; (ii) the powder is preheated and slightly sintered to increase mechanical stability and electrical conductivity of the layer. During the sintering process, a strong defocused electron beam scans the build area several times at remarkably high scan speed (up to 25,000 mm/s). The preheating parameters are chosen to keep the operating temperature above 950 °C and at a constant level. Preheating is crucial since superalloys like CMSX-4 are hard to sinter due to forming a stable  $\text{Al}_2\text{O}_3$  oxide layer at the particle surface. (iii) The powder is selectively melted using a focused electron beam that fuses the underlying material. The geometric data are given to the machine in a 2D layer information extracted from a 3D CAD model. (iv) The build platform is lowered, and the process cycle restarts again with the deposition of a new powder layer (Ramsperger et al., 2016).

The typical PDAS is in the range of 200 to 500  $\mu\text{m}$  for conventional Bridgman and LMC processes, depending on the withdrawal rate, the temperature gradient, and the size and geometry of casting samples (Brundidge et al., 2012). During S-EBM, remarkably high solidification velocities and temperature gradients are reached due to self-quenching. It results in 5-10 times smaller PDAS than after conventional solidification (**Figure I-8**). The smaller scale hence shortens the diffusion distances required for homogenization during HTs (Körner et al., 2018; Ramsperger et al., 2015; Rutttert et al., 2016).

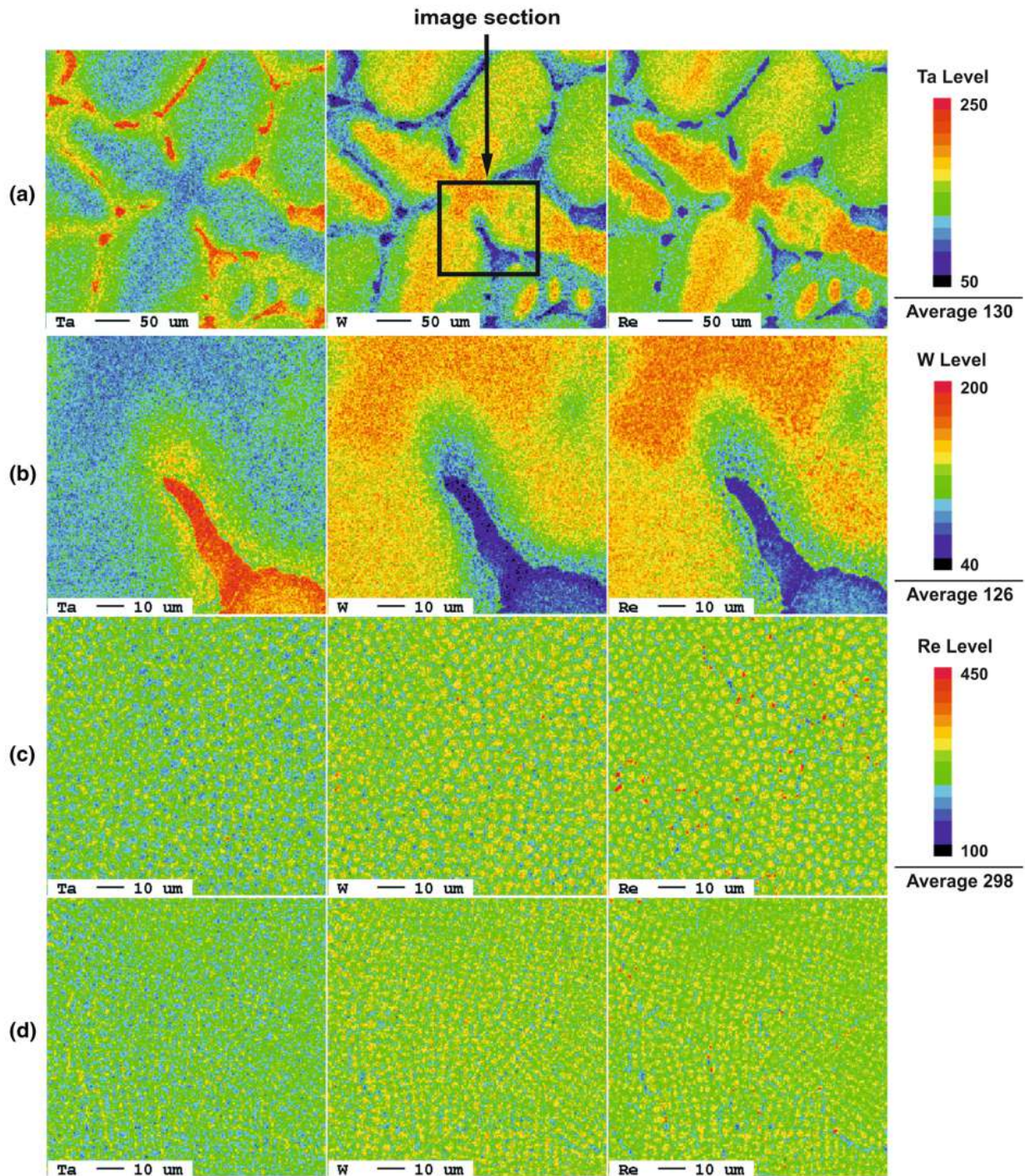


**Figure I-8** Qualitative microprobe mappings (normal to the built direction) of Ta, W, and Re. As-cast sample was analyzed with a spot size of  $2\ \mu\text{m}$  (a). Magnification of (a) in (b) with a spot size of  $0.5\ \mu\text{m}$ . S-EBM sample ( $P=510\ \text{W}$ ,  $v=600\ \text{mm/s}$ , line offset= $0.03\ \text{mm}$ ) and spot size of  $0.5\ \mu\text{m}$  (c). S-EBM sample ( $P=180\ \text{W}$ ,  $v=300\ \text{mm/s}$ , line offset= $0.1\ \text{mm}$ ) and spot size of  $0.5\ \mu\text{m}$  (d), (Ramsperger et al., 2016).

Further, the high homogeneity in the as-built state strongly influences the size distribution of the  $\gamma'$  precipitates and increases the solidus temperature ( $\approx 16$  °C). As a result, spherical pores corresponding to entrapped gas during the atomization process with a maximum diameter of  $\approx 5$   $\mu\text{m}$  are present in the superalloy. Further pores nucleate between secondary dendritic arms: the liquid can no longer reach the isolated channels to compensate the volume contraction with the liquid-to-solid transformation (like mechanism B in **sub-section 1.2**). Those pores are referred to as microshrinkage (Chauvet et al., 2018a). **Figure I-8** depicts the dendrite size and the chemical homogenization of CMSX-4 fabricated by PBF-E (Ramsperger et al., 2016).

### 1.5.2. Dislocation density

**Figure I-9** shows STEM micrographs taken with the beam direction close to [001] of a S-EBM processed CMSX-4. Dislocation segments of different microscopic crystallographic slip systems for an FCC crystal appear as small white lines in **Figure I-9a**. The micrograph shows localized areas of high dislocation densities that are associated to the formation of subgrains boundaries, which are located between dendrites (**Figure I-9b**). The misorientation between the subgrains is determined lower than  $3^\circ$  from the [001] direction. The high density of dislocations can lead to fatigue test issues, especially VHCF tests at high temperatures that are very sensitive to self-heating (Doudard et al., 2004; Favier et al., 2014, 2013; Plekhov et al., 2016; Zhao et al., 2020). ***In addition, from a technological point of view, this a high dislocation density indicates high internal stresses that may lead to earlier crack initiation.***

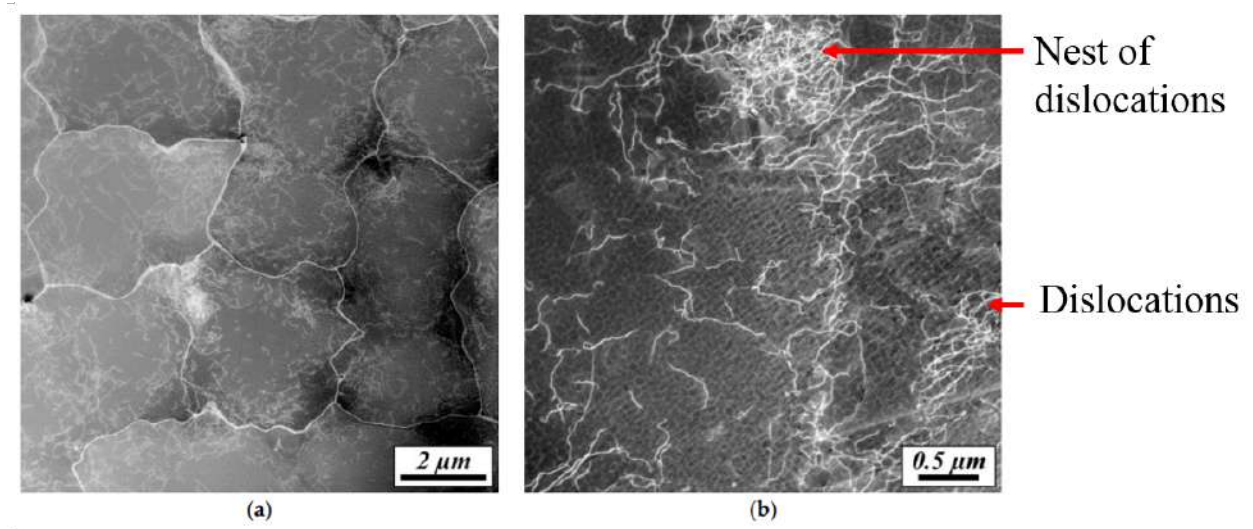


**Figure I-9** STEM-HAADF micrographs of the dislocation substructure in S-EBM CMSX-4 sample. Overall high dislocation density, subgrains boundary network, and ingrown nests of dislocations (a). Ingrown dislocation nest in an IZ at higher magnification (b), adapted from (Parsa et al., 2016).

### 1.5.3. CMSX-4 additive manufactured microstructure

The  $\gamma'$  particle size in the DZ is between 50 and 100 nm in the as-processed state (Parsa et al., 2016). The small particles do not exhibit the regular cuboidal shape (**Figure I-10a**), which characterizes larger  $\gamma'$  in conventional SX cast alloys (Fuchs, 2001). Even though, the  $\gamma'$  volume fraction is  $\approx 70\%$ . The partitioning behavior in the  $\gamma/\gamma'$  microstructure also follows the trends known from conventional SX cast materials (further detailed in **sub-section 2.1**). More specifically, Re partitions to the  $\gamma$  channels, and Al is enriched in the  $\gamma'$  phase (**Figure I-10b**) (Parsa et al., 2016).

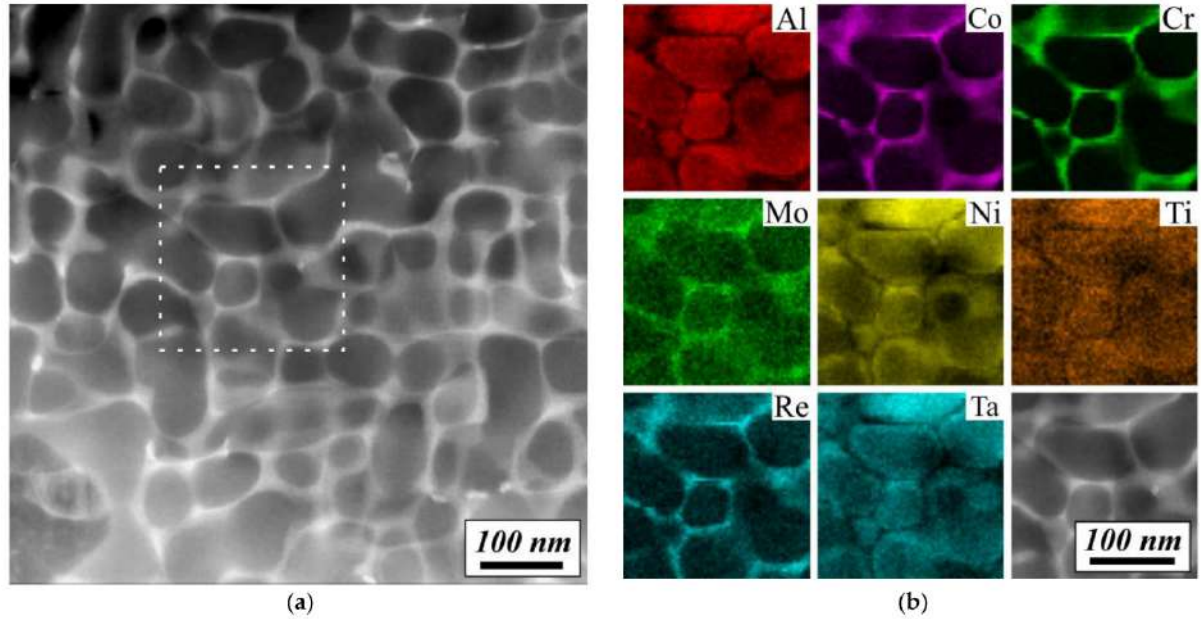


**Figure I-10** The  $\gamma/\gamma'$  microstructure of a CMSX-4 superalloy solidified by PBF-E method close to  $[001]$  direction (a). Corresponding element distribution maps (B), (Parsa et al., 2016).

## 2. Solution and aging heat treatments

### 2.1. Microsegregation, chemical homogenization and dissolution of eutectics

After the solidification, the dendritic morphology can be identified via the chemical segregation pattern inherited from processing. In cast Ni-based superalloys, eutectic  $\gamma/\gamma'$  nodules from solidification microsegregation are retrieved and may persist after the HT (Donachie and Donachie, 2002). They are identified as the off-equilibrium phase caused by elemental segregation, and its volume fraction decreases with the increase of the cooling rate during solidification (Seo et al., 2011).

**Figure I-11** shows the typical as-cast microstructures of CMSX-10 and CMSX-4 with the  $\gamma/\gamma'$  eutectic pools in the IZ. The presence of these  $\gamma/\gamma'$  eutectics pools decreases the superalloy ductility (Walston et al., 1991). Furthermore, the high dislocation density at  $\gamma/\gamma'$  eutectics and eutectic/matrix interfaces may promote recrystallized grains' nucleation (Wang et al., 2012).

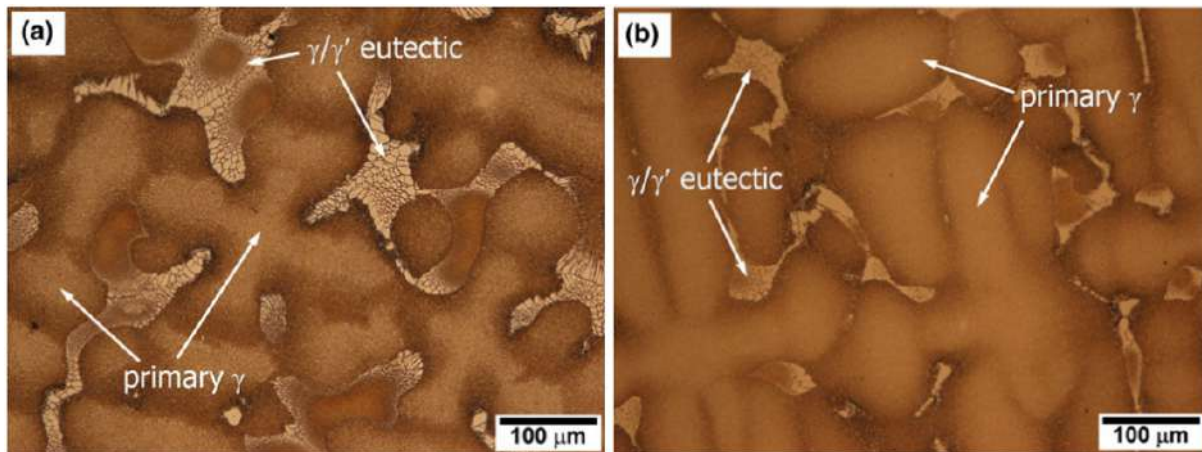


**Figure I-11** Typical as-cast microstructure of the alloy CMSX-10 (a) and CMSX-4 (b) solidified at about 10 °C/min, (Warnken et al., 2009).

Some of the components may be used in an as-cast state (e. g., vanes or shrouds) to reduce production costs and/or limit the development of defects during processing, such as recrystallization (RX) (Cormier and Gandin, 2021). However, components such as turbine blades have performances highly dependent to the microstructure at the precipitate scale. Consequently, the HT is a significant subject, relying on a high level of control and understanding of the primary solidification method (Pollock and Tin, 2008).

While the early alloys had relatively simple HT, the latest generations have a more complex HT due to the addition of the refractory elements. Traditionally, two heat treatments are used for Ni-based superalloys. First is the solution heat treatments (SHT), designed to homogenize the microstructure and reduce the effects of elemental segregation (Duhl, 1987). The second one is aging (AG), designed to develop a cuboidal  $\gamma/\gamma'$  microstructure and size uniformity of the  $\gamma'$  phase (Caron and Khan, 1983; Karunaratne et al., 2000; Wilson et al., 2003).

To overcome the microsegregation inherited from the solidification, SHTs were developed to achieve the best DZ/IZ homogenization, resulting in the dissolution of  $\gamma/\gamma'$  eutectic islands and further avoiding incipient melting (IM). The superalloy is first heated above the  $\gamma'$  solvus temperature and closest to the IM (or solidus) temperature to reduce the dendritic chemical inhomogeneity. Then, for practical cases it is held for the minimum time required to achieve the best chemical homogeneity (Duhl, 1987; Pettinari-Sturmel and Nazé, 2021; Reed, 2006),

The SHT is optimal when (i) most of the  $\gamma/\gamma'$  eutectics islands have been dissolved. Limiting or suppressing the  $\gamma/\gamma'$  eutectics islands is beneficial to the creep strength while the fraction of efficient  $\gamma'$  precipitates increases, (ii) the  $\gamma'$  size distribution is homogeneous across the dendrite structure. (Jackson et al., 1977). Heavy elements like Re, W, and Mo remain as a residual microsegregation impacting the  $\gamma'$  precipitate size in the DZ, with coarser precipitates and a higher volume of  $\gamma'$  precipitate within IZ as compared to DZ. This phenomenon degrades tensile and creep strengths of the alloy in a wide temperature range (Caron et al., 1988, 1986; Caron and Khan, 1983).

**Figure I-12** compares the microstructure of the CMSX-4 Plus superalloy in as-cast (**Figure I-12a**) and after two different HTs. The presence of remaining  $\gamma/\gamma'$  eutectics islands in **Figure I-12b** implies the non-complete homogenization of the system. **Figure I-12c** depicts a complete HT with no remaining  $\gamma/\gamma'$  eutectics.

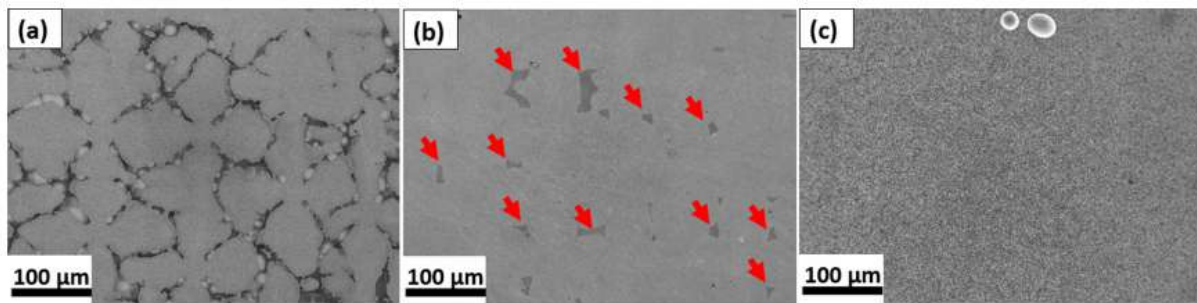


**Figure I-12** CMSX-4 Plus microstructures perpendicular to the  $[001]$  direction. The images were taken in the as-cast state (a). After a standard stepwise SHT 2 h/1,313 °C + 2 h/1,318 °C + 2 h/1,324 °C + 6 h/1,329 °C + 6 h/1,335 °C/AQ (b). After an SHT of 15 h/1,340 °C/AQ. The same AG treatments were applied in (b) and (c). The red arrows indicate the remaining  $\gamma/\gamma'$  eutectics islands, adapted from (Bortoluci Ormastroni et al., 2020a).

One of the consequences of SHT is the nucleation of H-pores in the IZ due to the imbalance of diffusing elements across the DZ (Link et al., 2006; Zhang et al., 2017). However, if the S-pores are critical to fatigue crack initiation, the H-pores do not have any noticeable impact on the mechanical properties (Epishin et al., 2014).

After the SHT, the AG treatments have the main purpose of adjusting the size and morphology of  $\gamma'$  precipitates to achieve a regular array of cubical precipitates having an average edge length of nearly 400 to 500 nm (Cormier and Gandin, 2021). In the literature, this microstructure is the most desirable to maximize creep, tensile, and fatigue properties of  $\approx [001]$  oriented components in a

large temperature range (i.e., from 700 °C up to 1,000 to 1,100 °C) whatever the alloy composition (Caron et al., 1988, 1986; Caron and Khan, 1983; Pollock and Tin, 2008; Reed, 2006; Steuer et al., 2014), by favoring a homogeneous plastic activity in the  $\gamma$  matrix (Pollock and Argon, 1992).

## 2.2. Hot isostatic pressing treatment

The casting pores can be suppressed by a hot isostatic pressing (HIP) technique. This technique was developed in the early 80s (Helle et al., 1985; Loh and Sia, 1992; Swinkels et al., 1983). It involves the simultaneous application of isostatic pressure and elevated temperature to a sample. Nowadays, Ni-based SX superalloys are HIPed at temperatures close to the solidus under remarkably high pressures, leading to a risk of recrystallization (RX) and incipient melting (IM). The employed pressure medium is an inert gas like argon (Ar) or nitrogen (N<sub>2</sub>) pressurized up to 200 MPa. *Therefore, the parameters of the industrial HIP (temperature, pressure, and duration) have to be carefully optimized at the conditions of complete pore annihilation, avoiding the RX, and minimization of processing costs* (Epishin et al., 2014).

### 2.2.1. HIPed pore's morphology

Two mechanisms of pore closure are discussed: (i) pore closure by plastic deformation and (ii) pore closure by a diffusional flow of vacancies emitted from the pore surface (Bokstein et al., 2007). Authors of the diffusion model (ii) give an explanation to the absence of RX during HIPing, which they expect to occur in the case of plastic pore closure. However, it was shown in the literature (Burgel et al., 2012) that while the high dislocation density (**Figure I-13a**) of cold pre-deformation is critical for RX at high temperature, the hot pre-deformation is less dangerous, and the dislocations annihilate dynamically (Epishin et al., 2013).

Epishin et al. (Epishin et al., 2014) investigated the pore closure phenomenon for the CMSX-4 superalloy. Indeed, they considered the pore “closure” by dislocation slip. **Figure I-13b** illustrates the pore obtained after the HIP treatment at 1,288 °C/103 MPa/0.5 h. **Figure I-13c** shows the distribution of the von Mises stress immediately after loading. At the pore's surface, the radial stress is equal to zero so that only compression in the tangential direction occurs. Due to the

anisotropy, the von Mises stresses are highly heterogeneous at the pore's surface. **Figure I-13d** shows the distribution of the plastic strains after 10 min. The pore has lost its sphericity, and corners with large localized plastic strains have formed (Epishin et al., 2013).

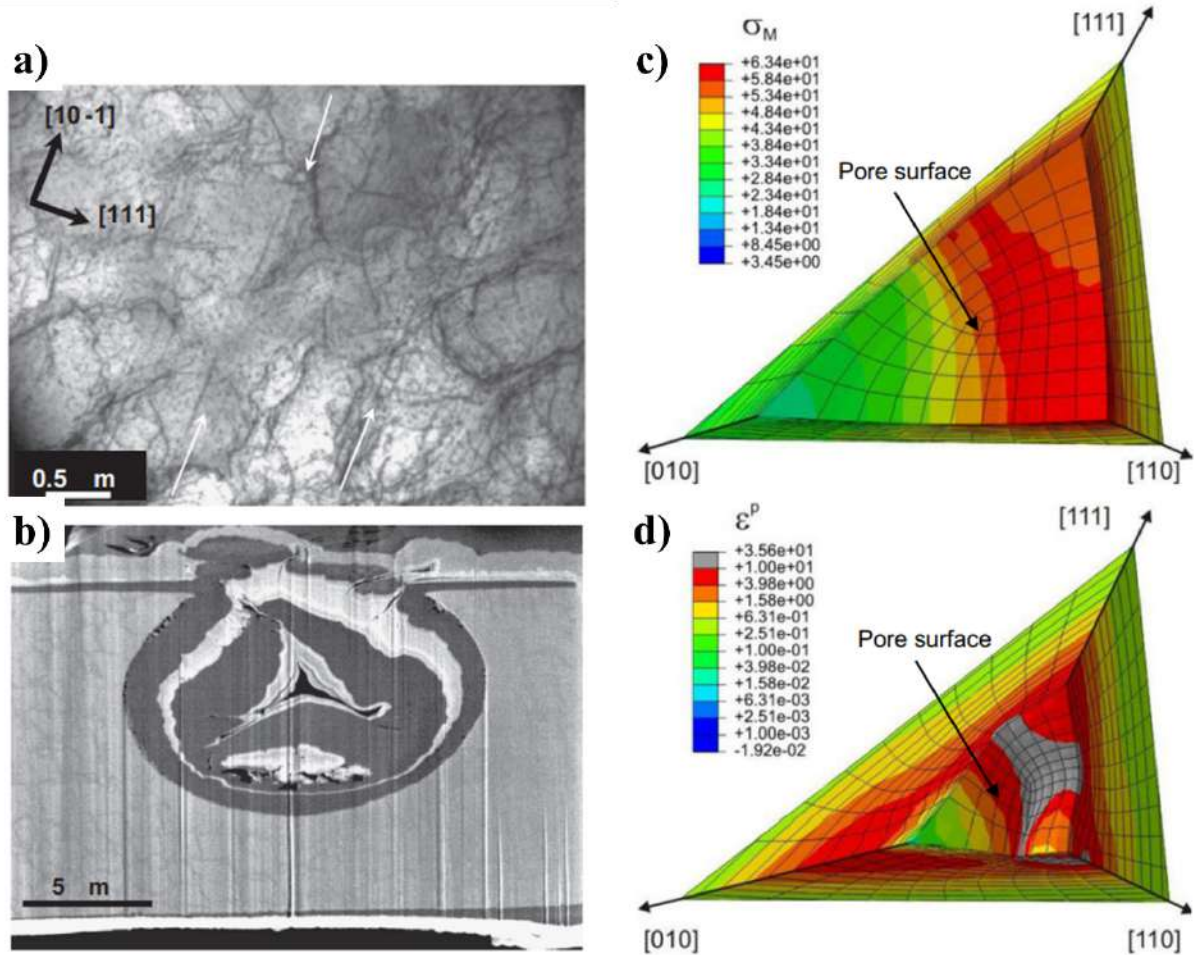


**Figure I-13** TEM image showing (111) slip planes in edge on the position marked by white arrows (a). Superalloy CMSX-4 after HIP at 1,288 °C/103 MPa/0.5 h. TEM foil cut by FIB. The pore is filled with Pt (b). Pore shape in superalloy CMSX-4 immediately after loading, distribution of von Mises stress is shown (c), and after 10 min holding at 1,288 °C at hydrostatic pressure of 103 MPa, equivalent plastic strain (d), adapted from (Epishin et al., 2013, 2014).

**Figure I-14** depicts the von Mises stress and plastic strain fields evolution obtained by finite element simulation around the irregularly shaped void during its closure. Void closure starts from the portion close to the sharp angle where the local von Mises stresses are high. Since the void shrinks gradually, the void-centered heterogeneous stress field shrinks, whereas the corresponding plastic strain field expands (Prasad et al., 2020). Prasad et al. (Prasad et al., 2020) compared three void

shapes. The most common, the irregular form (**Figure I-14**), presents the same asymmetric plastic strain pattern as seen by Epishin et al (Epishin et al., 2014).

The conditions to close a gas-filled pore depend on its diameter. The resistance offered by the trapped gas is negligible for larger pores (radius  $\geq 0.1 \mu\text{m}$ ) as the gas pressure does not reach exceedingly high values due to its shape. The smaller gas-filled pores have high gas pressures (orders of GPa) and offer significant resistance to further pore closure (Prasad et al., 2020).

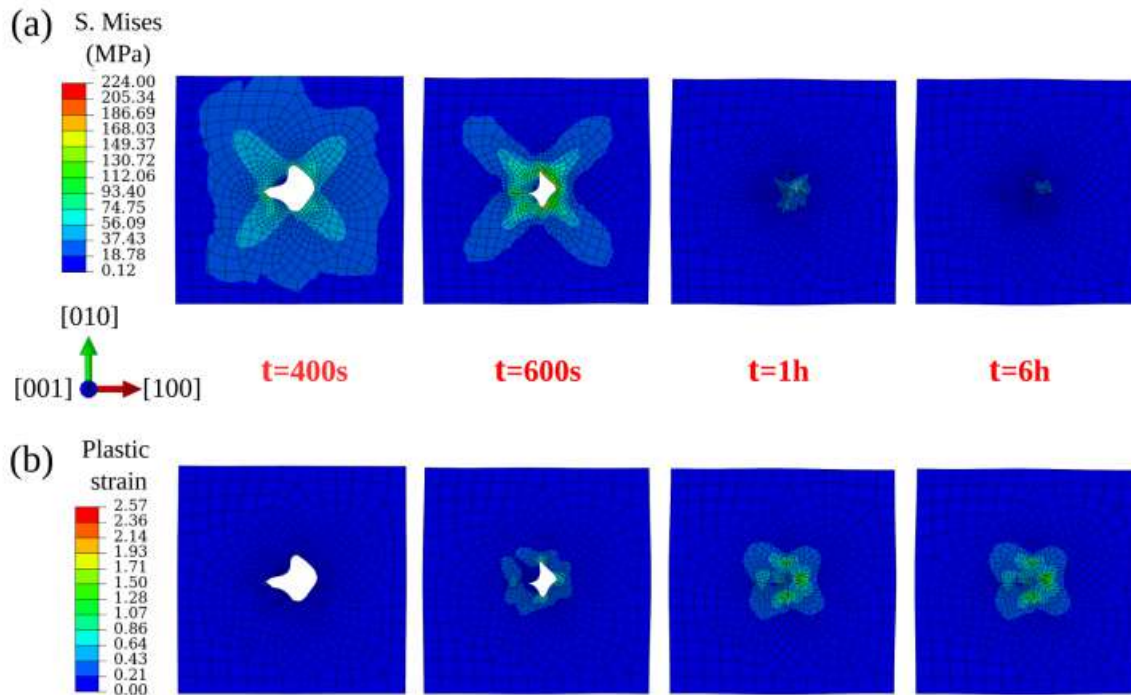


**Figure I-14** von Mises stress (a) and plastic strain (b) evolution around an irregular-shaped void (Quasi-2D) with increasing simulation time at 100 MPa isostatic pressure at 1,288 °C (Prasad et al., 2020).

### 2.2.2. HIP treatment of AM Ni-based SX

Rutttert et al. (Rutttert et al., 2016) investigated the HIP treatment strategies for S-EBM CMSX-4 SX superalloy. The fine dendritic microstructure obtained by S-EBM (**sub-section 1.5.1 and Figure I-8**) allows short holding times for the dissolution of primary  $\gamma'$  precipitates and eutectics. Further, the pore volume fraction of the AM superalloy is comparable to that of the cast material, whereas the pore size is significantly smaller and the pore density higher. A holding time of about 4 min at

1,315 °C and 100 MPa is sufficient to completely dissolve the primary  $\gamma'$  thanks to the shorter diffusion length resulting from the very fine dendritic structures. Thus, a short HIP heat treatment can reduce the porosity to less than 0.01 pct..

Indeed, the AM CMSX-4 superalloy SHT integrated with the HIP had to be above the  $\gamma'$ -solvus temperature. Resulting in unimodal  $\gamma'$  precipitates and a pore-free microstructure. Below the solvus-temperature,  $\gamma'$ -coarsening occurs, even after short holding times.

*Combining advanced processing routes (AM and HIP) makes it possible to create an almost defect-free microstructure with a high creep and fatigue strength potential. Materials processed by AM and treated by HIP are investigated in this work to understand failure mechanisms in very high cycle fatigue in the absence of (large) casting pores.*

### **3. High temperature mechanical properties of Ni-based superalloys and the impact of a bond coat**

For years, the improvement of high-temperature mechanical properties of the Ni-based superalloys was emphasized. Consequently time-dependent damage processes such as creep and environmental attack become important (Pineau and Antolovich, 2009). The desire for very long-time service has shifted emphasis toward improved oxidation and hot corrosion resistance. Despite the superalloys reaching a highly oxidation/corrosion resistance, the service temperature has also increased, and the coatings have been developed to protect superalloys from their environment. Nowadays, coatings are applied on “strong” base metals to form a “composite system” divided into superalloy, bond-coat (BC), the thermally grown oxide (TGO), and the ceramic topcoat (Lindblad, 1969; Perrut et al., 2018). Not only is the mechanical behavior of the substrate essential to be investigated, but also the entire system.

#### **3.1. Microstructure and mechanical behavior**

##### *3.1.1. Precipitates influence on tensile and creep properties*

Ni-based superalloys have relatively high yield and ultimate tensile strengths (YS and UTS), with YS often in the range of 900 - 1,300 MPa and UTS of about 1,200 - 1,600 MPa at room temperature

(Pollock and Tin, 2008). These attractive mechanical properties of Ni-based superalloys derive from the essential parameters determining superalloys strength as  $\gamma'$  particle size, interparticle spacing,  $\gamma'$  volume fraction (60 to 70 %), antiphase boundary (APB) hardening, coherency strain (due to lattice misfit), and the flow stress and modulus disparity between the  $\gamma/\gamma'$  precipitates. Most of these can be controlled by alloy chemistry and/or HT (Caron et al., 1988; Decker, 1974; Long et al., 2018; McLean et al., 1995).

For most Ni-base superalloys, the YS is constant from room temperature up to  $\approx 500$  °C, increasing up to  $\approx 700 - 800$  °C depending on the alloy's chemical composition (Reed, 2006). **Figure I-15a** shows the typical data for several single-crystal alloys tested along the [001] direction. For temperatures beyond 800 °C, the YS decreases quickly due to the progressive  $\gamma'$ -dissolution. Thus, at about 1,200 °C very low tensile resistance to plastic deformation is displayed.

Piearcey et al. (Piearcey et al., 1967) shed light on the role of the  $\gamma'$  phase in the high temperature deformation of the superalloys. They compared the evolution of the YS as a function of the temperature for the MAR-M200 alloy (60 % of  $\gamma'$ ) and the SX cube-oriented  $\text{Ni}_3\text{Al}$  (alloyed with a similar composition as the one of the  $\gamma'$ -phase of MAR-M200), see **Figure I-15b**. The strength of the  $\gamma'$  itself increases rapidly with increasing temperature up to about 700 °C, being the critical factor controlling the high temperature strength of  $\gamma/\gamma'$  superalloys, particularly for high  $\gamma'$  volume fraction alloys. The slight rise in the YS of the alloys at intermediate temperatures ( $\approx 850$  °C) is due to the unusual flow behavior of the  $\text{Ni}_3\text{Al}$   $\gamma'$  phase. The results confirm that at and beyond the peak stress, the behavior of the alloy is determined by the strength of the  $\gamma'$  phase. Moreover, the two-phase superalloys are much stronger than the matrix or precipitate in their bulk form (Pollock and Tin, 2008).

The  $\gamma'$  phase controls, as well, the creep resistance performance (Caron et al., 1986; Caron and Khan, 1983). In **Figure I-15c**, the YS CMSX-4 data is plotted along with the values of temperature. The hatched region indicates the conditions under which significant inelastic creep deformation is observed. These temperatures and stresses must be controlled if excessive creep deformation is not desired. Indeed, the creep deformation mechanisms in the [001]-oriented SX superalloy are very sensitive to acting temperature and stress (Reed, 2006).

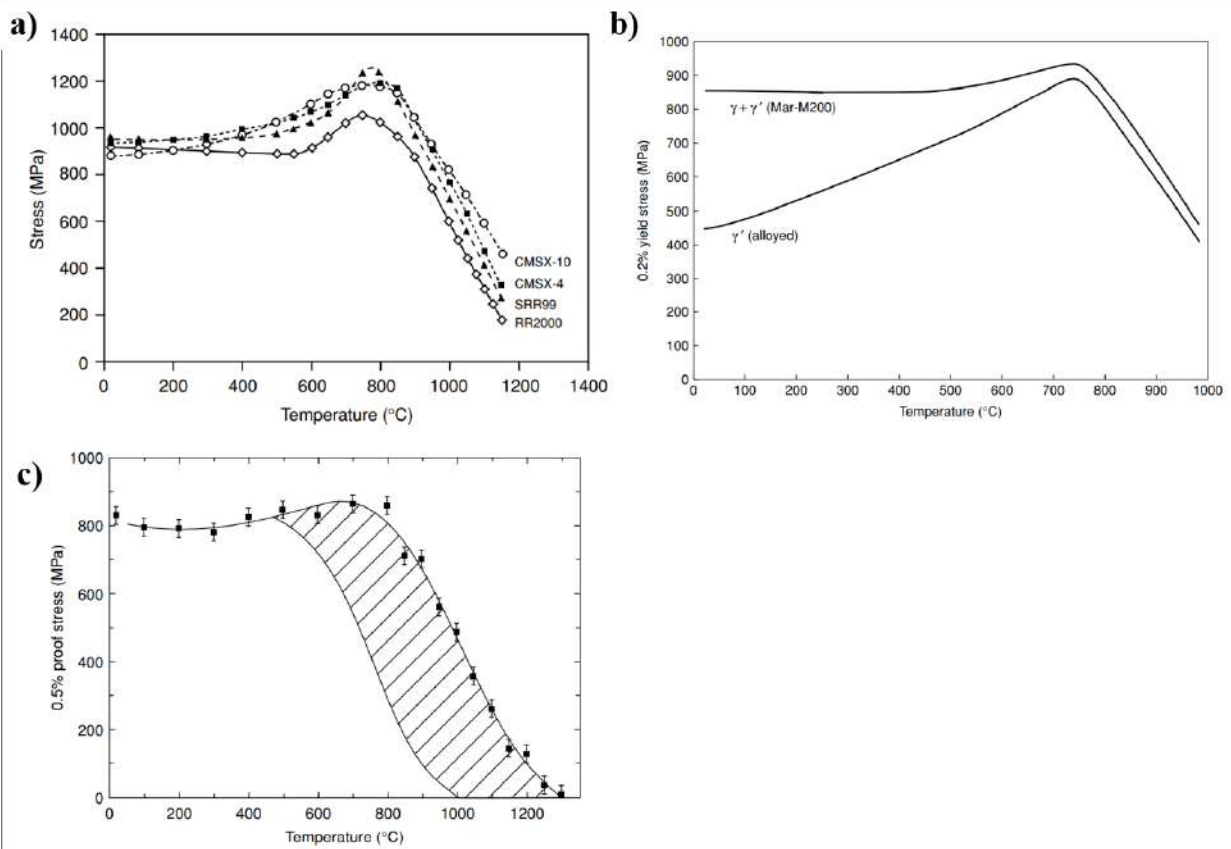


**Figure I-15** Variation of the yield stress of several single-crystal superalloys with temperature (a), variation with temperature of the yield strength of the MAR-M200 alloy in SX form, and a monolithic  $Ni_3Al$  alloy of composition equivalent to the  $\gamma'$  particles in MAR-M200 (b). Variation of the uniaxial 0.5 % yield stress of [001-oriented SX superalloy CMSX-4, showing (hatched region) the conditions under which significant inelastic creep deformation is observed (c). In all cases, the test was conducted along the [001] direction, adapted from (Pearcey et al., 1967; Reed, 2006).

### 3.1.2. Fundamentals of high temperature deformation mechanisms

In Ni-based superalloys, deformation at the microscopic scale is planar and discrete at low temperature ( $T \leq 750$  °C), taking the form of intense slip bands that vary in density and intensity depending on the interactions of dislocations (Betteridge and Shaw, 1987; Allan Harte et al., 2020; Reed, 2006). At high temperatures, thermally activated cross-slip leads to easier climb processes, and deformation becomes homogeneous, although slip is still predominantly planar, especially in superalloys with fine precipitates (Lerch et al., 1984; Shyam et al., 2002)

The precipitates have a very marked effect on the deformation behavior. In the very first stage of plastic deformation, the dislocations by-pass the precipitates (see **Figure I-16a**), influenced by the coherency hardening and the particle size distribution (Stoloff, 1972). Fine-ordered precipitates with low coherency strains lead to the localization of slip into a small number of intense slip bands from the beginning of deformation because of easy precipitate cutting and resultant slip band softening. Then the precipitates produce some fatigue hardening, which induces slip onto other planes and thus homogenizes the deformation, generally followed by fatigue softening as precipitate cutting starts (King, 1987).

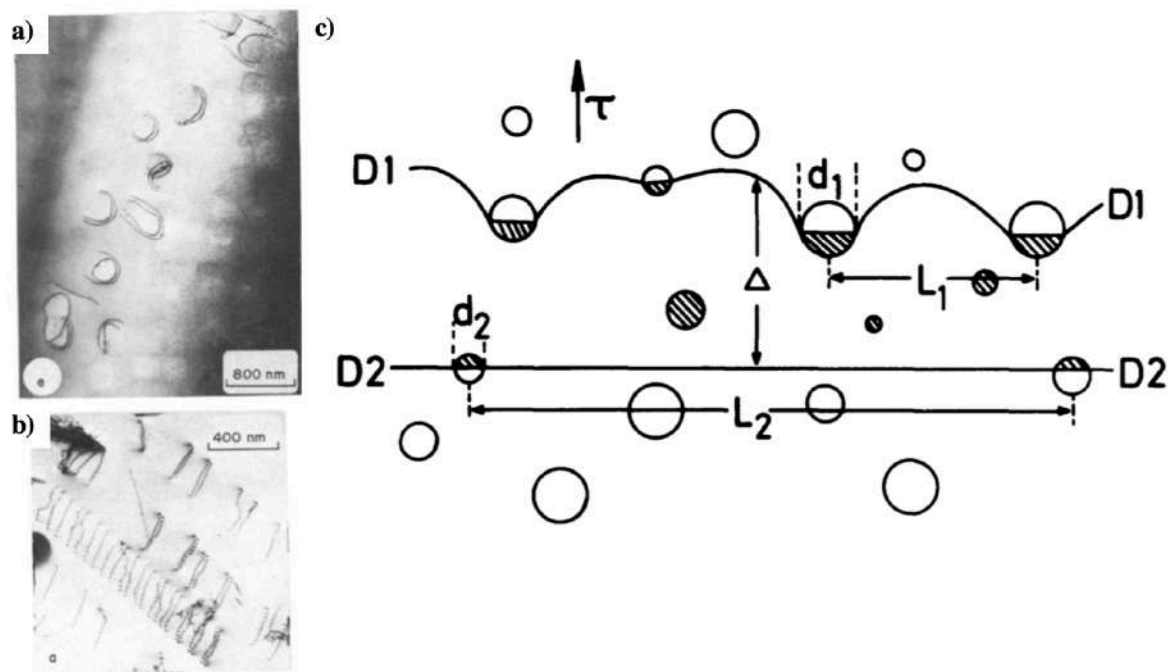


**Figure I-16** Bright-field TEM micrograph illustrating typical dislocation  $\gamma'$  particle interaction in Ni-based alloys. Orowan loops (a) and cutting (b), adapted from (Reppich et al., 1982). The paired dislocations D1 and D2 cutting the  $\gamma'$  precipitates in their common glide plane (c), adapted from (Nembach and Neite, 1985).

At high  $\gamma'$  volume fractions, where dislocations cannot bow between particles, or when  $\gamma/\gamma'$  lattice misfit is low, the particles are cut by dislocations. Cutting of the  $\gamma'$  particles by dislocations results in the production of an APB (hatched part at **Figure I-16c**) within the  $\gamma'$ , see **Figure I-16b** and **c**. Since it has positive energy associated, the pairing of dislocations results in the first dislocation introducing the APB and the second removing it. In addition to the low SFE of the matrix, this

dislocation pairing also encourages planar deformation by making cross-slip difficult. Cutting and dissolution of fine precipitates lead to softening on active slip planes, this deformation is not only planar but also very inhomogeneous in many alloys, producing very intense planar slip bands (King, 1987; Nembach and Neite, 1985; Reed, 2006).

### **3.2. High temperature oxidation of Ni-based superalloys: bare substrate**

For a practical design and application, it is essential to understand the superalloy oxidation kinetics and how it is influenced by alloy characteristics and exposure conditions (Smialek and Meier, 1987). Thus, several authors investigate the oxidation behavior of Ni-based SX superalloys in the literature. At temperatures over 900 °C, the superalloy exhibits a uniform scale consisting of several layers depending on the superalloy chemical composition. The 1<sup>st</sup> generation of Ni-based SX superalloys usually forms several layers: a NiO outer layer, the spinel-rich sublayer composed of a CrTaO<sub>4</sub>-rich layer, and an  $\alpha$ -Al<sub>2</sub>O<sub>3</sub> inner layer (Huang et al., 2006; Lindblad, 1969). Thermodynamically, an oxide will form on the surface of a metal when the oxygen potential in the environment is greater than the oxygen partial pressure in equilibrium with the oxide.

**Figure I-17** plots the standard Ellingham/Richardson diagram for the formation of oxides, including oxides typical for Ni-based superalloys, as a function of temperature. The diagram is used to obtain information about the partial pressure of oxygen required to form an oxide at temperatures between 0 and 2,400 °C (Khanna, 2012). The oxides shown at the bottom of the plot are difficult to form, while the easiest to form are shown on the upper part of the diagram. By analyzing the diagram, the  $\alpha$ -Al<sub>2</sub>O<sub>3</sub> is the slowest growing oxide at high temperatures, and it is known to form a dense, continuous, and adherent layer with excellent mechanical integrity.

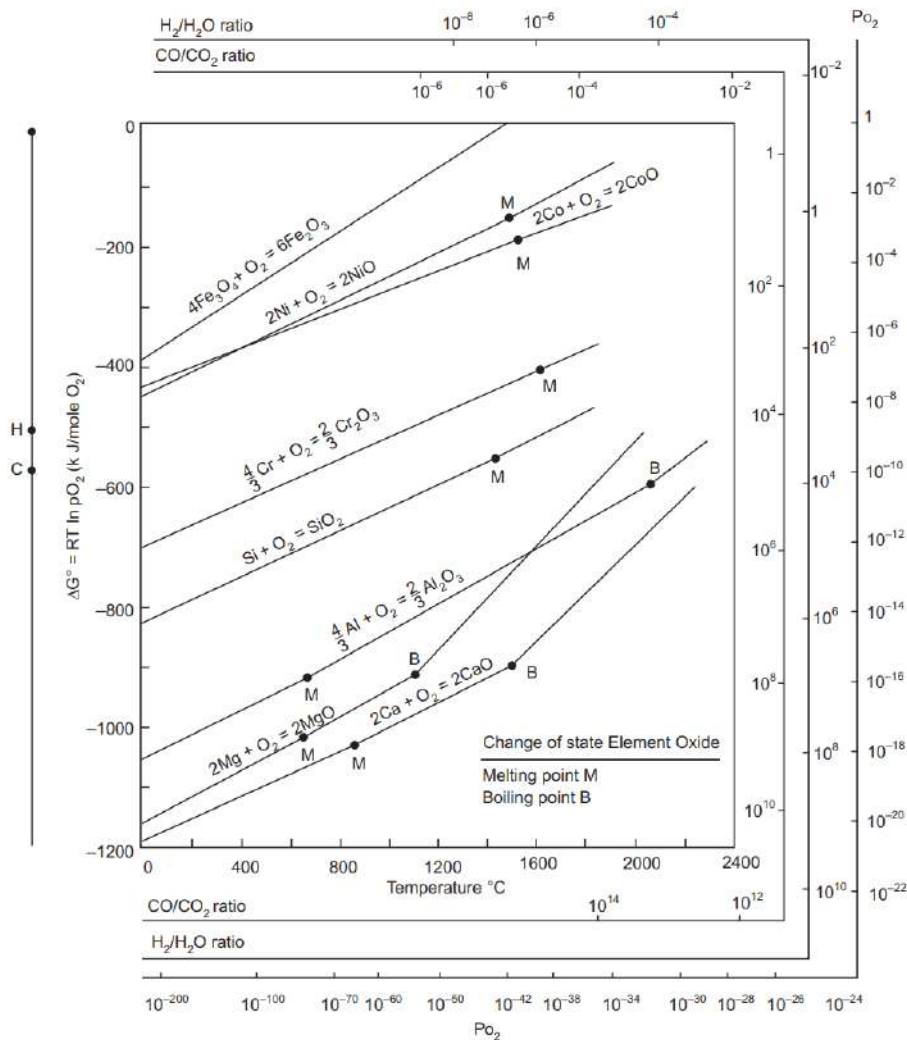


**Figure I-17** Ellingham diagram, showing the variation of free energy with temperature for various oxides, (Khanna, 2012).

During high temperature exposure of Ni-based superalloys, Al plays a critical role in the oxidation of  $\gamma'$ -strengthened superalloys. Ding et al. (Ding et al., 2015) observed the gradual transformation of the  $\gamma'$  phase into the  $\gamma$  phase, concluding that aluminum oxidation induced the  $\gamma'$  to  $\gamma$  phase transformation, resulting in aluminum depletion in the  $\gamma'$  phase and the formation of oxidation-resistant  $\alpha$ -aluminide (Smialek and Meier, 1987).

Recent studies have focused on the oxidation effect on the Ni-based SX superalloys microstructure. For example, Ding et al. (Ding et al., 2015) concluded that  $\{110\}$  planes are more difficult to be oxidized than  $\{100\}$  planes. The study carried out by Sato et al. (Sato et al., 2011)

observed the  $\text{Al}_2\text{O}_3$  scale difference between the DZ and IZ due to variations in local composition arising from residual microsegregation inherited from the casting process. **Figure I-18** is a micrograph of a Ni-based superalloy (5.0Co, 15.5Cr, 1.0Mo, 4.0W, 4.55Ta, 0.1Hf wt. pct. and Ni-bal) after the exposure at 1,000 °C indicating the DZ and the IZ oxides scale. Due to the Al partitioning preferences, the continuous  $\text{Al}_2\text{O}_3$  scale occurs preferentially at locations corresponding to the IZ. The  $\gamma'$  depletion is maximum in the DZ.

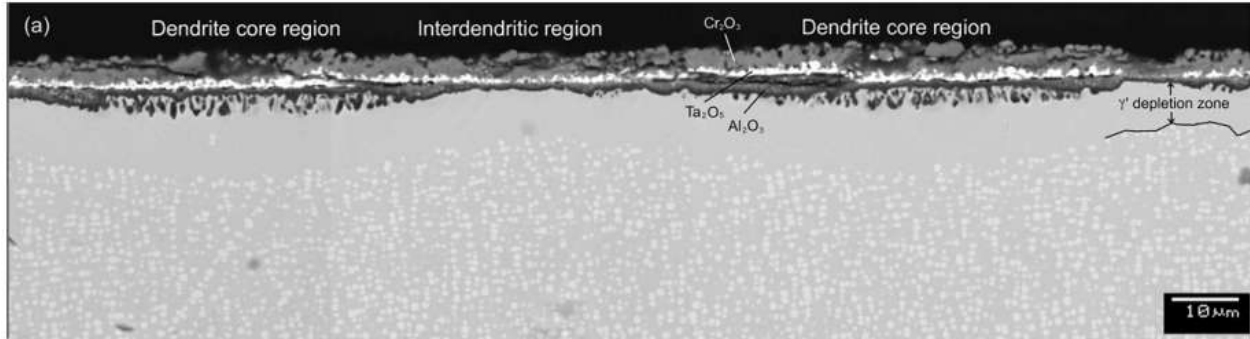


**Figure I-18** Micrographs of Ni-based superalloy with chemical composition (5.0Co, 15.5Cr, 1.0Mo, 4.0W, 4.55Ta, 0.1Hf wt. pct. and Ni-bal) after exposure at 1,000 °C during 100 h, adapted from (Sato et al., 2011).

### 3.3. Bond coat

The following sub-sections are dedicated to the aluminide bond coat and mechanical properties background. Special attention will be paid to the literature of the NiAl BC processing route developed by Pedraza and al. (Pedraza et al., 2012; Rannou et al., 2012) from the University of La Rochelle.

#### 3.3.1. Slurry aluminide bond coat

The so-called “slurry” coatings are produced by (i) applying aluminum or an aluminum alloy powder to the substrate surface by various methods like dipping, spraying, electrophoresis, and others. Indeed, the primary function is to provide a reservoir from which Al (or Cr) can diffuse to form a protective ( $\alpha\text{-Al}_2\text{O}_3$  and/or  $\text{Cr}_2\text{O}_3$ ) TGO layer (Pineau et al., 2016). (ii) The coating is subsequently formed by a diffusion treatment. (iii) Melting followed by solidification coincides with some inward diffusion of aluminum throughout the solid phases. Thus, the only particularity

of the “slurry” coating is the thin layer of slightly different microstructure at the outer surface of the slurry coating. This layer is the aluminum-nickel alloy solidification liquid (Goward and Boone, 1971).

The slurry-type Ni-Al BC investigated in this work was developed by Pedraza et al. (Pedraza et al., 2012) and the aging was investigated by Rannou et al. (Pedraza et al., 2012; Rannou et al., 2012) at LaSIE/University of La Rochelle-France. The slurry comprises Al microspheres mixed with water and polyvinyl alcohol (PVA), and it is deposited on the superalloy’s surface. The two-steps diffusion heat treatments in Ar (g) atmosphere finishes the formation of the composite layers.

The diffusion can be divided into four steps leading to the formation of aluminides and the subsequent growth of the aluminide layer: (i) After the aluminum powder melting, a network of molten aluminum forms within and between the particles, followed by (ii) the dissolution of nickel in the aluminum. Then, if enough Al is available, (iii) combustion synthesis between Ni and Al occurs. After this highly exothermic reaction, (iv) solid-state diffusion controls the subsequent formation of slurry coatings on the nickel substrate (Galetz et al., 2014).

### 3.3.2. *Aluminide BC elements diffusion, interdiffusion zone (IDZ), and second reaction zone (SRZ)*

The aluminide coating is divided into two main types of diffusion coatings formed on Ni-based superalloys: high-Al and low-Al activity. The inward diffusion of Al forms BC high-Al activity. The high Al activity causes the formation of the  $\delta(\text{Ni}_2\text{Al}_3)$  phase. Subsequent stabilizing HTs required for practical use of these types of BC cause some outward diffusion of Ni to form a three-zone  $\beta(\text{NiAl})$  coating (Goward and Boone, 1971).

The second type, BC of low-Al activity, is formed by outward diffusion of Al. Predominantly, the reaction between the outward diffusion of Ni with Al forms the  $\beta(\text{NiAl})$  phase. This process produces a two-zone  $\beta(\text{NiAl})$  coating: (i) the inner diffusion zone (consisting of  $\gamma$  phase in a  $\beta(\text{NiAl})$  matrix) is formed by outward diffusion of nickel from, and (ii) the resulting enrichment in Al in the substrate alloy (Goward and Boone, 1971).

The major issue for coated Ni-based SX superalloys is the chemical interaction between the superalloy substrate and the coating, occurring during the coating process and, later, in service at high temperatures. The interdiffusion phenomena can indeed lead to necessary chemical and microstructural modifications of both materials (Lindblad, 1969), forming specific layers:

**Interdiffusion zone (IDZ):** In coated 1<sup>st</sup> and 2<sup>nd</sup> generation, an interdiffusion layer modified the superalloy microstructure below the coating, creating a primary IDZ. This zone can contain precipitates rich in refractory elements, depending on the chemical composition of the superalloys and the coating. This primary IDZ is illustrated in **Figure I-19**.

**Secondary reaction zone (SRZ):** As discussed in **sub-section 1.3.2**, as the chemical composition of the 3<sup>rd</sup> and 4<sup>th</sup> Ni-based superalloys included more refractory elements (Liu et al., 2005), a deeper SRZ may develop in the alloy under the primary diffusion zone. An example for the MC-NG SX alloy protected by a NiAl(Pt) BC is shown in **Figure I-19** (Perrut et al., 2018).

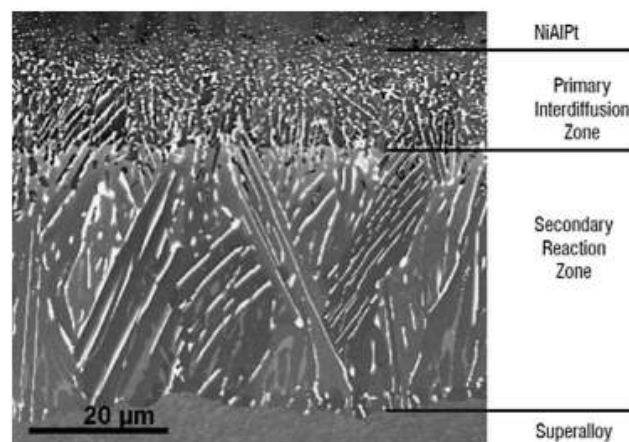


**Figure I-19** Microstructure of the diffusion zone in as-coated MC-NG SX (longitudinal section; observation in BSE mode) (Lavigne et al., 2004).

Depending on the coating characteristics and surface preparation, the SRZ can be continuous or occur in isolated cells. It is believed that the Al activity of the coating and the residual stress state at the surface play critical roles in determining the propensity of a specimen to form SRZ (W.S. Walston et al., 1996). Moreover, it was suggested that the SRZ layer could play a role as an effective “diffusion barrier,” inhibiting both outward and inward diffusion of Ni and Al elements during longtime exposures at high temperatures (Liu et al., 2005).

#### **4. Fatigue of Nickel-based single-crystal superalloys at high temperatures**

Turbine-engine components experience significant fluctuations in stress and temperature during their repeated take off/cruise/landing cycles (Pollock and Tin, 2008). Indeed, the abrupt changes in loading due to engine start-up and stops generate LCF damage. Thus, low cycle fatigue (LCF) is of interest to engine design. In the LCF domain, failure occurs typically within  $10^5$  cycles, with most of the fatigue life being spent in the propagation regime rather than in the crack initiation stage (Reed, 2006).

Likewise, engine vibrations and airflow between the stages of the turbine can result in high cycle fatigue and very high cycle fatigue (HCF/VHCF). It results in a rapid cycle accumulation in airfoils at much higher frequencies, in the kHz range (Pollock and Tin, 2008). For HCF, most of the fatigue life is spent in the initiation stage, and failure occurs at a lifetime higher than  $10^5$  cycles (Reed, 2006). The cycles can result in localized minor plastic strains.

Fatigue testing at high frequencies and high temperature are of great value not only because of reduced testing time to achieve a given number of cycles (Willertz, 1980). Moreover, the military and civil aircraft companies technical challenge is to reduce the turbine engine blade HCF failures, becoming an industrial subject of growing interest (Bhagi et al., 2013; Favier et al., 2013; Mazur et al., 2008; Morrissey and Golden, 2007). One of the technical challenges is that HCF/VHCF failure mainly results from a highly localized damage accumulation at a critical microstructure defect (pore, inclusion...), which is very difficult to monitor. Thus, probabilistic method approaches are required to identify the critical levels of prior microstructural damage (Ritchie et al., 1999).

The exact environment experienced by the turbine blades in service is also challenging to replicate precisely in the laboratory. Therefore, to be more representative than usual laboratory tests, Institut Pprime has developed a test bench capable of carrying out thermo-mechanical fatigue tests. The machine uses a burner to supply the hot gases having the advantage of low cost thermos-mechanical fatigue tests than a real engine test (Despres, 2021; Kromer, 2016; Kromer et al., 2019; Mattiello, 2018; Mauget et al., 2017, 2014, 2012). However, in this thesis, the characterization of fatigue performance at conditions that can be easily controlled, like the isothermal tests under uniaxial load, is still considered appropriate for evaluating the fundamental mechanical properties at extreme conditions.

Fundamental characterization of microstructural damage leading to fatigue/crack initiation under HCF/VHCF loading conditions was carried out for different alloys during the last 30 years. The researchers focus on defining the shape of the S-N curve with particular emphasis to the so-called “fatigue limit”. A typical fatigue life characterization is depicted in **Figure I-20** for most of the metallic materials. The presented graph is divided into four stages, according to the literature (Mughrabi, 2015; Nishijima and Kanazawa, 1999). The four stages can be characterized as:

- i. The finite fatigue life regime extends from the LCF to the HCF range → The fatal cracks are most commonly at the surface.
- ii. Conventional HCF fatigue limit.
- iii. Regime of finite VHCF life → The fatal cracks initiate most commonly at the bulk.
- iv. VHCF fatigue limit.

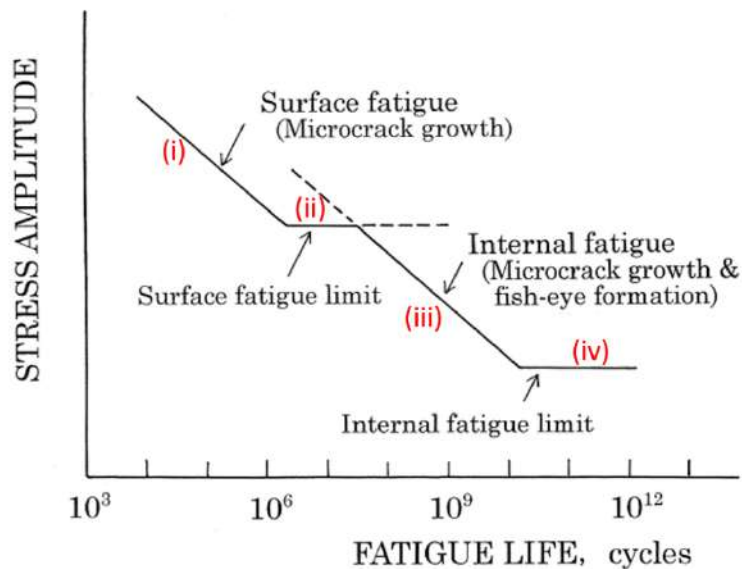


**Figure I-20** Schematic illustration of four-stages S-N curve, adapted from (Nishijima and Kanazawa, 1999).

One question that remains to be answered is the fatigue limit of defect-free Ni-based SX superalloys. The presence of a fatigue limit related to stage IV (**Figure I-20**) is still debated (Willertz, 1980). Some authors (Bathias and Paris, 2004) suggest a continuously decreasing stress-life

response and prefer introducing a fatigue strength associated with a given number of cycles rather than a fatigue limit. Others (Mughrabi, 2015) suggest the presence of a fatigue limit below the irreversibility threshold. The present work will try to answer, at least partially, this question at high temperatures for this class of alloys.

#### **4.1. Fatigue fundamentals**

LCF and HCF are distinguished by determining whether the dominant component of the strain imposed during cycling loading is elastic (HCF) or plastic (LCF), which in turn depends on the properties of the material and the magnitude of the stress (Bhagi et al., 2013). An illustration of the cyclic loading effect of both domains on the material is illustrated in **Figure I-21**.

Among different forms of cyclic plastic deformation, ratcheting has the highest detrimental effect on fatigue life, as the damage accumulates progressively during cycling and is responsible to severely deteriorate the performance of a component due to the cumulative effect of directional progressive plastic strain accumulation and fatigue damage (Paul, 2019). Three possible types of ratcheting behavior exist for the material. These are (i) decreasing ratcheting strain rate: leading to elastic/plastic shakedown where no additional ratcheting strain accumulation is noticed. This type of response usually is visible in severely cyclic hardened materials. However, elastic shakedown causes HCF, and plastic shakedown results in LCF in the material after initial ratcheting. (ii) Constant ratcheting strain rate: leading to a continuous accumulation of ratcheting strain. In this process, the material fails by fatigue crack initiation and propagation. Finally, (iii) increasing ratcheting strain rate: leads to a significant accumulation of ratcheting strain, which causes plastic instability and necking (Hübel, 1996; Paul, 2019).

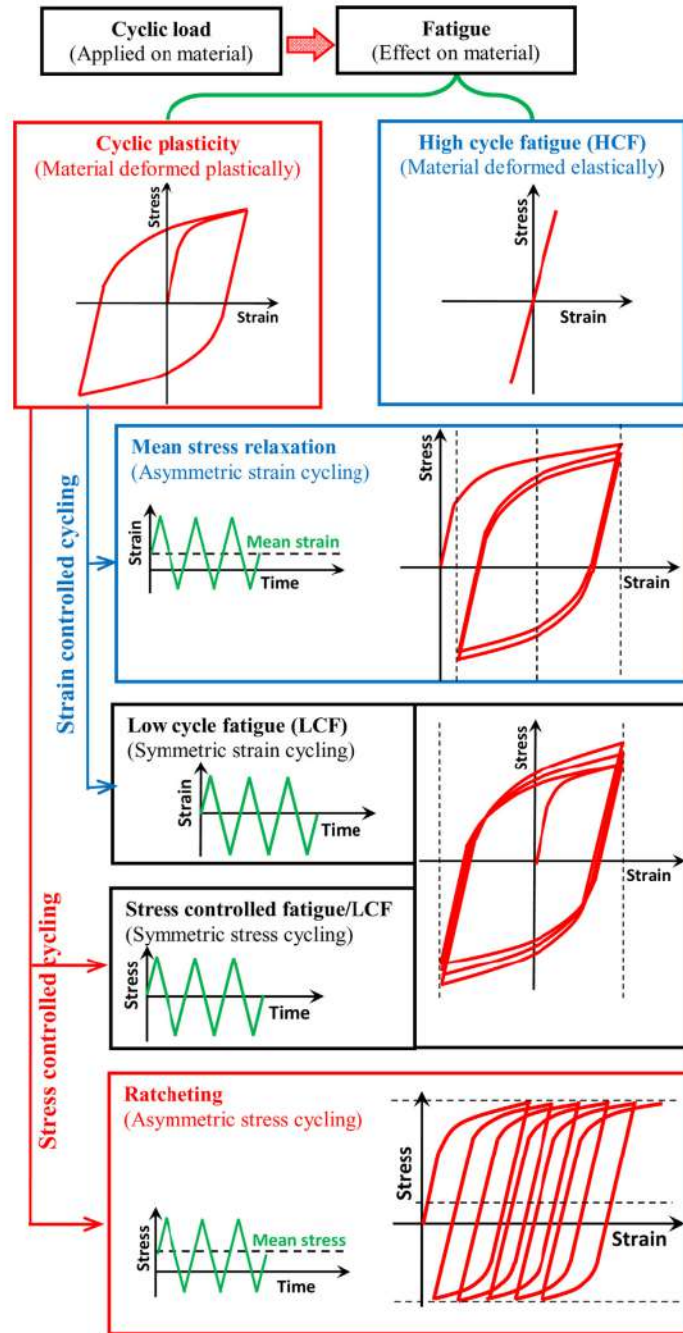


*Figure I-21 Different types of cyclic loading and corresponding material response (Paul, 2019).*

*During this project, two different fatigue frequencies range were chosen. A low frequency (0.5 Hz) and stress-controlled ( $R_o = 0.05$ ) with asymmetric stress cycling, and a very high frequency (20 kHz), fully reversed loading ( $R_\epsilon = -1$ ) and positive stress ratio ( $R = 0.5$ ).*

## 4.2. Internal or sub-surface crack initiation without the influence of oxidation

The pore size, shape, and distribution affect directly the LCF (Fritzemeier, 1988; Steuer et al., 2015), VHCF life (Cervellon et al., 2018; Liu et al., 2007), as well as creep properties to a lower degree (Cormier, 2016; Gancarczyk et al., 2019; le Graverend et al., 2017; Steuer et al., 2015).

### 4.2.1. Fatigue at low frequencies

At low temperatures of 650 °C, stress-controlled ( $R_\sigma = 0.05$ ) conditions, and maximum applied stress close to the superalloy YS, the CMSX-4 Plus superalloy presents systematically crack initiation at casting pores (Bortoluci Ormastroni et al., 2020a). New generations of superalloys as TMS-238 alloy present the same behavior at the same conditions (Bortoluci Ormastroni et al., 2020b). At the same temperature and conditions, SX or DS MAR-M200 present crack initiation at internal or at (sub-) surface MC carbides (Mataveli Suave, 2017). In these conditions, the carbides are more detrimental to the LCF life than any other defects as pores. Moreover, the bi-crystalline form of GTD-444 was tested at the same conditions, and the majority of samples presented crack initiation at casting pores outside of the (unique) grain boundary (see **Figure I-22**) (Mataveli Suave, 2017). *At low temperature, the superalloy chemistry is controlling the LCF life.*

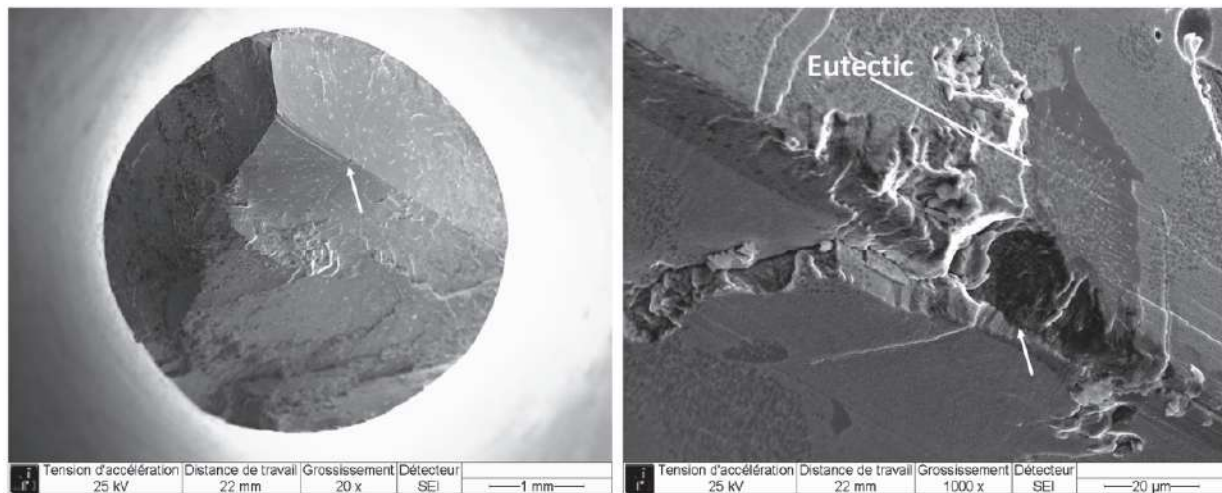


**Figure I-22** Typical crack initiation in LCF at 650 °C/ $f=0.5\text{Hz}/R_\sigma = 0.05$  for GDT-444 bi-crystalline specimens. White arrows are highlighting the pore serving as the crack initiation site (Mataveli Suave, 2017).

The solidification process influence on the fatigue life has been investigated by Steuer et al. (Steuer et al., 2015) at  $750\text{ }^{\circ}\text{C}/R_{\sigma} = -1/f = 0.5\text{ Hz}$ . **Figure I-23a** depicts the PDAS obtained after the Bridgman and the LMC solidification method, and **Figure I-23b** shows the critical casting pore at 650 MPa and 750 MPa. For both solidification routes, the samples fail at casting pores. **Figure I-23c** depicts the S-N diagram of this alloy in these conditions. An improvement of a factor of 3-4 is achieved after the LMC solidification method, indicating the casting pore size affects the fatigue life. For LCF conditions at higher temperatures ( $950\text{ }^{\circ}\text{C}/R_{\sigma} = -1/f = 0.5\text{ Hz}$ ) and under vacuum, the AM1 superalloy still presents crack initiation at casting pores (Perruchaut, 1997; Steuer et al., 2015). However, the critical casting pore is systematically near the surface, and several times connected to it. *During LCF loading at high temperature in vacuum (i.e., no oxidation), the casting defects (pores) near or at the surface control the LCF life.*

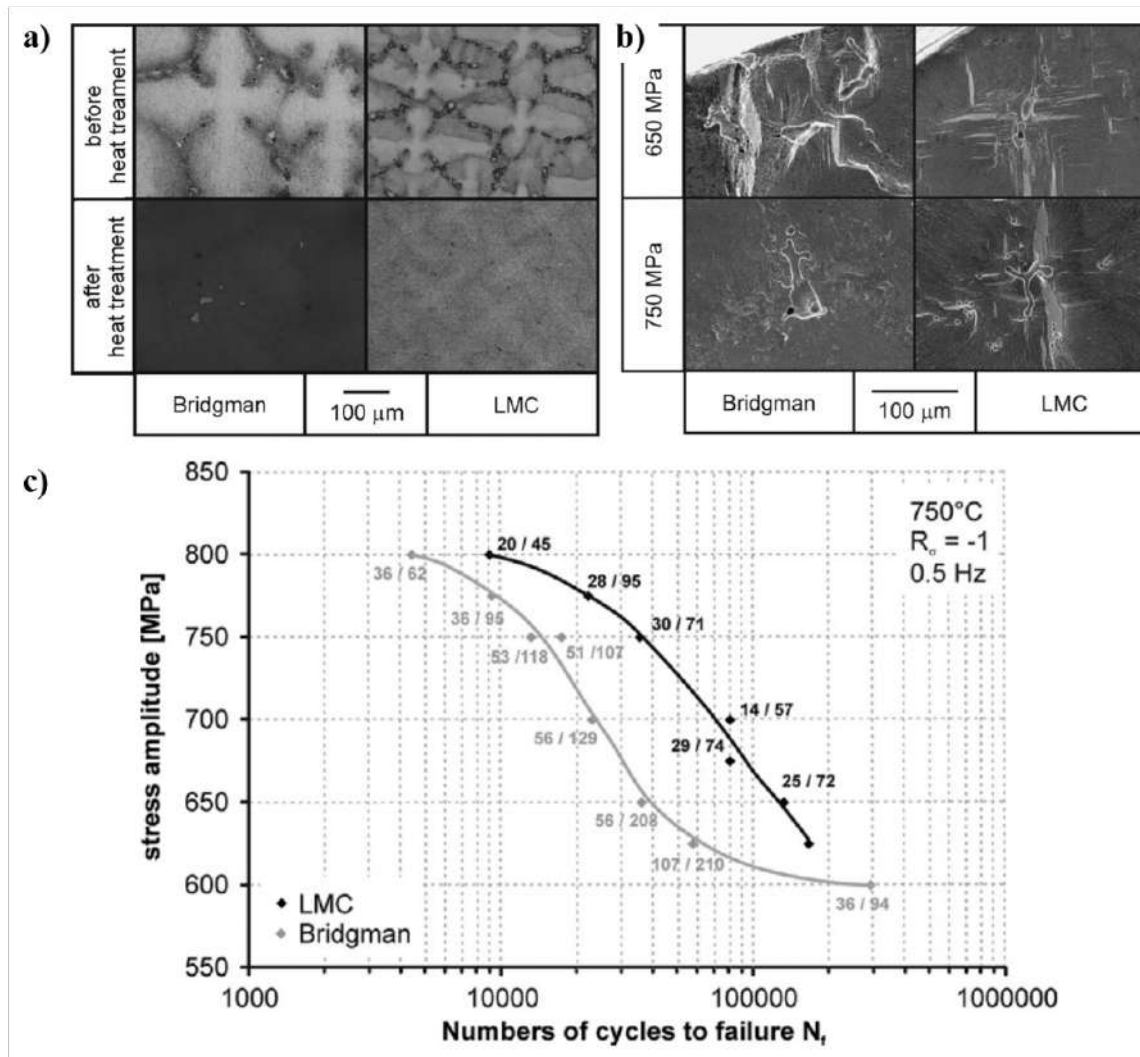


**Figure I-23** Dendritic microstructure before and after heat treatment for both casting techniques (conventional Bridgman and LMC) (a), Typical crack initiation sites at 750 °C for both samples at different stress levels. Cracks initiated at casting pores at internal or near-to-surface locations (b). S-N curves for AM1 tested in air at 750 °C,  $R_\sigma = -1$  and  $f = 0.5$  Hz, adapted from (Steuer et al., 2015).

#### 4.2.2. Fatigue at very high frequencies

Cervellon et al. (Cervellon et al., 2018) have investigated the VHCF life at 20 kHz, 1000 °C, and  $R_\sigma = -1$  for different Ni-based SX superalloys from different generations and one DS superalloy (DS200 + Hf), and the results are presented in **Figure I-24a**. All the results are inside the same trend with a trivial scatter. *One of the main conclusions of this work is that the very high cycle fatigue life is not controlled by the superalloy chemical composition.*

Furthermore, Cervellon affirms that up to  $10^9$ , most of the samples failed from large casting pores. At a very high number of cycles ( $> 10^9$  cycles), she observed occasionally a crack initiation site shift from casting pores to carbides, eutectics, and even to the surface from the oxidized layer.

**Figure I-24b** and **c** are examples of the main crack initiation site for two different AM1 samples processed with Bridgman (**Figure I-24b**) and LMC (**Figure I-24c**) methods. Cervellon observed the same trend for VHCF conditions as the one observed by Steuer et al. (Steuer et al., 2015). **Figure I-24d** depicts the VHCF fatigue life of the AM1 samples solidified by Bridgman and LMC methods and MC-NG samples with and without a HIP. The VHCF fatigue life increases with the decrease of the critical casting pore size. The increase of the fatigue life is also accompanied with a crack initiation shift from the internal casting pores to the oxidized layer in HIPed samples at low alternating stresses.

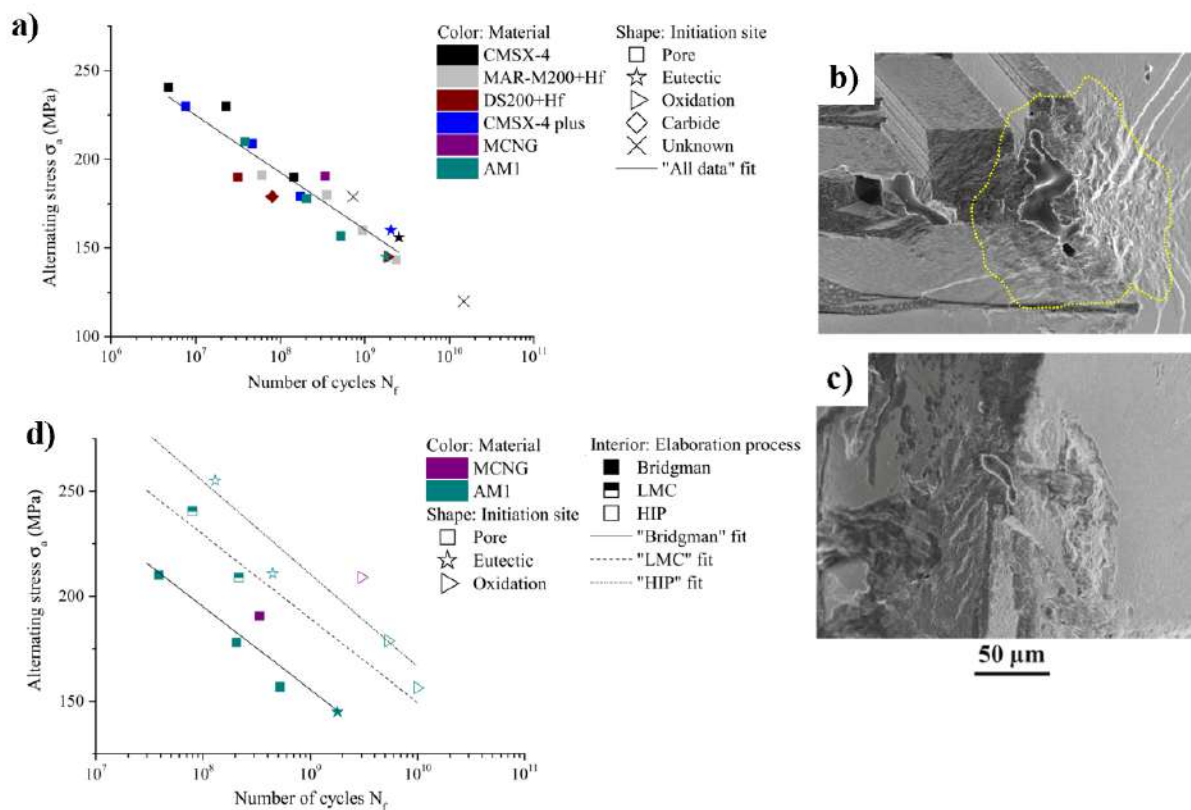


**Figure I-24** S–N diagram at 20 kHz, 1,000 °C, and  $R = -1$ : Bridgman processed superalloys (a); AM1 and MC-NG elaborated with different processes (d). Main crack initiation sites in: AM1 Bridgman (pore) tested at  $\sigma_a = 178$  MPa and failed at  $N_f = 2.04 \cdot 10^8$  cycles (b); AM1 LMC (pore) tested at  $\sigma_a = 240$  MPa and failed at  $N_f = 7.9 \cdot 10^7$  cycles (c). the yellow dotted line indicates the rough zone, adapted from (Cervellon et al., 2018).

Before Cervellon et al., Yi et al. (Yi et al., 2007) carried out VHCF tests under the same conditions using PWA 1484 superalloy HIPed samples, and their observations agree with the conclusions mentioned above. As the superalloy presented low porosity, the main crack initiation site observed by them was Ta-rich carbides. Moreover, they evidenced that under fully reversed loading, the crystallographic crack growth occurred on  $\{111\}$  octahedral slip planes.

**Figure I-24b** indicates a notable feature observed by Cervellon on the fracture surfaces after the VHCF tests by the yellow dotted line. The rough zone is very characteristic of these fatigue tests and has been the subject of investigation of Cervellon et al. (Cervellon et al., 2020a). They have concluded that the rough zone is characteristic of the crack initiation mechanism as near the critical casting pore (**Figure I-25a**), the rough zone corresponds to a localized and severe plastic activity. Furthermore, the high dislocation density (see **Figure I-25b, c, and e**) provided by the slip bands induces single-phase recrystallization and secondary phases precipitation (TCP phases, see **Figure I-25a-e**) via the redistribution of interacting solutes in the rough zone.

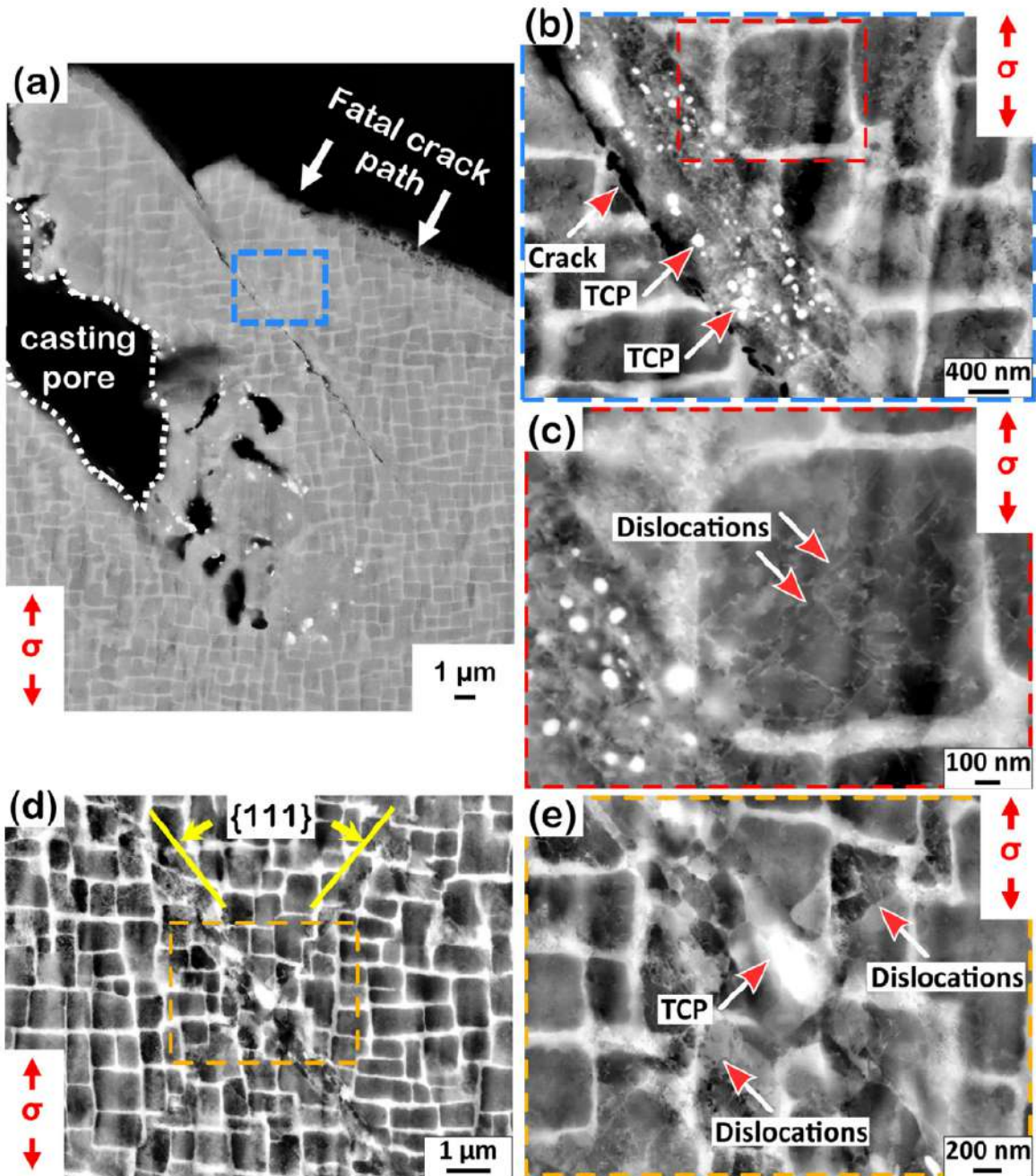


**Figure I-25** Crack initiation site on CMSX-4 Plus specimen tested at  $\sigma_a = 210$  MPa and failed at  $N_f = 4.6 \cdot 10^7$  cycles (a). Micrograph of blue rectangle in (a). In the slip bands core,  $\gamma'$  precipitates shape is substantially altered, and TCP phases have precipitated (b). Several dislocations in the precipitates are observed close to slip bands (c). ECCI micrograph in a zone close to the fatal crack path and distant from the crack initiation site shows TCP precipitation at a slip band intersection indicated by the yellow lines in (d) and magnification of the orange rectangle in (e). Dislocations are observed inside the slip bands, (Cervellon et al., 2020a).

A crack initiation mechanism for Ni-based SX alloys is proposed following the illustrations depicted in **Figure I-26**:

- i. **Figure I-26a** → Presence of a stress concentrator (casting pore) inside the  $\gamma/\gamma'$  microstructure before mechanic loading.
- ii. **Figure I-26b** → A combination of the applied stress and the stress concentration caused by the casting pore results in slip bands formed during the fatigue test in localized areas in the casting pore vicinity. These bands are induced by a high resolved shear stress on  $\{111\}\{110\}$  slip systems.

However, the stress intensity factor  $K_{\max}$  around the pore is lower than the macroscopic stress intensity threshold  $K_{\text{th,global}}$ . Thus, intense shearing of the microstructure occurs in these zones, cross-slip being inhibited at these conditions due to the extremely high strain rate at the conditions investigated, typically in the range of 70 - 200  $\text{s}^{-1}$  (Cervellon et al., 2017).

- iii. **Figure I-26c** → At 1,000 °C, the severe plastic deformation generated in these zones induces partial RX and cavitation. Utada et al. (Utada et al., 2021) recently observed short cracks initiated from a large casting pore after pre-deformation. The EBSD (**Figure I-27a** and **b**) analysis identified the presence of RX grains along the crack path, in agreement with the illustration proposed by Cervellon.

Moreover, depending on the chemical composition of the alloy, TCPs or carbides will also precipitate in the rough zone. Macroscopic crack propagation and then failure happen when the stress intensity factor  $K_{\max}$  around the rough zone reaches a threshold value  $K_{\text{th,global}}$ . The presence of voids and their coalescence is thought to assist crack growth, even if no evidence has been shown up to now.

*Thus, even though the chemical composition of the Ni-based SX superalloy does not control the very high cycle fatigue life, it may contribute to the development of features that decrease the local stress intensity threshold  $K_{\text{th,local}}$  which enables slip bands propagation.*

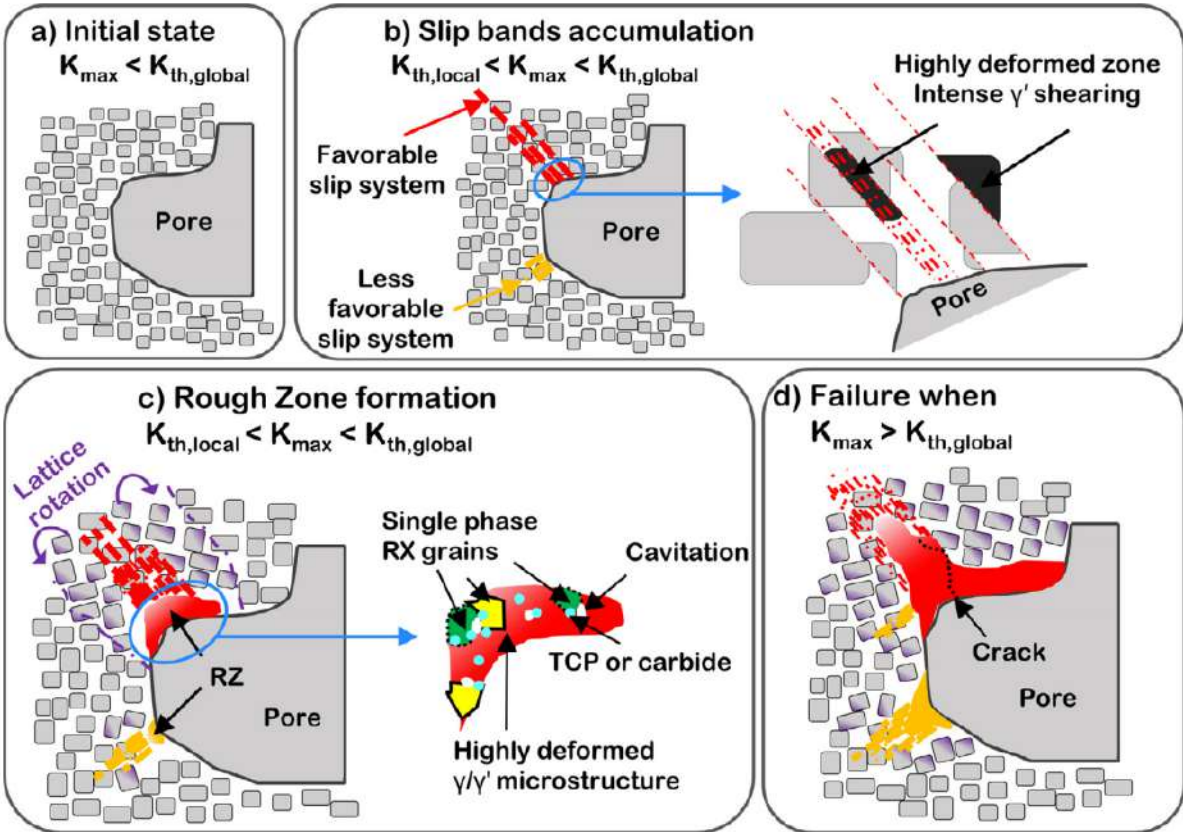


**Figure I-26** Mechanism of the rough zone formation proposed in Ni-based SX superalloys at high temperature  $R_e = -1$ ,  $f = 20$  kHz (Cervellon et al., 2020a).

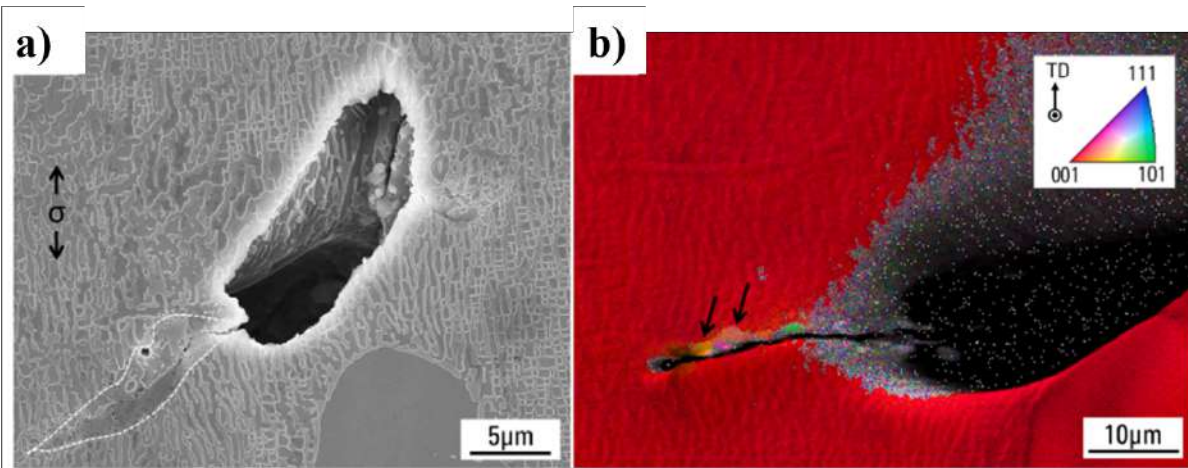


**Figure I-27** Microstructure observed along a longitudinal cut of AM1 pre-deformed specimen tested at  $1,000$  °C,  $f = 20$  kHz,  $R_e = -1$ ,  $\sigma_a = 209$  MPa. The dotted curve shows the evolved microstructure with crack propagation (a). IPF map of the area around the crack in (a) superimposed on forward scatter detector signal. Arrows show recrystallized grains along the crack path (b), adapted from (Utada et al., 2021).

### 4.2.3. Fatigue indicator parameter

As summarized in the sub-section above, internal casting pores control the crack initiation process in fatigue when oxidation does not control the crack initiation mechanisms. Therefore, to capture the fatigue life's dependence on the solidification-induced porosity size, a fatigue indicator parameter (FIP) was developed. This tool estimates the sample's fatigue life with a known casting pore size with an accuracy of a factor 2 - 3. The model was developed and adapted by Steuer et al. (Steuer et al., 2015), and it is used in several recent studies in the literature (Bortoluci Ormastroni et al., 2020a; Cervellon, 2018; Cervellon et al., 2018; Jiang et al., 2021b, 2021a).

The expression of the FIP proposed by Steuer et al. is presented in **Equation I-1**.

**Equation I-1** Fatigue indicator parameter defined at (Steuer et al., 2015).

$$FIP = \frac{\mu\Delta\sigma}{E} \left[ 1 + k \frac{\Delta K}{\Delta K_{threshold}} \right]$$

The FIP is estimated by the positive stress range over Young's modulus (E) multiplied by the Schmid factor ( $\mu$ , which is 0.408 for an octahedral slip with an applied stress along [001] direction). With this approach, the casting pore is considered as an internal notch, and the local threshold translates its influence on crack initiation.

The stress intensity factor in the vicinity of the pores used by Steuer is presented in **Equation I-2** and it was proposed by Murakami and Endo (Murakami and Endo, 1994).

**Equation I-2** Stress intensity factor defined at (Murakami and Endo, 1994).

$$K_I = Y\sigma \sqrt{\pi \sqrt{A_{defect}}}$$

Where Y is equal to 0.5 for internal and to 0.65 for near-to-surface initiations,  $\Delta\sigma$  is the applied positive stress and  $A_{defect}$  the area of the pore measured from a projection on a plane perpendicular to the stress axis. More recently, Cervellon et al. (Cervellon et al., 2020a) calculated the stress intensity factor in the vicinity of the rough zone, revealing an almost constant value of  $1.25 \pm 0.25$  MPa m<sup>1/2</sup> whatever the alloy. The value is more representative of a small crack threshold rather than a long crack threshold. However, Zhao et al. (Zhao et al., 2022) observe little dependence of the predicted fatigue life on the  $\Delta K_{th}$  value.

The stress intensity factor is then normalized by the value of the threshold stress intensity for long crack propagation. The parameter  $k$  is taken equal to 1 by Steuer et al. (Steuer et al., 2015) to achieve the best fit. The relationship between the number of cycles to failure and the FIP is depicted in **Equation I-3**, corresponding to a typical Basquin law.

***Equation I-3** Relationship between the number of cycles to failure and the FIP.*

$$N_f = a (FIP)^b$$

The coefficients  $a$  and  $b$  are calculated from the experimental results power trend line, as presented in **Figure I-28a** and **c**.

**Figure I-28a** depicts the FIP analysis of several results present in the literature using the stress intensity factor presented in **Equation I-2**. Moreover, the FIP analysis considering the contribution of the rough zone on the stress intensity factor is presented in **Figure I-28c**. Finally, the predicted life is presented in **Figure I-28b** and **d**, respectively.

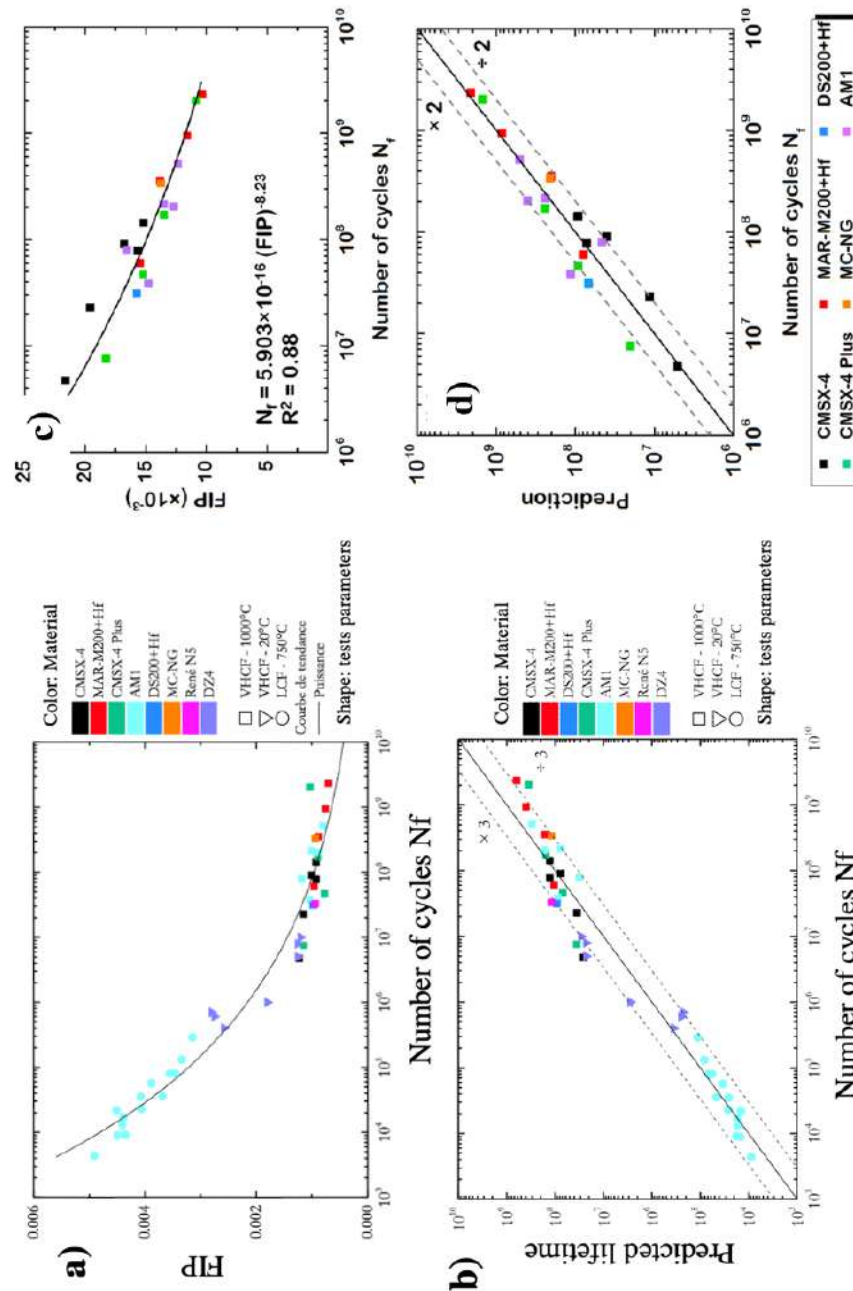


**Figure I-28** FIP as a function of the number of cycles (a), and the lifetime prediction by the fatigue indicator parameter (b) of several experimental results encountered in the literature for LCF à 750 °C (Steuer et al., 2015) and VHCF at 20 kHz and 1,000 °C (Nie et al., 2018). FIP as a function of the number of cycles using the corrected stress intensity factor (c) and the lifetime prediction by the fatigue indicator parameter (d) of several experimental VHCF results at 20 kHz and 1,000 °C, adapted from (Cervellon, 2018; Cervellon et al., 2020a).

The FIP approach seems to be useable for all Ni-based superalloys independently of the solidification method and the HT. Moreover, it seems to provide satisfying results in all fatigue regimes, temperatures, frequencies, and solidification methods. However, *it mainly depends on the stress intensity factor, which is influenced by the casting pore size and position, with no consideration on how the specific microstructures of alloys (i.e., incipient melting, local high dislocation density...) may affect the development of the rough zone.*

#### **4.3. Microstructure and its effect on the fatigue life**

The fatigue properties are known to be sensitive to the mean stress, particularly at elevated temperatures. Therefore, a Goodman approach to accounting for mean stresses is often used for the component design (Chan et al., 1987). Typically, the positive stress ratio and high temperatures lead to superalloy microstructure degradation ( $\gamma'$ -rafting), inducing cyclic softening, i.e., faster cyclic ratcheting at positive stress ratios (Gabb et al., 1986; Tetzlaff and Mughrabi, 2000) in stress controlled experiments. This phenomenon was mainly investigated and observed for the strain-controlled LCF experimental tests (Gabb et al., 1986; Perruchaut, 1997; Riallant, 2014; Tetzlaff and Mughrabi, 2000).

Indeed, the  $\gamma/\gamma'$  morphology controls the fatigue crack propagation and thus the fatigue life (Ott et al., 1999), as illustrated by the cyclic life for different microstructures in **Figure I-29a**. The crack propagation phenomenon is illustrated in **Figure I-29b** and **c**, where it shows a crack propagation stage favored by  $\gamma'$ -rafts perpendicular to the stress axis while the crack propagation rate is slowed down by a  $\gamma'$ -rafts parallel to the stress axis.

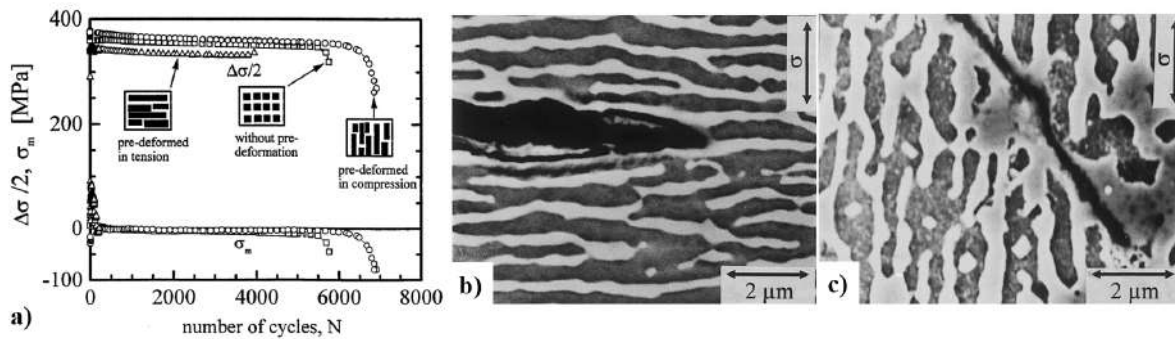


**Figure I-29** Cyclic deformation curves of fatigue tests on the alloy CMSX-6;  $T = 950\text{ }^{\circ}\text{C}$ ,  $\Delta\epsilon_{el} = 0.9\%$  with mean stress compensated (a). Fatigue crack tips of the alloy CMSX-4 samples tested at  $1,050\text{ }^{\circ}\text{C}$ ,  $t = 0.9\%$ . SEM-micrographs. A sample with  $\gamma'$ -rafts perpendicular to the stress axis (b), and a sample with  $\gamma'$ -rafts parallel to the stress axis (c), adapted from (Frenz et al., 1996; Ott et al., 1999).

At high frequencies and  $1,000\text{ }^{\circ}\text{C}$ , Cervellon et al. (Cervellon et al., 2017) compared the VHCF life of a reference CMSX-4 alloy with cubical precipitates (CMSX-4 R), a thermally aged alloy at  $1,100\text{ }^{\circ}\text{C}$  during 300 h (CMSX-4 A300), a pre-strained alloy at  $1,100\text{ }^{\circ}\text{C}$ , 120 MPa during 24 h (CMSX-4 P24), another pre-strained alloy at  $1,100\text{ }^{\circ}\text{C}$ , 120 MPa during 100 h (CMSX-4 P100). No influence of the microstructure degradation on the VHCF life of CMSX-4 superalloy at  $1,000\text{ }^{\circ}\text{C}$ /  $R_e = -1$  and  $f = 20\text{ kHz}$  was observed, see **Figure I-30a**. **Thus, the crack initiation under these conditions is not dependent on the superalloy microstructure.**

Conversely, at  $1,000\text{ }^{\circ}\text{C}$ ,  $R_e = 0.8$  and  $f = 20\text{ kHz}$ , the pre-aged samples have shown that at high maximum stresses, the VHCF life is 3 to 4 times lower than that of the reference samples, as shown in **Figure I-30b**. Again, the main factor controlling lifetime was creep damage, and the micro-propagation phase is also accelerated by the N-type rafted  $\gamma/\gamma'$  morphology. **The conclusions are like the observations of the influence of microstructure in the low cycle fatigue domain.**

In another study, Cervellon et al. (Cervellon et al., 2020b) showed that under  $1,000\text{ }^{\circ}\text{C}$ ,  $R_e = 0.8$  and  $f = 20\text{ kHz}$  conditions, the creep damage is the main factor controlling fatigue life (**Figure I-30c**). Furthermore, **the Ni-based SX superalloy developed to have better creep properties have the best VHCF lifetimes, at high  $R$  rates, even for a high frequency.**

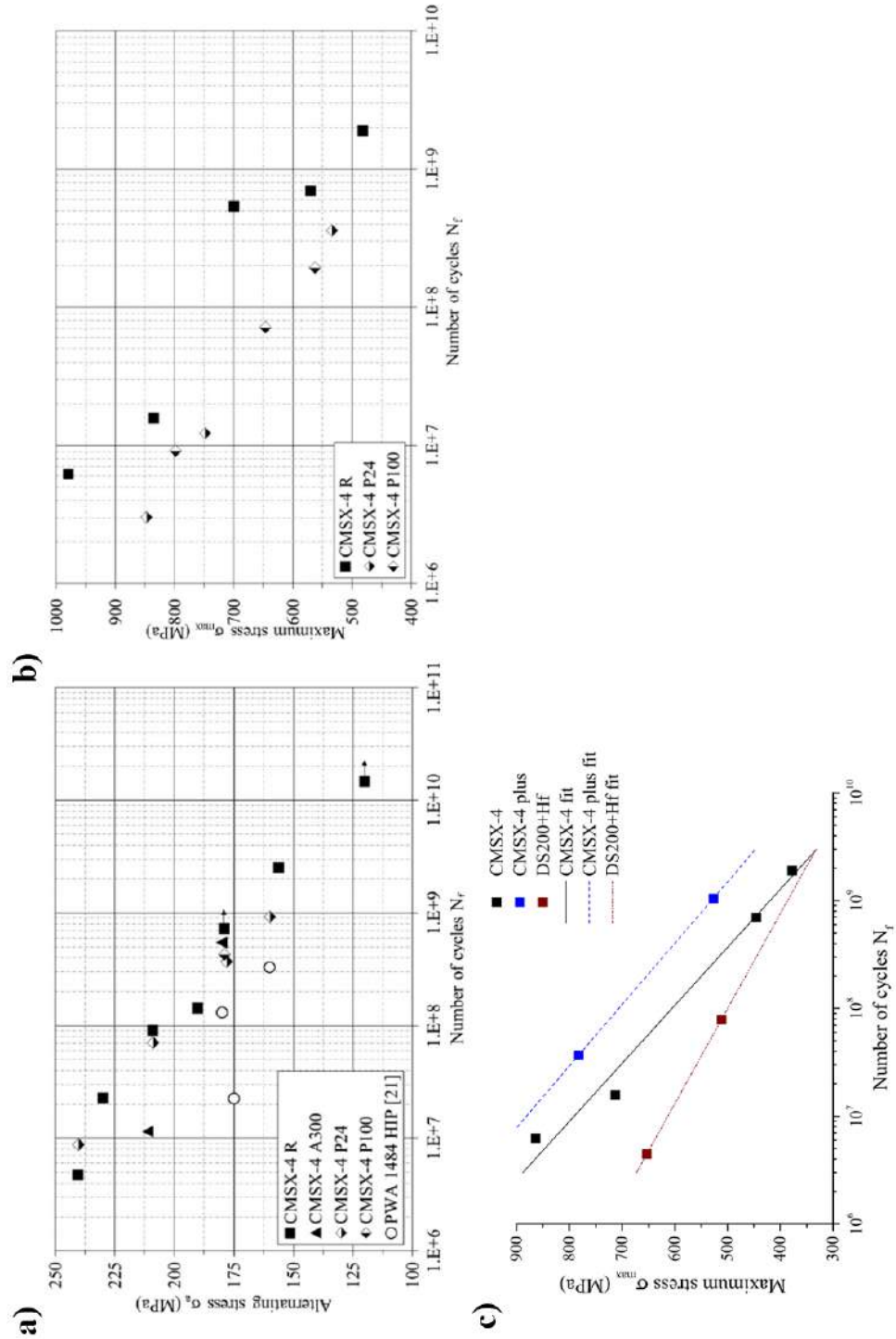


**Figure I-30** S-N diagram for 1,000 °C/  $R_\epsilon = -1$  and  $f = 20$  kHz. HIPed PWA 1484 is taken for comparison (Yi et al., 2007) (a). S-N diagram for 1,000 °C/  $R_\epsilon = 0.8$  and  $f = 20$  kHz on CMSX-4 R, P24 and P100. (b), S-N diagram at 20 kHz, 1000 °C, and  $R = 0.8$  (c). Reference CMSX-4 alloy with cubical precipitates (CMSX-4 R). Thermally aged alloy at 1,100 °C during 300 h (CMSX-4 A300). Pre-strained alloy at 1,100 °C, 120 MPa during 24 h (CMSX-4 P24). Pre-strained alloy at 1,100°C, 120 MPa during 100 h (CMSX-4 P100). Adapted from (Cervellon et al., 2018, 2017).

The crack initiation was further investigated by Utada et al. (Utada et al., 2021) for the Ni-based SX superalloy AM1 samples pre-strained at room-temperature, further heat treated and then tested in VHCF at a temperature of 1,000 °C,  $R_e = 0.5$ , and 20 kHz. A shift from the internal crack initiation to the surface was observed at high stress amplitudes. Utada et al. recognized bands lying on the former  $\{111\}$  slip planes (**Figure I-31a**) resulting from the prior pre-deformation. Therefore, it led to the surface roughness (**Figure I-31b**) and then to a surface recrystallization at high temperatures. Finally, it induces a mode I fatal crack initiation from the surface.

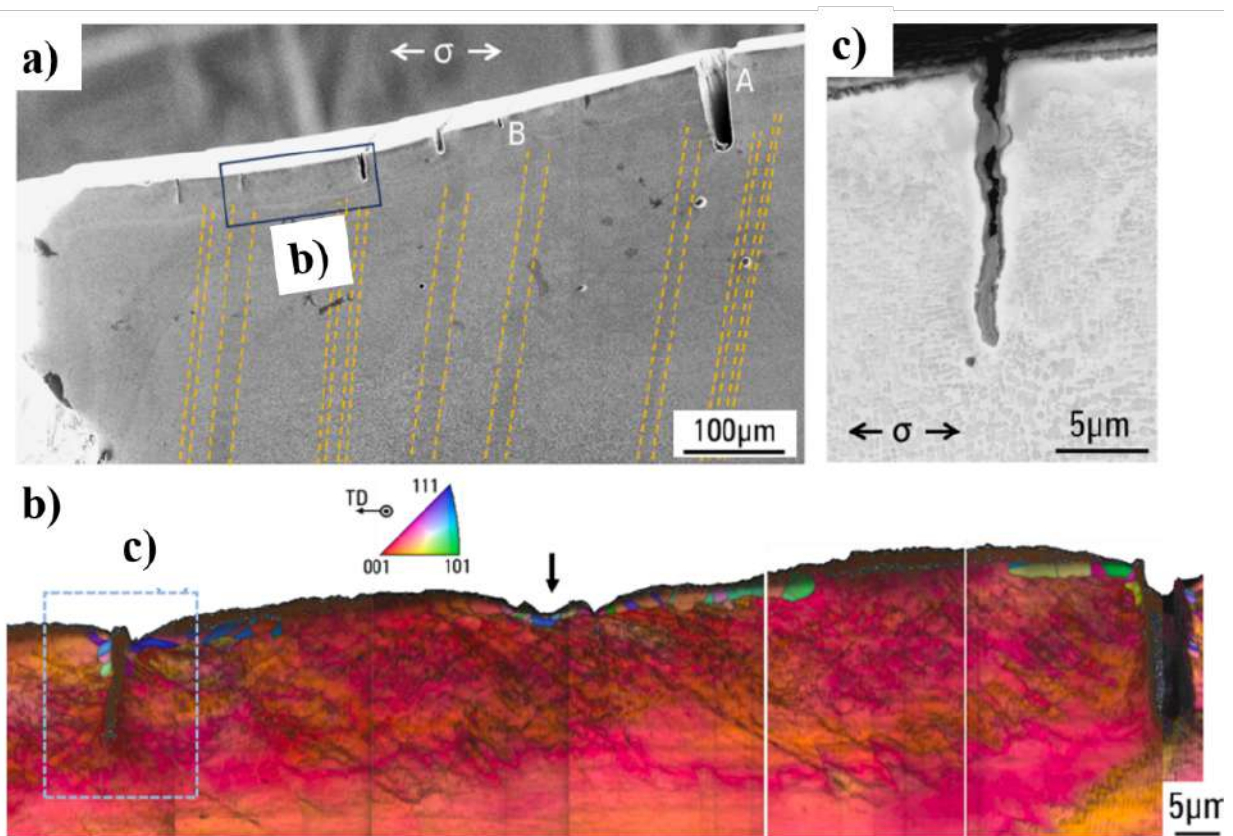


**Figure I-31** Microstructure observed along longitudinal cross-section ( $\approx (110)$  plane) of AM1 pre-deformed specimen tested at 1,000 °C,  $f = 20$  kHz,  $R_e = 0.5$ ,  $\sigma_{max} = 551$  MPa. Low magnification image is taken from the area with surface cracks. Dotted lines indicate the microstructure coarsened bands (a). Merged IPF + IQ maps at the surface layer indicated by the rectangle in (a). Arrow is pointing at the recrystallized area without a crack (b). Backscatter electron image of the area indicated by the blue rectangle in (b), (c), adapted from (Utada et al., 2021).

As previously shown, internal defects mainly controlled the fatigue endurance at  $R=-1$ . The studies presented in this sub-section have also shown that the fatigue life turns out to be affected by the  $\gamma/\gamma'$  morphology and the superalloy resistance to creep damage at positive stress ratios.

#### 4.4. Surface crack initiation due to oxidation

Fleury and Rémy (Fleury and Rémy, 1993) have investigated the AM1 superalloy at 650 °C, 950 °C and 1,100 °C,  $R_\epsilon = -1$ , and 0.05 Hz. As expected, the samples failed from internal sites under low temperatures and from the surface at high temperatures (**Figure I-32a**). The first surface cracks were detected in the first cycles, and most of the fatigue life was spent in the microcrack growth regime. At a temperature of 950 °C, they have identified two competing mechanisms: crack that nucleates from the surface or (sub-)surface casting pores, versus cracks that nucleate from the surface oxides.

In addition, they have observed that the oxides break under fatigue loading leading to the exposure of the substrate. The oxidation then takes place at the new surface. The repetition of this mechanism tends to localize oxidation and form a critical zone where a fatigue crack can develop quickly. *Crack initiation at high temperatures and low frequencies thus results from an interaction between fatigue and oxidation mechanism.*

**Figure I-32b** depicts a map that summarizes the fatigue crack initiation at different temperatures.

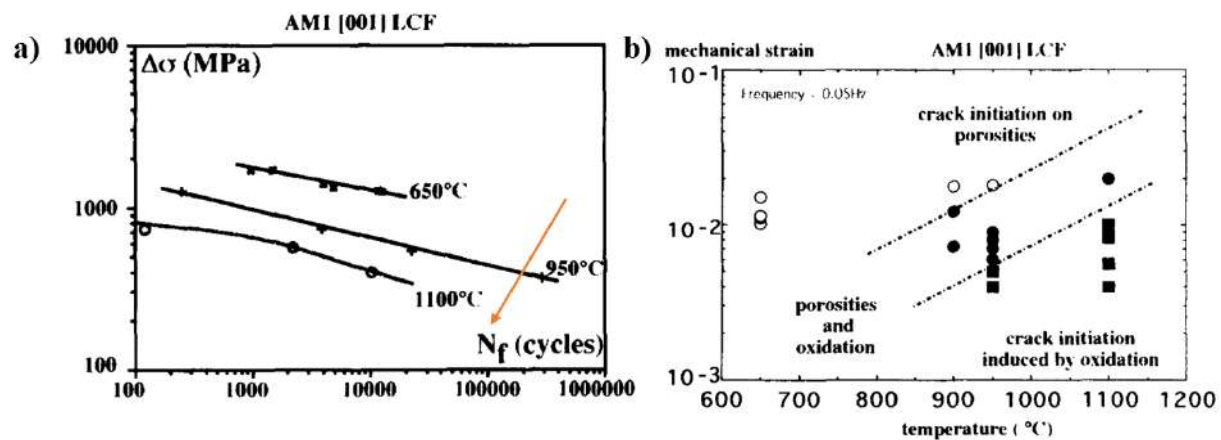


**Figure I-32** Comparison of the S-N diagram obtained for [001] specimens at 650 °C, 950 °C, and 1,100 °C (a), map of initiation mechanisms observed on [001] crystallographic orientation specimens (b). The orange arrow highlights the fatigue endurance from the low to the high temperature, adapted from (Fleury and Rémy, 1993).

More recently, Steuer et al. (Steuer et al., 2015) investigated the AM1 superalloy solidified by Bridgman and LMC methods tested at 950 °C,  $R_\sigma = -1$ , and 0.5 kHz in air and in vacuum. **Figure I-33a** shows that the fatigue life in air is independent of the casting technique. The samples from both solidification methods presented crack initiation from the surface, at oxides spikes, and subsequent crack propagation in mode I, see **Figure I-33b**. In vacuum, a dependence to the casting pore size was found again (see **Figure I-33a**). *Thus, the benefits provided by the LMC process in terms of pore size are not apparent when testing in the oxidizing environment without coatings.*

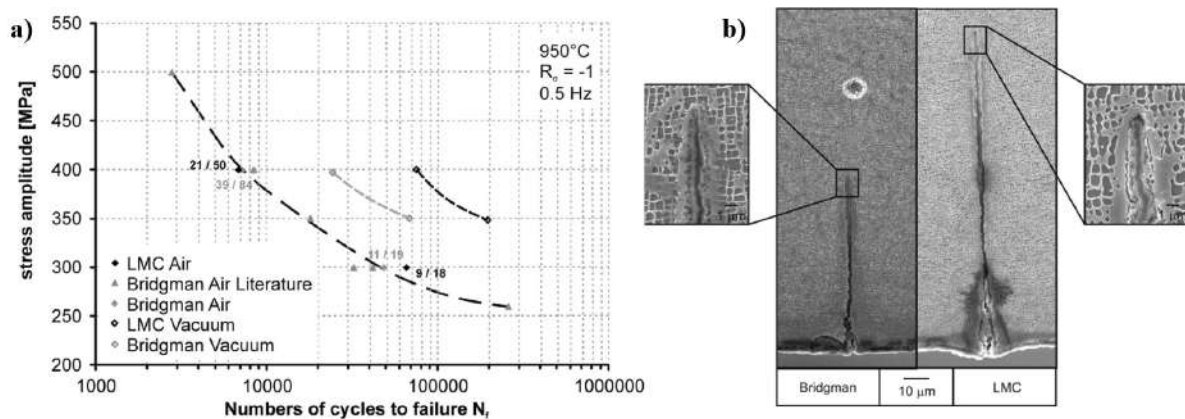


**Figure I-33** S-N diagram of AM1 samples solidified by Bridgman and LMC methods, tests carried out under air and vacuum, results from (Perruchaut, 1997) are added (a). Longitudinal section of AM1 samples tested in LCF at 950 °C,  $f=0.5$  Hz,  $\sigma_{alt}=300$  MPa and  $R_\sigma=-1$  (b), adapted from (Steuer et al., 2015).

This phenomenon was also observed and further investigated by Ohtani et al. (Ohtani et al., 2001) on the Ni-based SX superalloy CMSX-10 under stress-controlled ( $R_\sigma = -1$ ) fatigue tests at 1,000 °C, and higher frequency of 1 Hz and considering that most of the strain in fatigue cycles was elastic. A magnification of the oxides after 500 cycles is shown in **Figure I-34a**. The cracks grow along the oxide's grain boundaries. Thus, the granular oxidation on the surface can be recognized as a trigger for crack initiation. **Figure I-34b** depicts the crack morphology of interrupted tests at 5,000 cycles with the oxide layer, and **Figure I-34c** depicts the cracks morphology without the oxide layer. Thus, at 5,000 cycles, *the cracks already reached and developed in the superalloy substrate even though there was no macroscopic plastic deformation developing in the specimen.*

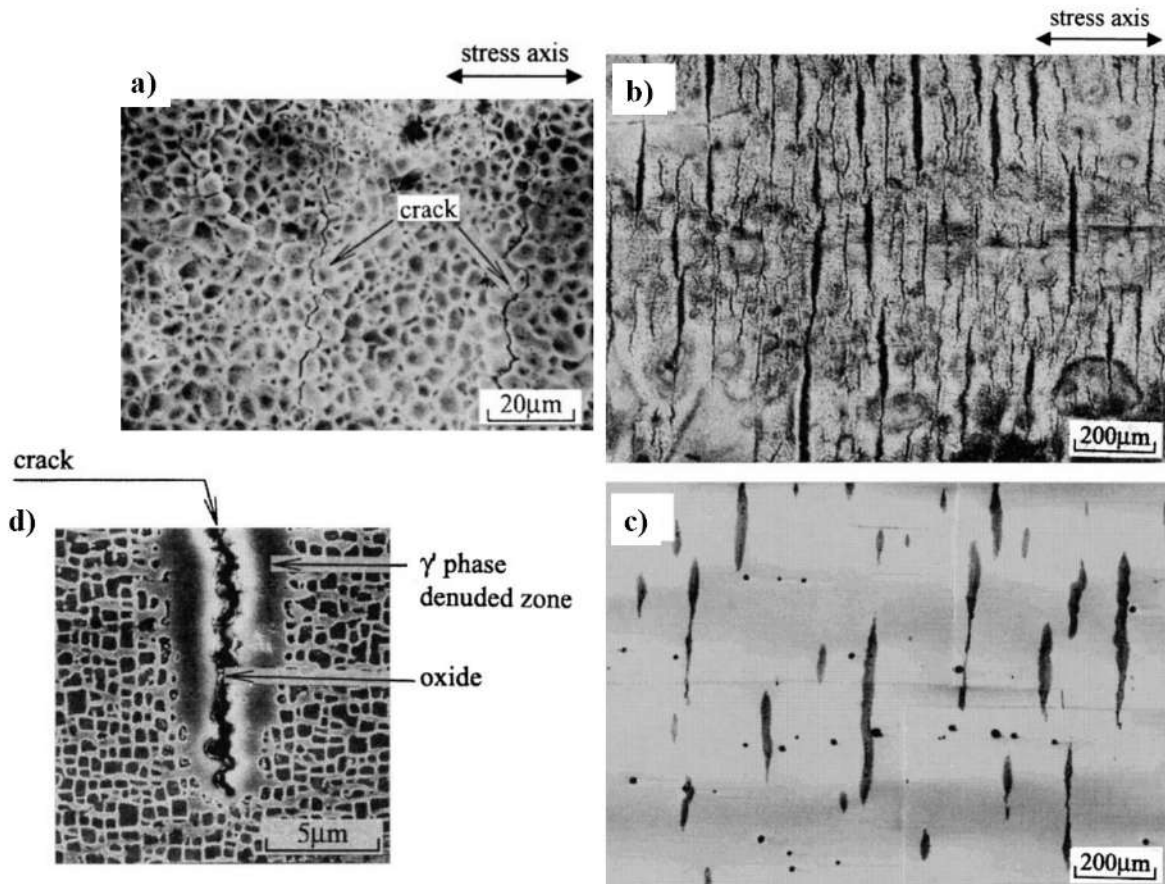


**Figure I-34** Surface cracks initiating and growing along the boundaries of granular oxides after 500 cycles in CMSX-10 tested at 1,000 °C/ $R_{\sigma}=-1/1\text{Hz}$  (a). Small cracks on the specimen surface at 5,000 cycles, oxide layer cracking (b), and (c) after removing the oxide layer from the surface. Microstructure length section in the vicinity of the crack tip (d), adapted from (Ohtani et al., 2001).

Under VHCF conditions, the crack initiation from the surface remains to be studied in more detail. Cervellon et al. (Cervellon et al., 2018), for example, observed a high oxidation activity at the fracture surface of an AM1 HIP sample tested at  $R_{\sigma} = -1$ ,  $f = 20$  kHz and high temperatures (1,000 °C), alternating stress of 190 MPa and  $5.3 \cdot 10^9$  cycles, see the graph in **Figure I-24d**. **Figure I-35a** depicts the fracture surface of this specimen and **Figure I-35b, c, and d** show the cross sections of cracks propagating from the oxide layer into the substrate material in mode I. **Figure I-35d** details the crack propagation mechanism from the crack tip. The crack propagates from the brittle oxide in the crack tip into the  $\gamma$  channels. Moreover, the slip bands (red arrows) indicate that a highly localized deformation is happening ahead of the crack tip in these conditions.

*In the absence of critical casting pores, the VHCF fatigue endurance may be controlled by the crack growth from the surface and no more by the crack initiation from an internal site. Moreover, the benefit of the HIP treatment to increase the fatigue life of SXs specimens may be counterbalanced by the alloy intrinsic oxidation resistance.*

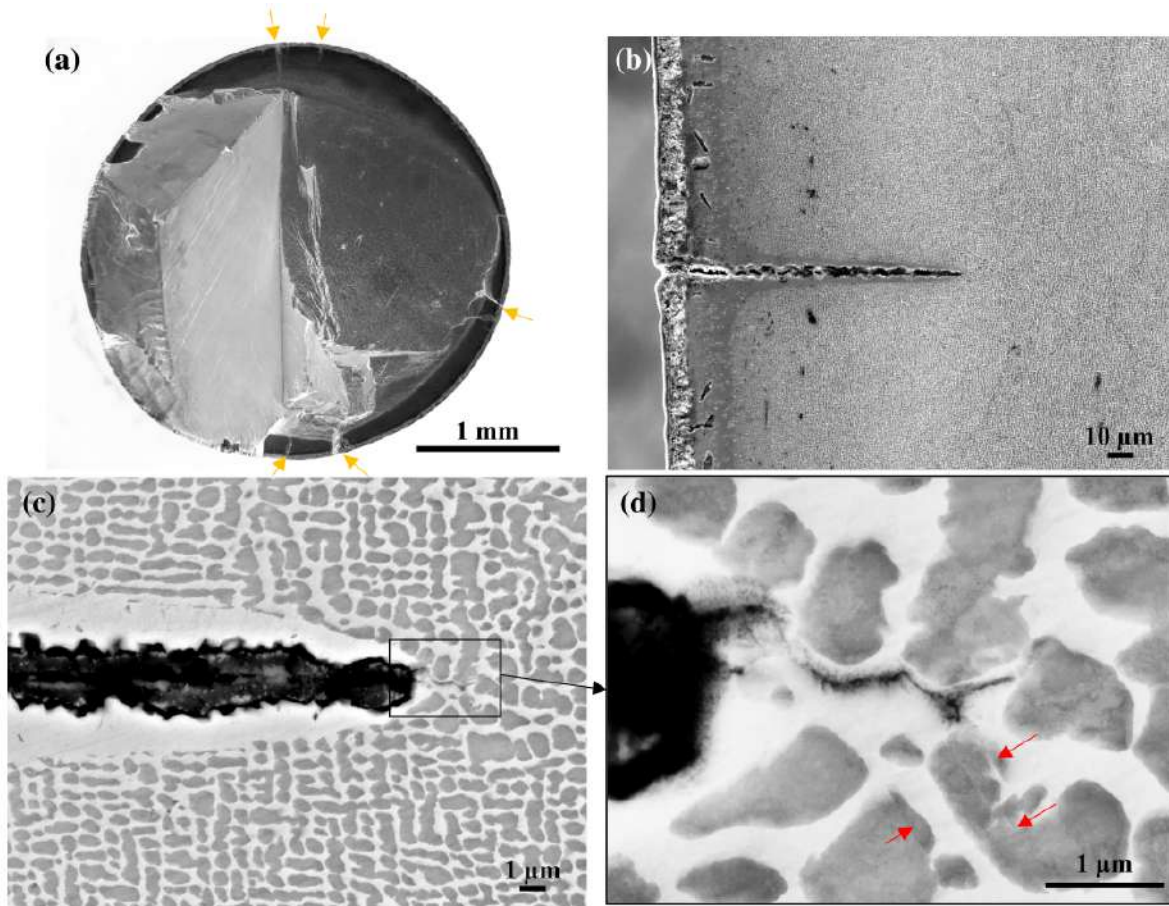


**Figure I-35** Fracture surface of an AM1 HIPed sample tested at 1,000 °C,  $f=20$  kHz,  $\sigma_a=190$  MPa, and  $R_e=-1$  (a), Crack in mode I (b), magnification of the crack tip (c) and crack propagation in the  $\gamma$  precipitates channel, (Cervellon et al., 2018).

Recently, Zhao et al. (Zhao et al., 2021a) presented the analysis of the internal to surface crack initiation transition under fully reversed loading, 20 kHz, and temperatures of 760 °C, 850 °C, 1,000 °C, and 1,100 °C for the Ni-based SX superalloy DD6. **Figure I-36a** depicts the VHCF life evolution as a function of temperature. The higher the temperature, the lower the VHCF life. As one can observe, all the samples at 1,100 °C failed from the surface, even though no HIP treatment

was applied. The SEM micrograph of one of the surface cracks is depicted in **Figure I-36b**, as well as EDS maps of Al (**Figure I-36c**), Ni (**Figure I-36d**), and Cr (**Figure I-36e**) showing oxides along the crack lips.

Moreover, they invoke the work of Cervellon et al. mentioned in **Figure I-30** where the VHCF fatigue life of the pre-oxidized samples CMSX-4 A300 are comparable to the fatigue life of the CMSX-4 without oxidation. Thus, they affirm that the dynamic nature of oxidation and associated fatigue cracking at 20 kHz may be the controlling factor of the crack initiation under VHCF conditions at 1,100 °C. All other specimens tested at lower temperatures failed from internal casting pores.

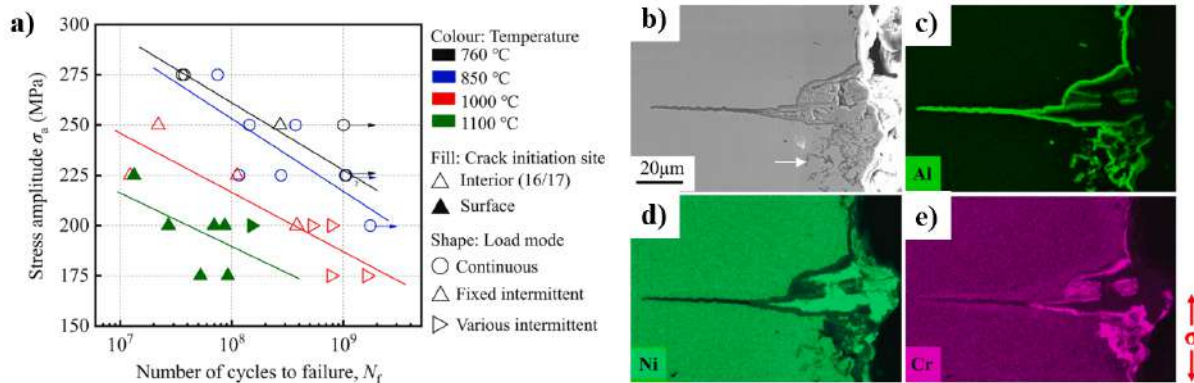


**Figure I-36** S-N diagram of DD6 alloy in the VHCF regime at 760, 850, 1,000 and 1,100 °C (a), SEM micrograph of a surface crack (b) and corresponding EDS mapping of aluminum in (c), nickel in (d) and chromium in (e). Measurements were performed on the as-polished surface of the longitudinal section of the specimen tested at  $\sigma_a = 200$  MPa and 1,100 °C, with a fatigue life of  $N_f = 8.6 \cdot 10^7$ , adapted from (Zhao et al., 2021a).

The authors proposed a schematic diagram to describe the crack initiation mechanisms assisted by oxidation under VHCF conditions and temperatures over 1,100 °C. First, aluminum-rich oxide formation creates a sub-surface region which appears to be  $\gamma'$ -depleted (**Figure I-37a**). Then, fatigue crack initiation occurs from heavily penetrated internal oxides (**Figure I-37b**). Finally, oxygen diffusion occurs during VHCF loading, and the diffusion distance can reach the fatigue crack tip.

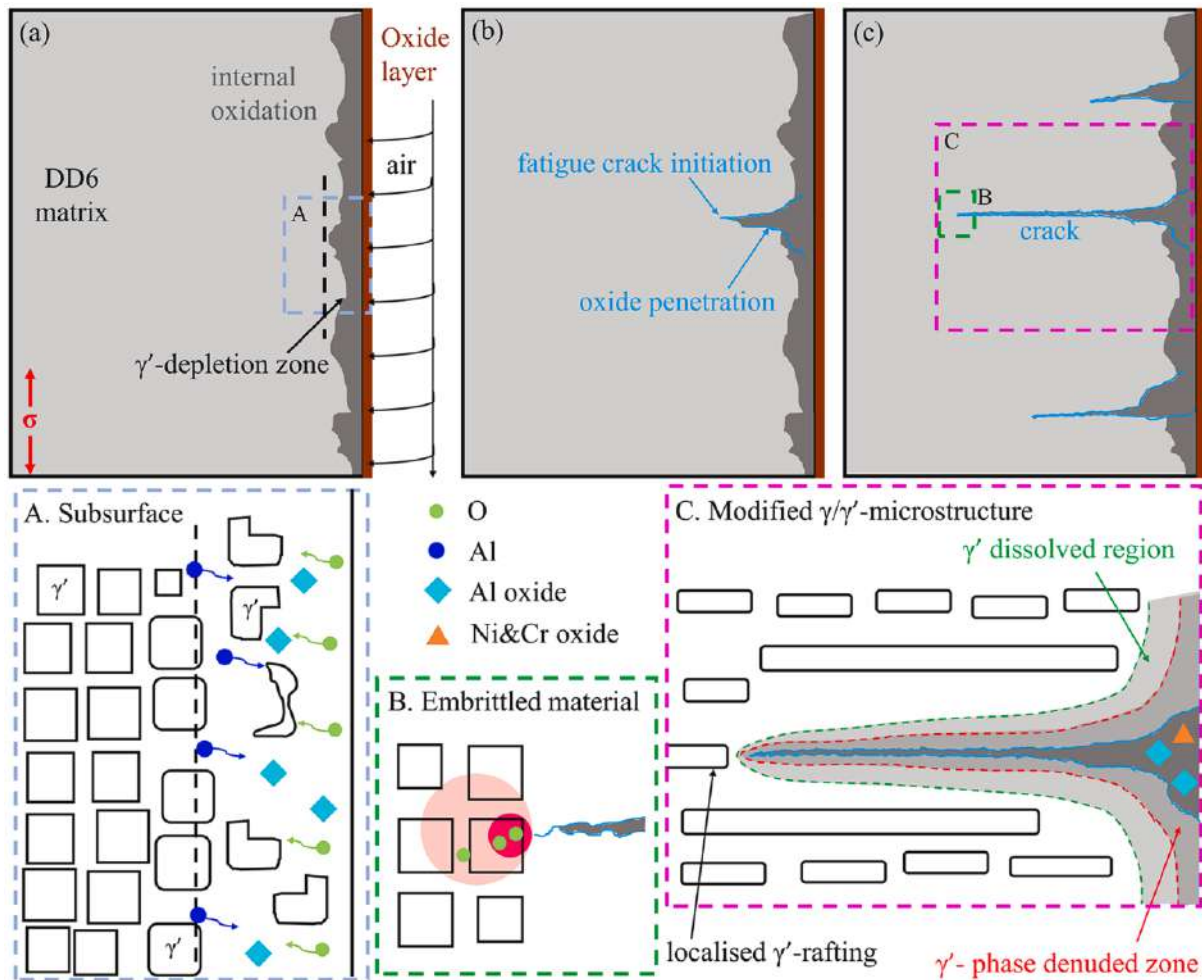


**Figure I-37** A schematic diagram describing the underlying mechanisms responsible for the transition from internal to surface crack initiation during VHCF loading: (a) formation of aluminum-rich internal oxides; (b) oxidation-assisted fatigue crack initiation; (c) propagating a crack under oxidation-fatigue interaction, (Zhao et al., 2021a).

The analysis presented in this work from Zhao et al (Zhao et al., 2021a) at different temperatures implies that the transition is mainly due to a more active oxidation induced damage at higher temperatures, i.e., transition due to the reduced superalloy's oxidation resistance at high temperatures. Indeed, the present work will carry out the same analysis under the same temperature (1,000 °C), stress ratio, and frequency, as the triggering transition from internal to surface crack initiation remains unclear.

## 4.5. Crack initiation in fatigue in coated specimens

### 4.5.1. Fatigue at low frequencies

The isothermal fatigue of a high-activity aluminide-coated nickel-base superalloy (high  $\gamma'$  volume fraction nickel-based SX superalloy with principal alloying additions of Co, Cr, Al, and Ti) was studied by Totemeier et al. (Totemeier and King, 1996) at 600 °C, 800 °C, and 1,000 °C under strain-controlled conditions, see **Figure I-38**. At low temperatures (**Figure I-38a**), fatigue life was significantly reduced for the coated specimens with respect to uncoated specimens by increasing the strain range. The lower fatigue endurance limits are mainly due to the brittle and fast crack initiation in the coating.

However, the effect of the coating becomes more complex once the ductile-to-brittle transition temperature of the coating is exceeded, i.e., 700/750 °C for the strain rate of  $10^{-5} \text{ s}^{-1}$  for NiAl coatings. At 800 °C (**Figure I-38b**) and high strain range, coated specimens still have lower fatigue endurance than the uncoated ones. Indeed, at 800 °C and low strain range, the coating seems to be beneficial to the fatigue life. This effect is due to the crack initiation, as in the first case, the cracks grew quickly from the coating into the substrate, and in the second case, the coating cracks were slowed or arrested by oxidation at the coating-substrate interfaces leading to internal crack initiation at casting pores. Finally, *the coating appeared to have minimal effect on the substrate fatigue life at high temperatures (Figure I-38c).*

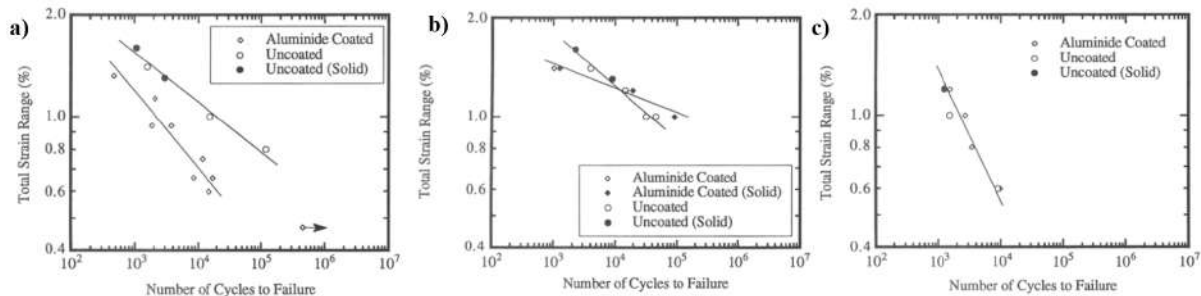


**Figure I-38** Fatigue life as a function of total strain range for coated and uncoated specimens: (a) 600 °C (b) 800 °C and (c) 1,000 °C. Solid for massif specimens. Adapted from (Totemeier et al., 1996).

However, even though the fatigue life of uncoated and coated samples is likely inside the same trend line at high temperatures and low frequencies, it does not mean that the crack initiation mechanism is the same in both conditions.

More recently, Pollock and al. (Pollock et al., 2011) investigated the Rene N5 superalloy with a PtAl and a NiAl (VPA) under isothermal (982 °C and 1,093 °C) strain-controlled conditions. The experiments revealed four successive stages of the failure process illustrated in **Figure I-39a and b**: (i) the bond coat cracks in the first few cycles. After that, however, the crack extension from the surface inside the bond coat takes approximately 80 % of the fatigue life, (ii) gradual cracking progress through the IDZ, (iii) and then to the superalloy substrate. Finally, (iv) the long crack growth into the superalloy bulk. In the final stage, coarse striations are visible on the fracture surface, indicating that rapid mixed-mode crack growth occurs in this final stage (**Figure I-39b**).

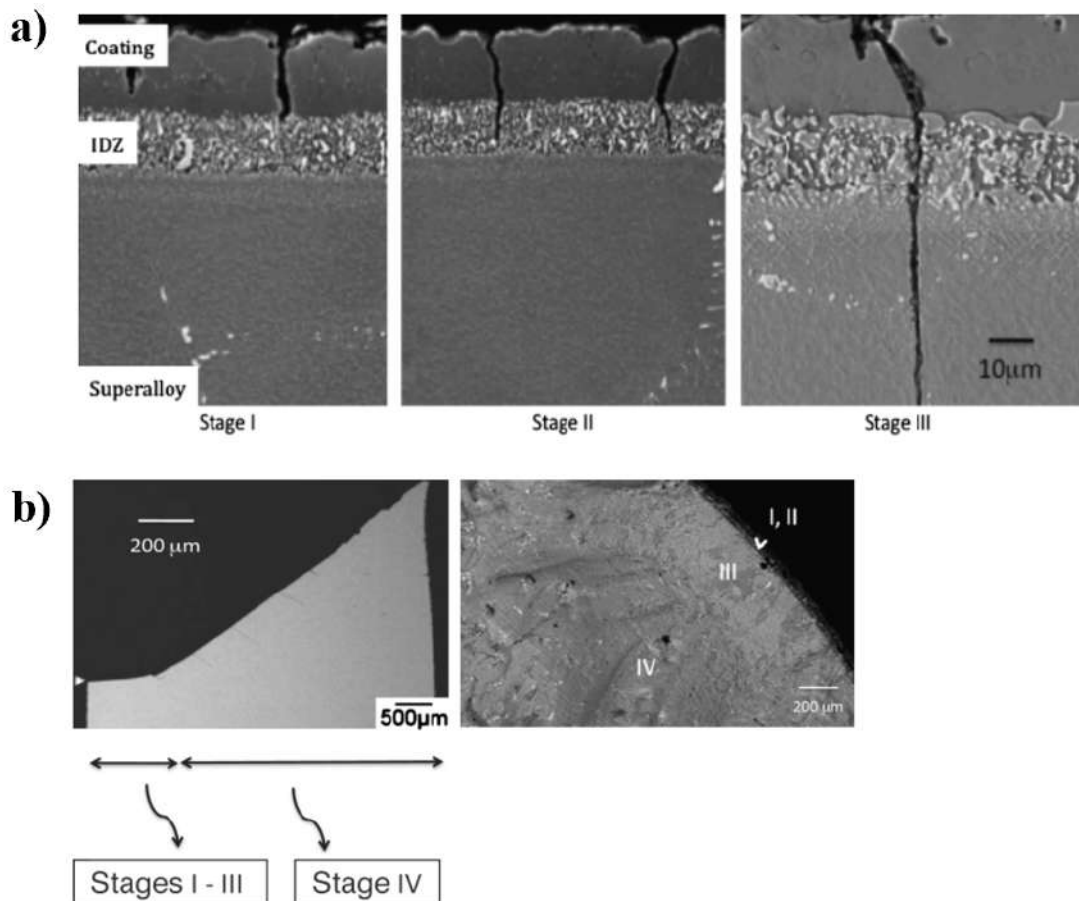


**Figure I-39** The first three stages of crack progression with cracking in the Pt aluminide bond coat (Stage I), interdiffusion zone (Stage II), and superalloy substrate (Stage III). Rene N5 was tested at 982 °C in strain-controlled conditions (a). Longitudinal section through a sample

showing the four stages of failure, with an inclined crack causing final failure in Stage IV (b), adapted from (Pollock et al., 2011).

To model the mechanism governing oxidation-assisted low cycle fatigue of superalloys, Evans et al. (Evans et al., 2009) have mechanically described the damage: (i) After a few straining cycles, tensile stress develops during the de-straining phase of the cycle because of creep illustrated in **Figure I-40**. (ii) This stress opens cracks in the material and exposes the surfaces to the atmosphere, causing thermal growth oxides (TGO). (iii) Dilatation occurs upon converting the alloy to oxide, with an associated strain rate that induces compressive growth stresses illustrated in **Figure I-40**. Finally, (iv) after that, during the re-straining phase of the cycle, a transverse extension of the substrate induces in-plane tension in the TGO, which “pushes” the TGO into the substrate along the crack front.

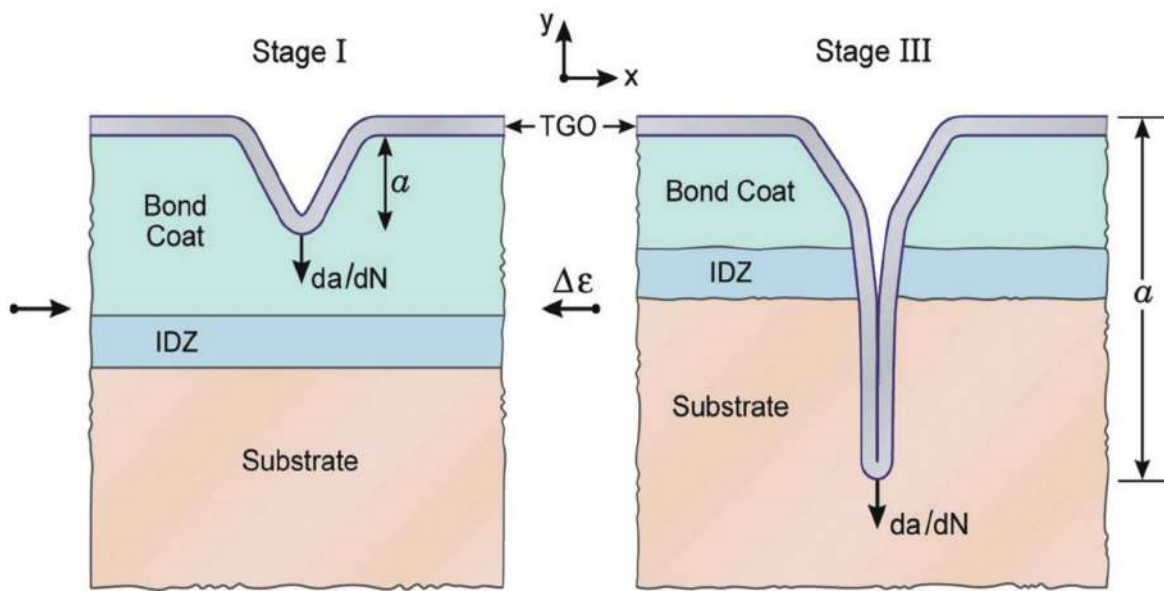


**Figure I-40** Two stages of development of a fatigue crack. V-shaped stage I cracks contained within the bond coat, and stage III parallel-sided cracks within the substrate, (Evans et al., 2009).

The creep and the fatigue strength were investigated by Riallant (Riallant, 2014), focusing on the system AM1/NiAlPt/TBC. Indeed, the low cycle fatigue damage is naturally linked with the plastic deformation; thus, the fatigue strength is intrinsically influenced by the creep effect, relating to the strain waveshape (Okazaki, 2001). At temperatures of 950 °C, it was observed that due to the test conditions, it is mainly the cracking mechanism at the substrate/bond coat that controls the coating

damage, i.e., the deformation and the substrate damage mainly control the creep rupture. However, under fatigue, the cracking mechanism at the bond coat triggers the sample failure.

Thus, changes in the strength of the coating layers and substrate strongly influence the crack propagation rates. *As the strength of the bond coat and IDZ approach that of the superalloy substrate strength, the rate of crack advance is substantially reduced* (Pollock et al., 2011).

#### 4.5.2. Fatigue at (very) high frequencies

Cervellon et al. (Cervellon et al., 2021) have investigated the damage mechanism of CMSX-4 SX superalloy coated with a MCrAlY bond coat which was applied on grit-blasted substrate surface. Tests were performed at  $R_e = -1/1,000$  °C and  $f = 20$  kHz (**Figure I-41**).

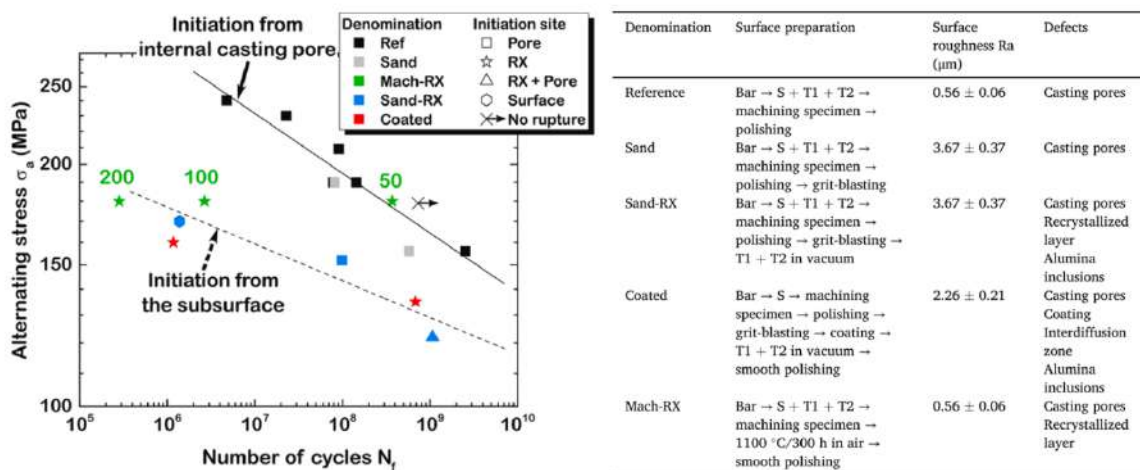


**Figure I-41** S-N diagram of CMSX-4 with different surface treatments (see table in the figure). The number close to the star symbol refers to the depth of the recrystallized layer in  $\mu\text{m}$ . Sand-RX and coated specimens have a recrystallized layer of about  $30 \mu\text{m}$  (Cervellon et al., 2021).

She reached two interesting conclusions. (i) The fatigue life of NiCoCrAlYTa coated CMSX-4 specimens is reduced compared to the uncoated specimens under high alternating stresses and inside the HCF/VHCF scatter band when lowering the stress amplitude, see **Figure I-41**. This is because the crack initiation occurs in the coating, and the IDZ governs the propagation and most of the fatigue life. The damage is accumulated by grain boundary oxidation-induced cracking and internal nitride precipitation in the recrystallized layer. (ii) As already seen for LCF tests (Ma et al.,

2019), an *RX layer thicker than the largest casting pore acts as the main crack initiation site and reduces the fatigue life without any influence of the environment*. Without surface RX, the environmental degradation does not affect the rupture mode or fatigue life. Coupled with an RX layer, the roughness that is introduced by grit-blasting degrades the fatigue life by accelerating the initiation and propagation of surface cracks, leading to stress concentration and final rupture along crystallographic planes. It is also shown that a surface RX of up to 50 – 60  $\mu\text{m}$  in thickness does not seem to affect VHCF life in these conditions.

A schematic model for both conclusions is proposed and is presented in **Figure I-42**.

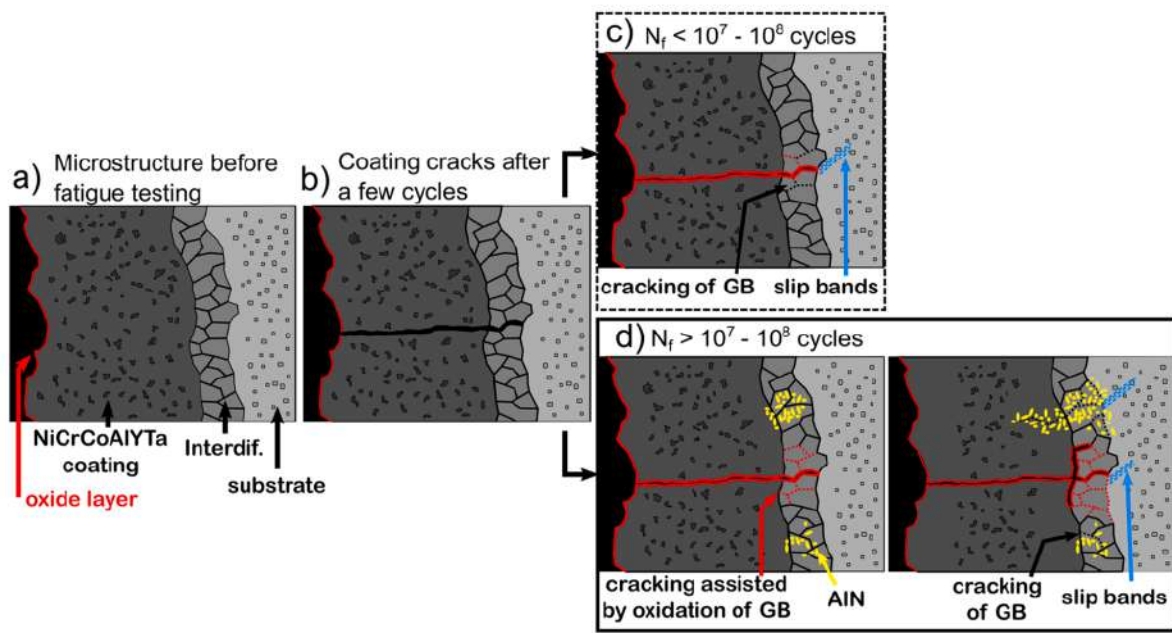


**Figure I-42** Schematic representation of damage mechanisms involved during VHCF in a NiCoCrAlYTa coated CMSX-4 (Cervellon et al., 2021).

#### 4.5.3. Summary

The coating reduces lifetime by crack initiation at coating features, especially at temperatures involving a brittle behavior of the bond-coat. At high temperatures, the main issue is the bond coat/substrate interface that turns out to be the main crack initiation site. Indeed, the coating may control the fatigue life whatever the solidification type of the substrate or even the HIP treatment effect on casting pores. To finish, a significant point to remember is the reduction of the load-

bearing section of the superalloy due to interdiffusion between the coating and the substrate that affects the creep, tensile, and LCF properties of Ni-based SX superalloys.

## **5. Summary and objectives**

Until recently, the alloy design strategies have been developed to increase the high temperature mechanical strength with less emphasis on the environmental resistance. The alloying philosophy has been that the protective coatings will overcome any requirement for achieving high temperature strengths. However, the coatings degrade over time in service, exposing the blade's bare surface to the engine's oxidizing and corrosive environment. Therefore, a deeper investigation of the time-dependent damage of coated systems is essential.

Within this context, the thesis work is dedicated to studying the (possible) oxidation contribution to the fatigue behavior under high temperatures of several superalloys from different generations, solidified by different methods, heat-treated employing different techniques and with and without coating. Therefore, the literature review could depict the main background studies so that the reader could be more familiar with the arguments mentioned in the following chapters.

The main question guiding the results and the discussion of the present work is the crack initiation transition from internal sites to the surface of Ni-based SX superalloys under cyclic loading and at high temperature. Even though the main conclusion of the literature review remains that the casting pore is critical in fatigue of bare Ni-based SX samples, the surface crack initiation seems to be triggered under specific conditions:

- At fixed stress ratio and low/moderate temperatures, the most critical internal defect controls the crack initiation site in very high frequencies conditions. The higher the temperature, the higher the contribution of oxidation, increasing the probability to have failure from the surface.
- By decreasing the stress/strain amplitude under the same temperature, very high frequencies, and fully reversed loading, higher number of cycles are obtained leading to a higher contribution of oxidation.
- For the coated samples, the higher the temperature, the weaker the influence of the coating on the durability of the system at low frequencies. Furthermore, the IDZ/SRZ will control the fatigue life at high temperatures and high frequencies.

Thus, many parameters like the solidification velocity, the heat treatment, the coating, the temperature, the stress ratio, the environment, and the frequencies impact the transition in crack initiation from internal defects to the sub-surface and then to the surface. Since there is a more detailed background on the fatigue properties and the crack initiation mechanisms of Ni-based SX superalloys tested in LCF compared to VHCF at high temperatures, and since VHCF characterization is essential to the design of rotating airfoils, this thesis work is mainly centered on the fatigue crack mechanism under very high frequencies.

# **Chapter II. Materials and experimental procedures**



# Matériaux étudiés et les procédures expérimentales

Ce chapitre décrit les procédures expérimentales utilisées pour caractériser les propriétés en fatigue à haute température de divers superalliages SX à base de Ni.

La première sous-section du chapitre décrit dix superalliages base Ni monogranulaires solidifiés par la méthode Bridgman, LMC ou PBF-E : MAR-M200 +Hf SX, AM1 de 1<sup>ère</sup> génération, Rene N5 et CMSX-4 de 2<sup>ème</sup> génération, ERBO/1, DD33, CMSX-4 Plus de 3<sup>ème</sup> génération, MC-NG, TMS-238 et TROPEA.

Les traitements de mise en solution, vieillissement et de compression isostatique à chaud appliqués (le cas échéant) et l'analyse de la microstructure  $\gamma/\gamma'$  « telle que reçue » et des micrographies de divers défauts ont été également présentés. Ensuite ce chapitre présente les paramètres de polissage de surface et le traitement/paramètres de dépôt des revêtements utilisés.

Le sujet de cette thèse est lié à l'amorçage des fissures de fatigue. Ainsi, il détaille deux machines de fatigue, une Instron 8562 électromécanique et un banc de fatigue ultrasonore. Des essais oligocyclique (0.5 Hz) ont été effectués à l'air, à 900 °C et 950 °C et à rapport de charge positif ( $R_\sigma = 0.05$ ). Des essais de traction ont été réalisés à l'air et à 900 et 950 °C pour permettre un choix des contraintes maximales appliquées en fatigue oligocyclique. D'autre part, des essais de fatigue gigacyclique (20 kHz) ont été effectués à l'air, à 1,000 °C et dans des conditions alternées ( $R_\epsilon = -1$ ). Le **Tableau 1** précise les essais mécaniques réalisés pour chaque superalliage base Ni monogranulaire.

La dernière sous-section décrit les principales caractérisations utilisées pour analyser les surfaces de rupture, la microstructure et les essais interrompus. Il décrit les équipements employés, les paramètres et la préparation des échantillons, en allant des techniques classiques telles que la microscopie optique et électronique à balayage (MEB), à des techniques plus spécifiques comme la spectroscopie à rayons X à dispersion d'énergie (EDS) et la diffraction des électrons rétrodiffusés (EBSD) sous MEB.

*Tableau 1 Synthèse des essais mécaniques relatifs à chaque superalliage base Ni monogranulaires. Traitement thermique (TT) et Revenus (R).*

<b>MAR-M200 +Hf SX</b>	Solidifié par la méthode Bridgman <ul style="list-style-type: none"> <li>▪ <b>Eprouvettes nues</b></li> <li>▪ <b>Eprouvettes revêtues via Slurry : TT + R1 + R2 + TT diffusion</b></li> </ul>	<b>Essais mécaniques :</b> <b>Traction : <math>5 \cdot 10^{-4} \text{ s}^{-1}</math> et <math>900 \text{ }^\circ\text{C}</math></b> <b>Fatigue oligocyclique : 0.5 Hz, <math>R_\sigma = 0.05</math> et <math>900 \text{ }^\circ\text{C}</math></b>
<b>AM1</b>	Solidifié par la méthode Bridgman <ul style="list-style-type: none"> <li>▪ <b>Eprouvettes nues</b></li> <li>▪ <b>Eprouvettes revêtues via Slurry et APVS : TT + TT diffusion + TT <math>\gamma'</math> optimisation</b></li> <li>▪ <b>Eprovettes revêtues via APVS: As-cast + TT diffusion</b></li> </ul>	<b>Essais mécaniques :</b> <b>Traction : <math>5 \cdot 10^{-4} \text{ s}^{-1}</math> et <math>950 \text{ }^\circ\text{C}</math></b> <b>Fatigue oligocyclique : 0.5 Hz, <math>R_\sigma = 0.05</math> et <math>950 \text{ }^\circ\text{C}</math></b> <b>Fatigue gigacyclique : 20 kHz, <math>R_\varepsilon = -1</math> et <math>1,000 \text{ }^\circ\text{C}</math></b>
<b>Rene N5</b>	Solidifié par la méthode Bridgman <ul style="list-style-type: none"> <li>▪ <b>Eprouvettes nues</b></li> <li>▪ <b>Eprouvettes revêtues via Slurry et APVS : TT + TT diffusion + TT <math>\gamma'</math> optimisation</b></li> </ul>	<b>Essais mécaniques :</b> <b>Traction : <math>5 \cdot 10^{-4} \text{ s}^{-1}</math> et <math>950 \text{ }^\circ\text{C}</math></b> <b>Fatigue oligocyclique : 0.5 Hz, <math>R_\sigma = 0.05</math> et <math>950 \text{ }^\circ\text{C}</math></b> <b>Fatigue gigacyclique : 20 kHz, <math>R_\varepsilon = -1</math> et <math>1,000 \text{ }^\circ\text{C}</math></b>
<b>CMSX-4</b>	Solidifié par la méthode Bridgman <ul style="list-style-type: none"> <li>▪ <b>Eprouvettes revêtues via Slurry : TT + R1 + R2 + TT diffusion</b></li> </ul>	<b>Essai mécanique :</b> <b>Fatigue gigacyclique : 20 kHz, <math>R_\varepsilon = -1</math> et <math>1,000 \text{ }^\circ\text{C}</math></b>
<b>ERBO/1</b>	Solidifié par la méthode Bridgman <ul style="list-style-type: none"> <li>▪ <b>Eprouvettes nues</b></li> <li>▪ <b>TT Classique</b></li> <li>▪ <b>CIC intégré</b></li> </ul>	<b>Essai mécanique :</b> <b>Fatigue gigacyclique : 20 kHz, <math>R_\varepsilon = -1</math> et <math>1,000 \text{ }^\circ\text{C}</math></b>
<b>CMSX-4</b>	Solidifié par la méthode PBF-E <ul style="list-style-type: none"> <li>▪ <b>Eprouvettes nues</b></li> <li>▪ <b>TT Classique</b></li> <li>▪ <b>CIC intégré</b></li> </ul>	<b>Essai mécanique :</b> <b>Fatigue gigacyclique : 20 kHz, <math>R_\varepsilon = -1</math> et <math>1,000 \text{ }^\circ\text{C}</math></b>
<b>DD33</b>	Solidifié par la méthode Bridgman <ul style="list-style-type: none"> <li>▪ <b>Eprouvettes nues</b></li> <li>▪ <b>TT Classique</b></li> <li>▪ <b>TT + CIC</b></li> </ul>	<b>Essai mécanique :</b> <b>Fatigue gigacyclique : 20 kHz, <math>R_\varepsilon = -1</math> et <math>1,000 \text{ }^\circ\text{C}</math></b>
	Solidifié par la méthode LMC <ul style="list-style-type: none"> <li>▪ <b>Eprouvettes nues</b></li> <li>▪ <b>TT Classique</b></li> </ul>	<b>Essai mécanique :</b> <b>Fatigue gigacyclique : 20 kHz, <math>R_\varepsilon = -1</math> et <math>1,000 \text{ }^\circ\text{C}</math></b>
<b>CMSX-4 Plus</b>	Solidifié par la méthode Bridgman <ul style="list-style-type: none"> <li>▪ <b>Eprouvettes nues</b></li> <li>▪ <b>Eprouvettes revêtues via Slurry : TT + R1 + R2 + BC TT diffusion</b></li> </ul>	<b>Essai mécanique :</b> <b>Fatigue gigacyclique : 20 kHz, <math>R_\varepsilon = -1</math> et <math>1,000 \text{ }^\circ\text{C}</math></b>
	Solidifié par la méthode Bridgman <ul style="list-style-type: none"> <li>▪ <b>Eprouvettes nues</b></li> <li>▪ <b>TT Classique</b></li> <li>▪ <b>TT+ CIC</b></li> </ul>	<b>Essai mécanique :</b> <b>Fatigue gigacyclique : 20 kHz, <math>R_\varepsilon = -1</math> et <math>1,000 \text{ }^\circ\text{C}</math></b>
<b>MC-NG</b>	Solidifié par la méthode Bridgman <ul style="list-style-type: none"> <li>▪ <b>Eprouvettes nues</b></li> <li>▪ <b>TT Classique</b></li> <li>▪ <b>TT + CIC</b></li> </ul>	<b>Essai mécanique :</b> <b>Fatigue gigacyclique : 20 kHz, <math>R_\varepsilon = -1</math> et <math>1,000 \text{ }^\circ\text{C}</math></b>

---

<b>TMS-238</b>	Solidifié par la méthode Bridgman <ul style="list-style-type: none"><li>▪ <b>Eprouvettes nues</b></li><li>▪ <b>TT Classique</b></li></ul>	<b>Essai mécanique :</b> <b>Fatigue gigacyclique : 20 kHz, <math>R_\epsilon</math></b> <b>= -1 et 1,000 °C</b>
<b>TROPEA</b>	Solidifié par la méthode Bridgman <ul style="list-style-type: none"><li>▪ <b>Eprouvettes nues</b></li><li>▪ <b>TT Classique</b></li></ul>	<b>Essai mécanique :</b> <b>Fatigue gigacyclique : 20 kHz, <math>R_\epsilon</math></b> <b>= -1 et 1,000 °C</b>

---



## 1. Introduction

This chapter describes the experimental procedures used to characterize the fatigue properties at high temperatures of various Ni-based SX superalloys.

The chapter's first sub-section describes ten Ni-based SX superalloys processed by Bridgman, LMC, or PBF-E method. The applied solution heat treatment, aging, and HIP treatments (if any) and the stereological analysis of the "as-received"  $\gamma/\gamma'$  microstructure and various defects micrographs are also presented. While **Chapter III** investigates the bare substrate, **Chapter IV** explores bond-coated samples. This chapter thus presents the surface polishing parameters and the employed BC processing/deposition.

The second sub-section presents the mechanical testing machines and tests conditions. It details two fatigue machines, an electro-mechanical Instron 8562 and an ultrasonic fatigue bench.

The last sub-section depicts the main characterization techniques employed to analyze the fracture surfaces and the microstructure. It describes the equipment, the parameters, and the samples preparation, opening with the classical techniques like optical and electronic microscopy, to more specific like Energy Dispersive X-ray Spectrometry (EDS) and Electron Backscatter Diffraction (EBSD).

## 2. Superalloys and bond coat details

Ten Ni-based SX superalloys have been used in this Ph.D. work. Five industrial superalloys are currently employed in the aircraft engines industry as turbine blades and vanes. MAR-M200 +Hf SX, AM1 from 1<sup>st</sup> generation, Rene N5 and CMSX-4 from 2<sup>nd</sup> generation, and CMSX-4 Plus from 3<sup>rd</sup> generation. The rods were provided by Safran Aircraft Engines (SAE) (MAR-M200 +Hf SX samples remaining from Mataveli Suave thesis project (Mataveli Suave, 2017)/ AM1/Rene N5), Safran Helicopter Engines (CMSX-4 samples remaining from Cervellon thesis project (Cervellon, 2018)) and Safran Tech/Cannon-Muskegon (CMSX-4 Plus).

Five of the superalloys (out of the ten studied) are primarily investigated in the research field. The superalloy inspired by the CMSX-4 chemistry called *Erlangen-Bochum* (ERBO/1) (Lopez-Galilea et al., 2016; Mujica Roncery et al., 2016) rods were kindly provided by its developers, the *Ruhr-University Bochum* (RUB) and the *University of Erlangen-Nürnberg* from Germany. They have also provided us with the CMSX-4 square bars built by the PBF-E method and the HIP treatments carried out for the ERBO/1 and CMSX-4 Plus/Bridgman rods. The *Institute of Metal Research* (IMR) from the *Chinese Academy of Science* provided the DD33 superalloy (Bridgman, LMC, and HIP treated rods) (Yang et al., 2019). The MC-NG samples are remaining from the Cervellon (Cervellon, 2018) thesis project. *National Institute for Materials Science* (NIMS) provided the 6<sup>th</sup> generation TMS-238 rods (Kawagishi et al., 2012). TROPEA is a PGM superalloy developed by Institut P/SAE, and it was kindly provided in this project by SAE (Rame et al., 2020).

The *Laboratoire des Sciences de l'Ingenieur pour l'Environnement* (LaSIE) provided the Slurry-type BC, while SAE provided the industrial BC “*Alumination en Phase Vapeur Snecma*” (APVS) used to protect turbine blades and vanes.

### 2.1. Ni-based SX superalloys chemical composition, solidification, and microstructure details

Each institute solidified the rods using its standard parameters. The industry/laboratories used the classic Bridgman method to solidify MAR-M200 +Hf, AM1, Rene N5, CMSX-4, ERBO/1, DD33 (thermal gradient: 30 - 40 K/mm), CMSX-4 Plus, MC-NG, TMS-238, and TROPEA rods. IMR also solidified the DD33 superalloy using the LMC method (thermal gradient: 80 - 100 K/mm).

The solidification was performed along a  $\approx$  [001] direction, admitting a maximum primary misorientation of  $10^\circ$  concerning the perfect [001] orientation. **Table II-1** depicts the chemical composition of each superalloy studied in the current project.

The MAR-M200 +Hf and MC-NG samples were machined from rods of 12 mm in diameter. AM1, Rene N5, CMSX-4, CMSX-4 Plus, TMS-238, TROPEA, and DD33 samples were machined from rods of 14 mm diameter. CMSX-4 Plus samples were also machined from 40 mm diameter (i.e., inducing larger casting pores) rods. Finally, ERBO/1 plates of 51 x 20 x 55 mm and CMSX-4 square bars of 12 mm edges built by PBF-E technique were provided by German colleagues for machining additional specimens.

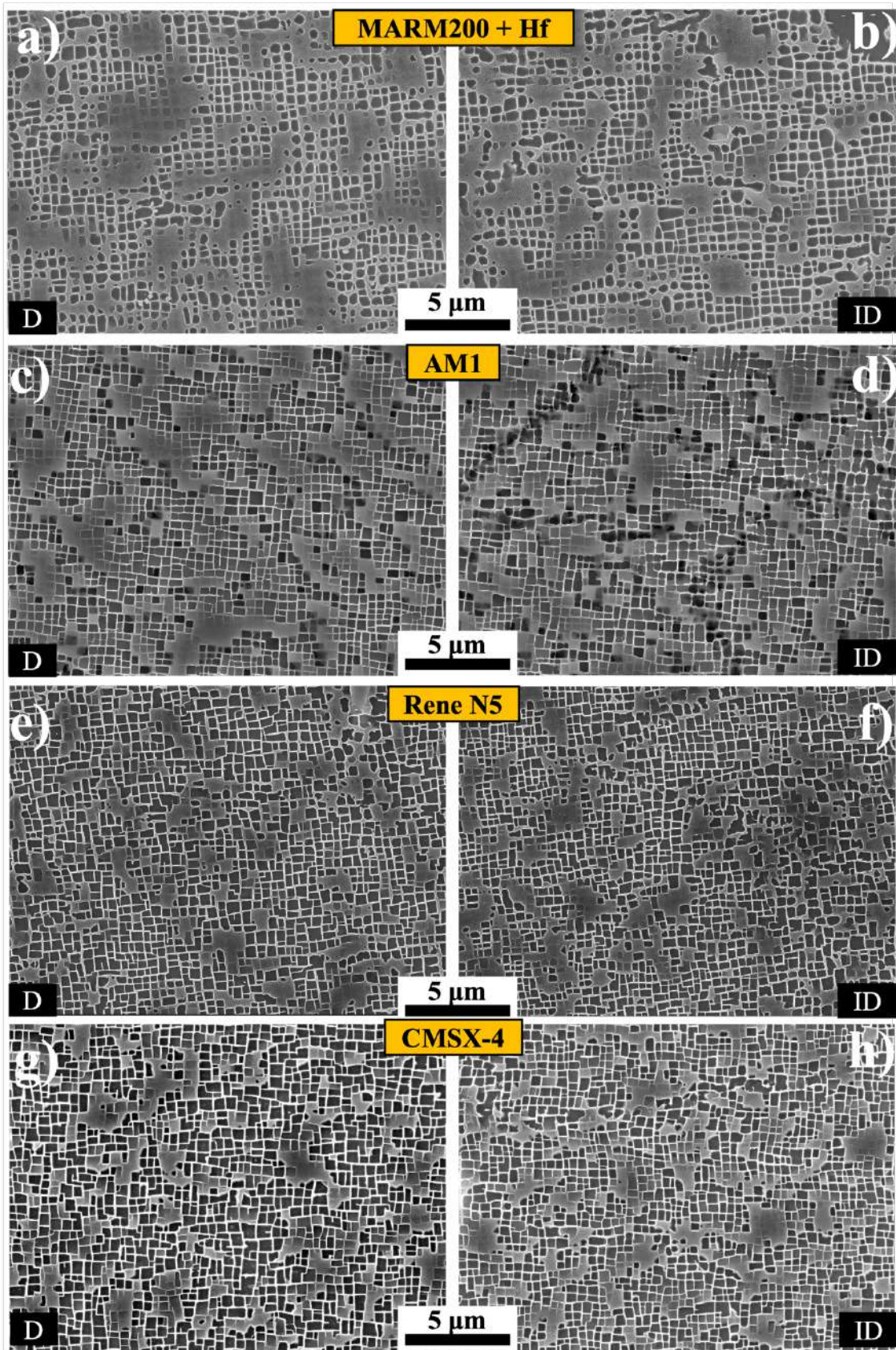
The CMSX-4/PBF-E, CMSX-4 Plus, MC-NG, ERBO/1, and DD33/Bridgman rods were divided into two batches. The first batch received the full HT and the second batch received HIP treatment. **Table II-2** summarizes the rods' solidification, SHT, AG, HIP treatment details. The SHT was carried out under the solidus temperature to avoid incipient melting zones, while the HIP was carried out close to the solidus temperature at RUB. **Figure II-1** illustrates the  $\gamma/\gamma'$  microstructure of the superalloys solidified via the Bridgman method and the microstructure of CMSX-4 PBF-E square bars.

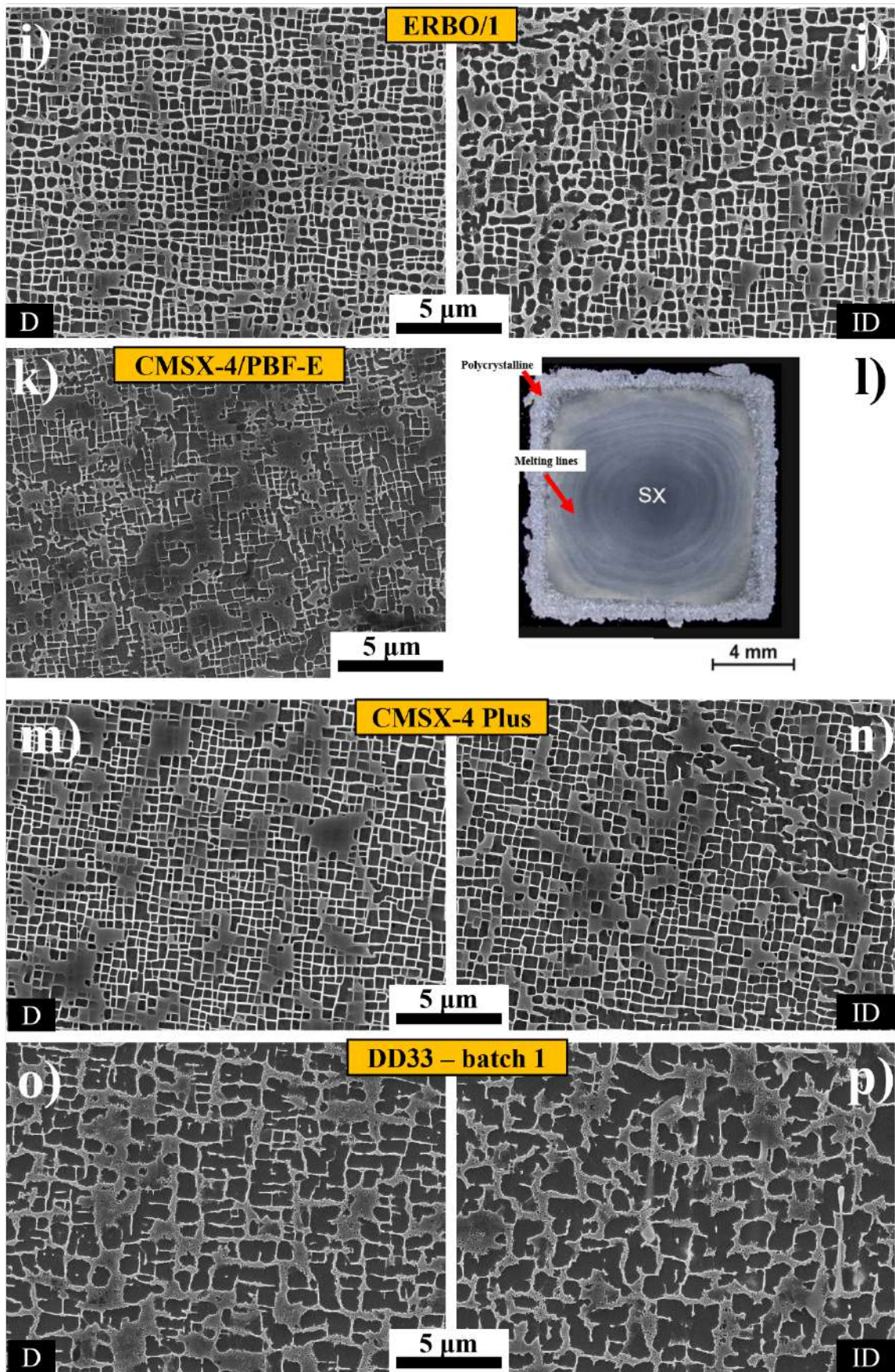
**Table II-1** Chemical composition (wt. pct.) of investigated superalloys. Nickel is the base element for all these alloys.

<b>Gen.</b>	<b>Alloy</b>	<b>Co</b>	<b>Cr</b>	<b>Mo</b>	<b>W</b>	<b>Al</b>	<b>Ti</b>	<b>Ta</b>	<b>Hf</b>	<b>Re</b>	<b>Others</b>	<b>Ref.</b>
	<b>MAR-M200 + Hf</b>	9.5	8.6	2.0	11.8	4.9	1.9	7.9	1.6		0.86 Nb 0.13 C	(Reed, 2006)
<b>1<sup>st</sup></b>	<b>AMI</b>	6.6	7.5	2.0	5.5	5.2	1.2	7.9	0.1			(Davidson et al., 1983)
	<b>Rene N5</b>	8.0	7.0	2.0	5.0	6.2	7.0	7.0	0.2	3.0		(Wukusick and Buchakjian Jr., 1991)
	<b>CMSX-4</b>	9.0	6.5	0.6	6.0	5.6	1.0	6.35	0.1	3.0		(Cervellon, 2018)
<b>2<sup>nd</sup></b>	<b>ERBO/1</b>	9.9	6.6	0.6	6.4	6.2	1.1	6.6	0.08	2.9		(Lopez-Galilea et al., 2016; Ruttart et al., 2016)
	<b>CMSX-4 atomized powder</b>	9.9	6.6	0.6	6.4	6.2	1.1	6.6	0.08	2.9		(Körner et al., 2018)
	<b>DD33</b>	12.0	3.0	1.0	6.0	6.0	8.0	8.0	0.1	4.0		(Yang et al., 2019)
<b>3<sup>rd</sup></b>	<b>CMSX-4 Plus</b>	10.0	3.5	0.6	6.0	5.7	0.9	8.0	0.1	4.8		(Wahl and Harris, 2016)
<b>4<sup>th</sup></b>	<b>MC-NG</b>	<0.2	4.0	1.0	5.0	6.0	0.5	5.0	0.1	4.0	4.0 Ru	(Caron, 2000)
<b>6<sup>th</sup></b>	<b>TMS-238</b>	6.5	4.6	1.1	4.0	5.9	7.6	7.6	0.1	6.4	5.0 Ru	(Kawagishi et al., 2012)
	<b>TROPEA</b>	8.9	6.4	0.6	6.1	5.4	1.0	9.1	0.08	1.0	1.95 Pt	(Rame and Cormier, 2019)

**Table II-2** Solidification method, heat treatment, and aging parameters of Ni-based SX superalloys investigated in the thesis work. AQ denotes for air quench.

Superalloy	Solidification method	Rods $\varnothing$ (mm)	Heat Treatment	Aging	Origin
MAR-M200 + Hf/SX	Bridgman	12	30 min/1,210 °C + 30 min/1,225 °C + 4 h/1,240 °C + cooling $\geq 45$ °C.min <sup>-1</sup> to 700 °C/AQ	4 h/1,100 °C/AQ + 16 h/870 °C/AQ	SAE
AMI	Bridgman	14	3 h/1300 °C/AQ	5 h/1,100 °C + 16 h/870 °C/AQ	SAE
Rene N5	Bridgman	14	1,150°C (0.7 °C.min <sup>-1</sup> ) $\rightarrow$ 1,270 °C + 1270 °C (1 °C.min <sup>-1</sup> ) $\rightarrow$ 1,300 °C + 2h/1,300 °C/AQ	6 h/1,080 °C + 4 h/900 °C/AQ	SAE
CMSX-4	Bridgman	14	3 h/1,296 °C + 3 h/1,304 °C + 2 h/1,313 °C + 2 h/1,316 °C + 2 h/1,318 °C + 2 h/1,321 °C/AQ	4 h/1,100 °C/AQ + 16 h/870 °C	Safran H. Eng.
ERBO/I	Bridgman	Plates of 51 x 20 x 55 mm	1 h/1,290 °C (20 °C.min <sup>-1</sup> ) + 6 h/1,300 °C (150 °C.min <sup>-1</sup> ) $\rightarrow$ 800 °C/AQ 1 h/1,290 °C (20 °C.min <sup>-1</sup> ) + 6 h/1,300 °C (150 °C.min <sup>-1</sup> ), 100 MPa Ar pressure/AQ	4 h/1,140 °C/AQ + 16 h/870 °C/AQ	RUB
CMSX-4	PBF-E	Square bars of 12 mm edge	35 min/1,315 °C/AQ QH-9HIP at 35 min/1,315 °C, 100 MPa Ar pressure/AQ	2 h/1,140 °C/AQ + 20 h/870 °C/AQ	Erlangen RUB
DD33	Bridgman	14	4 h/1,310 °C, 120 MPa + 10 h/1,325 °C/AQ	4 h/1,180 °C.AC + /24 h/870 °C/AQ	IMR
CMSX-4 Plus	Bridgman	14	15 h/1,340 °C/AQ	3 h/1,163 °C/AQ + 4 h/1,100 °C/AQ + 20 h/870 °C/AQ	Safran Tech HIP: RUB
MC-NG	Bridgman	12	QH-9 HIP at 12 h/1,345 °C/ + 3 h/1,350 °C, 100 MPa Ar pressure/AQ 1,310°C (3 °C.h <sup>-1</sup> ) $\rightarrow$ 3 h/1,340 °C/AQ 1,310°C (3 °C.h <sup>-1</sup> ) $\rightarrow$ 3 h/1,340 °C/AQ + 2 h/1,310 °C, 100 MPa Ar pressure/AQ	4 h/1,100 °C/AQ + 16 h/870 °C/AQ	SAE HIP: Bodycote
TMS-238	Bridgman	14	1 h/1,300 °C + 1 h/1,310 °C + 3 h/1,335 °C + 20 h/1,345 °C/AQ	2 h/1,150 °C/AQ + 20 h/870 °C/AQ	NIMS
TROPEA	Bridgman	14	1,200 (2 °C.min <sup>-1</sup> ) $\rightarrow$ 1,300 °C + 24 h/1,300 °C/AQ	1 h/1,200 °C/AQ + 16 h/870 °C/AQ	Institut P/SAE





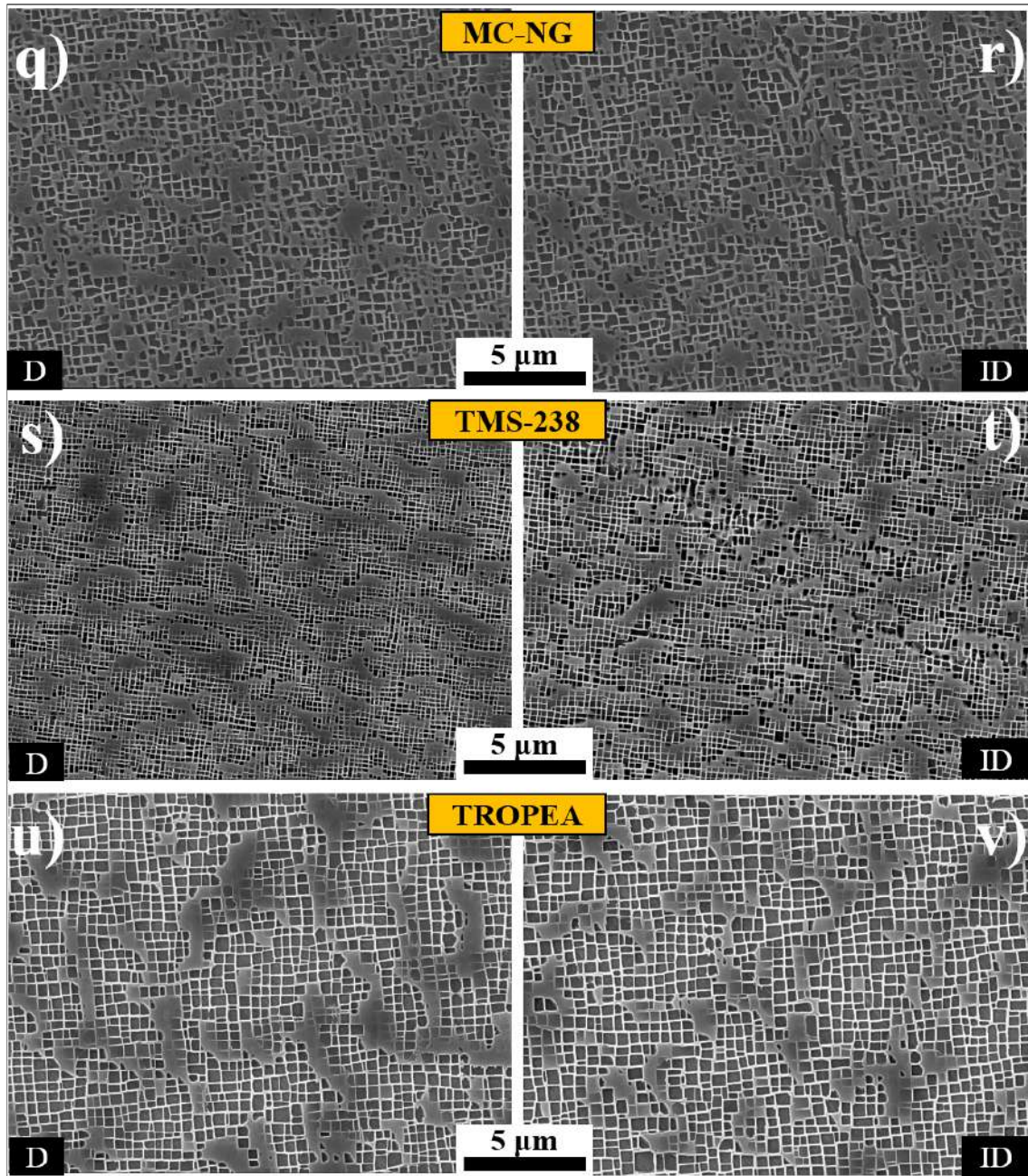


**Figure II-1**  $\gamma/\gamma'$  microstructure in the primary dendrite arms (D) and interdendrite zones (ID) of full HT superalloys: MAR-M200 +Hf (a and b resp.), AM1 (c and d resp.), Rene N5 (e and f resp.), CMSX-4 (g and h resp.), ERBO/1 (i and j resp.), DD33 (m and n resp.), CMSX-4 Plus (o and p resp.), MC-NG (q and r resp.), TMS-238 (s and t resp.), TROPEA (u and v resp.) solidified by Bridgman method, and CMSX-4 built via PBF-E (k and l). Observations performed in a  $\approx (001)$  plane.

Each superalloy's microstructure presents a particular size of  $\gamma'$  precipitate in the DZ and IZ. **Table II-3** summarizes the stereological analyses performed. Several superalloys have eutectics (Rene N5, DD33, and TROPEA), carbides (MAR-M200 + Hf SX, Rene N5, and DD33), high density of dislocations (CMSX-4 built via PBF-E), and most of them have casting pores. For example, CMSX-4 built via PBF-E presented pores diameter  $< 5 \mu\text{m}$  (Chauvet et al., 2018b).

**Table II-3** Defects encountered in the superalloy microstructure. *Y* for the presence and *N* for the absence of the specific defect.

<i>Superalloy</i>	<i>Casting pore</i>	<i>Eutectics</i>	<i>Carbides</i>	<i>High density of dislocations</i>
<b><i>Solidification via Bridgman method</i></b>				
<i>MAR-M200 +Hf SX</i>	<i>Y</i>	<i>N</i>	<i>Y</i>	<i>N</i>
<i>AMI</i>	<i>Y</i>	<i>N</i>	<i>N</i>	<i>N</i>
<i>Rene N5</i>	<i>Y</i>	<i>Y</i>	<i>Y</i>	<i>N</i>
<i>ERBO/1</i>	<i>Y</i>	<i>N</i>	<i>N</i>	<i>N</i>
<i>CMSX-4</i>	<i>Y</i>	<i>N</i>	<i>N</i>	<i>N</i>
<i>DD33</i>	<i>Y</i>	<i>Y</i>	<i>Y</i>	<i>N</i>
<i>CMSX-4 Plus</i> ( $\varnothing$ 14 and 40 mm)	<i>Y</i>	<i>N</i>	<i>N</i>	<i>N</i>
<i>MC-NG</i>	<i>Y</i>	<i>N</i>	<i>N</i>	<i>N</i>
<i>TMS-238</i>	<i>Y</i>	<i>N</i>	<i>N</i>	<i>N</i>
<i>TROPEA</i>	<i>Y</i>	<i>Y</i>	<i>N</i>	<i>N</i>
<b><i>Solidification via LMC method</i></b>				
<i>DD33</i>	<i>Y</i>	<i>N</i>	<i>Y</i>	<i>N</i>
<b><i>PBF-E method</i></b>				
<i>CMSX-4</i>	<i>N</i>	<i>N</i>	<i>N</i>	<i>Y</i>
<b><i>HIP</i></b>				
<i>ERBO/1</i>	<i>Compacted</i>	<i>N</i>	<i>N</i>	<i>Y</i>
<i>CMSX-4/PBF-E</i>	<i>N</i>	<i>N</i>	<i>N</i>	<i>Y</i>
<i>CMSX-4 Plus</i>	<i>Compacted</i>	<i>N</i>	<i>N</i>	<i>N</i>
<i>DD33</i>	<i>Compacted</i>	<i>N</i>	<i>Y</i>	<i>N</i>
<i>MC-NG</i>	<i>Compacted</i>	<i>N</i>	<i>N</i>	<i>N</i>

**Figure II-2** illustrates the several microstructural defects encountered in the superalloys before and after the full HT. **Figure II-2a** shows the dendrite (red square) and the interdendritic spacings (yellow square) of a CMSX-4 Plus as-cast microstructure. **Figure II-2b** depicts the casting pore (red arrow) size and morphology and the presence of  $\gamma/\gamma'$  eutectics pools (yellow arrow) in the interdendritic spacings. **Figure II-2c** and **d** compare the casting pore (red arrow) morphology in the fully heat treated state and after HIP treatment (black arrow), respectively. **Figure II-2e** and **f**

illustrate the DD33 features after the full HT. A carbide is indicated by the green arrow, the  $\gamma/\gamma'$  eutectic by the yellow arrow, and the RX feature by the blue arrow.

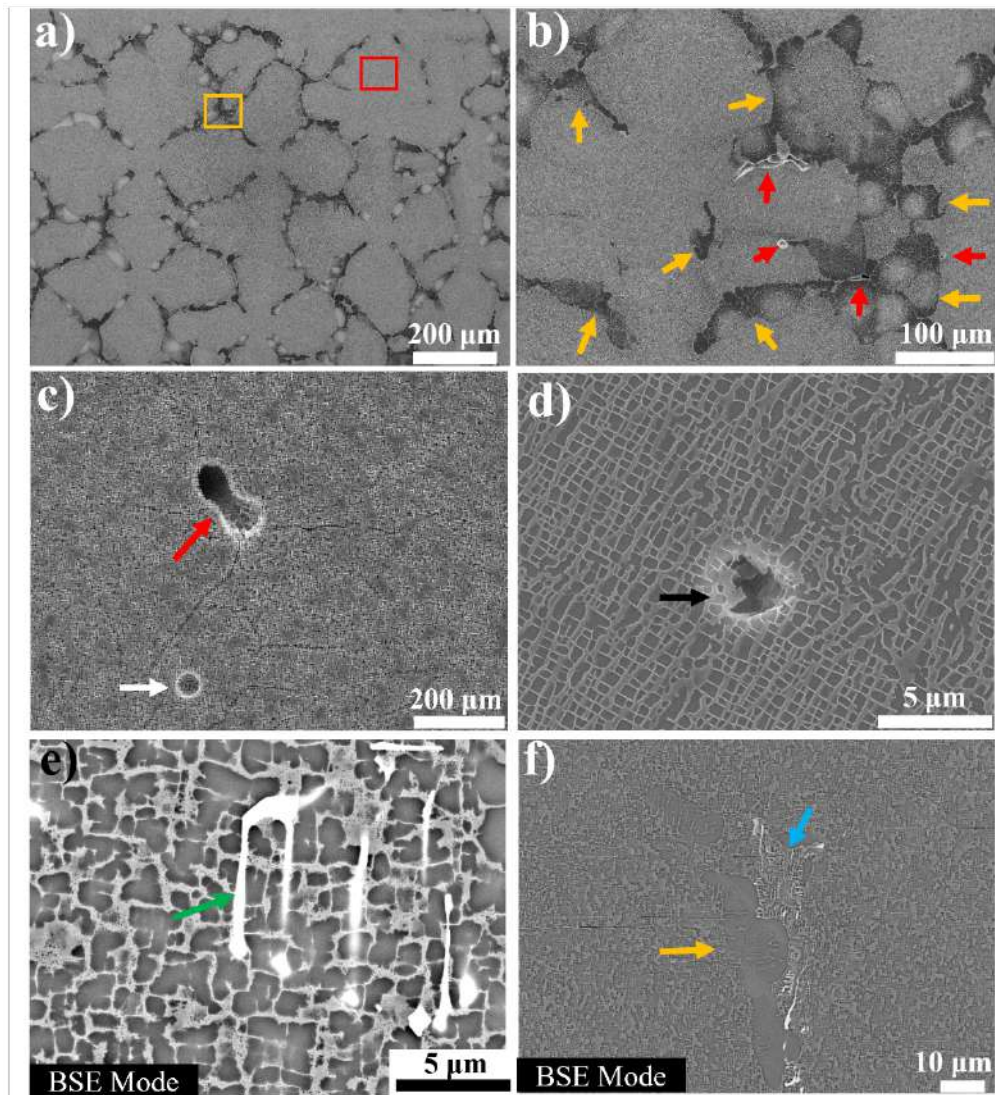


**Figure II-2** Example of CMSX-4 Plus as-cast microstructure emphasizing the dendrite (red square) and the interdendritic spacings (yellow square) (a). Higher magnification of as-cast microstructure illustrating the solidification pores (red arrows) and the  $\gamma/\gamma'$  eutectics pools (yellow arrows) before the SHT (b). Casting pore (red arrow) and homogenization pore (white arrow) after the full HT of ERBO/1 (c). Casting pore morphology after the ERBO/1 HIP treatment (black arrow) (d). An example of carbide after the full HT of DD33 batch 1 (green arrow) (e). A  $\gamma/\gamma'$  eutectic after the full HT of DD33 batch 1 (yellow arrow). A recrystallized zone (blue arrow) around the  $\gamma/\gamma'$  eutectic (yellow arrow) is surrounded by the carbides (f). All images were taken in SEI mode, except (e) and (f) which were taken in BSE mode.

The samples were extracted from SX rods by electro-discharge machining and subsequent machining to reach the final shape. CMSX-4 built via PBF-E does not have the classic SX rod shape. Instead, it has a central (bulk) single-crystalline part and radial grains at the surface (**Figure II-1j**). As a result, it increased the difficulty of machining heterogeneous structures. However, thanks to careful machining steps performed by the technical staff from our machining shop at Institut Pprime, it has been possible to avoid the polycrystalline zone in VHCF specimens.

The dimensions of the fatigue and creep specimens are detailed in **Figure II-3**. 0.2 mm thickness from the original diameter was systematically removed from each fatigue/creep sample by SiC grinding to remove residual stresses inherited from the machining steps. This step is essential to avoid possible surface recrystallization during the fatigue tests at high temperatures. The specimens tested without BC were then gently ground and polished until final mirror polish (1  $\mu\text{m}$  diamond suspension) with the final steps parallel to the loading axis.



## 2.2. Bond coat characteristics

Several samples machined from MAR-M200 +Hf, AM1, Rene N5, CMSX-4, and CMSX-4 Plus rods were bond coated with a NiAl BC developed by LaSIE via the Slurry route. The aluminide BC diffused thanks to AG heat treatments (1 h/400 °C + 2 h/700 °C + 2 h/1,100 °C/AQ), and creates an external layer of  $\alpha$ -Al<sub>2</sub>O<sub>3</sub>. Indeed, the  $\alpha$ -Al<sub>2</sub>O<sub>3</sub> layer provides a small thermal barrier insulation, an intermediate thermal oxide based on alumina, and an internal Al-rich  $\beta$ -NiAl diffusion coating (Galetz et al., 2014; Grégoire et al., 2019; Pedraza et al., 2012; Rannou et al., 2014).

Furthermore, several samples machined from AM1 and Rene N5 rods were coated by an industrial NiAl BC via the APVS technique. The method implies the coating application throughout a halogen gas and the diffusion through one-step HT (6 h/1,080 °C/AQ).

AM1 and Rene N5 rods were solution heat-treated but not aged before the BC deposition (**Table II-2**). Thus, these samples were aged to ensure a desired  $\gamma'$  precipitates size after the coating deposition. Further, one batch of AM1 samples without SHT (i.e., as-cast microstructure) was coated via the APVS method. These samples were not aged after the diffusion treatment, and the samples were polished/prepared at Safran Aircraft Engines. Finally, MAR-M200 +Hf, CMSX-4, and CMSX-4 Plus were fully HT before the BC deposition.

Before BC deposition, the specimens were polished with 180 SiC abrasive paper to remove 0.2 mm from the original surface. The specimens were not further polished, intending to achieve a roughness equivalent to the one obtained after an industrial sand-blasting.

The roughness (Ra) was measured with a profilometer (Someco) equipped with a diamond stylus according to the ISO4287 standard. Samples presented roughness of 0.103  $\mu$ m after 1  $\mu$ m diamond paste polishing, 1.331  $\mu$ m after coating via APVS, and 2.004  $\mu$ m after coating via the Slurry method. The roughness is not affected by the supplementary HT applied to optimize the  $\gamma'$  precipitate size distribution. **Table II-4** summarizes the polishing and the HT details before and after the BC deposition.

*Table II-4 Heat treatment parameters of the investigated coated superalloys.*

<i>Superalloy</i>	<i>Polishing</i>	<i>HT before the coat deposition</i>	<i>Deposition method</i>	<i>HT → Coating diffusion</i>	<i>HT → <math>\gamma'</math> size</i>
<b>MAR-M200 + Hf</b>	x180	SHT + R1 + R2	Slurry	1 h/400 °C + 2 h/700 °C + 2 h/1,100 °C/AQ	<b>x</b>
	x180	SHT	Slurry	1 h/400 °C + 2 h/700 °C + 2 h/1,100 °C/AQ	16 h/870 °C/AQ
<b>AM1</b>	x180	SHT	APVS	6 h/1,080 °C/AQ	16 h/870 °C/AQ
	SAE polishing process	As-cast	APVS	6 h/1,080 °C/AQ	<b>x</b>
<b>Rene N5</b>	x180	SHT	Slurry	1 h/400 °C + 2 h/700 °C + 2 h/1,100 °C/AQ	4 h/900 °C/AQ
	x180	SHT	APVS	6 h/1,080 °C/AQ	4 h/900 °C/AQ
<b>CMSX-4</b>	x180	SHT + R1 + R2	Slurry	1 h/400 °C + 2 h/700 °C + 2 h/1,100 °C/AQ	<b>x</b>
<b>CMSX-4 Plus</b>	x180	SHT + R1 + R2	Slurry	1 h/400 °C + 2 h/700 °C + 2 h/1,100 °C/AQ	<b>x</b>

**Figure II-4a** illustrates the bare substrate and the coated samples from a macroscopic view. **Figure II-4b** and **c** depict the microstructure of the AM1 superalloy after coating deposition via APVS (**Figure II-4b**) and Slurry (**Figure II-4c**). Both micrographs were taken after the HT to optimize the  $\gamma'$  precipitate size. Moreover, it is possible to observe the coating thickness, followed by the IDZ. The APVS deposition method resulted in a coating layer of 20  $\mu\text{m}$ , while the Slurry deposition method resulted in a coating layer of 50  $\mu\text{m}$ .

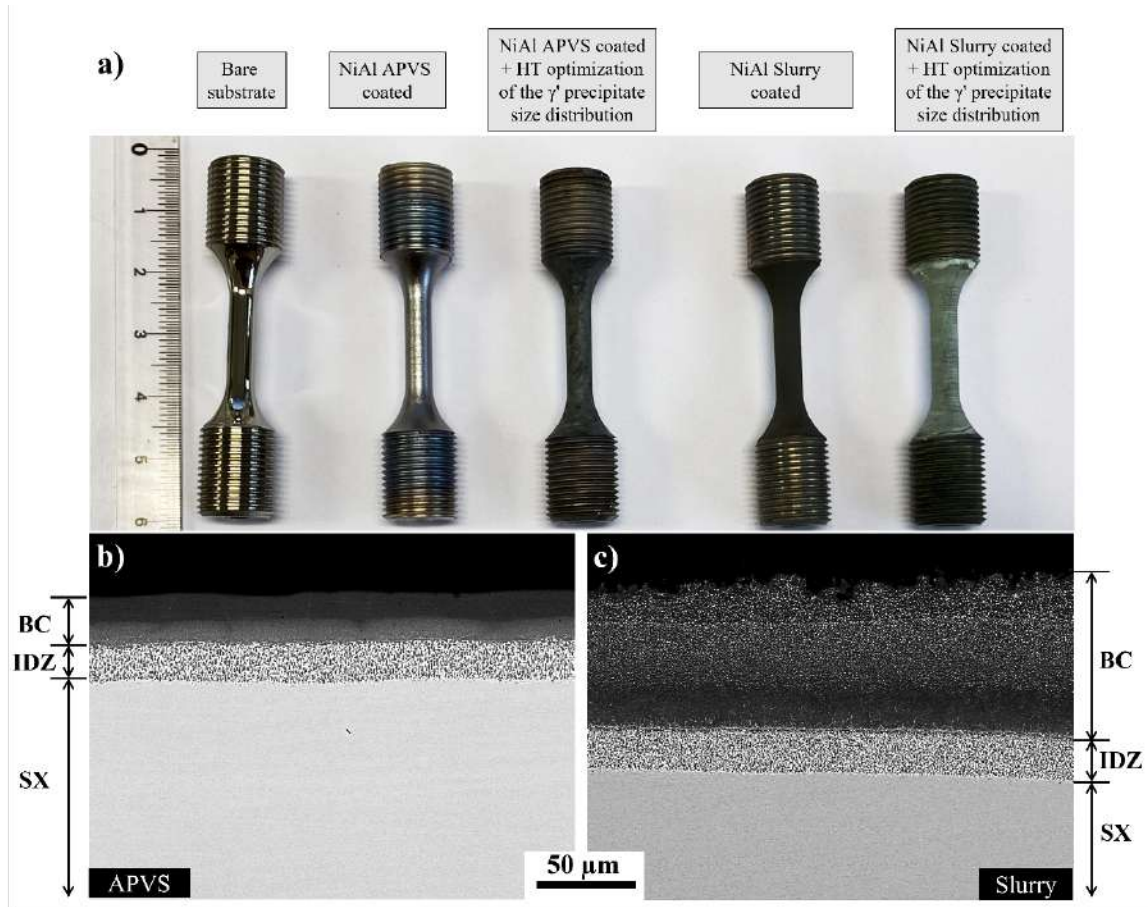


**Figure II-4** LCF fatigue samples with and without coating, before and after the heat treatment to normalize the  $\gamma'$  precipitate (a). AM1 fully HT APVS coated (b) and Slurry coated (c). Both micrographs were taken in BSE mode.

After the polishing procedure, the samples' diameter was measured by EPOI LP-6 profile projector. The coating deposition (i.e., the growth of the IDZ) led to a reduction of the load bearing section and it was not considered to calculate the initially applied loads. This fact will be commented in **Chapter IV**.

### 2.3. Summary

Figure II-5 illustrates the samples path from the machining to the mechanical tests.

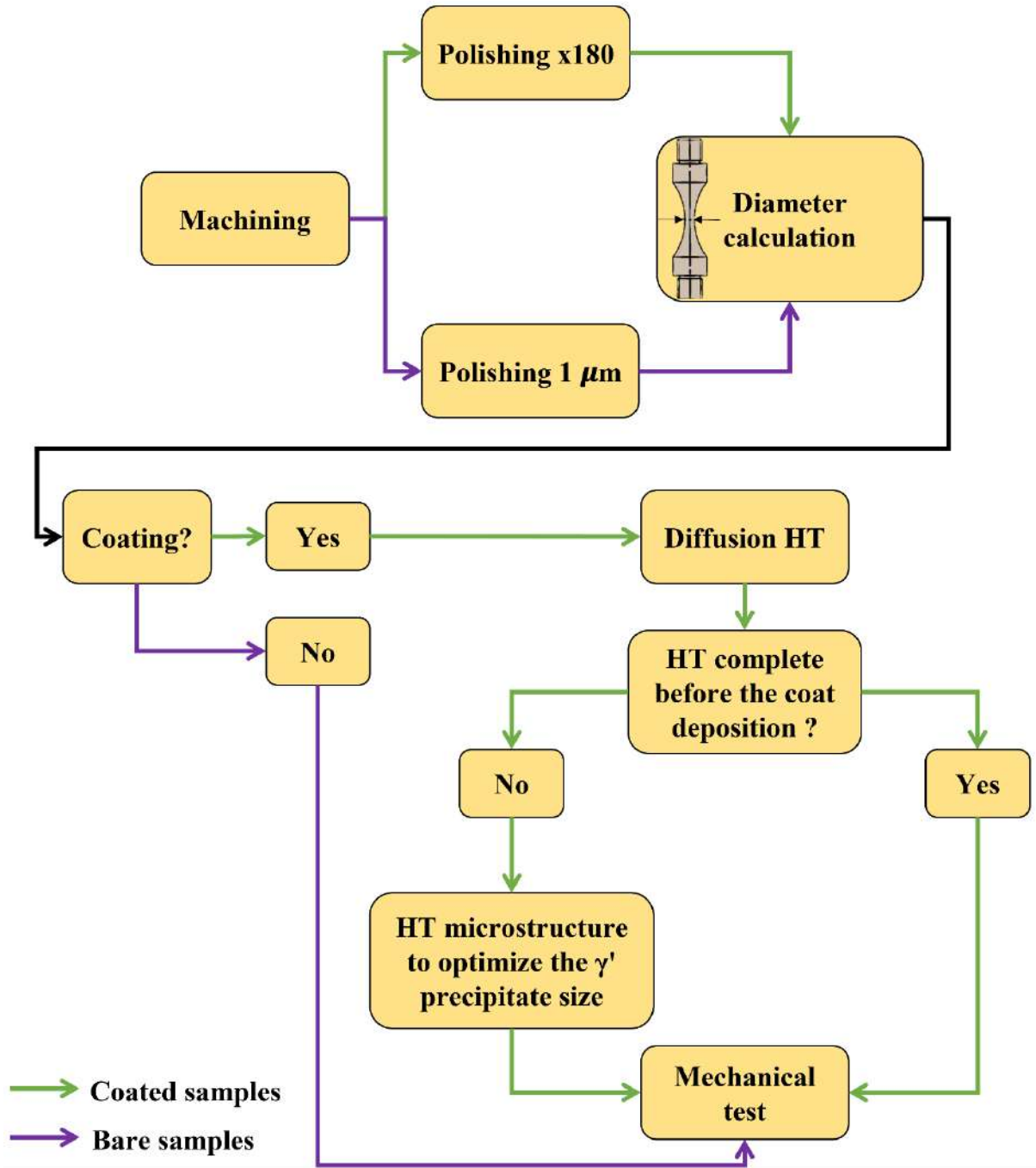


Figure II-5 Specimens preparation from the machining to the mechanical tests.

### 3. Mechanical testing procedures

Two different test machines are employed within this thesis. One of them is dedicated to the VHCF tests and the second one to the tensile and LCF tests. The fatigue and tensile tests are performed at high temperatures between 900 and 1,000 °C, in air.

The creep testing machine and procedures are not detailed in this chapter, as the results mainly support the discussion.

#### 3.1. Ultrasonic fatigue bench

The Institut Pprime has a uniaxial tensile/compression ultrasonic fatigue machine. Its operation principle is to make the specimen resonate at 20 kHz, i.e., it vibrates freely on its own frequency of resonance in tensile/compression excitation. These fatigue tests are strain-controlled by nature. Cervellon (Cervellon, 2018; Cervellon et al., 2017) details in her work the procedure to develop the high temperature apparatus and the samples' geometry by finite element modeling. The dimensions of the VHCF samples (**Figure II-3a**) and the machine parameters were preserved to maintain the same testing conditions as Cervellon's previous study. The following sub-sections summarize her work on the development of the apparatus and specimen design. More details can be found in **Chapter II.3** of her manuscript.

##### 3.1.1. Induction heating system

The induction system is composed of an Ambrell inductor with a maximum current of 750 A. The coil was developed at Institut Pprime with rectangular spirals to increase the temperature homogeneity within the VHCF specimen. The heating/cooling system is controlled during the test to avoid any temperature instability. **Figure II-6a** illustrates the ultrasonic fatigue bench and the induction heating system.

To be able to ensure the temperature on the samples' bulk and skin, the emissivity ratio ( $\varepsilon_1/\varepsilon_2$ ) must be measured. It relates the samples' emissivity  $\varepsilon_1$  and  $\varepsilon_2$  over the wavelengths  $\lambda_1$  and  $\lambda_2$ , correlating the temperatures of a pyrometer (skin,  $\varepsilon_1$ ) and a thermocouple (bulk,  $\varepsilon_2$ ). Cervellon (Cervellon, 2018) has developed a procedure to calculate the ratio for bare and coated specimens.

Employing this technique, the emissivity ratio was measured for each substrate. **Figure II-6b** shows the temperature measurement spot during a VHCF test.

Two linking bars were included in the fatigue assembly line to avoid damages the by high temperatures in the horn and transducer. Both have similar dimensions and shapes. The induction heating system enables the specimen's localized heating. However, it develops a thermal gradient in the fatigue assembly line. The temperature directly impacts the material Young's modulus, which in turn has a direct impact on the samples' dimensions. The finite element study carried out at Safran Helicopter Engines accounted for different thermal gradient measurements to define the final specimen dimension in **Figure II-3a**.

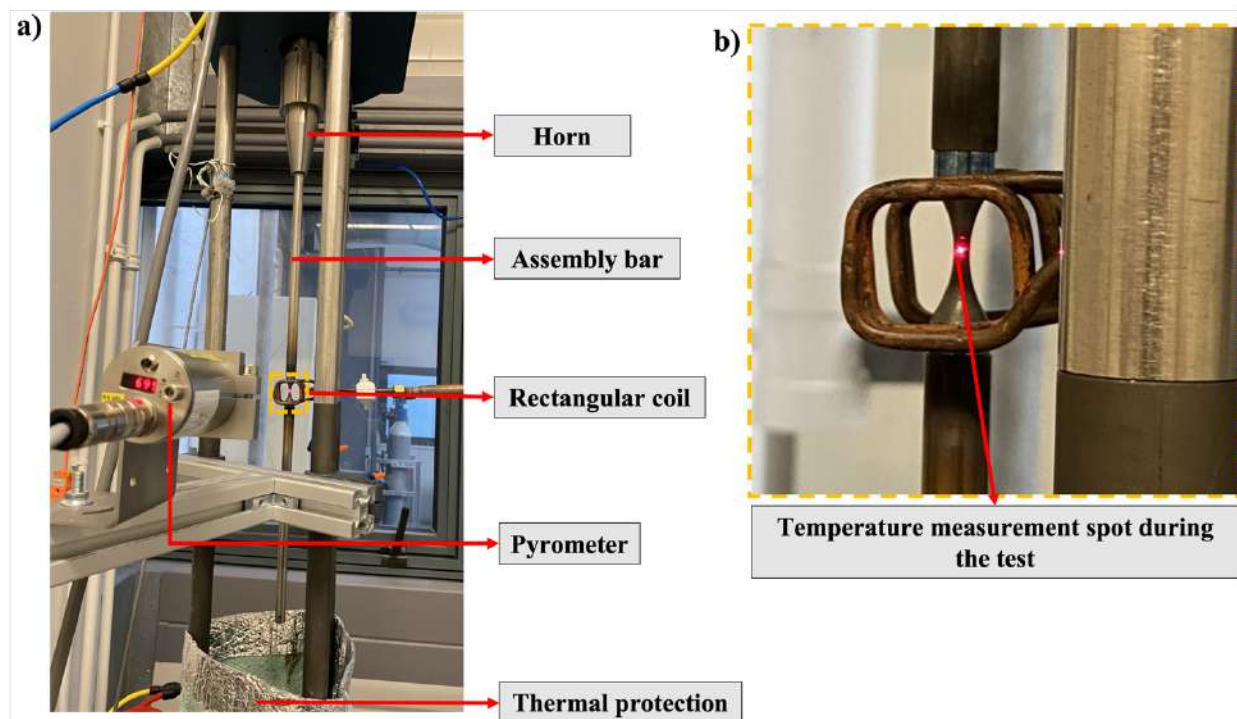


**Figure II-6** The ultrasonic fatigue bench components (a) the temperature measurement location during the fatigue tests (b).

### 3.1.2. Ultrasonic fatigue tests challenges

Several challenges are faced during VHCF tests carried out with an ultrasonic machine. Unfortunately, some of them will more or less interfere with the ultrasonic test results.

**Self-heating:** During ultrasonic fatigue tests at high temperatures and high alternating stresses, the elastic limit may locally be exceeded. It will induce localized plastic zones that introduce heat dissipation, a well-known challenge of ultrasonic tests carried out at  $\approx 20$  kHz (Munier et al., 2017; Roué, 2020). The self-heating can lead to samples' failure for different reasons: oxidation, fast microstructure evolution ( $R > 0$ ), or even material fusion. Several techniques were developed to avoid the problem using a pulse/pause excitation mode (Mayer, 1999). However, at Institut Pprime, since several tests are with the application of a high mean stress, we have decided to use a continuous excitation mode to avoid a contribution of creep at high temperatures during hold sequences. Thus, the temperature is close loop controlled during the loading to prevent the self-heating issue.

**Temperature distribution and its effect on the maximum stress:** The thermal gradient along the specimen's length is one of the particularities of induction heating. During the fatigue tests, a specific temperature profile will develop depending on the alternating stress. To evaluate the temperature profile along the specimens length axis, Cervellon (Cervellon, 2018) carried out a finite element calculation. Indeed, she concluded that the temperature drops by  $\approx 100$  °C between the sample's hourglass contour's central point and the fillet to the grips. Hence, it is constantly held at 1,000 °C in the center. At alternating stresses higher than 200 MPa, a steeper temperature profile is observed. She developed a system to correct it:

**At  $\sigma_a < 200$  MPa:** The error is neglected.

**At  $\sigma_a \geq 200$  MPa:** An increase of 5% of the maximum loading is added in the loading calculation.

Ex.: Maximum loading = 200 MPa

$$\text{Real loading} = 200 + 0.05 \times 200 = 210 \text{ MPa}$$

### 3.1.3. *Experimental procedure*

The ultrasonic fatigue tests procedure is divided into two main steps. The first stage consists in a temperature increase and stabilization to develop an oxide whose emissivity will be constant at 1,000 °C during the VHCF tests. Then, the VHCF test at  $20 \pm 0.5$  kHz and  $1,000 \pm 2$  °C is conducted.

*Table II-5 Heating steps for bare and coated samples.*

<i>Bare substrate</i>				
<i>Steps</i>	<i>Holding time (min)</i>	$\epsilon_1/\epsilon_2$	<i>Inductor setting</i>	<i>Objective</i>
1	5	1	25 % of its power	Avoid temperature overshoot
2	25	1	Automatic	Temperature stabilization + oxide development
3	10	1.024	Automatic	Match the samples' temperature in the bulk and skin
<i>Coated substrate</i>				
<i>Steps</i>	<i>Holding time (min)</i>	$\epsilon_1/\epsilon_2$	<i>Inductor setting</i>	<i>Objective</i>
1	10	1	25.6% of its power	Avoid temperature overshoot
2	30	Between 0.997 and 1.062	Automatic	Step 2 and 3 of bare substrate

$\epsilon_1/\epsilon_2$  is the emissivity ratio between the skin and the bulk.

Loading setting: Once the temperature is stable, the sample can be loaded mechanically. However, this study has adopted a systematic procedure to maintain a standard because several HIP and coated SX samples developed pronounced self-heating. Hence, to ensure reproducible results, the following procedure (**Table II-6**) was developed.

*Table II-6 Systematic loading procedure. (↓ to decrease.)*

<i>Steps</i>	<i>Method</i>	<i>Speed</i>	<i>Maximum alternating loading (MPa)</i>	<i>Objective</i>
1	Automatic	Instantly	100	Imposed by the software to spend a minimum number of cycles during the loading process – Minimum stress reached by the horn
2	Automatic	1 MPa/s	150	↓ temperature overshoot
3	Manually	Step-by-step 10, 5, or 1 MPa charging	240	↓ temperature overshoot + it is sensitive to the specific material alternating stress “limit”

#### 3.1.4. *Neglected points*

Diameter of the specimens: The software calculates the strain based on a fixed 3 mm diameter. As the samples are polished/coated, the diameter will fluctuate by  $\pm 0.2$  mm. Cervellon showed that this diameter range error is around 1.5 %. Consequently, this point was neglected in the following.

Temperature stability: During ultrasonic fatigue tests performed at Institut Pprime, the temperature may fluctuate by about  $\pm 2$  °C in the center of the specimen. This fluctuation is controlled using a closed loop with specific PID parameters, so it will not be further considered.

The number of cycles: **Table II-6** shows three loading stages before reaching the desired loading. During these stages, the number of cycles keeps running. It can last 15 seconds, although it can go up to 45 - 60 seconds, counting to  $10^6$  cycles. It was decided to neglect these cycles for short tests ( $< 10^6$  cycles) as it can significantly affect their fatigue lifetime.

#### 3.1.5. *Summary*

**Figure II-7** summarizes the specificities of the ultrasonic fatigue test bench at Institut Pprime.

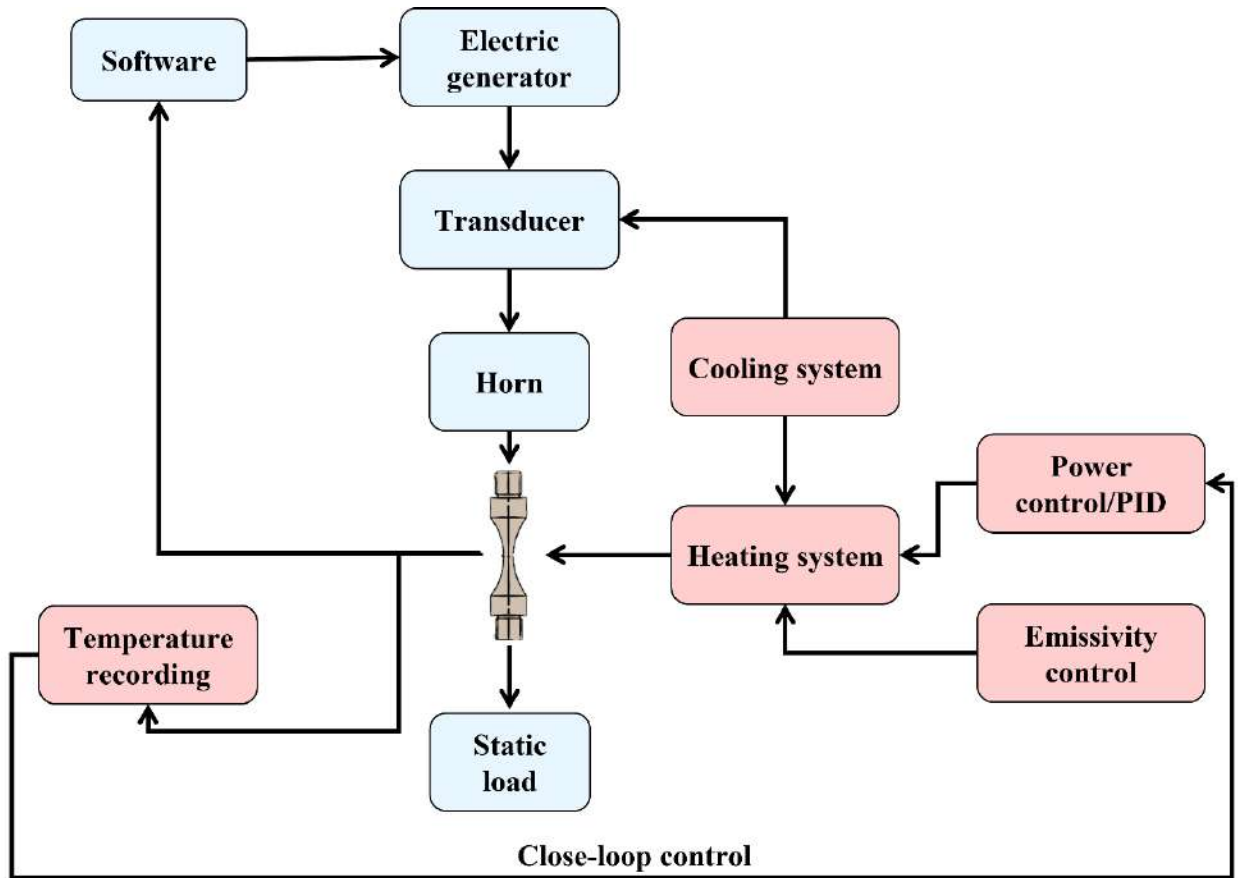


*Figure II-7 Ultrasonic fatigue bench components.*

### 3.2. Instron 8562

The Instron 8562 is an electro-mechanical machine supplied with a resistance furnace. The pre-heating program was established to cope with the sample and the machine components thermal expansion. **Table II-7** summarizes these steps. First, the furnace is divided into two heating zones, resulting in a  $\pm 2$  °C temperature variation between the center and the specimen's extremities. Next, a high-temperature ceramic extensometer is employed to follow the samples' displacement. The extensometer is positioned inside the furnace and in contact with the sample before starting the heating procedure. To avoid the extensometer sliding during tests, adhesive ceramic points are deposited at the surface of non-coated SX specimens. **Figure II-8a** and **c** illustrate the Instron 8562 machine before and after mounting the test assembly.

*Table II-7 Heating program established for the Instron 8562 resistance furnace.*

<i>Steps</i>	<i>Ramp (°C/min)</i>	<i>Maximum temperature</i>	<i>Time (min)</i>	<i>Pre-load (kN)</i>	<i>Objective</i>
1	15	$T_{\text{final}} - 30\text{ °C}$		0.1	Temperature rising
2	3	$T_{\text{final}}$		0.1	Specimen and machine components expansion
3	Dwell	$T_{\text{final}}$	30	0.1	Temperature homogenization within the specimen and machine components

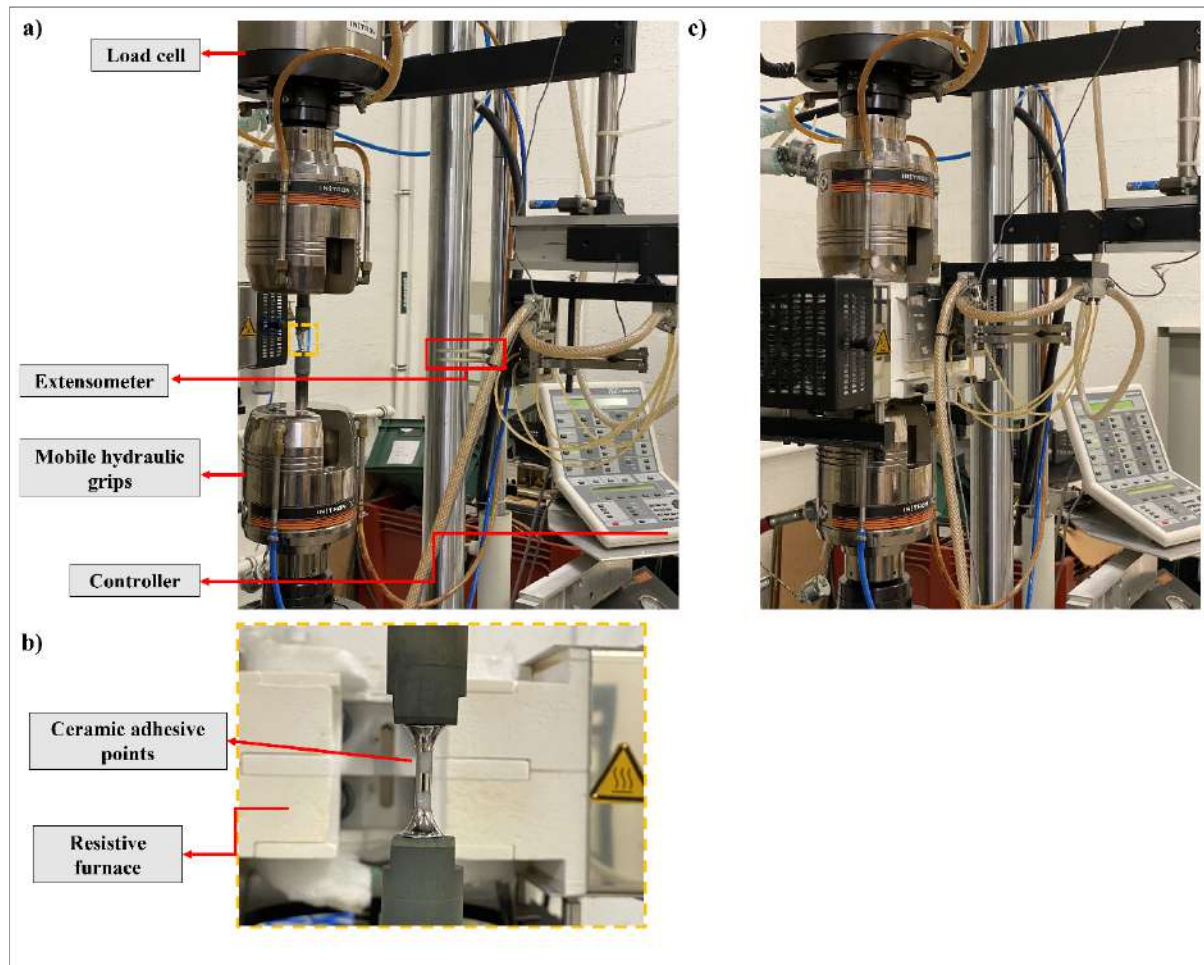


**Figure II-8** Instron 8562 machine with a non-coated specimen assembled. The details of the machine components (a). The specimen with two points of ceramic and the resistance furnace (b). Instron 8562 and the resistance furnace assembled with the extensometer positioned (c).

Low cycle fatigue tests: The LCF tests were performed at 0.5 Hz at temperatures of 900 / 950 °C, in stress-controlled mode, with a positive stress ratio ( $R_\sigma = 0.05$ ) and a sinusoidal waveform.

Tensile tests: The tensile tests were performed with an initial constant raw displacement rate corresponding to an initial strain rate of  $5 \cdot 10^{-4} \text{ s}^{-1}$  in the elastic part.

## **4. Characterization methods**

### **4.1. Non-destructive characterization**

Several non-destructive analyses were carried out. One of the main objectives of the study was to understand the crack initiation transition from internal sites to the surface. Hence, all the information given before destructive analysis is valuable. The equipment, techniques, and specimen preparation are detailed in this section.

#### *4.1.1. Microscopy*

Optical microscopy: Two optical microscopes were used, a Leica with a maximum  $\times 60$  magnification and a Zeiss equipped with an AxioCam and  $\times 1,000$  magnification. Both are useful to locate the surface cracks and define the further cutting planes.

Scanning Electron Microscope: The surface cracks are not visible through optical microscopy during the first fatigue cycles. Thus, the interrupted test samples' gage analysis was performed using a Scanning Electron Microscope (SEM) JEOL 6100 and acceleration voltage of 20 kV equipped with an accessory machine that allows turning the specimen inside the SEM chamber. The secondary electron imaging (SEI) mode was employed.

A Field Emission Gun Scanning Electron Microscope (FEG-SEM) JEOL 7000F was employed for fracture surface characterizations. Both SEI and back-scattered imaging mode were used. An accelerating voltage of 25 kV was used for the fracture surface observations. The casting pores' diameter was calculated from the fracture surface observations using the FIJI software.

## 4.2. Destructive characterizations

Destructive characterizations were aimed at analyzing the crack initiation site and the microstructure around it. As the crack initiation site can be located in the bulk or at the surface, it thus requires different analysis strategies for the sectioning and polishing routine.

### 4.2.1. Longitudinal analysis

The different methods illustrated below (**Figure II-9**) were developed for the sample's failure analysis. One of the advantages of the ultrasonic fatigue bench at Institut Pprime is to preserve at least one fracture surface from oxidation. Therefore, preserves the details usually hidden by oxides. Consequently, the samples with no surface oxidation were in priority.

The samples that failed from an internal site were carefully cut and polished up to intercepting the critical defect in the polishing plane, as shown by the black line indicating the cutting plane in **Figure II-9a**. The specimens that failed from the surface were cut to intercept the main critical crack propagated in mode I, see the cutting plane in **Figure II-9b**.

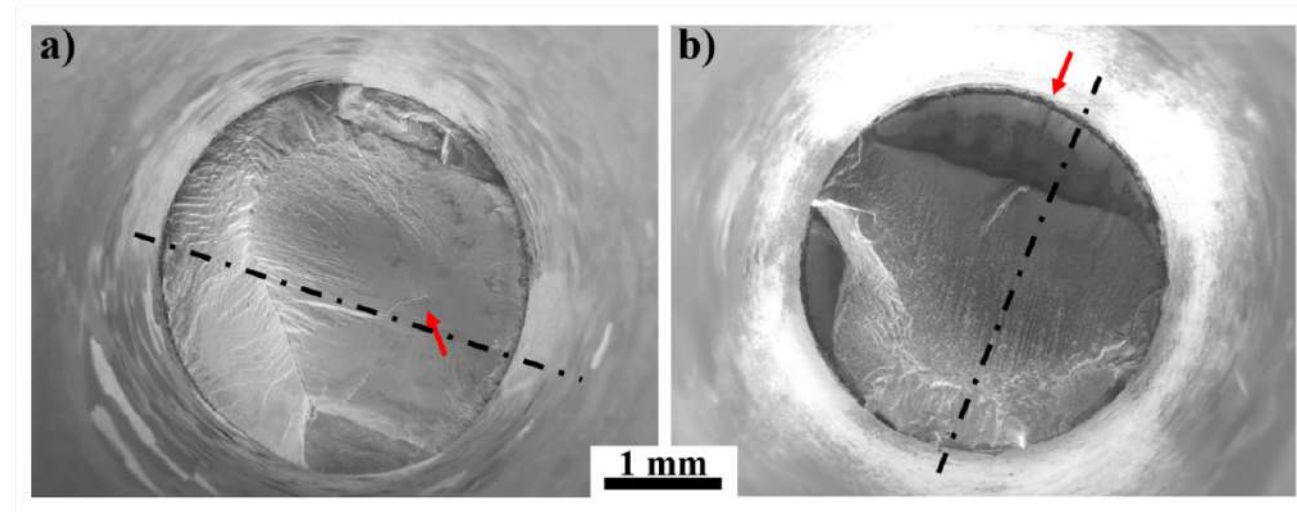


**Figure II-9** The longitudinal cutting plane is defined from the optical microscope observations. Samples with internal crack initiation (a). Samples with crack initiation from the surface (b). The black dotted lines illustrate the cutting planes. The red arrows indicated the crack initiation sites.

#### 4.2.2. *Microscopy*

Microstructure: To investigate the microstructure evolution around the crack initiation zone, the presence of deformed volume, and slip bands, the equipment FEG-SEM JEOL 7000F was employed with an acceleration voltage of 25 kV. The SEI and BSE modes were used. For this analysis, the samples were mirror polished and later polished with an active oxide polishing suspensions (OPS) for 30 minutes.

EDS: The local chemical composition was investigated by EDS analyses. It was carried out in the SEM JEOL 6100 and operated with an acceleration voltage of 20 kV and a working distance of 17 mm. The EDS detector is a Bruker AXS type Silicon drift connected, and Esprit's characterization software was used.

EBSD: The crystallographic orientation and texture close to the crack zone were analyzed by a second conventional SEM JEOL 6100 equipped with an EBSD detector operated with an acceleration voltage of 25 kV. The scanning step was chosen between 80 and 300 nm. The results were post-processed using the OIM software.

## 5. Mechanical tests summary

**Table II-8** summarizes the fatigue and tensile tests carried out throughout this work.

*Table II-8 Summary of mechanical tests related to each SX Ni-based superalloy.*

<b>MAR-M200 +Hf SX</b>	<b>Casting method:</b> Bridgman <ul style="list-style-type: none"> <li>▪ <b>Bare specimens</b></li> <li>▪ <b>Specimens Slurry coated:</b> HT + R1 + R2 + BC HT diffusion</li> </ul>	<b>Mechanical tests:</b> <b>Tensile:</b> $5 \cdot 10^{-4} \text{ s}^{-1}$ and $900 \text{ }^\circ\text{C}$ <b>LCF:</b> 0.5 Hz, $R_\sigma = 0.05$ and $900 \text{ }^\circ\text{C}$
<b>AM1</b>	<b>Casting method:</b> Bridgman <ul style="list-style-type: none"> <li>▪ <b>Bare specimens</b></li> <li>▪ <b>Specimens Slurry and APVS coated:</b> HT + BC HT diffusion + HT <math>\gamma'</math> optimization</li> <li>▪ <b>Specimens coated via APVS:</b> As-cast + BC HT diffusion</li> </ul>	<b>Mechanical tests:</b> <b>Tensile:</b> $5 \cdot 10^{-4} \text{ s}^{-1}$ and $950 \text{ }^\circ\text{C}$ <b>LCF:</b> 0.5 Hz, $R_\sigma = 0.05$ and $950 \text{ }^\circ\text{C}$ <b>VHCF:</b> 20 kHz, $R_e = -1$ and $1,000 \text{ }^\circ\text{C}$
<b>Rene N5</b>	<b>Casting method:</b> Bridgman <ul style="list-style-type: none"> <li>▪ <b>Bare specimens</b></li> <li>▪ <b>Specimens Slurry and APVS coated:</b> HT + BC HT diffusion + HT <math>\gamma'</math> optimization</li> </ul>	<b>Mechanical tests:</b> <b>Tensile:</b> $5 \cdot 10^{-4} \text{ s}^{-1}$ and $950 \text{ }^\circ\text{C}$ <b>LCF:</b> 0.5 Hz, $R_\sigma = 0.05$ and $950 \text{ }^\circ\text{C}$ <b>VHCF:</b> 20 kHz, $R_e = -1$ and $1,000 \text{ }^\circ\text{C}$
<b>CMSX-4</b>	<b>Casting method:</b> Bridgman <ul style="list-style-type: none"> <li>▪ <b>Specimens Slurry coated:</b> HT + R1 + R2 + BC HT diffusion</li> </ul>	<b>Mechanical test:</b> <b>VHCF:</b> 20 kHz, $R_e = -1$ and $1,000 \text{ }^\circ\text{C}$
<b>ERBO/1</b>	<b>Casting method:</b> Bridgman <ul style="list-style-type: none"> <li>▪ <b>Bare specimens</b></li> <li>▪ <b>Standard HT and HIP treatment</b></li> </ul>	<b>Mechanical test:</b> <b>VHCF:</b> 20 kHz, $R_e = -1$ and $1,000 \text{ }^\circ\text{C}$
<b>CMSX-4</b>	<b>Casting method:</b> PBF-E <ul style="list-style-type: none"> <li>▪ <b>Bare specimens</b></li> <li>▪ <b>Standard HT and HIP treatment</b></li> </ul>	<b>Mechanical test:</b> <b>VHCF:</b> 20 kHz, $R_e = -1$ and $1,000 \text{ }^\circ\text{C}$
<b>DD33</b>	<b>Casting method:</b> Bridgman <ul style="list-style-type: none"> <li>▪ <b>Bare specimens</b></li> <li>▪ <b>Standard HT and HIP treatment</b></li> </ul>	<b>Mechanical test:</b> <b>VHCF:</b> 20 kHz, $R_e = -1$ and $1,000 \text{ }^\circ\text{C}$
	<b>Casting method:</b> LMC <ul style="list-style-type: none"> <li>▪ <b>Bare specimens</b></li> <li>▪ <b>Standard HT</b></li> </ul>	<b>Mechanical test:</b> <b>VHCF:</b> 20 kHz, $R_e = -1$ and $1,000 \text{ }^\circ\text{C}$
<b>CMSX-4 Plus</b>	<b>Casting method:</b> Bridgman <ul style="list-style-type: none"> <li>▪ <b>Bare specimens</b></li> <li>▪ <b>Specimens Slurry coated:</b> HT + R1 + R2 + BC HT diffusion</li> </ul>	<b>Mechanical test:</b> <b>VHCF:</b> 20 kHz, $R_e = -1$ and $1,000 \text{ }^\circ\text{C}$
	<b>Casting method:</b> Bridgman <ul style="list-style-type: none"> <li>▪ <b>Bare specimens</b></li> <li>▪ <b>Standard HT and HIP</b></li> </ul>	<b>Mechanical test:</b> <b>VHCF:</b> 20 kHz, $R_e = -1$ and $1,000 \text{ }^\circ\text{C}$
<b>MC-NG</b>	<b>Casting method:</b> Bridgman <ul style="list-style-type: none"> <li>▪ <b>Bare specimens</b></li> <li>▪ <b>Standard HT and HIP treatment</b></li> </ul>	<b>Mechanical test:</b> <b>VHCF:</b> 20 kHz, $R_e = -1$ and $1,000 \text{ }^\circ\text{C}$
<b>TMS-238</b>	<b>Casting method:</b> Bridgman <ul style="list-style-type: none"> <li>▪ <b>Bare specimens</b></li> <li>▪ <b>Standard HT</b></li> </ul>	<b>Mechanical test:</b> <b>VHCF:</b> 20 kHz, $R_e = -1$ and $1,000 \text{ }^\circ\text{C}$
<b>TROPEA</b>	<b>Casting method:</b> Bridgman <ul style="list-style-type: none"> <li>▪ <b>Bare specimens</b></li> <li>▪ <b>Standard HT</b></li> </ul>	<b>Mechanical test:</b> <b>VHCF:</b> 20 kHz, $R_e = -1$ and $1,000 \text{ }^\circ\text{C}$



# **Chapter III. Very High Cycle Fatigue durability of uncoated substrates**



## Durée de vie en fatigue gigacyclique de substrats non-revêtus

Ce chapitre est consacré à l'étude de l'impact des méthodes de solidification et des traitements de compaction isostatique à chaud (CIC) des superalliages base de nickel monocristallins sur leur durée de vie en fatigue gigacyclique (VHCF). Ce chapitre a étudié neuf superalliages dans des conditions de fatigue de 1,000 °C, 20 kHz, rapport de charge négatif ( $R_e=-1$ ) et sans aucun traitement de surface.

Les méthodes de solidification classique (procédé Bridgman) conduisent à des pores de fonderie, dont la taille et la position sont les principaux facteurs contrôlant la durée de vie de la structure en VHCF. Selon les paramètres de solidification et la chimie du superalliage, le pore de fonderie critique peut présenter un diamètre équivalent aussi élevé que 200  $\mu\text{m}$  ou aussi bas que 40  $\mu\text{m}$ . Par conséquent, la durée de vie s'améliore en diminuant la taille de pore et la dispersion de la durée de vie en fatigue se réduit avec la diminution de la taille du diamètre des pores de fonderie. Une modélisation de type FIP (Fatigue Indicator Parameter) a été appliquée et comparée aux résultats, confirmant que cette approche est relativement adaptée à la modélisation de la durée de vie en fatigue en fonction de la taille et la position des pores les plus critiques. Cependant, il est essentiel de mentionner que ces conclusions ont déjà été rencontrées dans la littérature.

D'autre part, les méthodes de solidification à haute vitesse de refroidissement telles que le refroidissement par bain de métal liquide (LMC) ou la fabrication additive peuvent entraîner des durées de vie en fatigue très élevées (au-delà de  $10^{10}$  cycles sous faibles contraintes alternées) ou des durées de vie en fatigue très faibles (inférieures à  $10^6$  cycles sous faibles contraintes alternées) si des grains parasites sont présents dans le volume sollicité. L'analyse de la contribution des grains parasites aux mécanismes d'endommagement par fatigue est l'une des originalités de ce manuscrit. Il montre via une analyse par éléments finis et des résultats expérimentaux que les grains parasites augmentent la fréquence de résonance, et conduisent à une concentration de contrainte de cisaillement à l'interface superalliage/grains parasites. La surcharge locale entraîne en amorçage de fissure prématuré et, par conséquent, une durée de vie en fatigue plus faible.

De plus, et comme attendu, le traitement CIC améliore la durée de vie de la fatigue en diminuant/fermant les pores de fonderie. Cependant, après analyse EBSD, des sous-grains autour

des pores compactés ont été observés. La déformation plastique autour des pores compactés avait été réalisé par le passé. Aucune observation EBSD d'une véritable morphologie des pores compactés a pu être démontrée dans la littérature. Les observations montrent que les prédictions par éléments finis des pores compactés sont très proches des observations obtenues dans ce manuscrit. De plus, les pores compactés sont toujours critiques du point de vue de l'amorçage des fissures. Ainsi, il a été montré que le pore de fonderie est moins dommageable qu'un joint de grain avec une désorientation supérieure à  $20^\circ$  par rapport à l'orientation primaire du superalliage.

Enfin, et pour la première fois, une durée de vie en VHCF contrôlée par oxydation est présentée dans la littérature ouverte pour les superalliages base Ni monocristallins à haute température à  $R_\varepsilon = -1$  et sans aucun mécanisme de recristallisation à la surface. Un mécanisme d'amorçage de fissure en surface est proposé et, en l'absence de défauts tels que des pores de solidification, des grains parasites ou une couche recristallisée, la durée de vie intrinsèque en VHCF est contrôlée par la résistance chimique/environnementale de l'alliage. Ainsi, le mécanisme d'amorçage devient principalement contrôlé par l'amorçage et la (micro-) propagation depuis la surface. Ce mécanisme de rupture depuis la surface pour des durées de vie ultra-longues ( $N_f > 10^{10}$  cycles) remet en cause une éventuelle notion de limite de fatigue dans ces conditions.

## 1. Introduction

This chapter characterizes AM1, Rene N5, CMSX-4, ERBO/1, CMSX-4 Plus, DD33, MC-NG, TMS-238, and TROPEA superalloys under the fatigue conditions of 1,000 °C, 20 kHz, fully reversed loading, and no surface treatment.

The first sub-section is dedicated to the Ni-based SX superalloys processing conditions influence on the VHCF properties and crack initiation mode. It depicts the effect of casting pore's size on the fatigue lifetime for Bridgman solidified superalloys. Further, the LMC process illustrates the impact of higher cooling rates during superalloy solidification on fatigue life. Finally, the results presented in this chapter are compared with the FIP prediction model.

The second sub-section is dedicated to the HIP treatment as a possible processing route to close casting pores. However, the entire process can generate new challenges in the fatigue crack initiation domain. One of these challenges is the modification of the crack initiation mechanism by changing the casting pores morphology. Therefore, this sub-section elucidates the following question: which defect is more detrimental? The casting pore or the compacted casting pore with its surrounding modified microstructure?

The third sub-section is dedicated to the Ni-based SX superalloys samples built by the PBF-E method. It uncovers the mechanical behavior of these alloys with no “classical” remaining defects, and consequently, its new challenges. Further, the fourth sub-section presents the drawbacks of increasing the cooling rate during solidification: the stray grain formation can act as crack initiation site during ultrasonic fatigue tests.

Finally, the last sub-section investigates the samples with a very high number of cycles and, consequently, the crack initiation at the surface. It focuses more specifically on the role of the alloy's chemistry on its environmental resistance and fatigue limit. A crack initiation mechanism is proposed for Ni-based SX superalloys under VHCF conditions of 1,000 °C, 20 kHz, and  $R_e = -1$ .

## 2. Casting pore size and the solidification process impact

At elevated temperatures (1,000 °C) and ultrasonic fatigue conditions (20 kHz, and  $R_e=-1$ ) the casting pores are known to control the crack initiation process (Bortoluci Ormastroni et al., 2020a; Cervellon, 2018; Cervellon et al., 2018, 2017; Furuya et al., 2012; Morrissey and Golden, 2007; Stanzl-Tschegg, 2014; Yi et al., 2007; Zhao et al., 2020). Then, solidification methods and heat treatments were modified to control casting pore size and distribution. Consequently, it increased the superalloy performance under extreme environments. Classically, increasing the solidification rate using the LMC method improved the superalloy fatigue performances (Cervellon et al., 2018; Lamm and Singer, 2007; Steuer et al., 2015).

This sub-section investigates eight Bridgman processed superalloys, and one LMC processed superalloy. **Appendix A.1** depicts the fatigue database of this sub-section. **Table III-1** recalls eight Ni-based SX superalloys main solidification and defect information.

*Table III-1 Superalloys investigated in this sub-section. Y for presence, and N for absence.*

<i>Superalloy</i>	<i>Solidification methods</i>	<i>Rod <math>\varnothing</math> (mm)</i>	<i>Eutectics</i>	<i>Carbides</i>
<b>AM1</b>	Bridgman	14	N	N
<b>Rene N5</b>	Bridgman	14	<b>Y</b>	<b>Y</b>
<b>ERBO/1</b>	Bridgman	Plates 51 x 20 x 55	N	N
<b>DD33</b>	Bridgman	14	<b>Y</b>	<b>Y</b>
	LMC	14	<b>Y</b>	<b>Y</b>
<b>CMSX-4 Plus</b>	Bridgman	14	N	N
		40	N	N
<b>MC-NG</b>	Bridgman	12	N	N
<b>TMS-238</b>	Bridgman	12	N	N
<b>TROPEA</b>	Bridgman	14	<b>Y</b>	N

## 2.1. Bridgman processed Ni-based SX superalloys: pore's size effect

**Figure III-1** shows the alternating stress ( $\sigma_a$ ) as a function of the number of cycles to failure (Nf) diagram gathering the VHCF results obtained for the Bridgman processed superalloys. The symbols represent the superalloys, and the colors represent the crack initiation site. The lifetime increases with the decreasing of the critical casting pore diameter, see **Table III-2**. This figure has four AM1 datapoints and six CMSX-4 data points from the prior literature using the same setup and conditions (Cervellon, 2018).

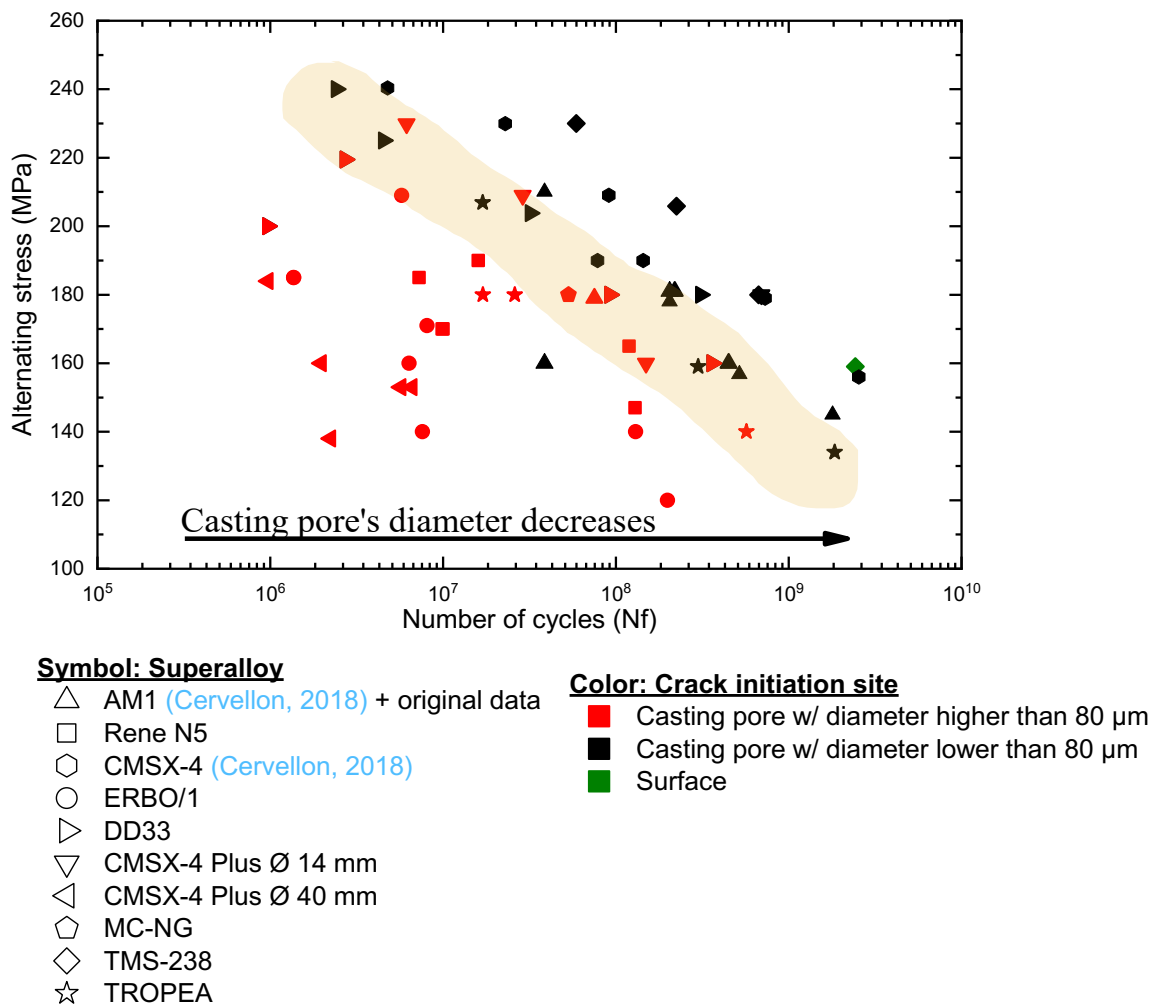


**Figure III-1** S-N diagram for 1,000 °C,  $R_e = -1$ , and  $f = 20$  kHz gathering the results achieved on Bridgman processed specimens. The diagram shows the alternating stress as a function of the number of cycles to failure. Part of the AM1 and the CMSX-4 data were extracted from the prior literature (Cervellon, 2018).

*Table III-2 Number of tested samples and critical casting pore diameter size in  $\mu\text{m}$ .*

<i>Superalloy</i>	<i>Number of samples tested</i>	<i>Casting pore maximum circumscribed diameter (<math>\mu\text{m}</math>)</i>
<b>AM1</b>	3 + 4 from (Cervellon, 2018)	70
<b>Rene N5</b>	5	200
<b>CMSX-4</b>	6 from (Cervellon, 2018)	80
<b>ERBO/1</b>	8	160
<b>DD33</b>	8	60
<b>CMSX-4 Plus Ø 14 mm</b>	4	80
<b>CMSX-4 Plus Ø 40 mm</b>	5	200
<b>MC-NG</b>	1	50
<b>TMS-238</b>	4	60
<b>TROPEA</b>	6	100

The specimens had crack initiation at internal casting pores, except for one TMS-238 sample that presented surface crack initiation. **Sub-section 6** details the specimens presenting surface crack initiation.

Three main zones can be identified in the S-N diagram presented in **Figure III-1**. The first zone covers the samples with a critical pore diameter greater than  $80 \mu\text{m}$  (illustrated by the red color symbol in **Figure III-1**). The second zone includes the samples with a critical pore diameter between  $70 - 90 \mu\text{m}$  (illustrated by the hatched yellow region in **Figure III-1**). Finally, the third zone covers the samples with a diameter of less than  $80 \mu\text{m}$  (illustrated by the black color symbol). As a result, the number of cycles to failure is about 4 decades higher for CMSX-4 Plus ( $\text{Ø } 40 \text{ mm}$ ) than for TMS-238 at  $\sigma_a = 180 \text{ MPa}$ .

Several samples were machined out from a thick SX plate (ERBO/1) or rods of 40 mm diameter (CMSX-4 Plus). Using the same casting parameters, larger SX castings are containing larger solidification pores, reducing the VHCF life (Bortoluci Ormastroni et al., 2020a; Cervellon et al., 2018). Therefore, the size of the critical pores in a specimen depends on the location from which specimen

is extracted from the cast plate. Indeed, for the 40 mm diameter rod, it was decided to machine symmetrically in the rod volume avoiding the central zone (i.e., last zone to solidify at the solidification front). Still, the pronounced scatter in VHCF life of ERBO/1 and CMSX-4 Plus ( $\varnothing$  40 mm) results from the significant variation in casting pore size. The effect of simply increasing the casting bar diameter from 14 mm to 40 mm decreases the samples' fatigue lifetime in at least two orders of magnitude, independently of the SHT applied (Bortoluci Ormastroni et al., 2020a).

**Figure III-2** depicts the fracture surface of representative specimens of each domain of **Figure III-1**. Note that the color code between **Figure III-1** and **Figure III-2** is kept. The fatigue ridges identify the initiation site, and the classic rough zone identifies the critical casting pore.

The CMSX-4 Plus sample machined from the 40 mm diameter rod (**Figure III-2a**) was tested at  $\sigma_a = 160$  MPa, resulting in a lifetime of  $1.9 \cdot 10^6$  cycles. The sample failed because of crack initiation at a casting pore of  $\approx 170 \mu\text{m}$  near the surface see **Figure III-2b**. Second, the platinum group metals (PGM) superalloy TROPEA sample (**Figure III-2c**) was tested at  $\sigma_a = 207$  MPa, resulting in a lifetime of  $1.7 \cdot 10^7$  cycles. The sample failed because of crack initiation at a casting pore of  $\approx 60 \mu\text{m}$  near the surface see **Figure III-2d**. The third is the 6<sup>th</sup> generation superalloy TMS-238 sample (**Figure III-2e**) tested at  $\sigma_a = 206$  MPa, resulting in a lifetime of  $2.2 \cdot 10^8$  cycles. The sample failed because of crack initiation at a casting pore of  $\approx 40 \mu\text{m}$  see **Figure III-2f**.

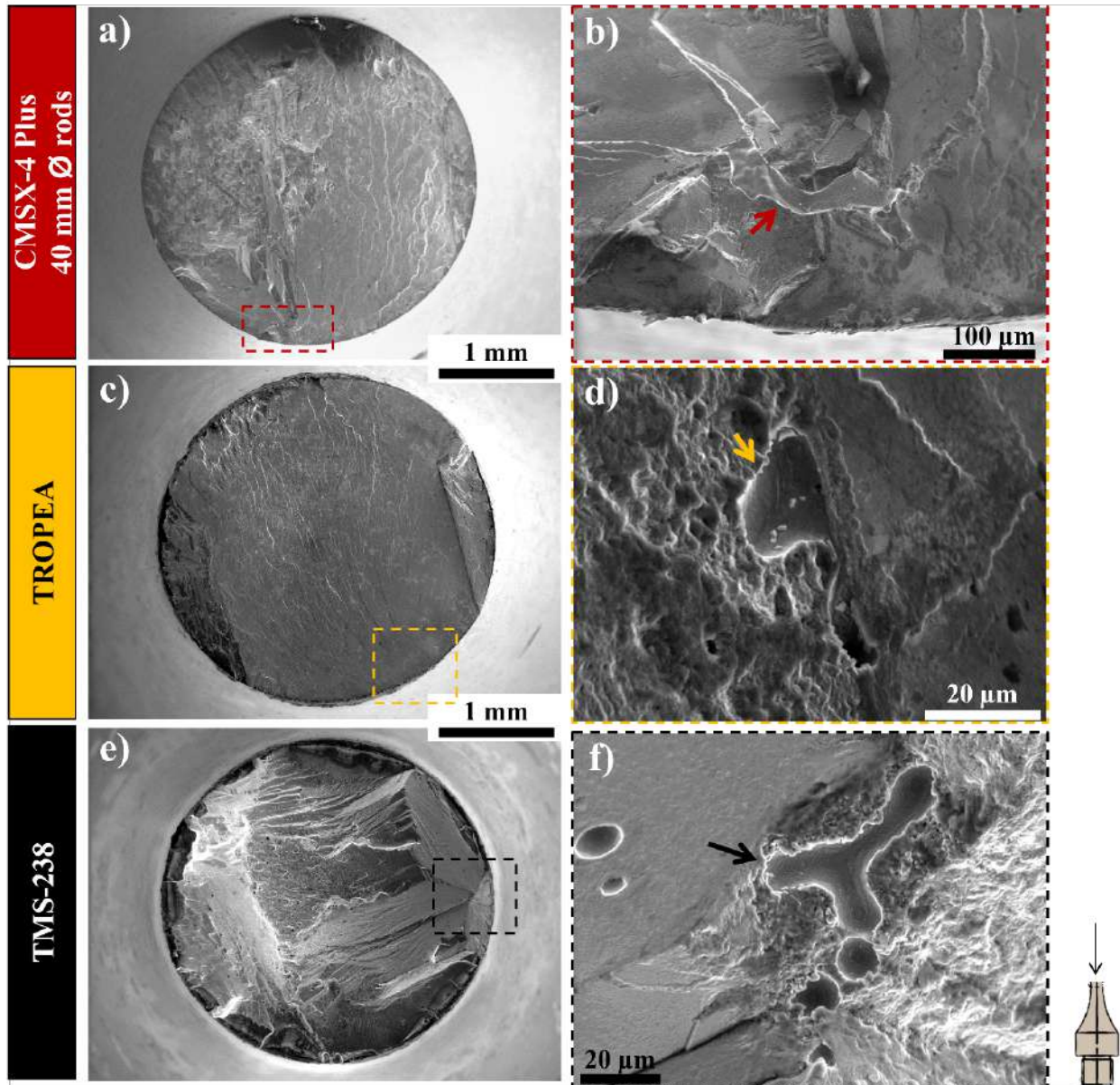


**Figure III-2** Fracture surface observations of CMSX-4 Plus, TROPEA, and TMSX-238 samples with main crack initiation at casting pores. CMSX-4 Plus ( $\sigma_a = 160$  MPa, with  $N_f = 1.9 \cdot 10^6$  cycles) (a), crack initiation zone magnification in (b), detail of the presence of a casting pore close to the surface with a diameter of  $\approx 170 \mu\text{m}$  indicated by the red arrow. TROPEA ( $\sigma_a = 207$  MPa, with  $N_f = 1.7 \cdot 10^7$  cycles) (c), crack initiation zone magnification in (d), detail of the presence of a casting pore with a diameter of  $\approx 60 \mu\text{m}$  indicated by the yellow arrow. TMS-238 ( $\sigma_a = 206$  MPa, with  $N_f = 2.2 \cdot 10^8$  cycles) (e), crack initiation zone magnification in (f), detail of the presence of a casting pore with a diameter of  $\approx 40 \mu\text{m}$  indicated by the black arrow.

From the present results, one may also speculate on the possible role of other non-metallic defects present within the alloys. In fact, DD33 presents the same critical pore's size diameter as TMS-238, although the DD33 specimens' fatigue life is approximately one decade lower compared with the TMS-238 specimens. Rene N5, another carbide-containing alloy (see **Table III-1**), known to have TaC carbides surrounding casting pores (Brundidge and Pollock, 2012), shows fatigue life values which are about one decade less than that of TMS-238 (see **Appendix A Figure A-1**) and further, the scatter of the lifetime values is higher in the case of Rene N5. **Figure III-3** shows two examples of casting pores serving as crack initiation sites surrounded by carbides.

**Figure III-3a** shows the crack initiation site of a Rene N5 sample tested at  $\sigma_a = 170$  MPa, resulting in fatigue life of  $9.9 \cdot 10^6$  cycles. The critical casting pore has a diameter of  $\approx 200 \mu\text{m}$ . **Figure III-3b** shows the crack initiation site of a DD33/Bridgman sample tested at 160 MPa, resulting in fatigue life of  $3.6 \cdot 10^8$  cycles. The critical casting pore has a diameter of  $70 \mu\text{m}$ . The orange arrows indicate the carbides.

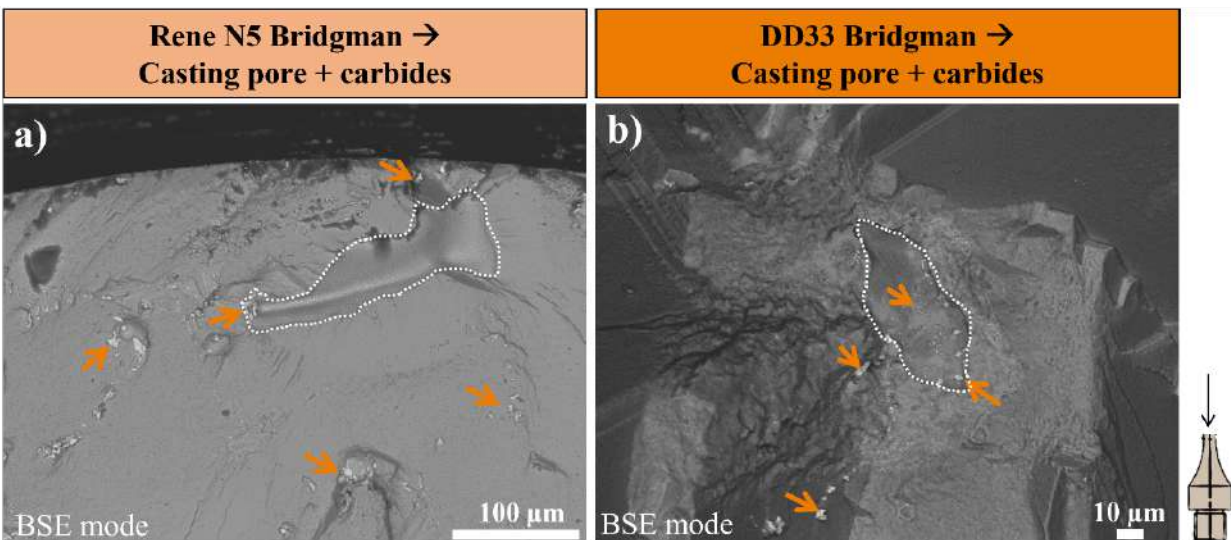


**Figure III-3** Examples of critical casting pores surrounded by carbides for Rene N5, and DD33/Bridgman samples tested at  $1,000 \text{ }^\circ\text{C}$ ,  $R_\epsilon = -1 / f = 20 \text{ kHz}$ . Rene N5 ( $\sigma_a = 170 \text{ MPa}$ , with  $N_f = 9.9 \cdot 10^6$  cycles) (a) and DD33/Bridgman ( $\sigma_a = 160 \text{ MPa}$ , with  $N_f = 3.6 \cdot 10^8$  cycles) (b). The orange arrows indicate the carbides. The white dotted lines define the casting pore shape.

The carbide-containing alloys represent the lower (and scattered) VHCF life in the literature (Cervellon et al., 2020b), and even though the presence of carbides influences the fatigue life (Govaere

et al., 2020; Huang et al., 2020). For both alloys (DD33 and Rene N5), the pore size seems to have a much stronger effect than the presence of other metallurgical defects like carbides (see **Appendix A, Figure A-1**). Therefore, the author of this work will consider carbides to have a secondary effect on the VHCF life if the crack initiation occurs at a large internal casting pore.

## **2.2. LMC processed Ni-based SX superalloy: cooling rate effect**

Two batches of DD33 superalloy solidified via the LMC method were provided by IMR to evaluate the cooling rate effect on the VHCF life. **Figure III-4** shows the  $\sigma_a$  as a function of the Nf diagram gathering all VHCF results for the Bridgman and LMC processed DD33 samples. Red symbols represent the crack initiation at casting pores with a diameter greater than 40  $\mu\text{m}$ , and the black ones initiation at casting pores with a diameter lower than 40  $\mu\text{m}$ . Blue symbols represent crack initiation at the high angle grain boundary (HAGB). Finally, green symbols represent crack initiation at the surface.

The LMC samples from the second batch failed mostly at casting pores with a diameter lower than 40  $\mu\text{m}$  and near the surface. Two samples failed from the surface at low alternating stresses, one from each batch; they will be further evaluated in **sub-section 6** of this chapter. Most samples from the first batch failed at HAGB, indicating RX during the solidification process and/or subsequent solution heat treatment. The HAGB crack initiation sites will be further discussed in **sub-section 5** of this chapter.

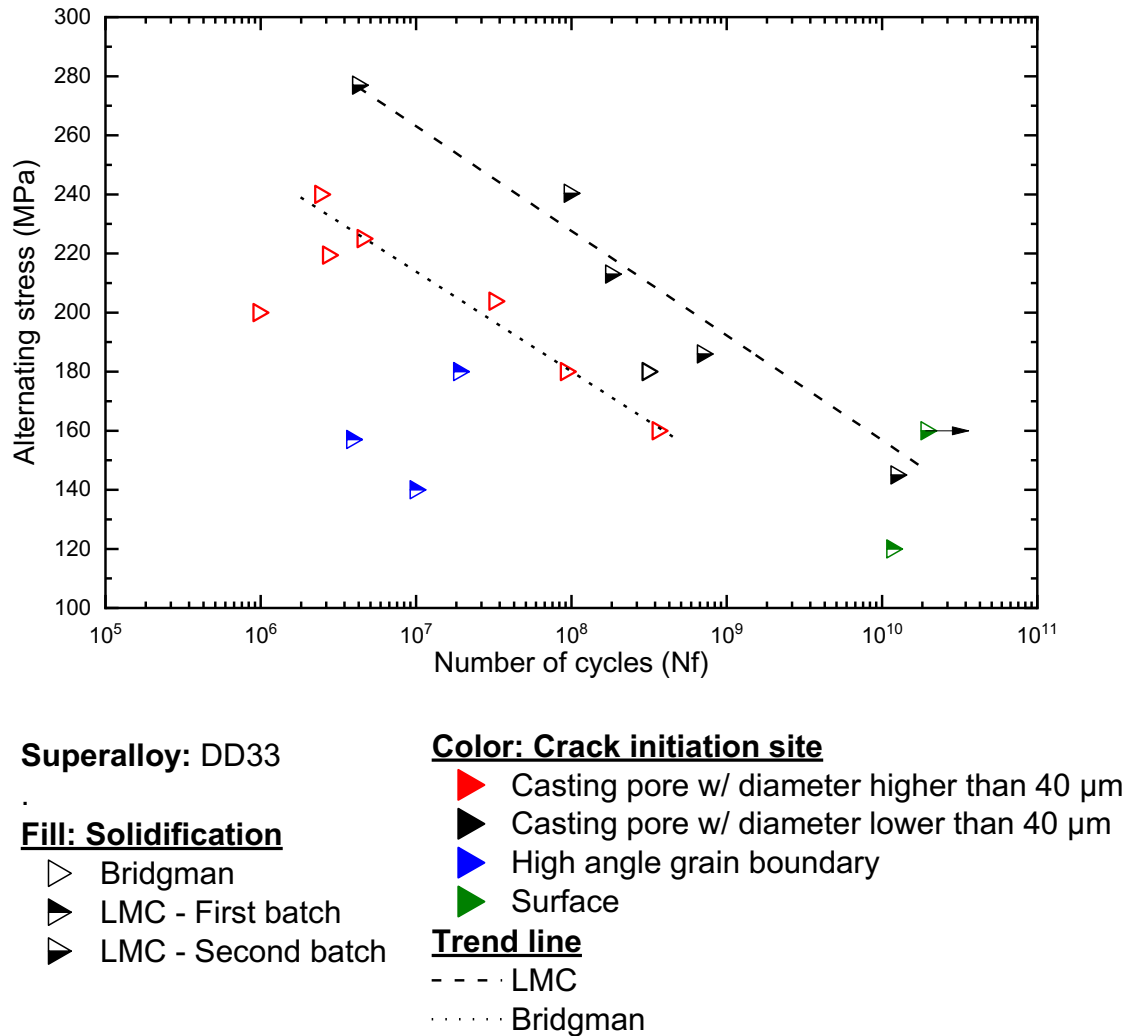


**Figure III-4** S-N diagram for 1,000 °C,  $R_e = -1$ , and  $f = 20$  kHz gathering the results from the samples machined from the DD33 LMC and Bridgman solidified rods. The alternating stress is plotted as a function of the number of cycles to failure.

**Figure III-5** depicts examples of fracture surfaces with crack initiation at casting pores, keeping the color code from **Figure III-4**. **Figure III-5a** shows an example of a DD33/Bridgman sample machined from the 2<sup>nd</sup> batch tested at 160 MPa and fatigue life of  $3.6 \cdot 10^8$  cycles and crack initiation at a casting pore with a  $\approx 70 \mu\text{m}$  diameter indicated by the red arrow (**Figure III-5b**). **Figure III-5c** presents a DD33/LMC sample machined from the 2<sup>nd</sup> batch tested at  $\sigma_a = 240$  MPa and fatigue life of  $9.7 \cdot 10^7$  cycles, with crack initiation at a casting pore with a  $\approx 30 \mu\text{m}$  diameter indicated by the black arrow, see **Figure III-5f**.

The DD33/LMC samples' fatigue life with crack initiation at casting pores is about one decade longer compared to the fatigue life of the Bridgman processed samples due to the reduced casting pore size. This phenomenon has already been described in the literature for AM1 (Steuer et al., 2015) at lower frequencies and AM1/MC-NG (Cervellon et al., 2018) at high frequencies. Again, the casting pores' size control the fatigue life. The following sub-section presents the prediction of the fatigue life by the fatigue indicator parameter developed by Steuer et al. (Steuer et al., 2015) and subsequently improved by (Cervellon et al., 2020a).

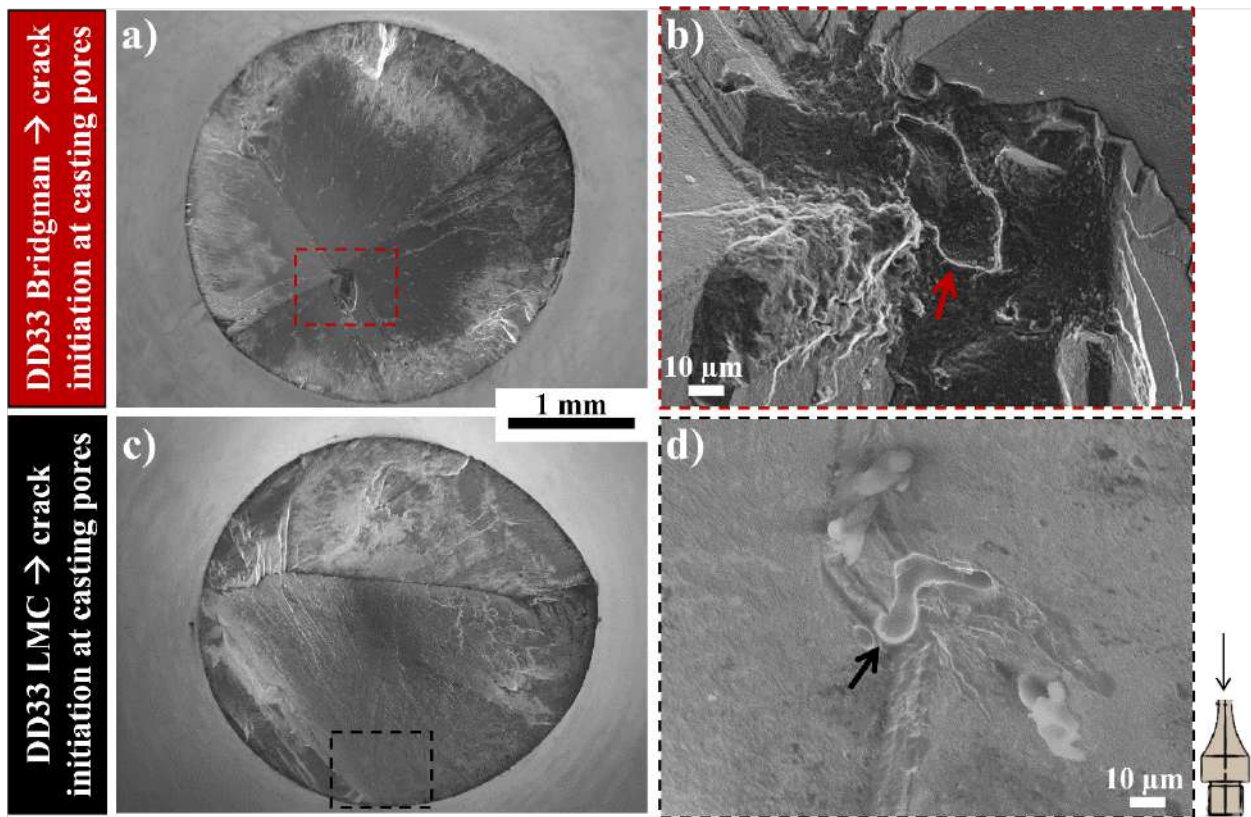


**Figure III-5** Fracture surface observations of DD33 specimens. DD33 Bridgman machined from the 2<sup>nd</sup> batch ( $\sigma_a = 160$  MPa, with  $N_f = 3.6 \cdot 10^8$  cycles) (a), crack initiation zone magnification in (b), detail of a casting pore with a diameter of  $\approx 70 \mu\text{m}$  indicated by the red arrow. DD33 LMC machined from the 2<sup>nd</sup> batch ( $\sigma_a = 240$  MPa, with  $N_f = 9.7 \cdot 10^7$  cycles) (c), crack initiation zone magnification in (d), details the presence of a casting pore with a diameter of  $\approx 30 \mu\text{m}$  indicated by the black arrow.

### 2.3. Fatigue indicator parameter

The casting pore size and position are the main parameters controlling HCF/VHCF fatigue life without significant oxidation, RX, or other nonmetallic defects contribution. Therefore, using the measurements of the size and position of the casting pore serving as crack initiation site and assuming that the total lifetime is mainly spent in micro crack propagation, the model developed by Steuer et al. (Steuer et al., 2015), introduced in **Chapter I sub-section 4.2.3**, was used to compare the predicted and the experimental lifetimes.

The model gathers the fatigue results from Steuer et al. (Steuer et al., 2015) for AM1 superalloy solidified by Bridgman and by LMC method and tested under fully reversed loading,  $f = 0.5$  Hz and  $750$  °C, and the fatigue results from the previous **sub-section 1.1** for the superalloys solidified by Bridgman and LMC methods and tested under fully reversed loading,  $f = 20$  kHz and  $1,000$  °C.

**Table III-3** shows the parameters adopted to **Equation III-1** and **Equation III-2**. They are like those adopted by Steuer et al. and Cervellon et al. (Cervellon et al., 2020a, 2018). The casting pore size was characterized by its maximum circumscribed diameter, as already adopted by Steuer et al. (Steuer et al., 2015) and Cervellon et al. (Cervellon et al., 2020a, 2018), i.e., the diameter of a circle surrounding the critical casting pore.

**Table III-3** Parameters and the values adopted to model the fatigue results.  $k$  is a constant.

$\mu$	$E$ (MPa)	$k$	$\Delta K_{threshold}$ (MPa.m <sup>1/2</sup> )	$Y$
0,408	91600	1	10	0.5 for internal crack initiation 0.65 for sub-surface crack initiation

**Equation III-1** Fatigue indicator parameter defined by (Steuer et al., 2015).

$$FIP = \frac{\mu \Delta \sigma}{E} \left[ 1 + k \frac{\Delta K}{\Delta K_{threshold}} \right]$$

**Equation III-2** Stress intensity factor defined by (Murakami and Endo, 1994).

$$K_I = Y \sigma \sqrt{\pi \sqrt{A_{defect}}}$$

**Figure III-6** depicts the FIP calculation obtained after applying **Equation III-1**.

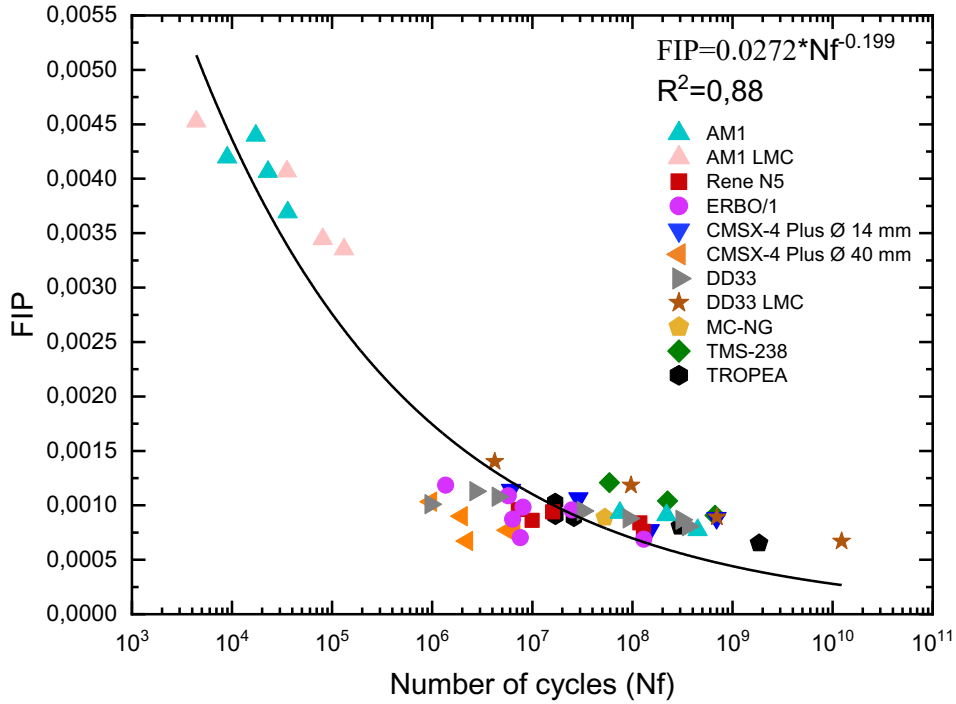


**Figure III-6** FIP versus the number of cycles up to failure for AM1 ( $R_e=-1$ ,  $f=0.5$  Hz and  $750$  °C) from (Steuer et al., 2015) and AM1, Rene N5, ERBO/1, CMSX-4 Plus, DD33, MC-NG, TMS-238, TROPEA ( $R_e=-1$ ,  $f=20$  kHz and  $1,000$  °C) samples studied in this work and processed using different solidification techniques.

The master curve was identified by the results obtained from the samples solidified by the Bridgman and LMC methods. Due to the pore's size calculation method, the lifetime of the samples is scattered, influencing the model accuracy. Still, the parameters were identified, and then the predicted lifetime was calculated using **Equation III-3**.

**Equation III-3** Relationship between the number of cycles to failure and the FIP.

$$Nf = a (FIP)^b$$

As a result, the predicted fatigue life was plotted as a function of the actual life (see **Figure III-7**) to check the model accuracy.

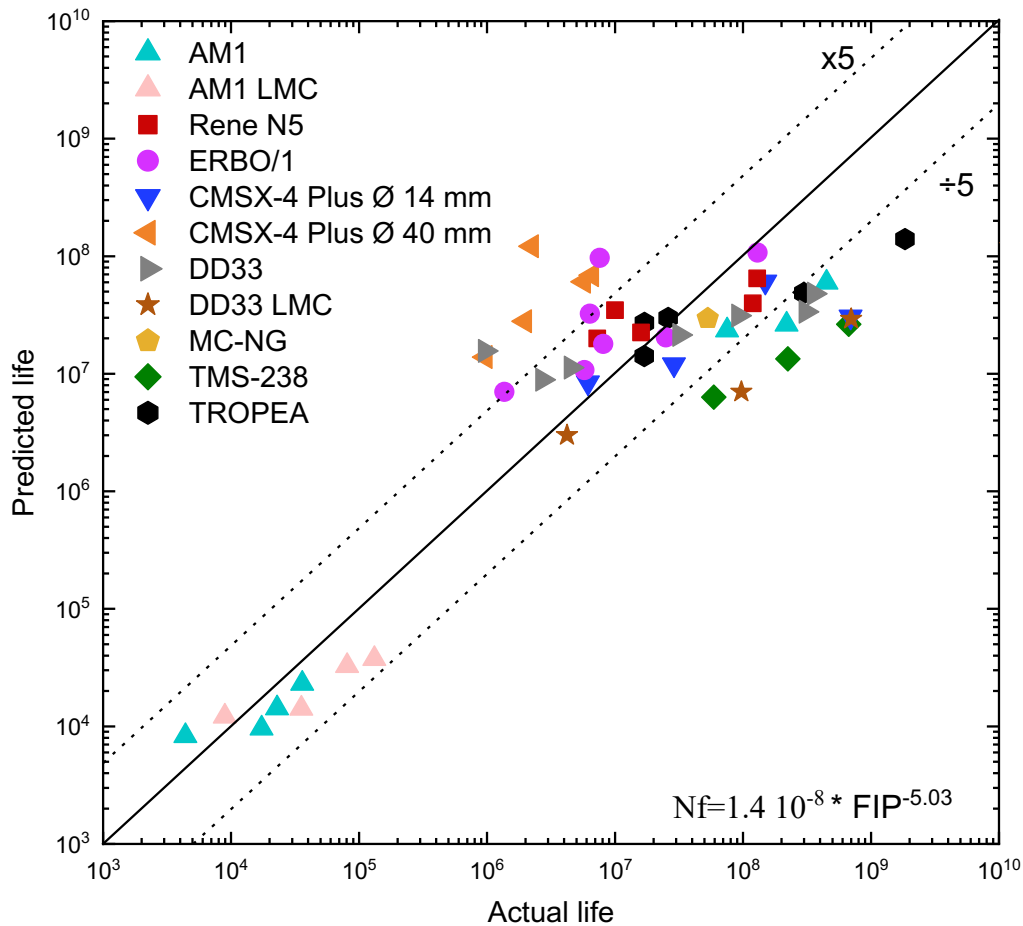


**Figure III-7** Predicted lives using the FIP approach versus the actual life of AM1 ( $R_e=-1$ ,  $f=0.5$  Hz and  $750\text{ }^\circ\text{C}$ ) from (Steuer et al., 2015) and of AM1, Rene N5, ERBO/1, CMSX-4 Plus, DD33, MC-NG, TMS-238, TROPEA ( $R_e=-1$ ,  $f=20$  kHz and  $1,000\text{ }^\circ\text{C}$ ) specimens studied in this work.

In this figure, the continuous bisectrix line represents the perfect modeling, and most data points are inside a factor 5 of accuracy. The accuracy of this modeling approach could be improved considering the actual Young's modulus and a maximum Schmidt factor for each individual specimen by knowing the exact crystallographic orientation of each sample, as well as identifying  $\Delta_{\text{threshold}}$  for long cracks for each alloy.

The objective of the modeling approach is to evaluate the fatigue life, knowing the largest pore size, known to be dependent to the solidification parameters (i.e., thermal gradient, withdrawal rate...) (Brundidge et al., 2011; Brundidge and Pollock, 2012). Therefore, this model's usefulness is to

predict the fatigue life in HCF/VHCF knowing these casting parameters, using e.g., simulations tools like PROCAST modeling.

## 2.4. Summary

The superalloys' chemical composition seems to have almost no (or minor) impact on the VHCF lifetime under fully reversed conditions when an internal crack initiation at a casting pore is observed (Cervellon et al., 2020a). **Appendix C, Figure C-1** and **C-2** show that at  $R = 0.5$  the creep damage coexists with fatigue damage. In fact, the superalloy's chemistry seems to influence the VHCF lifetime at high temperatures and positive stress ratio.

At  $1,000\text{ }^{\circ}\text{C}$  and  $R_e = -1$ , the casting pores' size and position define the superalloys' HCF/VHCF fatigue life. If the casting pore size controls the fatigue life of cast Ni-based SX superalloys, the idea to suppress or decrease the casting pore size seems obvious once the objective is to increase the materials' operating lifetime/temperature. Methods as HIPing and/or AM can be used to obtain "defect-free" "cast" SX superalloys. Indeed, the consequences of these practices will be detailed in the two following sub-sections.

## 3. HIP treatment and compacted casting pores

The HIP treatment is usually employed to suppress or decrease the effect of critical casting pores on the fatigue life. Indeed, according to the literature, there is no full understanding of the influence of this treatment on the VHCF crack initiation mechanism(s). In the present work, rods of four superalloys were solidified by the Bridgman method and then HIPed with specific conditions. **Appendix A.2** depicts the HIP tests database.

**Table III-4** recalls the details of the superalloys investigated in this section. Self-heating was observed for the ERBO/1 tests, indicating the presence of a high density of dislocations, further confirmed at the RUB (Parsa et al., 2016).

**Table III-4** Superalloys investigated in the present sub-section. SHT stands for solution heat treatment and AG for aging.

<i>Superalloy</i>	<i>Rod <math>\varnothing</math> (mm)</i>	<i>Institution</i>	
<b>ERBO/1</b>	Plates 51 x 20 x 55	RUB	SHT (under pressure) → AG
<b>DD33</b>	14	IMR	SHT (under pressure) → AG
<b>CMSX-4</b>	40	RUB	SHT + AG (both under pressure)
<b>Plus</b>	14	CM	SHT 1 → SHT 2 (under pressure) → AG
<b>MC-NG</b>	14	SAE	SHT 1 → SHT 2 (under pressure) → AG

### 3.1. Impact of the HIP process on the VHCF life

Two different HIP treatments were carried out for the CMSX-4 Plus rods. Five CMSX-4 Plus specimens machined from the 40 mm diameter rods were homogenized in the QIH-9 HIP for 12 h/1,345 °C/ + 3 h/1,350 °C, 100 MPa Ar pressure, carried out by RUB. Three CMSX-4 Plus specimens machined from 14 mm diameter rods were first homogenized at 2 h/1,315 °C + 2 h/1,326 °C + 6 h/1,332 °C + 8 h/1,337 °C + 4 h/1,340 °C/AQ, then HIP treated at 4 h/ 1,287 °C/AQ at 103 MPa and finally aged at 6 h/ 1,162 °C/AQ + 20 h/871 °C with no load, carried out by Cannon-Muskegon.

**Table III-2** depicts the maximum casting pore size for the Bridgman solidified bars. The casting pore size of the CMSX-4 Plus solidified in 14 mm diameter rods is about three times smaller than the one observed for CMSX-4 Plus solidified in 40 mm diameter rods. Therefore, after the HIP treatment, the casting pore was expected to be smaller or even suppressed. **Figure III-8** shows the  $\sigma_a$  as a function of the Nf diagram gathering all VHCF results obtained for the CMSX-4 Plus with and without HIP treatment.

The samples HIPed by Cannon-Muskegon presented crack initiation at internal casting pores with a diameter range of 30 – 90  $\mu\text{m}$  (see the fracture analyses in **Figure A-2, Appendix A**). In addition, the critical casting pore diameter decreased by a factor of  $\approx 2$  compared to the “original diameter” (**Table III-2**). Therefore, the fatigue life is almost similar between the results obtained with and

without the HIP treatment (compare red triangles and black squares around the dotted trend in **Figure III-8**).

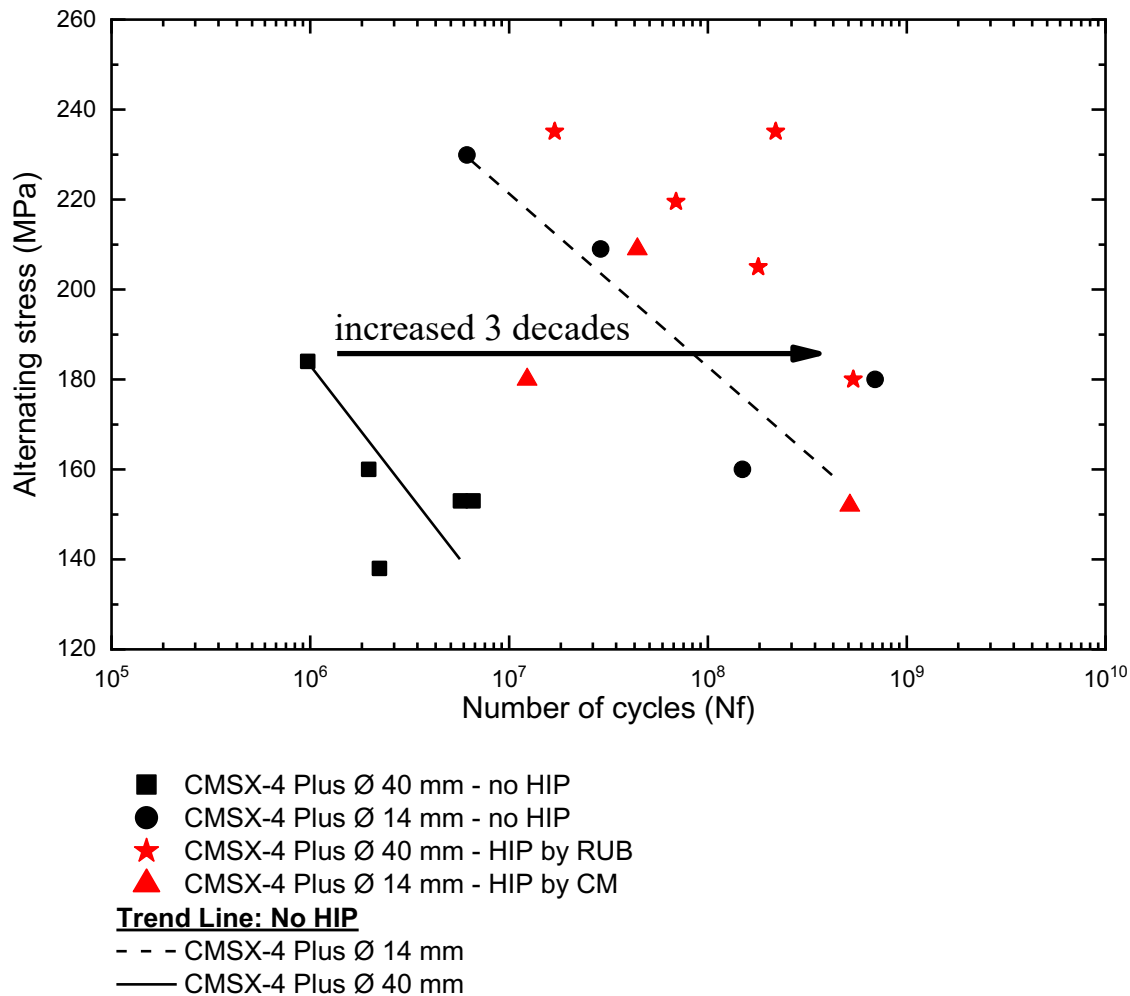


**Figure III-8** S-N diagram for 1,000 °C,  $R_e = -1$ , and  $f = 20$  kHz, gathering the CMSX-4 Plus specimens' life with and without HIP treatment. The alternating stress is plotted as a function of the number of cycles to failure.

The samples HIPed by RUB presented crack initiation at internal features. The fatigue life was enhanced by up to three decades after the integrated HIP treatment compared to the original material without HIPing. The fracture surface analysis and the discussion about the role of the compacted pore microstructure are the subjects of the following sub-section.

The fatigue results indicate that the HIP process of CMSX-4 Plus is temperature dependent. The HIP temperature adopted by RUB is within the  $\gamma'$  super-solvus domain, a practice previously

adopted for the HIP treatment of CMSX-4 in the literature (Epishin et al., 2013). Epishin et al. indicate that temperatures above the  $\gamma'$ -solvus increase the material plastic flow kinetics, leading to a successful pore closure by viscoplasticity. According to the results in **Figure III-8**, HIPing at higher temperatures leads to better VHCF lives, especially considering that RUB performed HIPing on larger castings (i.e., larger pores).

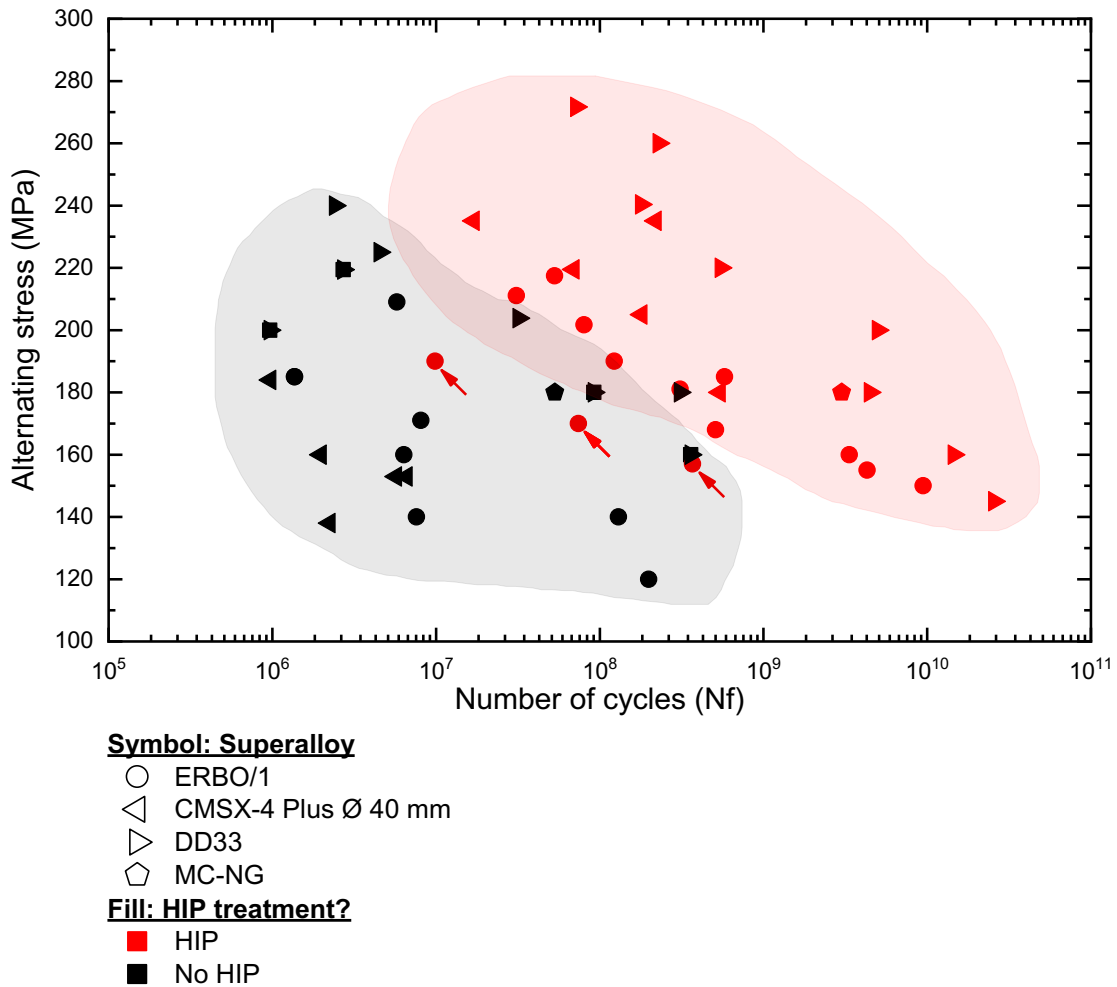
One should also note that no self-heating was identified during the VHCF tests of CMSX-4 Plus HIPed specimens, indicating that the process did not introduce high dislocations density affecting fatigue tests.

*The following sub-sections are dedicated to HIP treatment with crack initiation at features other than casting pores. Therefore, the CMSX-4 Plus HIPed at Cannon-Muskegon will not be further considered in this work.*

### 3.2. VHCF endurance and crack initiation after HIP treatment

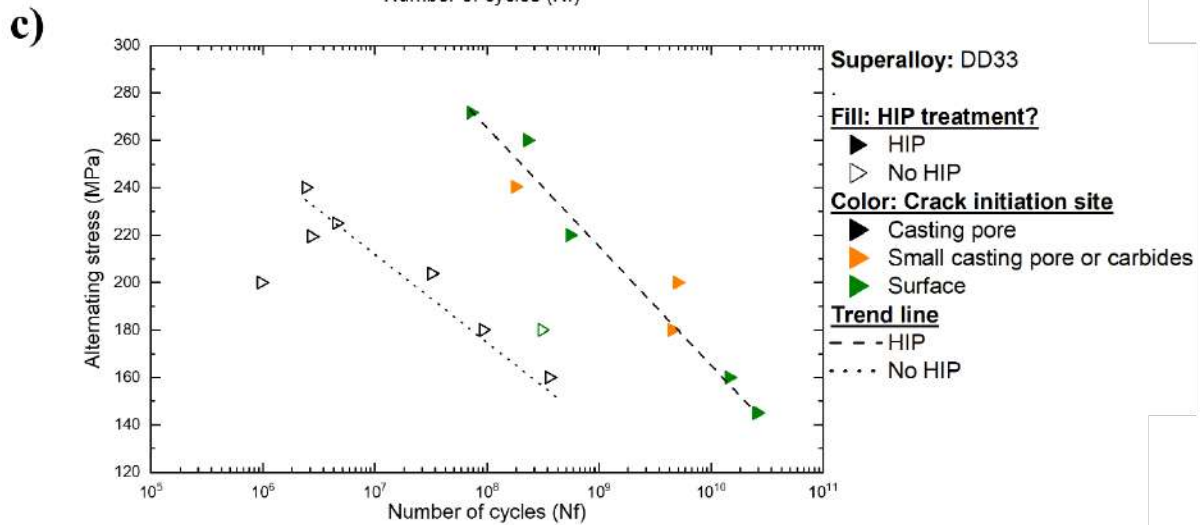
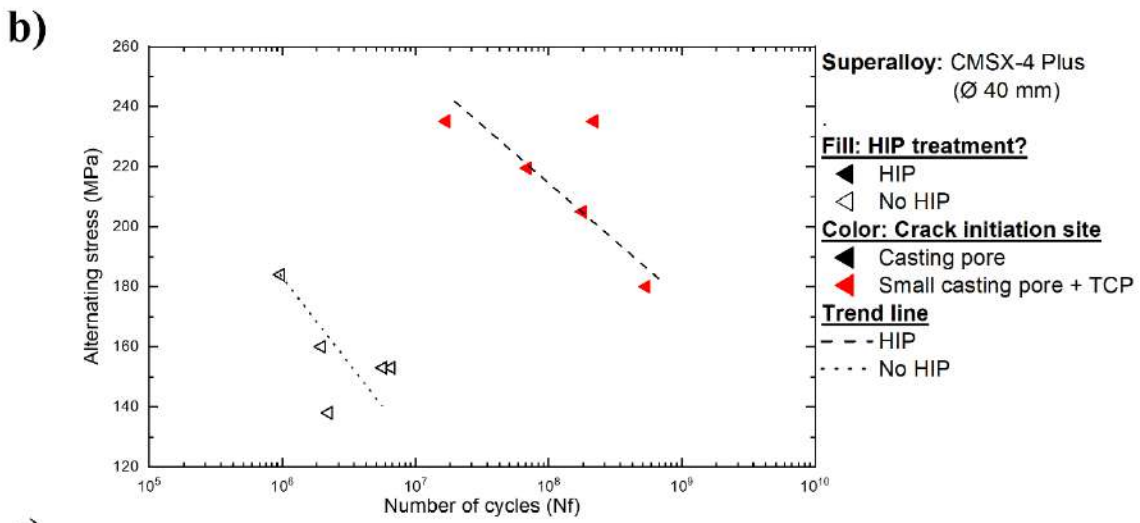
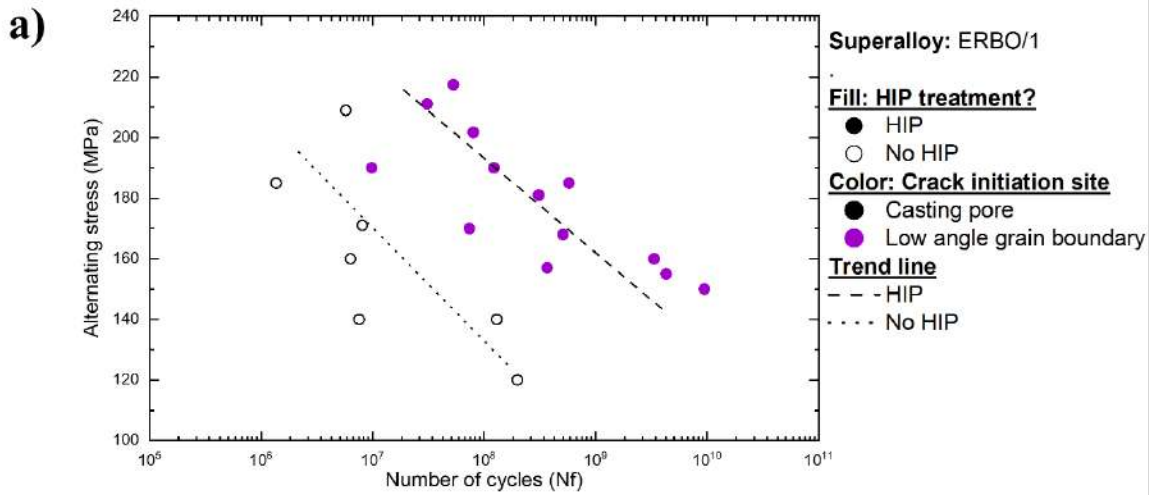
**Figure III-9** shows the S-N diagram of ERBO/1, CMSX-4 Plus ( $\varnothing$  40 mm), DD33, and MC-NG before and after HIPing.

The first analysis is devoted to fatigue life. Compared to the samples fully heat treated (black symbols in **Figure III-9**), the HIPed samples (red symbols in **Figure III-9**) have an improved fatigue life of up to four decades in the [140 – 200 MPa] alternating stress range. Conversely, three ERBO/1 HIPed samples presented fatigue life similar or sometimes lower to the standard group (see red arrows in **Figure III-9**). These specimens are requiring a deeper investigation as it means that HIP treatment provides scatter in fatigue life.



**Figure III-9** S-N diagram for 1,000 °C,  $R_\epsilon = -1$ , and  $f = 20$  kHz gathering the ERBO/1, CMSX-4 Plus ( $\varnothing$  40 mm), DD33, and MC-NG results with and without HIP treatment. The alternating stress is plotted as a function of the number of cycles to failure.

**Figure III-10** depicts each superalloy S-N diagram detailing the crack initiation site for each sample. The ERBO/1 (**Figure III-10a**) HIPed specimens failed at low angle grain boundary (LAGB) features. Note that, the investigation and definition of LAGB will be detailed in the following sub-section. The CMSX-4 Plus ( $\varnothing$  40 mm) (**Figure III-10b**) HIPed specimens failed from small pores filled with TCP. Several DD33 (**Figure III-10c**) HIPed specimens probably failed at small casting pores and/or at carbides. Moreover, some DD33 HIPed specimens and the MC-NG (**Figure III-10d**) sample failed from the surface. The surface crack initiation is the subject of **section 6** of this chapter.



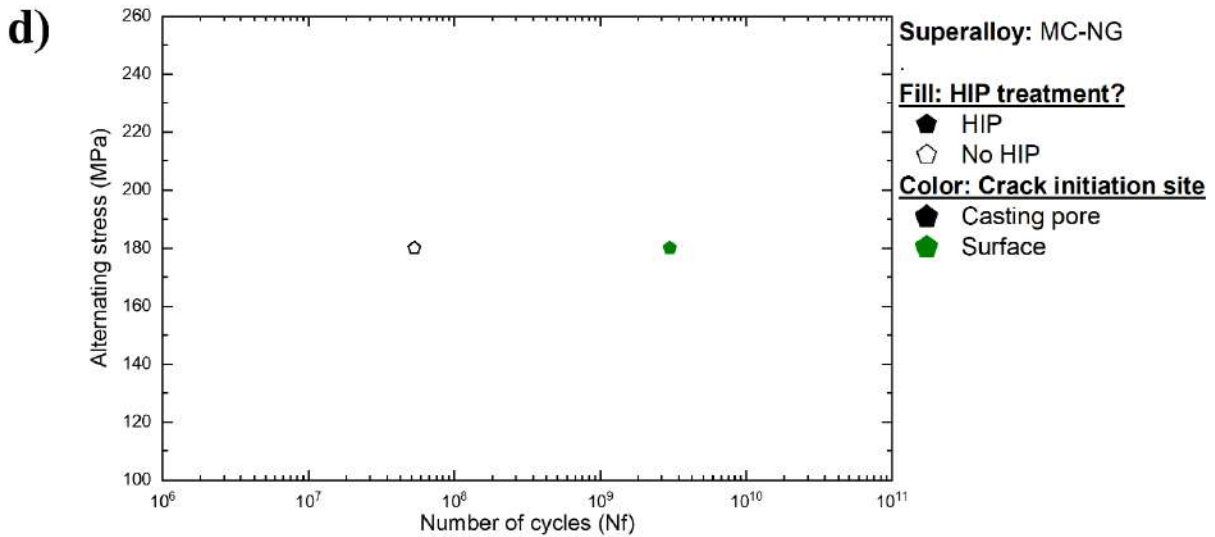


**Figure III-10** Individual *S-N* diagrams for 1,000 °C,  $R_c = -1$ , and  $f = 20$  kHz for ERBO/1 (a), CMSX-4 Plus ( $\varnothing 40$  mm) (b), DD33 (c), and MC-NG (d) with and without HIP treatment results.

**Figure III-11** shows the fracture surface of three specimens. **Figure III-11a** depicts an ERBO/1 sample tested at alternating stress of 190 MPa, resulting in a fatigue life of  $9.8 \cdot 10^6$  cycles. The slightly misoriented grain acting as crack initiation site has a  $\approx 100$   $\mu\text{m}$  diameter, highlighted by a pink arrow (see **Figure III-11b**). This specimen is one of three specimens that presented fatigue life inside the standard HT group, i.e., lifetime lower than the HIP treated samples group (point highlighted by a red arrow and outside the red hatched region in **Figure III-9**).

**Figure III-11c** illustrates a fracture surface for the CMSX-4 Plus HIPed sample tested at alternating stress of 180 MPa, resulting in a fatigue life of  $5.4 \cdot 10^8$  cycles. The rough zone indicates the main internal crack initiation site, see pink arrow in **Figure III-11d**. Unfortunately, it was not possible to clearly define the nature of the crack initiation site from an observation. However, the rough zone indicates plastic activity at a feature that may act as crack initiation site.

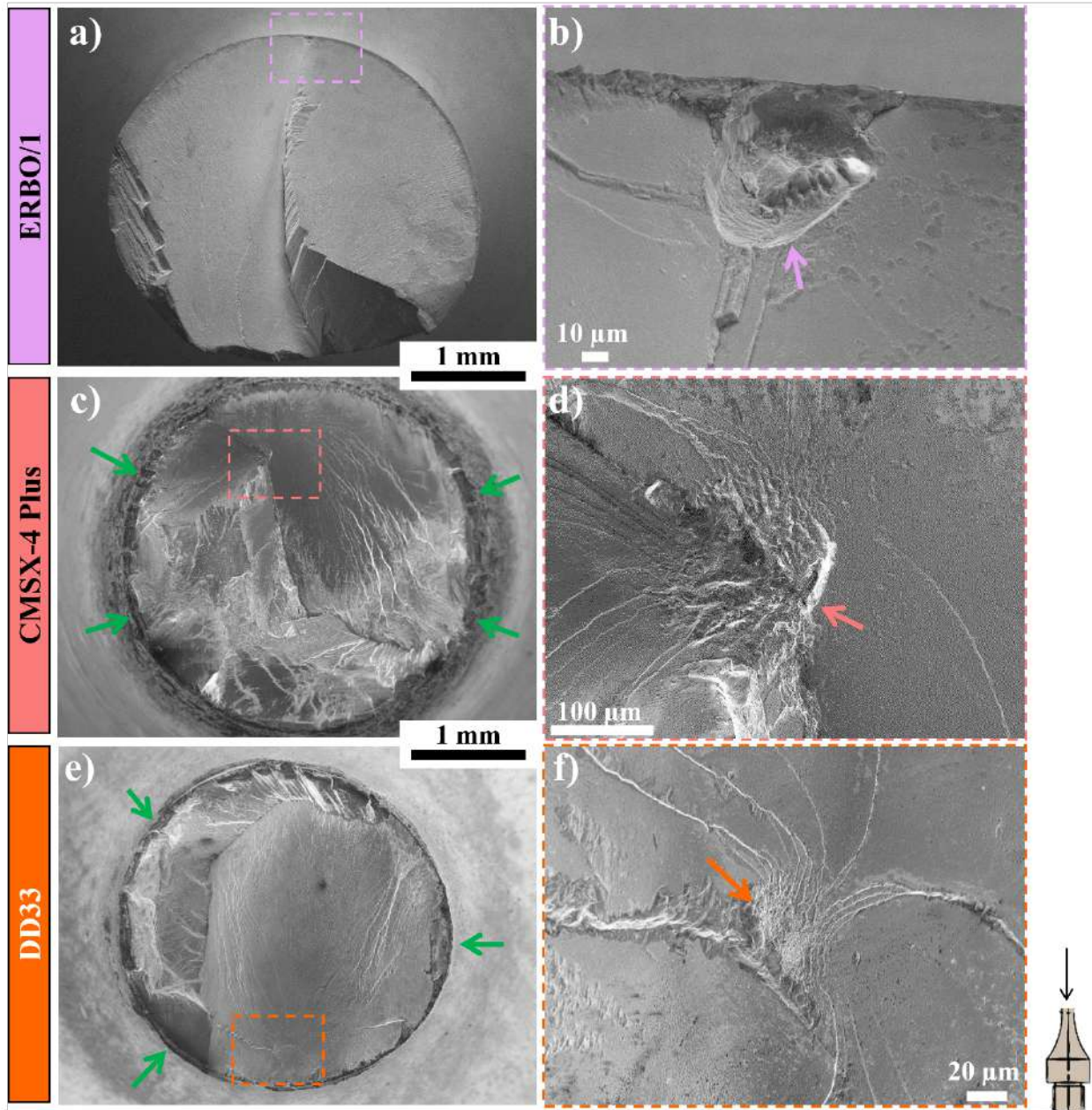


**Figure III-11** Fracture surface observations of ERBO/1 HIPed ( $\sigma_a = 190$  MPa, with  $N_f = 9.8 \cdot 10^6$  cycles) (a), crack initiation zone magnification in (b), detail of the presence of a feature with a diameter of  $\approx 100 \mu\text{m}$  indicated by the purple arrow. CMSX-4 Plus ( $\text{Ø } 40$  mm) sample HIPed ( $\sigma_a = 180$  MPa, with  $N_f = 5.4 \cdot 10^8$  cycles) (c), crack initiation zone magnification in (d), detail of the presence of rough zone indicated by the red arrow. DD33 sample HIPed ( $\sigma_a = 180$  MPa, with  $N_f = 4.5 \cdot 10^9$  cycles) (e), crack initiation zone magnification in (f), detail of the presence of rough zone indicated by the red arrow. The green arrows indicate surface crack initiation site in (c) and (e).

**Figure III-11e** illustrates the DD33 HIPed sample fracture surface. The sample was tested under alternating stress of 180 MPa, resulting in a lifetime of  $4.5 \cdot 10^9$  cycles. The DD33 HIPed example has the same characteristic as the CMSX-4 Plus example. The crack initiation site cannot be identified by fracture analysis. However, the rough zone indicated, again, a local intense plastic activity. **Figure III-11f** is the magnification of the crack initiation zone.

In addition, CMSX-4 Plus/DD33 presented secondary cracks from the surface indicated by the green arrows in **Figure III-11c** and **Figure III-11e**.

### 3.3. Compacted pores morphology

**Figure III-12** shows a longitudinal section intercepting the crack initiation site of the ERBO/1 HIPed sample shown in **Figure III-11a**. The crack initiation site is indicated by the red dotted square in **Figure III-12a**. Indeed, **Figure III-12b** and **c** show a non-fully closed pore at the top of the fracture surface, indicated by the blue arrows. **Figure III-12d, e, and f** also show a non-planar crack propagation. The trajectory is not expected for Ni-based SX superalloys failing in VHCF, which usually show a crystallographic crack path out of the rough zone (Bortoluci Ormastroni et al., 2020a; Cervellon, 2018; Cervellon et al., 2018, 2017; Furuya et al., 2012; Morrissey and Golden, 2007; Stanzl-Tschegg, 2014; Yi et al., 2007; Zhao et al., 2020). The  $\gamma/\gamma'$  microstructure around the HIPed casting pores is heterogeneous (see green dotted lines in **Figure III-12d**). The healing volumes around pores are indicated by yellow arrows in **Figure III-12g, h, and i**. These healing interfaces are identified by the  $\gamma/\gamma'$  microstructure inhomogeneity around the casting pore.

**Figure III-12d, e, and f** show that the crack propagates along cavities. Thus, the author believes that it happens to be the crack initiation site. Furthermore, TCP phases precipitate within the vicinity of the cavities (see white arrows in **Figure III-12d, e, and f**). These characteristics are comparable to the rough zone description of Cervellon et al. (Cervellon et al., 2020a). The green dotted lines in **Figure III-12d** indicate the  $\gamma$  channels direction with an angle being not perfectly  $90^\circ$  across the boundary. Unfortunately, due to the position of the feature and the polishing method, it was not possible to characterize accurately the local orientation by EBSD.

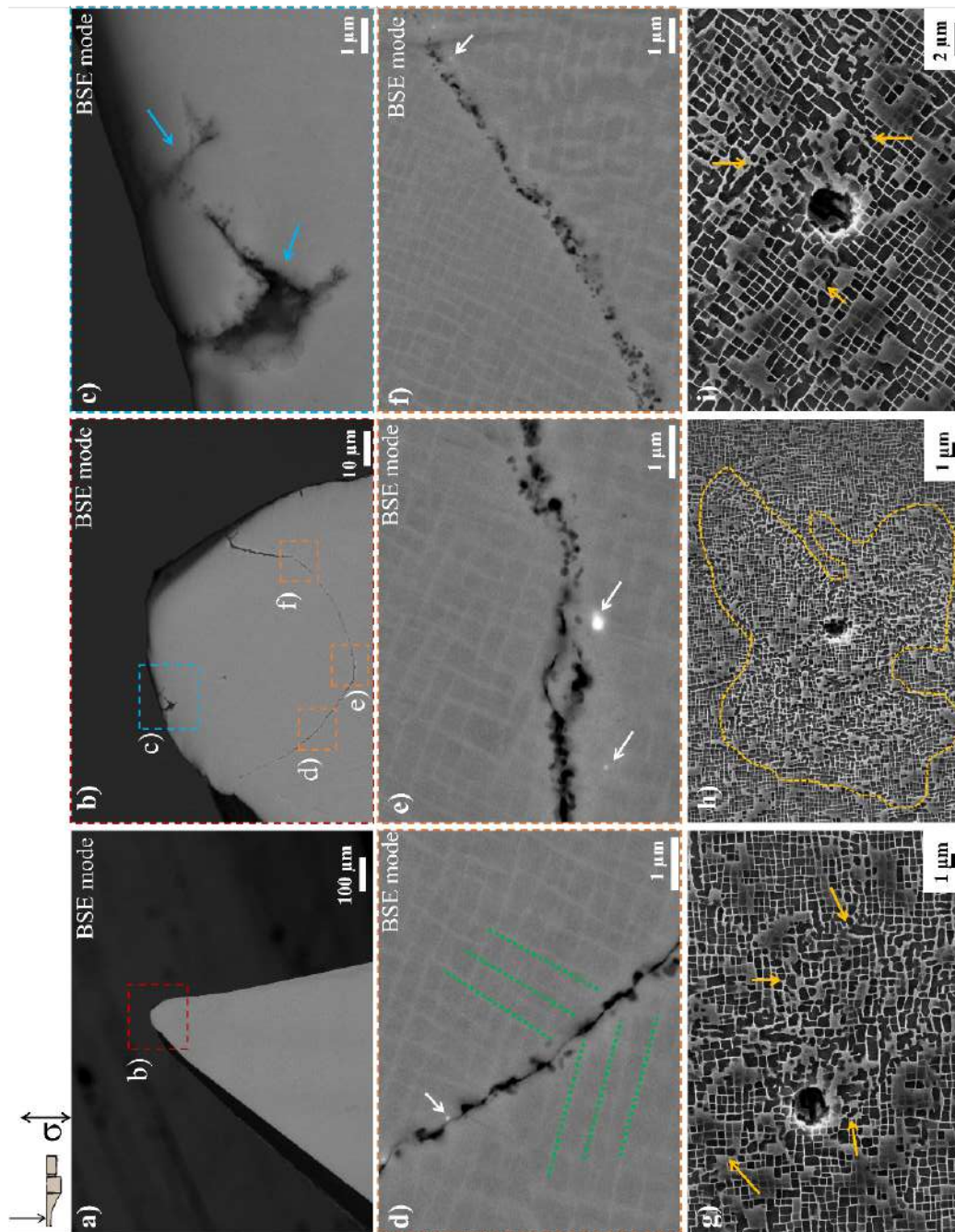


**Figure III-12** Longitudinal section of **Figure III-11a**, ERBO/I HIPed sample ( $\sigma_a = 190$  MPa, with  $N_f = 9.8 \cdot 10^6$  cycles). Analysis of the crack initiation site (a), magnification of top zone indicated by the red square (b). Magnification of a casting pore after the HIP treatment indicated by the blue square in (b) and the blue arrows (c), magnification of the crack initiation zone around the HIPed casting pore in (d), (e), and (f). These SEM observations were done in BSE mode. The white arrows indicate the TCP phases. The green dotted lines in (d) indicate the  $\gamma$  channels “main” direction. HIPed casting pores are presented in (g), (h), and (i). The yellow arrows indicate the healed interfaces. The Yellow dotted line in (h) indicates the heterogeneous microstructure zone.

**Figure III-13a** is the EBSD map with image quality (IQ) superimposed to the inverse pole figure (IPF map) close to what we believe to be an almost-closed casting pore. The fracture surface is recognized to be along the (111) plane (see **Figure III-13a**), a typical crack propagation for Ni-based SX superalloys. The IQ and IPF maps indicate a crystallographic orientation gradient inside the SX bulk. These features were identified close to the fracture surface (**Figure III-13**) and at several internal positions of the HIPed ERBO/1 specimens (see **Appendix A.2, Figures A-3 and A-4**). **Figure III-13c** and **d** indicate the presence of a pore of about 10  $\mu\text{m}$ . **Figure III-13e** up to **h** show the analyses of the regions using different EBSD data post-processing. These features were not identified in the Bridgman processed specimens after VHCF tests.

**Figure III-13g** shows the IQ analysis with the grain reference orientation deviation (GROD) that measures the misorientation gradient compared to the substrate's  $\approx [001]$  orientation. This specific case shows that the misorientation is heterogeneous around the remaining casting pores. This is probably a consequence of the superalloy anisotropic elastic and viscoplastic behavior during the HIP treatment. The graduation between  $\approx 5$  and  $18^\circ$  is a great indication of this heterogeneity. In addition, the GROD reveals that plastic activity occurred in the vicinity of the remaining casting pores in good agreement with Epishin et al. simulations of pore closure during HIPing (see **Figure I-13** and **Figure I-14** in **Chapter I**) (Epishin et al., 2013).

The Kernel average misorientation (KAM) is depicted in **Figure III-13h** with  $15^\circ$  as average misorientation. These areas which are slightly misoriented with respect to the macroscopic single crystal likely to be preferential sites for nucleating grain boundaries during HIPing (Kerisit et al., 2010). The intragranular misorientation indicates that *the investigated features can be defined as LAGB ( $< 15^\circ$ )*.

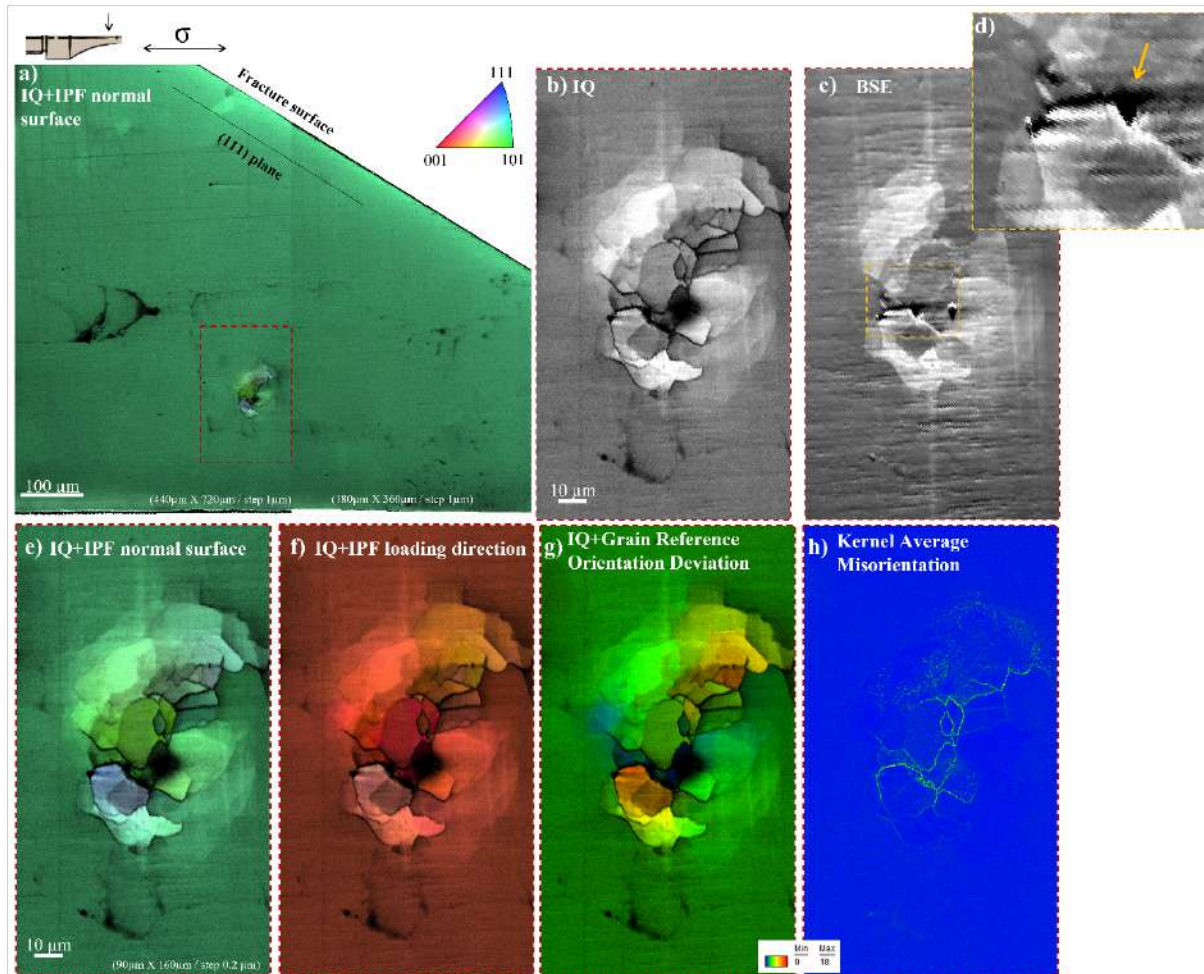


**Figure III-13** EBSD characterization of ERBO/1 HIPed sample illustrated in **Figure III-11a** ( $\sigma_a = 190$  MPa, with  $N_f = 9.8 \cdot 10^6$  cycles) focusing on an almost fully-closed pore. The analysis was carried out close to the fracture surface. Sample's image quality (IQ) superimposed to the inverse pole figure (IPF) map (a). Magnification of the feature indicated by the red dotted rectangle, IQ (b), BSE mode (c), magnification of the yellow dotted square presenting a poorly closed pore (yellow arrow) (d), IQ superimposed to the IPF map normal to the surface (e), IQ superimposed to the IPF map relative to loading direction (f), IQ superimposed to the grain reference orientation deviation (g), and Kernel average misorientation (h).

According to the fracture surface and longitudinal observations, the pore closure mechanism occurred by viscoplastic deformation forming such a feature with  $\approx 100 \mu\text{m}$  size as the one observed in **Figure III-11b**. In addition, specimens were HIPed at super-solvus temperature, increasing the plastic flow rate under these extreme temperatures. The orientation deviation around the features depicted in this sub-section correlates to the plastic strain distribution calculated by

finite elements in the literature (Epishin et al., 2013, 2014; Prasad et al., 2020). Indeed, Epishin et al. show that the von Mises stresses are highly heterogeneous at the pore surface during the compression, leading to significant and localized plastic strains. Even though it is not possible to quantify plastic strain within individual grains using EBSD derived misorientation values, the relationship between misorientation and plastic strain is affected by the heterogeneity in slip (discontinuous) and lattice rotation (continuous) activity (A. Harte et al., 2020).

*In short, after the HIP treatment, the compacted casting pore morphology was defined as a sub-grain structure with low angle grain boundaries (LAGB). What remains a question is how damaging these structures are? Are they more damaging than a casting pore of the same size in terms of fatigue crack initiation life?*

#### **3.4. Solidification pores vs. compacted pores**

The sub-grain structure in **Figure III-13** has a  $\approx 100 \mu\text{m}$  diameter, the sub-grain structure shown in **Figure A-3** has a  $\approx 30 \mu\text{m}$  diameter, and the sub-grain structure shown in **Figure A-4** has a  $\approx 5 \mu\text{m}$  diameter within the analysis presented. Thus, the diameter of the sub-grains structures is as scattered as the casting pores in the non-HIPed specimens. The author believes that the length scale of the compacted features is directly proportional to the pre-existing casting pore size. Indeed, the HIP treatment improved the lifetime of ERBO/1, CMSX-4 Plus, DD33, and MC-NG by two decades, even when the sub-grain structures have diameters of  $\approx 100 \mu\text{m}$ . Therefore, the features presented appear to be less damaging than the casting pores in VHCF life.

Furthermore, the crack initiation and propagation mechanism seem to be comparable. First, in **Figure III-12d, e and f** cavities and TCP precipitates at the interfaces between the sub-grain structure and the superalloy bulk were identified. These zones are very similar to the rough zone characteristics uncovered by Cervellon et al. (Cervellon et al., 2020a).

Based on **Figure III-13**, **Figure A-4**, and **Figure A-5**, one of the key questions is how the local misorientation introduced near closing pores during the HIP process may affect the VHCF life. In fact, it is known from Cervellon et al. (Cervellon et al., 2018) that the presence of LAGB in DS Ni-based superalloys does not significantly affect the VHCF life at  $1,000 \text{ }^\circ\text{C}/R_\epsilon = -1$  compared to the pure single-crystalline alloy (at same solidification parameters).

*Hence, the question is whether between a region near to the healed compacted pore and the macroscopic SX orientation can be more damaging than the casting pore?*

To answer the question, a finite element (FEM) analysis using Abaqus CAE software was carried out to support the discussion. The analysis details are presented in **Appendix D.1**. **Figure III-14** depicts the evolution of the von Mises stress ratio as a function of the diameter of the (pore/sub-grain) inserted in the specimen. This ratio is defined as the maximum von Mises stress in the vicinity of the defect divided by the von Mises stress in the smooth specimen without defect.

Supported by the mechanical results, **Figure III-14** shows that the von Mises stress around a casting pore is higher than the von Mises stress around a grain with the same diameter, located at the same position, with a misorientation lower than  $20^\circ$ . On the other hand, the von Mises stress around the grains with a primary misorientation of  $> 20^\circ$  is higher than the von Mises stress around the casting pore. The finite element analysis does not consider the size effect.

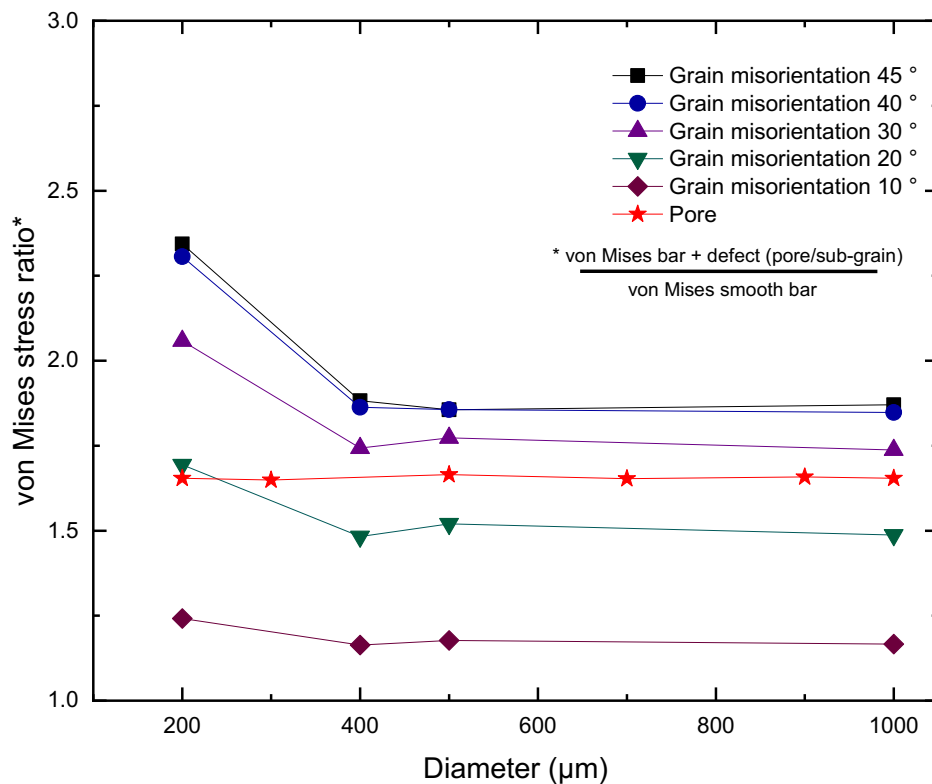


**Figure III-14** Finite element results using the Abaqus software for a spherical grain having a diameter between 200 - 1,000  $\mu\text{m}$  and primary misorientation ( $\theta$ ) in the range of  $10 - 45^\circ$ , and a spherical casting pore designed with diameter between 200 - 1,000  $\mu\text{m}$ .

*In conclusion, the compacted pores with sub-grains misorientated of up to 18 ° from the superalloy mean orientation is considered less harmful than the casting pores under the conditions investigated in this sub-section.*

### **3.5. Impact of incipient melting during the HIP treatment on VHCF life**

**Figure III-15** shows the longitudinal analysis of the specimen shown in **Figure III-11c** CMSX-4 Plus (Ø 40 mm) HIPed sample. The crack initiation site is not intercepted in the observation plane. On the other hand, **Figure III-15** shows the analysis of three compacted casting pores encountered in the sample's bulk. **Figure III-15a** and **b** show a pore of less than 1  $\mu\text{m}$  diameter surrounded by a homogeneous  $\gamma/\gamma'$  microstructure. The red dotted square shows the pore at high magnification. The compacted casting pores are surrounded by a heterogeneous microstructure indicated by orange dotted lines in **Figure III-15c**, and **e**.

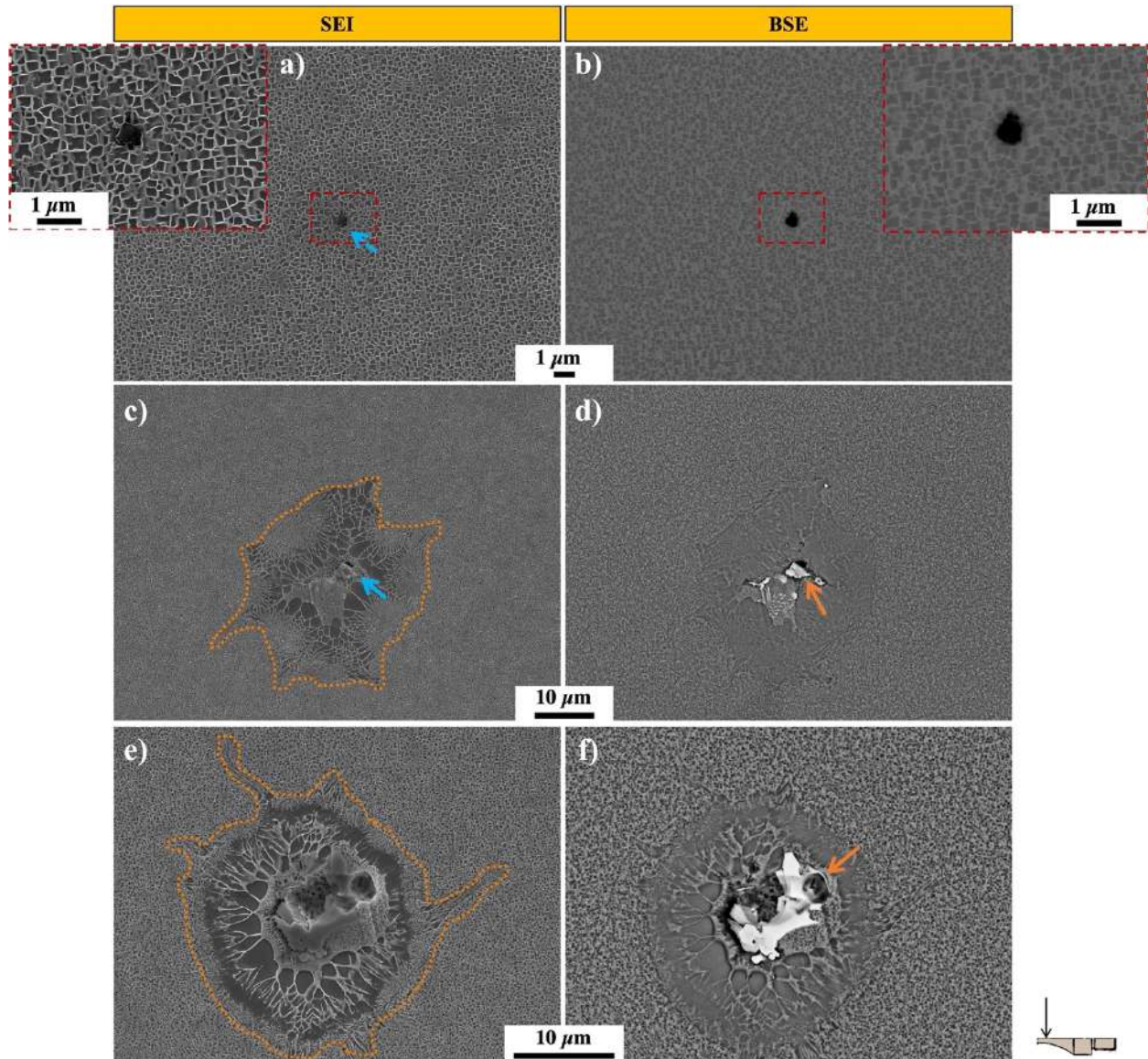


**Figure III-15** Longitudinal analysis of **Figure III-11c** CMSX-4 Plus ( $\varnothing$  40 mm) sample HIPed ( $\sigma_a = 180$  MPa, with  $N_f = 5.4 \cdot 10^8$  cycles). Compacted pore morphology surrounded by homogeneous microstructure (a and b) and the magnification of the dotted red square. Pore surrounded by a heterogeneous microstructure indicated by the orange dotted line (c), and (e). The blue arrow indicated the compacted casting pores. The orange arrows indicate white phases in (d) and (f).

The SEI images do not give much information about the feature encountered around the casting pores. However, the BSE mode images show white particles at the interface of the casting pore and the heterogeneous microstructure (see orange arrows in **Figure III-15d** and **f**). The author believes that the heterogeneous structures around the casting pores are local incipient melting (IM)

pockets developed during the HIPing process since it has already been shown previously that the IM areas may develop even for HT at close-solvus conditions and since, in the present case, HIP was performed at nearly solidus conditions. One has to note that under isostatic pressure, both  $\gamma'$  solvus and IM temperature are rising (Bortoluci Ormastroni et al., 2020a). The white particles observed in **Figure III-15d** and **f**) are surrounded by  $\gamma'$  deformed precipitates.

The EBSD characterization of the incipient melting developed during the hot isostatic pressing process is presented in **Figure III-16**. IQ superimposed to the IPF map relative to the loading direction of an incipient melting (**Figure III-16b** and magnification in **Figure III-16e**) shows that after the “resolidification” this melted zone has the same crystallographic orientation as the parent SX material. A second incipient melting was analyzed by EBSD characterization (see **Figure A-5**). The EBSD characterization shows TCP phases inside the compacted pores surrounded by the IM (see **Figure III-16f** and **Figure A-5e**). Prior characterizations from the authors have shown that these white particles are very rich in Re, with a local Re content of up to 30 wt. pct. in CMSX-4 Plus (Bortoluci Ormastroni, 2018).

Introducing nearly 20 % of IM in CMX4- Plus/Bridgman rods did not influence the LCF, HCF, VHCF fatigue life or the high temperature tensile and creep properties (Bortoluci Ormastroni et al., 2020a). Furthermore, no crack initiation was identified at IM by Bortoluci et al. (Bortoluci Ormastroni et al., 2020a) in CMSX-4 Plus. Despite these TCP phases are known to be brittle at low temperatures and to lead to interfacial decohesion in LCF conditions at a high temperatures of 950 °C (Simonetti and Caron, 1998) no specific impact has been observed here in CMSX-4 Plus. This may be a result of their small size compared to the other defects within the specimens.

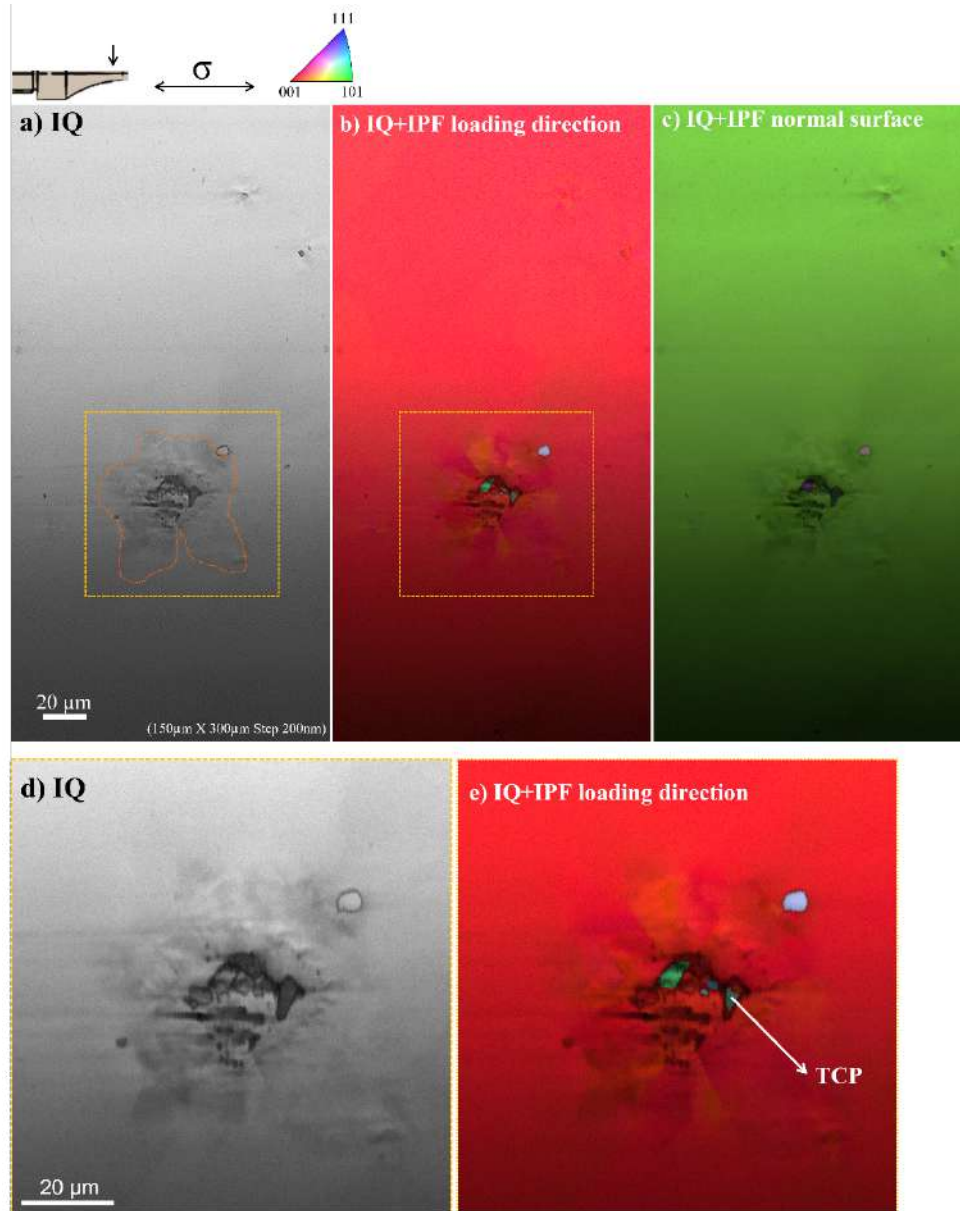


**Figure III-16** EBSD characterization of CMSX-4 Plus ( $\varnothing$  40 mm) sample HIPed ( $\sigma_a = 180$  MPa, with  $N_f = 5.4 \cdot 10^8$  cycles) illustrated in **Figure III-11c** focusing on an incipient melting (surrounded by the orange dotted line). Sample's image quality (IQ) (a). IQ superimposed to the IPF map normal to the relative loading direction (b), IQ superimposed to the IPF map to the normal direction (c). Magnification of the IM (yellow dotted square) in IQ (d) and IQ superimposed to the IPF map normal to the relative loading direction (e). The TCP phase is indicated by the white arrow.

### 3.6. Summary

According to our experiments, a HIP treatment performed between  $\gamma'$ -solvus temperatures and the incipient melting temperature seems to provide the best subsequent VHCF durability. Furthermore, as pore closure during HIPing occurs by plastic deformation, nucleation of low angle grain boundaries/sub-grains in the vicinity of former casting pores are observed. For the first time in the literature, it is shown that these sub-grain structures can lead to an earlier fatigue crack initiation if local misorientations larger than  $20^\circ$  (i.e., High Angle Grain Boundaries) are encountered.

Moreover, if no LAGB develops during the HIP process, the crack initiation site takes place at small (not completely closed) pores filled by TCP phases. The incipient melting areas were observed to have the same orientation as the parent material under HIP treatment and there is no evidence that the IM reduces the fatigue life of Ni-based SX superalloys under VHCF conditions at high temperatures.

## 4. PBF-E processed Ni-based SX superalloy: toward defect-free single-crystals?

The PBF-E CMSX-4 SX samples are divided into different groups depending on whether they have received a HIP treatment or not and on the atomized powders' quality. A first batch called AM/HT/REC (AM: Additive manufacturing, HT: Heat treated, REC: Recycled atomized powder) specimens built with recycled powder, HT by the standard method in the air at  $1,315^\circ\text{C}/35$  min and finally aged at  $1,140^\circ\text{C}/2$  h/AQ (air quench) and  $870^\circ\text{C}/20$  h/AQ, has been characterized.

For the second batch, called AM/HIP (HIP: HIP treatment), the specimens were homogenized in the QIH-9 HIP at  $1,315^\circ\text{C}/35$  min under 100 MPa Argon pressure. The material was directly quenched after holding by applying the fast-cooling capability of the HIP set-up to achieve ultrafine  $\gamma'$  precipitates. Then, the material was subjected to the same AG treatment as defined for the non-HIPed material. The CMSX-4 PBF-E stereological characterization is detailed in the literature (Pistor and Körner, 2019; Ramsperger et al., 2015; Ruttert et al., 2016).

The AM/HIP samples were received in two different sub-batches, the first one with eight bars built with recycled powder (AM/HIP/REC) and the second one with four bars built with fresh powder (AM/HIP/FRS) (FRS: Fresh atomized powder). **Table III-5** details the nomenclature employed

for AM samples. **Appendix A.1** and **Appendix A.2** present the fatigue tests database of this subsection.

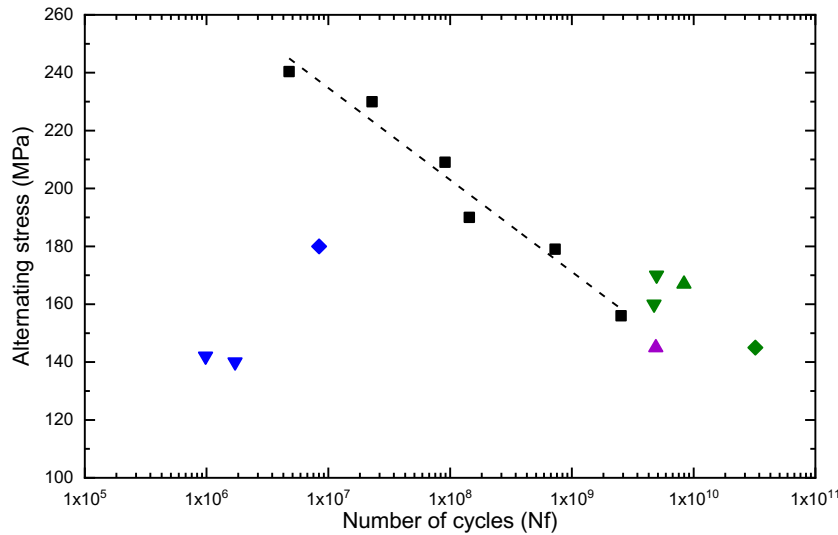
**Table III-5** Sample's nomenclature. *HT* is the denomination for full heat treatment. *AQ* is the denomination for air quench. *PBF-E* is the denomination for electron beam-based powder bed fusion.

<i>Superalloy</i>	<i>Number of samples</i>	<i>Superalloy/Solidification process/Heat treatment</i>
AM/HT/REC	2	Additive manufacturing (PBF-E) samples-built w/ recycled CMSX-4 atomized powder → SHT in air at 1,315 °C/35 min and AG steps at 1,140 °C/2 h/AQ and 870 °C/20 h/AQ
AM/HIP/REC	8	Additive manufacturing (PBF-E) samples-built w/ recycled CMSX-4 atomized powder → HIP homogenization at 1,315 °C/35 min under 100 MPa Argon pressure
AM/HIP/FRS	4	Additive manufacturing (PBF-E) samples-built w/ fresh CMSX-4 atomized powder → HIP homogenization at 1,315 °C/35 min under 100 MPa Argon pressure

#### 4.1. VHCF performance of PBF-E SX

**Figure III-17** presents the S-N diagram gathering all VHCF results obtained for the PBF-E samples. Fatigue lives ranging from  $\approx 10^6$  cycles to  $\approx 3.0 \cdot 10^{10}$  cycles were obtained at  $\sigma_a = 145$  MPa. The latter result is probably the longest test ever performed on this alloy class at high temperatures (Cervellon, 2018; Zhao et al., 2022, 2021b).

The AM results are compared to the CMSX-4/Bridgman results from the literature (Cervellon et al., 2018). The symbols define the superalloy by its processing method, HT, and atomized powder quality. The colors indicate the crack initiation type in agreement with **Figure III-4** and **Figure III-10**.



- Shape: Superalloy**
- CMSX-4/Bridgman (Cervellon, 2018)
  - ◆ AM samples built w/ recycled CMSX-4 atomized powder → Standard HT (AM/HT/REC)
  - ▲ AM samples built w/ recycled CMSX-4 atomized powder → HIP HT (AM/HIP/REC)
  - ▼ AM samples built w/ fresh CMSX-4 atomized powder → HIP HT (AM/HIP/FRS)
- Color: Crack initiation site**
- Solidification pore
  - High angle grain boundary
  - Low angle grain boundary
  - Surface
- Trend line**
- - - CMSX-4/Bridgman

**Figure III-17** S-N diagram for 1,000 °C,  $R_\epsilon = -1$ , and  $f = 20$  kHz gathering the PBF-E SX results. The alternating stress is plotted as a function of the number of cycles to failure. The CMSX-4/Bridgman data, represented with black squares, were extracted from the literature (Bortolucci Ormastroni et al., 2022; Cervellon, 2018; Cervellon et al., 2018).

From **Figure III-17**, AM processed samples are presenting very different VHCF lives, either very long ones of more than  $5 \cdot 10^9$  cycles or short ones below  $10^7$  cycles. Six AM/HIP/REC samples failed from stray grains, presumably formed during the PBF-E and/or HIPing processes, further discussed in **sub-section 5**. In the following no specific distinction will be made between the HAGB and stray grain.

The successful tests using PBF-E processed specimens (i.e., AM/HT/REC, AM/HIP/REC, and AM/HIP/FRS samples) with VHCF lives close to the CMSX-4/Bridgman trend line mostly failed from a surface crack initiation and one specimen failed from an internal site see **Figure III-17**.

As mentioned in the literature, see **Chapter I, sub-section 1.5.2**, a high density of “processing” dislocations is stored in the SX superalloy bulk after the PBF-E process. A high initial density of dislocations limited the maximum alternating stress values reachable ( $\sigma_a \leq 170$  MPa for

AM1/HT/REC and  $\sigma_a \leq 165$  MPa for AM1/HIP/REC and AM1/HIP/FRS) due to self-heating issues. In fact, the VHCF set-up at Institut Pprime is working with a continuous excitation mode (i.e., no possibility of pulse-pause mode), leading to complex temperature management during self-heating periods. As the AM SX samples are difficult to obtain, the author decided to test them under the maximum allowable alternating stress reached without self-heating phenomena.

The fracture analysis of CMSX-4/Bridgman specimens was already presented in detail by Cervellon et al. (Cervellon, 2018). Regarding the successful results shown in **Figure III-17** for PBF-E processed specimens (i.e., no consideration of specimens containing high angle grain boundaries), most AM/HT/REC, AM/HIP/REC, and AM/HIP/FRS samples presented crack initiation at the surface. These specimens will be further analyzed and compared in **section 6**. Thus, this sub-section will investigate only AM/HIP/REC ( $\sigma_a = 145$  MPa,  $N_f = 4.9 \cdot 10^9$  cycles) the sample with crack initiation from an internal site (see **Figure III-18**).

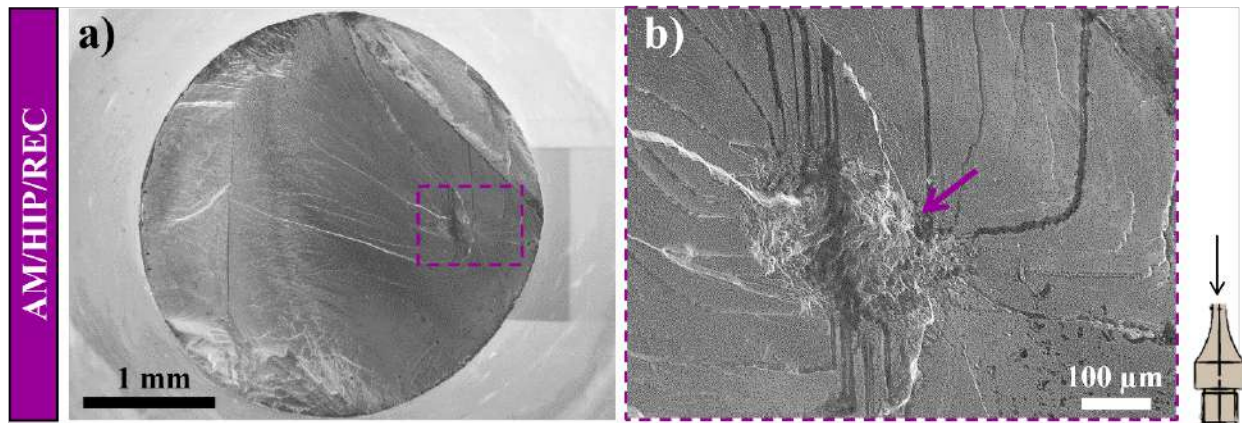


**Figure III-18** Fracture surface observations of AM/HIP/REC ( $\sigma_a = 145$  MPa,  $N_f = 4.9 \cdot 10^9$  cycles) with an internal crack initiation, presenting the characteristic rough zone indicated by the purple arrow.

#### 4.2. Crack initiation from an internal site: AM/HIP/REC specimen

**Figure III-18b** depicts the characteristic rough zone commonly observed at the main crack initiation site of samples tested in VHCF conditions at  $R_e = -1$  (Cervellon et al., 2020a). However, it was not possible to conclude on the exact nature of this crack initiation site from fractographic observations, and further observations along longitudinal cuts were thus performed.

**Figure III-19** shows a high magnification observation along a longitudinal section intercepting the initiation site of the main crack initiation depicted in **Figure III-18b**. **Figure III-19a** shows a secondary crack in the sample's surface indicated by the white square. In addition, the crack initiation site is indicated by the blue dotted square (see its magnification in **Figure III-19b**). The green square region indicates the EBSD analysis zone.

Different imaging modes were employed to try to determine the exact nature of the crack initiation site. **Figure III-19c** and **d** show the TCP precipitates identified by the red arrows, and the white arrows indicate discontinuities like voids in the rough zone. These characteristics are typical of a rough zone due to locally very high deformation magnitude, as previously observed by Cervellon et al. (Cervellon et al., 2020a). Thus, the crack initiation zone is like the one uncovered in **Figure III-12** for a cast version of CMSX-4.

**Figure III-20** shows the EBSD analysis performed below the crack initiation site according to the green rectangle's localization provided in **Figure III-19a**. The IQ+IPF images show that most of this region below the crack initiation site presents angular variations lower than  $1^\circ$  indicating the absence of recrystallization. However, a small "RX" zone of  $\approx 60 \mu\text{m}$  in extension (see a yellow rectangle in **Figure III-20a-c**) was observed close to the crack initiation zone. It comprises several low angle grain boundaries of local misorientation typically lower than  $10^\circ$  (see **Figure III-20d**).

**Figure III-13** and **Figure III-20** identify sub-grains regions of  $30 - 100 \mu\text{m}$  with low internal angle grain boundary to the ERBO/1 and AM/HIP/REC macroscopic SX. Therefore, the author concluded that the crack initiation of AM/HIP/REC ( $\sigma_a = 145 \text{ MPa}$ ,  $N_f = 4.9 \cdot 10^9$  cycles) sample is due to the presence of LAGB, suchlike the crack initiation sites shown in **sub-section 3.3**.

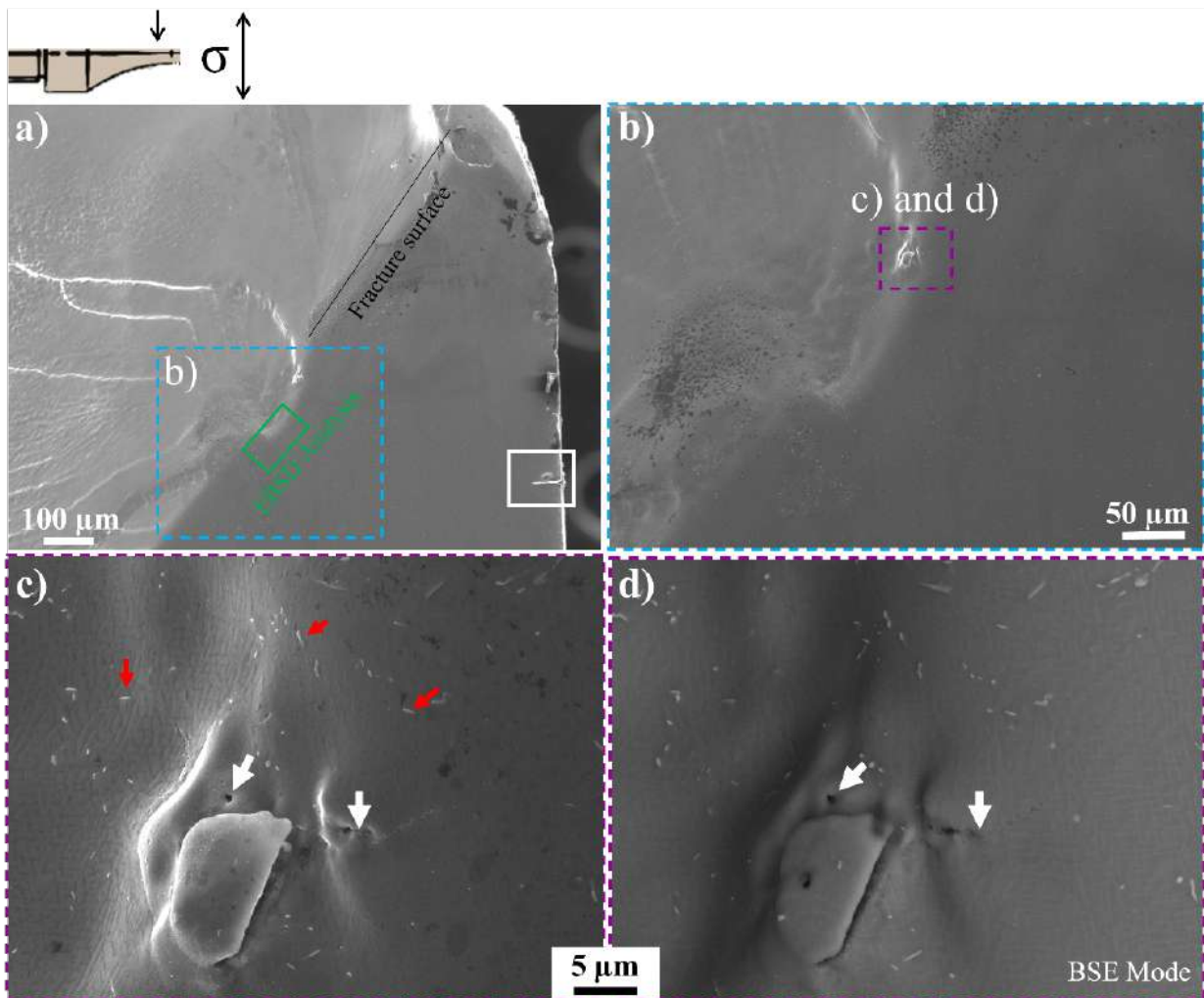


**Figure III-19** Crack initiation site of AM/HIP/REC ( $\sigma_a = 145$  MPa,  $N_f = 4.9 \cdot 10^9$  cycles) observed along a longitudinal section. Few secondary cracks are observed at the surface (see white square) (a). Magnification of the crack initiation site identified by the rough zone (b), and the magnified images of the crack initiation site using the SEI (c), and BSE imaging mode (d). The white arrow indicates cavities, and the red arrows indicate the presence of TCP precipitates. The green square in (a) shows the location where the EBSD analyses were performed.

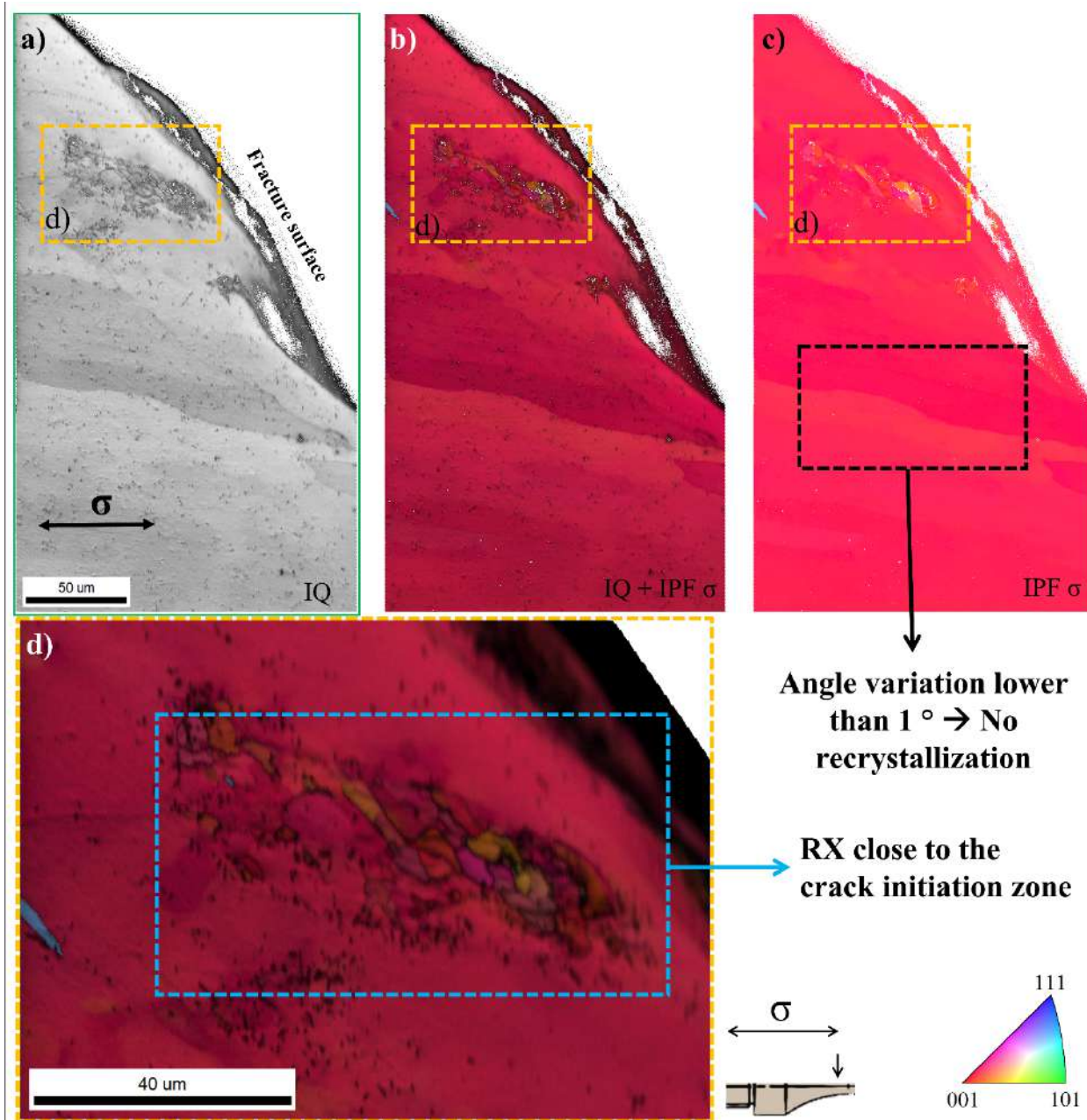


**Figure III-20** EBSD characterization of AM/HIP/REC ( $\sigma_a = 145$  MPa,  $N_f = 4.9 \cdot 10^9$  cycles) crack initiation zone (yellow rectangle in **Figure III-20a**) including image quality (IQ) (a), IQ, superimposed to the inverse pole figure (IPF map) (b), and IPF map relative to the loading direction (c). The black dotted rectangle shows an angle variation lower than  $1^\circ$ . The region (dotted yellow rectangles in (a-c)) contains several recrystallized cells with low angle grain boundaries (d).

### 4.3. Summary

Ni-based SX superalloy specimens PBF-E processed were investigated in the VHCF conditions for the first time in the literature. The VHCF life was shown to be comparable or higher than the one of Bridgman solidified Ni-based SX superalloys for the specimens with no stray grains present within the gage part of the specimens. Part of the samples failed by surface crack initiation, part at high angle grain boundaries features, and one sample failed at a low angle grain boundary. The last ones were considered defect “free” inherent from the additive manufacturing process. Moreover, the presence of “processing” stored dislocations in the material bulk limited the maximum reachable alternating stress.

## 5. Processing defects: stray grains

The presence of stray grains within the gage part of VHCF specimens, particularly close to the surface, results in very low VHCF lives for LMC solidified and PBF-E built superalloys. Indeed, failure during the initial ramping-up in alternating stress to reach the desired value in  $\sigma_a$  was obtained for six AM/HIP/REC samples. **Figure III-21** depicts two different examples of PBF-E samples with immediate failure at stray grains.

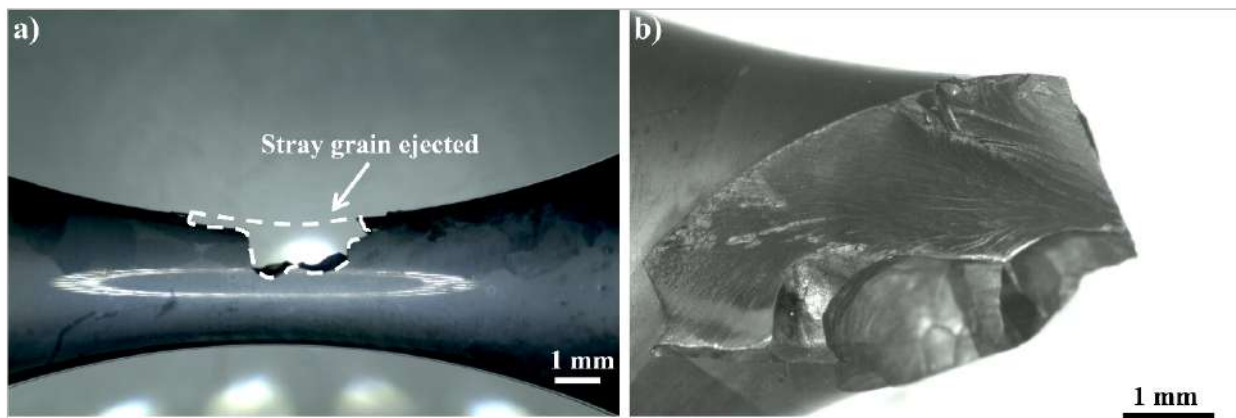
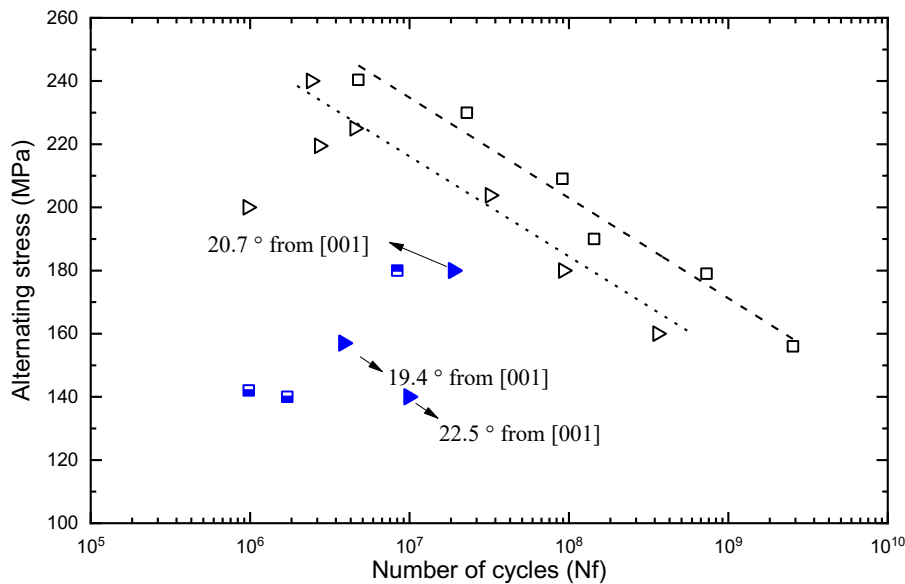


**Figure III-21** Optical microscope observations of two AM/HIP/REC samples that presented immediate failure. The white dotted region in (a) illustrates the location of a stray grain ejected from the specimen gage part during the application of the alternating stress. A specimen with complete failure at stray grains (b).

**Figure III-22** gathers all “successful” results obtained for DD33/LMC (**Figure III-4**) and CMSX-4/PBF-E (**Figure III-17**), including those with crack initiation at HAGB. The grain boundaries within the gage part of specimens appear to be detrimental to the VHCF life of AM and LMC processed specimens and may lead to fatigue lives well below the ones obtained for Bridgman processed alloys. According to EBSD characterizations performed at IMR, grain boundaries with misorientation larger than  $15^\circ$  from the [001] direction were observed on low fatigue life DD33/LMC specimens (see **Figure III-23**). **Figure III-23** depicts typical fracture surface observations of AM/HT/REC, AM/HIP/FRS, and DD33 LMC.



**Symbol: Superalloy/Solidification process**

- CMSX-4/Bridgman (Cervellon, 2018)
- AM samples built w/ recycled CMSX-4 atomized powder  
→Standard HT (**AM/HT/REC**)
- AM samples built w/ fresh CMSX-4 atomized powder  
→HIP HT(**AM/HIP/FRS**)
- ▷ DD33/Bridgman
- ▶ DD33/LMC

**Color: Crack initiation site**

- Solidification pore
- High angle grain boundary

**Trend line**

- - - CMSX-4/Bridgman
- ..... DD33/Bridgman

**Figure III-22** S-N diagram for  $1,000^\circ\text{C}$ ,  $R_\epsilon = -1$ , and  $f = 20\text{ kHz}$  gathering the results with crack initiation at high angle grain boundary from **Figure III-4** and **Figure III-17**. The alternating stress is plotted as a function of the number of cycles to failure. Special attention has been paid to the grain boundary orientation deviation from the main [001] crystallographic orientation. The CMSX-4/Bridgman data, represented with black opened squares, were extracted from the literature (Cervellon, 2018; Cervellon et al., 2018).

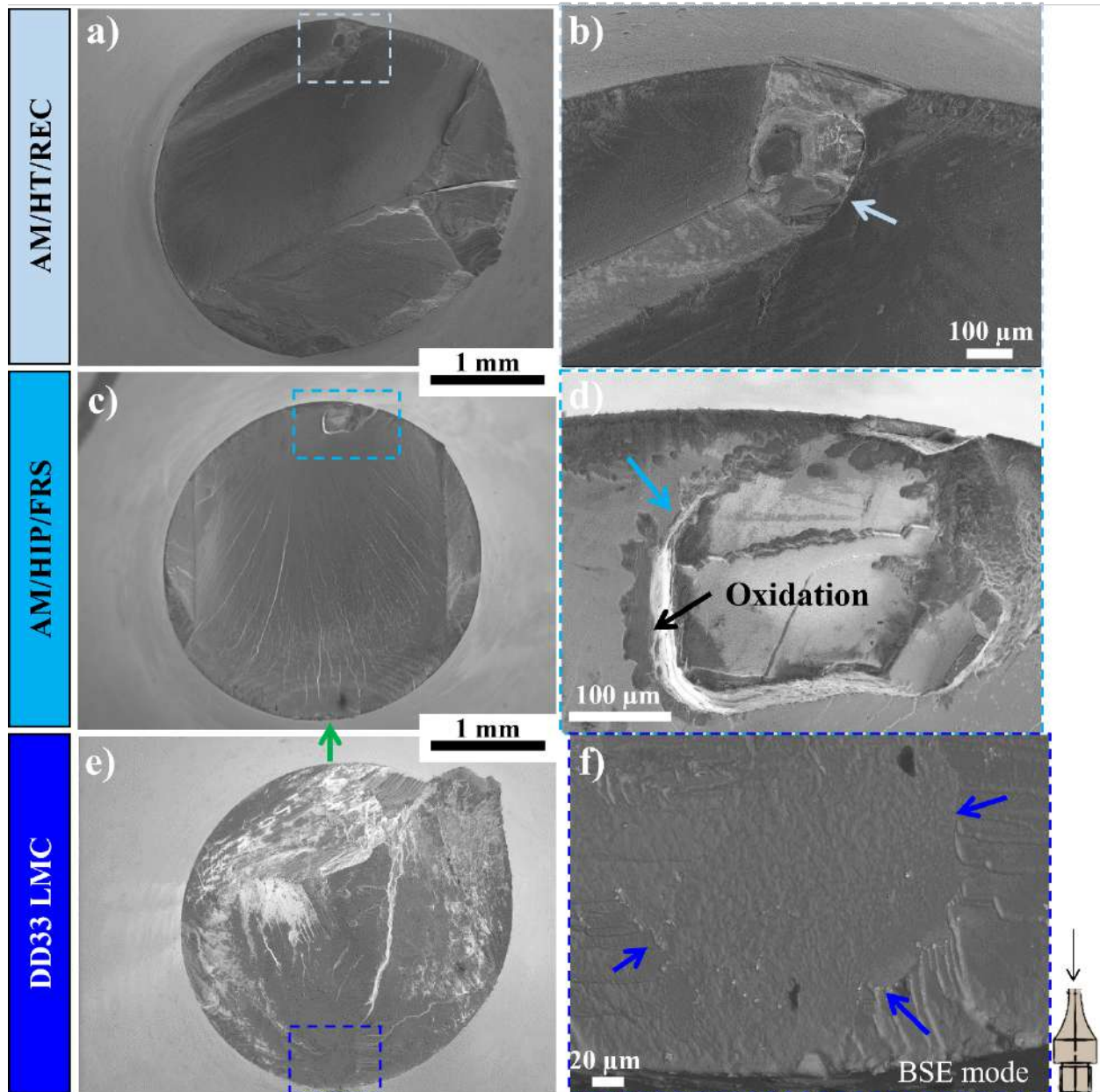


**Figure III-23** Fracture surface observations of AM/HT/REC ( $\sigma_a = 180$  MPa, with  $N_f = 8.4 \cdot 10^6$  cycles) (a), crack initiation zone magnification in (b). AM/HIP/FR ( $\sigma_a = 140$  MPa, with  $N_f = 1.7 \cdot 10^6$  cycles) (c), crack initiation zone magnification in (d). DD33 LMC processed from the first batch ( $\sigma_a = 157$  MPa, with  $N_f = 3.9 \cdot 10^6$  cycles) sample (e), crack initiation zone magnification in (f). The green arrow highlights a surface crack initiation.

From **Figure III-23**, crack initiation from a small grain immersed in the  $\approx \langle 001 \rangle$  substrate can be observed in each case. **Figure III-23c** shows a competition between the failure at the stray grain

and the crack initiation at the surface. **Figure III-23d** even shows oxidation at the grain boundaries.

According to **Figure III-22**, the presence of stray grains within the gage part of VHCF specimens induces a spectacular deficit in fatigue life. These grains are inherited from either the LMC solidification process or the building process/heat treatment of the AM specimens. The impact of the oxides in the PBF-E process is not yet fully understood. However, the author believes that the stray grains are present in the material bulk right after the AM process and before the HIP treatment. The HIP treatment does not seem to be the determining factor for the development of recrystallization in the PBF-E samples, as just one no HIPed sample AM/HT/REC (**Figure III-23a**) shows a fracture at a HAGB feature.

While (surface) recrystallization is known to decrease the LCF life of Ni-based single-crystalline superalloys (Ma et al., 2020, 2015), no prior study reported the consequence of stray grain on the VHCF life at high temperatures of Ni-based SX superalloys, according to the author's very best knowledge. Indeed, the directionally solidified alloy (DS200+Hf), presenting several  $\approx \langle 001 \rangle$  columnar grains within the gage part of VHCF specimens (i.e., low angle grain boundaries concerning the loading direction (Mataveli Suave et al., 2016)), just performs slightly worse in VHCF at  $1,000 \text{ }^\circ\text{C}/R_\epsilon = -1/f = 20 \text{ kHz}$  compared to SX specimens solidified with the same casting parameters (Cervellon et al., 2018). In fact, a decrease in VHCF life of a factor of 2-3 has been observed compared to SX alloys, far below the 2-3 decades decrease observed in **Figure III-22**.

Hence, highly misoriented grains from the perfect [001] crystallographic orientation is critical to the VHCF life. As VHCF specimens used in the present study are designed to obtain a frequency of resonance in tension/compression of  $20 \text{ kHz} \pm 500 \text{ Hz}$  (Cervellon, 2018), these recrystallized grains have Young's modulus far higher than the one with a [001] orientation (i.e., 93 GPa for CMSX-4/Bridgman) modifying the specimens stiffness.

Like in **sub-section 3.4**, FE analyses using Abaqus CAE were carried out to understand the impact of the presence of stray grain at the sample's surface on the VHCF life. The analysis is presented in **Appendix D.2**. **Figure III-24** depicts the results obtained from the FEM analysis.

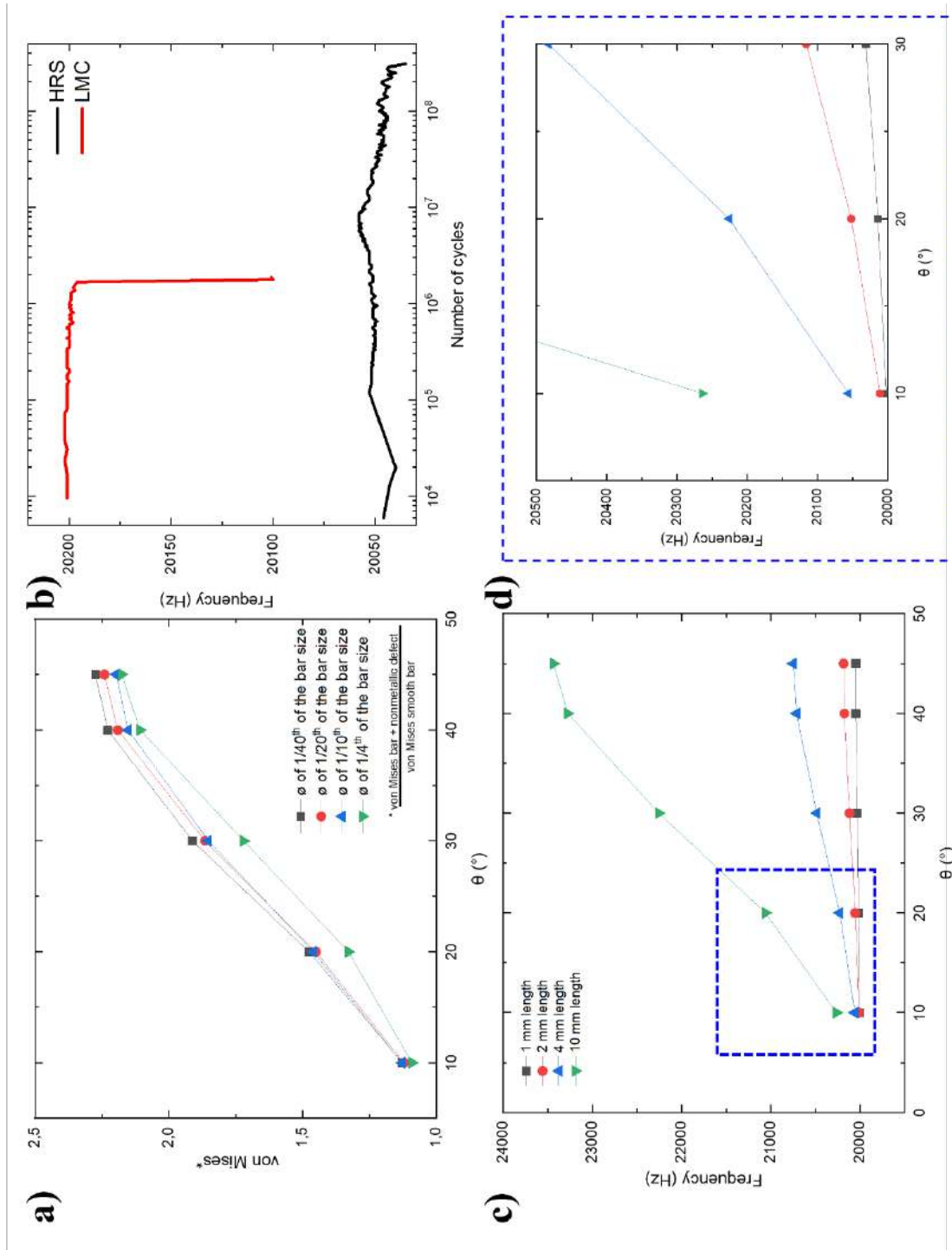


**Figure III-24** Results obtained by FEM of a stray grain with misorientation ( $\theta = 10$  up to  $45^\circ$ ) inside a perfectly orientated [001] SX bar. von Mises stress around the stray grain interface (a). The experimental frequency of VHCF tests of DD33 HRS (without the stray grain) and LMC (with the stray grain) (b). The frequency of resonance evolution as a function of the stray grain size and orientation (c). Magnification of the highlighted region from (c) in (d).

**Figure III-24a** shows that the von Mises stress around the stray grain increases continuously with the increase in misorientation. From this figure, the stray grain size does not significantly affect the local von Mises stress at fixed  $\theta$  misorientation. However, and as expected, the results show that the larger the stray grain, the higher the influence of the misorientation over the frequency of resonance (**Figure III-24c and d**). For example, at  $\theta > 20^\circ$ , the frequency is higher than 20kHz reaching 20,200 Hz for stray grains with a diameter of  $1/10^{\text{th}}$  of the bar size.

The higher resonance frequency of DD33/LMC containing recrystallized grains (**Figure III-24b**) indicates that the stray grain disturbs the sample's frequency of resonance. The author believes that the grain's apparent modulus will be very different from the superalloy's when pulling in the stress axis of the specimen. Therefore, this affects the specimen's frequency of resonance and the maximum stress at the center of the specimen. Failure in shear mode at the grain boundary is obtained in this condition as suggested by fractographic observation in **Figure III-23**.

## 5.1. Summary

The new "solidification" techniques like LMC and AM lead to an increased probability of having stray grains in "SX" components. These defects were not widely investigated in the literature, especially under very high frequency cyclic loading. From the present study, stray grains increase the frequency of resonance, leading to a shear stress concentration in the superalloy/stray grain interface. The local overload leads to earlier fatigue damage and, consequently, a lower fatigue life.

## 6. Crack initiation from the surface

Gathering the results from the previous sub-sections of this chapter, many samples failed with a very high number of cycles. Indeed, most of them presented surface crack and propagation in mode I assisted by oxidation. Thus, independently of the chemical composition, different superalloys seem to fail through a process assisted by oxidation when the defects (pores, stray grains...) are suppressed or small enough to avoid the microplastic deformation in their vicinity responsible for crack initiation and propagation.

The subsequent question, associated with a transition in crack initiation site from an internal site toward the surface, is to discuss if there is a fatigue limit in these conditions.

**Table III-6** details the superalloys and the respective number of samples that failed from the surface.

*Table III-6 The superalloys and the respective number of samples with surface crack initiation investigated in this section. Y for yes and N for No.*

<i>Superalloy</i>	<i>Nº of samples with surface crack initiation</i>	<i>Completely broken?</i>
<b>CMSX-4/PBF-E</b>	4	<b>Y</b>
<b>DD33/LMC</b>	2	N
<b>DD33/HIP</b>	5	<b>Y</b>
<b>MC-NG</b>	1	<b>Y</b>
<b>TMS-238</b>	1	<b>Y</b>

### 6.1. VHCF endurance and surface crack initiation

**Figure III-25** shows the S-N diagram gathering all VHCF results obtained within this PhD thesis at 1,000 °C,  $R_e = -1$ , and  $f = 20$  kHz. The database is defined by the superalloy (symbol shape), the solidification process or HIP treatments if it is applicable (symbol filling), and the crack initiation type (color). The samples with crack initiation at the surface are highlighted by the green hatched zone, presenting a very high number of cycles up to failure in both high and low alternating stress domains.

**Figure III-26** shows the fracture surface observations for different samples and alternating stress between 145 - 180 MPa. Surface cracks assisted by oxidation as deep as 0.8 mm were observed after failure. Fracture surfaces are showing a subsequent crack propagation zone in mode I (highlighted by yellow arrows), which is oxidized according to the SEM/SEI contrast. Then a final failure in shear mode can be observed. In addition, most of the samples presented well-developed secondary cracks zones (black arrows) assisted by oxidation in the main fracture surface. Thus, oxidation seems to play an essential role during the crack initiation, propagation, and rupture process for these specimens.

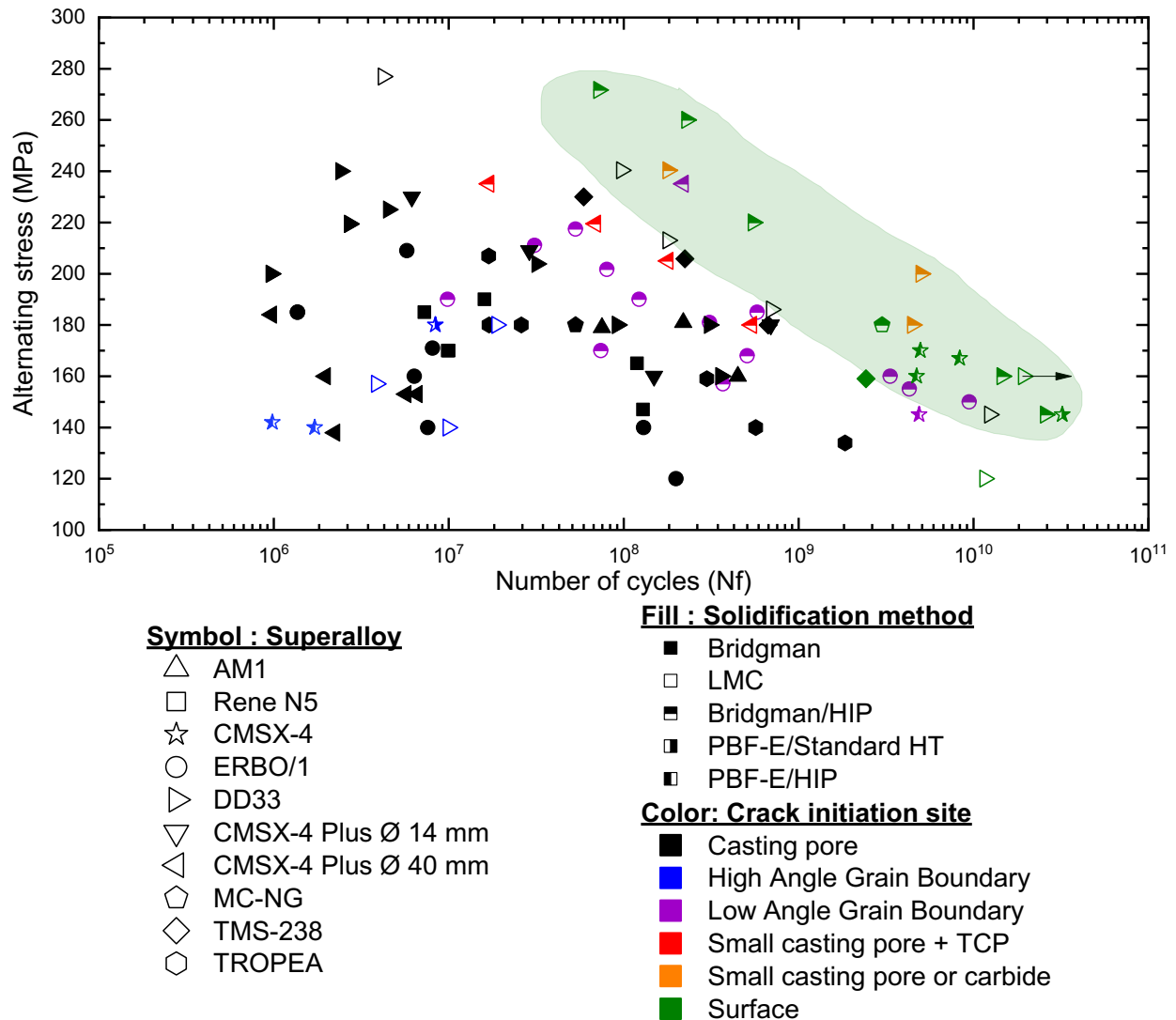


**Figure III-25** S-N diagram for 1,000 °C,  $R_e = -1$ , and  $f = 20$  kHz gathering the results of **Figure III-1**, **Figure III-4**, **Figure III-9** and **Figure III-17**. The alternating stress is plotted as a function of the number of cycles to failure — special attention to the specimens that failed at surface initiation highlighted by the hatched green zone.

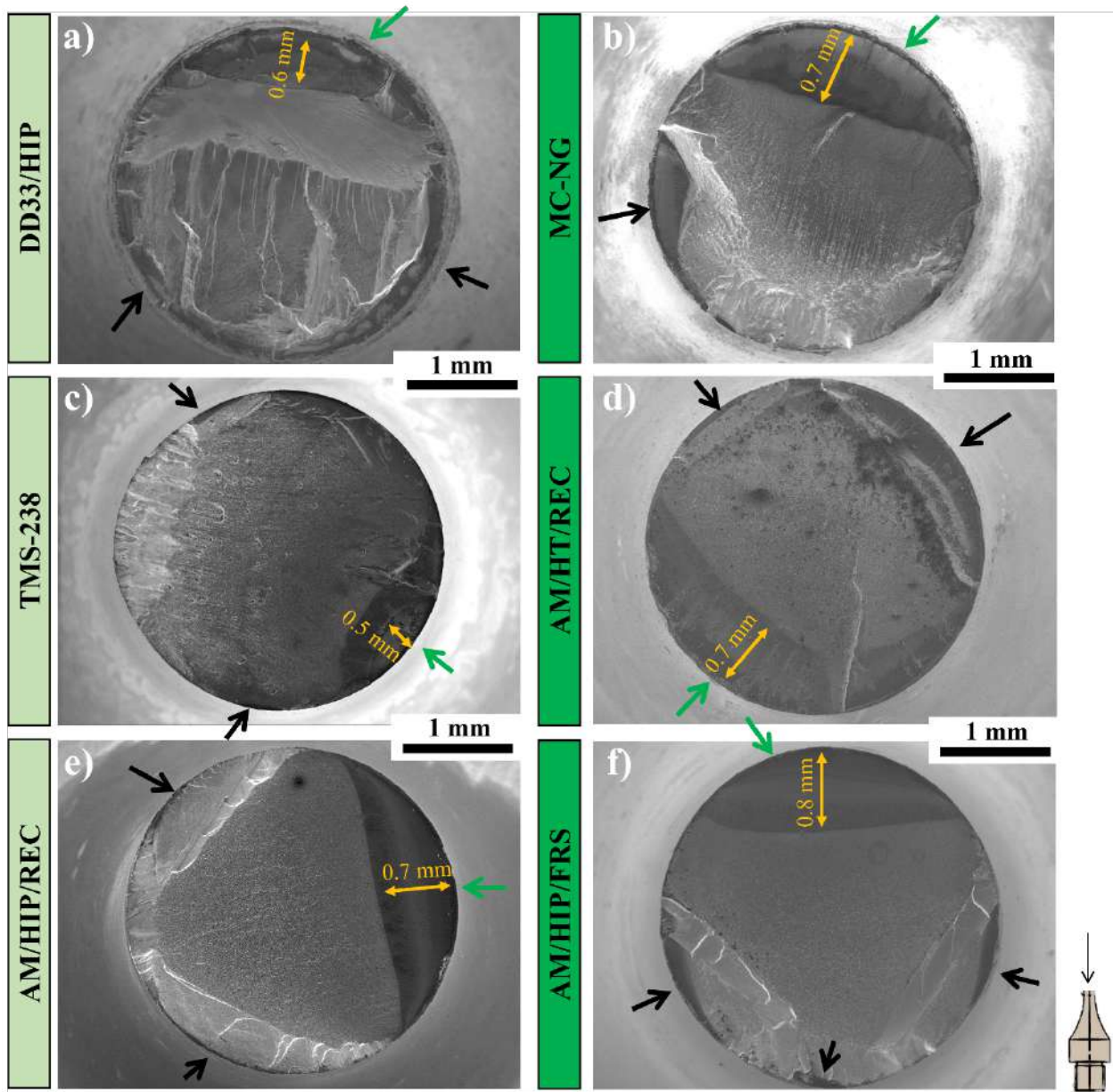


**Figure III-26** Fracture surface observations of samples with main crack initiation from the surface: DD33/HIP ( $\sigma_a = 160$  MPa,  $N_f = 1.4 \cdot 10^{10}$  cycles) sample (a), MC-NG/HIP ( $\sigma_a = 180$  MPa, with  $N_f = 3.0 \cdot 10^9$  cycles) sample (b), TMS-238 ( $\sigma_a = 159$  MPa, with  $N_f = 2.4 \cdot 10^9$  cycles) sample (c), AM/HT/REC ( $\sigma_a = 145$  MPa,  $N_f = 3.2 \cdot 10^{10}$  cycles) sample (d), AM/HIP/REC ( $\sigma_a = 167$  MPa,  $N_f = 8.3 \cdot 10^9$  cycles) sample (e), AM/HIP/FRS-3 ( $\sigma_a = 160$  MPa,  $N_f = 4.7 \cdot 10^9$  cycles) sample (f). The main crack initiation is highlighted by the green arrow and the secondary crack initiations are highlighted by the black arrows. The maximum depth of the main fatal crack initiated at the surface is added for each specimen.

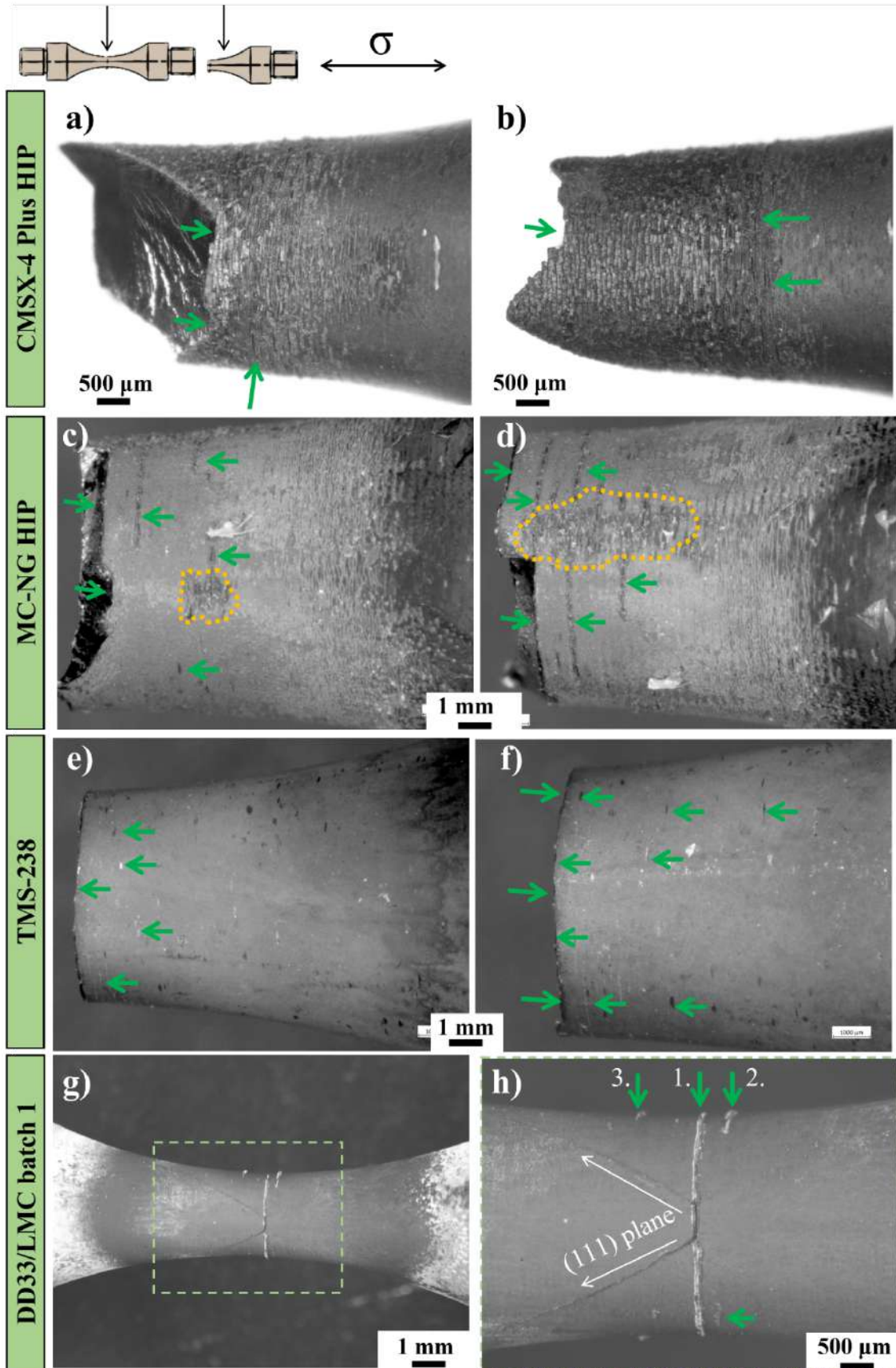
## 6.2. Role of oxidation in VHCF and high temperatures

The specimens analyzed in this section are presenting several secondary cracks perpendicular to the main loading axis, as shown in **Figure III-27**. Six different samples are presented hereafter according to the number of cycles up to failure.

**Figure III-27a** and **b** are optical microscope observations of a CMSX-4 Plus HIP ( $\sigma_a = 180$  MPa,  $N_f = 5.4 \cdot 10^8$  cycles) sample. Even though the CMSX-4 Plus HIP samples do not present crack initiation at the surface, the oxidation was present at the sample's surface after the VHCF tests.

**Figure III-27c** and **d** are observations carried out of the MC-NG HIP ( $\sigma_a = 180$  MPa,  $N_f = 3 \cdot 10^9$  cycles) sample. MC-NG sample presented fewer secondary cracks compared to the CMSX-4 Plus HIP sample. Still, dotted yellow lines indicate that most of the severely oxidized zones are localized in the central part of the VHCF specimens and cracks are developed. **Figure III-27e** and **f** are observations of TMS-238 ( $\sigma_a = 159$  MPa,  $N_f = 2.4 \cdot 10^9$  cycles). This specimen has even fewer secondary cracks compared to CMSX-4 Plus.

**Figure III-27g** is a DD33/LMC ( $\sigma_a = 120$  MPa,  $N_f = 1.1 \cdot 10^{10}$  cycles) sample from the 1<sup>st</sup> batch, and it is a none-completely broken specimen. This specimen presents at least four secondary cracks (green arrow) with a final crystallographic failure along  $\{111\}$  planes, see **Figure III-27h**. **Figure III-27i** is a DD33/LMC ( $\sigma_a = 160$  MPa,  $N_f = 1.9 \cdot 10^{10}$  cycles) sample from the 2<sup>nd</sup> batch, and it is an interrupted test. The sample presents several secondary cracks propagated from the specimen's surface, see **Figure III-27j**. **Figure III-27k** is the AM/HT/REC ( $\sigma_a = 145$  MPa,  $N_f = 3.2 \cdot 10^{10}$  cycles) sample with the highest fatigue lifetime at high temperatures reached at Institut Pprime. The magnification shows several localized secondary cracks (see **Figure III-27l**). The green arrows indicate several secondary cracks present at the sample's surface.



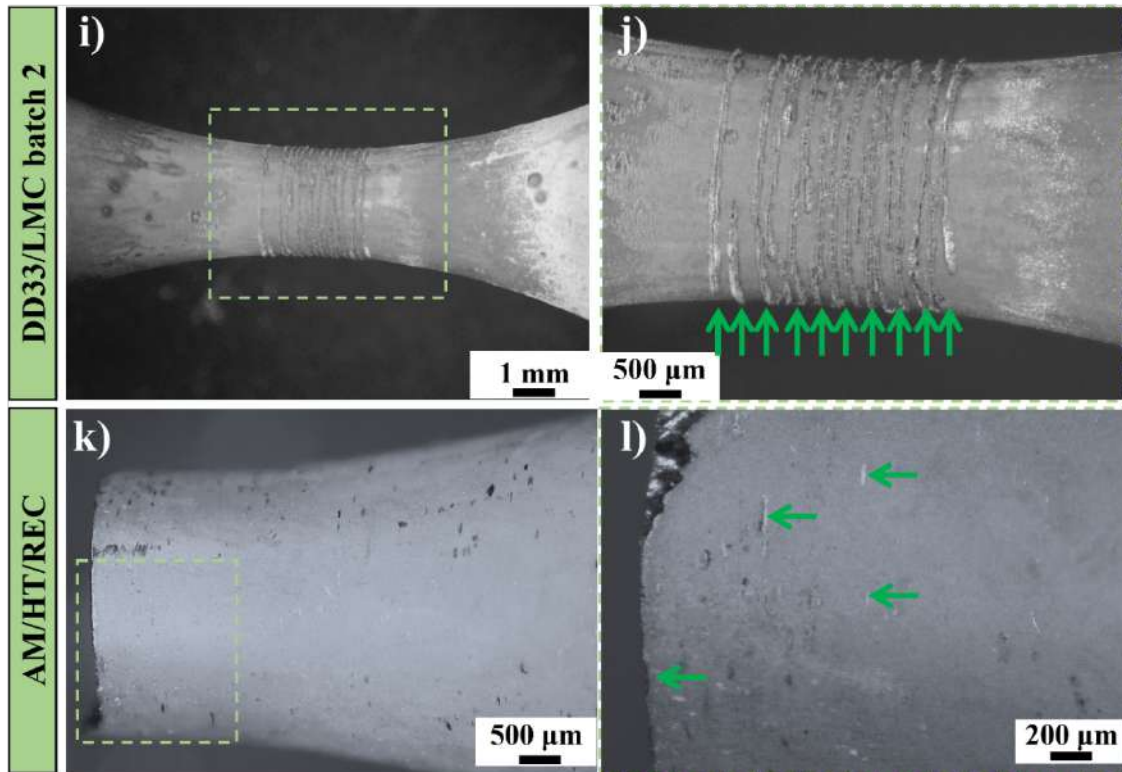


**Figure III-27** Optical microscope observations of several samples showing surface cracks morphology/density. CMSX-4 Plus HIP ( $\sigma_a = 180$  MPa,  $N_f = 5.4 \cdot 10^8$  cycles) (a) and (b); MC-NG HIP ( $\sigma_a = 180$  MPa,  $N_f = 3 \cdot 10^9$  cycles) (c) and (d). TMS-238 ( $\sigma_a = 159$  MPa,  $N_f = 2.4 \cdot 10^9$  cycles) (e) and (f); DD33/LMC batch 1 ( $\sigma_a = 120$  MPa,  $N_f = 1.1 \cdot 10^{10}$  cycles) (g), the specimen was not completely broken (h); DD33/LMC batch 2 ( $\sigma_a = 160$  MPa,  $N_f = 1.9 \cdot 10^{10}$  cycles) (i), it is an interrupted test (j); AM/HT/REC ( $\sigma_a = 145$  MPa,  $N_f = 3.2 \cdot 10^{10}$  cycles) (k) and (l). The secondary cracks are highlighted by the green arrows.

We can learn from the present observations that *surface crack initiation does not seem to be restricted to one specific alloy having a bad oxidation resistance*.

Then, it was decided to perform longitudinal observations of these specimens. First, the specimens with VHCF lives less than  $10^{10}$  cycles are analyzed. **Figure III-28** Shows the longitudinal section analysis of CMSX-4 Plus HIP ( $\sigma_a = 180$  MPa,  $N_f = 5.4 \cdot 10^8$  cycles) in **Figure III-28a** and **b**, MC-NG HIP ( $\sigma_a = 180$  MPa,  $N_f = 3 \cdot 10^9$  cycles) in **Figure III-28c** and **d** and TMS-238 ( $\sigma_a = 159$  MPa,  $N_f = 2.4 \cdot 10^9$  cycles) in **Figure III-28e** and **f**.

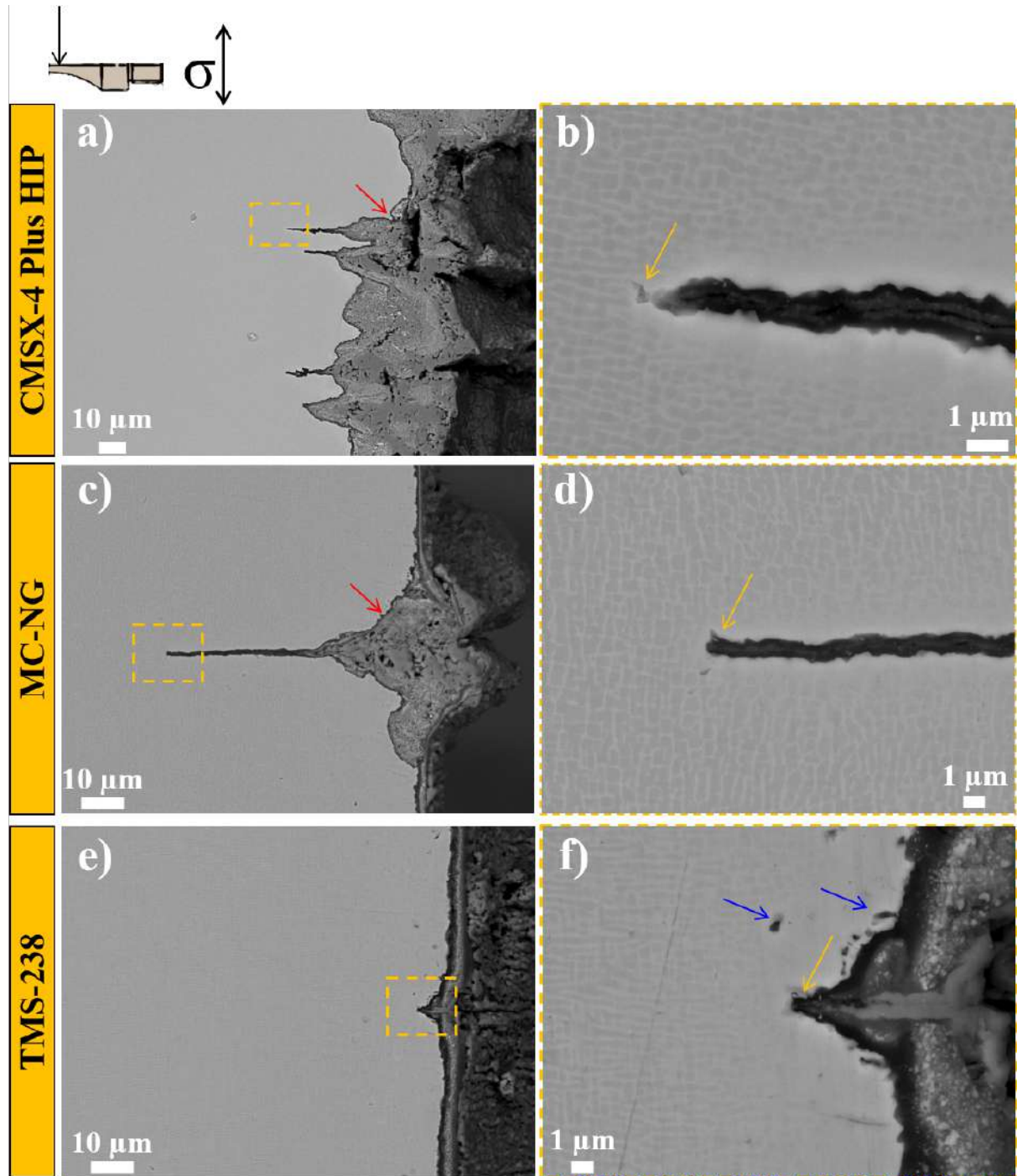


**Figure III-28** Microstructure characterizations along a longitudinal section of CMSX-4 Plus/HIP ( $\sigma_a = 180$  MPa,  $N_f = 5.4 \cdot 10^8$  cycles) sample (a), high magnification overview of a crack tip (b). MC-NG/HIP ( $\sigma_a = 180$  MPa,  $N_f = 3 \cdot 10^9$  cycles) sample (c), high magnification overview of a crack tip (d). TMS-238 ( $\sigma_a = 159$  MPa,  $N_f = 2.4 \cdot 10^9$  cycles) sample (e), high magnification overview of a crack tip (f). Red arrows indicate the oxides' spinel. Yellow arrows indicate the crack tip. Blue arrows indicate the presence of sub-surface precipitates.

The BSE analysis reveals some similar characteristics of the secondary cracks whatever the alloy. **Figure III-28a** and **c** present a highly oxidized surface composed of several layers. Crack tip magnifications in **Figure III-28b** and **d** show that the crack propagation is assisted by oxidation, and oxides are filling the crack. CMSX-4 Plus longest crack in **Figure III-28a** has a 50  $\mu\text{m}$  length, and MC-NG crack has a 60  $\mu\text{m}$  length. As expected, it is possible from **Figure III-28e** to identify thin oxide layers and fewer secondary cracks. The crack tip magnification in **Figure III-28f** shows that first, the oxides developed in the sub-surface, and then the crack propagates into the material's bulk. Blue arrows indicate the presence of precipitates at the sub-surface of TMS-238.

**Figure III-29** and **Figure III-30** show the features found along longitudinal sections of the DD33/LMC from the 1<sup>st</sup> batch and AM/HT/REC sample, respectively. Both samples have a fatigue life higher than  $10^{10}$  cycles. **Figure III-29** depicts three cracks with 150, 100, and 80  $\mu\text{m}$  of depth, respectively. All of them are filled with oxides. The author assumes that crack 1 (**Figure III-27h**) illustrated in **Figure III-29a** first formed and was then deep enough to lead to a subsequent transition to a crystallographic propagation along a (111) plane. The magnification shows the presence of oxide at the crack deviation point (see red arrow in **Figure III-29b**). The author believes that a plausible mechanism for this transition in crack mode (from mode I to crystallographic) may result from the fact that a local obstacle (e.g., small casting pore, low angle grain boundary full of carbides – specific to DD33 alloys) led to a crack deviation. However, the 2D observations presented in **Figure III-29** are not sufficient to check this assumption.

**Figure III-29c** and **e** illustrate the longitudinal section of cracks 2 and 3 (**Figure III-27h**). Crack 2 presented oxide at the sample's surface/sub-surface (see red arrows in **Figure III-29c**). The crack tips are presented in **Figure III-29b**, **d**, and **f** for cracks 1, 2, and 3 in **Figure III-27h**. All cracks presented sub-surface black precipitates (blue arrows). In addition, it was identified white precipitates at the crack tip in **Figure III-29d** (see green arrows).

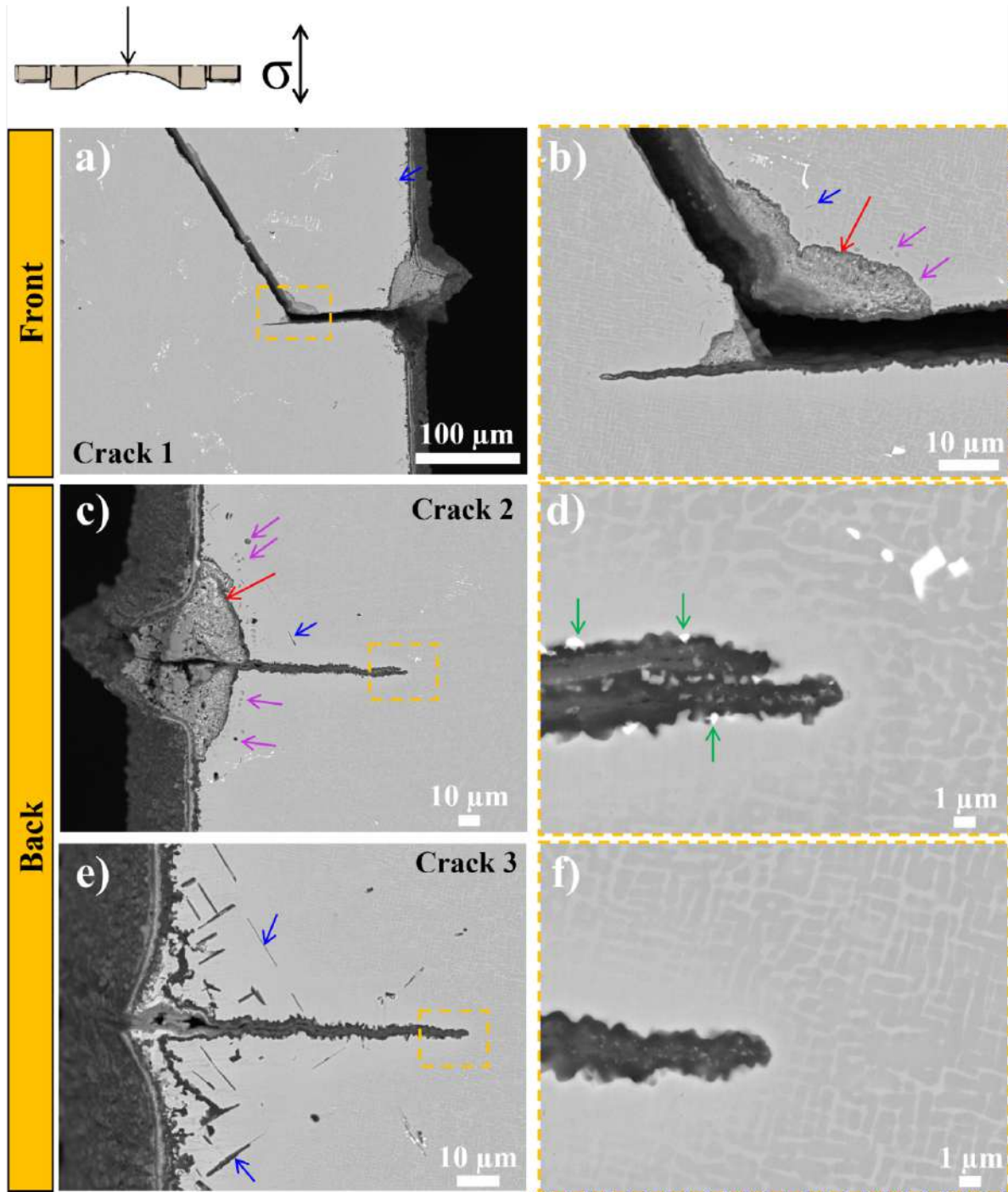


**Figure III-29** Microstructure characterizations along a longitudinal section of DD33/LMC batch 1 ( $\sigma_a = 120$  MPa,  $N_f = 1.1 \cdot 10^{10}$  cycles) sample. High magnification overview of crack 1 (a), crack 2 (c), and crack 3 (indicated in **Figure III-27h**). Magnification of crack tip in (b), (d), and (f). Red arrows indicate the oxides in the surface. The green arrows indicate white precipitates, and the blue arrows indicate black precipitates. The purple arrows indicated Kirkendall type voids. These SEM observations were taken in BSE mode.

**Figure III-30** illustrates a secondary crack with a depth of  $\approx 70 \mu\text{m}$  in AM CMSX-4 alloy. This crack is filled with oxides up to its tip. **Figure III-30b** and **c** are observations in BSE and SEI modes, respectively, highlighting significant features like the square-like precipitates around the crack initiation zone and the oxidation inside the crack. A layer of  $\approx 30 \mu\text{m}$  with Kirkendall porosity and precipitates of different shapes appear underneath the surface (**Figure III-30d** and **e**). The precipitates are comparable to the ones identified for DD33/LMC in **Figure III-29**. **Figure III-30e** illustrates the oxides growing outwardly and leaving behind Kirkendall voids.

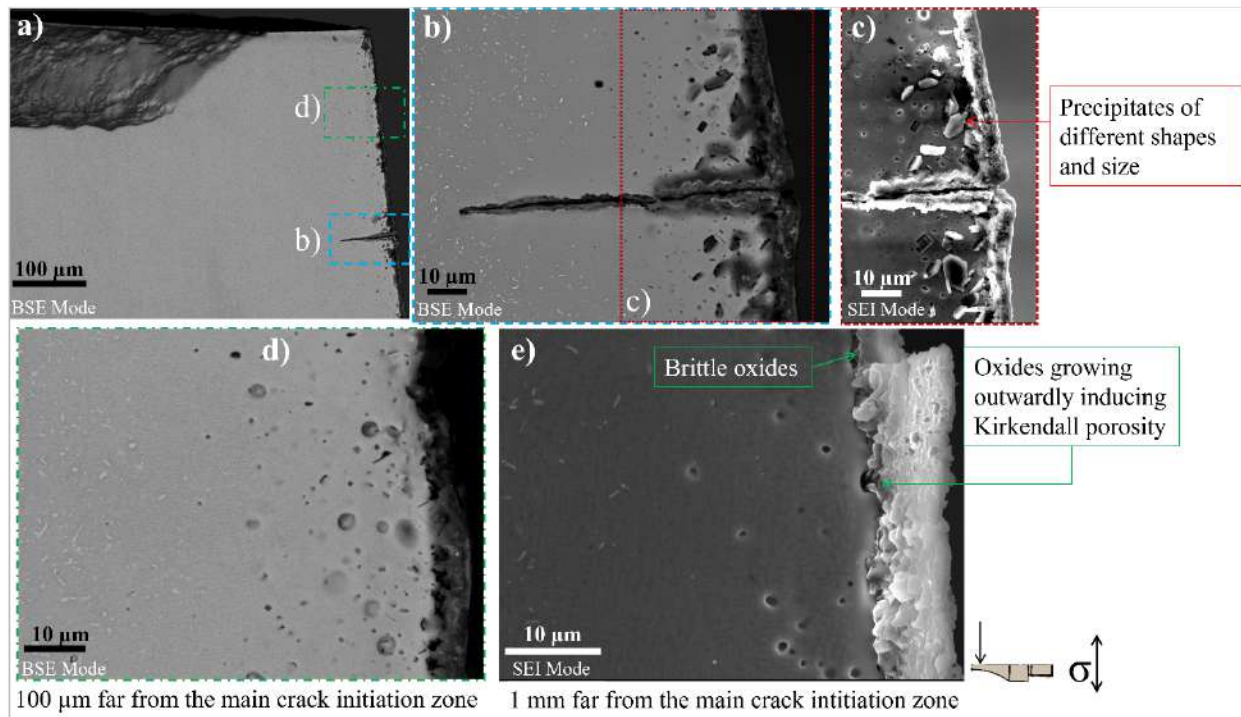


**Figure III-30** Microstructure characterizations of AM/HT/REC ( $\sigma_a = 145 \text{ MPa}$ ,  $N_f = 3.2 \cdot 10^{10}$  cycles) along a longitudinal section: high magnification overview of one side of the sample, SEM observation in BSE mode (a). Secondary crack (blue dotted rectangle in (a)) SEM observation in BSE mode (b) and SEI mode (c). Surface detail (green dotted rectangle in (a)) close to the main crack initiation site, SEM observation in BSE mode (d) and 1 mm far from the main crack initiation zone in SEI mode (e). Precipitates and Kirkendall voids are observed in the sub-surface.

As a common feature for all specimens showing failure from the surface, highly localized oxidation activity is observed (see red arrows in **Figure III-28**, **Figure III-29**, and yellow arrow in **Figure III-30e**). Two distinct oxidation activities can be identified from these characterizations: (i) a high oxidation activity, with the oxides growing outwardly to the samples' surface (**Figure**

**III-28a** and **c**, **Figure III-29a** and **c**); and (ii) a low oxidation activity, with oxides growing inwardly to the samples' sub-surface (**Figure III-28e**, **Figure III-29e** and **Figure III-30b**).

The presence of other kinds of precipitates (black precipitates indicated by the blue arrows in **Figure III-28** and **Figure III-29**, and red arrow in **Figure III-30**) and Kirkendall voids in the sub-surface of the specimens with a very high number of cycles ( $> 10^{10}$  cycles) is just an indication of the superalloy chemical evolution during the VHCF tests. None of these features were previously observed either in CMSX-4/Bridgman, MC-NG/Bridgman in VHCF at 1,000 °C by Cervellon et al. (Cervellon et al., 2018) or in the CMSX-4 PBF-E samples after LCF tests at 950 °C by Meid et al. (Meid et al., 2019a), probably due to shorter duration of the tests.

In what follows, the author will neglect the presence of small amounts of S (sulfur) in the superalloys' chemical composition (typically less than 5-6 ppm) and its consequences on the oxidation behavior at high temperatures (McVay et al., 1992).

**Figure III-28b**, **d**, and **f**, **Figure III-29d** and **f** also show  $\gamma'$  depletion around the crack tip. It seems that most of the fatigue life is spent in oxidizing the surface/sub-surface, and the subsequent crack propagation can be quite fast. Thus, even though the BSE/SEI analyses uncover essential features, other techniques are required to better characterize sub-surface evolution as the EDX technique.

**Figure III-31** shows the EDX maps of several chemical elements that constitute the oxides and the precipitates in the sub-surface of the samples analyzed in **Figure III-28**, **Figure III-29**, and **Figure III-30**. In addition, **Figure III-32** shows the chemical profile showing an Al gradual depletion from the surface, especially for the AM/HT/REC specimen.

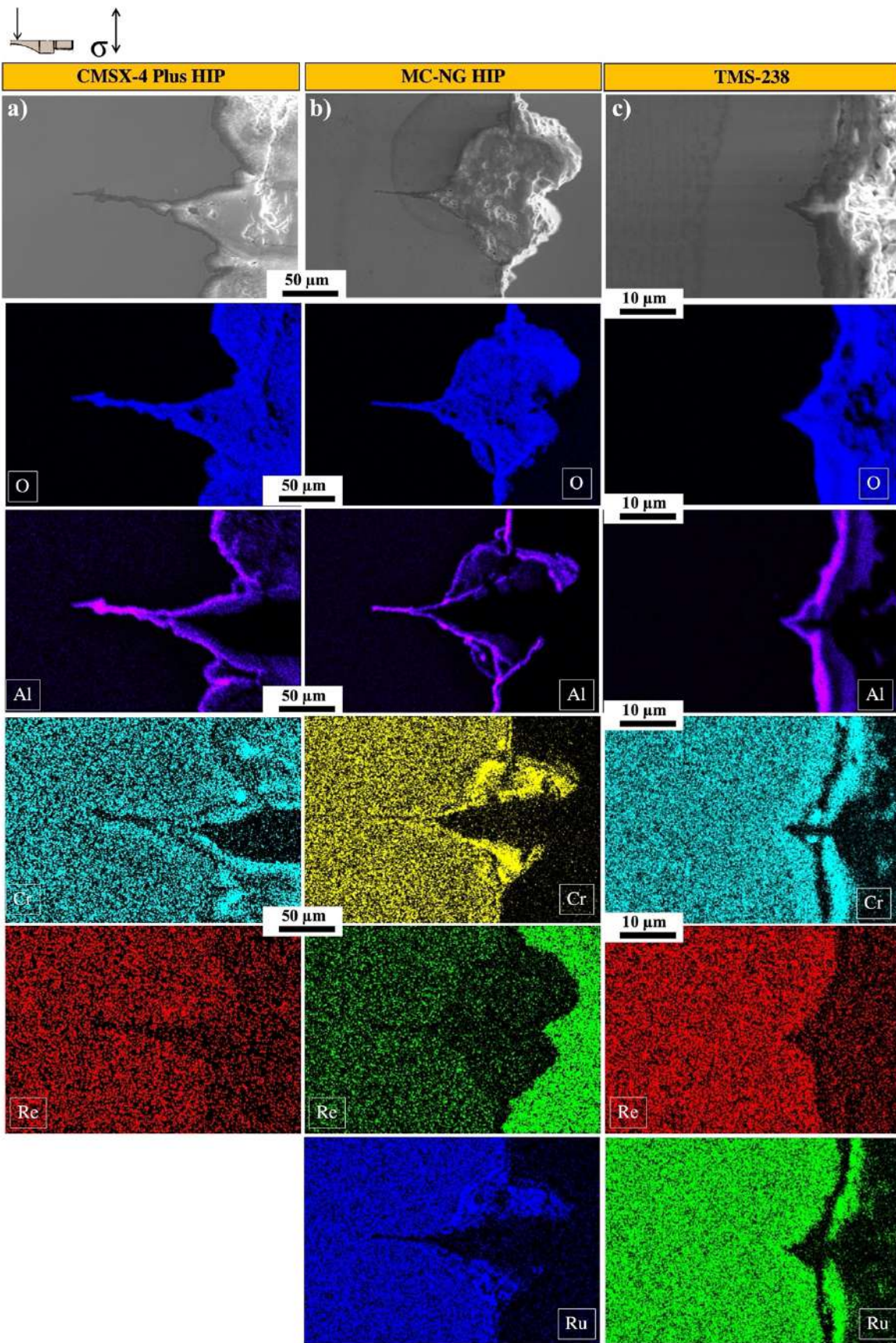
The external oxide scale is rich in O, Ni, Al, and Cr for CMSX-4 Plus, DD33, and AM/HT/REC, and of O, Ni, Al, Cr, and Ru for MC-NG and TMS-238. In addition, the crack tips were filled with Ta and Ti oxides. The oxide is divided into at least three main layers: an external NiO, an intermediate Cr<sub>2</sub>O<sub>3</sub>, and an internal Al<sub>2</sub>O<sub>3</sub> layer.

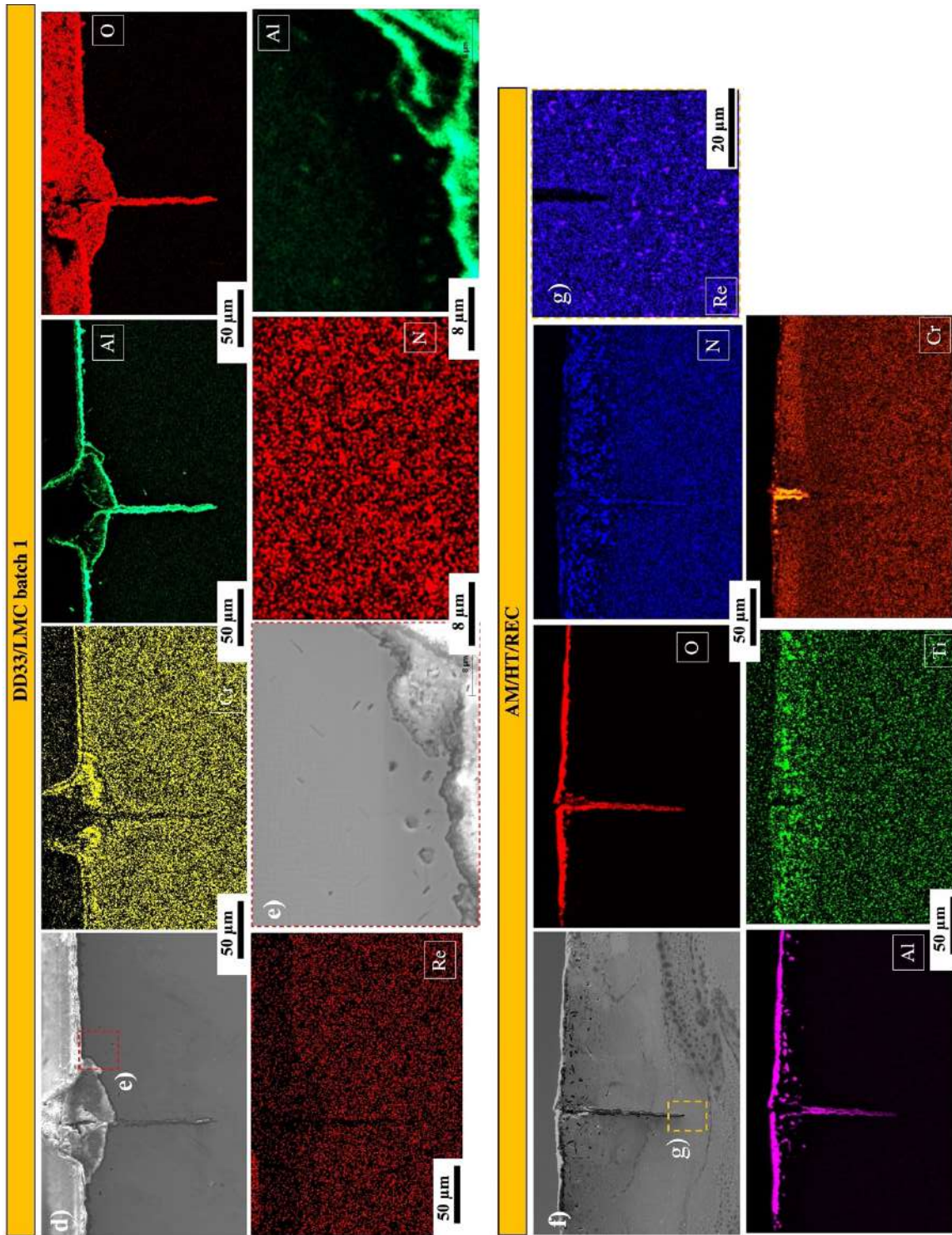
The black precipitates in the sub-surface (indicated by the blue arrows in **Figure III-28** and **Figure III-29**, and red arrow in **Figure III-30**) were identified by the EDX maps as Al and Ti nitrides. In addition, several large precipitates were identified to be composed of Ta, W, and Hf in the AM/HT/REC sample. **Figure III-31e** indicates the presence of Al nitrides in the sub-surface of

DD33/LMC and **Figure III-31f** the presence of Ti and Al nitrides in the sub-surface of AM/HT/REC.

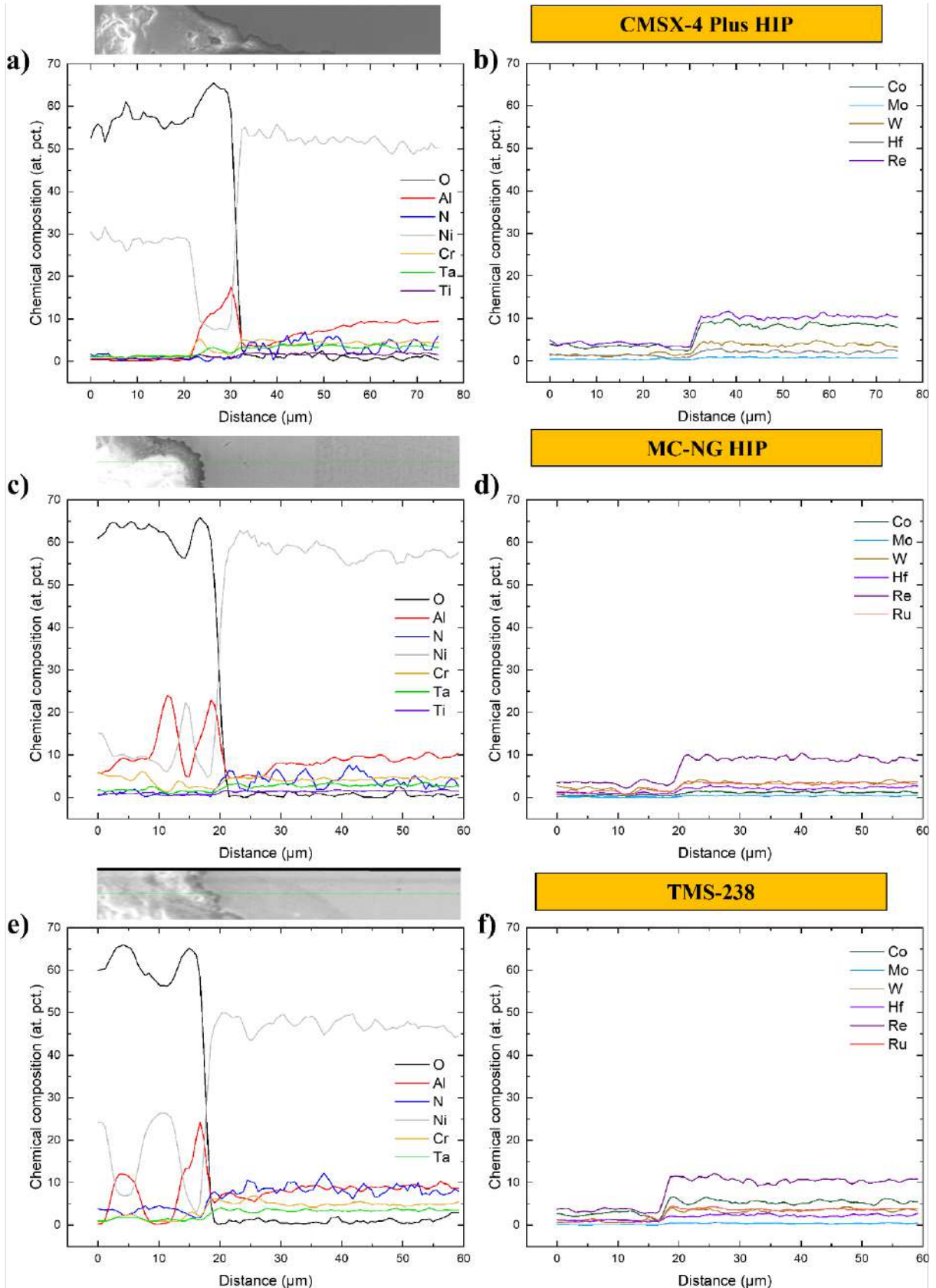
As the oxygen is being consumed by the Ni, Al, and Cr elements to form the oxide layer, the oxygen pressure locally drops, and the 78 % of N<sub>2</sub> present in the air diffuses in the substrate reacting with Al and Ti. Nitrides are known to be brittle structures, decreasing the mechanical properties of superalloys, especially in fatigue at low temperatures (Govaere et al., 2020; Texier et al., 2016b, 2016a). The Ta/W/Hf-rich carbides previously observed in MAR-M247 (Szczołok and Rodak, 2012) and Mar-M200+Hf/DS200+Hf (Mataveli Suave et al., 2018) are also known to favor crack initiation in LCF (Mataveli Suave, 2017).

Needle-shaped Re-rich precipitates identified in **Figure III-30b** are probably TCP ones (see Rhenium in **Figure III-31e**), presumably  $\mu$  or P phases, based on their morphology and the very high Re content (Rae and Reed, 2001). At 1,000 °C, the superalloy CMSX-4/Bridgman is known to be prone to TCP precipitates (Cheng et al., 2011; Giraud, 2014; Lopez-Galilea et al., 2016; Rae and Reed, 2001; Yi et al., 2007) that are well known to influence the crack initiation (le Graverend et al., 2012; Simonetti and Caron, 1998). This TCP precipitation is also known to be enhanced at high temperature by the introduction of pre-deformation (Meid et al., 2019b) or by the very high local plastic deformation in the rough zone close to stress raisers in VHCF (Cervellon et al., 2020a). Pistor et al. (Pistor and Körner, 2019) have already investigated the processes of TCP precipitation in PBF-E CMSX-4 alloy at high temperatures (around 1,050 °C) and for longtime exposures. Moreover, AM/HT/REC sample test lasted  $\approx$  447 h, i.e., long enough to be in the precipitation domain of TCP phases at high temperatures according to previous literature (Cheng et al., 2011; Dubiel et al., 2018; Lopez-Galilea et al., 2016). Further, the local change in chemical composition due to the depletion of the other alloying elements to form the oxides, especially Cr and W, are known to favor TCP precipitation in CMSX-4/Bridgman (Dubiel et al., 2018). In addition, it explains the TCP density discrepancy between the surface and the bulk see **Figure III-31e**.





**Figure III-31** SEM-SEI analysis and EDX maps of secondary cracks. SEI image of a secondary crack at CMSX-4 Plus HIP (a), MC-NG HIP (b), TMS-238 (c), DD33/LMC batch 1 (d), magnification of the sub-surface precipitates (d) in (e), AM/HT/REC (f), magnification of the crack tip (f) in (g).



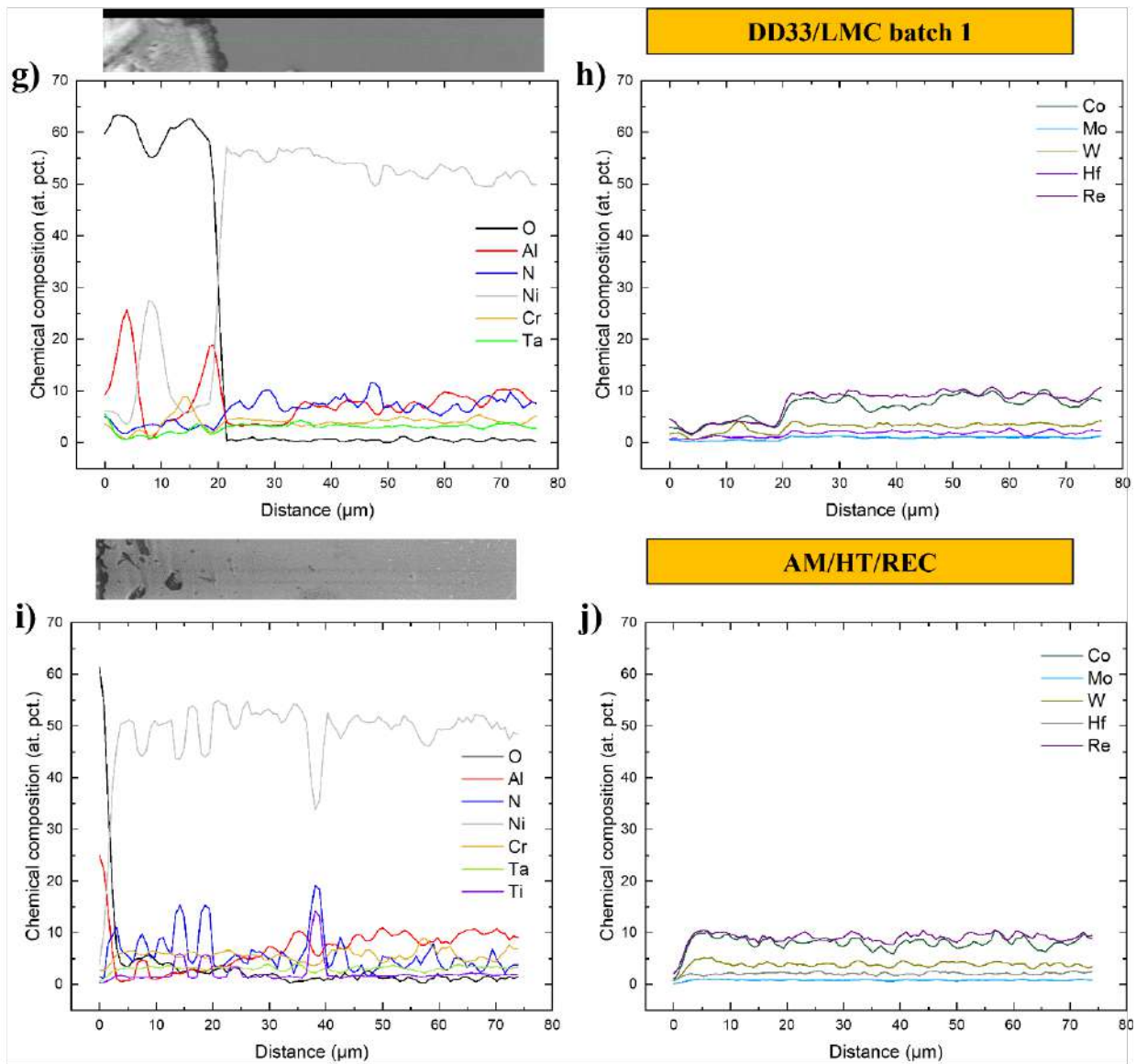


**Figure III-32** Chemical composition profiles (at. pct.) for each sample from the surface of VHCF specimens. The chemical elements Al, Ni, Cr, Ta, Ti plus O and N (a,) (c), (e), (g), and (i). Co, Mo, W, Hf, Re, and Ru (b), (d), (f), (h), and (j).

A high density of voids is observed in **Figure III-29b** and **c**, and **Figure III-30d** and **e** after VHCF tests. The voids appearing just beneath the oxide layer have been previously observed after the high-temperature oxidation of various Ni-based superalloys (Berthod, 2005; Shida et al., 1981) and are related to the vacancy supersaturation, according to Evans et al. (Evans, 1988). These vacancies originate from significant outward (cationic) diffusion and the countercurrent injection of

vacancies into the bulk resulting in the well-known Kirkendall porosity (Kirkendall, 1942). Indeed, **Figure III-32a, c, e, g, and j** illustrate the depletion of Al near the surface with respect to the Al content in the bulk, which results in a local increase in Re and W contents. Overall, Kirkendall voids are clear indication of imbalance in diffusion flows of atoms, a greater flow from the bulk towards the surface being present.

One shall notice that the Kirkendall porosity often driven by the gradient of chemical potential (Desgranges et al., 2013) was not observed in **Figure III-28**. This finding suggests that greater outward diffusion was most likely enhanced through the dislocations introduced upon the VHCF tests with fatigue life greater than  $10^{10}$  cycles (Ma et al., 2020), allowing to reach voids of up to a  $\approx 5 \mu\text{m}$  diameter. One may also speculate on the high dislocations' density inherited from the very PBF-E additive manufacturing process that can also foster oxidation. Regarding oxidation, Juillet et al. (Juillet et al., 2018) demonstrated that the instantaneous parabolic rate ( $k_p$ ) constants could not be calculated in an AM IN-718 superalloy due to enhanced growth of the oxides in comparison with the forged counterparts and related this to the significantly higher density of internal defects assessed by transmission electron microscopy (TEM). As a result, the selective outward diffusion of the most oxidizable elements to form the oxide scale brings about the precipitation of the strong carbide and nitride formers underneath (Pedraza et al., 2020).

### **6.3. Surface damage mechanism**

For the first time in this thesis, a VHCF life controlled by oxidation is presented for Ni-based SX superalloys at high temperatures in fully reversed loading and without any surface recrystallization mechanisms. In fact, two secondary cracks from two distinct samples are depicted in **Figure III-33**, showing no evidence of local recrystallization at the oxidized surface leading to crack initiation.

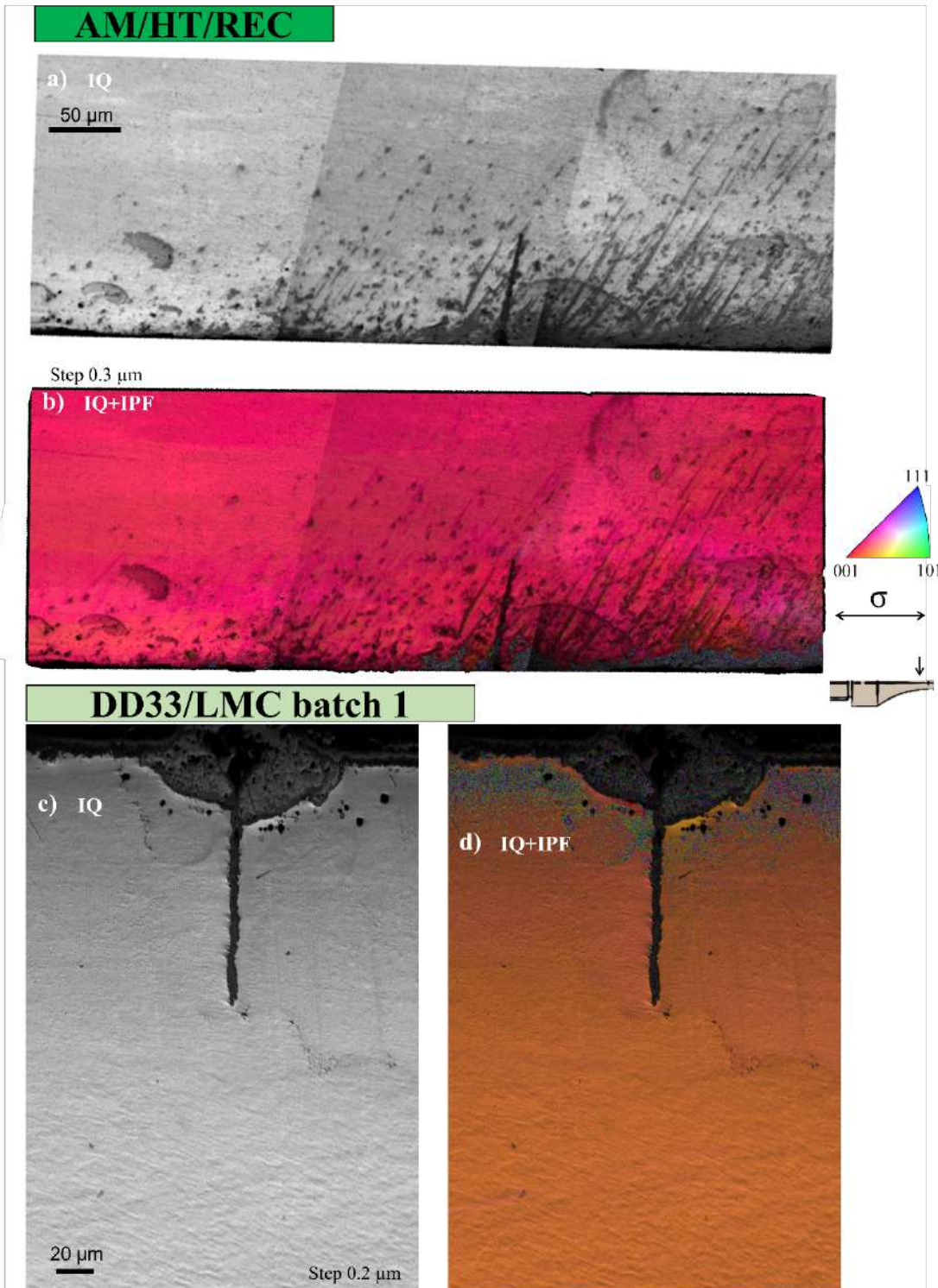


**Figure III-33** EBSD characterization of AM/HT/REC ( $\sigma_a = 145 \text{ MPa}$ ,  $N_f = 3.2 \cdot 10^{10}$  cycles) and DD33/LMC batch 1 ( $\sigma_a = 120 \text{ MPa}$ ,  $N_f = 1.1 \cdot 10^{10}$  cycles) crack initiation including image quality (IQ) (a) and (c), IQ superimposed to the inverse pole figure (IPF map) relative to the loading direction (b), and (d).

Cervellon already observed that surface cracks may develop in fatigue with  $R_e = -1$  at the same temperature for long VHCF tests (Cervellon et al., 2018, 2017), but the main crack initiation (almost) always occurred at an internal site (a large casting pore). Previous examples of fatal crack initiation from the surface in VHCF resulted from the presence of RX grains (associated or not to a coating deposition process) (Cervellon et al., 2021; Zhao et al., 2021a) or from a stress concentration at the surface of specimens, due to a prior plastic deformation before testing specimens in VHCF at  $1,000\text{ }^\circ\text{C}/R = 0.5/f = 20\text{ kHz}$  (Utada et al., 2021).

From the longitudinal and chemical analysis investigated in **sub-section 6.2** the author concluded that the oxidation process in VHCF at  $1,000\text{ }^\circ\text{C}/R_e = -1/f = 20\text{ kHz}$  is more or less damaging depending on the superalloy's chemistry. Further, **Figure III-34** proposes a crack initiation and propagation mechanism detailing the scenario built from the events uncovered in this section.

Starting from the initial optimized  $\gamma/\gamma'$  microstructure (**Figure III-34a**) that likely contains intrinsic processing defects (e.g., a high dislocation density), oxidation rapidly occurs at the specimens' surface, leading to a rougher surface and the depletion of (mostly) Al and Cr. As a result, the surface oxides are brittle and may crack due to the fatigue-oxides interaction (Reger and Rémy, 1988a), leaving the surface open to further oxygen and nitrogen diffusion into the bulk (Fleury and Rémy, 1993). Consequently, there is subsequent precipitation of nitrides below the surface (**Figure III-34b**) (Sato et al., 2011; Zhao et al., 2021a).

Dislocation climbing may be fostered by the VHCF loading, resulting in enhanced outward vacation diffusion and the derived formation of Kirkendall microvoids (i.e., invisible with the magnification available) just below the free surface (Evans, 1988). Furthermore, the early stages of fatigue cracks propagation were found to occur at preferentially oxidized interdendritic zones (Reger and Rémy, 1988a) since the interdendritic areas present stress/strain concentrations (e.g., pores, eutectics, carbides) that favor the matrix oxide scale fracture. Conversely, the author believes that in the absence of critical defects, the  $\gamma'$  maximum depletion in the DZ (Sato et al., 2011) is critical to the crack initiation as the mechanical resistance is related to the presence of  $\gamma'$  precipitates. The heterogeneous consumption results in “weak” zones more likely to form oxides and secondary cracks. In the defect “free” specimens, the superalloys with lower degree of chemical homogenization between DZ and IZ should present a higher density of secondary cracks at localized zones (**Figure III-27d**). Indeed, superalloys with high homogenization between DZ and

IZ are presenting fewer secondary cracks as TMS-238 (**Figure III-27e, f**) and AM/HT/REC (**Figure III-27 k and l**).

The oxidation combined with voids/intermetallic inclusions leads to crack initiation at a void or hard particles like nitrides or TCPs. These cracks are filled with a spinel of oxides, and the author believes that most of the fatigue life is spent consuming the elements that build the oxide's spinel. The author does not have a clear conclusion about the role of alternating stress in the way it may enhance oxidation kinetics (**Figure III-34c**).

This micro-crack can be considered as a notch in a sub-surface layer composed of voids and a  $\gamma$  matrix depleted from its main refractory elements filled with quite brittle particles (nitrides, carbides). Finally, it propagates in mode I through the microstructure, assisted by oxidation, up to failure (**Figure III-34d and e**).

Still, if oxidation seems to be clearly controlling the crack initiation phase in the absence of more critical defects, like casting pores or stray grains, one of the remaining key questions is to know how it may affect the very first stages of crack propagation from the surface, in mode I. Characterizing crack-propagation rate in VHCF in air and in a protective environment would be necessary to answer this question.

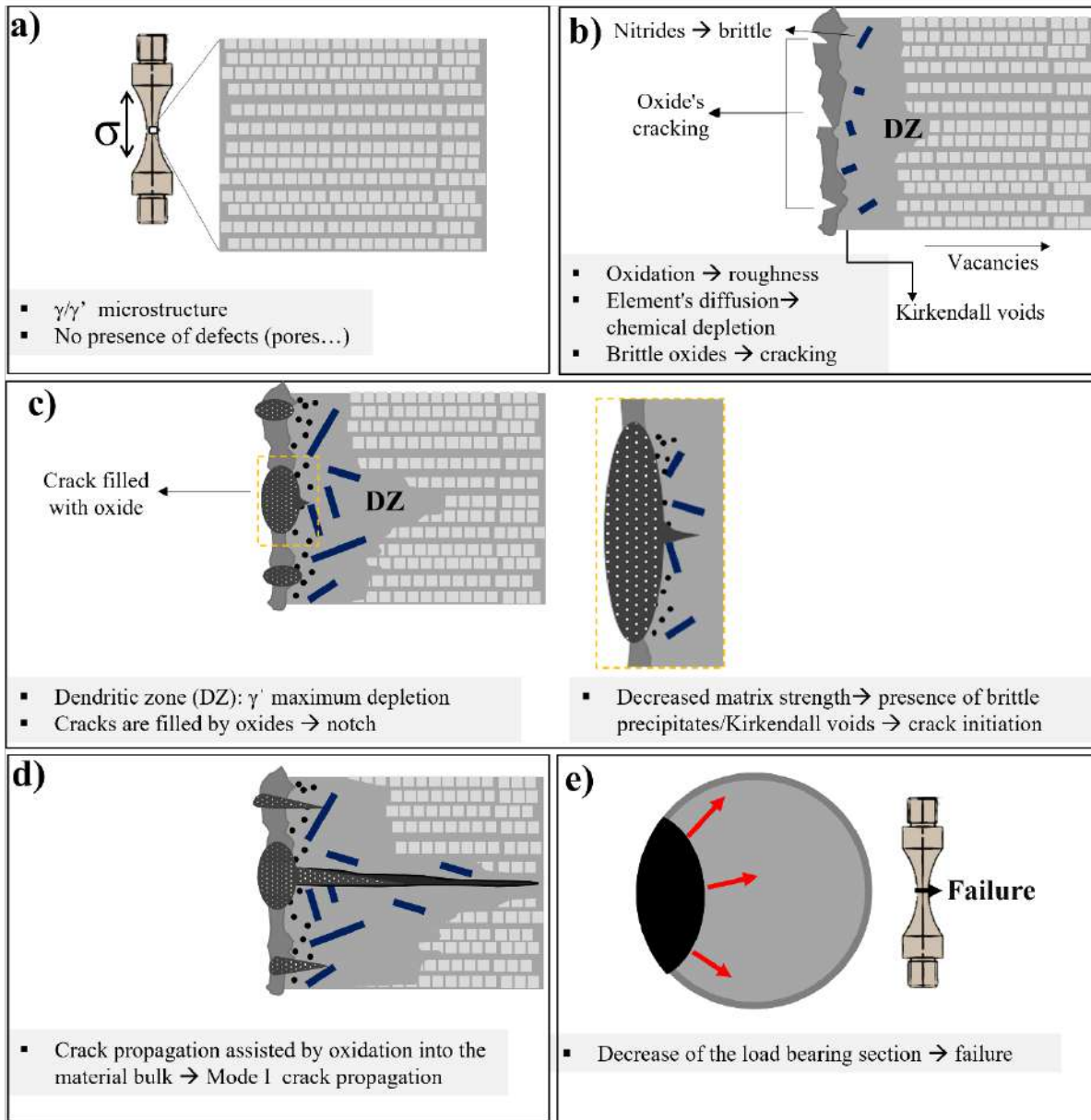


**Figure III-34** Schematic illustration of SX Ni-based superalloys' oxidation-controlled crack initiation mechanism in VHCF conditions at  $1,000\text{ }^\circ\text{C}/R_e = -1/f = 20\text{ kHz}$ . The initial optimized  $\gamma/\gamma'$  microstructure (a) is oxidized, leading to surface roughness. Subsequently, the brittle oxides crack, leaving the surface open to oxygen and nitrogen diffusion toward the bulk. Thus, the oxidation leads to the precipitation of small nitrides just below the free surface (b). The cracks filled by oxides inside a weak  $\gamma$  matrix combined with these voids/intermetallic precipitates lead to a surface crack initiation at a void or a nitride particle (c). The micro-crack then propagates in mode I through the microstructure, assisted by oxidation, until failure (d and e).

#### 6.4. Summary

Several Ni-based SX superalloys failed by crack initiation at the surface, even though no recrystallization was identified. The lifetime of the specimens that fail at the surface at  $R_e = -1$  is at least one decade higher than that of the specimens that failed at small casting pores. The crack initiation mechanism seems to be independent of the superalloy chemistry, as Ni-based SX superalloys from different generations developed secondary cracks. Due to the exposure to the temperature and then to the oxidation activity, a chemical evolution was observed, which results in differences in chemical composition of the regions in the specimens bulk and near the surface, respectively. A surface crack initiation mechanism was proposed from the results obtained in this sub-section determining that in the absence of critical defects such as casting pores, stray grains, or RX layer, the intrinsic VHCF life is controlled by the alloy's chemistry/environmental resistance.

## 7. Conclusions

This chapter was dedicated to studying the benefits and the consequences of the solidification methods and HIP treatments of nickel-based single-crystalline superalloys on the VHCF life. This chapter investigated nine superalloys under the fatigue conditions of 1,000 °C, 20 kHz, fully reversed loading, and no surface treatment.

Casting techniques involving moderate to low solidification rate led to casting pores, and their size and position are the main features controlling the fatigue life. Depending on the casting parameters and the superalloy chemistry, the critical casting pore can present a diameter as high as 200 μm or as low as 40 μm. Consequently, the fatigue life scatter decreases with the casting pore diameter size decreasing. A particular FIP modeling approach was applied confirming that this approach can be suitable for modeling fatigue life when the largest pore size and position control crack initiation.

On the other hand, fast solidification methods as liquid melting cooling or additive manufacturing can result in very high fatigue lives (beyond  $10^{10}$  cycles under low alternating stresses) or very low fatigue lives (lower than  $10^6$  cycles under low alternating stresses) if stray grain nucleation occurs. The analysis of the stray grain contribution to the fatigue damage mechanism is one of the original analyses of this work. It shows by means of finite element analysis and experimental results that the presence of stray grains increases the frequency of resonance, leading to a shear stress concentration at the interface between the macroscopic SX and the stray grain. The local overload leads to severe fatigue damage, earlier crack initiation, and consequently, a lower fatigue life.

The HIP treatment has shown to improve fatigue lives. However, it can lead to a much more scatter of fatigue life. According to EBSD analysis, sub-grains were observed to develop around the compacted pores. The plastic strain around the compacted pores was the subject of finite element studies in the literature. However, no prior EBSD observations of a HIPed pore was presented in the literature up to now. HIPed pores are still controlling the VHCF life if sub-grains are present in their vicinity. It was also shown by means of FEM simulations that a casting pore is less damaging than the quasi-recrystallized region of the same size but with a misorientation higher than 20 ° from the superalloy's primary <001> orientation.

Moreover, if no subgrains develop during the HIP treatment, the crack initiation starts at not completely closed casting pores filled with TCP phases. Even though these very small casting pores are surrounded by incipient melting, it was shown by EBSD characterizations that no recrystallization occurs due to incipient melting. There is, thus, no evidence that the IM leads to the crack initiation under these conditions.

Finally, for the first time, a VHCF life controlled by oxidation is presented in the open literature for Ni-based SX superalloys at high temperatures in fully reversed loading and without any surface recrystallization mechanisms. Moreover, a surface crack initiation mechanism is proposed, and in the absence of critical defects like casting pores, stray grains, or RX layer, the alloy's chemistry /environmental resistance control the intrinsic VHCF life.

These results also suggest that there is no fatigue limit in these VHCF conditions as oxidation may always be the source of crack initiation at the lowest alternating stresses at high temperatures.

## **Chapter IV. Fatigue life of coated Ni-based single crystal superalloys**



## **Durée de vie en fatigue de superalliages base-Ni monocristallins revêtus**

Le chapitre III a été consacré aux mécanismes d'endommagement des superalliages base Ni monogranulaire en fatigue gigacyclique sans aucun revêtement. Au contraire, le chapitre IV est consacré à l'impact des conditions de surface telles que la présence d'un revêtement sur la durée de vie en fatigue du superalliage. Il a été vu dans le chapitre précédent qu'une fois que les défauts tels que les pores sont absents, la durée de vie en fatigue gigacyclique peut être contrôlée par l'oxydation pour les très fortes durées de vie. Dans le présent chapitre, une analyse détaillée des mécanismes d'amorçage depuis la surface sera présentée pour les alliages monogranulaires base Ni revêtus par NiAl.

Deux types de revêtements NiAl ont été étudiés, l'un étant déposé par un procédé de dépôt industriel (APVS) et une seconde par un procédé de type barbotine (Slurry). Des paramètres de fatigue spécifiques ont été choisis pour reproduire l'environnement opérationnel, y compris les conditions de fatigue oligocyclique et gigacyclique. De plus, les alliages MAR-M200 +Hf SX, AM1, Rene N5, CMSX-4 et CMSX-4 Plus ont été étudiés dans cette section.

Premièrement, il a été montré que le traitement thermique de mise en solution et le vieillissement contrôlent à la durée de vie en fatigue en LCF, rapport de charge positif et températures élevées. Dans ces conditions, le revêtement NiAl n'a pas eu d'impact sur la vie en fatigue des superalliages Rene N5 et AM1. Cependant, il a un impact important sur la durée de vie en fatigue du superalliage MAR-M200 + Hf, même en corrigeant la section portante en prenant en compte la couche d'interdiffusion du revêtement avec le substrat. L'interaction chimique entre le MAR-M200 +Hf SX et le revêtement NiAl Slurry semble être très néfaste pour la tenue mécanique du superalliage.

Des fissures perpendiculaires à l'axe de chargement se sont développées depuis la surface dans les tous premiers cycles et les essais réalisés sous vide ont prouvé que l'amorçage de la fissure n'était pas assisté par l'oxydation. Ainsi, l'oxyde joue un rôle moins important dans le mécanisme d'amorçage comparativement aux observations de la littérature. De plus, il a été possible d'identifier des fissures à l'interface entre la matrice et le précipité dans la couche d'interdiffusion (IDZ). En effet, la fragilité locale du revêtement conduit à l'amorçage de fissures en surface et

dans l'IDZ, indiquant une faible ductilité du revêtement NiAl sous les chargements de fatigue et à des températures de 900 - 950 °C.

Deuxièmement, à une température plus élevée, des fréquences très élevées et à  $R_\epsilon = -1$ , l'auteur a observé que la durée de vie en fatigue des échantillons revêtus pouvait être fortement influencée par l'interaction chimique entre le revêtement et les défauts de fonderie. Tout comme en LCF, des fissures se forment dès les tous premiers cycles de VHCF, indiquant à nouveau une faible ductilité du revêtement sous ces conditions, malgré une température plus élevée.

Deux mécanismes d'amorçage caractéristiques ont pu être identifiés dans ces conditions : (i) amorçage au voisinage d'une couche recristallisée qui arrête la propagation des fissures et qui ne semble pas impacter la durée de vie en VHCF. (ii) Un amorçage avec une interaction entre un pore de fonderie et la zone d'interdiffusion qui contrôle la durée de vie intrinsèque du VHCF. Ce dernier mécanisme est induit par l'évolution chimique locale entraînant une déformation microplastique prématurée (formation de la zone rugueuse). Par conséquent, dans ces conditions, l'amorçage de fissure sur un pore de fonderie proche de la zone d'interdiffusion semble être plus dangereux que l'amorçage de fissure au niveau des couches recristallisées à l'interface revêtement/substrat d'épaisseur d'environ 50  $\mu\text{m}$  ou depuis la surface.

## 1. Introduction

**Chapter III** was devoted to intrinsic damage mechanism of Ni-based SX superalloys in VHCF without any coating. On the contrary, **Chapter IV** is dedicated to the impact of the presence of (bond) coat on the superalloy's fatigue life.

Most of the results presented in this sub-section are part of an industrial project aiming to decrease the time and the costs of the turbine blades' refurbishment. Two types of NiAl bond coats were studied, one being deposited by an industrial (APVS) deposition process and a second one through a slurry-type process. Specific fatigue parameters were chosen to reproduce the operative environment including LCF and VHCF conditions. In addition, MAR-M200 +Hf SX, AM1, Rene N5, CMSX-4, and CMSX-4 Plus alloys were investigated in this section.

The first sub-section investigates the bond coat's damage mechanism at low frequency and high temperatures of MAR-M200 +Hf SX, AM1, and Rene N5 superalloys. The objective is to examine the effect of surface conditions on the LCF life.

The second sub-section investigates the bond coat's impact on the superalloys damage mechanism in the VHCF regime at high temperatures of AM1, Rene N5, CMSX-4, and CMSX-4 Plus superalloys. Based on the fatigue lives and the microstructure investigations, a damage mechanism of coated systems is proposed.

## 2. Impact of the bond-coat on the LCF durability

This sub-section is dedicated to the stress-controlled fatigue tests performed at 900 and 950 °C with a frequency of 0.5 Hz and a stress ratio of 0.05. Typically, in these conditions and high temperatures of 900 - 1,000 °C, the crack initiation is at the surface at oxide spikes (Chan et al., 1987; Lerch and Antolovich, 1990; MacLachlan and Knowles, 2001). Moreover, the fatigue tests carried out with a positive stress ratio imply that creep damage will contribute to the failure mode (Cervellon et al., 2020b; Kobayashi et al., 2014; Meid et al., 2019a). Therefore, creep tests and monotonic tensile tests were performed for AM1 and Rene N5 samples to support the discussion. The creep results are depicted in **Appendix E**.

Three superalloys are investigated in this sub-section: AM1, Rene N5, and MAR-M200 +Hf SX alloys, the last being remaining samples from the Mataveli thesis (Mataveli Suave, 2017). **Table IV-1** recalls the testing conditions applied to these three alloys. As a reminder, heat treatments and the bond coat diffusion treatments have already been presented in **Chapter II**. **Appendix B** presents the database of this sub-section and several supplementary fracture surface analyses.

*Table IV-1 AM1, Rene N5, and MAR-M200 +Hf SX tensile and fatigue tests parameters.*

<i>Mechanical test parameters</i>	<i>AM1</i>	<i>Rene N5</i>	<i>MAR-M200 +Hf SX</i>
Tensile rate (s <sup>-1</sup> )		5 10 <sup>-4</sup>	
Tensile temperature (°C)	950	950	900
LCF parameters		R <sub>σ</sub> = 0.05 and f = 0.5 Hz	
LCF temperature	950	950	900
Slurry coat method	✓	✓	✓
APVS coat method	✓	✓	×
Microstructure	AM1: As-cast + HT BC diffusion AM1 and Rene N5: SHT + HT BC diffusion + HT to normalize the γ' size		SHT + R1 + R2 + HT BC diffusion

### 2.1. Tensile strength of bond-coated specimens

The main objective of the tensile tests at 900 °C and 950 °C was to get information for interpreting LCF. **Figure IV-1a** shows the tensile curves for AM1 (dotted line) and Rene N5 (solid line) samples with a bare substrate and NiAl-coated samples via the Slurry and the APVS methods. **Figure IV-1b** shows the tensile curves of the MAR-M200 +Hf SX sample with bare substrate and a NiAl-coated sample via the Slurry method.

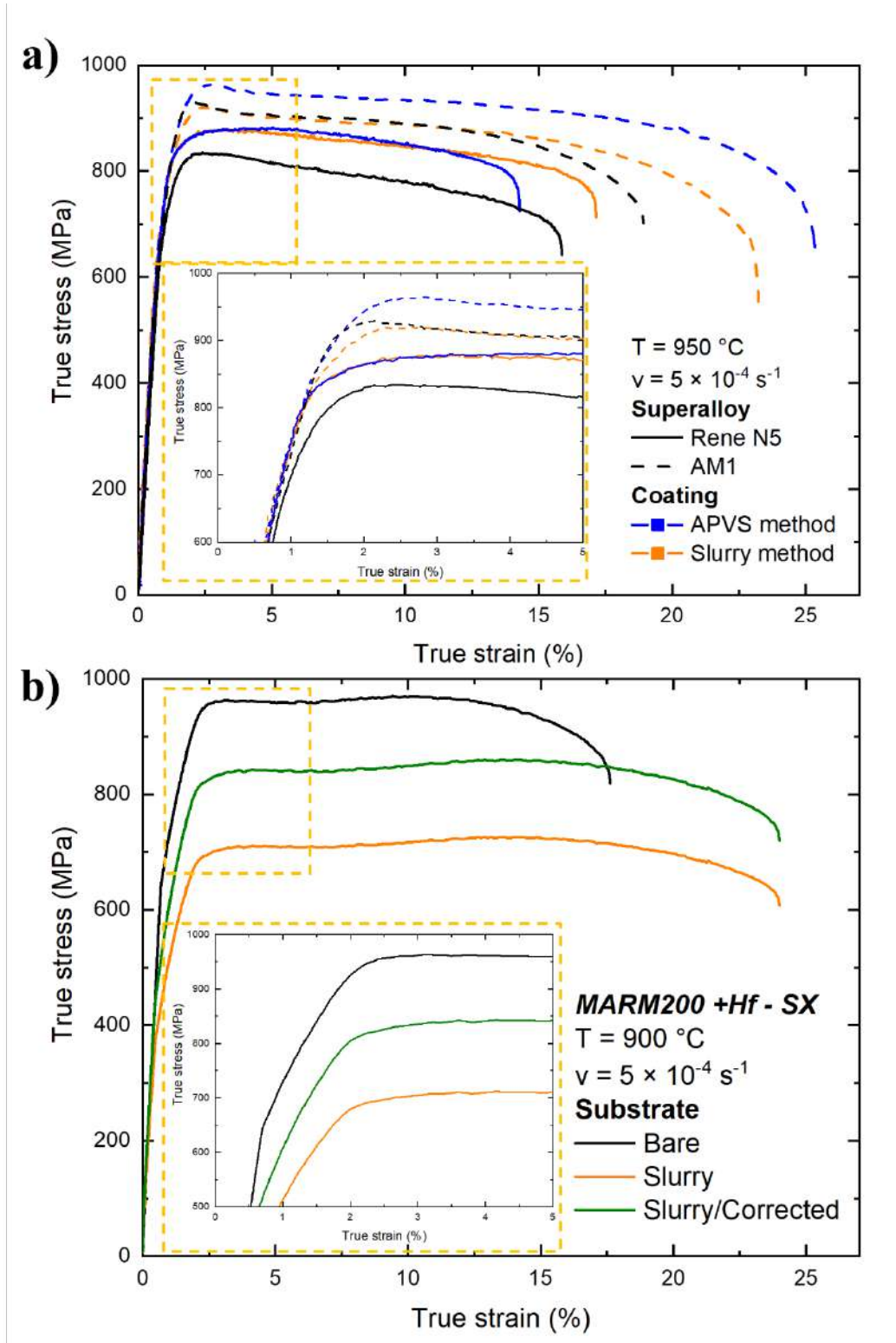
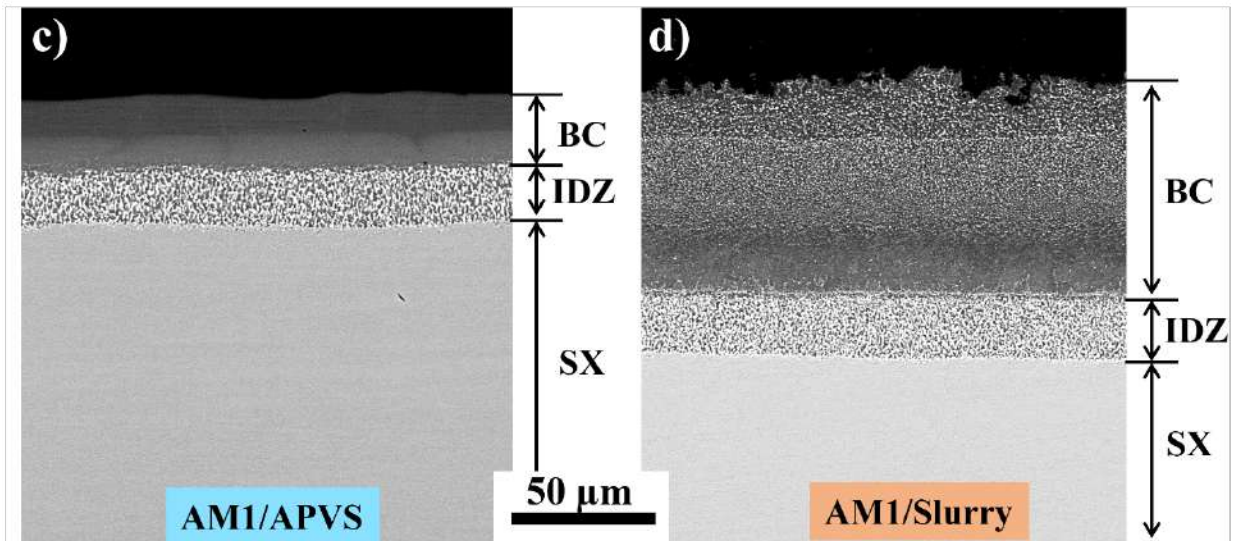
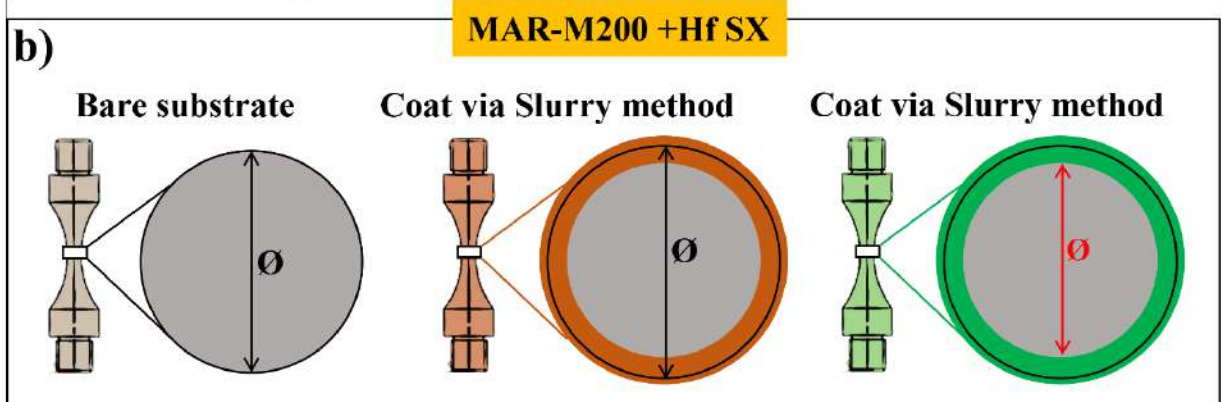
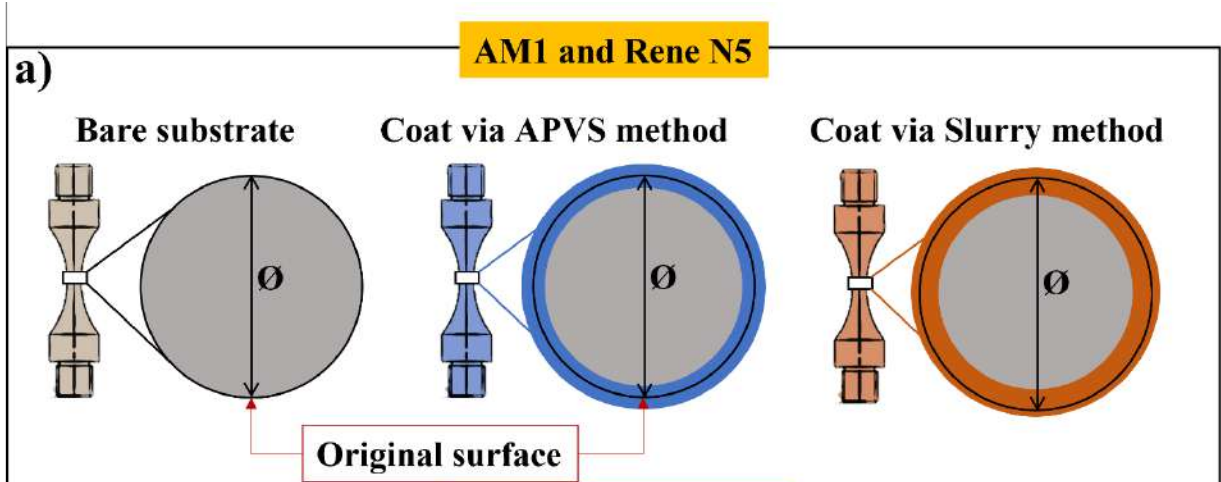


**Figure IV-1** Tensile curves representing the true stress (MPa) vs. the true strain (%) at  $950\text{ }^{\circ}\text{C}/5 \times 10^{-4}\text{ s}^{-1}$  for AM1 and Rene N5 (a) and at  $900\text{ }^{\circ}\text{C}/5 \times 10^{-4}\text{ s}^{-1}$  for MAR-M200 +Hf SX (b).

The tensile curves in each plot were calculated considering the bare substrate diameter as already depicted in **Chapter II sub-section 2.2**. Neither the coating thickness nor the interdiffusion zone were considered in the calculation of the load-bearing section. From **Figure IV-1**, a weak impact of the BC is noticed on AM1 and Rene N5 tensile behavior at 950 °C. Rene N5 is observed to have a lower tensile strength compared to AM1 with and without a NiAl BC. A small improvement in tensile strength is observed for Rene N5 after BC deposition. However, for the MAR-M200 +Hf SX sample, the NiAl BC induces a spectacular decrease of the specimen's tensile strength. To better analyze this decrease in tensile strength, the BC diffusion layer thickness was measured and the total of both ( $\approx 1$  mm, 500  $\mu\text{m}$  on each side) was subtracted from the original diameter, assuming no loading bearing capacity of the coating/IDZ (see **Figure IV-2**). The green curve in **Figure IV-1b** represents the tensile strength of the MAR-M200 +Hf SX calculated with this load-bearing section correction. A similar approach has also been done for AM1 and Rene N5, the results being depicted in **Table IV-2**.

According to **Figure IV-1**, *the MAR-M200 +Hf SX tensile strength are highly impacted by a Slurry type BC deposition, even after correcting the load-bearing diameter* (green curve in **Figure IV-1b**).

The green curve and the black curve in **Figure IV-1b** should be superimposed if the loss of tensile strength would only result from the loss of load bearing section due to the diffusion/interdiffusion of the NiAl coating with the MAR-M200 +Hf SX substrate. However, as seen in **Figure IV-1** and **Table IV-2**, the yield stress ( $\sigma_{\epsilon 0.2\%}$ ) was still 14 % lower, and the ultimate tensile strength (UTS) was 100 MPa lower than the uncoated sample's tensile strength after this correction, meaning that the loss of the tensile strength is not only resulting from this loss of load bearing section.



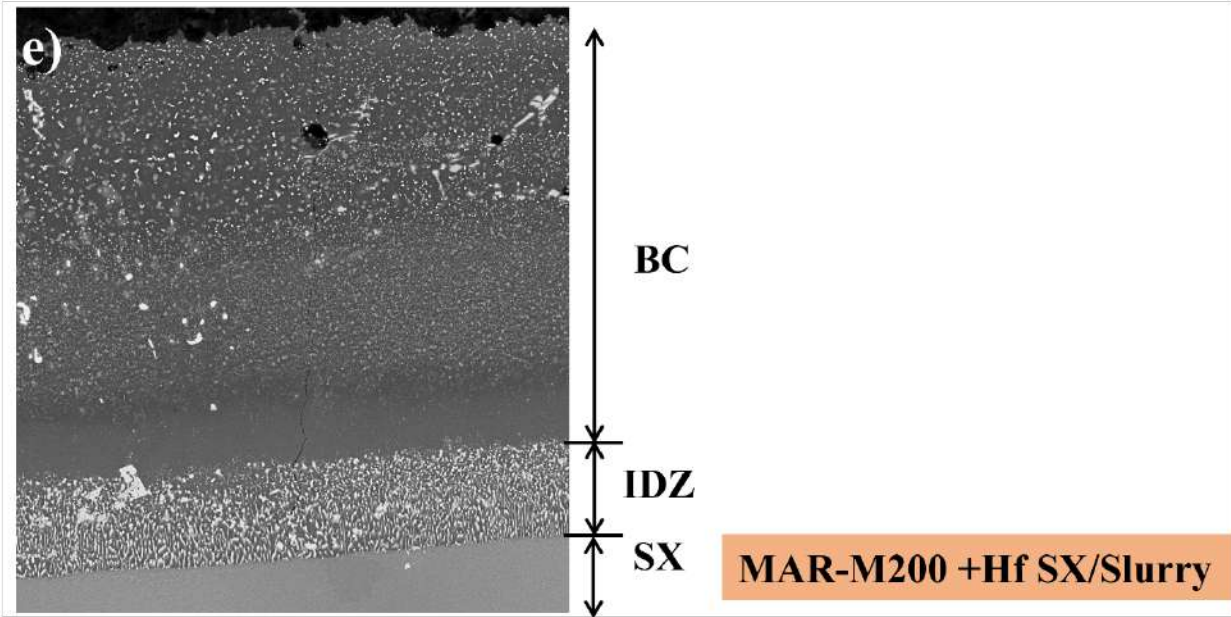


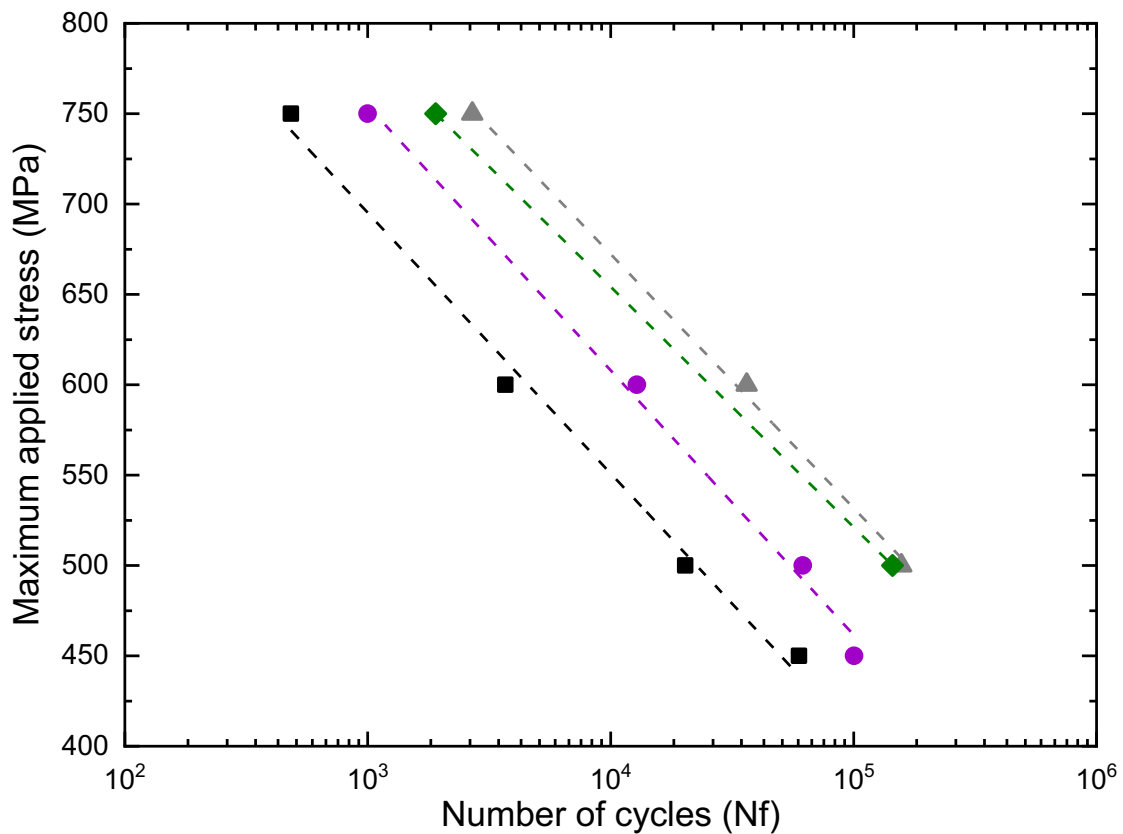
**Figure IV-2** Load bearing section calculation for AMI and Rene N5 (a) and MAR-M200 +Hf SX (b). The gray color represents the bare substrate, the blue one the samples coated via APVS method, and orange are the samples coated via Slurry method. The green color represents the load-bearing section calculated by subtracting the coating diffusion layer and IDZ from the original diameter. AMI coated with the NiAl BC via APVS (c) and Slurry (d). MAR-M200 +Hf SX coated with the NiAl BC via Slurry (d).

**Table IV-2** Tensile strength at 900 °C for MAR-M200 +Hf SX and 950 °C for AMI and Rene N5 samples at  $5 \cdot 10^{-4} \text{ s}^{-1}$ .  $\sigma_{e 0.2\%}$  is the yield stress at 0.2% plastic offset, UTS is the ultimate tensile strength and A the elongation at failure.

<i>Tensile test data</i>	<i>AMI</i>	<i>Rene N5</i>	<i>MAR-M200 +Hf SX</i>
<b>Bare substrate</b>			
Temperature (° C)	950	950	900
$\sigma_{e 0.2\%}$ (MPa)	766	726	957
UTS (MPa)	927	834	970
A (%)	19	15	17
<b>Coated via APVS</b>			
$\sigma_{e 0.2\%}$ (MPa)	788/821	783/798	
UTS (MPa)	962/995	896/911	
A (%)	25	14	
<b>Coated via Slurry</b>			
$\sigma_{e 0.2\%}$ (MPa)	781/1,082	783/992	698/825
UTS (MPa)	918/1,084	875/1,034	725/860
A (%)	23	17	24

## 2.2. Microstructure, polishing, and bond coat: which parameter primarily controls the LCF life?

First, the impact of the surface preparation on the AM1 LCF life was investigated. **Figure IV-3** show the maximum applied stress ( $\sigma_m$ ) as a function of the number of cycles to failure ( $N_f$ ) diagram gathering the obtained LCF results. **Figure IV-3** shows the results obtained for AM1 superalloys with three different microstructures: as-cast (represented by black symbols), solution heat treated (i.e., no aging) (represented by purple symbols), and fully heat treated specimens. Further, AM1 samples with the full HT were either polished up to a SiC grade 320 paper (represented by green symbols) or up to 1  $\mu\text{m}$  minor finish (represented by gray symbols). The samples presented a roughness ( $R_a$ ) of 0.103  $\mu\text{m}$  after mirror polishing and 0.535  $\mu\text{m}$  after 320 SiC paper polishing. It is recalled that the surface preparation with a SiC 320 polishing was evaluated since it has been determined to be representative of the roughness necessary to ensure a good deposition process for NiAl bond coats processed by APVS and Slurry. All specimens presented in **Figure IV-3** failed from the surface (see **Figure IV-4**).



**AM1 bare substrate**

$R = 0.05 / T = 950 \text{ }^\circ\text{C} / f = 0.5 \text{ Hz}$

**Heat treatment and polishing:**

- ▲ Full HT + 1  $\mu\text{m}$
- ◆ Full HT + x 320
- SHT + x 320
- As-cast + x 320

**Crack initiation site: Surface**

**Trend line**

- - - Full HT + 1  $\mu\text{m}$
- - - Full HT + x 320
- - - HT + x 320
- - - As-cast + x 320

**Figure IV-3** S-N diagram at  $950 \text{ }^\circ\text{C}$ ,  $R_\sigma = 0.05$ , and  $f = 0.5 \text{ Hz}$  gathering the uncoated AM1 low cycle fatigue results. The diagram shows the maximum stress as a function of the number of cycles to failure.

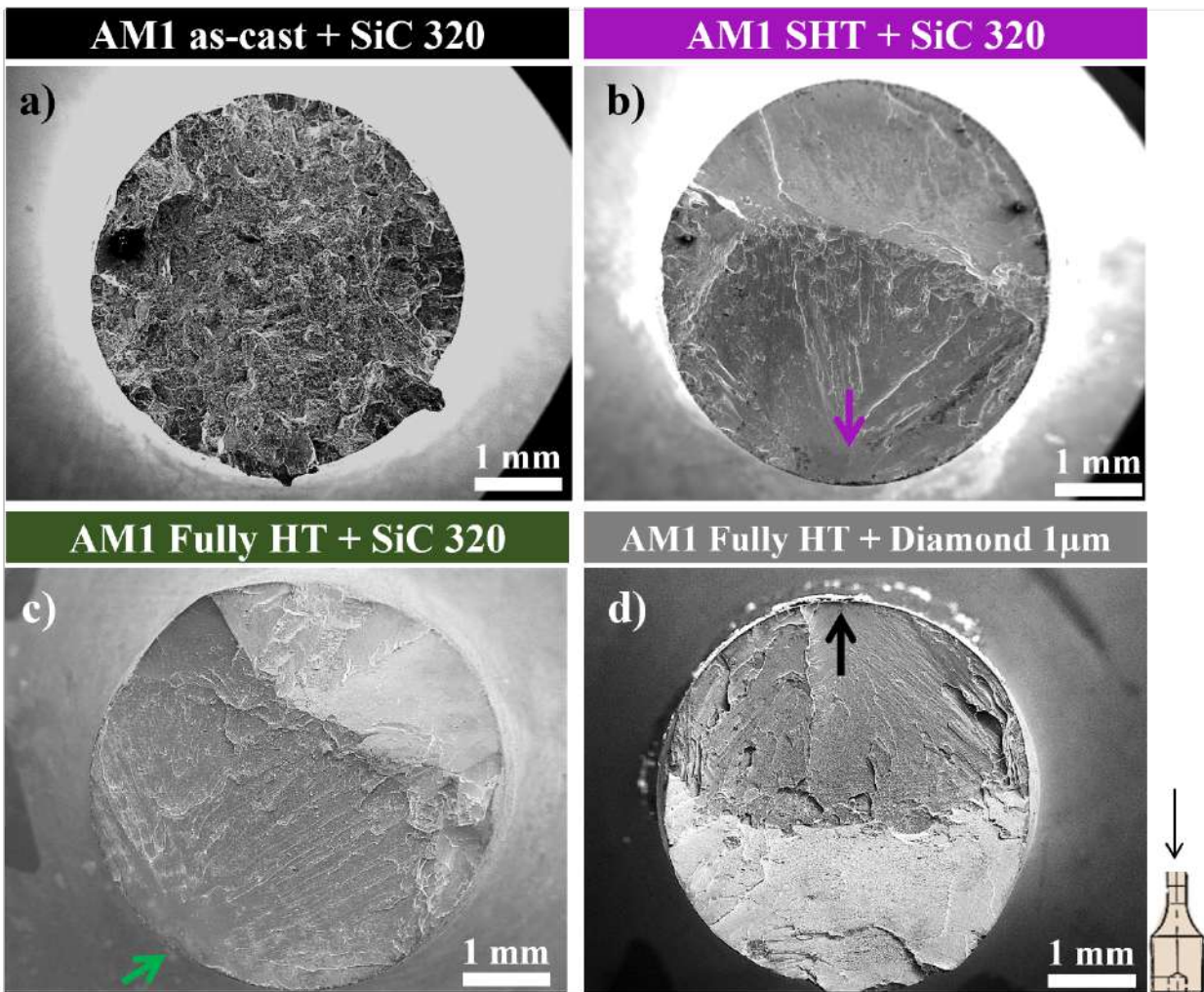


**Figure IV-4** Fracture surface observation of AM1 bare substrate specimens. As-cast specimen ( $\sigma_m = 600$  MPa, with  $N_f = 3.7 \cdot 10^3$  cycles) (a), SHT (3 h/1,300 °C) ( $\sigma_m = 600$  MPa, with  $N_f = 1.3 \cdot 10^4$  cycles) (b), fully HT ( $\sigma_m = 500$  MPa, with  $N_f = 1.4 \cdot 10^5$  cycles) (c) specimens polished up to a SiC grade 320 paper, and specimen polished up to 1  $\mu\text{m}$  minor finish ( $\sigma_m = 600$  MPa, with  $N_f = 3.6 \cdot 10^4$  cycles) (d). The arrows indicate the crack initiation zone.

The samples' fatigue life was improved by a factor of  $\approx 5$  after the SHT and by a factor of  $\approx 10$  after the full HT. Hence, bulk microstructure seems to be more LCF life controlling compared to the surface preparation. In fact, according to **Figure IV-5**, the AM1 superalloy creep life increases by  $\approx 100$  h after the full HT. **Figure IV-6** shows further analyses of the fatigue specimens' deformation indicating a less pronounced cyclic ratcheting once the SHT is applied to the alloy, due to a better creep resistance of the alloy. The sample fully HT APVS coated illustrates an even

greater improvement due to a more regular  $\gamma/\gamma'$  microstructure of the substrate, as observed in **Figure IV-7**. *In these conditions, LCF life is mainly controlled by the bulk alloy microstructure and resistance to creep damage.*

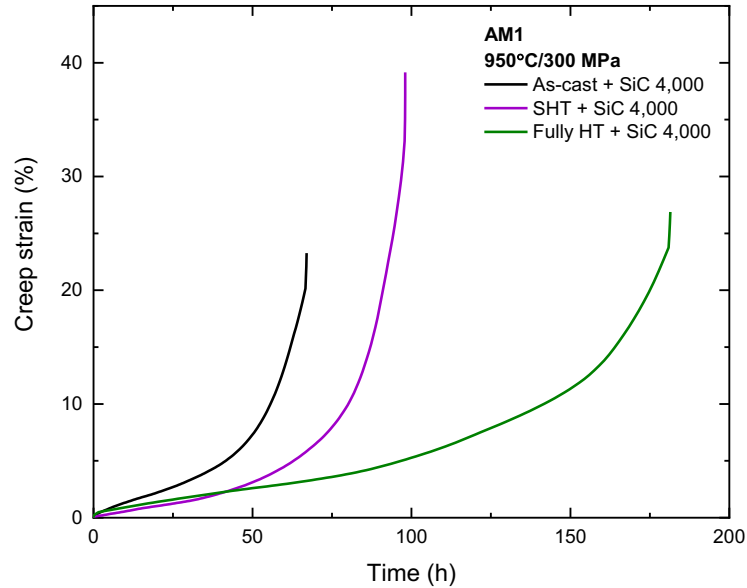


**Figure IV-5** Creep curves for the Ni-based SX superalloy AM1 bare substrate in different microstructural states at 950 °C/300 MPa.

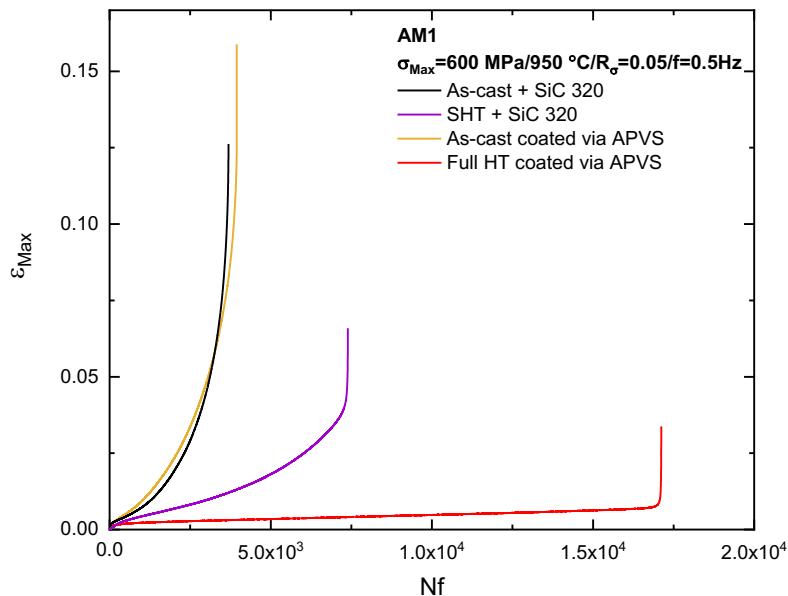


**Figure IV-6** Evolution of the maximum mechanical strain as a function of the number of cycles for the AM1 superalloy in different microstructural states and with/without an APVS coating. The fatigue test was carried out at  $\sigma_{Max}=600$  MPa/950 °C,  $R_{\sigma} = 0.05$ , and  $f = 0.5$  Hz. Note that the curve of the uncoated fully HT specimen is not presented due to extensometer sliding.

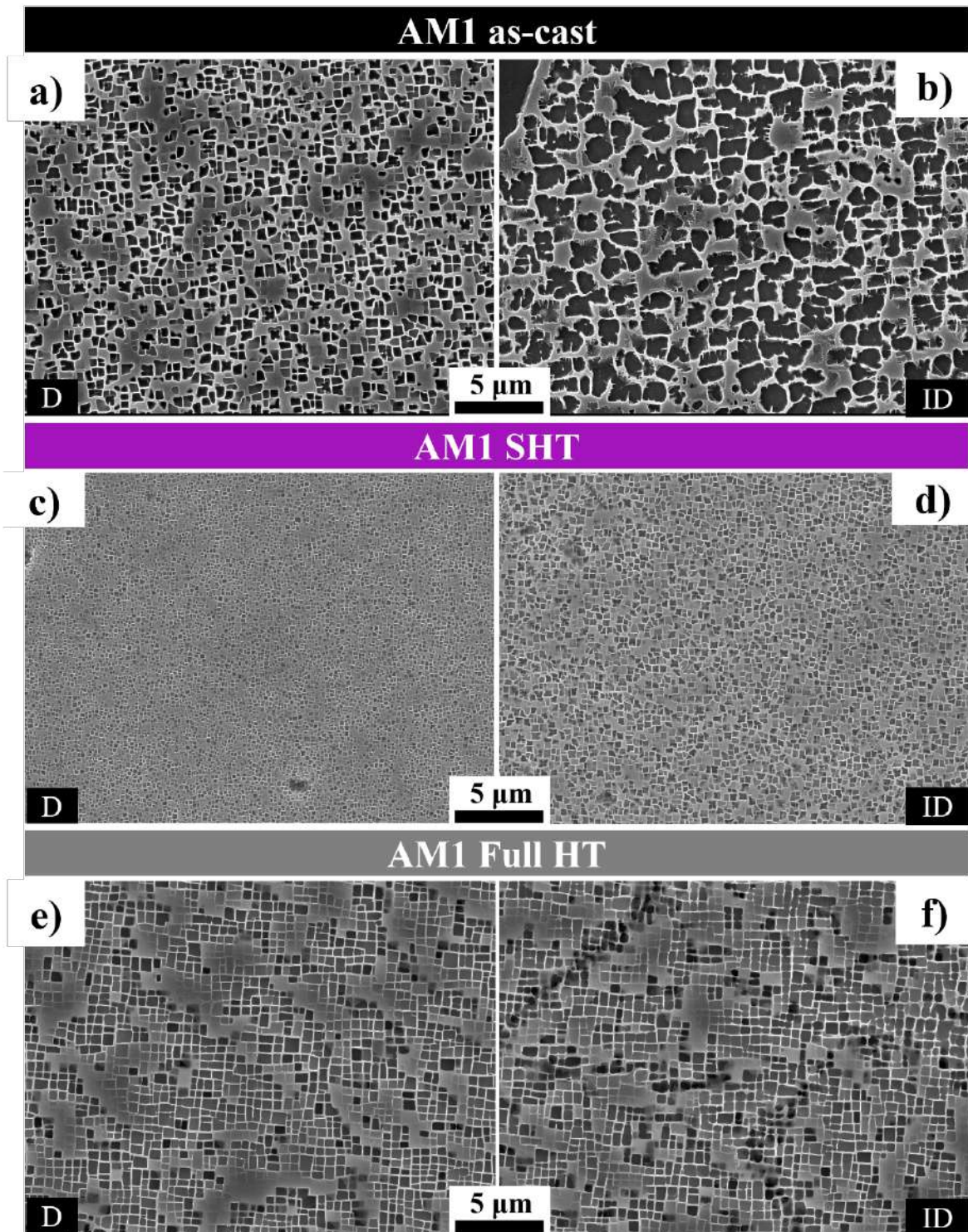
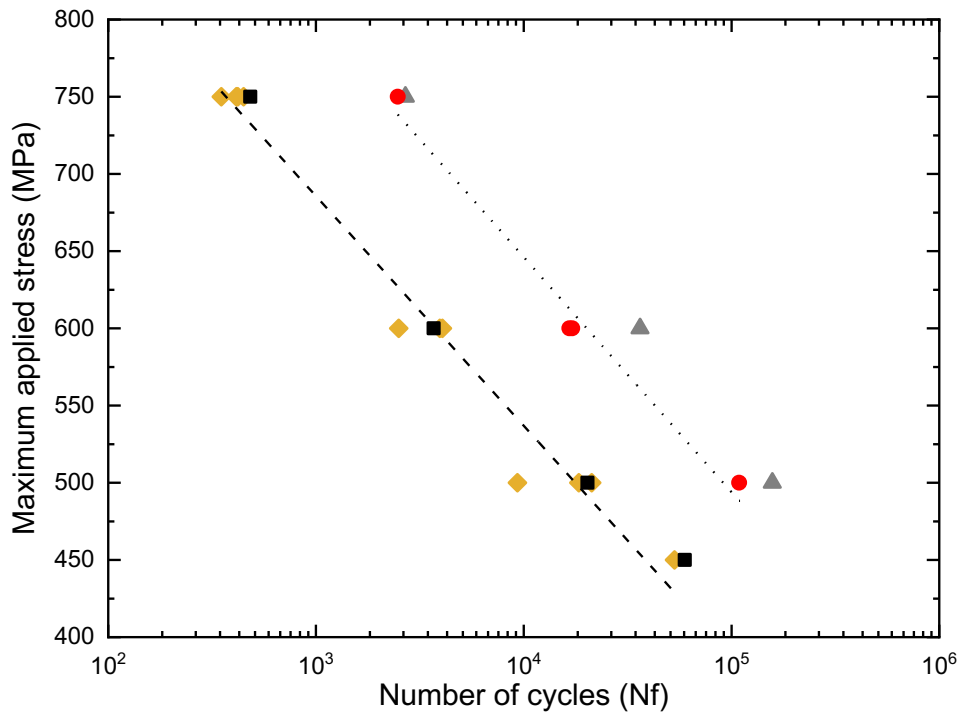


**Figure IV-7**  $\gamma/\gamma'$  microstructure in the primary dendrite arms (D) and interdendrite zones (ID) of AM1 as-cast (a and b resp.), AM1 SHT (3 h/1,300 °C) (c and d resp.), and AM1 full HT (e and f resp.). Observations performed in a  $\approx (001)$  plane.

LCF tests in the same conditions were also performed using coated specimens. It is recalled that the applied stress range for all coated specimens was calculated from the specimens' diameters before coating deposition. **Figure IV-8** depicts the AM1 LCF results of as-cast (black and yellow symbols) and fully HT (gray and red symbols) samples with bare (black and gray symbols) and coated (red and yellow symbols) substrates. In this figure, the coating is the industrial NiAl deposited via the APVS method. Again, the specimens failed from a surface crack initiation site detailed in **Figure IV-9**.



**AM1**

**NiAl coated by APVS method**

$R = 0.05 / T = 950 \text{ }^\circ\text{C} / f = 0.5 \text{ Hz}$

**Heat treatment and substrate:**

- As-cast/Bare
- ▲ Full HT/Bare
- ◆ As-cast/Coated
- Full HT/Coated

**Crack initiation site: Surface**

**Trend line**

..... Full HT

----- As-cast

**Figure IV-8** S-N diagram at  $950 \text{ }^\circ\text{C}$ ,  $R_\sigma = 0.05$ , and  $f = 0.5 \text{ Hz}$  gathering the AM1 low cycle fatigue results. The diagram shows the maximum stress as a function of the number of cycles to failure.

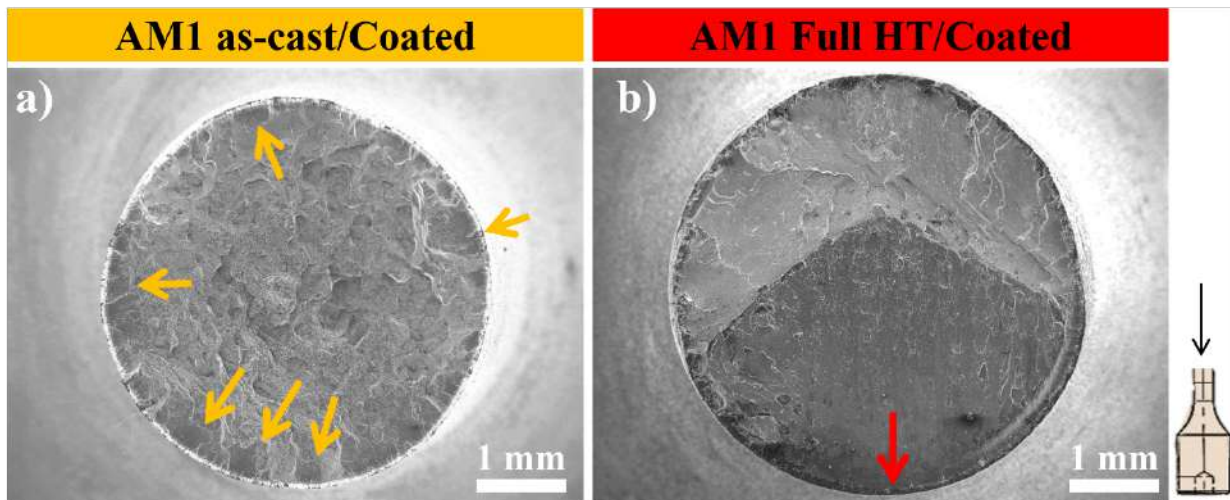


**Figure IV-9** Fracture surface observation of AM1 coated via APVS specimens. As-cast specimen ( $\sigma_m = 600$  MPa, with  $N_f = 3.9 \cdot 10^3$  cycles) (a), full HT specimen ( $\sigma_m = 600$  MPa, with  $N_f = 1.7 \cdot 10^4$  cycles) (b). The arrows indicate the crack initiation zone.

According to **Figure IV-8**, the bond coat does not seem to affect the alloy's fatigue life under these conditions. Just a small decrease of the LCF life can be observed in the fully HT state once an APVS NiAl BC is applied. Thus, the critical factor is still the microstructure. The result is not really surprising since fatigue tests under stress-controlled and positive stress ratio were already observed to be strongly dependent on creep damage accumulation (Cervellon et al., 2020b; Fleury and Rémy, 1993; Perruchaut, 1997; Pollock and Tin, 2008).

The impact of the process of BC deposition on the LCF life is presented in **Figure IV-10**, for fully HT AM1 specimens. Slurry type BC appears to have almost no influence on the LCF life, except perhaps at the lowest applied stress. However, due to the low number of representative samples, the results are inside the LCF typical scatter, i.e., any possible impact of the coating cannot be concluded. Again, all the specimens failed from the surface (**Figure IV-11**).

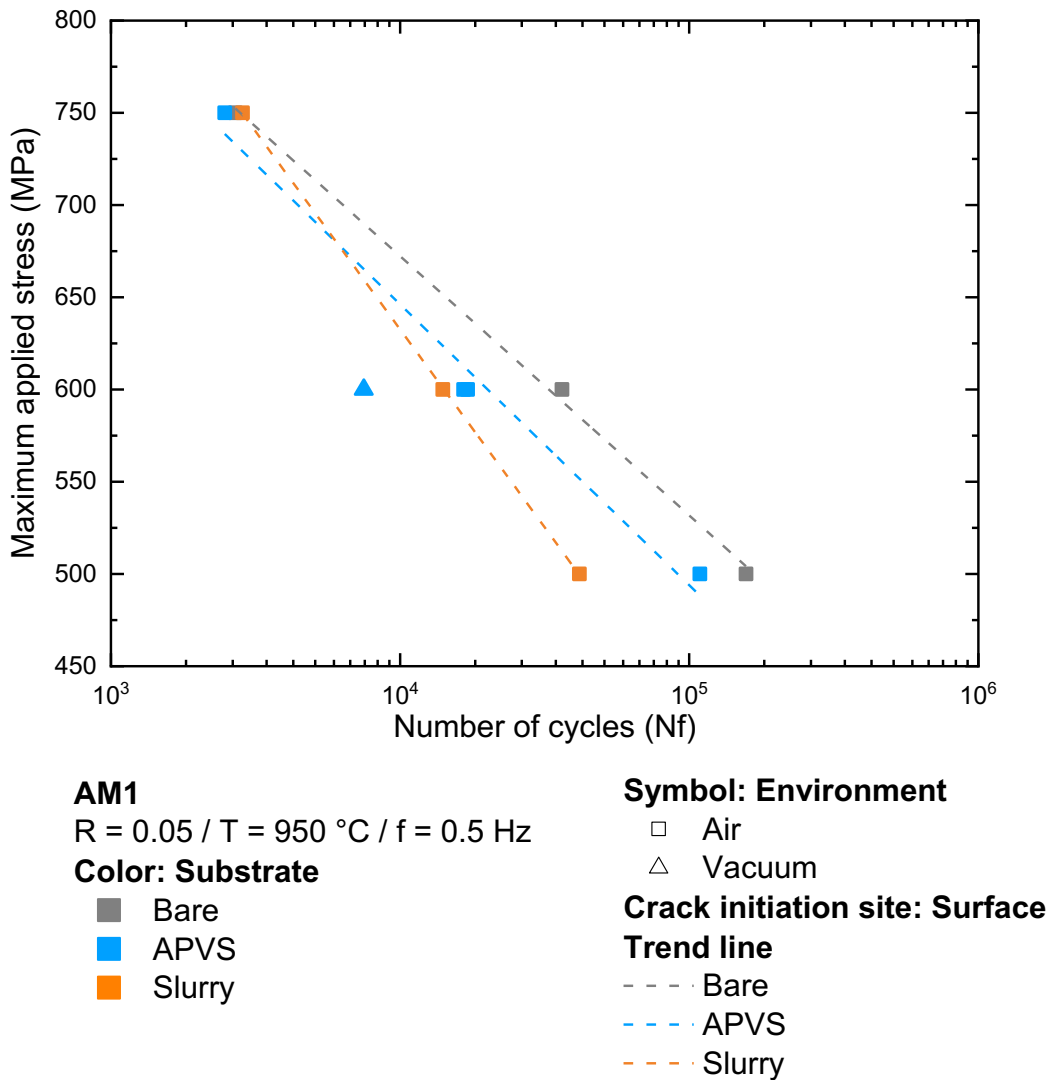


**Figure IV-10** S-N diagram at 950 °C,  $R_\sigma = 0.05$ , and  $f = 0.5 \text{ Hz}$  gathering all achieved LCF results on fully HT AM1. The diagram shows the maximum stress as a function of the number of cycles to failure.

The absence of any noticeable impact of the NiAl BC on the LCF life can be understood from the fact that bond-coated specimens have almost the same creep life at 950 °C/300 MPa, see **Appendix E, Figure E-1c**.

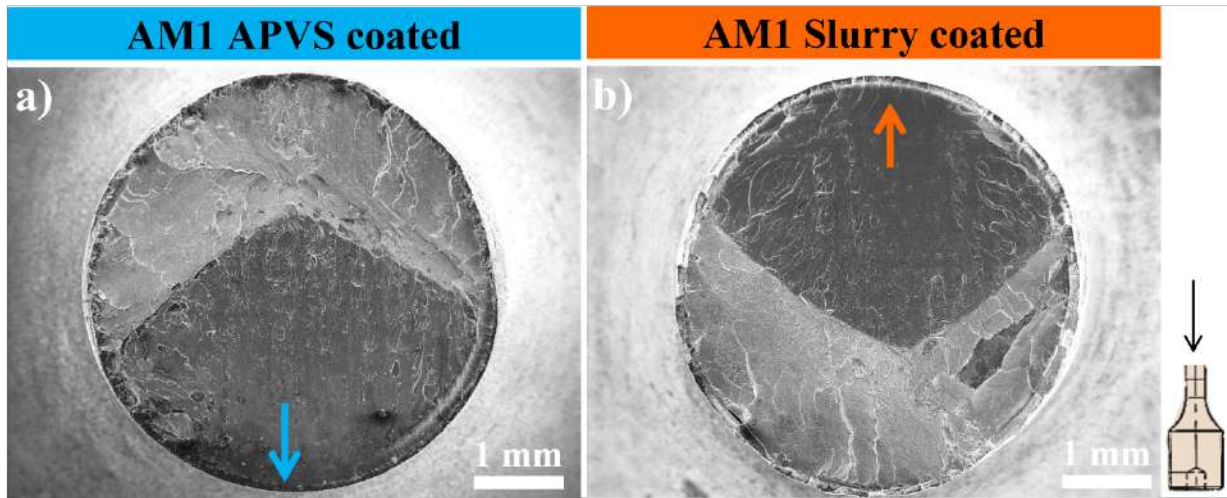
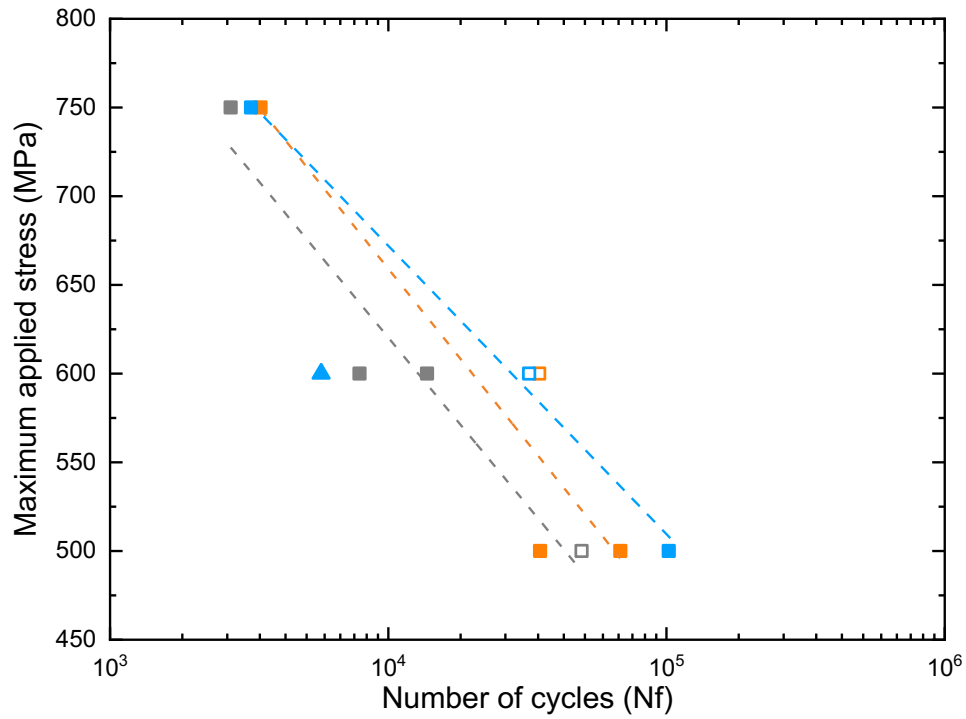


**Figure IV-11** Fracture surface observation of AM1 APVS coated ( $\sigma_m = 600$  MPa, with  $N_f = 1.7 \cdot 10^4$  cycles) (a), and Slurry coated ( $\sigma_m = 600$  MPa, with  $N_f = 1.4 \cdot 10^4$  cycles) (b). The arrows indicate the crack initiation zone.

The same tests have also been performed using Rene N5 alloy. **Figure IV-12** shows the Rene N5 LCF results of bare and coated samples. In this case, three samples tested under low maximum applied stress failed from casting pores near the surface surrounded by carbides (see **Figure IV-13**). Like for AM1, the presence of a NiAl BC seem to have a low influence on the creep life at 950 °C/300 MPa (see **Appendix E**). **Figure IV-14** shows a less pronounced cyclic ratcheting for the coated Rene N5 specimens (APVS and Slurry) compared to the bare ones. This may explain the slightly improved fatigue lives of the coated specimens.



**Rene N5**

R = 0.05 / T = 950 °C / f = 0.5 Hz

**Color: Substrate**

- Bare
- APVS
- Slurry

**Symbol: Environment**

- Air
- △ Vacuum

**Fill: Crack initiation site**

- Surface
- Casting pore

**Trend line**

- - - Bare
- - - APVS
- - - Slurry

*Figure IV-12 S-N diagram at 950 °C,  $R_\sigma = 0.05$ , and  $f = 0.5$  Hz gathering the Rene N5 low cycle fatigue results. The diagram shows the maximum stress as a function of the number of cycles to failure.*

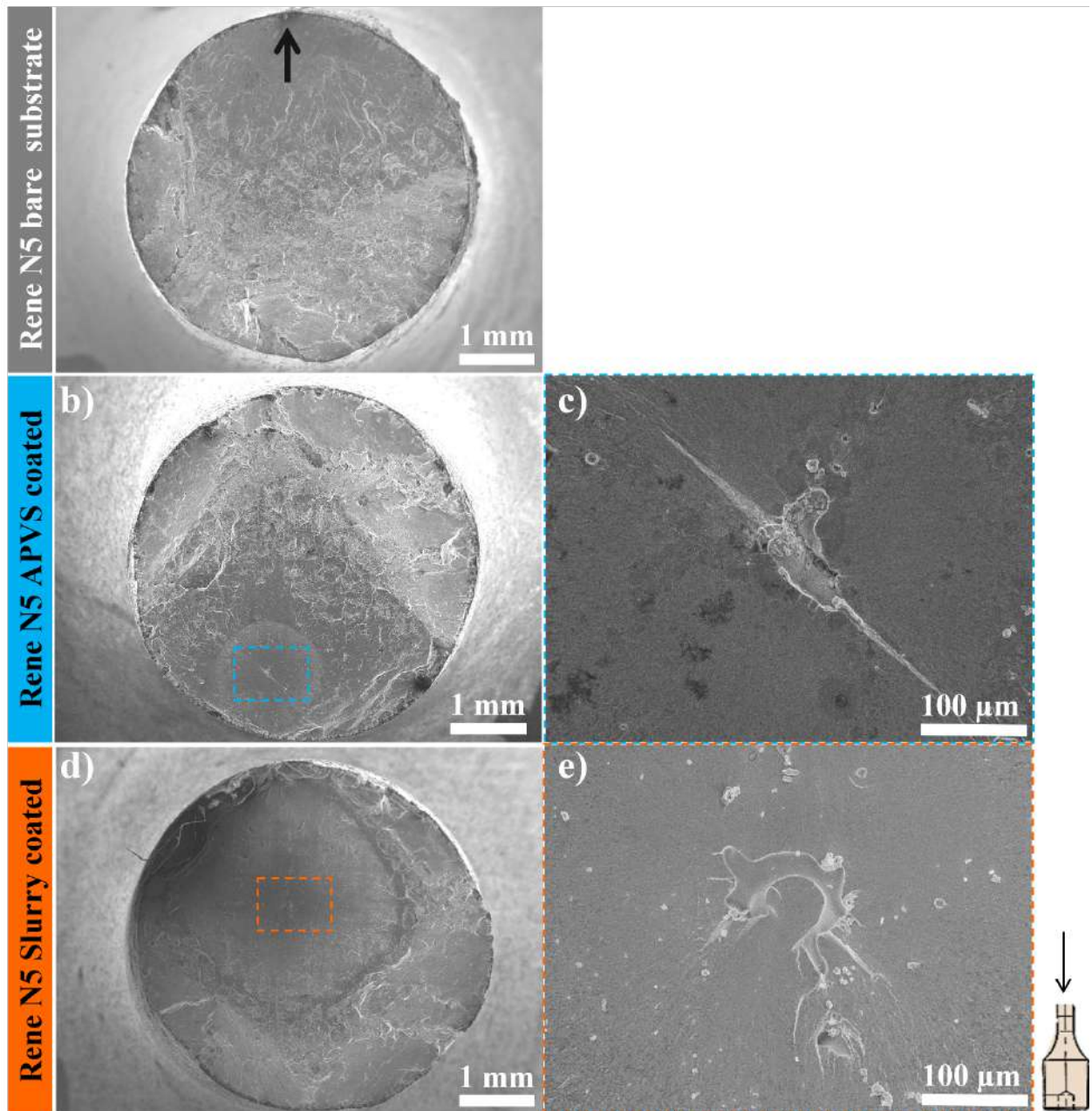


**Figure IV-13** Fracture surface observation of Rene N5 bare substrate ( $\sigma_m = 600$  MPa, with  $N_f = 1.4 \cdot 10^4$  cycles) (a). Rene N5 APVS coated ( $\sigma_m = 600$  MPa, with  $N_f = 3.2 \cdot 10^4$  cycles) (b), and magnification of the crack initiation zone (c). Rene N5 Slurry coated ( $\sigma_m = 600$  MPa, with  $N_f = 3.6 \cdot 10^4$  cycles) (d), and magnification of the crack initiation zone (e). The arrow indicates the crack initiation zone.

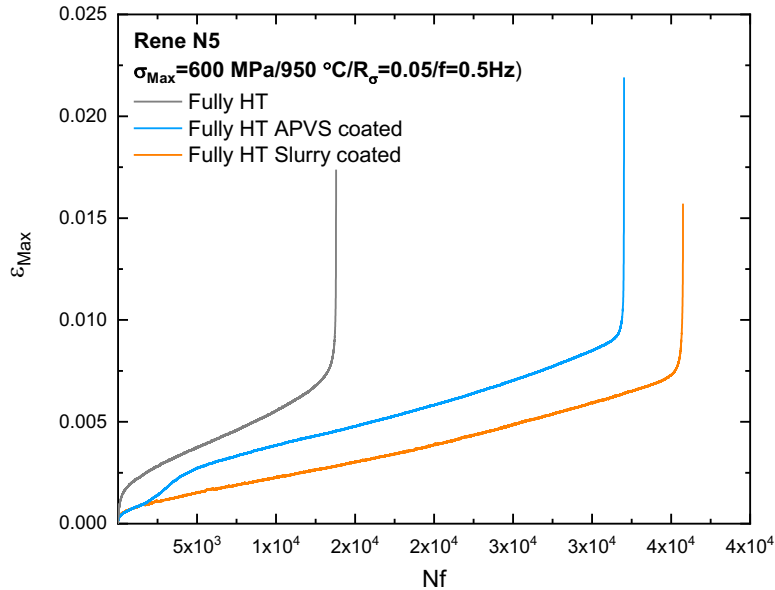


**Figure IV-14** Evolution of the maximum mechanical strain as a function of the number of cycles for the Rene N5 superalloy at  $\sigma_{Max}=600$  MPa/950 °C,  $R_\sigma = 0.05$ , and  $f = 0.5$  Hz, with and without a NiAl bond coat.

Contrary to the AM1 sample results, coated Rene N5 seems to present slightly improved LCF life. However, the author considered that the results are still inside a scatter expected in these fatigue conditions.

One AM1 and one Rene N5 APVS coated specimen were tested in high vacuum (triangular symbols in blue in **Figure IV-10** and **Figure IV-12**). Both failed by surface crack initiation (**Figure IV-15**). The objective of these tests was to evaluate the coating damage mechanisms in a controlled atmosphere. Both samples presented a reduced fatigue life in vacuum. For Rene N5, it was by a factor of 10, and for AM1, by a factor of 5. the behavior could have been expected as oxidation has been shown to be beneficial by increasing the crack propagation threshold for long cracks (Mataveli Suave, 2017).

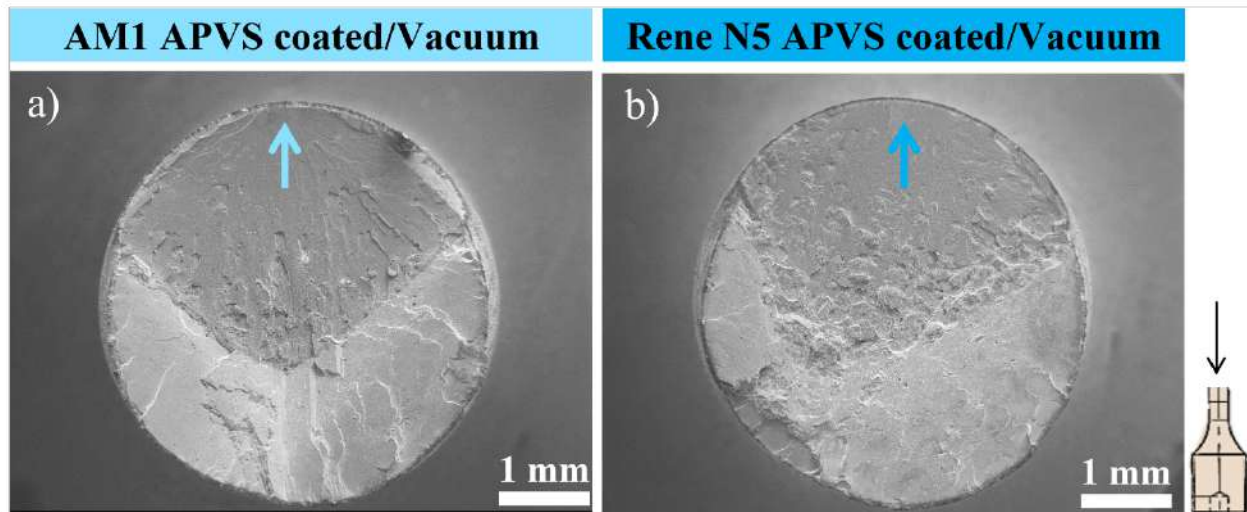


**Figure IV-15** Fracture surface observation of specimens tested in high vacuum. AM1 APVS coated ( $\sigma_m = 600$  MPa, with  $N_f = 5.7 \cdot 10^3$  cycles) (a), and Rene N5 APVS coated ( $\sigma_m = 600$  MPa, with  $N_f = 7.5 \cdot 10^3$  cycles) (b). The arrows indicate the main crack initiation zone.

**Figure IV-16** compares the AM1 and the Rene N5 results in fully HT state. The samples' LCF life under maximum applied stress of 750 MPa is similar, whatever the coating route or the substrate. However, at a lower maximum applied stress of 500 MPa, the fatigue life is scattered by a factor of  $\approx 5$ , which is considered as limited considering possible applications. Therefore, from an application point of view the author concluded that the LCF performance of bare and coated samples is similar for both AM1 and Rene N5 superalloys in these conditions.

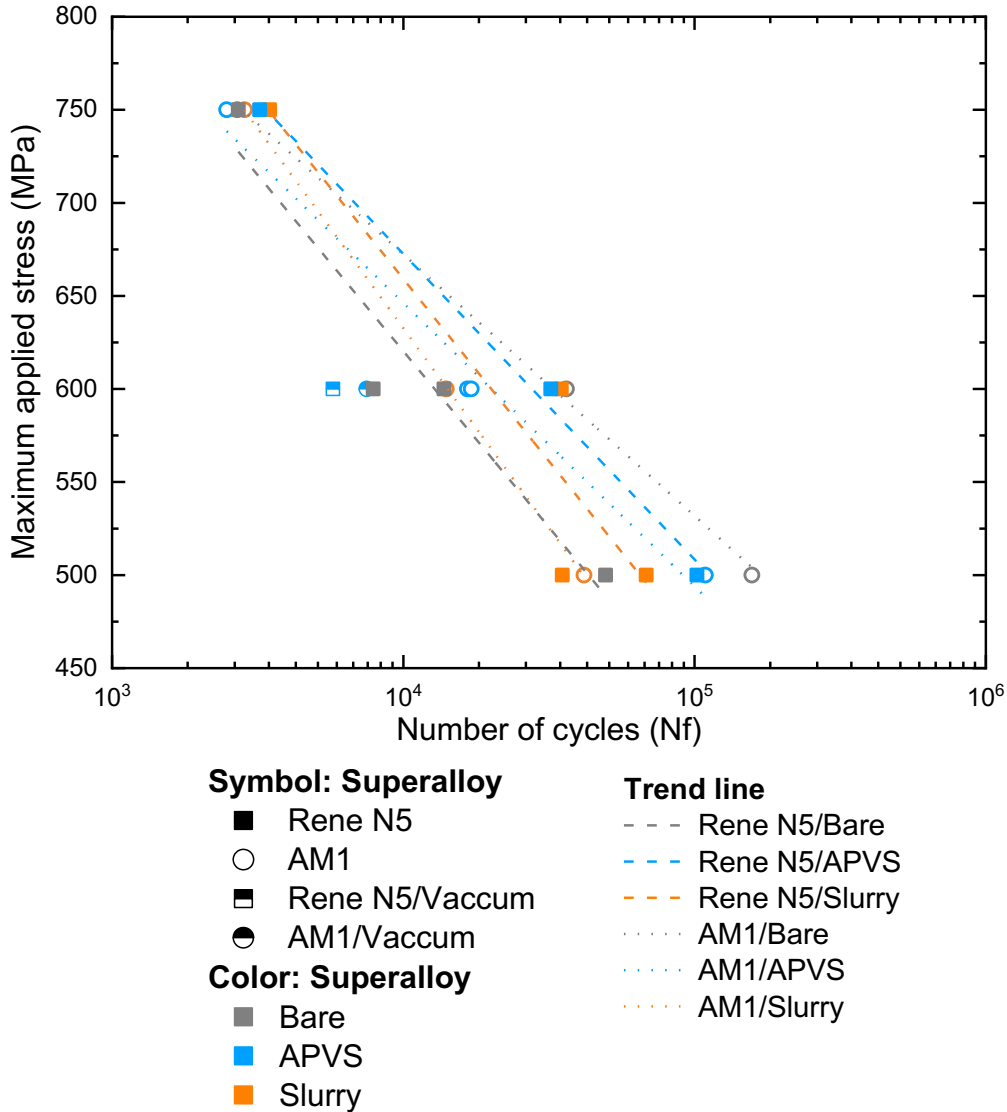


**Figure IV-16** S-N diagram at 950 °C,  $R_\sigma = 0.05$ , and  $f = 0.5$  Hz gathering the fully HT AM1 and Rene N5 low cycle fatigue results. The diagram shows the maximum stress as a function of the number of cycles to failure.

From this sub-section, the regularity of the  $\gamma/\gamma'$  microstructure obtained through the application of a full HT, is key in controlling the LCF life at 950 °C/ $R_\sigma = 0.05$ / $f = 0.5$  Hz. It has a greater impact than the quality of surface polishing or the presence of a NiAl bond coat. Moreover, AM1 and Rene N5 superalloys have been shown to have very similar LCF performances in these conditions. Most of the samples failed by surface crack initiation, a prevalent damage mechanism under LCF

and high-temperature conditions (Chan et al., 1987; Crompton and Martin, 1984; Lerch and Antolovich, 1990; Mataveli Suave, 2017; Perruchaut, 1997; Steuer et al., 2015; Telesman and Ghosn, 1996).

*Still, the absence of any pronounced effect of the BC on the LCF life remains questionable and will be further detailed hereafter more specifically for MAR-M200 +Hf alloy.*

### 2.3. Impact of a slurry-type bond coat on MAR-M200 +Hf SX LCF life

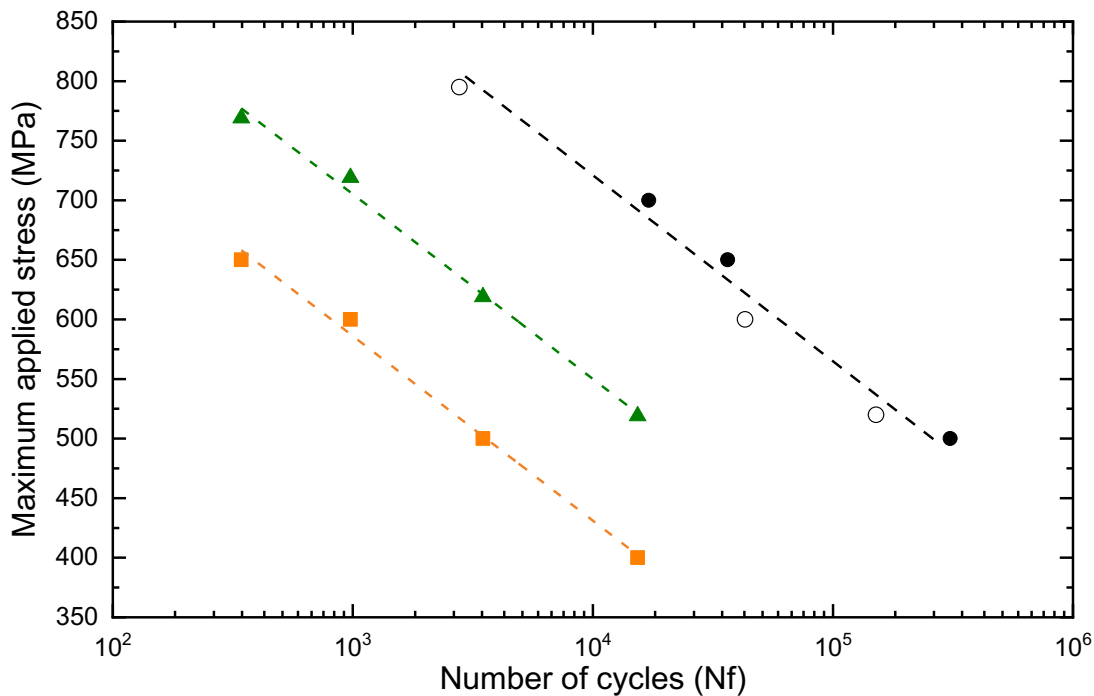
**Figure IV-17** shows the S-N diagram in LCF of MAR-M200 +Hf SX at 900 °C. The results from the bare and coated samples are compared with the results obtained by Mataveli Suave (Mataveli Suave, 2017). Contrary to the results of AM1 and Rene N5, the samples coated via the Slurry method presented a fatigue life decrease by two decades when compared with the bare substrate results, whatever the maximum applied stress. Again, all samples failed through a surface crack initiation process (**Figure IV-18** and **Figure B-1a** and **b**).

The load-bearing section was corrected using the same principle as illustrated in **Figure IV-2**. Again, the green symbols represent the corrected results. Still, the fatigue life reduction is of  $\approx$  one decade. As already mentioned in the sub-section above, the idea of disregarding the IDZ theoretically means that the load bearing is only ensured by the superalloy substrate, and no load bearing capacity of the bond coat/IDZ is considered. Therefore, there is a spectacular fatigue life reduction, weather the IDZ is considered or not. Thus, *from the macroscopic ratcheting behavior the slurry-type bond coat deposition procedure affects the MAR-M200 +Hf SX LCF life.*

**Figure IV-18a, b** and **c** show the fracture surface observations of coated MAR-M200 +Hf SX and tested at 600 MPa (fatigue life of  $9.8 \cdot 10^2$  cycles). **Figure IV-18b** and **c** show magnifications of the BC/IDZ at different positions of the specimen after failure. The analyses were performed in BSE mode, indicating carbides rich in Nb/Hf and Ti (Mataveli Suave, 2017; Mataveli Suave et al., 2018). The coating depth highlighted by the white arrows is of  $\approx 120 \mu\text{m}$ . This depth is approximately twice thicker than the one observed for the Slurry coated AM1 superalloy (presented in **Figure IV-18d**).

Further, the IDZ depth is of  $\approx 25 \mu\text{m}$ , the same as the one seen for the AM1 superalloy (see **Figure IV-18**). Finally, a third layer extending from the IDZ up to red arrows presented in **Figure IV-18** is observed corresponding to a mode I crack propagation zone. Final failure of coated MAR-M200

+Hf seems to be ductile. Crack initiation in the coated MAR-M200 +Hf specimens seems to be occurring everywhere at the surface indicating a “brittle” behavior of the coating, or, at least, a BC with a very limited ductility in good agreement with specimens results from Totemeier et al. (Totemeier et al., 1996; Totemeier and King, 1996). Moreover, LCF failure of coated MAR-M200 +Hf specimens is very different from the one obtained for non-coated ones, in which cracks are developing from discrete locations at the surface, from oxidized carbides (Mataveli Suave, 2017).



**MAR M200 +Hf - single crystalline**

R = 0.05 / T = 900 °C / f = 0.5 Hz

**Fill: Data**

■ Original

□ Database (Mataveli Suave, 2017)

**Color/Symbol: Substrate**

● Bare

■ Slurry → coated substrate

▲ Slurry → coated substrate w/o IDZ

**Crack initiation site: Surface**

**Trend line**

- - - Bare

- - - Slurry → coated substrate

- - - Slurry → coated substrate w/o IDZ

**Figure IV-17** S-N diagram at 900 °C,  $R_\sigma = 0.05$ , and  $f = 0.5$  Hz gathering the MAR-M200 +Hf SX low cycle fatigue results. The diagram shows the maximum stress as a function of the number of cycles to failure. The green color curve represents the load-bearing section calculated by subtracting the coat diffusion layer + IDZ thickness from the original diameter, database from (Mataveli Suave, 2017).

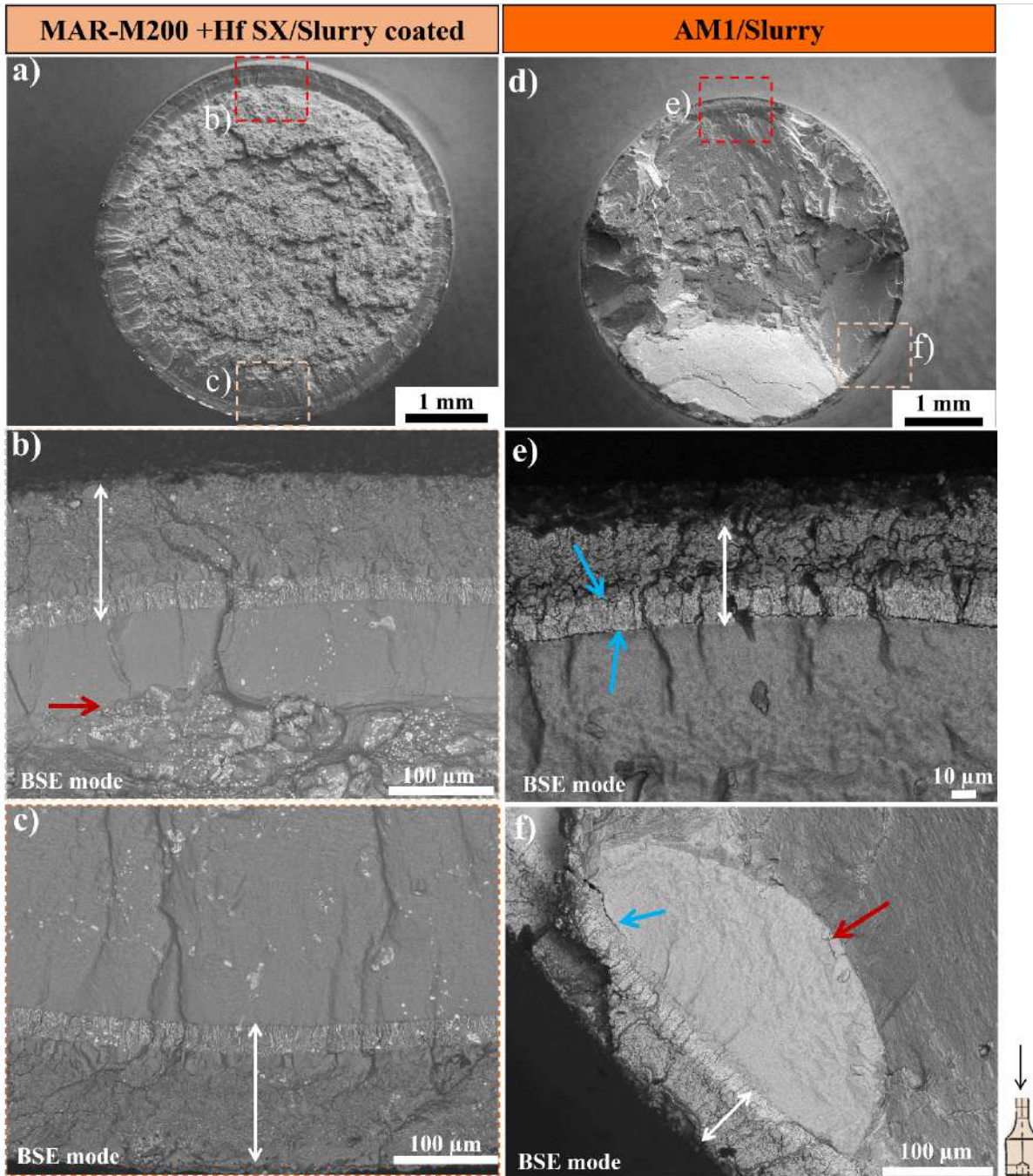


**Figure IV-18** Fracture surface observation of the Slurry MAR-M200 +Hf SX coated sample ( $\sigma_m = 600$  MPa, with  $N_f = 9.8 \cdot 10^2$  cycles) (a), and magnifications of areas (b and c) indicated in (a). Slurry AM1 coated sample ( $\sigma_m = 750$  MPa, with  $N_f = 2.8 \cdot 10^3$  cycles) (d), and magnifications (e and f) areas indicated in (d). The (b), (c), (e), and (f) are observations done in BSE mode. The white arrows indicate the coating thickness. The blue arrows indicate the IDZ/substrate cracks. The red arrow indicates the interface between the crack propagation and the fracture. The white particles are carbides rich in Nb/Hf/Ti present in the MAR-M200 +Hf substrate (Mataveli Suave, 2017).

As a matter of comparison and to support the next sub-section analysis, **Figure IV-18d** shows a fracture surface of the AM1 sample coated via the Slurry method under maximum stress of 750 MPa and fatigue life of  $2.8 \cdot 10^3$  cycles (i.e., very similar LCF life to the analyzed MAR-M200 +Hf) specimen in **Figure IV-18**. The crack initiation is at the surface (**Figure IV-18e**). However, several secondary cracks were identified as the one presented in **Figure IV-18f**. After a mode I crack propagation in the IDZ, further propagation along crystallographic planes in the substrate may be observed. Still, no extended propagation from the surface is observed in BC AM1 specimens and cracks only develop at some specific locations.

**Figure IV-19** shows the spectacular increase in cyclic ratcheting of the Slurry coated MAR-M200 +Hf sample tested at 600 MPa compared to the bare substrate MAR-M200 + Hf sample tested at the same maximum applied stress. This figure also shows a decrease of strain at failure.

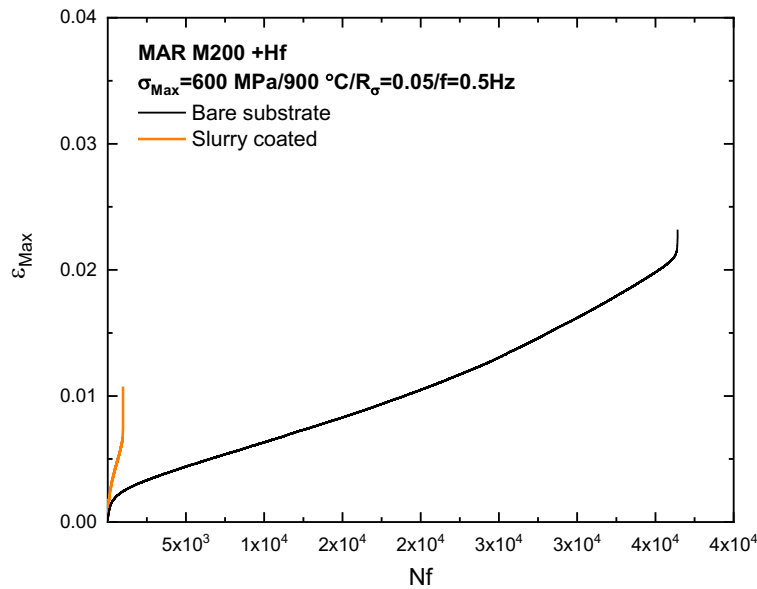


**Figure IV-19** Evolution of the maximum mechanical strain as a function of the number of cycles for the MAR-M200 +Hf superalloy with and without a NiAl Slurry-type bond coat at 900 °C/ $R_{\sigma} = 0.05$ / $f = 0.5 \text{ Hz}$ / $\sigma_{Max} = 600 \text{ MPa}$ .

**Figure IV-20** shows the  $\gamma/\gamma'$  microstructure in both bare and coated MAR-M200 +Hf SX in different positions of the dendritic structure.

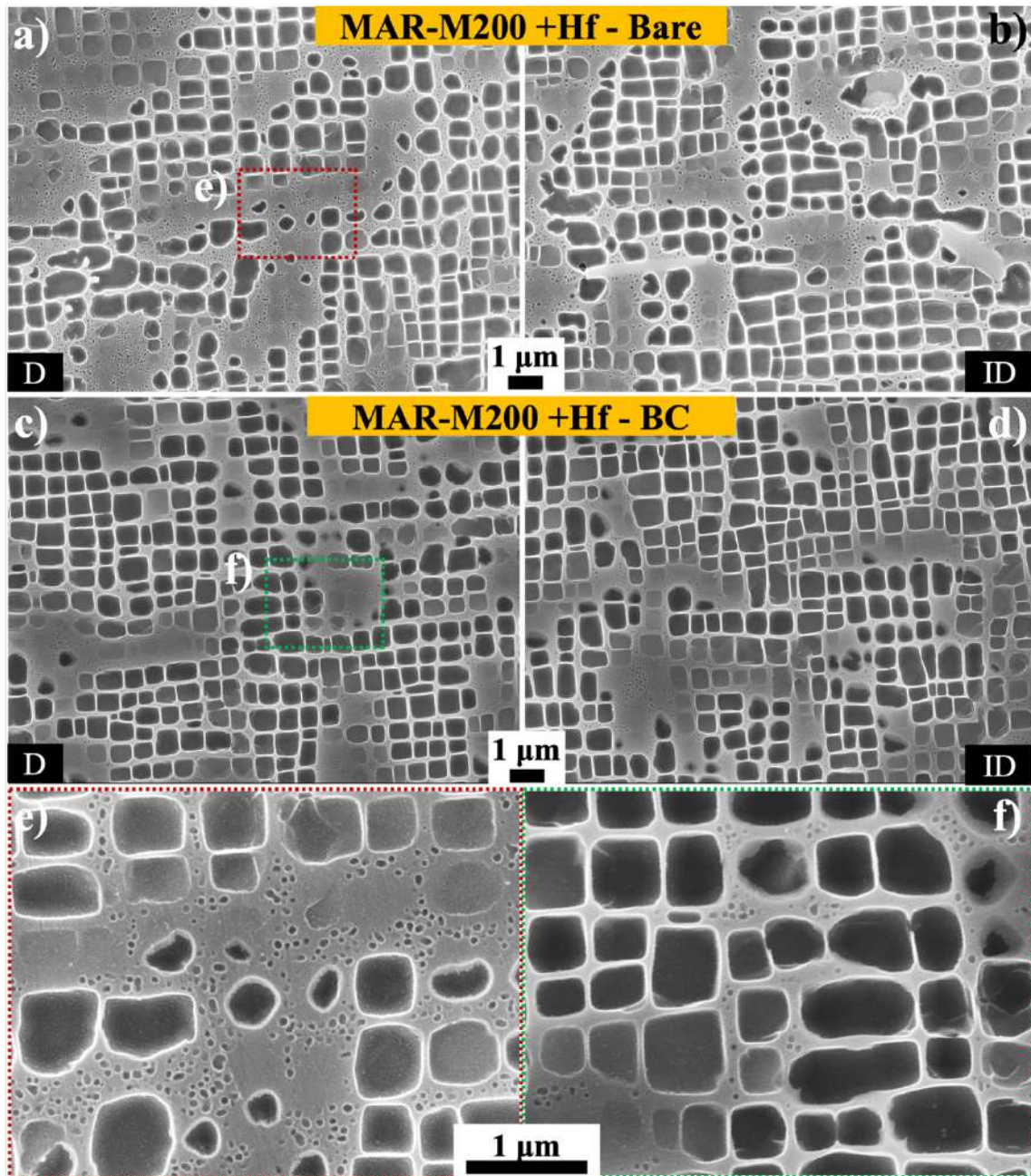


**Figure IV-20**  $\gamma/\gamma'$  microstructure in the primary dendrite arms (D) and interdendrite zones (ID) of MAR-M200 + Hf bare substrate (a and b resp.), and MAR-M200 + Hf Slurry coated (c and d resp.). Magnification of the fine  $\gamma'$  precipitates for the bare and Slurry coated MAR-M200 + Hf specimens (e and f resp.). Observations performed in a  $\approx (001)$  plane.

The secondary precipitates are slightly coarser in the coated specimens, due to the longer heat treatment sequence. However, the main difference is that a lower density of tertiary  $\gamma'$  precipitates is observed in the coated specimens (compare **Figure IV-20e** and **Figure IV-20f**). The faster ratcheting in this condition probably results from this lower fraction of tertiary precipitates. Still, the lower ductility observed in **Figure IV-19** is probably a result of the lack of ductility of the slurry-type BC, probably contributing to the loss of LCF properties shown in **Figure IV-17**, in addition to the loss in creep resistance. This would remain to be checked through creep tests.

#### 2.4. NiAl bond coat behavior at high temperatures

This subsection is divided into two main parts, and each one is dedicated to the investigation of NiAl bond coat mechanical behavior related to its deposition method. Thus, several samples tested at high temperatures were analyzed. **Table IV-3** summarizes the details of these samples.

**Table IV-3** AM1 and MAR-M200 +Hf SX specimens investigated in this sub-section. SHT for solution heat treatment and HT for heat treatment.

<i>Superalloy</i>	<i>AM1</i>	<i>MAR-M200 +Hf SX</i>
<b>Coated via APVS method</b>		
<b>Microstructure</b>	As-cast + HT BC diffusion	
<b>Maximum applied stress (MPa)</b>	750	
<b>Environment</b>	Air	
<b>Coated via Slurry method</b>		
<b>Microstructure</b>	SHT + HT BC diffusion + HT to normalize the $\gamma'$ size	SHT + R1 + R2 + HT BC diffusion
<b>Maximum applied stress (MPa)</b>	750	650
<b>Environment</b>	Vacuum/air	Vacuum/air

##### 2.4.1. Bond coat deposition via the APVS method

The AM1 as-cast samples coated via the APVS method were tested in air, with maximum applied stress of 750 MPa and temperature of 950 °C. The first sample is an interrupted test after seven cycles, and the second is an interrupted test after 414 cycles. **Figure IV-21** shows the SEM and OM observations of the gage length for both samples after these interruptions.

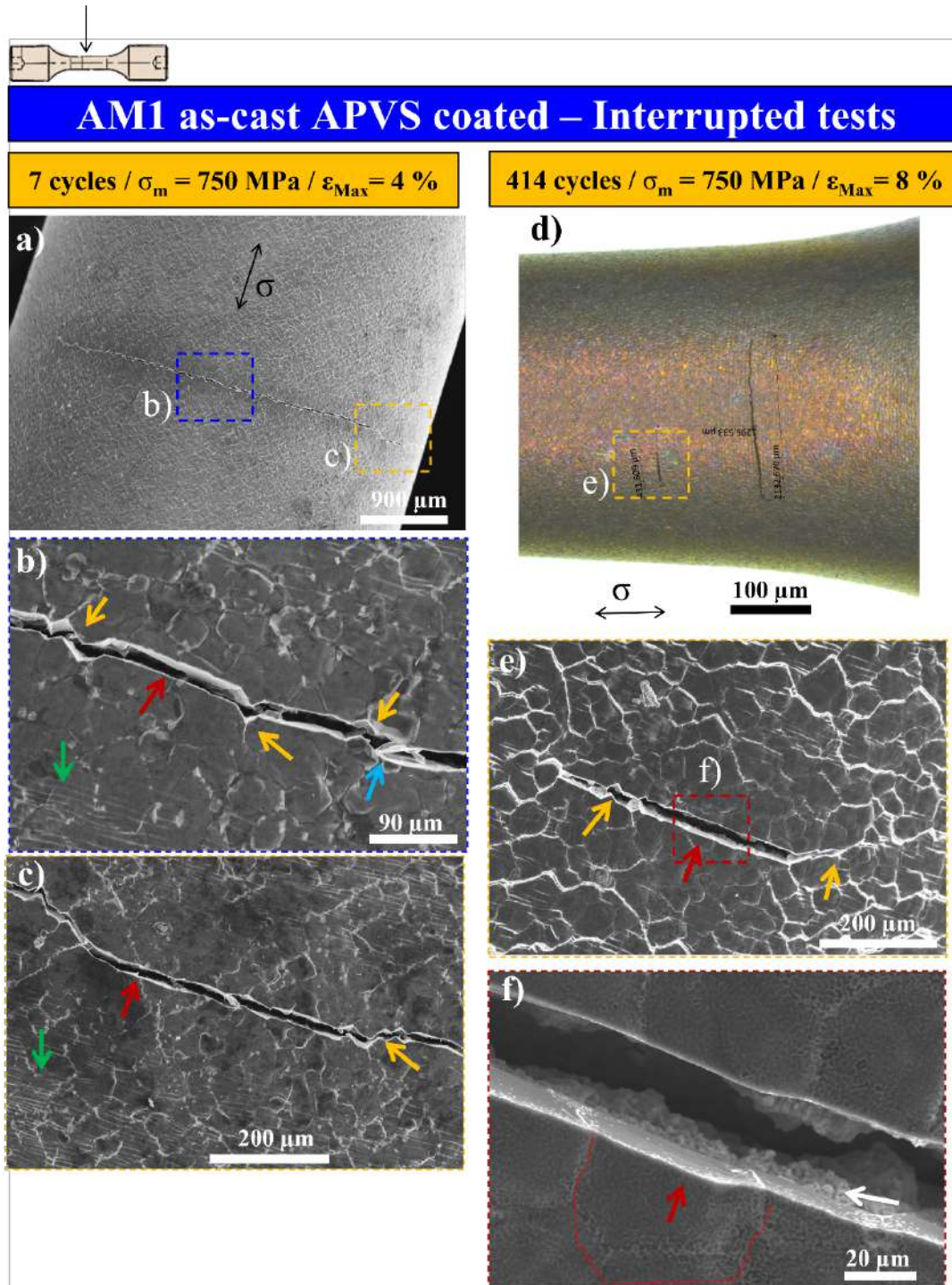


**Figure IV-21** Observations of the gage length for as cast APVS coated AM1 samples and tested under LCF and 950 °C/ $R_{\sigma}=0.05/f=0.5$  Hz conditions. A crack after 7 cycles (a) and magnifications in (b) and (c). Two surface cracks after 414 cycles (d) and magnifications in (e) and (f). Yellow arrows indicate the intergranular crack propagation, red arrows indicate transgranular crack propagation, green arrow indicates the slip traces, blue arrow indicates the connection of cracks, white arrow indicates the superalloy bulk, and red dotted lines indicate a  $\beta$ -NiAl grain cracked.

Surface cracks are observed in both samples. **Figure IV-21a** shows several cracks developing in the NiAl BC after very few cycles. Indeed, the cracks are very similar on both samples' surfaces. The red arrows in **Figure IV-21b, c, e, and f** show a mostly transgranular crack propagation. **Figure IV-21b**, for example, shows that just after seven cycles, a crack perpendicular to the loading axis developed in the gage diameter and propagated into the superalloy bulk (indicated by the white arrow).

Crack propagation appears to be both transgranular and intergranular (see yellow and red arrows in **Figure IV-21b, c, e, and f**). The high density of cracks in the BC indicates that this APVS coating has a limited ductility compared to the substrate. In fact, the mechanical strain amplitudes presented in this figure are mainly carried out by the substrate.

From the longitudinal section shown in **Figure IV-22**, cracks are developing from both the surface and the IDZ (see **Figure IV-22c and d**). Further, the propagation in the first few cycles is assisted by oxidation into the substrate mostly in interdendritic areas (see **Figure IV-22b**). The cracking mechanism of the BC is very similar to the ones observed in the previous literature (Grube et al., 2002; Perruchaut, 1997) and it may only be affected by the nature of the test environment and the BC intrinsic ductility.

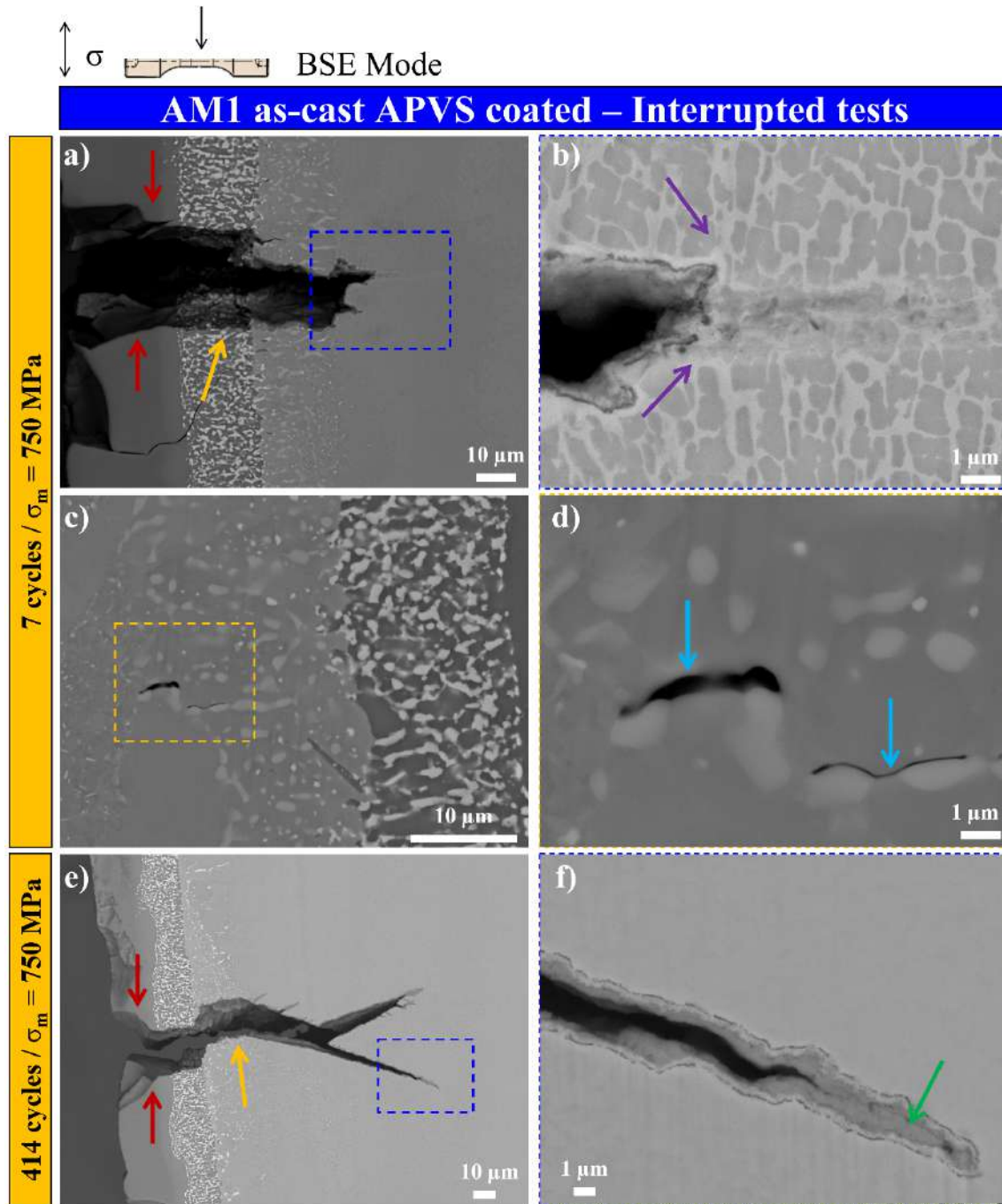


**Figure IV-22** Longitudinal section observations of APVS AM1 coated specimens tested under 950 °C /  $R_\sigma=0.05/f=0.5$  Hz conditions. A crack after 7 cycles (a) and the crack tip magnification (b). The presence of cracks in the IDZ (c) and its magnification in (d). Crack after 414 cycles (e) and the magnification of the oxidized crack tip in (f). Red arrows indicate the crack opening, yellow arrows indicate the crack propagation into the superalloy bulk, purple arrows indicate the microstructure in the crack tip, blue arrows indicate the crack in the interface of the  $\gamma$  and  $\gamma'$  precipitate, green arrows indicate the crack tip filled with oxides, and the white arrow indicates crack propagation inside the oxides.

### 2.4.2. Slurry-type bond coat

Interrupted LCF tests after 5 cycles were performed in vacuum using AM1 and MAR-200 +Hf SX specimens coated via the Slurry method. According to **Figure IV-23**, surface cracks have propagated up to the IDZ/substrate interface, where bifurcation is observed (see blue arrows in **Figure IV-23c** and **f**). Further, cracks are already penetrating the substrate. Contrary to the observations of Mataveli Suave (Mataveli Suave, 2017) in LCF conditions for the uncoated material, primary carbides do not seem to serve as crack initiation site and no specific damage in their vicinity has been observed (see **Figure IV-23d** and **e**) in our case. Moreover, no pore or other feature was identified as a crack initiation site.

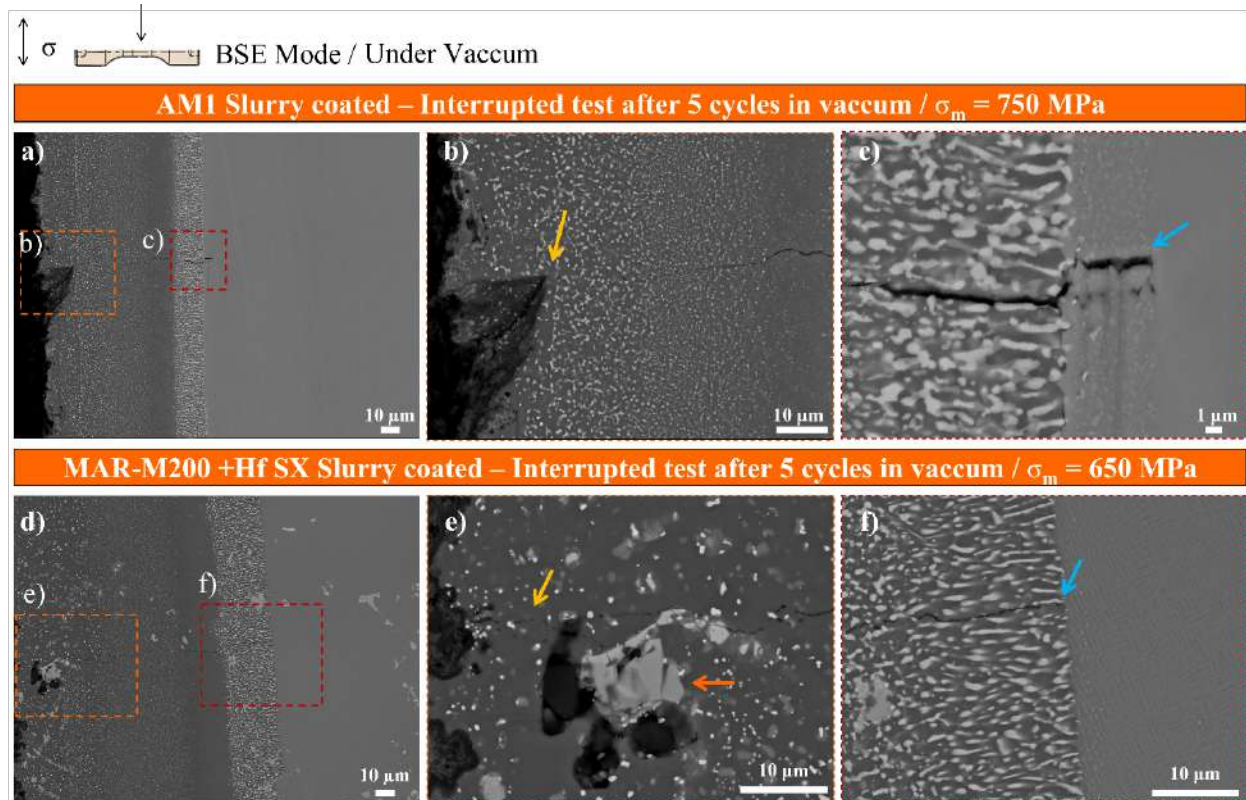


**Figure IV-23** Longitudinal section observations of AM1 and MAR-M200 +Hf SX samples coated via the Slurry method. The LCF tests were carried out in vacuum, 950 °C/ $\sigma_m=750$  MPa, and 900 °C/ $\sigma_m=650$  MPa respectively. A crack is illustrated for the AM1 sample in (a), and for MAR-M200 +Hf SX sample in (d). The magnifications of the crack initiation at the free surface are shown in (b) and (e). The crack tip magnifications are shown in (c) and (f). Blue arrows indicate the crack tip, orange arrows indicate the presence of carbides rich in Nb/Hf/Ti in the MAR-M200 +Hf SX superalloy, and yellow arrows indicate the cracks at the surface.

Identifying well-developed cracks after five cycles in vacuum means that the bond coat damage mode does not appear to be dependent on the oxidation. LCF tests were carried out under a positive stress ratio. The damage mode mainly depends on the bond coat's brittle/ductile character. The brittle/ductile transition temperature is usually observed to be in the 750 and 950 °C temperature range for this kind of bond coat (Boudot, 1999; Hancock et al., 1990). *The author thus believes that the NiAl coating is brittle under such conditions, and the difference of the creep-fatigue properties between the matrix and the brittle precipitates leads to earlier onset of LCF cracks.*

**Figure IV-24** presents the longitudinal sections carried out for two samples after complete rupture. Both samples were tested in air and at the maximum applied stress range studied for both alloys, tests inducing pronounced cyclic ratcheting.

As expected, a higher density of cracks is observed, most of them running up to the IDZ, sometimes with a bifurcation at the IDZ/SX interface (see **Figure IV-24a**, and **c**). Cracks propagation in the substrate is clearly assisted by oxidation, as observed in **Figure IV-24b** and **d**).

Despite a lower testing temperature and a shorter LCF tests, *MAR-M200 +Hf is clearly more sensitive to oxidation compared to AM1*, as cracks propagating in the substrate are filled with oxides up to the crack tip. The oxidation is probably the reason of multiple crack branching (Grube et al., 2002), as observed in **Figure IV-24c**. The oxides developing along the crack path in MAR-M200 +Hf are typically composed of Cr<sub>2</sub>O<sub>3</sub> outer layer and Al<sub>2</sub>O<sub>3</sub> rich inner layer (Aghion et al., 1991; Mataveli Suave, 2017; Mataveli Suave et al., 2018).

These observations and comparisons to AM1 specimens tested in almost the same LCF conditions strongly suggests a lack of ductility of the BC at 900 °C and 950 °C in these LCF conditions.

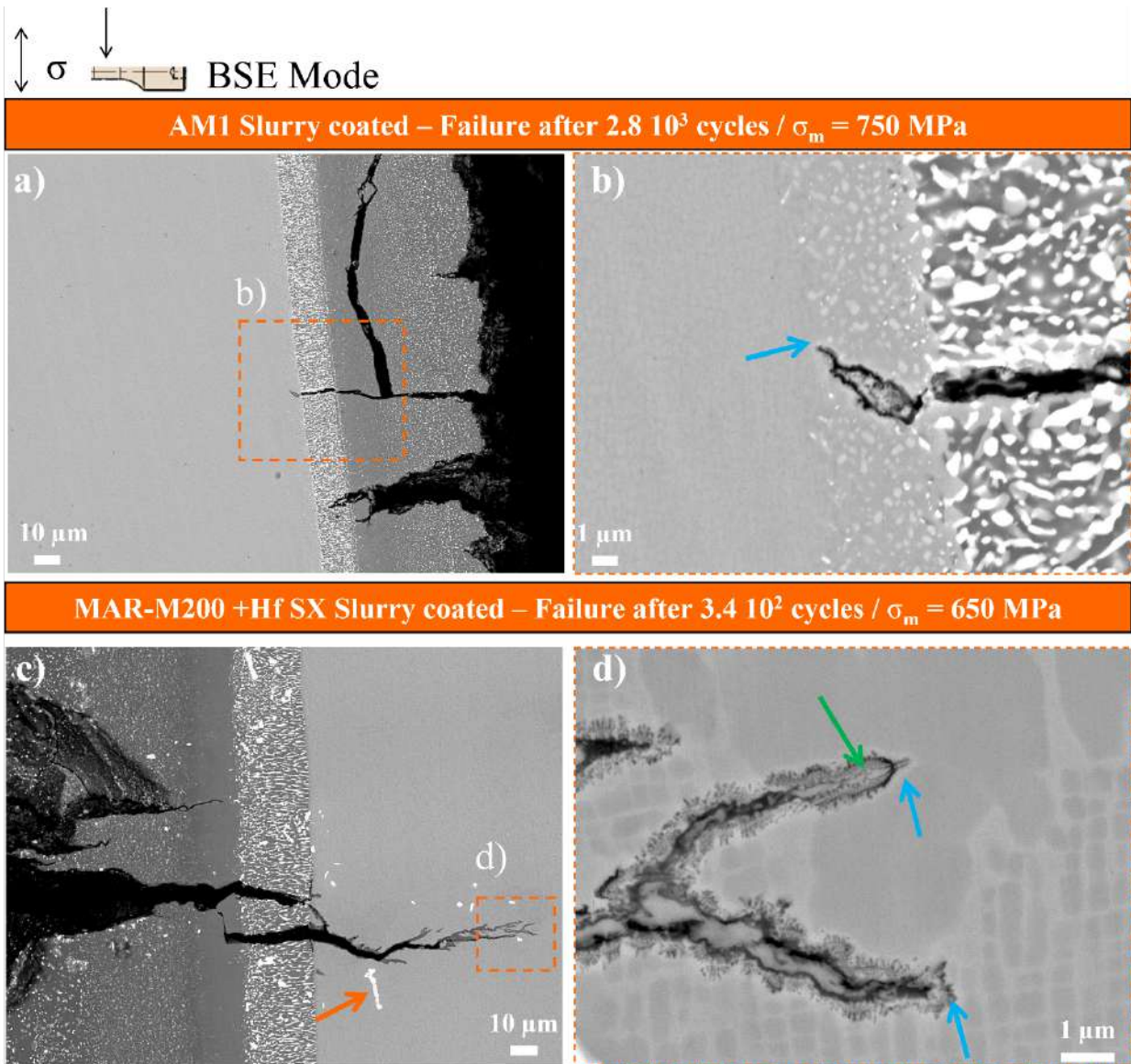


**Figure IV-24** Longitudinal section observations of AMI and MAR-M200 +Hf SX Slurry coated specimens. The LCF tests were carried out in air, at  $950\text{ }^\circ\text{C}/\sigma_m=750$  MPa, and  $900\text{ }^\circ\text{C}/\sigma_m=650$  MPa respectively. A typical crack is illustrated for the AMI sample in (a), and for the MAR-M200 +Hf SX sample in (c). Crack tip magnifications are shown in (b) and (d). Blue arrows show the crack tip. Orange arrows show the presence of carbides into the MAR-M200 +Hf SX superalloy. The green arrow indicates the crack filled with oxides.

## 2.5. Damage mechanism and durability of NiAl bond coated samples in LCF at high temperatures

It has been observed that neither the polishing nor the coating severely influences the LCF life at  $950\text{ }^\circ\text{C}/R_\sigma = 0.05/f = 0.5\text{ Hz}$ . The solution heat treatment and aging have a more pronounced effect on the LCF behavior in these conditions.

Not surprisingly, the full HT leads to a microstructure that improves the creep properties (Cormier and Gandin, 2021). In addition, the better chemical homogenization between the DZ and IZ increases the substrate resistance to oxidation (Sato et al., 2011) and favors homogeneous plastic activity (Pollock and Argon, 1992). Comparing **Figure IV-22a**, and **c**, **Figure IV-24 a** and **b** *the oxidation and the plastic deformation are much more severe in the as-cast sample* after 414 cycles (14 minutes) than the fully heat-treated sample with  $2.8 \cdot 10^3$  cycles (94 minutes).

The NiAl bond coat resulting from the APVS deposition method and investigated on the AM1 superalloy substrate showed a low ductility under the chosen conditions. A similar behavior was observed for the slurry-type bond coating method. Blunted cracks in the outer surface (see **Figure IV-22f** and **Figure IV-24d**) are propagating up to the IDZ in the very first few cycles, decreasing the load-bearing section. No recrystallization was identified in the crack propagation path (**Figure B-3**, **Appendix B.2**). Similar behavior was already observed in the literature (Baufeld et al., 2008).

Tests performed in vacuum confirmed that long cracks are forming from the free surface up to the IDZ in the very first few cycles. Further, these tests proved that the crack initiation and propagation in the coating/IDZ layer are not assisted by oxidation indicating a lack of ductility of this slurry-processed BC too. Oxidation may only become the leading actor once cracks are propagating into the superalloy bulk.

Even though it is difficult to estimate the intrinsic mechanical properties of the bond coat itself like the characterizations done by Texier et al. (Texier et al., 2020, 2017, 2016c), *the author believes that the crack initiation is due to a lack of ductility of the bond coat in these LCF conditions and the suspected brittleness of the IDZ layer at high temperatures*. The result is somehow in contradiction with the tensile characterizations performed by Texier et al. using freestanding (Pt-) NiAl bond-coats processed by APVS and showing a tensile elongation of at least 15 % at  $T \geq 900\text{ }^\circ\text{C}$  (Texier et al., 2020).

Moreover, as mentioned in the first paragraph, the microstructure plays an important role in controlling the mechanical properties under high temperatures. For AM1 and Rene N5 the NiAl BC deposition does not influence the tensile nor the fatigue properties. However, for the MAR-M200 +Hf SX, there is a high influence of the BC deposition process.

**Figure IV-19** shows that the cyclic ratchetting of the Slurry coated MAR-M200 +Hf sample was highly influenced by the BC deposition when compared with Rene N5 (see **Figure IV-14**) or AM1 (**Figure IV-6**). If the  $\gamma/\gamma'$  regularity is widely known to control creep properties (Caron and Khan, 1983; Cormier and Gandin, 2021) and hence, to control the cyclic ratchetting of the AM1, the size and density of the ultrafine  $\gamma'$  precipitates is believed to control the mechanical properties of the MAR-M200 +Hf superalloy.

MAR-M200 +Hf SX specimens were in fact fully HT before the coating process, the “extra” BC diffusion heat treatment led to the coarsening and dissolution of the fine  $\gamma'$  precipitates decreasing its density (and increasing its size) on the  $\gamma$  matrix (see **Figure IV-20e** and **f**). In fact, the fine  $\gamma'$  precipitates are known to provide strength against the dislocation motion (le Graverend et al., 2016; Murakumo et al., 2004), influencing the creep properties (Kakehi, 1999; Murakumo et al., 2004) and the overaging conditions was proved to influence the creep properties of the Ni-based superalloys by changing the fine  $\gamma'$  precipitates size and density (Jackson and Reed, 1999). Consequently, *the author believes that the pronounced reduction of fatigue life seen for MAR-M200 +Hf Slurry coated in these LCF conditions inducing cyclic ratcheting is due to the microstructure evolution during the BC diffusion.*

## 2.6. Summary

The Ni-based SX superalloy microstructure (the regularity of the  $\gamma/\gamma'$  and the fine  $\gamma'$  precipitates) seems to be the main life controlling factor in the LCF conditions of  $R_\sigma = 0.05$ , and  $f = 0.5$  Hz and temperatures of 900 °C and 950 °C for all investigated systems. The diffusion heat treatment of the Slurry type BC has highly influenced the MAR-M200 +Hf SX resulting in a decrease of the superalloy tensile and fatigue properties. On the contrary, the diffusion heat treatment has not impacted the tensile or the fatigue life of the AM1 nor Rene N5 since they have higher  $\gamma'$  solvus

temperatures. This is an important result for industrial practices, as the refurbishment of turbine blades is carried out after the full HT cycle of the blades.

A second remark is a quite brittle behavior of the NiAl bond coat. It was seen that whatever the superalloy, under these conditions of LCF and at temperatures of 900/950 °C, the NiAl bond coat has a limited ductility and cracks up to the interdiffusion zone are forming in the very first LCF cycles. This behavior induces to premature cracks decreasing the load bearing section, leading to crack propagation into the substrate assisted by oxidation. Therefore, a remaining question is the influence of a “brittle” coating under VHCF regime and high temperatures.

### **3. Impact of the bond coat in Very High Cycle Fatigue**

The largest casting pore typically controls the ultrasonic VHCF tests for Bridgman/LMC solidified specimens without any coating (Bortoluci Ormastroni et al., 2020a; Cervellon, 2018; Cervellon et al., 2018; Liu et al., 2007; Miao et al., 2009; Yi et al., 2007), as show in **Chapter III**. However, the surface treatments can influence the specimens mechanical behavior at 1,000 °C (Cervellon et al., 2021) and induce a crack initiation transition from the bulk to the (sub-)surface. Recently, Cervellon et al. (Cervellon et al., 2021) analyzed different surface treatments of CMSX-4 specimens. They observed a transition from internal to (sub-)surface crack initiation using NiCoCrAlYTa coated specimens, showing that the presence of a coating is the limiting factor controlling the VHCF lifetime under these conditions. Therefore, the main motivation of this study is to know if we still have a trend and if the VHCF life is sensitive to the BC deposition process.

Several samples were investigated in this sub-section to propose a reasonable damage mechanism. The investigated superalloys are AM1, Rene N5, CMSX-4, and CMSX-4 Plus, and the tests were carried out in fully reversed loading, 20 kHz and 1,000 °C. **Table IV-4** recalls the essential information to the following investigation. **Appendix A.3** depicts the database of this sub-section.

**Table IV-4** The fatigue samples and the fatigue conditions details studied in this sub-section.

<i>Experimental parameters</i>	<i>AM1</i>	<i>Rene N5</i>	<i>CMSX-4</i>	<i>CMSX-4 Plus</i>
<b>VHCF parameters</b>	$R_e = -1, f = 20 \text{ kHz}$ and $T = 1,000 \text{ }^\circ\text{C}$			
<b>Slurry coat method</b>	✓	✓	✓	✓
<b>APVS coat method</b>	✓	✓	×	×
<b>Microstructure</b>	SHT + HT BC diffusion + HT to normalize the $\gamma'$ size		SHT + R1 + R2 + HT BC diffusion	

### 3.1. VHCF endurance and crack initiation

**Figure IV-25** shows the alternating stress ( $\sigma_a$ ) as a function of the number of cycles to failure (Nf) diagram gathering the VHCF results obtained for AM1, Rene N5, CMSX-4, and CMSX-4 Plus superalloys (identified by different shapes) tested with and without NiAl coating (identified by the symbol filling arrangement). The BC deposition techniques are APVS (symbol half-down filled) and Slurry (symbol half-up filled) methods. The colors identify the crack initiation site.

Two trend lines distinguish the samples' mechanical behavior. The first represents lifetime data of bare substrate samples with a main crack initiation site at internal casting pores. A weak impact of oxidation has been observed for these specimens. The second trend represents lifetime data of coated samples with a primary crack initiation site at a casting pore close to the free surface or at least close to the IDZ. The crack initiation mechanism is suspected (at this point) to be sensitive to the local chemical modifications resulting from the IDZ development during the coating process and further VHCF tests.

**Figure IV-26** depicts the fracture surface observations of representative coated samples for each type of crack initiation. Again, the color code accounting for the type a crack initiation mode is kept for **Figure IV-25** and **Figure IV-26**. The fatigue ridges allow the identification of the initiation site, and the classic rough zone identifies the critical casting pore (see **Figure IV-26b**). A clear crack initiation from the surface of Slurry coated CMSX-4 Plus is observed in **Figure IV-26f**. Further to this observation, oxidation seems to assist crack propagation.

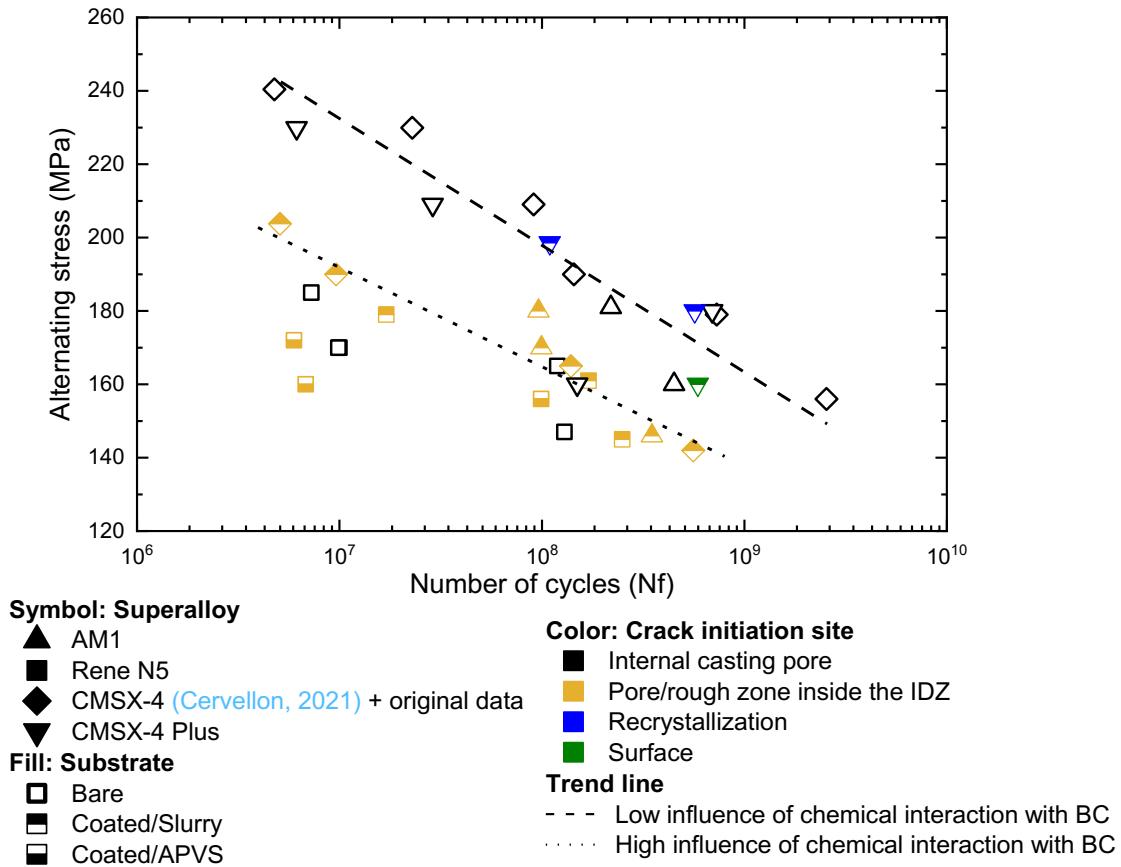


**Figure IV-25** S-N diagram for 1,000 °C,  $R_\epsilon = -1$ , and  $f = 20$  kHz gathering the AM1, Rene N5, CMSX-4 and CMSX-4 Plus superalloys results. The samples were tested with bare substrate and coated via APVS and Slurry method. The diagram shows the alternating stress  $\sigma_a$  as a function of the number of cycles to failure. Part of the CMSX-4 bare substrate data was extracted from the literature (Cervellon, 2018).

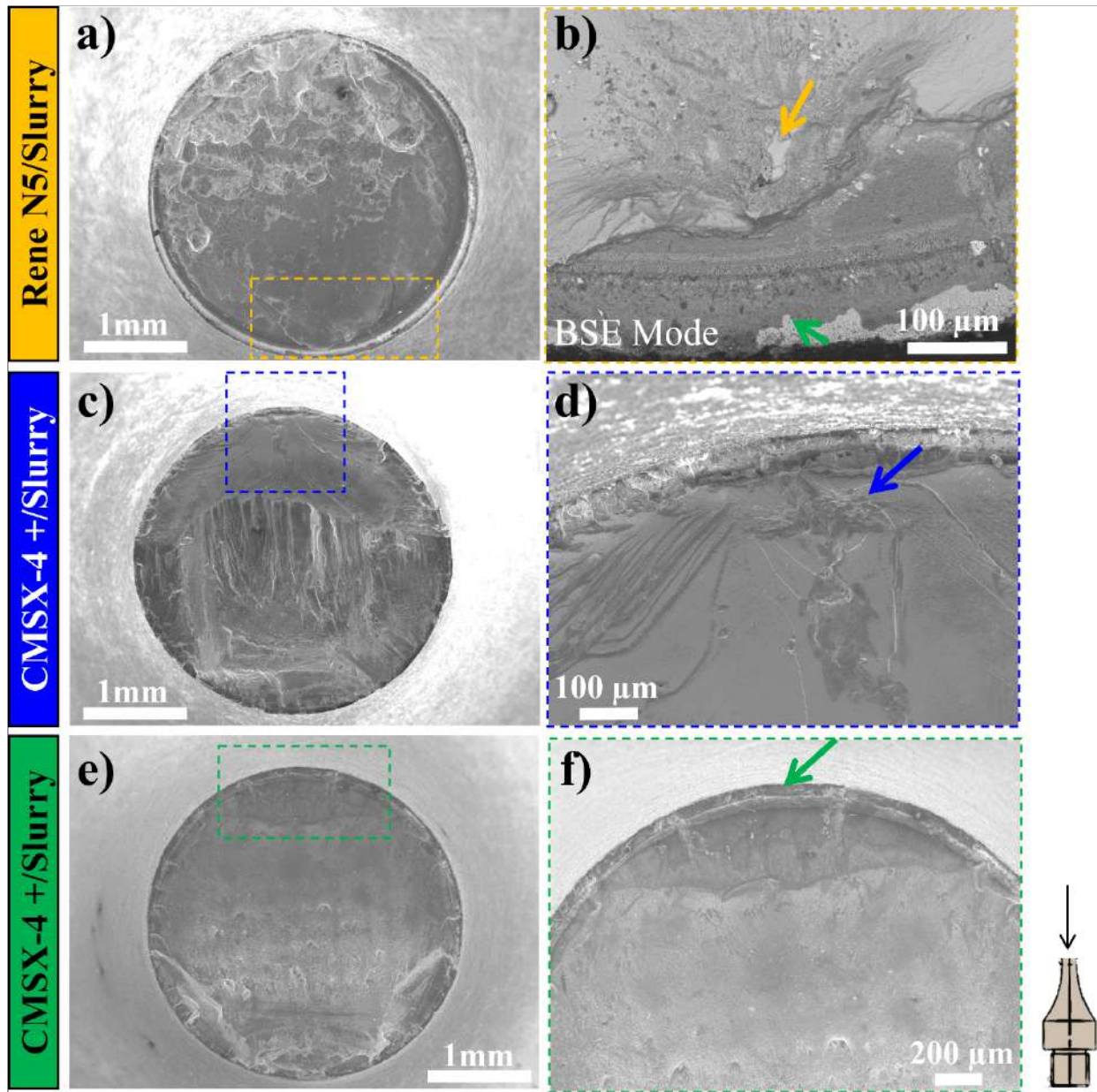


**Figure IV-26** Fracture surface observations of Slurry coated Rene N5 and CMSX-4 Plus specimens. Rene N5 ( $\sigma_a = 145$  MPa, with  $N_f = 2.5 \cdot 10^8$  cycles) (a), crack initiation zone magnification in (b), details the presence of a casting pore close to the surface with a diameter of  $\approx 70 \mu\text{m}$  (indicated by the yellow arrow) and an oxide layer (indicated by the green arrow). CMSX-4 Plus ( $\sigma_a = 214$  MPa, with  $N_f = 9.2 \cdot 10^7$  cycles) (c), crack initiation zone magnification in (d), detail of a rough zone close to the surface (indicated by the blue arrow). CMSX-4 Plus ( $\sigma_a = 160$  MPa, with  $N_f = 5.9 \cdot 10^8$  cycles) (e), crack initiation zone magnification in (f), and detail of the coating (indicated by the green arrow).

**Figure IV-26a** is the fracture surface of the Rene N5 sample tested under alternating stress of 146 MPa and fatigue life of  $3.5 \cdot 10^8$  cycles. The sample failed by crack initiation at a casting pore close to the IDZ (see yellow arrow in **Figure IV-26b**). However, the green arrow indicates an oxidized cracking path, meaning that an already developed secondary crack at the surface reached the rough zone, or the opposite (i.e., the rough zone reached the secondary crack). The white precipitates visible by using the BSE mode are the carbides present in the Rene N5 microstructure. **Figure IV-26c** and **e** are the fracture surface of the CMSX-4 Plus samples tested under an alternating stress of 214 MPa and fatigue life of  $9.2 \cdot 10^7$  cycles, and an alternating stress of 160 MPa and fatigue life of  $5.9 \cdot 10^8$  cycles, respectively. It was impossible to identify the crack initiation feature by the fracture surface observations in **Figure IV-26c**, even though there is a rough surface in **Figure IV-26d**. The second sample (**Figure IV-26e**) failed from the surface.

### 3.2. Coating damage under VHCF conditions

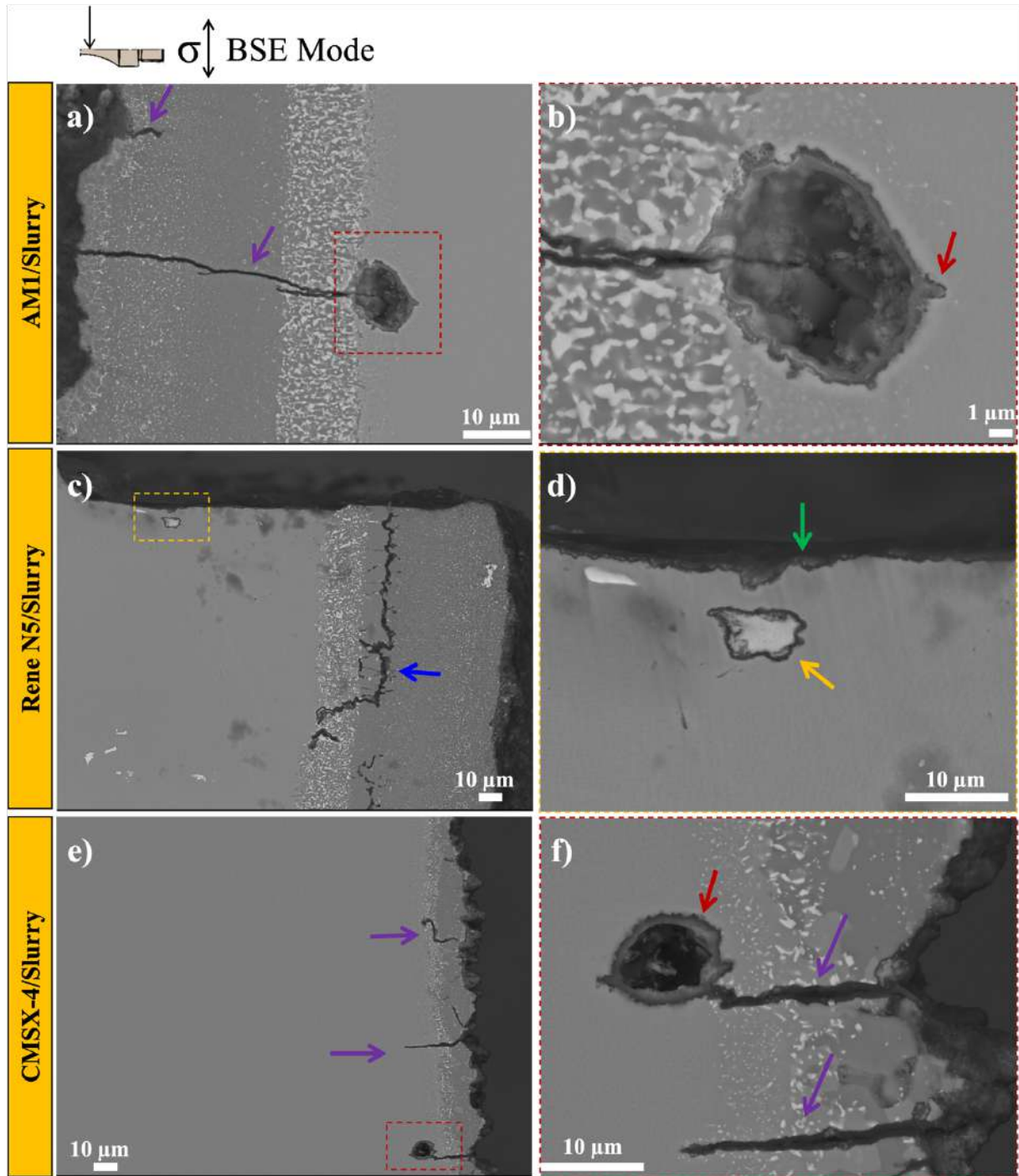
**Figure IV-27** shows the longitudinal sections of samples representing each superalloy coated via the Slurry route. The first three specimens failed from a casting pore close/inside the IDZ. The last one failed from the surface.

**Figure IV-27a** and **b** show the interaction between a secondary crack and a pore filled with oxides encountered after the longitudinal analysis of the AM1 sample tested under alternating stress of 145 MPa and fatigue life of  $2.5 \cdot 10^8$  cycles. **Figure IV-27c** and **d** show the longitudinal section of the Rene N5 sample shown in **Figure IV-26a**. Oxidation at the surface was observed (see the green arrow in **Figure IV-27d**), indicating a secondary crack path into the bulk in mode I. Further, oxidized crack path near to the coating/IDZ and IDZ/substrate interfaces was observed for this system (see dark blue arrow in **Figure IV-27c**). As observed from the longitudinal analysis of the AM1 sample, **Figure IV-27e** and **f** show the interaction of a pore filled with oxides and a secondary crack after the longitudinal section of the CMSX-4 sample tested under alternating stress of 142 MPa and fatigue life of  $5.6 \cdot 10^8$  cycles.

**Figure IV-27g** up to **j** show the CMSX-4 Plus longitudinal section of the **Figure IV-26e** sample. Several secondary cracks were identified on the sample's surface. They propagate perpendicular to the loading axis (i.e., [100] plane) or parallel to the loading axis in the recrystallized layer in the

sub-surface, below the IDZ. **Figure IV-27h** is a magnification of the tip of the most extended crack ( $\approx 150 \mu\text{m}$ ). A blue dotted curve identifies in **Figure IV-27g** and **j** the recrystallized layer from the coating up to the substrate. The light blue arrows indicate the high oxidation activity inside the IDZ for this specimen.

**Figure IV-28** shows that the oxides formed at the surface of the slurry BC are composed mainly of  $\text{Cr}_2\text{O}_3$  and  $\text{TiO}_2$  for AM1, and  $\text{Al}_2\text{O}_3$  for the three other systems. CMSX-4 and CMSX-4 Plus samples presented precipitates rich in Re in the IDZ (see **Figure IV-28c** and **d**). For all four systems,  $\text{Al}_2\text{O}_3$  is the oxide mostly found along secondary crack propagation in the BC/IDZ. The cracks identified by the purple arrows propagated into the substrate in mode I (see **Figure IV-27a**, **e**, and **f**), do not present a high oxidation activity in the IDZ as the ones indicated by the light blue arrows in **Figure IV-27g**, **i**, and **j**. **Figure IV-29** shows the EDS maps of a zone with high oxidation activity, and the cracks are filled with oxides presumably being of  $\text{Al}_2\text{O}_3$ ,  $\text{Cr}_2\text{O}_3$ , and  $\text{TiO}_2$ .



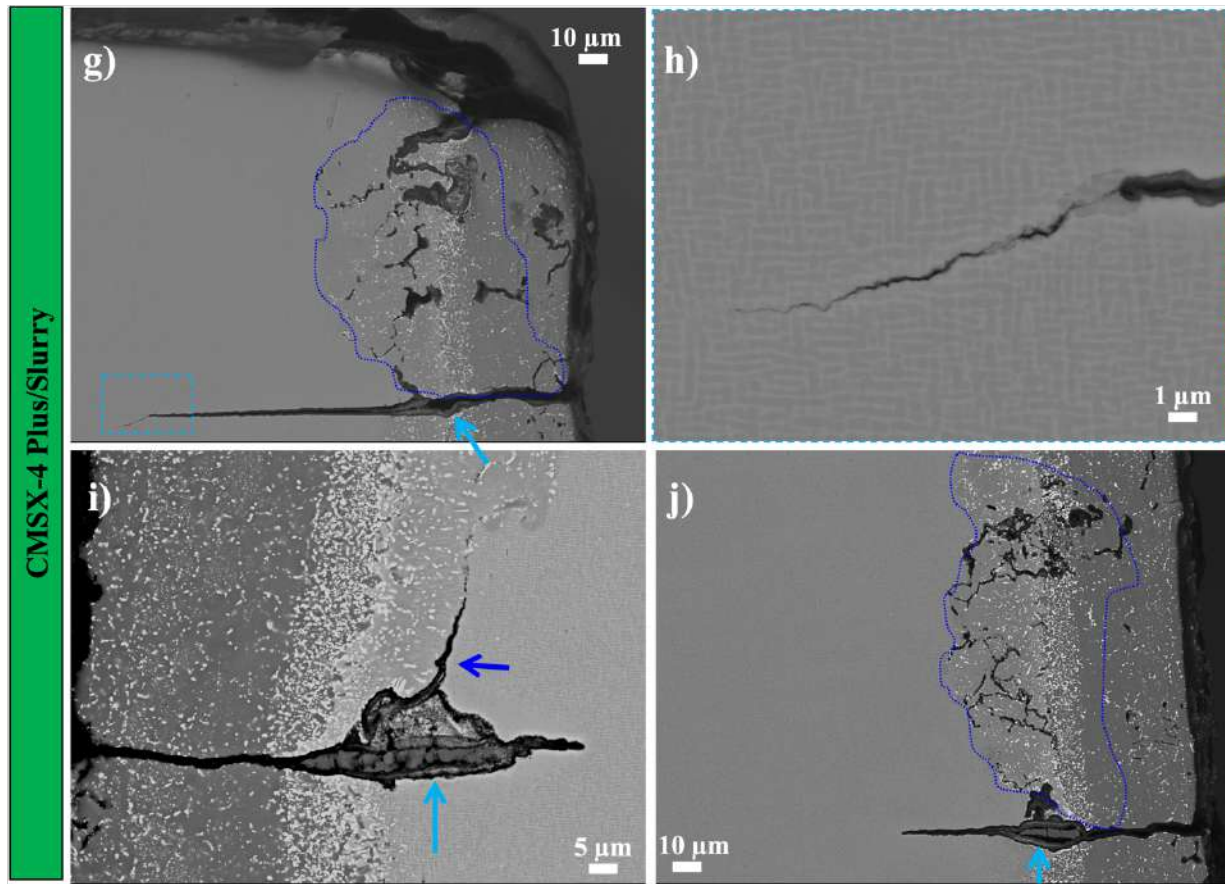


**Figure IV-27** Longitudinal analysis of several samples coated via the Slurry method. AM1 ( $\sigma_a = 146$  MPa, with  $N_f = 3.5 \cdot 10^8$  cycles) sample (a), magnification of the crack interaction with a pore (b). Rene N5 ( $\sigma_a = 145$  MPa, with  $N_f = 2.5 \cdot 10^8$  cycles) sample (c), magnification of an oxidized carbide in (d). CMSX-4 ( $\sigma_a = 142$  MPa, with  $N_f = 5.6 \cdot 10^8$  cycles) sample (e), magnification of the secondary cracks in (f). CMSX-4 Plus ( $\sigma_a = 160$  MPa, with  $N_f = 5.9 \cdot 10^8$  cycles) sample (g), (i), and (j), magnification of the crack tip in (h). Purple arrows indicate the secondary cracks propagating in mode I, red arrows indicate the oxidized casting pore in the IDZ interface, dark blue arrows and dotted lines indicate crack propagation in RX layer, the yellow arrow indicates an oxidized carbide, the green arrow indicates the oxidized surface, and light blue arrows indicate the oxidation inside the crack surfaces.

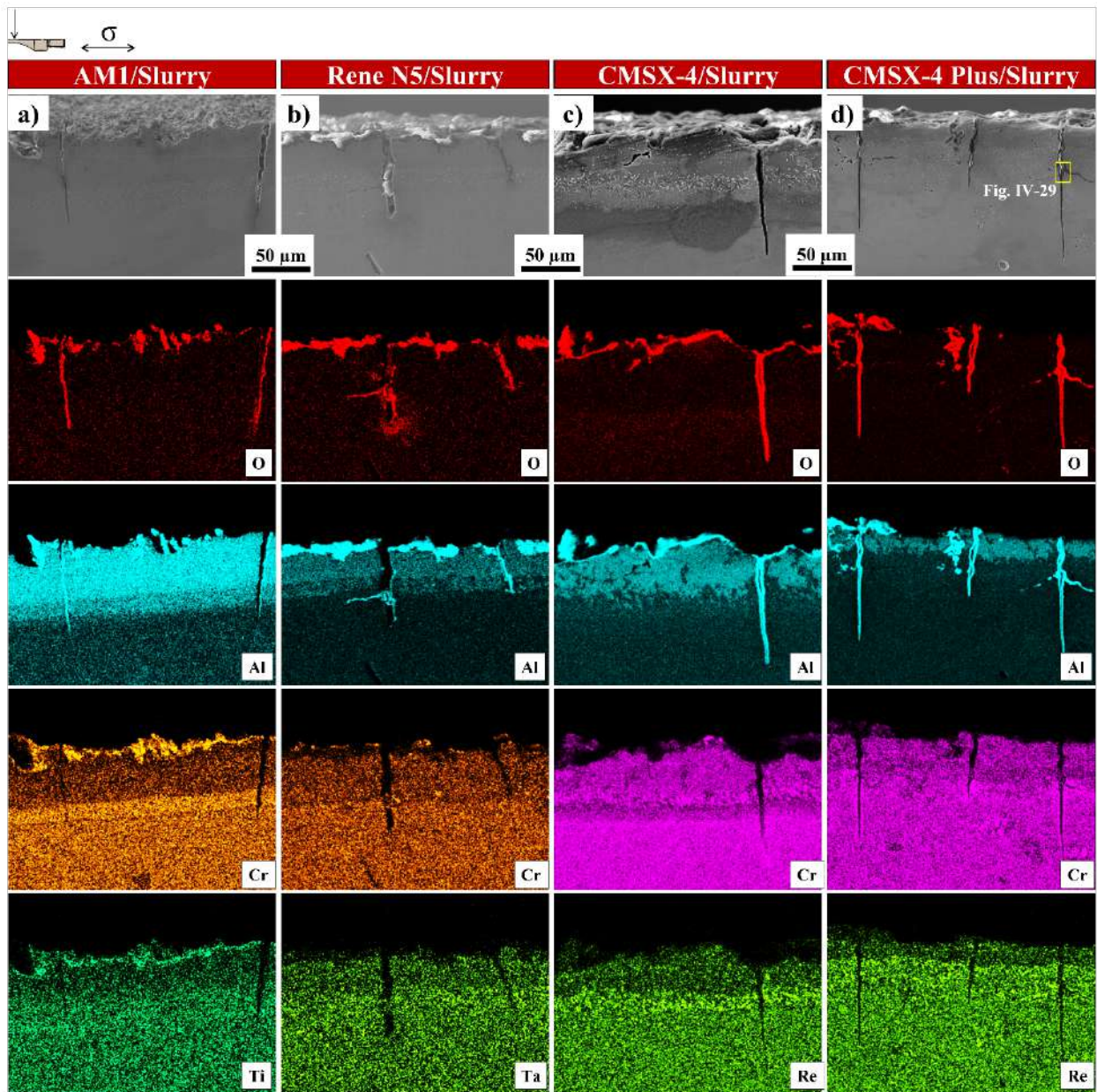


**Figure IV-28** SEI analysis and EDS maps of secondary cracks of **Figure IV-27** longitudinal analysis. AMI (a), Rene N5 (b), CMSX-4 (c), and CMSX-4 Plus (d) samples coated via Slurry method. The EDS maps of: O, Al, Cr, Ti, and Re elements.

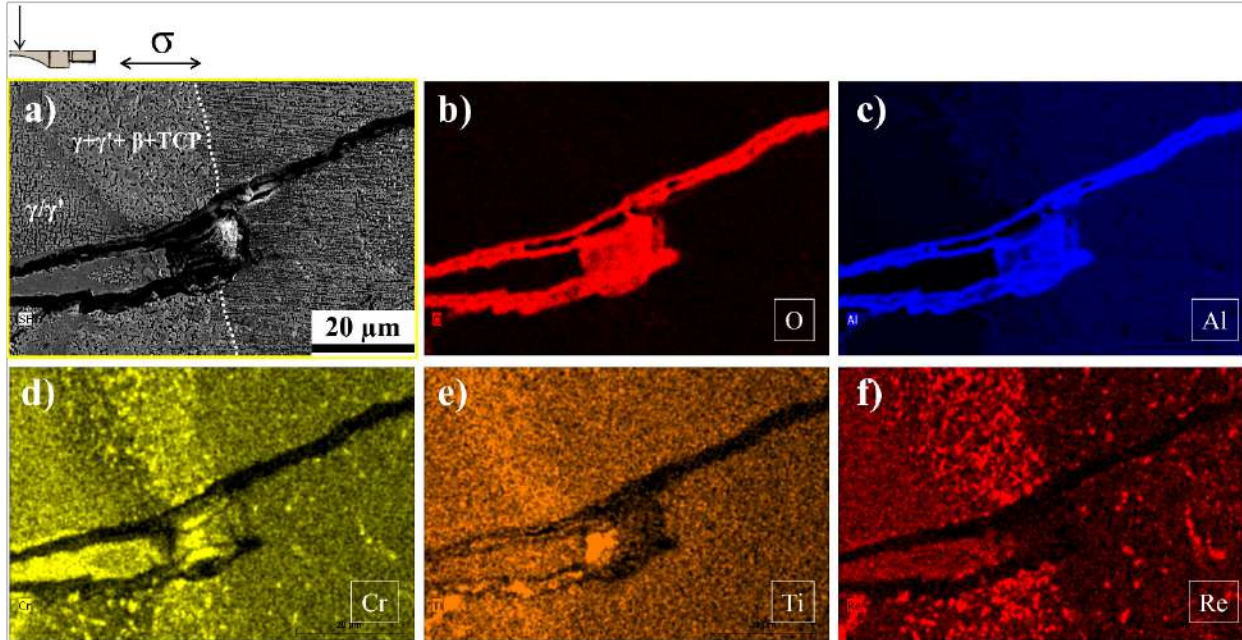


**Figure IV-29** SEI analysis and EDS maps of the secondary cracks like those encountered in **Figure IV-28d**. SEI (a), and EDS maps of: O (b), Al (c), Cr (d), Ti (e), and Re (f). The white dotted curve identifies the interface between the bond coat and the IDZ.

### 3.3. Casting pore vs. recrystallized layer

Secondary crack propagation parallel to the loading axis was observed after the longitudinal analysis of the Rene N5 (see dark blue arrow in **Figure IV-27c**) and CMSX-4 Plus (see dark blue arrows and dotted line in **Figure IV-27g, i, and j**). To investigate the phenomenon, EBSD analyses were performed along longitudinal sections of CMSX-4 (**Figure IV-27e**) and CMSX-4 Plus (**Figure IV-27g**) samples, and the results are depicted in **Figure IV-30**.

**Figure IV-30a** shows a crack close to the fracture surface of the Slurry coated CMSX-4 sample, and **Figure IV-30b** shows a crack  $\approx 3$  mm far from the rupture surface. No recrystallization was identified in the substrate below the BC/IDZ. On the other hand, **Figure IV-30e** illustrates two secondary cracks close to the rupture surface for Slurry coated CMSX-4 Plus.

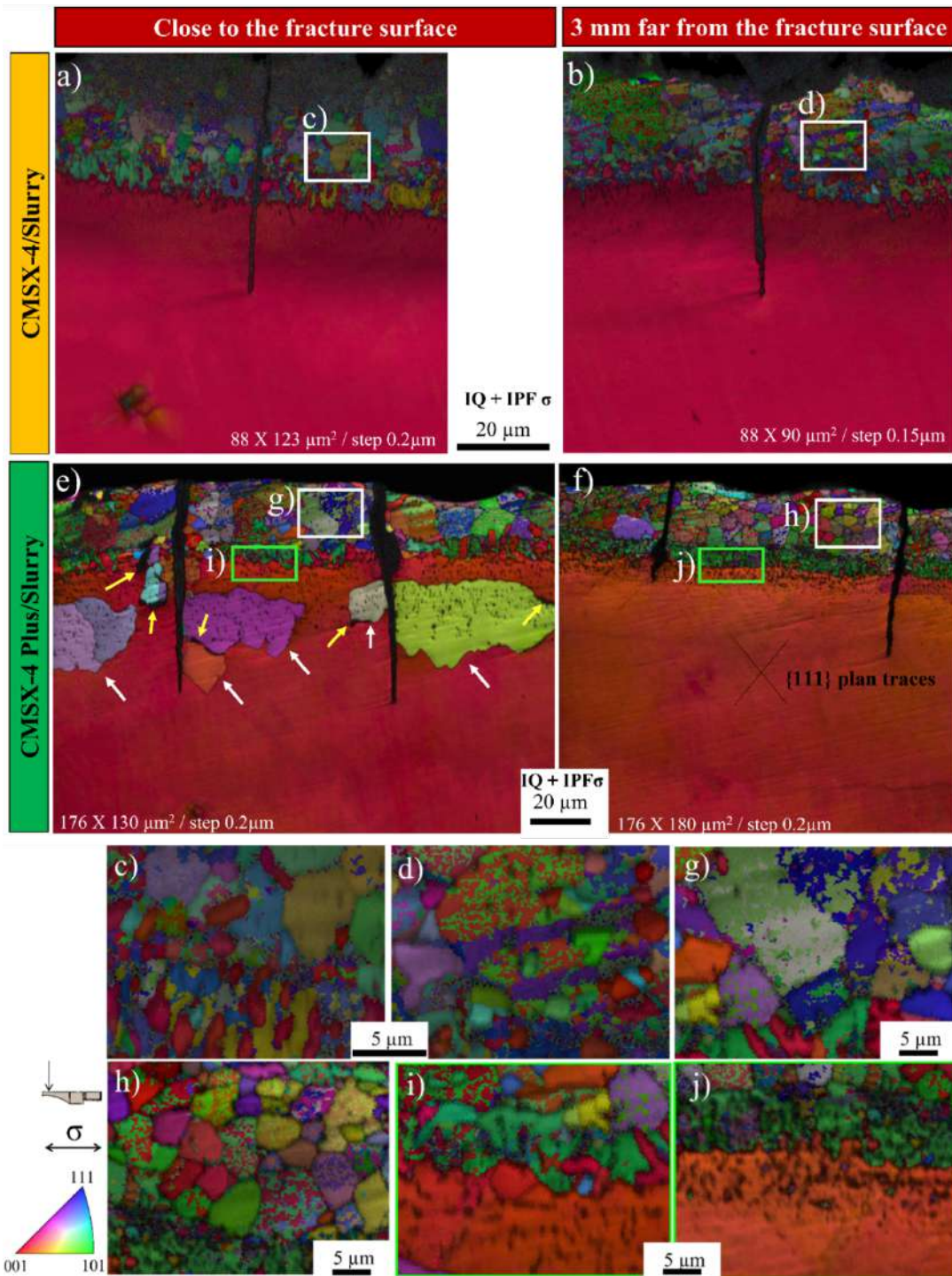


**Figure IV-30** EBSD characterization of Slurry coated CMSX-4 and CMSX-4 Plus specimens close to the rupture surface (IQ+IPF map) (a and e resp.) and  $\approx 3$  mm far from the rupture surface (IQ+IPF map) (b and f resp.). Magnification of the grains in the bond coat in (c and g resp.) and (d and h resp.). Magnification of the CMSX-4 Plus IDZ grains (i) and (j). Color coding is performed along the loading direction. White arrows indicate the grains in the substrate, and yellow arrows indicate cracks at grain boundaries.

**Figure IV-30e** also shows the nucleation of grains with a  $\approx 50 - 100 \mu\text{m}$  size with high misorientation from the [001] direction (see the white arrows in **Figure IV-30e**) below the IDZ of the CMSX-4 Plus sample. The recrystallized layer thicker than the largest casting pore of the substrate may be more critical than the casting pore itself under the VHCF conditions (Cervellon et al., 2021). In fact, several cracks following the nucleated grain boundaries are also observed (see yellow arrows in **Figure IV-30e**). **Figure IV-30f** illustrates two additional cracks  $\approx 3 \text{ mm}$  far from the rupture surface and no recrystallization in the cracks' vicinity.

For both specimens tested in VHCF, a grain growth in the BC is observed in the central part of the specimens, close to the fracture surface (compare **Figure IV-30c** and **d**, **Figure IV-30g** and **h**). This is a result of both (i) a locally higher temperature (a  $\approx 10 - 15 \text{ }^\circ\text{C}$  temperature inhomogeneity is observed in these tests between the middle of the gage length and 3 mm away of the central point (Cervellon, 2018)) and (ii) a higher strain amplitude in this central area.

**Figure IV-31** presents a more detailed analysis of the Slurry coated CMSX-4 Plus sample already investigated in **Figure IV-26e**, **Figure IV-27g-j**, and **Figure IV-30 e** and **f**, with main crack initiation from the surface. Remarkably (and luckily!), the longitudinal section analysis reached a cracked pore (indicated by the dotted red square in **Figure IV-31a** and magnified in **Figure IV-31e**). The critical internal pore has a minimum diameter of over  $50 \mu\text{m}$ , and the voids in **Figure IV-31e** indicate the development of a rough zone. Further, the crack presented in **Figure IV-31f** propagates along the  $\{111\}$  type plane while the stress intensity factor exceeds the threshold value (Cervellon et al., 2020a).

**Figure IV-31b** shows RX layer (**Figure IV-30**) indicated by the dotted blue curve. The recrystallized layer has a depth of  $50 - 100 \mu\text{m}$ , developing in the IDZ, and the substrate layers below the BC. **Figure IV-31c** is the magnification of the high oxidation in the IDZ. **Figure IV-31d** clearly shows a network of secondary cracks developing in the IDZ/RX layer below the IDZ, whose propagation is assisted by oxidation. This damage mechanism is very similar to the one observed in CMSX-4 coated by a processed NiCoCrAlYTa BC (Cervellon et al., 2021).

*Thus, from this observation, an obvious competition in crack initiation mode is observed, and, presumably, in crack propagation rate (i.e., propagation from the surface assisted by oxidation and propagation in the bulk).* The competition was already observed in Utada et al., after pre deformation (Utada et al., 2021), but at positive stress ratio

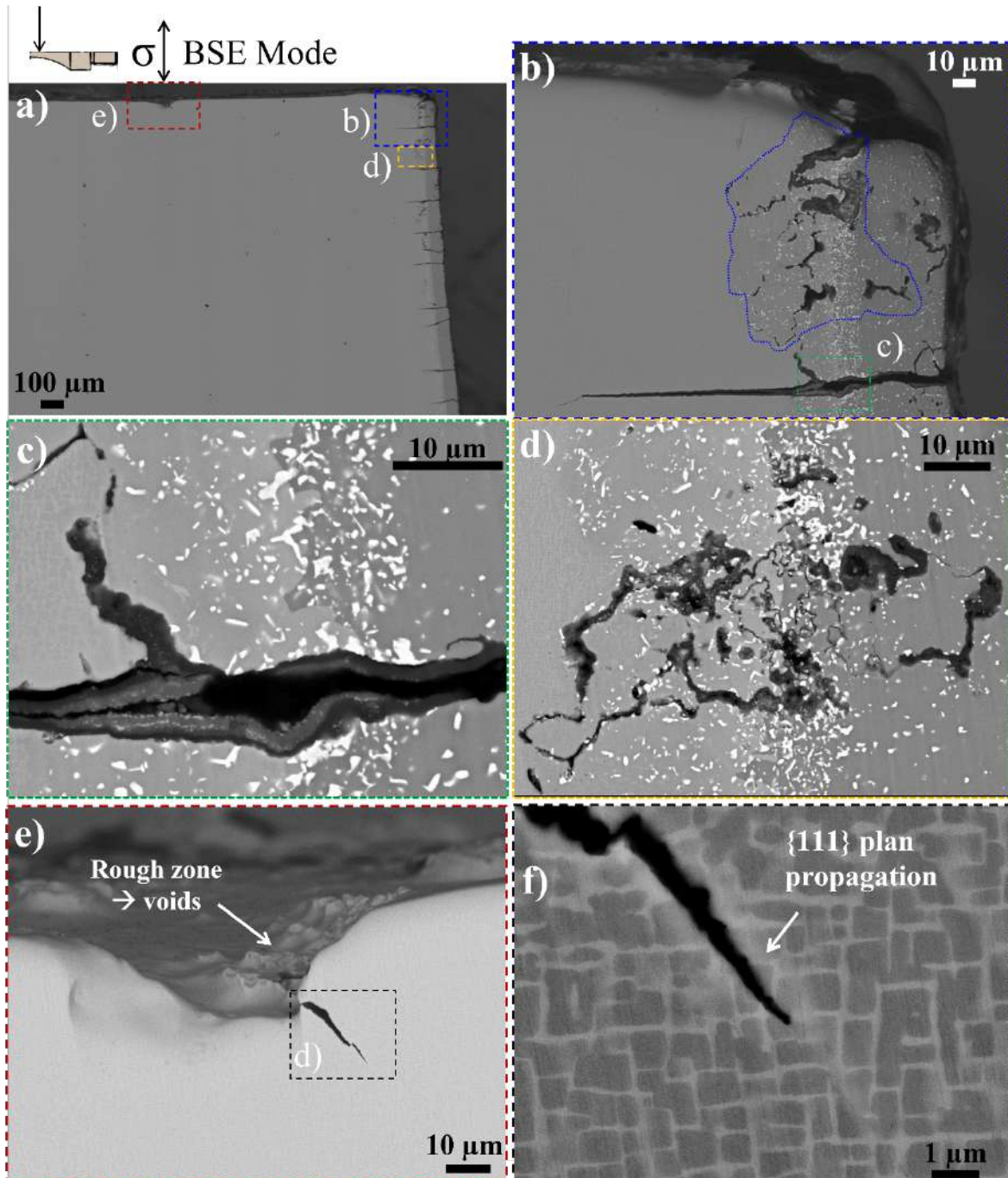


**Figure IV-31** Longitudinal analysis of CMSX-4 Plus sample (**Figure IV-27g**) (a) and presence of RX layer below the BC (b). Magnification of the IDZ (c). Magnification of the network of secondary cracks developing in the IDZ (d). Magnification of the casting pore developing a crack (e), that propagates along a  $\{111\}$  plane (white arrow) (f).

It is usually considered that most of the VHCF lifetime is spent in crack initiation (typically 90 - 95 % of the total life) considering time-independent crack initiation mechanism (Cervellon et al., 2018; Furuya et al., 2012; Miao et al., 2009; Morrissey and Golden, 2007; Yi et al., 2007). However, additional interrupted tests (see **Appendix A.3** and **Figure A-6**) performed to support the discussion showed that the (sub-)surface cracks can develop during the very first cycles ( $\approx 18$  % of the total life) in VHCF for coated samples. As observed from previous results in LCF, the bond coat has a very low ductility in these conditions and may even be brittle at a very high strain rate ( $\epsilon \approx 10^1 - 10^2 \text{ s}^{-1}$ ). Thus, while the crack observed in **Figure IV-31f** develops during the very last fatigue cycles, the (sub-)surface crack propagation assisted by oxidation overcomes the internal crack propagation during the very last cycles, finally controlling failure.

*The remaining question is to know why crack initiation at the (sub-)surface in the BC/IDZ results in a VHCF life comparable with the one of uncoated specimens?*

The crack observed in **Figure IV-31c** has been sitting in the IDZ for a long time, given the observed high local oxidation activity resulting in an oxide spinel indicated by **Figure IV-29**. The mechanism is really similar to the mechanism described by Cervellon et al. (Cervellon et al., 2021) for an MCrAlY coated CMSX-4.

**Figure IV-32** shows the chemical composition profile from the coating layer to the substrate for the Slurry coated CMSX-4 and CMSX-4 Plus samples investigated in **Figure IV-30**.

The CMSX-4 Plus high Al activity towards the substrate is believed to reduce the substrate's sinking effect of Al. Consequently, the Al diffusion from the coating to the substrate is accumulated at the coating/substrate interface (compare **Figure IV-32a** and **c**, blue dotted square). This high Al activity is believed to cause a misorientation of approximately  $20^\circ$  between the superalloy bulk and the vicinity of the subgrains' interface right after the BC deposition (see **Figure A-7** in **Appendix A.3**). The Al-rich layer seems to be the rate-controlling factor in these VHCF conditions since once initiated, cracks are sitting at this IDZ/SX interface for a very long time, up to a point when oxidation helps further crack propagation toward the substrate.

Despite CMSX-4 Plus is known to be sensitive to SRZ formation in the presence of NiAl type BC industrially processed (Saboundji et al., 2020), the author believes that this Al layer is key in controlling the crack propagation from the surface, through the oxidation mechanisms at the crack

tip. Indeed crack tip blunting by oxidation and volume expansion of oxides at the crack tip are known to slow down the crack propagation rate (Cruchley et al., 2015; Mataveli Suave, 2017; Perruchaut, 1997).

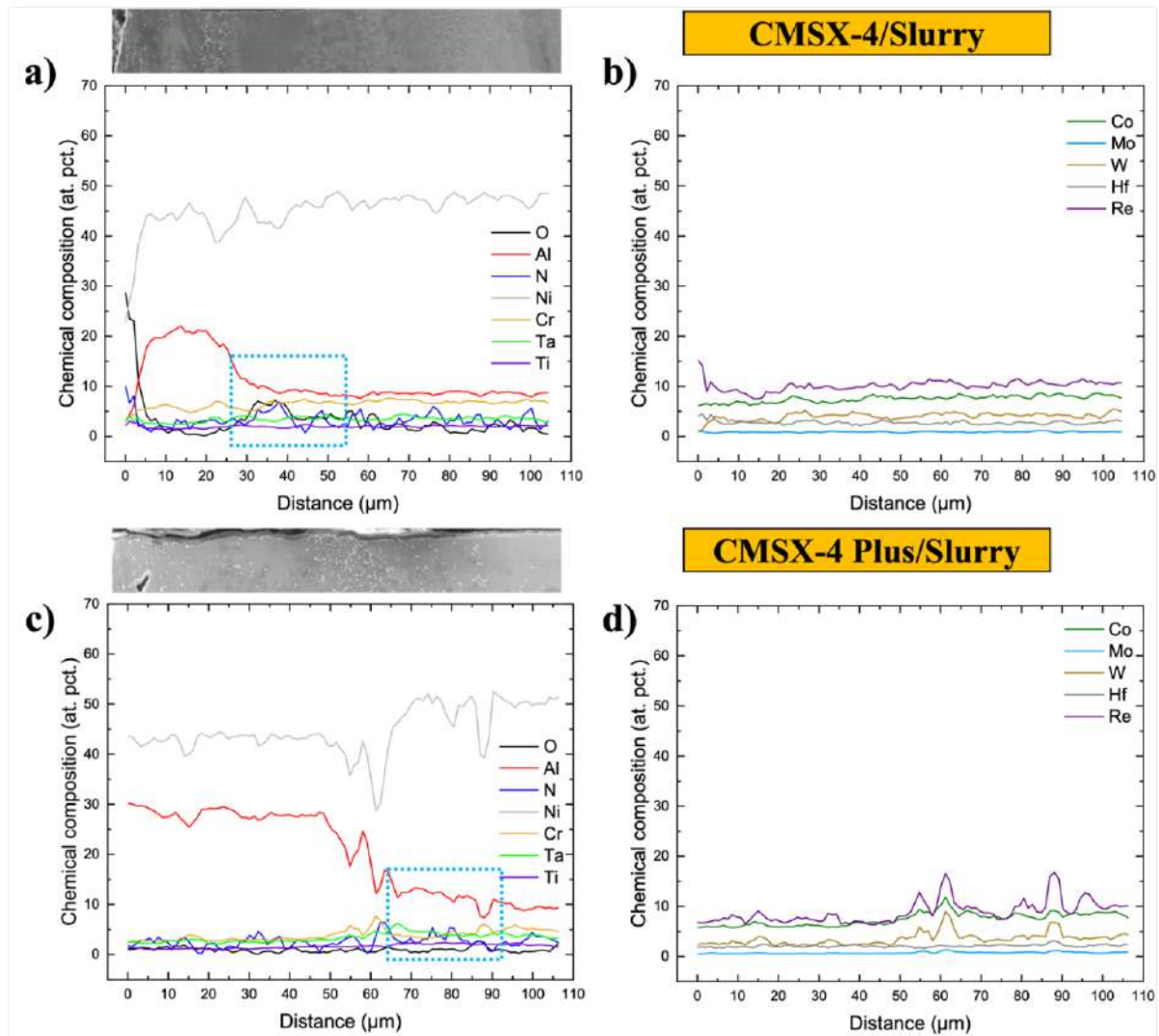


**Figure IV-32** EDS profiles from the surface toward the substrate showing the evolution of the chemical composition (at. pct.) for each sample after the VHCF tests. The chemical elements Al, Ni, Cr, Ta, Ti plus O and N (a) and (c). Co, Mo, W, Hf, and Re (b) and (d).

From the present observations, the better VHCF life of Slurry-type bond-coated CMSX-4 Plus seems to mainly results from a slower crack propagation from the surface compared to the other three systems, despite RX below the IDZ. On the other hand, AM1, CMSX-4, and Rene N5 failed at casting pores close to the IDZ without any RX contribution. Therefore, recrystallization is less

detrimental (by a factor of 10) than features as casting pores at IDZ (see **Figure IV-25**). A *final key question is to understand the interaction between casting pores and the IDZ*.

### 3.4. Casting pore/IDZ interaction in VHCF

**Figure IV-33** illustrates a typical casting pore configuration for bond-coated AM1/Rene N5/CMSX-4 leading to a deficit in VHCF life compared to uncoated substrates.

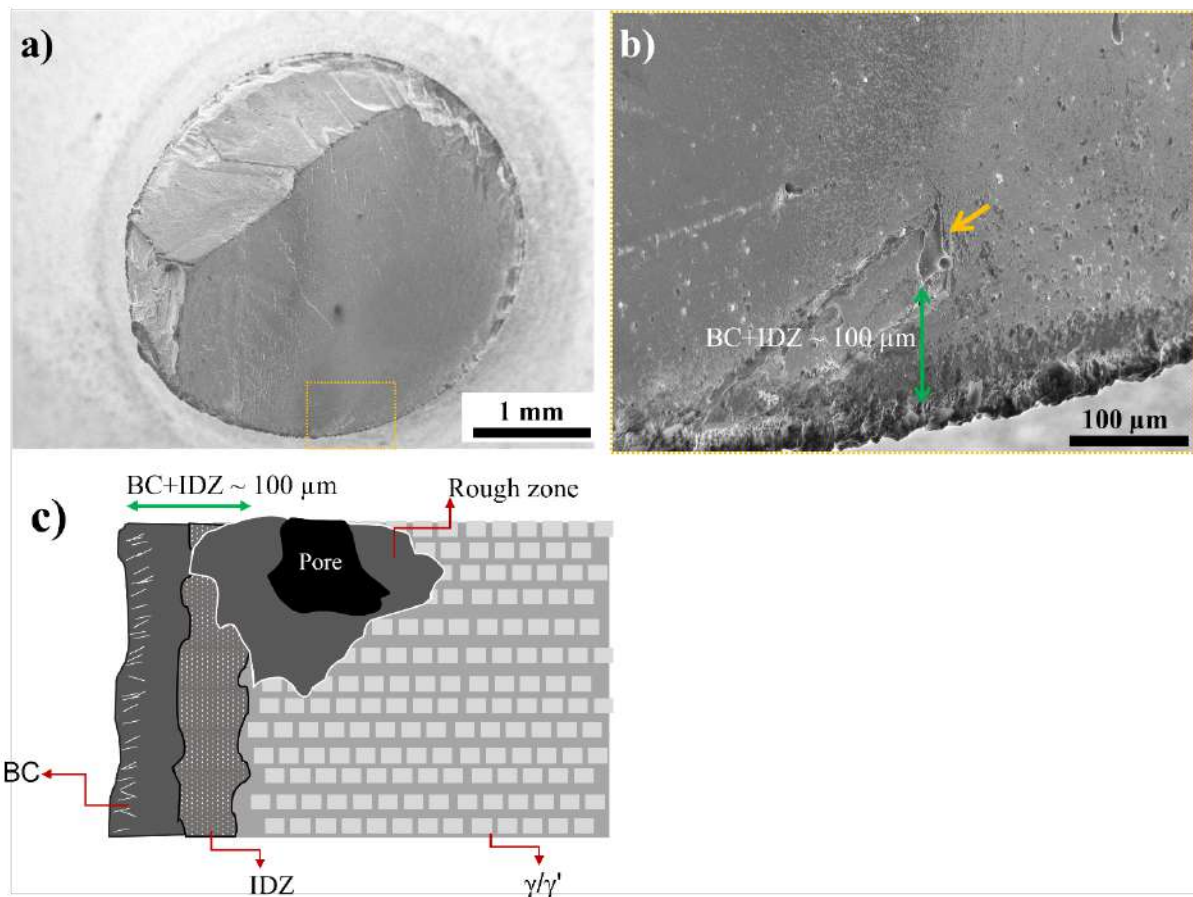


**Figure IV-33** Fracture surface observations of Slurry CMSX-4 coated sample ( $\sigma_a = 204$  MPa, with  $N_f = 5.1 \cdot 10^6$  cycles) (a), crack initiation zone magnification in (b), details the presence of a casting pore close to the surface with a diameter of  $\approx 50 \mu\text{m}$  (indicated by the yellow arrow). 2D schematic illustration of a casting pore + the rough zone/IDZ interaction (c).

Since all single-crystalline bars were solidified using almost the same casting parameters, the size of the casting pores is expected to be inside the same range (60 – 100  $\mu\text{m}$ ) (Bokstein et al., 2007; Reed, 2006). Hence, the author believes that the VHCF life dependence on the pore size presented in

**Chapter III sub-section 2** can be disregarded for the present analysis. After the fracture surfaces observation (example at **Figure IV-26a** and **Figure IV-33a**), the author observed that even though the casting pores were not always located at a distance lower than  $100\ \mu\text{m}$  from the surface, the projected area of casting pores plus the rough zone was in the vicinity of the IDZ interface (**Figure IV-33b** and a schematic illustration in **c**).

Knowing that the bond coat diffuses inward, possibly reaching defects (i.e., casting pores, carbides), and knowing that the cracks develop very fast during the first cycles in VHCF (**Figure A-6**), the VHCF life can be controlled by the interaction of the superalloy/coating inside the IDZ, which locally induce a deficit in the mechanical strength of the substrate. In fact, the evolved microstructure in the IDZ is suspected to be favorable for the rough zone development.

**Figure IV-34** is illustrating a damage mechanism proposed by the author based on this section's observations and analysis. **Figure IV-34a** represents a longitudinal section of a Ni-based SX superalloy NiAl-coated. It first proposes the interaction between a (small) casting pore close to the interface of the substrate/IDZ and a larger casting pore inside the sample's substrate (i.e., far from the IDZ interface). The bond coat is known to develop cracks in the first cycles up to the IDZ (**Figure IV-34b**). The crack stops in the IDZ before propagating into the superalloy bulk. Simultaneously, chemical elements like Al and Ti (typical  $\gamma'$  elements) are consumed in the substrate/IDZ interface. Thus, the small casting pore is now located in a chemically and mechanically (i.e.,  $\gamma'$  dissolution) unstable zone, while, simultaneously, slip bands accumulate in the vicinity of the casting pores along the favorable slip system (Cervellon et al., 2020a) (**Figure IV-34c**).

Then, an earlier development of the rough zone in the vicinity of the pore close to the IDZ is obtained compared to internal casting pores because of the local microstructure evolution at the IDZ/SX interface and dissolution of the  $\gamma'$  phase due to oxidation (**Figure IV-34d**). Finally, the crack propagates from the smaller casting pore through the rough zone due to the microstructure degradation, leading to the sample's failure (**Figure IV-34e**). Consequently, it results in a lifetime of at least one decade lower than the one obtained for specimens without any coating (see **Figure IV-25**).

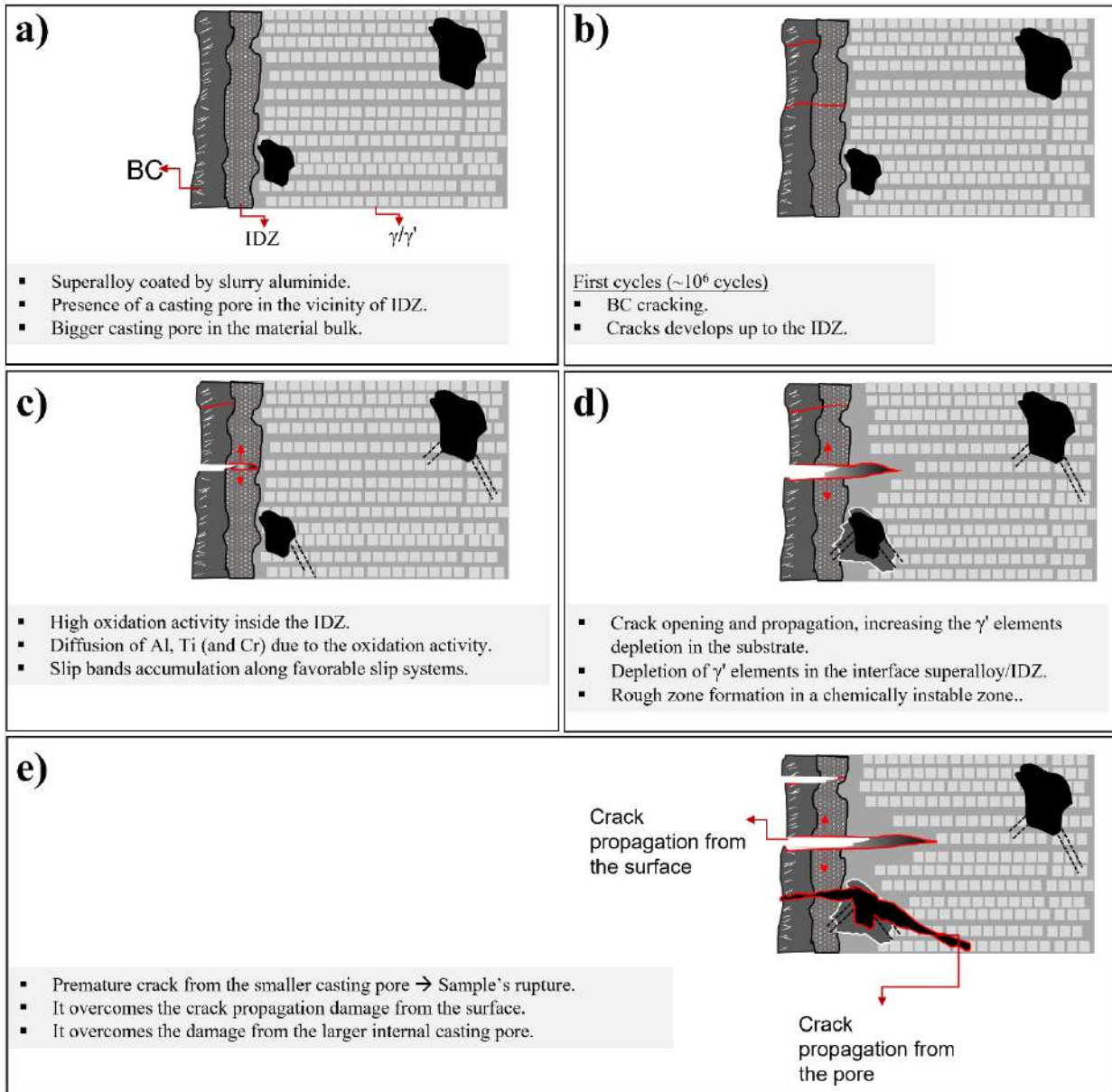


**Figure IV-34** Schematic illustration of SX Ni-based superalloys' aluminide coated crack initiation mechanism in VHCF conditions at  $1,000\text{ }^\circ\text{C}/R_\epsilon = -1/f = 20\text{ kHz}$ . The initial optimized  $\gamma/\gamma'$  microstructure, the bond coat, and the IDZ. The superalloy has two pores, one bigger far from the free surface and one smaller in the IDZ/substrate interface (a). During the first cycles, the BC cracks up to the IDZ (b). The oxidation activity in the IDZ blocks the crack initiated at the surface consuming the  $\gamma'$  elements like Al, Ti, and Cr. Thus, the slip bands accumulate in the casting pores' vicinity along favorable slip system(s) (c). The dissolution of  $\gamma'$  precipitates and the chemical instability leads to earlier rough zone formation close to the smaller pore (d). The crack propagates toward the smaller casting pore leading to the sample's failure (e).

### **3.5. Summary**

CMSX-4 Plus failed by the presence of a recrystallized layer leading to (i) (sub-)surface crack initiation with the presence of a rough zone, or (ii) surface crack initiation. They were proved to hardly affect the fatigue life, as the crack remains sitting in the IDZ for a long time, given the local oxidation activity. The author believes that the presence of a layer of recrystallized grain below the IDZ plus the higher Al concentration in this zone controls the crack propagation.

AM1, CMSX-4, and Rene N5 superalloys failed from a casting pore close to the IDZ/bond coat zone. The author believes that cracks propagating in the very first cycles up to the IDZ increase the diffusion activity near the IDZ/coat zone. Consequently, this zone becomes chemically and mechanically unstable, with high stress concentration, and thus it favors the rough zone development, then leading to a premature failure of the specimens at smaller sub-surface pores.

## 4. Conclusions

This chapter was dedicated to studying the impact of a bond-coat deposition on the cyclic life of Ni-based SX superalloys. This chapter investigated five superalloys from different generations and two aluminide coating methods. The tests were carried out in LCF at 0.5 Hz/900 – 950 °C/ $R_{\sigma} = 0.05$  and in VHCF at 20 kHz/1,000 °C/ $R_{\sigma} = -1$ .

First, it was shown that the solution heat treatment and the aging are key parameters controlling the LCF life in these conditions. In fact, these heat-treatments are usually applied to improve the homogeneity of the  $\gamma'$  microstructure and hence, the creep properties. These heat treatments are shown to limit LCF ratcheting, leading to a better LCF life. Moreover, under the same conditions, the aluminide coating did not influence the LCF life of Rene N5 and AM1 alloys. The diffusion heat treatment of the Slurry type BC has highly affected the MAR-M200 +Hf SX resulting in a decrease of the superalloy tensile and fatigue strength due to the “extra” BC diffusion heat treatment. In fact, it led to the coarsening of the fine  $\gamma'$  precipitates decreasing its density (and increasing its size) directly influencing the superalloy monotonic mechanical properties at 950 °C.

Cracks perpendicular to the loading axis are developing in the very first LCF cycles in the bond coat leading to the conclusion that the bond-coats, whether processed by APVS or by Slurry route, have a low ductility at 900 – 950 °C. Tests carried out in vacuum proved that the crack initiation was not assisted by oxidation. Moreover, the quasi-brittle behavior of the NiAl bond coat has been observed to be independent of the frequency (0.5 or 20 kHz), the superalloy or the stress ratio.

In VHCF conditions, 1,000 °C and fully reversed loading this quasi-brittle behavior of the BC does not seem to affect the fatigue life. In fact, the opposite transition (from the surface to the internal remaining defects) was observed for several superalloys. Thus, for the first time, the chemical interaction around a casting pore located close to the coated surface is supposed to impact the fatigue life of Ni-based SX superalloys coated systems tested in VHCF conditions and 1,000 °C.

In short, the VHCF life of the coated samples is controlled by: (i) a recrystallized layer below the surface where the crack propagation is stopped with a VHCF life hardly affected compared to uncoated specimens. (ii) Casting pore close to the IDZ controlling the VHCF life due to a favorable local microstructure for rough zone development. This second situation leads to a VHCF life deficit for all superalloys investigated.

# **Chapter V. Analysis of crack initiation mechanism transition from internal sites to the surface in the very high cycle fatigue regime**



## **Analyse de la transition de l'amorçage des fissures des sites internes vers la surface en régime de fatigue gigacyclique**

Les deux chapitres précédents ont été consacrés à l'étude du mécanisme d'amorçage des fissures en régime gigacyclique pour les substrats non revêtus (Chapitre III) et pour les échantillons revêtus NiAl (Chapitre IV). À partir de toutes ces caractérisations, ce dernier (et court) chapitre a pour objectif principal d'analyser et de discuter des conditions/paramètres favorisant une transition de l'amorçage des fissures des sites internes vers la surface.

Pour discuter la transition de l'amorçage de la fissure des grands aux petits pores de fonderie puis à la surface, la condition de chargement mécanique considérée est de 1,000 °C,  $R_e = -1$ , 20 kHz, à l'air. Cette condition a été choisie car c'est la plus « populaire » étudiée dans cette thèse et car elle n'implique pas d'endommagement de type fluage. De plus, les méthodes de solidification et traitement HIP seront corrélés pour illustrer la transition.

Le chapitre répond à trois questions principales :

- Comment se déroule le mécanisme de transition de l'amorçage interne à l'amorçage en surface sous 1,000 °C,  $R_e = -1$  et 20 kHz ?

Pour les échantillons de substrat nu et les conditions de 1,000 °C,  $R_e = -1$  et 20 kHz, ce sont les paramètres de procédé de solidification ou de traitement de compression isostatique à chaud qui contrôlent la transition d'amorçage de fissure de l'intérieur vers la surface.

- Limite de fatigue à 1,000 °C,  $R_e = -1$  et 20 kHz.

Si les défauts internes restants (par exemple, les phases TCP, les petits pores restants et les carbures) sont suffisamment petits pour limiter/éviter les sites de concentration de contraintes, les conditions environnementales (c'est-à-dire la température et le temps d'exposition) conduisent à la transition de l'amorçage de fissure en fatigue des sites internes à la surface.

- Comment se produit l'amorçage de la fissure après application d'un revêtement NiAl visant à protéger le superalliage SX base Ni de l'oxydation ?

D'une part, pour les échantillons nus, l'amorçage des fissures est fortement influencé par les paramètres de traitement du superalliage, tandis que d'autre part, la durée de vie en fatigue gigacyclique des échantillons revêtus est contrôlée principalement par le comportement intrinsèque du revêtement (c'est-à-dire fragile vs ductile) dans les mêmes conditions.

The two previous chapters have been dedicated to investigate the crack initiation mechanism in VHCF for uncoated substrates (**Chapter III**) and in NiAl-coated specimens (**Chapter IV**). From all these characterizations, this last (short) chapter has the main aim to analyze and discuss conditions/parameters favoring a transition in crack initiation from internal sites to the surface.

The different experimental studies available in the literature have highlighted the different parameters controlling the fatigue crack initiation mechanism from internal and surface features under a wide variety of conditions (Cervellon, 2018; Fleury and Rémy, 1993; Mataveli Suave, 2017; Ohtani et al., 2001; Perruchaut, 1997; Steuer et al., 2015; Utada et al., 2021; Zhao et al., 2021a). Therefore, the literature is relatively abundant for several of them (i.e., at low frequencies) (Fleury and Rémy, 1993; Mataveli Suave, 2017; Ohtani et al., 2001; Perruchaut, 1997; Steuer et al., 2015) although very scarce in the VHCF regime (Cervellon, 2018; Utada et al., 2021; Zhao et al., 2021a, 2022) at high temperatures.

To discuss the crack initiation transition from large to small casting pores and then to the surface, the mechanical loading condition considered is 1,000 °C,  $R_\epsilon = -1$ , 20 kHz, in air. This condition was chosen, as it is the most “popular” one investigated in this thesis and as it does not involve creep-type damage. In addition, the SX processing parameters (solidification methods and HIP treatment) will be correlated to illustrate the transition.

i. *How does the transition from internal to surface crack initiation occurs at 1,000 °C,  $R_\epsilon = -1$  and 20 kHz?*

**Figure V-1** presents data extracted from **Figure III-25**. Color backgrounds used in this figure highlight three zones:

- Red hatched zone: Crack initiation at large internal casting pores with a diameter higher than 80  $\mu\text{m}$  or high angle grain boundaries (HAGB).
- Yellow hatched zone: Crack initiation at casting pore with a diameter lower than 80  $\mu\text{m}$  or low angle grain boundaries (LAGB).
- Green hatched zone: Main crack initiation from the surface.

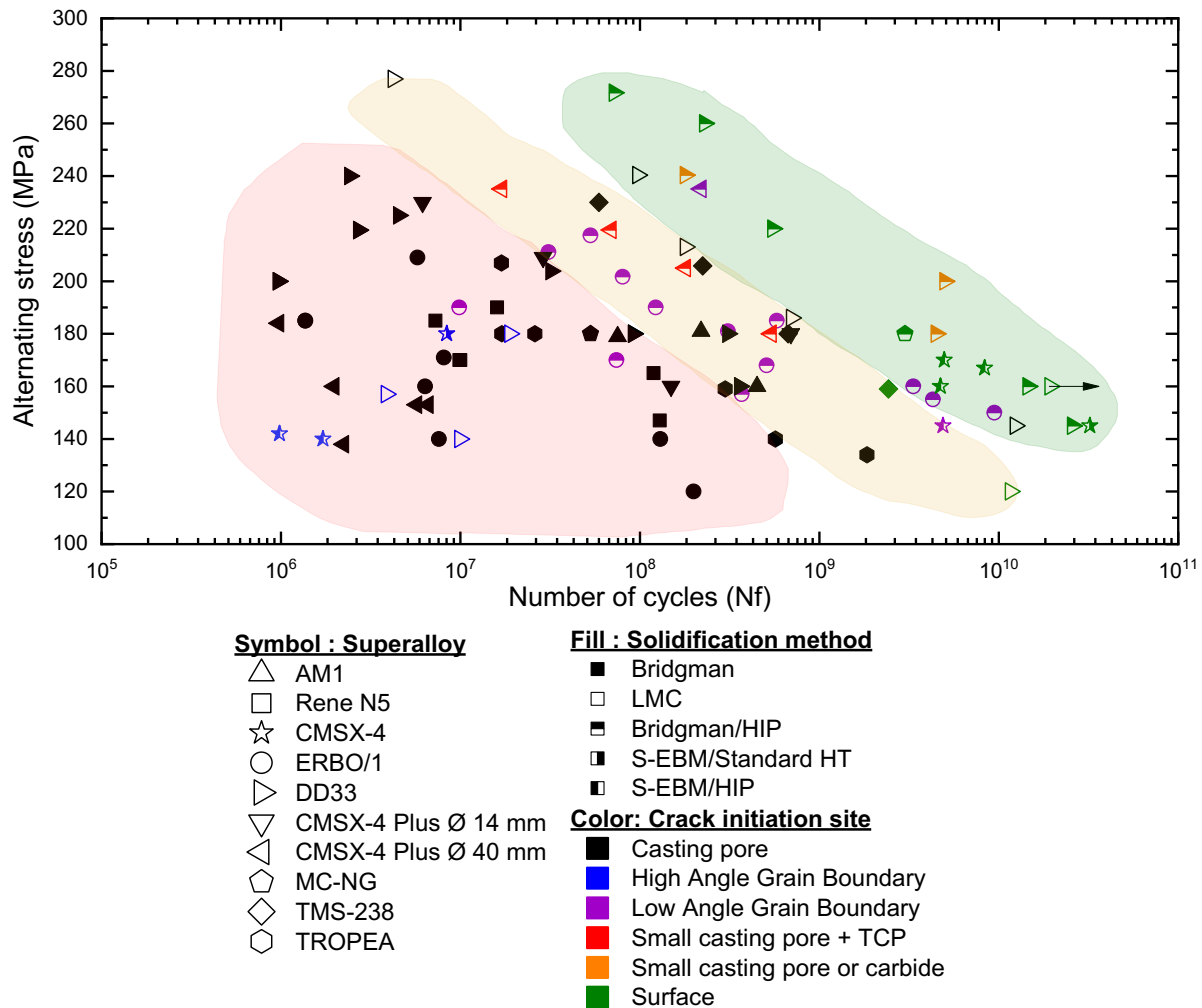


**Figure V-1** S-N diagram for 1,000 °C,  $R\epsilon = -1$ , and  $f = 20$  kHz gathering the results of **Figure III-25**. The alternating stress  $\sigma_a$  is plotted as a function of the number of cycles to failure.

The red zone shows that HAGBs lead to a VHCF life as low and scattered as the large internal casting pores. Thus, it should be considered that while high solidification rates (LMC and AM) are usually desirable to improve the fatigue life of Ni-based SX (Brundidge and Pollock, 2012; Cervellon et al., 2018; Steuer et al., 2015), they could generate defects/RX as critical as large internal casting pores. *It means that using these kind of accelerated solidification routes, while providing improved fatigue performance in principle, can also introduce defects that are more critical.*

The yellow hatched zone show that even though several HIP treatments lead to a local LAGB development, the VHCF life of these samples was improved. However, the samples that failed at

LAGB features show a higher scatter in lifetime the samples with small casting pores and no HIP, possibly decreasing the usefulness of processing routes from a component design point of view. Even though the size and fraction of internal defects were decreased by AM solidification or HIP treatment, remaining defects as TCP phases (e.g., CMSX-4 Plus HIPed samples), carbides (e.g., DD33), or very small casting pores ( $\approx 5 \mu\text{m}$  diameter) can still be present in the samples.

The CMSX-4 Plus superalloy is known to have a high concentration of Re in its composition (Wahl and Harris, 2016). From the results obtained in **Chapter III sub-section 3**, it was not possible to identify a clear role of features as TCP phases in the crack initiation mechanism. However, for the CMSX-4 Plus HIPed samples, 100% of them failed at (very) small internal casting pores filled with TCP phases. **Figure III-16** shows that the small remaining features present in the CMSX-4 Plus superalloy microstructure are structures very similar to the TCP phases (Dubiel et al., 2018; Rae and Reed, 2001). Even though the TCP phases are known to have a small influence on the creep life (Simonetti and Caron, 1998), and almost no influence on the fatigue life (Pessah et al., 1992; Simonetti and Caron, 1998). The author believes that the presence of the brittle feature as the TCP phases (Simonetti and Caron, 1998) inside remaining small casting pores influenced the internal crack initiation of the CMSX-4 Plus HIPed samples.

Three DD33 HIPed specimens failed at remaining unclosed pores probably filled with carbides (**Figure III-3b**). The carbides are known to degrade the fatigue life, especially when they are located at the (sub-)surface (Govaere et al., 2020; Huang et al., 2006; Mataveli Suave, 2017). Despite a transition zone can be identified at  $10^9$  cycles mentioned by Cervellon (Cervellon, 2018), where internal defects like TCP phases, remaining eutectics or even carbides can be critical crack initiation zones. The author believes that inside this transition zone, the nature of the crack initiation mechanism is still highly related to the presence of small remaining pores from the processing techniques (e.g., LMC, AM or HIP). However, *the brittle intermetallic particles inside or in the vicinity of the remaining pores act as stress concentration zones due to their weak interface with the superalloy.*

As observed in **Figure V-1**, the fatigue life highly increased between the red and the green hatched zone by up to 4 decades. Moreover, most of the specimens in the green hatched zone are breaking

from the surface. It then leads to the question to know if increasing superalloys resistance to oxidation would benefit to the VHCF life of Ni-based SX alloys if they were (almost) defect-free.

**Figure III-33** has shown that the crack initiation from the surface is not assisted by the superalloy (sub-)surface recrystallization. In addition, no carbides were identified as crack initiation sites. Thus, the onset of surface crack initiation was not entirely identified in this thesis. No additional mechanism has been proposed by Zhao et al. (Zhao et al., 2021a) regarding crack initiation at the surface of this specimens tested in VHCF at 1,100 °C/20 kHz/ $R_e = -1$ . In the literature, several authors indicate that the crack initiation at the surface is triggered by the oxides spallation during the cyclic loading (Fleury and Rémy, 1993; Ohtani et al., 2001; Steuer et al., 2015) or even by the presence of remaining pores in the (sub-)surface (Fleury and Rémy, 1993; Steuer et al., 2015). Even though the  $\alpha$ -Al<sub>2</sub>O<sub>3</sub> oxide layer is known to be very stable and adherent at high temperatures (Khanna, 2012), it may crack due to the intrinsic brittleness of this kind of oxide under these mechanical tests. In the present thesis, the author proposed that in the VHCF regime, the local  $\gamma/\gamma'$  microstructure evolution leading to a  $\gamma'$  depletion, and nitrides are weakening the superalloy surface and it is one of the possible scenarios leading to favoring sub-surface crack initiation.

Even though the surface failure observed in DD33, MC-NG and S-EBM HIPed specimens were correlated to longer lives, the respective crack initiation and propagation contributions to the fatigue life in this kind of failure is not completely clear. An analysis carried out for several steels has shown that the VHCF life is still mainly influenced by the crack initiation when it starts at the surface (Marines-Garcia et al., 2007). However, these studies have never been carried out for the Ni-based SX superalloys. The author believes that a great fraction of the VHCF life is still spent in the crack initiation regime. To answer the question, crack rate measurement should be carried out under these conditions. However, the technique is still in development (Liu et al., 2008) and would be very complex at these high temperatures and frequencies.

Moreover, analyzing the same alternating stress of 160 MPa in **Figure V-1** (specimens: TMS-238/Bridgman, CMSX-4/PBF-E built, DD33/HIPed, and DD33/LMC), the microstructure degradation seems to be controlled not only by the superalloy intrinsic resistance to oxidation, but also by the surface and (sub-)surface evolution. TMS-238 should have shown a VHCF life higher than both other superalloys, because of its high resistance to oxidation (Kawagishi et al., 2012). However, as the TMS-238 superalloy was Bridgman processed, the interaction between the

intrinsic microstructure defects (e.g., (sub-)surface casting pores) and the oxidation play an important role leading to the crack initiation at the surface. Between the CMSX-4/PBF-E and DD33/HIPed samples, the VHCF life is comparable, and the author believes that it was mostly controlled by the intrinsic resistance to oxidation of the Ni-based SX superalloys.

One may also question the slope the yellow and the green hatched zones in the S-N diagram in **Figure V-1**, as naturally, it should not be the same due to differences in crack initiation mechanisms. Indeed, there are some evidences in the literature that oxidation is strongly enhanced by fatigue cycling in the superalloys (Barret et al., 1973; Ma et al., 2020; Reger and Rémy, 1988b, 1988a; Rémy et al., 2007; Reuchet and Rémy, 1983). Even though the fatigue-oxidation interactions were proved to be enhanced under cyclic loading (Ma et al., 2020), accelerating strengthening elements' depletion and usually leading to a lower life in the LCF regime (Clavel et al., 1979; Pineau and Antolovich, 2015), no decrease in fatigue life or change in the S-N diagram slope has been observed in the VHCF regime. This clearly means that surface failure assisted by oxidation is an intrinsic mechanism and the improved VHCF life compared to specimens failing from internal casting pore is mainly a result of the time dependence of the oxidation process. Still, the author believes that the question of mechanical loading/environment interaction could be better answered if the VHCF could be carried out in a protective environment (e.g., vacuum or Argon flow).

The **Appendix C, Figure C-1** presents the results of MAR-M200 +Hf SX, AM1, Rene N5 and DD33 in VHCF conditions 1,000 °C, and  $R = 0.5$ . Most of the samples failed at internal casting pores. However, two results of the superalloy MAR-M200 +Hf SX have presented a main crack initiation at the surface. Contrary to the results obtained for the tests obtained at  $R_e = -1$ , the samples that failed at the surface at  $R = 0.5$  have shown a lifetime lower or like the samples that failed from internal casting pores. These results have shown that the creep-fatigue interaction may be more detrimental to the fatigue life than the environment when the crack initiation is at the surface.

*Finally, for the bare substrate samples tested at 1,000 °C,  $R_e = -1$  and 20 kHz, the processing parameters control the crack initiation transition from the internal to the surface.*

ii. *Fatigue limit at 1,000 °C,  $R_\epsilon=-1$  and 20 kHz*

As mentioned in the first chapter of this work, the fatigue limit in VHCF at high temperature is not only of interest from a fundamental viewpoint. It is also of practical importance for designing “flying” components (Bathias, 2013; Laird, 1976; Pyttel et al., 2011). Laird (Laird, 1976) mentioned that a true fatigue-stress or fatigue-strain limit exists for most crystalline materials. Moreover, this study mentioned that the fatigue stress limit decreases markedly with increasing temperature. Thus, the time-dependent mechanisms can highly influence the crack initiation depending on the combination of specific conditions as temperature and frequency (i.e., time of exposition). However, it can be highly dependent to other factors like pre-strain deformation or the stress ratio. Therefore, the failure will always be a combination of several scenarios.

**Figure V-2** gathers all the VHCF results from the Institut Pprime/ISAE-ENSMA database from this thesis and Cervellon thesis work (Cervellon, 2018). It is important to point out that the results from the internal database established at Institut Pprime/ISAE-ENSMA have been obtained using “legacy” Ni-based SX superalloys as DS200 +Hf, MAR-M200 +Hf SX, AM1, Rene N5 and CMSX-4 but also newer generations as CMSX-4 Plus, DD33, ERBO/1, TMS-238, MC-NG, and TROPEA. Their chemical composition is given in **Table II-1**. Further, they were solidified using a Bridgman or an LMC process. The superalloys are not identified because in these VHCF conditions, the failure mechanism is independent of the chemical composition (Cervellon et al., 2018).

Up to now, most of the authors focused their investigations on VHCF damage mechanisms from either casting pores or from non-metallic inclusions (TCP phases, eutectics, carbides...) (Cervellon, 2018; Cervellon et al., 2018, 2017; Yi et al., 2007), i.e., from process related “defects”. When nearly all defects are removed from the material, and if a good surface preparation of specimens is performed to avoid any surface recrystallization, an intrinsic VHCF life controlled by the alloy’s chemistry can be obtained. In these conditions, the VHCF life of single crystalline Ni-based superalloys is hence controlled by the environmental resistance, i.e., by the alloys’ chemistry.

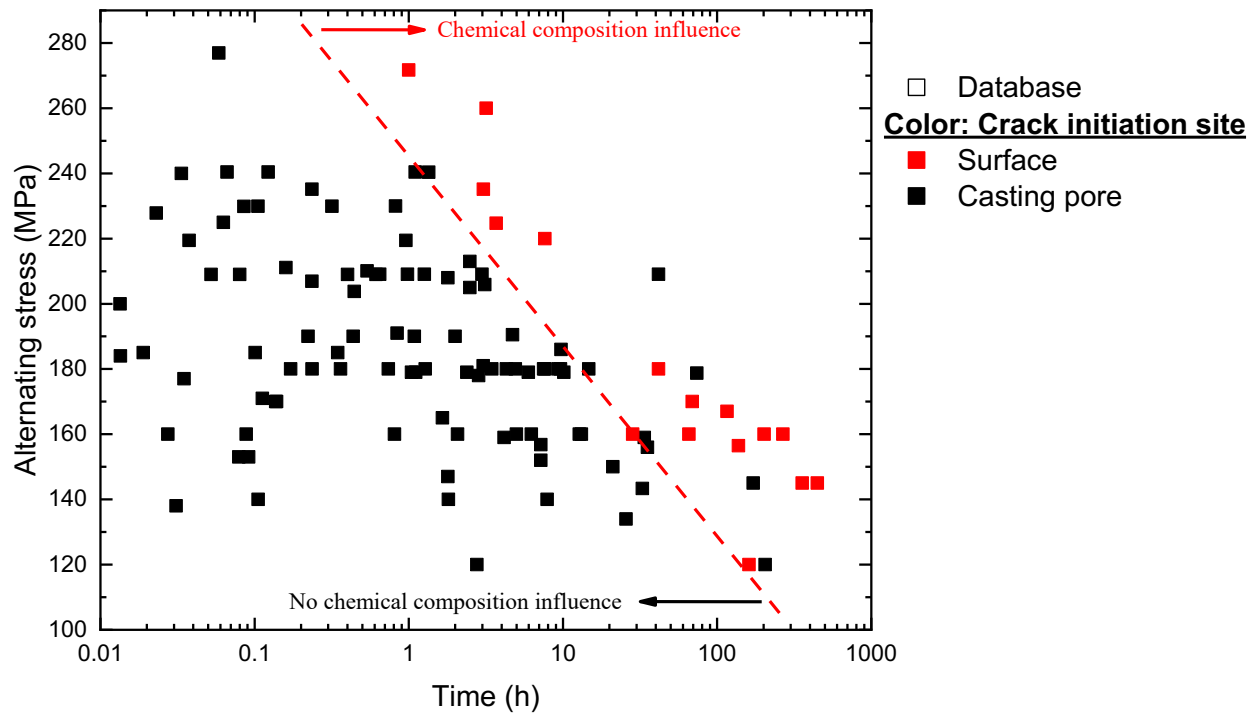


**Figure V-2** Alternating stress as a function of the testing duration diagram at 1,000 °C,  $R_e = -1$ , and  $f = 20$  kHz gathering the results from Institut Pprime from this thesis and (Cervellon, 2018) database.

*Finally, if the remaining internal defects (e.g., TCP phases, small remaining pores, and carbides) are small enough to limit/avoid stress concentration sites, the environmental conditions (i.e., temperature and time of exposition) lead to the transition of the crack initiation from the internal features to the surface.*

The present study also suggests that if processing parameters can be controlled in a way to avoid internal defects, *no fatigue limit exists in these fatigue conditions at high temperature*, but this question should also be investigated at higher and lower temperatures to get a better picture of oxidation controlled VHCF crack initiation mechanisms.

iii. How does the crack initiation occur after applying a bond coat aiming at protecting the Ni-based SX superalloy from oxidation?

In **Chapter IV**, the VHCF life of coated samples has been investigated. From the results and analysis presented in this chapter, the crack initiation behavior of coated samples seems to be controlled by other parameters than SX substrate properties. The surface cracks are mainly controlled by mechanical properties of the BC and the substrate/BC chemical and mechanical interaction as already mentioned in the literature (Cervellon et al., 2021; Evans et al., 2009; Pollock et al., 2011; Totemeier et al., 1993). **Figure V-3** depicts the results of **Figure IV-25** added in **Figure V-1** containing only the 3 labeled areas to compare the impact of the coating on the crack initiation mechanism.

The results of bond-coated specimens are lying inside the red and the yellow hatched zone. However, most of the results are inside the red zone.

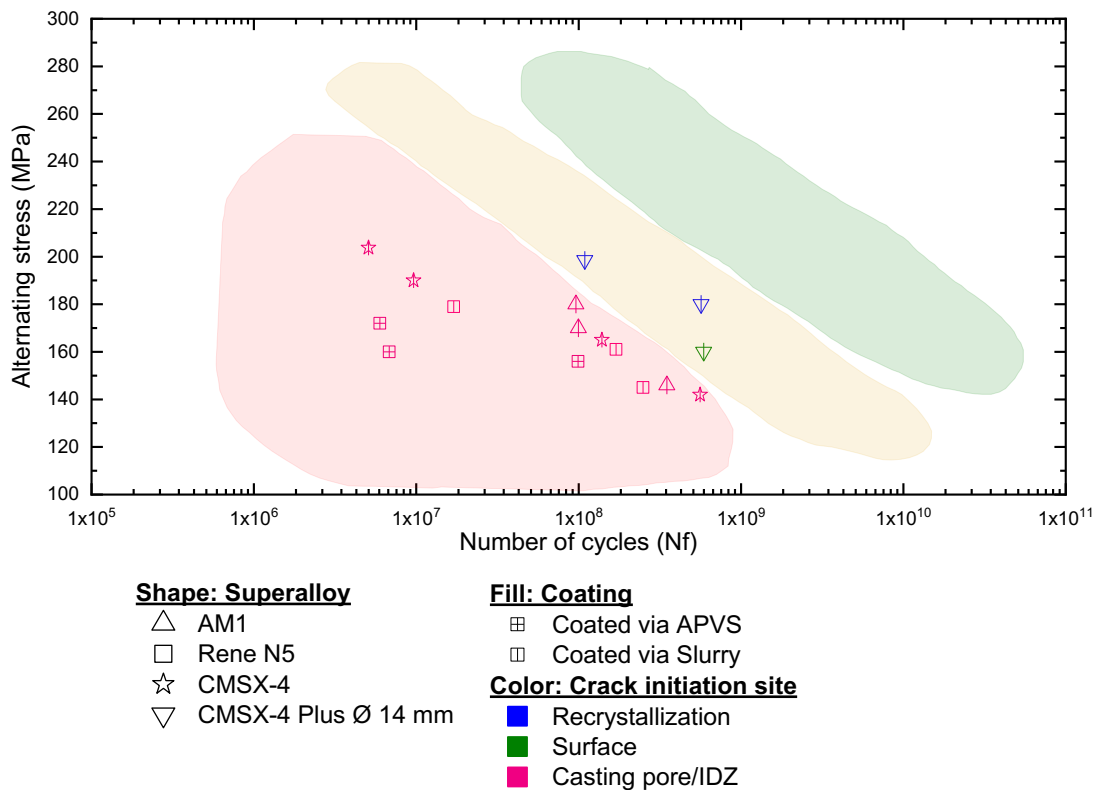


**Figure V-3** S-N diagram for 1,000 °C,  $R_c = -1$ , and  $f = 20$  kHz gathering the results of **Figure IV-25** and the three labeled areas of **Figure V-1**. The alternating stress  $\sigma_a$  is plotted as a function of the number of cycles to failure.

From the results obtained in **Chapter IV**, the crack initiation at the coating surface takes place in the very first cycles. The propagation into the substrate then becomes the main contribution to the fatigue life of the samples that fails through a surface crack initiation process. The NiAl BC studied in this thesis was shown to have a very low ductility at 1,000 °C whatever the deposition method, the test frequency or test stress ratio. Consequently, a “brittle” coating leads to a fatigue life degradation (Totemeier et al., 1993).

Thus, having BC more ductile would be very useful to assess the impact of the BC behavior on the VHCF life of the coated specimens. For example the Ni(Pt,Al) coating that turns to be ductile at high temperatures due to the phase transformation from  $\beta$  phase to  $\gamma+\gamma'$  is known to increase the ductility (Alam et al., 2013; Maurel et al., 2021). Moreover, a similar effect was observed by Cervellon et al. (Cervellon et al., 2021) on aged coated (NiCoCrAlYTa) specimens. The overaging has induced the transformation of  $\beta$  phase into  $\gamma+\gamma'$  precipitates, increasing the BC mechanical resistance to cracking at high temperatures, and even though a RX formed in the superalloy (sub-)surface, the transformation ( $\beta \rightarrow \beta + \gamma + \gamma' \rightarrow \gamma + \gamma'$ ) was beneficial to the specimen VHCF life. A similar trend was also observed in the AM1 + NiAlPt/EB-PVD top coat loaded in out-of-phase thermo-mechanical fatigue (Mauget et al., 2017).

We then came to the following fact that, on the one hand, for the bare samples, the crack initiation is highly influenced by the superalloy processing parameters; while on the other hand, *the coated samples VHCF life is controlled mainly by the BC intrinsic behavior (i.e., brittle vs ductile) in these conditions.*

**Figure V-4** shows how the coating influences the fatigue limit. The results obtained in **Figure IV-25** are compared with the results depicted in **Figure V-2**. In addition, the results obtained by Cervellon et al. (Cervellon et al., 2021) for the NiCoCrAlYTa coated samples are also added to the plot. As one can observe, the fatigue limit for the coated samples was shifted by almost 50 h at high alternating stresses and by  $\approx 500$  h at low alternating stresses. Thus, it evidences that the mismatch of physical properties of the multilayered system influences the residual stresses and strains and temperature-related service stresses and strains as the crack pass from the bond coat to the interdiffusion zone into the substrate (Pollock et al., 2011), leading to early crack initiation.

The effect of these heterogeneous physical properties can be enhanced by the substrate and coating preparation as well as by the substrate/coating compatibility. Indeed, it determines the oxidation resistance of aluminized Ni-based SX superalloys. For example, systems with grit-blasted surfaces reveal a worse oxidation resistance during tests because of the detrimental effect of remaining alumina particles originating from the surface grit-blasting on the diffusion processes at high temperatures, increasing the local stress magnitude at the coating/substrate interface during the heating (Cervellon et al., 2021; Kromer et al., 2018; Nowak et al., 2019). On the other hand, laser patterning of the substrate surface changes the top-coat stress distribution improving the time to spallation in creep and thermal cycling oxidation (Kromer et al., 2018).

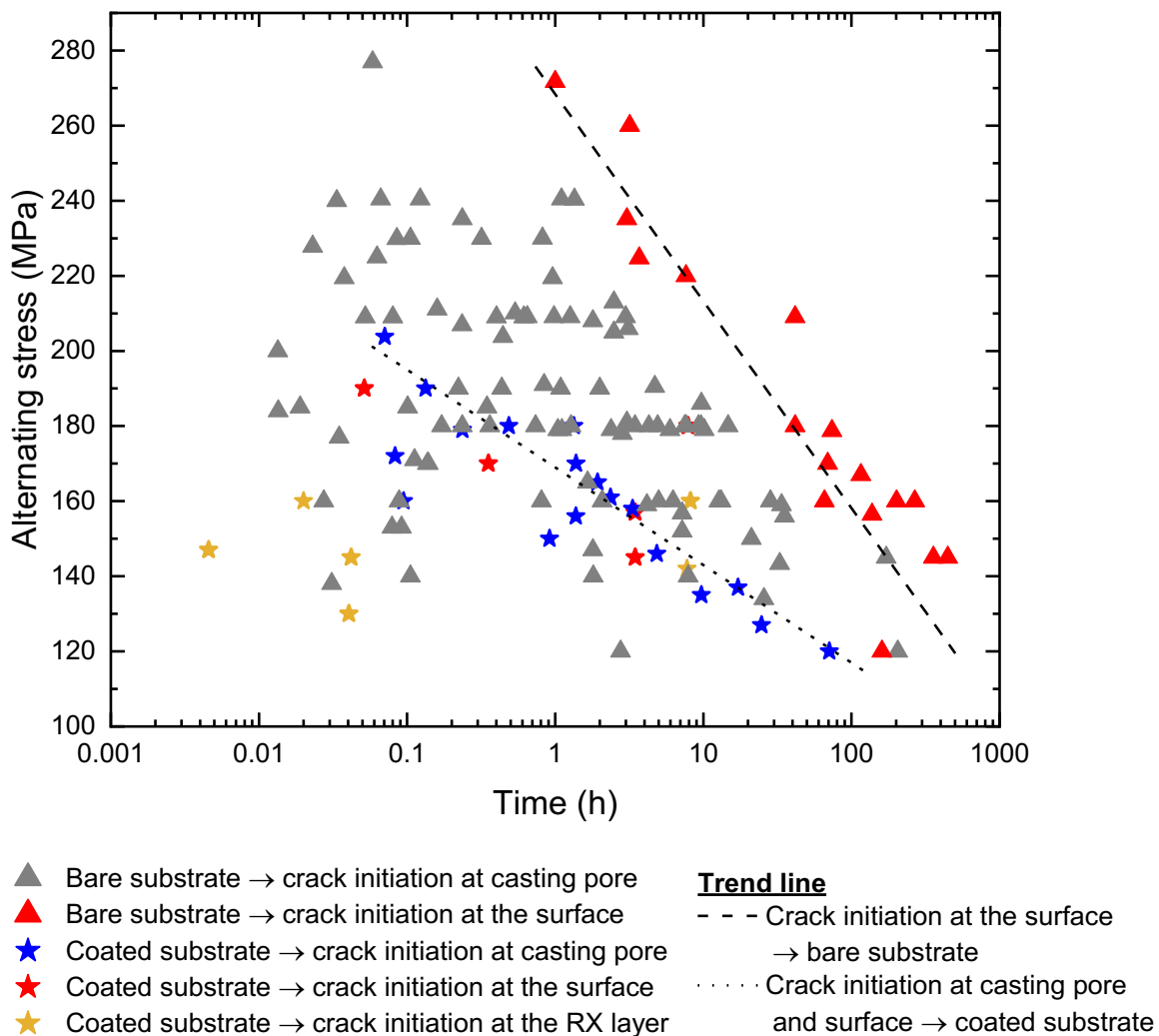


**Figure V-4** Alternating stress as a function of test duration diagram at 1,000 °C,  $R_e = -1$ , and  $f = 20$  kHz gathering the results from Institut Pprime from this thesis and database from (Cervellon, 2018).

## **General conclusions and future prospects**



The focus of this PhD thesis was the investigation of the crack initiation transition from internal sites to the surface at high temperatures and at very high frequencies with and without a coating deposition for different Ni-based SX superalloys. First, for the nine uncoated Ni-based SX superalloys, fast solidification processes (LMC and AM) and the HIP treatment were the focus of study in the VHCF ( $R_e=-1$ , 20 kHz, and 1,000 °C) regime. Second, for the five Ni-based SX superalloys NiAl coated via APVS or Slurry, two fatigue regimes were investigated: LCF ( $R_\sigma = 0.05$ , 0.5 Hz, and 900/950 °C) and VHCF.

The two main conclusions obtained from this PhD thesis are listed below:

- *For uncoated specimens, once the internal defects are small enough, the crack initiation switches to the surface, increasing the VHCF life by a factor of at least one decade compared to the specimens that fails at small casting pores (10 - 20  $\mu\text{m}$  diameter). The fatigue life is then controlled by the oxidation at 1,000 °C. Thus, the alloy's chemistry /environmental resistance control the intrinsic VHCF life. A new surface damage mechanism for "defect-free" specimens has been revealed. The author suggests that there is no fatigue limit in these VHCF conditions as oxidation may always be the source of crack initiation at the lowest alternating stresses.*
- *For NiAl coated specimens, despite the very fast crack initiation in the bond coat, the casting pore positioned close to the IDZ are controlling the VHCF life of at least three Ni-based SX superalloys. It was suggested that the local microstructure close to the IDZ is favorable to induce a premature development of the rough zone. This second situation leads to a VHCF life deficit of at least one decade. A (new) second damage mechanism was proposed to describe such original scenario.*

Several additional conclusions are summarized below:

#### Uncoated specimens:

- The VHCF tests demonstrated that the chemical composition of the Ni-based SX alloys has almost no impact on the fatigue life under fully reversed loading when the main crack initiation site is a casting pore. An impact has only been observed at positive ratio due to the contribution of creep damage in addition to the fatigue one.

- The casting pores size (diameters larger than 30  $\mu\text{m}$ ) and position define the superalloys' VHCF life. The larger the casting pore's diameter, the shorter the VHCF life.
- The HIPing process increases the fatigue life of the Ni-based SX superalloys by at least two decades when performed accurately. However, two consequences can result from this a method: recrystallization or incipient melting. The first one has been shown to be more detrimental to the fatigue life than a casting pore of the same size if the misorientation is higher than 20 ° (i.e., HAGB). Even though the incipient melting develops under high pressure (100 MPa), the melted areas have been shown to solidify with the same orientation as the parent material and they do not influence the crack damage mechanism and the VHCF life.
- Additive manufacturing can lead to a defect “free” Ni-based SX superalloy increasing the fatigue life and switching the crack initiation from the internal defects to the surface. However, the “processing” related stored dislocations in the material's bulk is another issue inherent to the additive manufacturing technique that could result in a premature internal failure. Both LMC and additive manufacturing solidification can lead to HAGB. These defects were proven to decrease the VHCF life by at least two decades at best or inducing immediate failure as soon as the specimen resonate in the worst case. The study proposes that these HAGB grains increase the frequency of resonance leading to a shear stress concentration in the superalloy/grain interface and a premature failure.
- The HIPing and the additive manufacturing processes, if well controlled, demonstrated to be the best methods to increase the fatigue life of the Ni-based SX superalloys up to its chemical limit.

#### NiAl coated specimens:

- An irregular  $\gamma/\gamma'$  microstructure is more detrimental to the LCF endurance than a poor polishing, or even the diffusion of a bond coat. Even though the diffusion heat treatment did not influence the microstructure of the AM1 and Rene N5 alloys, it has highly decreased the tensile and LCF endurance of the MAR-M200 + Hf alloy because of the dissolution of ultrafine tertiary  $\gamma'$  precipitates.
- A lack of ductility of the NiAl bond coat at high temperature was observed whatever the superalloy and the deposition method. The bond coat cracks in the very first few cycles in air or in vacuum, under low or even under very high frequencies, under positive or negative stress

ratio proving that the crack initiation and propagation up to the IDZ is intrinsic to the BC at these temperatures (i.e., 900 - 1,000 °C).

- The VHCF life of NiAl coated CMSX-4 Plus was controlled by a recrystallized layer below the surface where the crack propagation is stopped by the oxidation activity in an Al rich layer with a VHCF life hardly affected compared to uncoated specimens.

Finally, from all this PhD work, the author is proposing **Table 2** as a summary of conditions favoring fatigue crack initiation at the surface/at internal sites.

**Table 2** Summary of processing and mechanical parameters influencing the crack initiation mechanism. ↓ for decrease/low. ↑ for increase/high. !! for attention. RX for recrystallization.

<i>Processing parameters</i>	<i>Main contributions</i>	<i>Promotes the crack initiation at</i>
<b>Fast solidification rate (e.g., LMC)</b>	↓ casting pores size !! RX	Surface
<b>Slow solidification rate (e.g., Bridgman)</b>	↑ casting pores size	Internal
<b>Additive manufacturing (PBF-E)</b>	↓ casting pores size !! RX !! ↑ dislocations' density	Surface
<b>Heat treatment</b>	↑ the homogenization → ↑ oxidation resistance	Internal
<b>HIP treatment</b>	↓ the casting pores size !! RX	Surface
<b>Coated substrate</b>	↑ oxidation resistance !! interaction casting pore + IDZ !! RX	Surface
<i>Mechanical loading</i>	<i>Main contribution</i>	<i>Promotes the crack initiation at</i>
<b>High temperatures</b>	↑ Oxidation + faster element's diffusion	Surface
<b>Intermediate temperatures</b>	≈ Oxidation + stacking fault shearing	Internal/surface
<b>Low temperatures</b>	↓ Oxidation + APB shearing	Internal
<b>Low frequencies</b>	↑ time + plastic deformation	Surface
<b>Very high frequencies</b>	↓ time + elastic deformation	Internal
<b>R=-1 and low frequency</b>		Surface
<b>R=-1 and high frequency</b>		Internal if defects
<b>High maximum applied stress (R&gt;0)</b>	↑ $\Delta k_{local}$ + ↑ ratcheting	Surface
<b>Low maximum applied stress (R&gt;0)</b>	↓ $\Delta k_{local}$ + ↓ plastic deformation	Internal
<b>Vacuum</b>	↓ Oxidation	Internal
<b>Air</b>	↑ Oxidation	Surface

## Future prospects

Even if a huge experimental database has been generated in this work to understand the crack initiation transition from the internal casting defects to the surface, many other questions remain. Still, further analysis and characterizations to understand the mechanisms proposed should be carried out in the future. Hereafter, the author proposes further analyses/characterizations:

- For internal crack initiation mechanisms, the crack initiation phase is the major contribution to the total VHCF life. However, the respective contributions of initiation and propagation to the total VHCF life are still unclear when a crack initiation at the surface is observed. The author suggests that VHCF tests using notched specimens could be useful to elucidate such a question.
- For surface crack initiation, the author also suggests that it would be ideal to perform VHCF tests in vacuum or, at least, in a protective environment. Being able to measure the crack propagation rates in these VHCF conditions at high temperature would be very useful. However, to answer this question, it would be necessary to develop a specific VHCF fatigue bench.
- Working around the question of VHCF life modeling is still of great importance from a component design point of view. Further improving a FIP approach and correlating it with processing parameters would be useful to develop process-sensitive modeling tools.
- Further analysis of  $\gamma/\gamma'$  bond-coated superalloys (i.e., bond coats with ductility at high temperature) under the VHCF regime and high temperatures would be interesting to analyze if the crack initiation would completely shift to the internal defects.
- The aging heat treatment of the superalloy/bond-coat system must be adapted to the substrate to diminish the effect of the “extra” treatment on the superalloy microstructure and thus the mechanical properties. This is of utmost importance from a component refurbishment point of view.
- VHCF durability in corrosive environment must also be investigated given the increase in operation temperatures of newer generations aero-engines, leading to new “under-platform” corrosion damage (Koizumi et al., 2020; Kovalchuk and Gleeson, 2020).
- Creep deformed coated specimens must be investigated to evaluate the impact of the IDZ/substrate microstructure degradation on VHCF durability.

# Appendices



## Appendix A. Very high cycle fatigue $R_e=-1$

The following database tests were carried out at 1,000 °C, fully reversed loading, and 20 kHz.

### Appendix A.1. Bare substrate

The Bridgman processed Ni-based SX superalloys database analyzed in **Chapter III** is depicted in **Table A-1**. The samples were polished with a 1  $\mu\text{m}$  grade diamond spray. The alternating stress, the number of cycles, the initiation site, and the casting pore diameter serving as crack initiation site, and the distance from the initiation site up to the free surface are detailed.

*Table A-1 Fatigue tests at 1,000 °C,  $R_e=-1$  and 20 kHz for different superalloys Bridgman, LMC, and PBF-E processed. RZ for the rough zone. HAGB for high angle grain boundary. SG for stray grain.  $\emptyset$  is the casting pore diameter.  $D$  is the distance between the casting pore and the surface.*

<i>Superalloy</i>	$\sigma_a$ (MPa)	$N_f$	<i>Initiation site</i>	$\emptyset$ ( $\mu\text{m}$ )	$d$ ( $\mu\text{m}$ )
<b>Bridgman</b>					
AM1	181	219,103,895	Casting pore + RZ	73	487
AM1	160	449,336,583	Casting pore + RZ	40	192
Rene N5	165	119,166,396	Casting pore + RZ + carbides	48	560
Rene N5	147	129,147,474	Casting pore + RZ + carbides	105	924
Rene N5	170	9,998,722	Casting pore + RZ + carbides	194	8
Rene N5	185	7,265,135	Casting pore + RZ + carbides	94	101
Rene N5	170	9,879,292	Casting pore + RZ + carbides	117	198
ERBO/1	160	6,359,517	Casting pore + RZ	168	26
ERBO/1	140	7,596,723	Casting pores + RZ	117	354
ERBO/1	120	199,025,186	Casting pore + RZ	128	249
ERBO/1	171	8,083,627	Casting pore + RZ	162	66
ERBO/1	140	130,119,786	Casting pore + RZ	78	652
ERBO/1	209	5,761,433	Casting pore + RZ	93	76
ERBO/1	185	1,367,306	Casting pore	87	29
ERBO/1	185	24,945,862	Casting pore + RZ	110	136
DD33 batch 1	240	2,412,117	Casting pore + carbides	26	34

<i>Superalloy</i>	$\sigma_a$ (MPa)	<i>Nf</i>	<i>Initiation site</i>	$\emptyset$ ( $\mu\text{m}$ )	<i>d</i> ( $\mu\text{m}$ )
<b>DD33 batch 1</b>	225	4,521,301	Casting pore + RZ + carbides	16	37
<b>DD33 batch 1</b>	180	309,213,042	Casting pore + RZ + carbides	29	242
<b>DD33 batch 1</b>	204	31,924,080	Casting pore + RZ + carbides	7	54
<b>DD33 batch 2</b>	219	2,708,530	Casting pore + RZ + carbides	62	53
<b>DD33 batch 2</b>	160	359,175,981	Casting pore + RZ + carbides	73	431
<b>DD33 batch 2</b>	180	92,029,650	Casting pore + RZ + carbides	42	154
<b>DD33 batch 2</b>	200	964,841	Casting pore + carbides	64	92
<b>CMSX-4 Plus <math>\emptyset</math> 14 mm</b>	209	28,885,622	Casting pore + RZ	40	18
<b>CMSX-4 Plus <math>\emptyset</math> 14 mm</b>	230	6,146,832	Casting pore + RZ	39	194
<b>CMSX-4 Plus <math>\emptyset</math> 14 mm</b>	180	694,242,760	Casting pore + RZ	85	93
<b>CMSX-4 Plus <math>\emptyset</math> 14 mm</b>	160	149,329,836	Casting pore + RZ	77	170
<b>CMSX-4 Plus <math>\emptyset</math> 40 mm</b>	153	6,596,872	Casting pore + RZ	228	89
<b>CMSX-4 Plus <math>\emptyset</math> 40 mm</b>	153	5,690,909	Casting pore + RZ	99	234
<b>CMSX-4 Plus <math>\emptyset</math> 40 mm</b>	160	1,970,084	Casting pore + RZ	172	32
<b>CMSX-4 Plus <math>\emptyset</math> 40 mm</b>	138	2,229,789	Casting pore + RZ	98	916
<b>CMSX-4 Plus <math>\emptyset</math> 40 mm</b>	184	970,722	Casting pore + RZ	105	166
<b>MC-NG</b>	180	53,132,742	Casting pore + RZ	53	867
<b>TMS-238</b>	159	2,429,899,526	Surface + oxidation	/	/
<b>TMS-238</b>	206	223,971,167	Casting pore + RZ	38	188
<b>TMS-238</b>	230	59,031,546	Casting pore + RZ	44	83

<i>Superalloy</i>	$\sigma_a$ (MPa)	<i>Nf</i>	<i>Initiation site</i>	$\emptyset$ ( $\mu\text{m}$ )	<i>d</i> ( $\mu\text{m}$ )
TMS-238	180	669,261,739	Casting pore + RZ	62	189
TROPEA	180	26,018,942	Casting pore + RZ	72	72
TROPEA	140	569,296,201	Casting pore + RZ	97	86
TROPEA	207	16,939,858	Casting pore + RZ	62	223
TROPEA	159	299,201,877	Casting pore + RZ	95	83
TROPEA	180	16,998,273	Casting pore + RZ	79	217
<i>LMC</i>					
DD33 batch 1	120	11,582,424,312	Surface	/	/
DD33 batch 1	140	9,894,453	HAGB SG	/	/
DD33 batch 1	180	1,882,115	HAGB SG	/	/
DD33 batch 1	157	3,857,631	HAGB SG	/	/
DD33 batch 2	240	97,107,068	Casting pore + RZ	28	80
DD33 batch 2	160	19,261,575,394	Surface	/	/
DD33 batch 2	277	4,216,616	Casting pore + RZ	35	140
DD33 batch 2	186	699,159,135	Casting pore + RZ	24	109
DD33 batch 2	213	179,161,605	Casting pore + RZ	Deformed by the RZ	
DD33 batch 2	145	12,339,914,707	Casting pore + RZ	Deformed by the RZ	
<i>PBF-E</i>					
CMSX-4	145	32,181,329,931	Surface	/	/
CMSX-4	180	8,386,636	HAGB SG	/	/

Two samples without polishing (the surface conditions after the machining) were tested under the VHCF conditions. The tests were carried out to evaluate the residual stresses' influence on the samples' VHCF fatigue life. *No influence of the surface polishing on the fatigue life was observed in these VHCF conditions.* The alternating stress, the number of cycles, the initiation site, the casting pore diameter, and the distance from the initiation site up to the free surface are detailed in **Table A-2**

**Table A-2** Fatigue tests at 1,000 °C,  $R_e=-1$  and 20 kHz for different superalloys Bridgman processed and no polishing. RZ for the rough zone.  $\emptyset$  is the casting pore diameter.  $d$  is the distance between the casting pore and the surface.

Superalloy	$\sigma_a$ (MPa)	$N_f$	Initiation site	$\emptyset$ ( $\mu\text{m}$ )	$d$ ( $\mu\text{m}$ )
<b>Bridgman</b>					
AM1	179	75,073,307	Casting pore + RZ	40	284
Rene N5	190	16,100,743	Casting pore + RZ + carbides	136	76

**Figure A-1** shows the S-N diagram gathering all VHCF results for the Bridgman processed DD33 and Rene N5 samples. The diagram complements the brief discussion about the influence of carbides on the VHCF life in **Chapter III sub-section 2.1**. The red square symbols represent the Rene N5 samples. The black triangle symbols represent the DD33 specimens. The Rene N5 results presented scattered fatigue life when compared with the DD33 results.

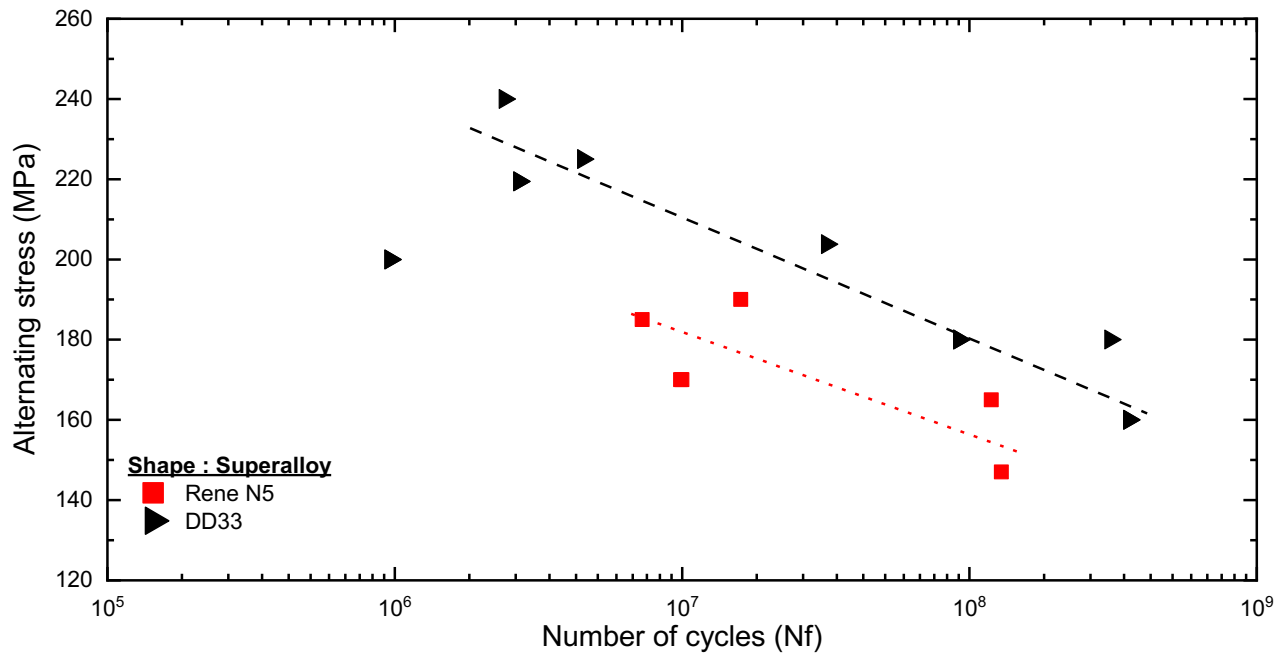


**Figure A-1** S-N diagram for 1,000 °C,  $R_e = -1$ , and  $f = 20$  kHz gathering the results from the samples machined from the DD33 and Rene N5 Bridgman solidified rods. The alternating stress is plotted as a function of the number of cycles to failure.

**Appendix A.2. Samples HIP treated**

The HIPed Ni-based SX superalloys database analyzed in **Chapter III** is depicted in **Table A-3**. The alternating stress, the number of cycles, the initiation site, the casting pore diameter, and the distance from the initiation site up to the free surface are detailed.

*Table A-3 PBF-E processed, and HIP treated specimens. LAGB for low angle grain boundary. HAGB for high angle grain boundary. SG for stray grain. RZ for the rough zone.  $\emptyset$  is the casting pore diameter.  $D$  is the distance between the casting pore and the surface.*

<i>Superalloy</i>	<i>HIPing location</i>	<i><math>\sigma_a</math> (MPa)</i>	<i>Nf</i>	<i>Initiation site</i>	<i><math>\emptyset</math> (<math>\mu\text{m}</math>)</i>	<i>d (<math>\mu\text{m}</math>)</i>
<b>Bridgman</b>						
<b>ERBO/1</b>	<i>RUB</i>	181	309,273,937	LAGB subgrain	/	/
<b>ERBO/1</b>	<i>RUB</i>	202	80,193,163	LAGB subgrain + RZ	/	/
<b>ERBO/1</b>	<i>RUB</i>	157	369,228,766	LAGB subgrain + RZ	/	/
<b>ERBO/1</b>	<i>RUB</i>	170	74,097,724	LAGB subgrain + RZ	/	/
<b>ERBO/1</b>	<i>RUB</i>	211	30,980,799	LAGB subgrain + RZ	/	/
<b>ERBO/1</b>	<i>RUB</i>	190	122,659,404	LAGB subgrain + RZ	/	/
<b>ERBO/1</b>	<i>RUB</i>	220	34,704,077	LAGB subgrain	/	/
<b>ERBO/1</b>	<i>RUB</i>	168	509,178,791	LAGB subgrain + RZ	/	/
<b>ERBO/1</b>	<i>RUB</i>	160	3,339,620,848	LAGB subgrain + RZ	/	/
<b>ERBO/1</b>	<i>RUB</i>	185	579,232,516	LAGB subgrain + RZ	/	/
<b>ERBO/1</b>	<i>RUB</i>	217	53,048,657	LAGB subgrain + RZ	/	/
<b>ERBO/1</b>	<i>RUB</i>	155	4,299,681,800	LAGB subgrain + RZ	/	/
<b>ERBO/1</b>	<i>RUB</i>	150	9,451,006,935	LAGB subgrain + RZ	/	/
<b>ERBO/1</b>	<i>RUB</i>	190	9,864,642	LAGB	/	/
<b>DD33 batch 2</b>	<i>IMR</i>	200	4,999,749,503	Small casting pore or carbides	/	/
<b>DD33 batch 2</b>	<i>IMR</i>	240	179,092,567	Small casting pore or carbides	/	/
<b>DD33 batch 2</b>	<i>IMR</i>	160	14,519,266,427	Surface	/	/
<b>DD33 batch 2</b>	<i>IMR</i>	260	229,166,809	Surface	/	/
<b>DD33 batch 2</b>	<i>IMR</i>	272	71,897,480	Surface	/	/
<b>DD33 batch 2</b>	<i>IMR</i>	220	549,129,029	Surface + RZ	/	/
<b>DD33 batch 2</b>	<i>IMR</i>	180	4,469,637,350	Small casting pore or carbides	/	/
<b>DD33 batch 2</b>	<i>IMR</i>	145	25,700,972,811	Surface	/	/

<i>Superalloy</i>	<i>HIPing location</i>	$\sigma_a$ (MPa)	<i>Nf</i>	<i>Initiation site</i>	$\emptyset$ ( $\mu\text{m}$ )	<i>d</i> ( $\mu\text{m}$ )
<b>CMSX-4 Plus</b>	CM	152	517,199,023	Surface and casting pore	56	193
<b>CMSX-4 Plus</b>	CM	180	12,330,822	Casting pore + RZ	35	50
<b>CMSX-4 Plus</b>	CM	209	44,139,858	Casting pore + RZ	88	647
<b>CMSX-4 Plus</b>	<i>RUB</i>	235	16,955,964	Small casting pore +TCP phases	/	/
<b>CMSX-4 Plus</b>	<i>RUB</i>	205	179,251,003	Small casting pore +TCP phases	/	/
<b>CMSX-4 Plus</b>	<i>RUB</i>	235	219,200,706	Small casting pore +TCP phases	/	/
<b>CMSX-4 Plus</b>	<i>RUB</i>	219	69,078,618	Small casting pore +TCP phases	/	/
<b>CMSX-4 Plus</b>	<i>RUB</i>	180	539,232,119	Small casting pore +TCP phases	/	/
<b>MC-NG</b>	SAE	180	2,999,887,109	Surface	/	/
<b>PBF-E</b>						
<b>CMSX-4</b>	<i>RUB</i>	167	8,344,413,212	Surface	/	/
<b>CMSX-4</b>	<i>RUB</i>	145	4,890,333,142	LAGB SG + RZ	/	/
<b>CMSX-4</b>	<i>RUB</i>	142	980,910	HAGB SG	/	/
<b>CMSX-4</b>	<i>RUB</i>	170	4,970,459,405	Surface	/	/
<b>CMSX-4</b>	<i>RUB</i>	160	4,730,445,724	Surface	/	/
<b>CMSX-4</b>	<i>RUB</i>	140	1,712,883	HAGB SG + RZ	/	/
<b>CMSX-4</b>	<i>RUB</i>			HAGB SG	/	/
<b>CMSX-4</b>	<i>RUB</i>			HAGB SG	/	/
<b>CMSX-4</b>	<i>RUB</i>			HAGB SG	/	/
<b>CMSX-4</b>	<i>RUB</i>			HAGB SG	/	/
<b>CMSX-4</b>	<i>RUB</i>			HAGB SG	/	/
<b>CMSX-4</b>	<i>RUB</i>			HAGB SG	/	/

**Figure A-2a** shows an exemplary crack initiation site of one tested Cannon-Muskegon HIPed specimen. The white arrow indicates the crack initiation site, the magnification of which is presented in **Figure A-2b**. The critical casting pore has a diameter of  $\approx 60 \mu\text{m}$ .

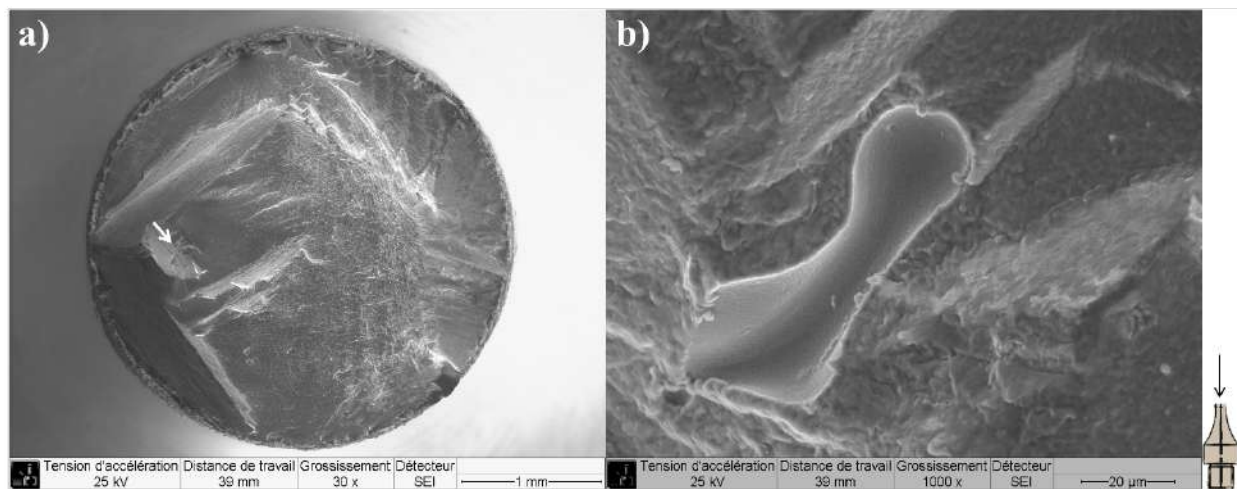


**Figure A-2** Fracture surface observations of CMSX-4 Plus HIPed ( $\sigma_a = 180$  MPa, with  $N_f = 1.2 \cdot 10^7$  cycles). The white arrow indicates the crack initiation site.

Several EBSD characterizations of ERBO/1 HIPed sample ( $\sigma_a = 190$  MPa, with  $N_f = 9.8 \cdot 10^6$  cycles) were presented in **Chapter III sub-section 3**. **Figure A-3** and **Figure A-4** show two complementary analysis of the crystallography around compacted pores.

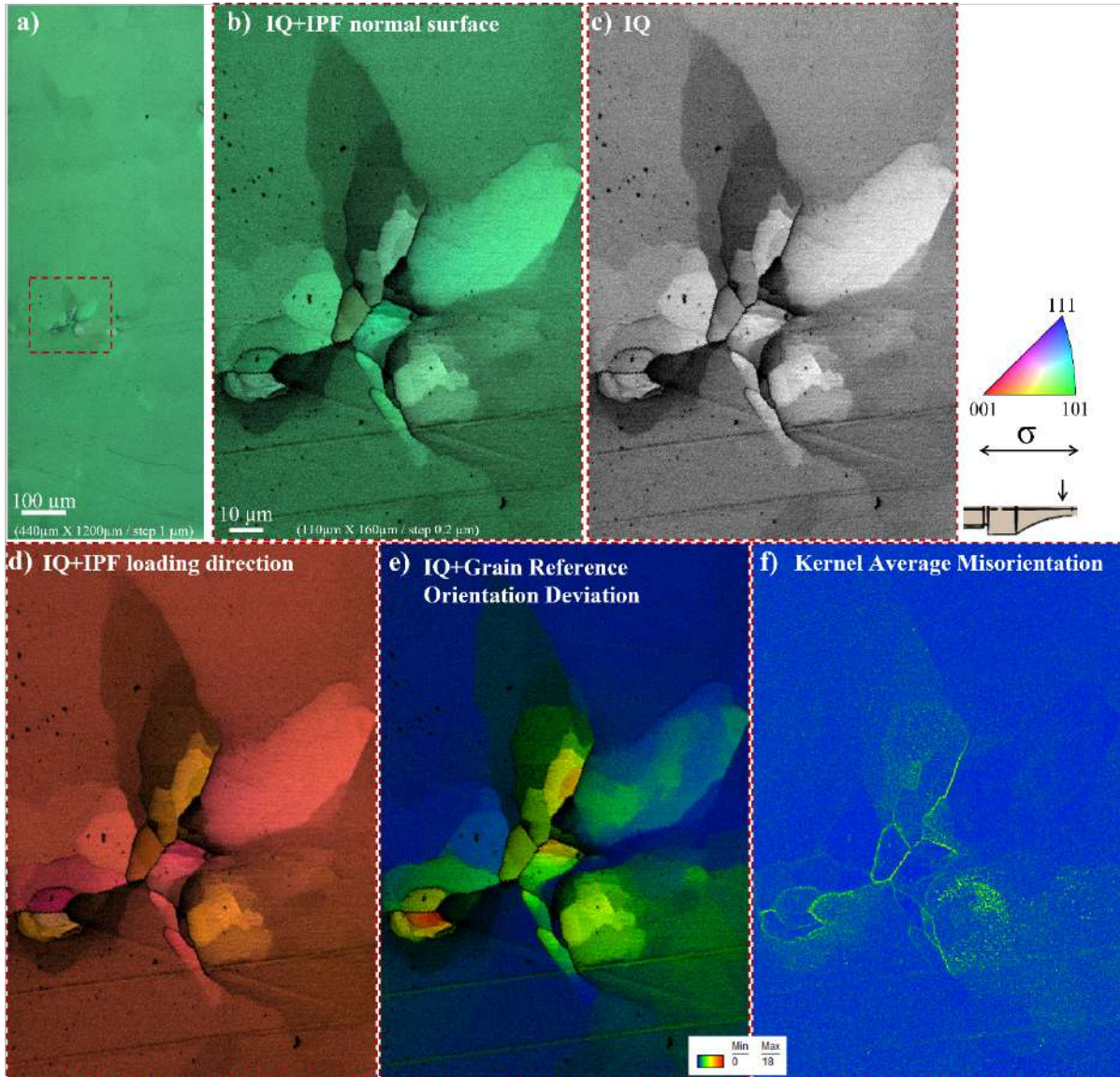


**Figure A-3** EBSD characterization of ERBO/1 HIPed sample illustrated in **Figure III-11a** ( $\sigma_a = 190$  MPa, with  $N_f = 9.8 \cdot 10^6$  cycles). The analysis was carried out far from the fracture surface. Sample's image quality (IQ) superimposed to the inverse pole figure (IPF map) (a). Magnification of the feature indicated by the red dotted square, IQ superimposed to the IPF map (b), IQ (c) IQ superimposed to the IPF map normal to the surface (d), IQ superimposed to the grain reference orientation deviation (e), and Kernel average misorientation (f).

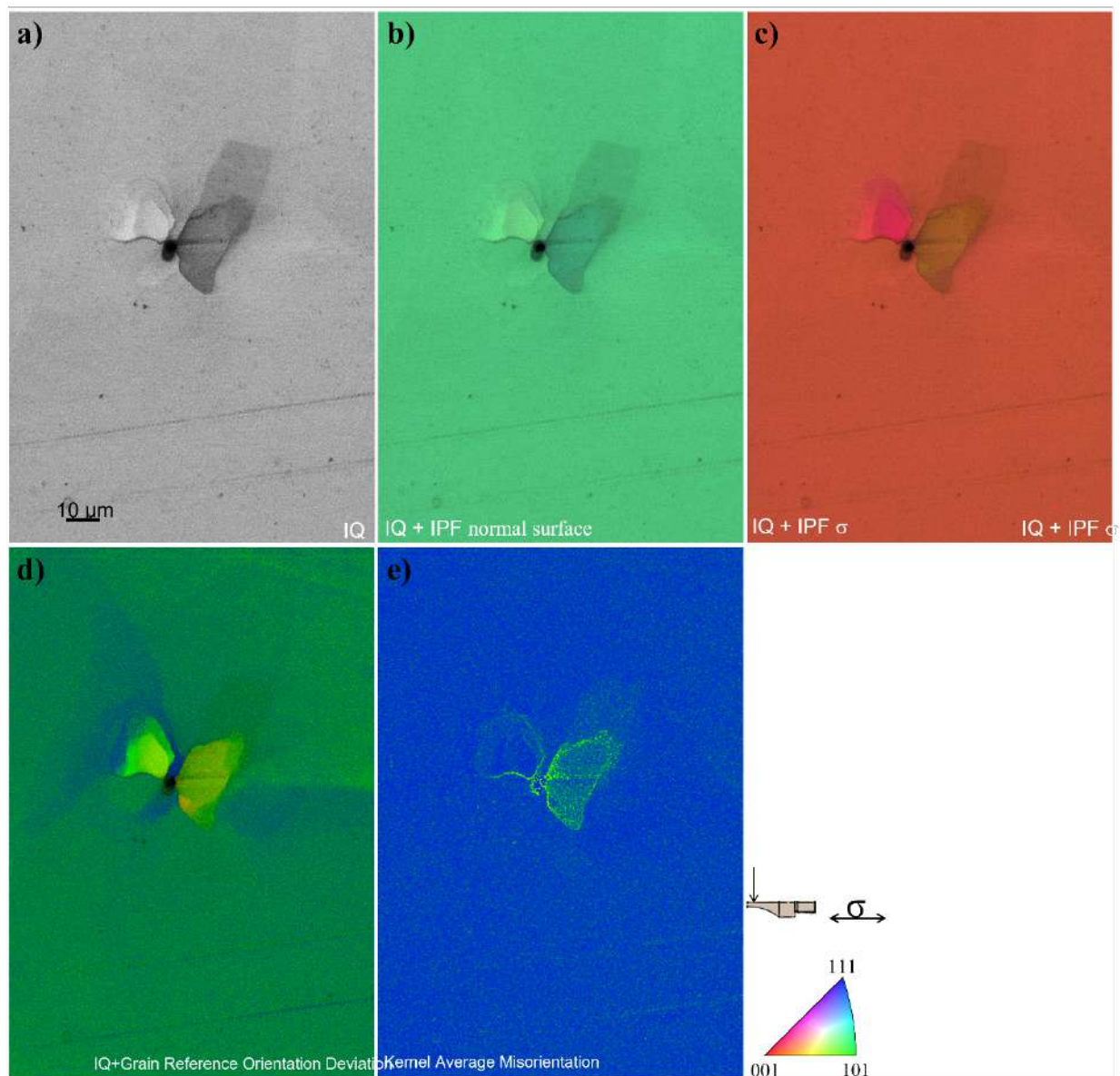


**Figure A-4** EBSD characterization of ERBO/1 HIPed sample illustrated in **Figure III-11a** ( $\sigma_a = 190$  MPa, with  $N_f = 9.8 \cdot 10^6$  cycles). The analysis was carried out far from the fracture surface. Sample's image quality (IQ) (a). IQ superimposed to the inverse pole figure (IPF map) normal to the surface (b), IQ superimposed to the IPF map in the loading direction (c) IQ superimposed to the grain reference orientation deviation (GROD) (d), and Kernel average misorientation (KAM) (e).

Several EBSD characterizations of CMSX-4 Plus ( $\varnothing$  40 mm) sample HIPed ( $\sigma_a = 180$  MPa, with  $N_f = 5.4 \cdot 10^8$  cycles) were presented in **Chapter III, sub-section 3**. **Figure A-5** show one complementary analysis of the incipient melting.

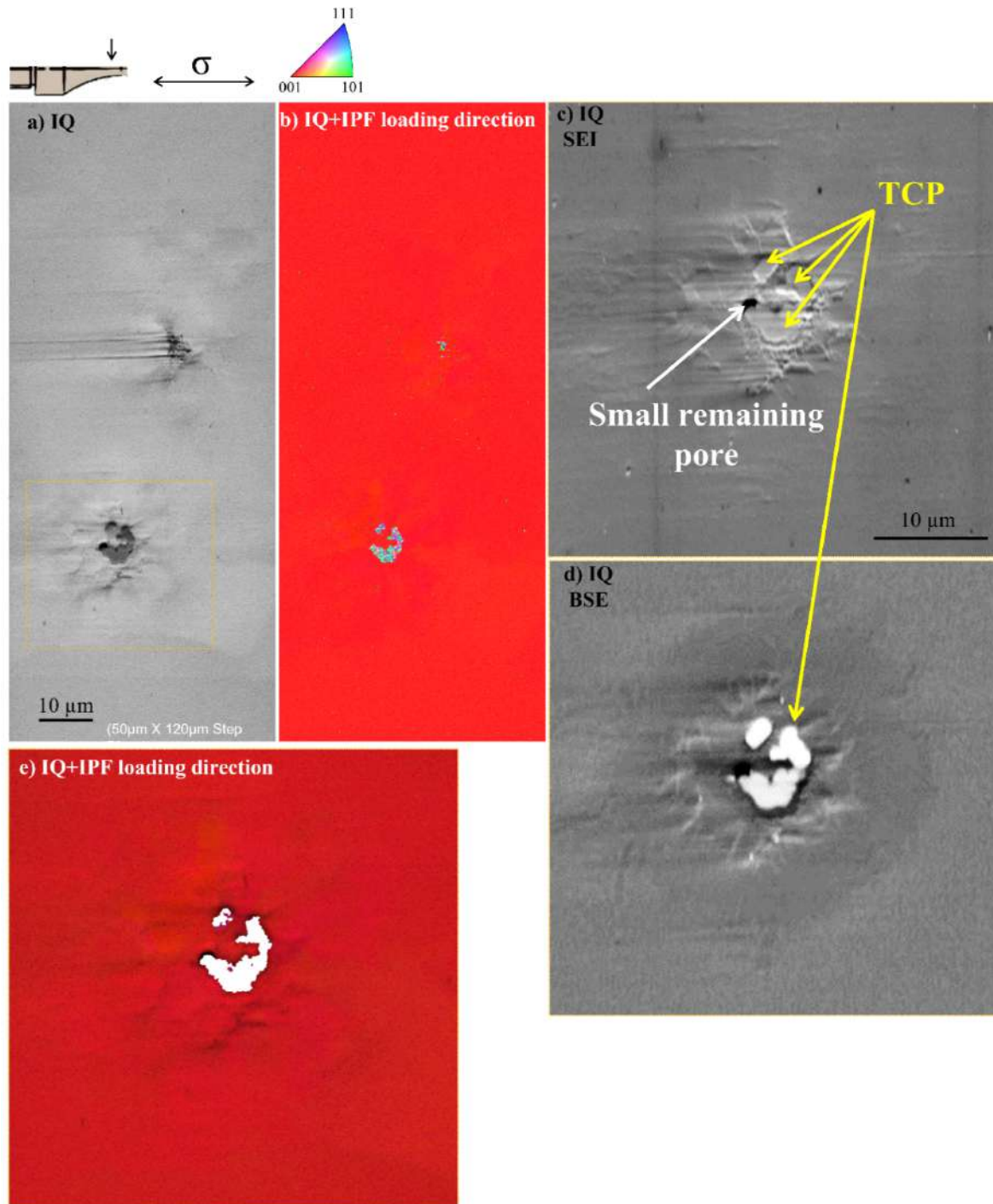


**Figure A-5** EBSD characterization of CMSX-4 Plus ( $\varnothing$  40 mm) sample HIPed ( $\sigma_a = 180\ \text{MPa}$ , with  $N_f = 5.4 \cdot 10^8$  cycles) in **Figure III-11c**. Sample's image quality (IQ) (a) and IQ superimposed to the inverse pole figure (IPF) map in the loading direction (b). Magnification of the incipient melting in IQ SEI (c), BSE (d) mode, and IQ superimposed to the IPF map in the loading direction (e).

**Appendix A.3. Coated substrate**

The bond coated Ni-based SX superalloys database analyzed in **Chapter IV** is depicted in **Table A-4**. The alternating stress, the number of cycles, the initiation site, and the diameter of the casting pore serving as the crack initiation site, and the distance from the initiation site up to the free surface are detailed.

*Table A-4 Fatigue tests at 1,000 °C,  $R_e=-1$  and 20 kHz for different superalloys Bridgman processed and NiAl coated via the Slurry and the APVS method. RZ for the rough zone. IDZ for the interdiffusion zone.  $\emptyset$  is the casting pore diameter.  $D$  is the distance between the casting pore and the surface.*

<i>Superalloy</i>	<i><math>\sigma_a</math> (MPa)</i>	<i>Nf</i>	<i>Initiation site</i>	<i><math>\emptyset</math> (<math>\mu\text{m}</math>)</i>	<i>d (<math>\mu\text{m}</math>)</i>
<b>Slurry</b>					
<b>AM1</b>	146	349,240,114	Casting pore + RZ + IDZ	74	85
<b>AM1</b>	180	96,173,964	Casting pore + RZ + IDZ	63	65
<b>AM1</b>	170	99,581,687	Casting pore + RZ + IDZ	69	110
<b>Rene N5</b>	161	169,921,632	Casting pore + RZ + IDZ + carbides	138	125
<b>Rene N5</b>	179	17,023,339	Casting pore + RZ + IDZ + carbides	109	90
<b>Rene N5</b>	145	249,263,803	Casting pore + RZ + IDZ + carbides	55	84
<b>Rene N5</b>	150	66,003,382	Casting pore + RZ + IDZ + carbides	208	251
<b>CMSX-4</b>	204	5,085,000	Casting pore + RZ + IDZ	52	92
<b>CMSX-4</b>	165	139,095,843	Casting pore + RZ + IDZ	74	224
<b>CMSX-4</b>	190	9,618,259	Casting pore + RZ + IDZ	83	140
<b>CMSX-4</b>	142	559,341,874	Casting pore + RZ + IDZ	80	227
<b>CMSX-4 Plus</b>	160	589,406,512	Surface	/	/
<b>CMSX-4 Plus</b>	199	109,246,925	IDZ + RZ	/	/
<b>CMSX-4 Plus</b>	180	568,139,000	IDZ + RZ	/	/
<b>CMSX-4 Plus</b>	214	92,096,879	IDZ + RZ	/	/
<b>APVS</b>					
<b>AM1</b>	170	25,510,486	Surface	/	/
<b>AM1</b>	190	3,705,422	Surface	/	/
<b>AM1</b>	157	249,256,179	Surface	/	/
<b>Rene N5</b>	156	99,203,266	Casting pore + RZ + IDZ	126	181

<i>Superalloy</i>	$\sigma_a$ (MPa)	<i>Nf</i>	<i>Initiation site</i>	$\varnothing$ ( $\mu\text{m}$ )	<i>d</i> ( $\mu\text{m}$ )
<b>Rene N5</b>	172	5,967,068	Casting pore + RZ + IDZ	208	147
<b>Rene N5</b>	160	6,813,964	Casting pore + RZ + IDZ	97	240

An interrupted test was carried out on a Slurry coated AM1 sample. The test was stopped after 10 seconds ( $\approx 2 \cdot 10^5$  cycles), and a longitudinal sectioning was performed. The SEI images are depicted in **Figure A-6**. The objective was to identify the first stage of crack initiation and propagation in the bond coat and interdiffusion zone. A casting pore of  $\approx 50 \mu\text{m}$  was identified in the observation plane (see red arrow in **Figure A-6**). In addition, several surface cracks along the system BC/IDZ/substrate were identified and are marked by yellow arrows in **Figure A-6**. Thus, *it shows that the BC/IDZ cracks quickly under VHCF conditions at high temperatures.*

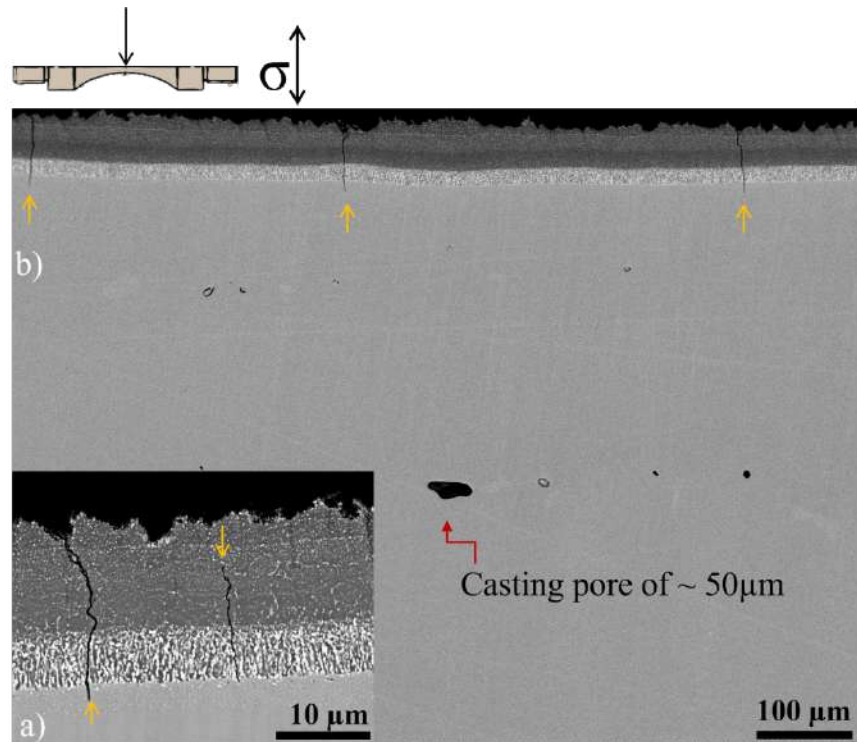


**Figure A-6** Longitudinal analysis of a Slurry coated AM1 sample interrupted with  $2 \cdot 10^5$  cycles: high (a) and low (b) magnification SEI image. The red arrow indicates a casting pore of  $\approx 50 \mu\text{m}$ . The yellow arrows indicate the cracks in the bond coat/IDZ/substrate.

A Slurry coated CMSX-4 Plus sample was characterized via EBSD before the VHCF test. **Figure A-7** depicts the characterizations. **Figure A-7a** shows that the CMSX-4 Plus specimen has a layer of recrystallized grains between the IDZ and the substrate. **Figure A-7b** shows a misorientation of  $19^\circ$  of the bulk (i.e.,  $260\ \mu\text{m}$  from the recrystallized grains layer) up to the subgrains' interface. Finally, **Figure A-7c** demonstrates that after the coating deposition, a misorientation between  $15^\circ$  and  $20^\circ$  happens.

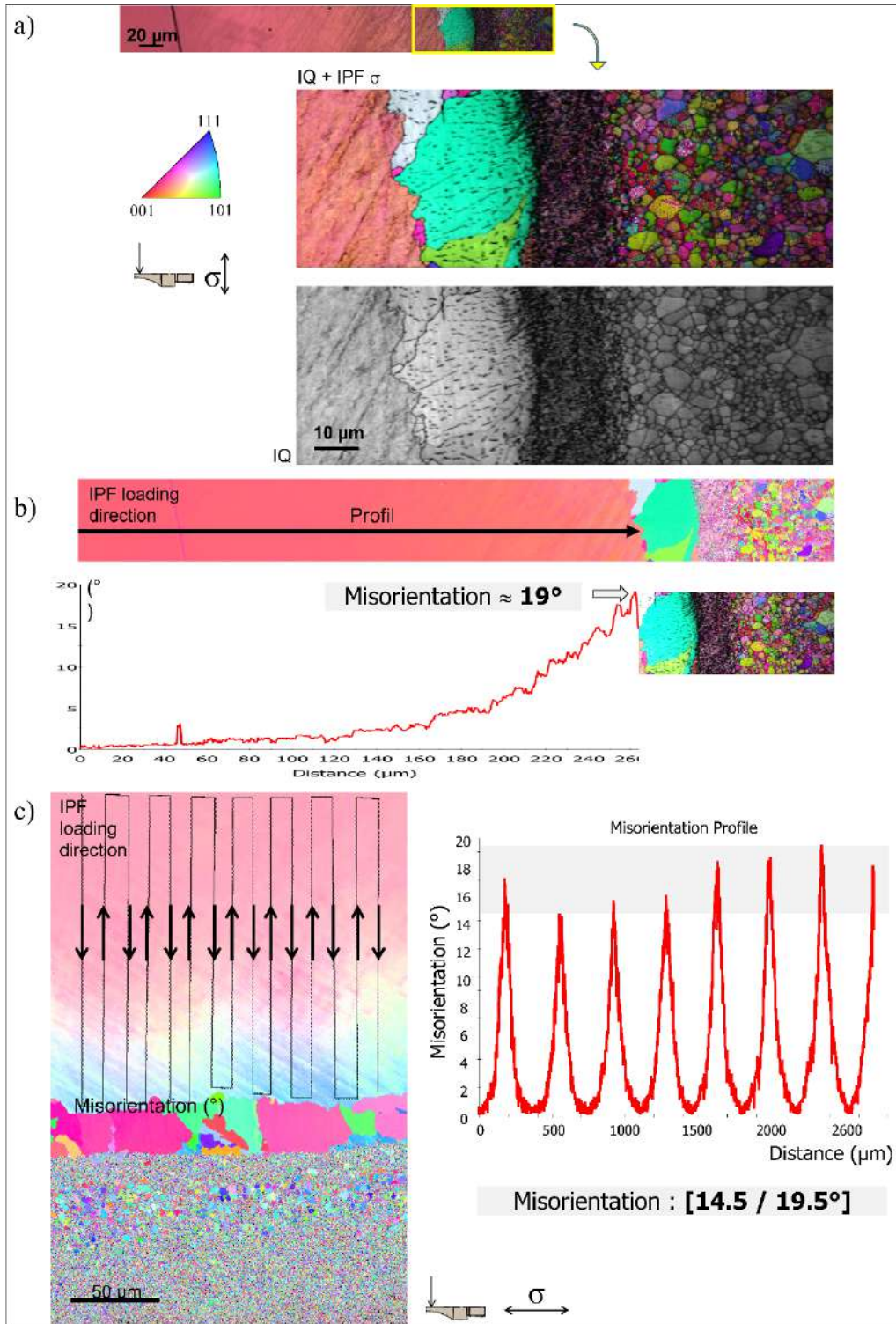


**Figure A-7** EBSD characterization of CMSX-4 Plus sample bond coated via Slurry before the VHCF test. The analysis was carried out far from the fracture surface. Sample's image quality (IQ) superimposed to the inverse pole figure (IPF map) in the loading direction (a). Misorientation analysis from the bulk up to the IDZ (b and c).

**Appendix B. Low cycle fatigue  $R_\sigma=0.05$**

The following database tests were carried out at 900 °C and 950 °C,  $R_\sigma=0.05$ , and 0.5 Hz.

**Appendix B.1. Bare substrate**

The Ni-based SX superalloys specimens analyzed in **Chapter IV sub-section 2** are presented in **Table B-1**. The maximum applied stress, the number of cycles, and the crack initiation site are detailed. For the superalloy AM1, it was detailed the applied heat treatment and polishing.

*Table B-1 Fatigue tests at different temperatures,  $R_\sigma=0.05$  and 0.5 Hz for MAR-M200 + Hf SX, AM1, and Rene N5 superalloys.*

<i>Superalloy</i>	<i>T (°C)</i>	<i><math>\sigma_m</math> (MPa)</i>	<i>Nf</i>	<i>Initiation site</i>
<b>MAR-M200 +Hf SX</b>	900	700	17,083	Surface
<b>MAR-M200 +Hf SX</b>	900	650	36,417	Surface
<b>MAR-M200 +Hf SX</b>	900	500	308,003	Surface
<b>Rene N5</b>	950	750	2,715	Multiples cracks from the surface
<b>Rene N5</b>	950	600	13,797	Surface
<b>Rene N5</b>	950	500	49,518	Internal highly oxidized
<b>Rene N5</b>	950	600	7,888	Surface
<b>AM1 superalloy</b>				
	<b>Polishing</b>	<b><math>\sigma_m</math> (MPa)</b>	<b>Nf</b>	<b>Initiation site</b>
<b>As-cast</b>	SiC 320	750	483	Surface
<b>As-cast</b>	SiC 320	600	3687	Surface
<b>As-cast</b>	SiC 320	500	20265	Surface
<b>As-cast</b>	SiC 320	450	59619	Surface
<b>SHT</b>	SiC 320	600	12,825	Surface
<b>SHT</b>	SiC 320	450	100,500	Surface
<b>SHT</b>	SiC 320	500	61,816	Surface
<b>SHT</b>	SiC 320	750	1,000	Surface
<b>Full HT</b>	SiC 320	750	1,903	Surface
<b>Full HT</b>	SiC 320	500	144,493	Surface
<b>Full HT</b>	Diamond 1 $\mu$ m	500	157,328	Surface
<b>Full HT</b>	Diamond 1 $\mu$ m	750	2,694	Surface
<b>Full HT</b>	Diamond 1 $\mu$ m	600	36,335	Surface

**Figure B-1a** shows a fracture surface of a MAR-M200 +Hf sample tested at maximum stress of 500 MPa and  $3.0 \cdot 10^5$  cycles. **Figure B-1b** illustrates the fracture surface of an AM1 fully HT sample tested at maximum stress of 750 MPa and  $1.6 \cdot 10^5$  cycles. **Figure B-1c** and **d** depicts two fracture surfaces of Rene N5 samples. **Figure B-1c** illustrates the crack initiations at the sample's surface tested at maximum stress of 750 MPa and  $2.7 \cdot 10^3$  cycles, and **Figure B-1d** at the internal feature of the sample tested at maximum stress of 500 MPa and  $4.9 \cdot 10^5$  cycles. The objective is to illustrate the fracture mode of these superalloys under LCF conditions and 950 °C and bare substrate, as it was not illustrated in **Chapter IV**.

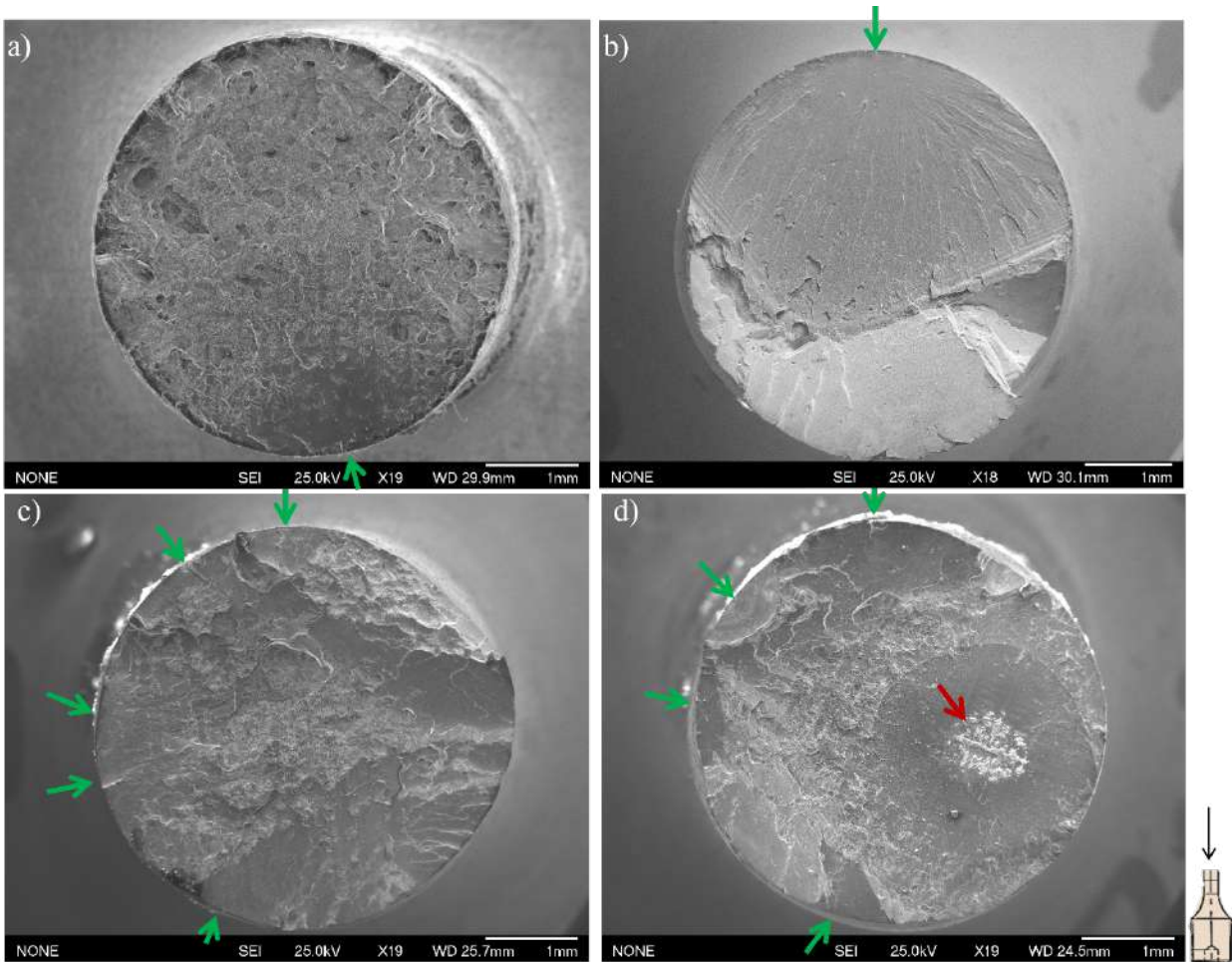


**Figure B-1** Fracture surface observations of MAR-M200 +Hf (a), and AM1 full HT sample (b) with surface crack initiation. Rene N5 sample with surface (c) and internal (d) crack initiation. The green arrows indicate surface initiation. The red arrow indicates the internal crack initiation site.

**Appendix B.2. Coated substrate**

The bond coated Ni-based SX superalloys database analyzed in **Chapter IV** is depicted in **Table B-2** and **Table B-3**. The maximum applied stress, the number of cycles, the initiation site, and the diameter of the casting pore serving as crack initiation site, and the distance from the initiation site up to the free surface are detailed.

*Table B-2 Fatigue tests at different temperatures,  $R_\sigma=0.05$  and 0.5 Hz for superalloys Bridgman processed, and NiAl coated via the Slurry and APVS method.  $\emptyset$  is the casting pore diameter.  $D$  is the distance between the casting pore and the surface.*

<i>Superalloy</i>	$\sigma_m$ (MPa)	<i>Nf</i>	<i>Initiation site</i>	$\emptyset$ ( $\mu\text{m}$ )	<i>d</i> ( $\mu\text{m}$ )
<b>Slurry</b>					
MAR-M200 +Hf SX	650	343	Surface	/	/
MAR-M200 +Hf SX	400	15,358	Surface	/	/
MAR-M200 +Hf SX	500	3,485	Surface	/	/
MAR-M200 +Hf SX	600	977	Surface	/	/
AM1	750	2,851	Surface	/	/
AM1	500	41,726	Surface	/	/
AM1	600	14,055	Surface	/	/
Rene N5	500	68,248	Surface	/	/
Rene N5	750	3,475	Surface	/	/
Rene N5	600	35,854	Casting pore	130	1365
<b>APVS</b>					
AM1	500	108,988	Surface	/	/
AM1	750	2,475	Surface	/	/
AM1	600	16,598	Surface	/	/
AM1	600	17,118	Surface	/	/
AM1 As-cast	600	3,944	Surface	/	/
AM1 As-cast	750	7	Interrupted		
AM1 As-cast	750	414	Interrupted		
AM1 As-cast	750	448	Surface	/	/
AM1 As-cast	600	2,501	Surface	/	/
AM1 As-cast	750	350	Surface	/	/
AM1 As-cast	750	420	Surface	/	/
AM1 As-cast	500	21,241	Surface	/	/

<i>Superalloy</i>	$\sigma_m$ (MPa)	<i>Nf</i>	<i>Initiation site</i>	$\emptyset$ ( $\mu m$ )	<i>d</i> ( $\mu m$ )
AM1 As-cast	600	4,059	Surface	/	/
AM1 As-cast	500	18,414	Surface	/	/
AM1 As-cast	500	9,313	Surface	/	/
AM1 As-cast	450	53,191	Surface	/	/
Rene N5	500	101,862	Internal highly oxidized	?	?
Rene N5	750	3,213	Surface	/	/
Rene N5	600	32,121	Casting pore	113	540

The fracture surface of the AM1 and MAR-M200 + SX samples coated via Slurry are already depicted in Chapter IV. **Figure B-2a** shows the surface crack initiation for the Slurry coated Rene N5 sample tested at 750 MPa and  $3.5 \cdot 10^3$  cycles. **Figure B-2b** shows the APVS coated Rene N5 sample surface crack initiation for the sample tested at 500 MPa and  $3.2 \cdot 10^3$  cycles. **Figure B-2c** shows the surface crack initiation of the APVS coated AM1 fully HT sample tested at 500 MPa and  $Nf = 1.1 \cdot 10^5$  cycles. **Figure B-2d** shows the surface crack initiation of the Slurry coated MAR-M200 +Hf SX tested at 500 MPa and  $Nf = 3.5 \cdot 10^3$  cycles.

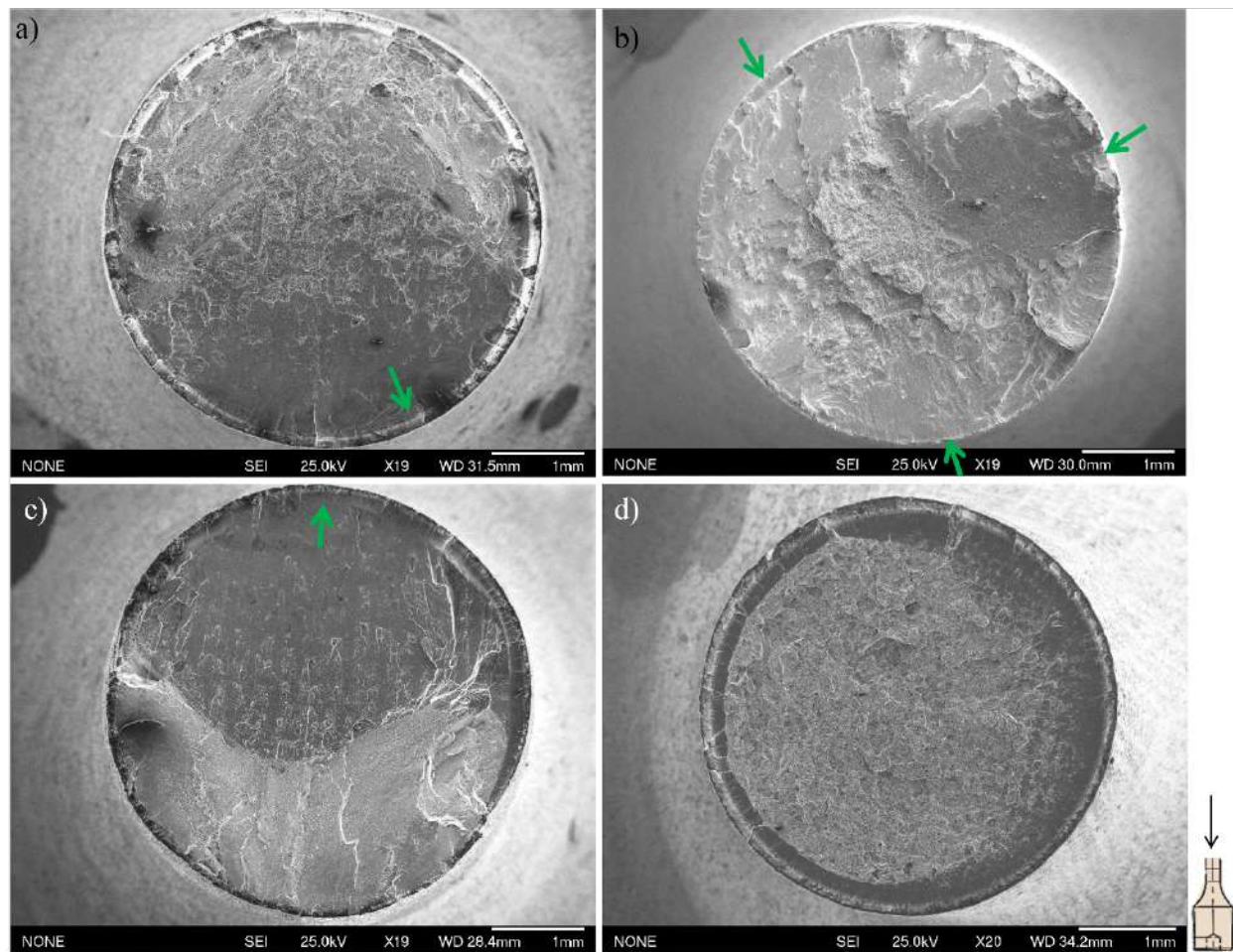


**Figure B-2** Fracture surface observations of Slurry coated Rene N5 sample with surface crack initiation (a) crack initiation. APVS coated Rene N5 sample with surface crack initiation (b). APVS coated AM1 sample fully HT with surface crack initiation (c). Slurry coated MAR-M200 +Hf sample with surface crack initiation (d). The green arrows indicate surface initiation. The red arrow indicates the internal crack initiation site.

**Figure B-3** depicts the EBSD characterization of an AM1 As cast sample coated via APVS ( $\sigma_m = 750$  MPa, with  $N_f = 448$  cycles under air). Three cracks were analyzed, and ***no recrystallization was observed in the crack path or near the crack lips.***

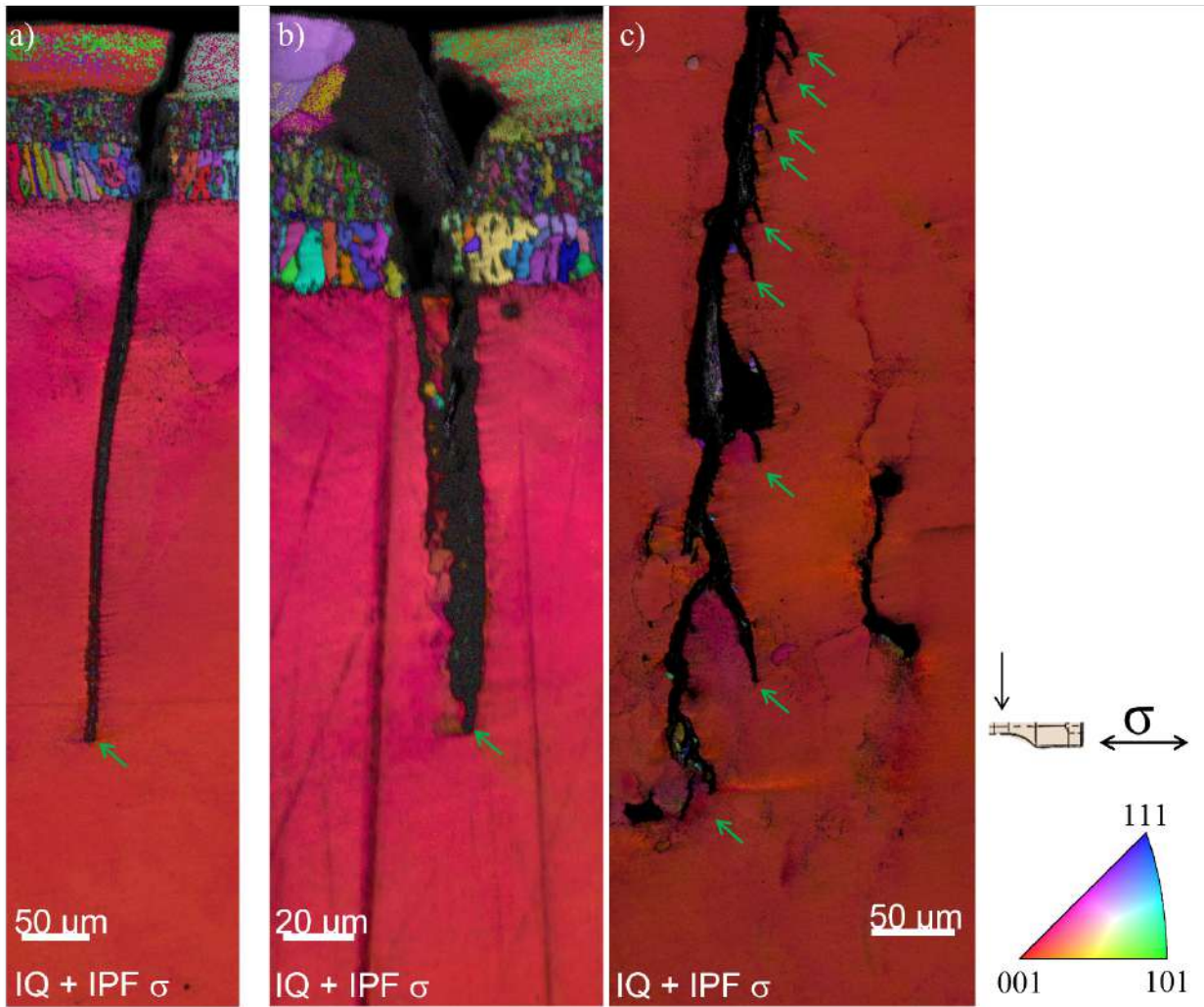


**Figure B-3** EBSD characterization of AM1 As cast sample coated via APVS tested at 950 °C,  $R_\sigma = 0.05$  and 0.5 Hz ( $\sigma_m = 750$  MPa, with  $N_f = 448$  cycles). The analysis was carried out close to the fracture surface. The sample's image quality (IQ) + inverse pole figure (IPF map) in the loading direction of three cracks (a, b, and c).

**Table B-3** depicts the fatigue tests carried out in high vacuum for the MAR-M200 + Hf, AM1, and Rene N5 superalloy. Two fatigue tests were carried up to the rupture, and two were interrupted after 5 cycles.

**Table B-3** Fatigue tests under vacuum at 950 °C,  $R_\sigma=0.05$  and 0.5 Hz for AM1 and Rene N5 superalloys NiAl coated via the APVS method.

<i>Superalloy</i>	$\sigma_m$ (MPa)	<i>Nf</i>	<i>Initiation site</i>
AM1	600	5,736	Surface
Rene N5	600	7,495	Surface
<b>Interrupted tests</b>			
MAR-M200 + Hf SX	650	5	Surface
AM1	750	5	Surface

## Appendix C. Very high cycle fatigue R=0.5

The following tests were carried out at 1,000 °C, positive stress-ratio (R=0.5), and 20 kHz. These results were not mentioned in this PhD thesis as damage mechanisms are different from the ones obtained in pure fatigue conditions. However, the author judged it valuable to present the data to support the subject and part of the final analysis performed in **Chapter V**.

### Appendix C.1. Bare substrate

The Ni-based SX superalloys database for the VHCF tests carried out at a positive stress ratio is depicted in **Table C-1**. The maximum applied stress, the number of cycles, and the initiation site are detailed.

*Table C-1 VHCF tests at 1,000 °C, R = 0.5 and 20 kHz for different superalloys Bridgman and LMC processed. HAGB for high angle grain boundary.*

<i>Superalloy</i>	<i><math>\sigma_m</math> (MPa)</i>	<i>N<sub>f</sub></i>	<i>Initiation site</i>
<b>Bridgman</b>			
<b>MAR-M200 +Hf SX</b>	428	744,514	Surface
<b>MAR-M200 +Hf SX</b>	330	749,107,103	Casting pore
<b>MAR-M200 +Hf SX</b>	303	583,646,082	Surface
<b>MAR-M200 +Hf SX</b>	415	64,065,114	Casting pore
<b>AM1</b>	423	839,339,714	Casting pore
<b>AM1</b>	573	13,967,721	Casting pore
<b>AM1</b>	748	128,856	Surface
<b>AM1</b>	398	3,339,940,874	Casting pore
<b>AM1</b>	623	5,657,660	Casting pore
<b>AM1</b>	528	22,022,382	Casting pore
<b>Rene N5</b>	411	139,234,877	Casting pore
<b>Rene N5</b>	505	449,386,618	Casting pore
<b>Rene N5</b>	523	48,000	Casting pore
<b>Rene N5</b>	490	3,133,156	Casting pore
<b>DD33 batch 1</b>	560	329,894,174	Casting pore
<b>DD33 batch 1</b>	396	4,124,408,559	Internal
<b>DD33 batch 1</b>	638	159,219,626	Casting pore
<b>LMC</b>			
<b>DD33 batch 1</b>	626	16,996,793	HAGB

<i>Superalloy</i>	$\sigma_m$ (MPa)	$N_f$	<i>Initiation site</i>
DD33 batch 1	548	291,166,430	HAGB

**Figure C-1** shows the maximum applied stress ( $\sigma_m$ ) as a function of the number of cycles to failure ( $N_f$ ) diagram gathering all VHCF results obtained for the bare substrate samples.

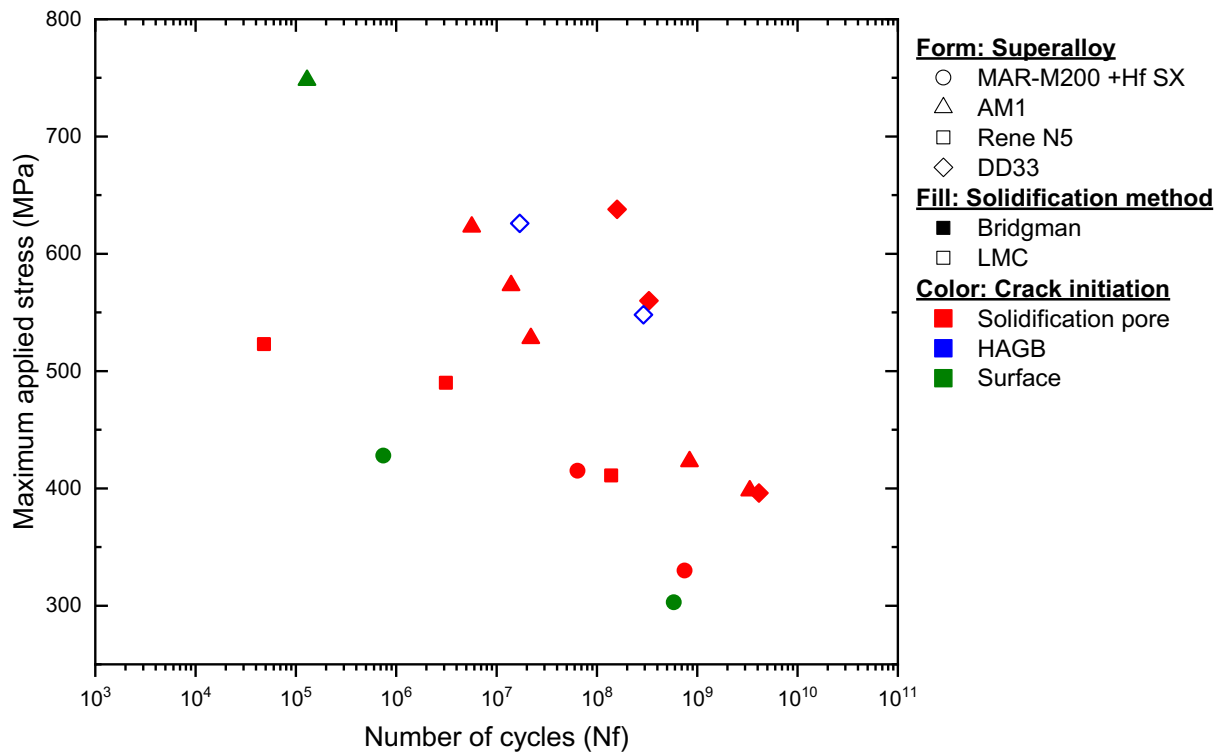


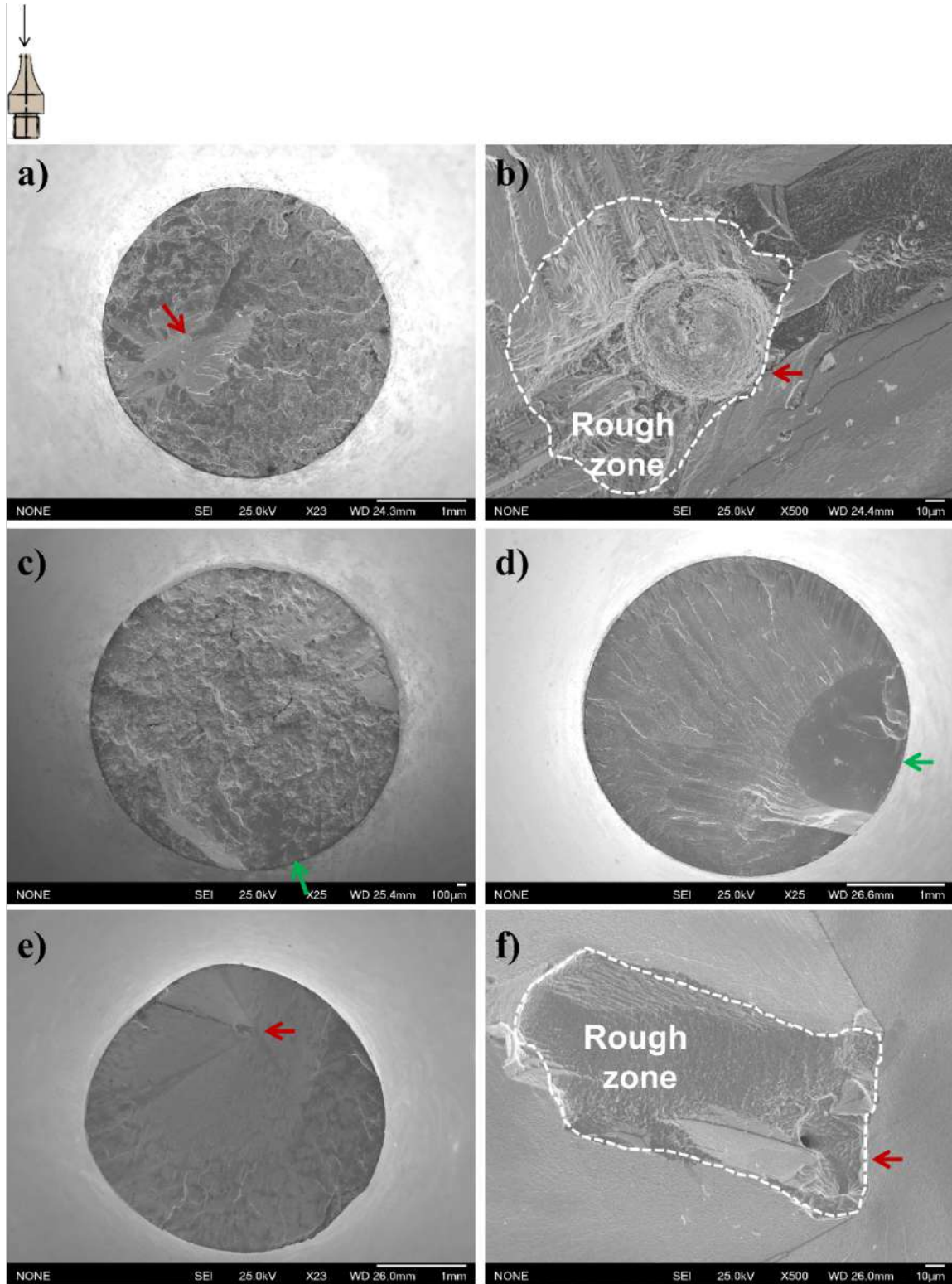
**Figure C-1** S-N diagram for 1,000 °C,  $R = 0.5$ , and  $f = 20$  kHz, gathering the results of the bare samples. The maximum applied stress is plotted as a function of the number of cycles to failure.

From **Figure C-1**, one can see that DD33 performs better in these VHCF conditions, followed by AM1, Rene N5, and then MAR-M200 + Hf SX. This confirms that VHCF properties at positive R ratios are following the respective creep resistance of the alloys (Cervellon et al., 2020b, 2017).

**Figure C-2** depicts the fracture surface observations for samples tested under very high frequencies, positive stress ratio, and high temperatures. Most of the samples failed by internal crack initiation at casting pores: MAR-M200 +Hf SX (**Figure C-2a** and **b**) tested under a

maximum applied stress of 330 MPa and  $7.5 \cdot 10^8$  cycles, AM1 (**Figure C-2e** and **f**) tested at a maximum applied stress of 398 MPa and  $3.3 \cdot 10^9$  cycles, Rene N5 (**Figure C-2g** and **h**) tested at a maximum applied stress of 505 MPa, with  $N_f = 4.5 \cdot 10^8$  cycles, and DD33 Bridgman processed (**Figure C-2i** and **j**) tested at a maximum applied stress of 638 MPa and  $1.6 \cdot 10^8$  cycles. Two examples of samples that failed at the surface are MAR-M200 Hf+ SX (**Figure C-2c**) tested at a maximum applied stress of 428 MPa and  $7.4 \cdot 10^5$  cycles, and AM1 (**Figure C-2d**) tested at a maximum applied stress of 748 MPa and  $1.3 \cdot 10^5$  cycles. Finally, one example of the DD33 LMC processed (**Figure C-2k** and **l**) that probably failed at a HAGB interface. The sample was tested at a maximum applied stress of 548 MPa and  $2.9 \cdot 10^8$  cycles.

In one hand, **Figure C-2b** and **f** show the rough zone (see the white dotted line) around the casting pores, i.e., the main crack initiation site. On the other hand, **Figure C-2h** shows a mode I crack propagation (see the yellow dotted line) around a large casting pore. It seems that at these conditions, there is a mixture of fatigue damage that can be more or less influenced by the superalloy creep properties under the mean stress and high temperature of 1,000 °C.



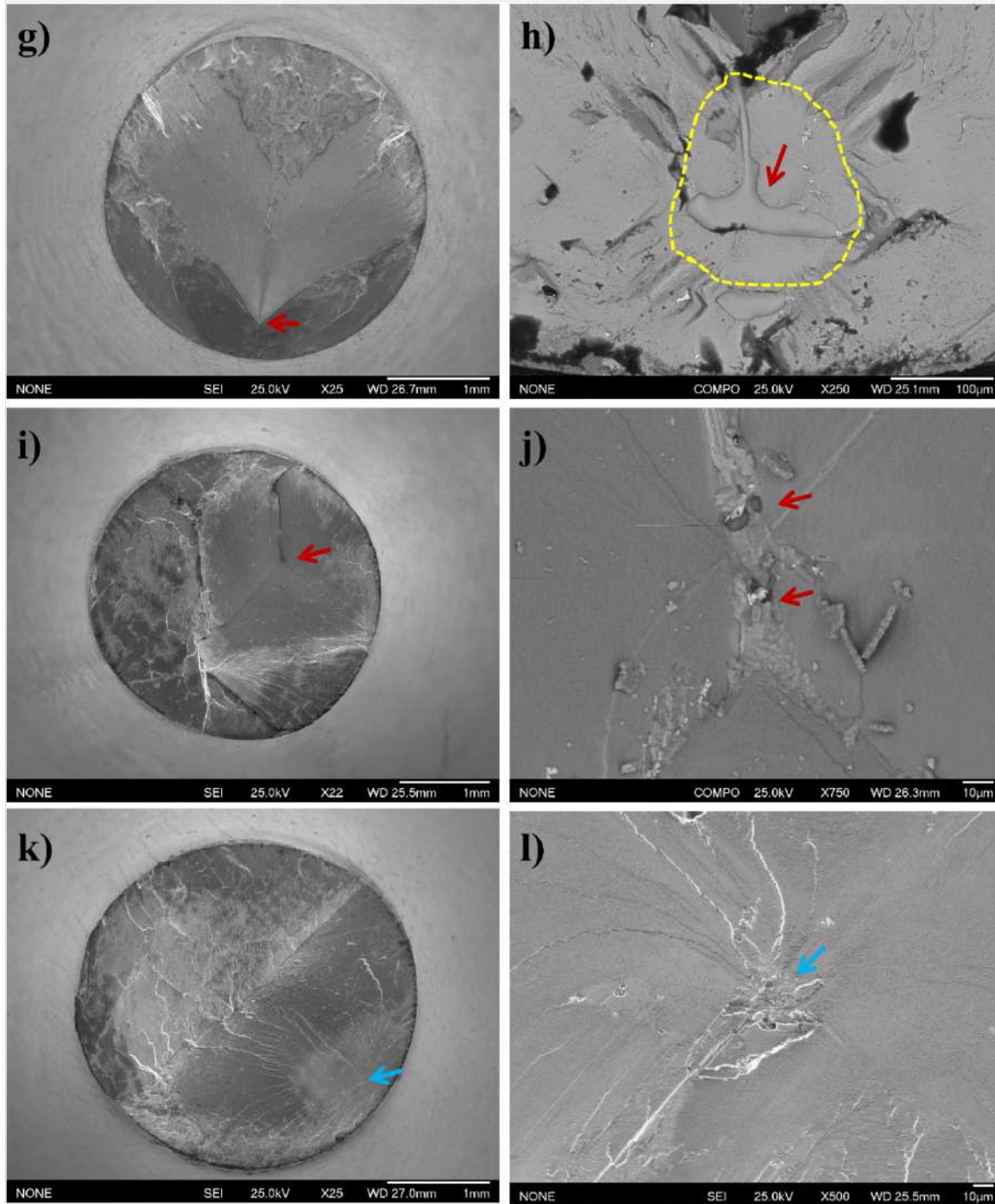


**Figure C-2** Fracture surface observations of samples tested under positive stress ratio. MAR-M200 +Hf SX with internal (a, magnification in b) and surface (c) crack initiation. AMI with surface (d) and internal (e and magnification in f) crack initiation. Rene (g and magnification in h), DD33 Bridgman processed (i and magnification in j), and DD33 LMC processed (k and magnification in l) with internal crack initiation. The green arrows indicate the surface crack initiation site. The red arrows indicate the internal crack initiation site. The blue arrows indicate the crack initiation at HAGB stray grains.

**Appendix C.2. Coated substrate**

The bond coated Ni-based SX superalloys database for the VHCF tests carried out at a positive stress ratio is depicted in **Table C-2**. The maximum applied stress, the number of cycles, and the initiation site are detailed.

*Table C-2 VHCF tests at 1,000 °C, R =0.5 and 20 kHz for different superalloys Bridgman processed and NiAl coated via the Slurry and the APVS method.*

<i>Superalloy</i>	<i><math>\sigma_m</math> (MPa)</i>	<i>Nf</i>	<i>Initiation site</i>
<b>Slurry</b>			
AM1	476	109,121,927	Casting pore
AM1	570	125,000	Surface
Rene N5	580	297,268	Internal
Rene N5	485	479,353,869	Internal
Rene N5	447	709,339,258	Casting pore
CMSX-4	513	150,000	Surface
CMSX-4	354	259,111,846	Surface
CMSX-4 Plus	425	20,000,000,000	Surface
CMSX-4 Plus	517	60,793,585	Surface
<b>APVS</b>			
AM1	576	189,211,214	Casting pore
AM1	347	1,058,513,661	Surface
Rene N5	532	238,750	Casting pore
Rene N5	451	2,618,813	Casting pore

**Figure C-3** shows the  $\sigma_m$  as a function of the Nf diagram gathering all VHCF results obtained for the bond coated samples via Slurry and APVS. The Slurry coated CMSX-4 Plus specimens presented a fatigue life three decades higher than the Slurry coated CMSX-4 specimens, even though all specimens presented crack initiation from the surface. The AM1 specimens presented crack initiation at casting pores or at the surface, and astonishing scattered results that was not observed for the same superalloy no coated under the same conditions of test.

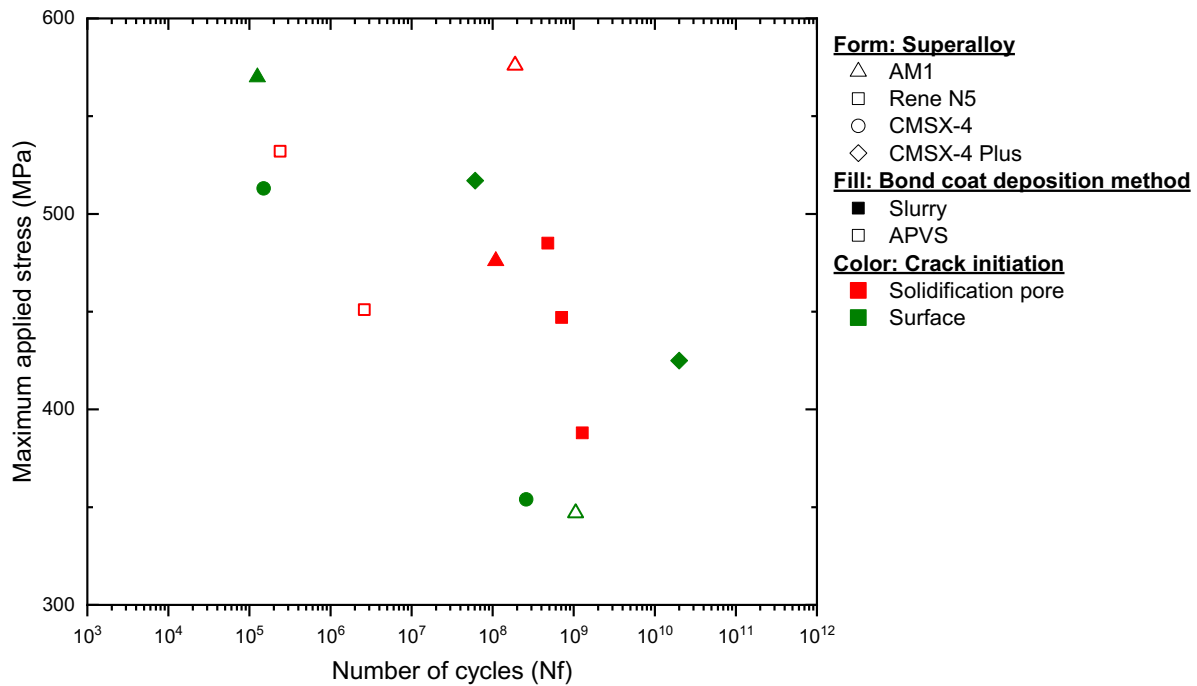


**Figure C-3** S-N diagram for 1,000 °C,  $R = 0.5$ , and  $f = 20$  kHz, gathering the results of the bond coated samples. The maximum applied stress is plotted as a function of the number of cycles to failure.

**Figure C-4** and **Figure C-5** depict the fracture surface observations for bond coated samples tested at very high frequencies, positive stress ratio, and high temperatures. The samples failed by internal crack initiation at casting pores: AM1/Slurry (**Figure C-4a** and **b**) tested under a maximum applied stress of 476 MPa and  $1.1 \cdot 10^8$  cycles, AM1/APVS (**Figure C-5a** and **b**) tested under a maximum applied stress of 576 MPa and  $1.9 \cdot 10^8$  cycles, Rene N5/Slurry (**Figure C-4e** and **f**) tested at a maximum applied stress of 447 MPa and  $7.1 \cdot 10^8$  cycles, and Rene N5/APVS (**Figure C-5d** and **e**) tested at a maximum applied stress of 451 MPa and  $2.6 \cdot 10^6$  cycles.

Several samples failed from the surface: AM1/Slurry (**Figure C-4c** and **d**) tested at a maximum applied stress of 570 MPa and  $1.2 \cdot 10^5$  cycles, AM1/APVS (**Figure C-5c**) tested at a maximum applied stress of 347 MPa and  $1.0 \cdot 10^9$  cycles, CMSX-4/Slurry (**Figure C-4g**) tested at a maximum applied stress of 354 MPa and  $2.6 \cdot 10^8$  cycles, and CMSX-4 Plus (**Figure C-4h**) tested at a maximum applied stress of 517 MPa and  $6.1 \cdot 10^7$  cycles.

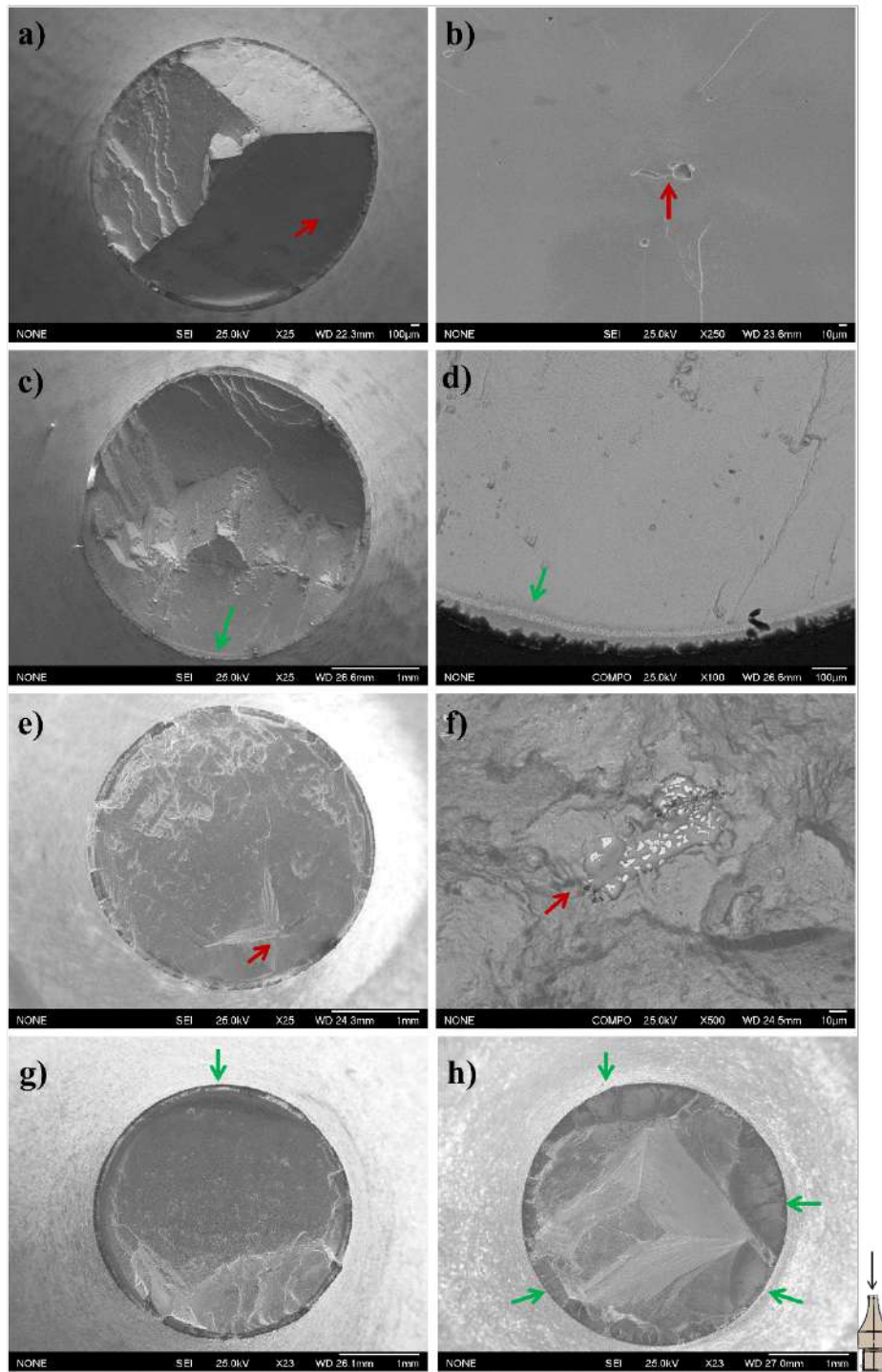


**Figure C-4** Fracture surface observations of samples bond coated via Slurry tested under positive stress ratio. AM1 with internal (a, magnification in b) and surface (c, magnification in d) crack initiation. Rene N5 (e and magnification in f) with internal crack initiation. CMSX-4 (g), and CMSX-4 Plus processed (h) with internal crack initiation. The green arrows indicate the surface crack initiation. The red arrows indicate the internal crack initiation site.

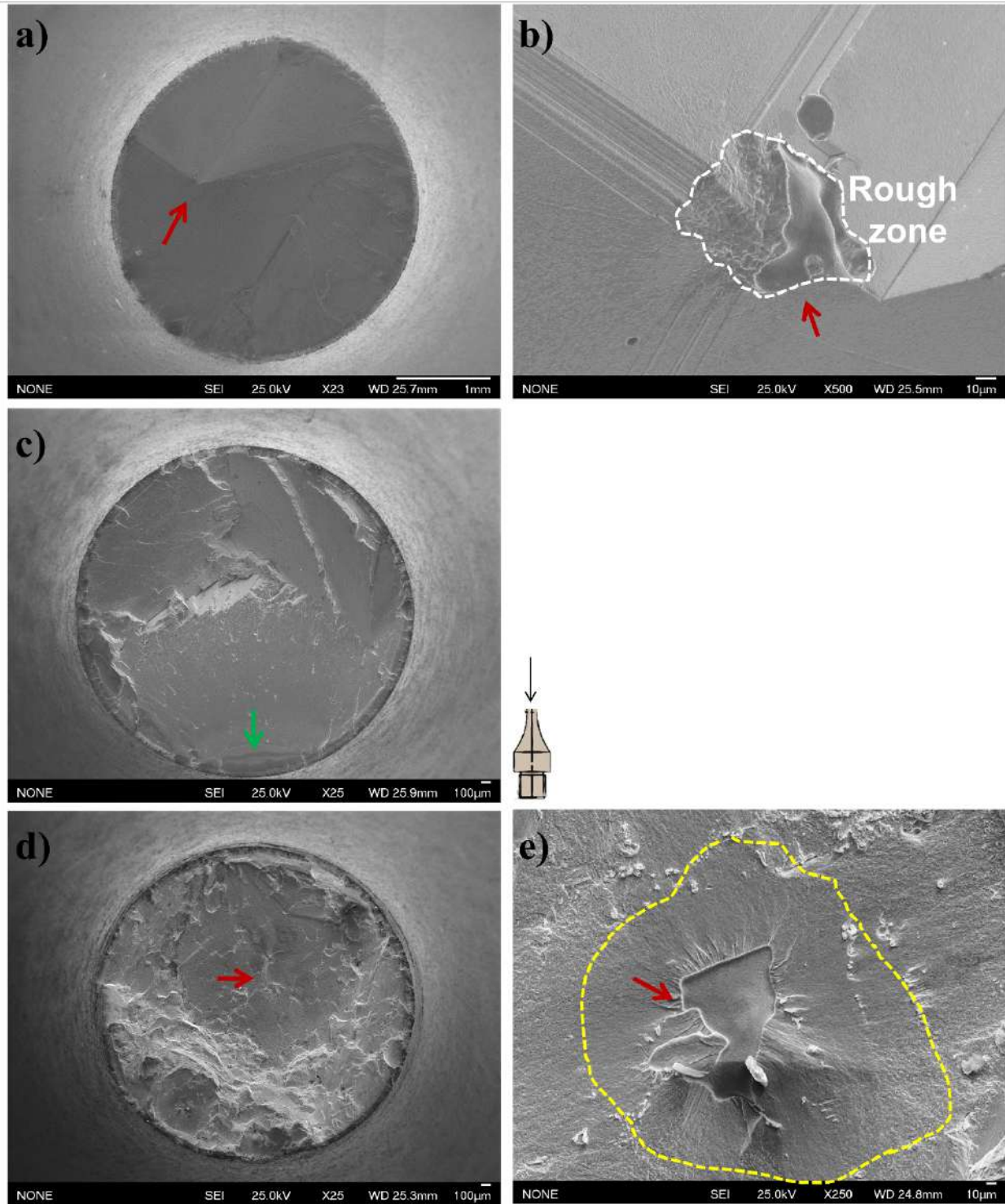


**Figure C-5** Fracture surface observations of samples bond coated via APVS tested under positive stress ratio. AMI with internal (a, magnification in b) and surface (c) crack initiation. Rene N5 with internal crack initiation (d, magnification in e). The green arrows indicate the surface crack initiation. The red arrows indicate the internal crack initiation.

**Figure C-5b** shows characteristic rough zone around the casting pore (see the dotted white line) and **Figure C-5e** shows the crack propagation in mode I around the casting pore (see the yellow dotted line), a typical crack propagation of the fatigue-creep interaction. At the same conditions and for the uncoated specimens, **Figure C-2** shows the same mixture of crack propagation.

## **Appendix D. Finite element analysis**

The finite element analysis was carried out to support the discussion of **sub-section 3 and 5** of **Chapter III**. Simulations were performed using Abaqus CAE, version 2017. The samples were represented as a solid cylindrical bar with a 75.5 mm length and 20 mm diameter. The length and the diameter are precisely calculated to reach the frequency of resonance 20 kHz. The density and the tensor of elastic constants adopted for these calculations are related to the AM1 superalloy properties at 1,000 °C (Mazot and de Fouquet, 1962). The material's behavior was defined as elastic/cubic, and the bar was perfectly orientated along the [001] direction. Further, the applied amplitude was chosen as periodic. The elements type used is C3D8R and the simulation is linear perturbation/frequency.

**Figure D-1a** is a schematic illustration of the maximum von Mises stress calculation for the smooth specimen without any defect. **Figure D-1b** is the von Mises stress distribution.

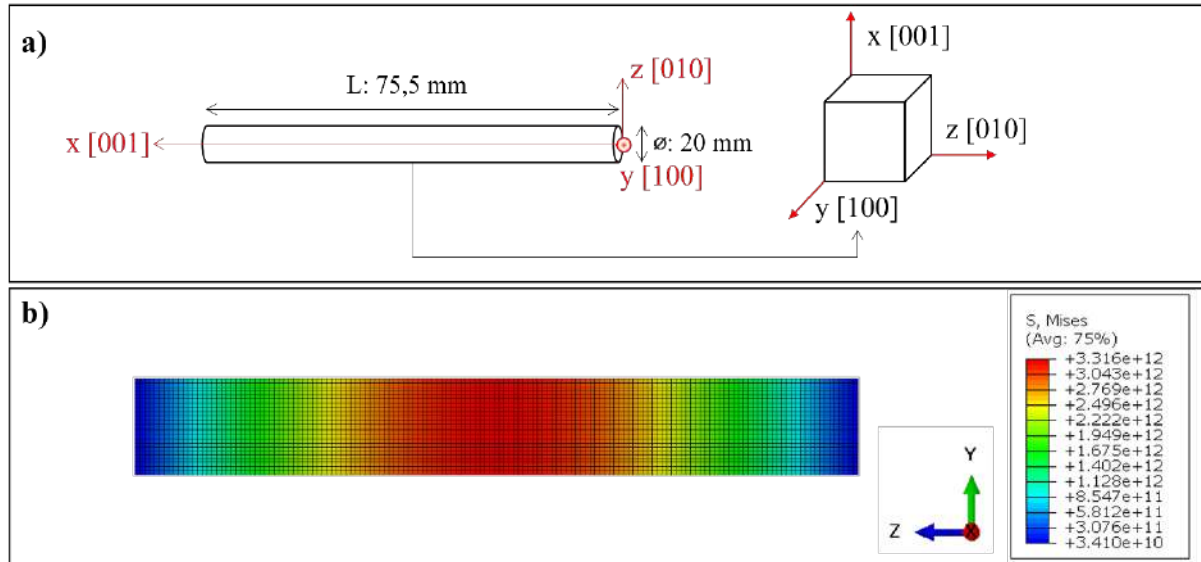


**Figure D-1** Schematic illustration of the specimen dimensions (a). Results of the maximum von Mises stress of the smooth bar under 20 kHz (b).

#### Appendix D.1. Compacted pore

A sphere was designed symmetrically to the bar axis. As a first simulation, the sphere was empty to simulate an internal casting pore, and the calculation was performed for diameters ranging between 200 and 1,000  $\mu\text{m}$ . The sizes in these simulations have been adjusted to keep the same relative size of defects compared to experimental results. Indeed, the diameter is relative to the VHCF sample having a 3 mm diameter in the gage zone and the critical casting pores with a diameter between 30 and 150  $\mu\text{m}$ . The frequency of resonance of a bar, including an internal casting pore, fluctuated between 19,999 and 19,996 Hz, respectively, from the minimum up to the maximum pore diameter. The element type used is C3D10 for simulations containing pores.

Next, a sphere of the same density and the same stiffness as the entire bar was introduced in the middle of the bar, with a primary misorientation of  $\theta$  degrees from the perfect [001] diameter. The misorientation of the “inclusion” was applied by introducing a rotation of  $\theta$  degrees around the [100] direction (see **Figure D-2a**). The  $\theta$  values were chosen between 10 and 45°. As a result, the von Mises stress calculation frequency fluctuated between 19,999 and 20,012 Hz, respectively, for misorientation ranging from 10 to 45°. **Figure D-2b** is the maximum von Mises stress in the vicinity of the grain (10° and 45° from the [001] direction) and pore with 1 mm diameter.

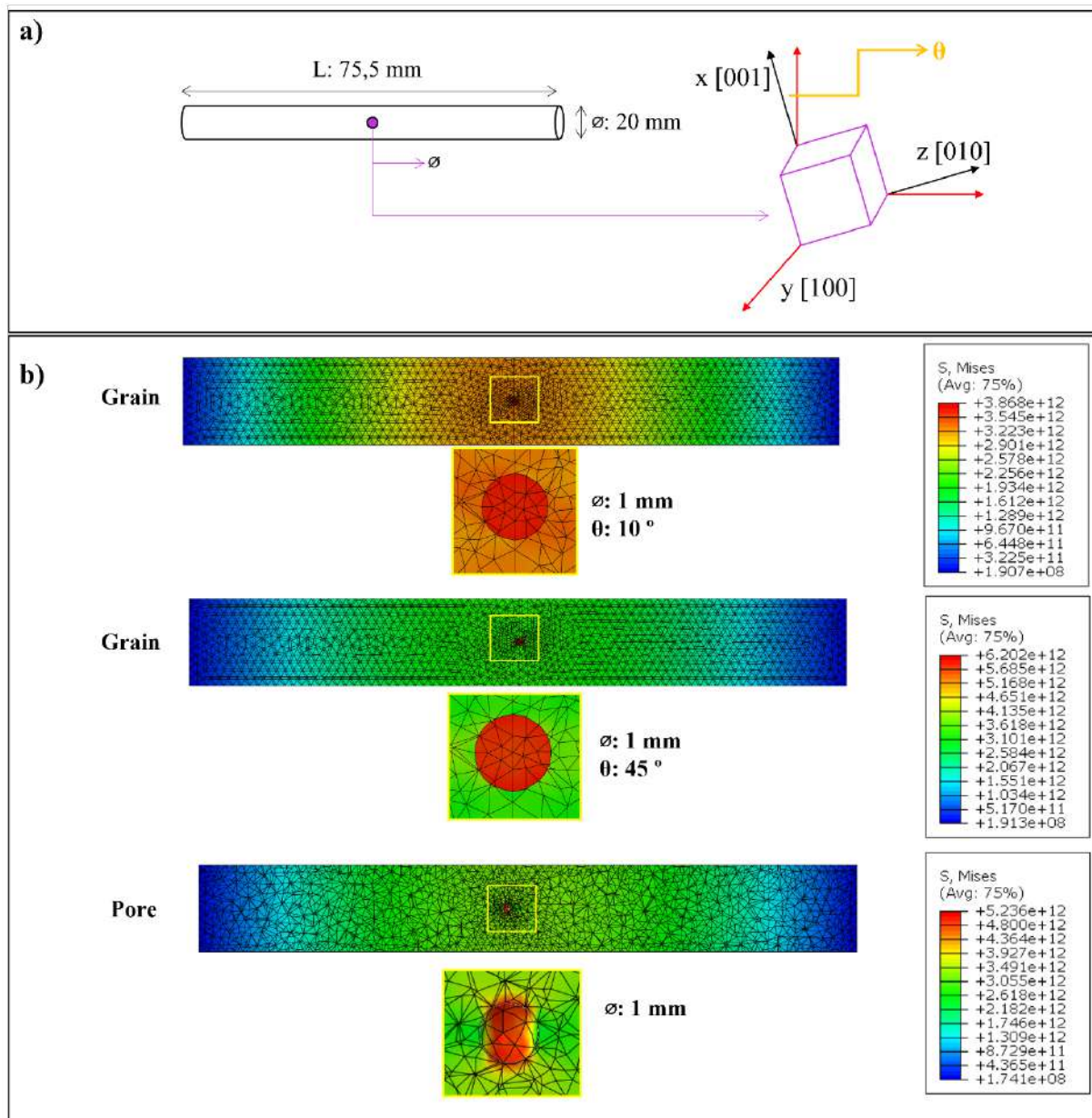


**Figure D-2** Schematic illustration of the spherical grain orientation (a). Maximum von Mises stress in the vicinity of the grain ( $10^\circ$  and  $45^\circ$  from the  $[001]$  direction) and the pore with 1 mm diameter (b).

**Appendix D.2. Stray grains**

**Figure D-3a** shows the schematic illustration of a stray grain connected to the surface of the gage part of VHCF specimens. It was designed with a 10 mm diameter (i.e., depth from the free surface) and length ranging between 1 mm (a 2/151, aspect ratio) up to 10 mm (a 20/151, aspect ratio). The

stray grain was defined to have the same density and elastic constants of the superalloy substrate, however misorientated by  $\theta^\circ$  from the [001] direction, according to **Figure D-3a**. The  $\theta$  values were chosen between 10 and 45 °. **Figure D-3b** illustrates the maximum von Mises stress in the vicinity of the stray grain. The elements type used for these simulations is C3D10.

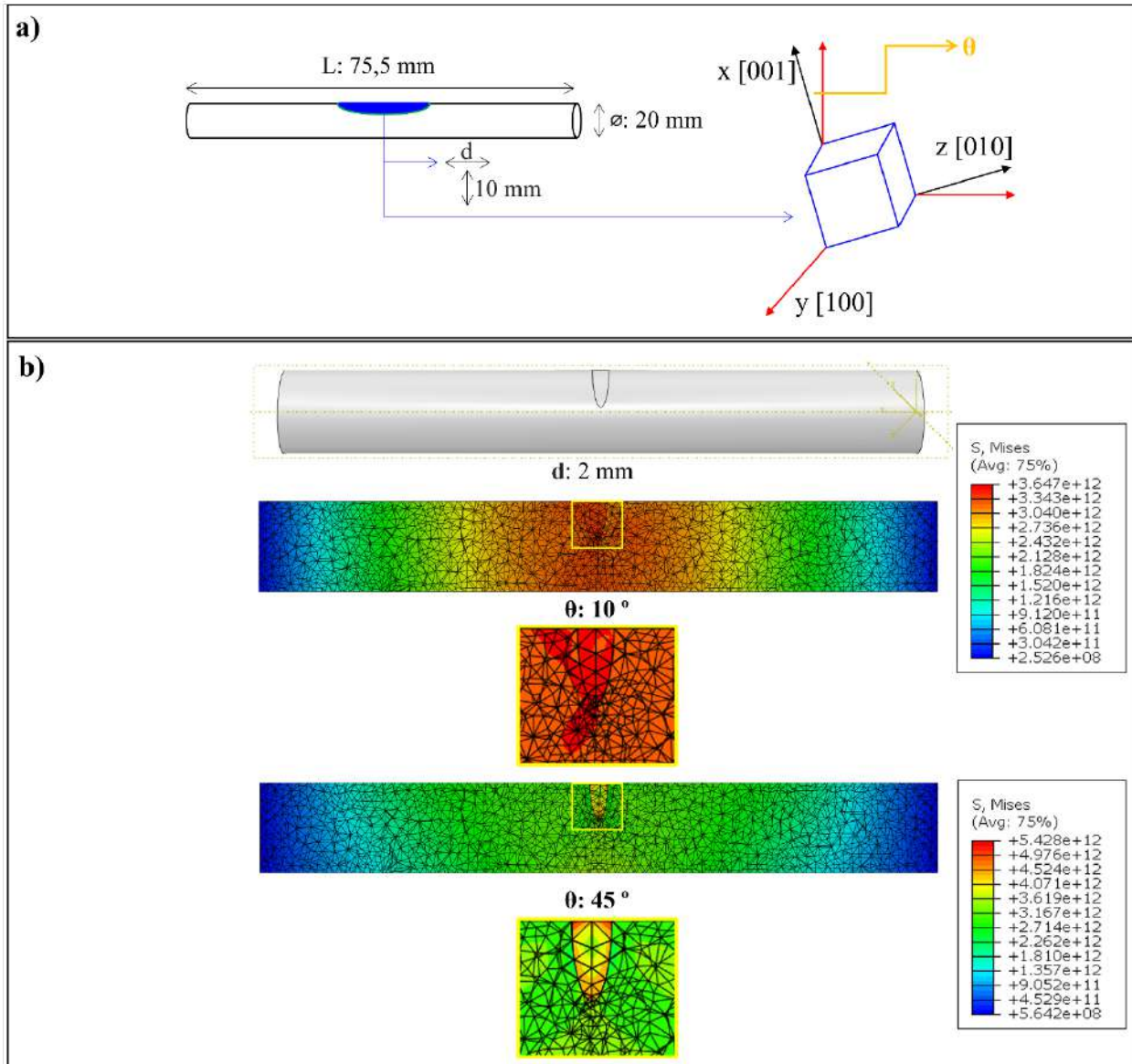


**Figure D-3** Schematic illustration of the elliptical stray grain orientation (a). Maximum von Mises stress in the vicinity of the stray grain ( $10^\circ$  and  $45^\circ$  from the [001] direction) (b).

## Appendix E. Creep

To support the discussion of **Chapter IV** creep tests were performed at 950 °C/500 MPa (**Figure E-1a**), 850 °C/500 MPa (**Figure E-1b**), 950 °C/300 MPa (**Figure E-1c**), and 1,050 °C/140 MPa (**Figure E-1d**). The results are depicted in **Table E-1** and **Figure E-1**.

*Table E-1 Isothermal creep properties.*

<i>Superalloy</i>	<i><math>\sigma_{max}</math> (MPa)</i>	<i>T (°C)</i>	<i>Creep life (h)</i>
<b>Bare</b>			
AM1	950	500	4.4
AM1	850	500	650.2
AM1	950	300	181.4
AM1	1,050	140	726.7
Rene N5	950	500	5.3
Rene N5	850	500	440.5
Rene N5 (No aging)	950	300	147.1
Rene N5	950	300	136.5
Rene N5	1,050	140	485.6
<b>Slurry</b>			
AM1	850	500	557.3
AM1	950	300	128.4
AM1	1,050	140	243.5
Rene N5	850	500	536.1
Rene N5	950	300	159.2
Rene N5	1,050	140	290.5
<b>APVS</b>			
AM1	950	300	161.5
AM1	1,050	140	664.8
Rene N5	950	300	162.2
Rene N5	1,050	140	378.7

**Figure E-1b** and **c** show that the coating did not influence the creep life of the superalloys AM1 and Rene N5. Moreover, both types of coating perform similarly under 950 °C and 300 MPa. However, **Figure E-1d** shows that there is a shorter creep life for the slurry coated specimens.

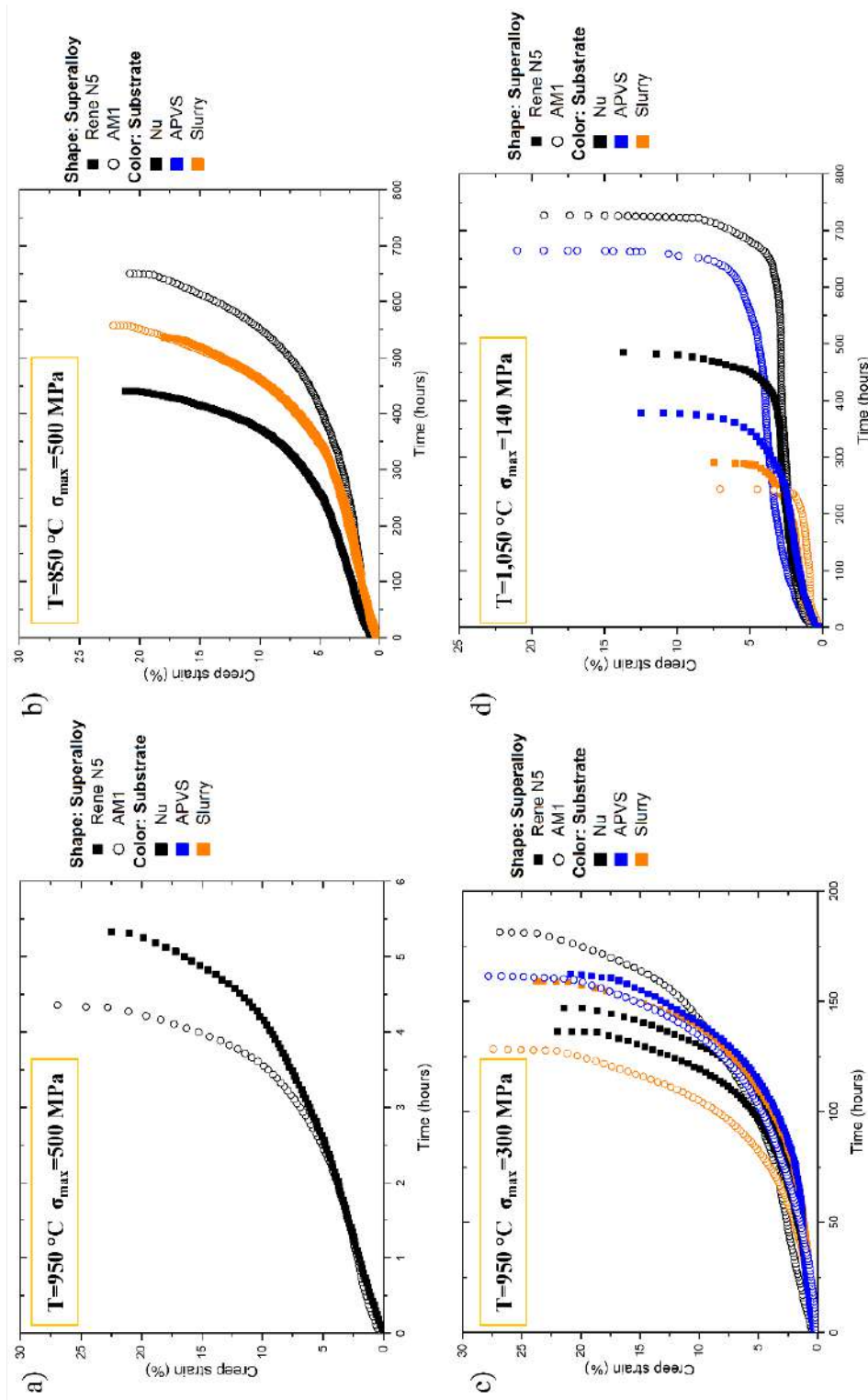


**Figure E-1** Creep curves for the Ni-based SX superalloys AM1 and Rene N5 (bare substrate and bond coated) at 950 °C/500 MPa (a); 850 °C/500 MPa (b); 950 °C/300 MPa (c); and 1,050 °C/140 MPa (d).

## Appendix F. Tomography

The XCT technique was employed to investigate coated samples' crack initiation modes. It provides 3D information on the sample's volume. It allows the analysis of crack initiations from the surface or IDZ without destroying the sample. The equipment manufactured by RX Solutions was operated at 150 kV, 47 mA, and a 10 mm from the source (Distance between specimen's and source of less than 3 mm) and 80 mm from the sensor. The software employed for the image treatment and reconstruction were FIJI and Paraview.

Interrupted tests were carried out to support the discussion topic by X-ray tomography analysis. **Figure F-1** shows a gray layer that represents the BC. Unfortunately, it was impossible to avoid the casting/homogenization pore features. The green arrows indicate the sub-surface cracks. The authors could observe that the sub-surface cracks developed in the first cycles ( $\approx 18\%$  of the fatigue life). After that, for the time-dependent mechanism, most of the VHCF lifetime was spent in the propagation.

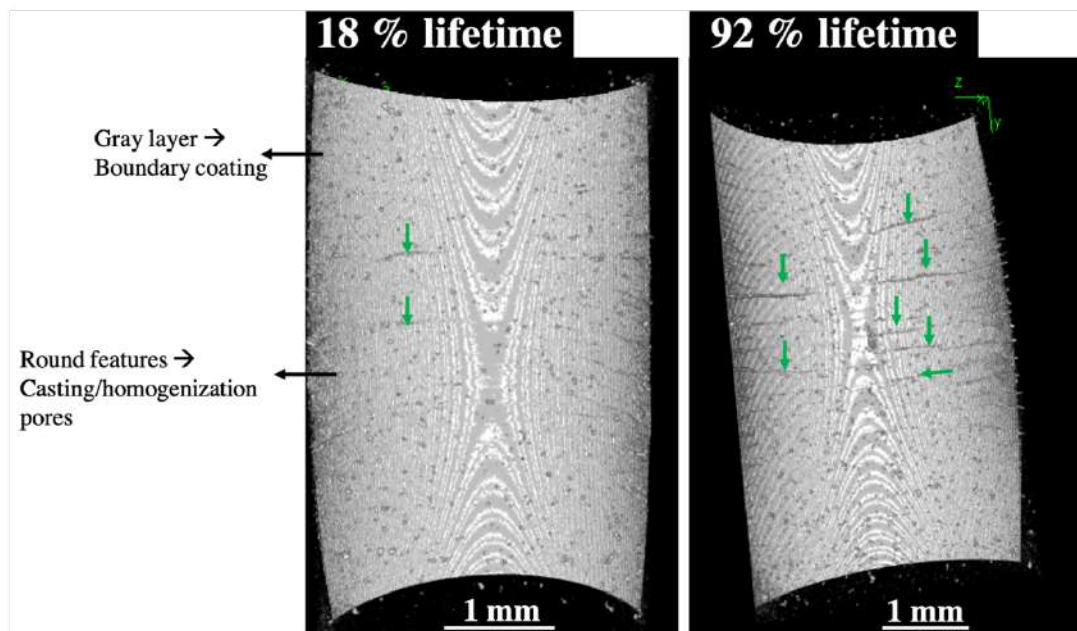


**Figure F-1** X-ray tomography analysis of an interrupted test of a specimen coated by aluminide. The specimen analysis could be taken at 18% and 92% of real fatigue. The gray layer represents the BC layer. The round features are casting/homogenization pores from the substrate. The features pointed by the green arrows are sub-surface cracks. The images were treated with FIJI software



## References



- Aghion, E., Bamberger, M., Berkovits, A., 1991. High-temperature low-cycle fatigue of a nickel-based MAR-M200 + Hf alloy in AR and AR + 20% O<sub>2</sub> environment. *J. Mater. Sci.* 26, 1873–1881.
- Alam, Z., Kamat, S. V., Jayaram, V., Das, D.K., 2013. Tensile behavior of a free-standing Pt-aluminide ( PtAl ) bond coat. *Acta Mater.* 61, 1093–1105.
- Anand Kumar, S., Rajkumar, V., Nagesha, B.K., Kumar Tigga, A., Barad, S., Suresh, T.N., 2021. Single crystal metal deposition using laser additive manufacturing technology for repair of aero-engine components. *Opt. Laser Technol.* 45, 5395–5399.
- Barret, C.A., Santoro, G.J., Lowell, C.E., 1973. Isothermal and cyclic oxidation at 1000C and 1100 C of four Nickel-base alloys: Nasa-Trw Via, B-1900, 713C, and 738X, Nasa Technical Note NASA TN D-7484. Ohio.
- Bathias, C., 2013. *Fatigue limit in metals*, 1st ed. John Wiley & Sons, London.
- Bathias, C., Paris, P.C., 2004. *Gigacyclique fatigue in mehcanical practice*. CRC Press, New York.
- Baufeld, B., Bartsch, M., Heinzemann, M., 2008. Advanced thermal gradient mechanical fatigue testing of CMSX-4 with an oxidation protection coating. *Int. J. Fatigue* 30, 219–225.
- Berthod, P., 2005. Kinetics of High Temperature Oxidation and Chromia Volatilization for a Binary Ni–Cr Alloy. *Oxid. Met.* 64, 235–252.
- Betteridge, W., Shaw, S.W.K., 1987. Development of superalloys. *Mater. Sci. Technol.* (United Kingdom) 3, 682–694.
- Bhagi, L.K., Gupta, P., Rastogi, V., 2013. A Brief Review on Failure of Turbine Blades. *Proc. STME-2013 Smart Technol. Mech. Eng.* 6, 1–8.
- Boesch, W., 1989. *Introduction—Superalloys*, 1st ed, *Superalloys Supercomposites Superceramics*. Academic Press, INC., New Hartford, New York.
- Boettinger W.J., 1974. The structure of directionally solidified two-phases Sn–Cd peritectic alloys. *Met. Trans.* 5, 2023–2031.
- Bokstein, B.S., Epishin, A.I., Link, T., Esin, V.A., Rodin, A.O., Svetlov, I.L., 2007. Model for the porosity growth in single-crystal nickel-base superalloys during homogenization. *Scr. Mater.* 57, 801–804.
- Bortoluci Ormastroni, L.M., 2018. Effect of microstructure defects on lifetime variability of CMSX-4 plus. Chasseneuil-du-Poitou.
- Bortoluci Ormastroni, L.M., Lopez-Galilea, I., Pistor, J., Rutttert, B., Körner, C., Theisen, W.,

- Villechaise, P., Pedraza, F., Cormier, J., 2022. Very high cycle fatigue durability of an additively manufactured single-crystal Ni-based superalloy. *Addit. Manuf.* 54, 102759.
- Bortoluci Ormastroni, L.M., Mataveli Suave, L., Cervellon, A., Villechaise, P., Cormier, J., 2020a. LCF, HCF and VHCF life sensitivity to solution heat treatment of a third-generation Ni-based single crystal superalloy. *Int. J. Fatigue* 130, 105247.
- Bortoluci Ormastroni, L.M., Utada, S., Rame, J., Mataveli Suave, L., Kawagishi, K., Harada, H., Villechaise, P., Cormier, J., 2020b. Tensile, Low Cycle Fatigue, and Very High Cycle Fatigue characterizations of advanced single crystal Nickel-based superalloys, in: Tin, S., Hardy, M., Clews, J., Cormier, J., Feng, Q., Marcin, J., O'brien, C., Suzuki, A. (Eds.), *Proceedings of the International Symposium on Superalloys 2020*. Springer US, Seven Springs, PA, USA, pp. 341–351.
- Boudot, A., 1999. Propriétés des revêtements de protection haute température pour pales de turbine haute pression. PhD Thesis - Institut national polytechnique (INP), Toulouse, France.
- Brundidge, C.L., Miller, J.D., Pollock, T.M., 2011. Development of dendritic structure in the liquid-metal-cooled, directional-solidification process. *Metall. Mater. Trans. A Phys. Metall. Mater. Sci.* 42, 2723–2732.
- Brundidge, C.L., Pollock, T.M., 2012. Processing to Fatigue Properties: Benefits of High Gradient Casting for Single Crystal Airfoils, in: Huron, E.S., Reed, R.C., Hardy, M.C., Mills, M.J., Montero, R.E., Portella, P., Telesman, J. (Eds.), *Proceedings of International Symposium on Superalloys 2012*. Springer US, Seven Springs, PA, USA, pp. 379–385.
- Brundidge, C.L., Van Drasek, D., Wang, B., Pollock, T.M., 2012. Structure refinement by a liquid metal cooling solidification process for single-crystal nickel-base superalloys. *Metall. Mater. Trans. A Phys. Metall. Mater. Sci.* 43, 965–976.
- Burgel, R., Portella, P.D., Preuhs, J., 2012. Recrystallization in Single Crystals of Nickel Base Superalloys, in: Pollock, T.M., Kissinger, R.D., Bowman, R.R., Green, K.A., McLean, M., Olson, S., Schirra, J.J. (Eds.), *Proceedings of the International Symposium on Superalloys 2012*. Springer US, Seven Springs, PA, USA, pp. 229–238.
- Caron, P., 2016. Le développement des superalliages monocristallins à base de nickel, in: *Journées Annuelles de La SF2M*. HAL, Albi.
- Caron, P., 2000. High gamma prime solvus new generation Nickel-based superalloys for single crystal turbine blade applications, in: Pollock, T.M., Kissinger, R.D., Bowman, R.R., Green,

- K.A., McLean, M., Olson, S., Schirra, J.J. (Eds.), Proceedings of International Symposium on Superalloys 2000. Springer US, Seven Springs, PA, USA, pp. 737–746.
- Caron, P., Henderson, P.J., Khan, T., McLean, M., 1986. On the effects of heat treatments on the creep behaviour of a single crystal superalloy. *Scr. Metall.* 20, 875–880.
- Caron, P., Khan, T., 1983. Improvement of Creep strength in a nickel-base single-crystal superalloy by heat treatment. *Mater. Sci. Eng.* 61, 173–184.
- Caron, P., Ohta, Y., Nakagawa, Y.G., Khan, T., 1988. Creep Deformation Anisotropy in Single Crystal Superalloys, in: Reichman, S., Duhl, D.N., Maurer, G., Antolovich, S., Lund, C. (Eds.), Proceedings of the International Symposium on Superalloys 1988. Springer US, Seven Springs, PA, USA, pp. 215–224.
- Cervellon, A., 2018. Propriétés en fatigue à grand et très grand nombre de cycles et à haute température des superalliages base nickel monogranulaires. PhD Thesis - Ecole Nationale Supérieure de Mécanique et d'Aérotechnique (ISAE-ENSMA), Poitiers, France. <https://theses.fr/2018ESMA0009>.
- Cervellon, A., Bortoluci Ormastroni, L.M., Hervier, Z., Pollock, T.M., Pedraza, F., Cormier, J., 2021. Damage mechanisms during very high cycle fatigue of a coated and grit-blasted Ni-based single-crystal superalloy. *Int. J. Fatigue* 142, 105962.
- Cervellon, A., Cormier, J., Mauget, F., Hervier, Z., 2017. VHCF life evolution after microstructure degradation of a Ni-based single crystal superalloy. *Int. J. Fatigue* 104, 251–262.
- Cervellon, A., Cormier, J., Mauget, F., Hervier, Z., Nadot, Y., 2018. Very high cycle fatigue of Ni-based single crystal superalloys at high temperature. *Metall. Mater. Trans. A* 49, 3938–3950.
- Cervellon, A., Hémerly, S., Kürnsteiner, P., Gault, B., Kontis, P., Cormier, J., 2020a. Crack initiation mechanisms during very high cycle fatigue of Ni-based single crystal superalloys at high temperature. *Acta Mater.* 188, 131–144.
- Cervellon, A., Yi, J.Z., Corpacci, F., Hervier, Z., Rigney, J., Wright, P.K., Torbet, C.J., Cormier, J., Jones, J.W., Pollock, T.M., 2020b. Creep, fatigue, and oxidation interactions during High and very high cycle fatigue at elevated temperature of nickel-base single crystal superalloys, in: Tin, S., Hardy, M., Clews, J., Cormier, J., Feng, Q., Marcin, J., O'Brien, C., Suzuki, A. (Eds.), Proceedings of the International Symposium on Superalloys 2020. Springer US, Seven Springs, PA, USA, pp. 185–195.

- Cetel, A.D., Duhl, D.N., 1988. Second-generation nickel-base single crystal superalloy, in: Reichman, S., Duhl, D.N., Maurer, G., Antolovich, S., Lund, C. (Eds.), Proceedings of the International Symposium on Superalloys 1988. Springer US, Seven Springs, PA, USA, pp. 235–244.
- Chan, K.S., Hack, J.E., Leverant, G.R., 1987. Fatigue crack growth in MAR-M200 single crystals. *Metall. Trans. A* 18, 581–591.
- Chauvet, E., Kontis, P., Jäggle, E.A., Gault, B., Raabe, D., Tassin, C., Blandin, J.J., Dendievel, R., Vayre, B., Abed, S., Martin, G., 2018a. Hot cracking mechanism affecting a non-weldable Ni-based superalloy produced by selective electron Beam Melting. *Acta Mater.* 142, 82–94.
- Chauvet, E., Tassin, C., Blandin, J.J., Dendievel, R., Martin, G., 2018b. Producing Ni-base superalloys single crystal by selective electron beam melting. *Scr. Mater.* 152, 15–19.
- Cheng, K., Jo, C., Jin, T., Hu, Z., 2011. Precipitation behavior of  $\mu$  phase and creep rupture in single crystal superalloy CMSX-4. *J. Alloys Compd.* 509, 7078–7086.
- Clavel, M., Levallant, C., Pineau, A., 1979. Creep-fatigue-environment interactions, in: Pelloux, R., Stoloff, N.S. (Eds.), Metallurgical Society of AIME. pp. 24–25.
- Coffin, L.F., 1974. The effect of frequency on the cyclic strain and fatigue behavior of cast Rene at 1600 F. *Metall. Trans.* 5, 1053–1060.
- Cormier, J., 2016. Thermal cycling creep resistance of Ni-based single crystal superalloys, in: Hardy, M.C., Huron, E., Glatzel, U., Griffin, B., Lewis, B., Rae, C., Seetharaman, V., Tin, S. (Eds.), Proceedings of the International Symposium on Superalloys 2016. Springer US, Seven Springs, PA, USA, pp. 385–394.
- Cormier, J., Gandin, C.-A., 2021. Processing of directionally cast nickel-base superalloys: solidification and heat treatments, in: Cailletaud, G., Cormier, J., Eggeler, G., Maurel, V., Naze, L. (Eds.), Nickel Base Single Crystals across Length Scales. Elsevier, Amsterdam, pp. 193–221.
- Crompton, J.S., Martin, J.W., 1984. Crack growth in a single crystal superalloy at elevated temperature. *Metall. Trans. A* 15, 1711–1719.
- Cruchley, S., Li, H.Y., Evans, H.E., Bowen, P., Child, D.J., Hardy, M.C., 2015. The role of oxidation damage in fatigue crack initiation of an advanced Ni-based superalloy. *Int. J. Fatigue* 81, 265–274.
- Darolia, R., 2018. Development of strong, oxidation and corrosion resistant nickel-based

- superalloys: critical review of challenges, progress and prospects. *Int. Mater. Rev.* 6608, 1–26.
- Davidson, J.H., Fredholm, A., Khan, T., Théret, J.-M., 1983. French Patent. 2 557 598.
- Decker, R.F., 1974. *High temperature materials in gas turbine*. Elsevier, Amsterdam.
- Desgranges, C., Lequien, F., Aublant, E., Nastar, M., Monceau, D., 2013. Depletion and voids formation in the substrate during high temperature oxidation of Ni-Cr alloys. *Oxid. Met.* 79, 93–105.
- Despres, L., 2021. *Comportement en fatigue thermomécanique à haute température d'un système barrière thermique texturé par laser*. PhD Thesis, Université Bourgogne Franche-Comte, Sévenans, France. <https://theses.fr/2020UBFCA030>.
- Ding, Q., Shen, Z., Xiang, S., Tian, H., Li, J., Zhang, Z., 2015. In-situ environmental TEM study of  $\gamma'$ - $\gamma$  Phase transformation induced by oxidation in a nickel-based single crystal superalloy. *J. Alloys Compd.* 651, 255–258.
- Donachie, M.J., Donachie, S.J., 2002. *Superalloys A Technical Guide*, 1st ed, The Materials Information Society. ASM International, New York.
- Doudard, C., Calloch, S., Hild, F., Cugy, P., Galtier, A., 2004. Identification de la dispersion des limites d'endurance à l'aide d'un essai d'échauffement. *Comptes Rendus - Mec.* 332, 795–801.
- Dubiel, B., Indyka, P., Kalembe-Rec, I., Kruk, A., Moskalewicz, T., Radziszewska, A., Kaç, S., Kopia, A., Berent, K., Gajewska, M., 2018. The influence of high temperature annealing and creep on the microstructure and chemical element distribution in the  $\gamma$ ,  $\gamma'$  and TCP phases in single crystal Ni-base superalloy. *J. Alloys Compd.* 731, 693–703.
- Duhl, D.N., 1987. *Superalloys II*. Wiley and Sons, New York.
- Durand-Charre, M., 1997. *The microstructure of superalloy*. Gordon and Breach, Amsterdam.
- Epishin, A., Fedelich, B., Link, T., Feldmann, T., Svetlov, I.L., 2013. Pore annihilation in a single-crystal nickel-base superalloy during hot isostatic pressing: Experiment and modelling. *Mater. Sci. Eng. A* 586, 342–349.
- Epishin, A.I., Link, T., Fedelich, B., Svetlov, I.L., Golubovskiy, E.R., 2014. Hot isostatic pressing of single-crystal nickel-base superalloys: Mechanism of pore closure and effect on Mechanical properties. *MATEC Web Conf.* 14, 08003.

- Erickson, G.L., 1996. The Development and Application of CMSX®-10, in: Kissinger, R.D., Deye, D.J., Anton, D.L., Cetel, A.D., Nathal, M. V., Pollock, T.M., Woodford, D.A. (Eds.), Proceedings of the International Symposium on Superalloys 1996. Springer US, Seven Springs, PA, USA, pp. 035–044.
- Evans, A.G., He, M.Y., Suzuki, A., Gigliotti, M., Hazel, B., Pollock, T.M., 2009. A mechanism governing oxidation-assisted low-cycle fatigue of superalloys. *Acta Mater.* 57, 2969–2983.
- Evans, H.E., 1988. Cavity formation and metallurgical changes induced by growth of oxide scale. *Mater. Sci. Technol. (United Kingdom)* 4, 1089–1098.
- Favier, V., Blanche, A., Phung, N.L., Ranc, N., Chrysochoos, A., 2014. Energy dissipation and self-heating due to microplastic deformation mechanisms at very high cycle fatigue for single-phase ductile metals. *Mater. Sci. Forum* 783–786, 2278–2283.
- Favier, V., Phung, N.L., Ranc, N., Bretheau, T., Gros-lafaige, J., Roger, G., Seiler, W., Valès, F., Wagner, D., Wang, C., Bathias, C., Cedelle, J., Ranc, I., Chrysochoos, A., Blanche, A., Wattrisse, B., Camp, G., Clary, A., El kaim, Y., Jourdan, F., Grégori, F., Bacroix, B., Galtier, A., Thoquenne, G., Mughrabi, H., 2013. Microplasticity and energy dissipation in very high cycle fatigue. *Fatigue Des.* 2011 1–8.
- Fleury, E., Rémy, L., 1993. Low cycle fatigue damage in nickel-base superalloy single crystals at elevated temperature. *Mater. Sci. Eng. A* 167, 23–30.
- Flood, S.C., Hunt, J.D., 1987. Columnar and equiaxed growth. II. Equiaxed growth ahead of a columnar front. *J. Cryst. Growth* 82, 552–560.
- Frasier, D.J., Whetstone, J.R., Harris, K., Erickson, G.L., Schwer, R.E., 1990. Process and alloy optimization for CMSX-4 superalloy single crystal airfoils *High Temperature Materials for Power Engineering. Proc. Cost Conf. Liege* 1291–1297.
- Frenz, H., Kinder, J., Klingelhoffer, H., Portella, P.D., 1996. Behaviour of single crystal superalloys under cyclic loading at high temperatures, in: Kissinger, R.D., Deye, D. j., Anton, D.L., Cetel, A.D., Nathal, M. V., Pollock, T.M., Woodford, D.A. (Eds.), Proceedings of International Symposium on Superalloys 1996. Springer US, Seven Springs, PA, USA, pp. 305–312.
- Fritzemeier, L.G., 1988. The influence of high thermal gradient casting, hot isostatic pressing and alternate heat treatment on the structure and properties of a single crystal nickel base superalloy, in: Reichman, S., Duhl, D.N., Maurer, G., Antolovich, S., Lund, C. (Eds.),

- Proceedings of International Symposium on Superalloys 1988. Springer US, Seven Springs, PA, USA, pp. 265–274.
- Fuchs, G.E., 2001. Solution heat treatment response of a third generation single crystal Ni-base superalloy. *Mater. Sci. Eng. A* 300, 52–60.
- Furuya, Y., Kobayashi, K., Hayakawa, M., Sakamoto, M., Koizumi, Y., Harada, H., 2012. High-temperature ultrasonic fatigue testing of single-crystal superalloys. *Mater. Lett.* 69, 1–3.
- Gabb, T.P., Gayda, J., Miner, R. V., 1986. Orientation and temperature dependence of some mechanical properties of the single-crystal nickel-base superalloy René N4: Part II. Low cycle fatigue behavior. *Metall. Trans. A* 17, 497–505.
- Galetz, M.C., Montero, X., Mollard, M., Günthner, M., Pedraza, F., Schütze, M., 2014. The role of combustion synthesis in the formation of slurry aluminization. *Intermetallics* 44, 8–17.
- Gancarczyk, K., Zubko, M., Hanc-Kuczkowska, A., Kościelniak, B., Albrecht, R., Szeliga, D., Motyka, M., Ziaja, W., Sieniawski, J., 2019. The effect of withdrawal rate on crystal structure perfection, microstructure and creep resistance of single crystal castings made of CMSX-4 nickel-based superalloy. *Materials (Basel)*. 12.
- Geddes, B., Leon, H., Huang, X., 2010. *Superalloys alloying and performance*, 1st ed. ASM International, New York.
- Giamei, A.F., Tschinkel, J.G., 1976. Liquid metal cooling: A new solidification technique. *Metall. Trans. A* 7, 1427–1434.
- Giraud, R., 2014. Influence de l’histoire thermique sur les propriétés mécaniques à haute et très haute température du superalliage monocristallin CMSX-4®. PhD Thesis - Ecole Nationale Supérieure de Mécanique et d’Aérotechnique (ISAE-ENSMA), Poitiers, France.
- Govaere, A., Rouffie, A.-L., Franchet, J.M., Galy, D., Dumont, C., Devaux, A., Crozet, C., Kontis, P., Villechaise, P., Cormier, J., 2020. Is the Carbon Content Really an Issue for the LCF Durability of Forged  $\gamma/\gamma'$  Ni-Based Disk Alloys?, in: Tin, S., Hardy, M., Clews, J., Cormier, J., Feng, Q., Marcin, J., O’Brien, C., Suzuki, A. (Eds.), *Proceedings of the International Symposium on Superalloys 2020*. Springer US, Seven Springs, PA, USA, pp. 591–602.
- Goward, G.W., Boone, D.H., 1971. Mechanisms of formation of diffusion aluminide coatings on nickel-base superalloys. *Oxid. Met.* 3, 475–495.
- Greatrix, D.R., 2012. *Powered flight: The engineering of aerospace propulsion*, 1st ed, Powered

- Flight: The Engineering of Aerospace Propulsion. Springer, London.
- Grégoire, B., Bonnet, G., Pedraza, F., 2019. Development of a new slurry coating design for the surface protection of gas turbine components. *Surf. Coatings Technol.* 374, 521–530.
- Grube, F., Affeldt, E.E., Mughrabi, H., 2002. Thermo-mechanical fatigue behavior of an aluminide-coated monocrystalline Ni-base superalloy, in: Kalluri, S., McGaw, M.A., J, B., Peteves, S.D. (Eds.), *Thermomechanical Fatigue Behavior of Materials*. ASTM STP 1428. West Conshohocken: American Society for Testing and Materials, pp. 164–179.
- Hancock, P., Chien, H.H., Nicholls, J.R., Stephenson, D.J., 1990. In situ measurements of the mechanical properties of aluminide coatings. *Surf. Coatings Technol.* 43–44, 359–370.
- Harris, K., Erickson, G.L., Schwer, R.E., 1999. *Directionally Solidified and Single Crystal Superalloys*, 1st ed. ASM International, New York.
- Harris, K., Erickson, G.L., Schwer, R.E., 1984. MAR M 247 derivations - CM 247 LC DS alloy CMSX single crystal alloys properties and performance. *Mettallurgical Soc. AIME* 221–230.
- Harris, K., Wahl, J.B., 2016. High strength single crystal superalloy. U. S. Patent 9518311.
- Harte, A., Atkinson, M., Preuss, M., Quinta da Fonseca, J., 2020. A statistical study of the relationship between plastic strain and lattice misorientation on the surface of a deformed Ni-based superalloy. *Acta Mater.* 195, 555–570.
- Harte, Allan, Atkinson, M., Smith, A., Drouven, C., Zaefferer, S., Quinta da Fonseca, J., Preuss, M., 2020. The effect of solid solution and gamma prime on the deformation modes in Ni-based superalloys. *Acta Mater.* 194, 257–275.
- Helle, A.S., Easterling, K.E., Ashby, M.F., 1985. Hot-isostatic pressing diagrams: New developments. *Acta Metall.* 33, 2163–2174.
- Huang, L., Sun, X.F., Guan, H.R., Hu, Z.Q., 2006. Oxidation behavior of the single-crystal Ni-base superalloy DD32 in air at 900, 1000, and 1100°C. *Oxid. Met.* 65, 391–408.
- Huang, Y., Wang, D., Shen, J., Lu, Y., Lou, L., Zhang, J., 2020. Initiation of fatigue cracks in a single-crystal Nickel-based superalloy at intermediate temperature, in: Tin, S., Hardy, M., Clews, J., Cormier, J., Feng, Q., Marcin, J., O'brien, C., Suzuki, A. (Eds.), *Proceedings of International Symposium on Superalloys 2020*. Springer, Seven Springs, PA, USA, pp. 208–217.
- Hübel, H., 1996. Basic conditions for material and structural ratcheting. *Nucl. Eng. Des.* 162, 55–65.

- Jackson, J.J., Donachie, M.J., Gell, M., Henricks, R.J., 1977. The effect of volume percent of fine gamma prime on creep in DS Mar-M200 + Hf. *Metall. Trans. A* 8, 1615–1620.
- Jackson, M.P., Reed, R.C., 1999. Heat treatment of UDIMET 720Li: The effect of microstructure on properties. *Mater. Sci. Eng. A* 259, 85–97.
- Jiang, W., Li, P., Yao, W.X., Rui, S.S., Shi, H.J., Huang, J., 2021a. The effect of porosity size on the high cycle fatigue life of nickel-based single crystal superalloy at 980 °C. *Int. J. Fatigue* 147, 106191.
- Jiang, W., Yao, W., Li, P., Luo, P., 2021b. A fatigue life prediction method distinguishing fracture modes for Ni-based single crystal superalloys considering porosity defect. *Theor. Appl. Fract. Mech.* 112, 102883.
- Johnson, A.S., Shao, S., Shamsaei, N., Thompson, S.M., Bian, L., 2017. Microstructure, Fatigue Behavior, and Failure Mechanisms of Direct Laser-Deposited Inconel 718. *JOM* 69, 597–603.
- Jullet, C., Oudriss, A., Balmain, J., Feugas, X., Pedraza, F., 2018. Characterization and oxidation resistance of additive manufactured and forged IN718 Ni-based superalloys. *Corros. Sci.* 142, 266–276.
- Takehi, K., 1999. Influence of secondary precipitates and crystallographic orientation on the strength of single crystals of a Ni-based superalloy. *Metall. Mater. Trans. A Phys. Metall. Mater. Sci.* 30, 1249–1259.
- Karunaratne, M.S. a, Cox, D.C., Carter, P., Reed, R.C., 2000. Modelling of the microsegregation in CMSX-4 superalloy and its homogenisation during heat treatment, in: Pollock, T.M., Kissinger, R.D., Bowman, R.R., Green, K.A., McLean, M., Olson, S., Scirra, J.J. (Eds.), *Proceedings of International Symposium on Superalloys 2000*. Springer US, Seven Springs, PA, USA, p. 263.
- Kawagishi, K., Yeh, A.C., Yokokawa, T., Kobayashi, T., Koizumi, Y., Harada, H., 2012. Development of an Oxidation-Resistant High-Strength Sixth-Generation Single-Crystal Superalloy TMS-238, in: Huron, E.S., Reed, R.C., Hardy, M.C., Mills, M.J., Montero, R.E., Portella, P.D., Telesman, J. (Eds.), *Proceedings of International Symposium on Superalloys 2012*. Springer US, Seven Springs, PA, USA, pp. 189–195.
- Kerisit, C., Jacomet, S., Bozzolo, N., Houillon, M., Geslin, W., Llorca, V., Logé, R.E., 2010. Mesures des hétérogénéités de déformation du tantale déformé à froid et conséquences sur la

- recristallisation, in: *Materiaux 2010*. Nantes.
- Khanna, A.S., 2012. *High Temperature Oxidation*, Second Edition. ed, *Handbook of Environmental Degradation of Materials: Second Edition*. Elsevier Inc.
- King, J.E., 1987. Fatigue crack propagation in nickel-base superalloys – effects of microstructure, load ratio, and temperature. *Mater. Sci. Technol.* 3, 750–764.
- Kirkendall, E.O., 1942. Diffusion of Zinc in Alpha Brass. *Trans. Metall. Soc. AIME* 147, 104.
- Kobayashi, D., Miyabe, M., Achiwa, M., Sugiura, R., Yokobori, A.T., 2014. Creep-fatigue crack growth behaviour based on EBSD observations for notched specimen made of directionally solidified Ni-base superalloy. *Mater. High Temp.* 31, 326–333.
- Koizumi, Y., Kawagagishi, K., Yokokawa, T., Yuyama, M., Takata, Y., Harada, H., 2020. Hot Corrosion and creep properties of Ni-base single crystal superalloys, in: Tin, S., Hardy, M., Clews, J., Cormier, J., Feng, Q., Marcin, J., O’Brien, C., Suzuki, A. (Eds.), *Proceedings of International Symposium on Superalloys 2020*. Springer US, Seven Springs, PA, USA, pp. 747–752.
- Koizumi, Y., Kobayashi, T., Yokokawa, T., Zhang, J., Osawa, M., Harada, Hiroshi, Aoki, Y., Arai, M., 2004. Development of next-generation Ni-base single crystal superalloys, in: Green, K.A., Pollock, T.M., Harada, H., Howson, T.E., Reed, R.C., Schirra, J.J., Walston, S. (Eds.), *Proceedings of the International Symposium on Superalloys 2004*. Springer US, Seven Springs, PA, USA, pp. 35–43.
- Körner, C., Ramsperger, M., Meid, C., Bürger, D., Wollgramm, P., Bartsch, M., Eggeler, G., 2018. Microstructure and Mechanical Properties of CMSX-4 Single Crystals Prepared by Additive Manufacturing. *Metall. Mater. Trans. A Phys. Metall. Mater. Sci.* 49, 3781–3792.
- Kounitzky, A., Wortmann, J., Agarwal, P.N., 1991. A single crystal casting process for high-temperature components. *Mater. Des.* 12, 323–330.
- Kovalchuk, M., Gleeson, B., 2020. laboratory-scale replication of deposition-induced degradation of high-temperature turbine components, in: Tin, S., Hardy, M., Clews, J., Cormier, J., Feng, Q., Marcin, J., O’Brien, C., Suzuki, A. (Eds.), *Proceedings of the International Symposium on Superalloys 2020*. Springer US, Seven Springs, PA, USA, pp. 789–797.
- Kromer, R., 2016. Etude des effets des préparations de surface avant projection thermique : application barrière thermique. PhD Thesis - Université de technologie Belfort-Montbéliard (utbm), Belfort, France. <https://theses.fr/2016BELF0297>.

- Kromer, R., Cormier, J., Costil, S., Courapied, D., Berthe, L., Peyre, P., 2018. High temperature durability of a bond-coatless plasma-sprayed thermal barrier coating system with laser textured Ni-based single crystal substrate. *Surf. Coatings Technol.* 337, 168–176.
- Kromer, R., Mauget, F., Despres, L., Costil, S., Cormier, J., 2019. Thermo-mechanical fatigue evaluation of a thermal barrier coating bond-coatless system. *Mater. Sci. Eng. A* 756, 130–141.
- Kurz, W., Fisher, D.J., 1986. *Fundamentals of solidification*, 3rd ed. Trans Tech Publications, Michigan.
- Laird, C., 1976. The fatigue limits of metals. *Mater. Sci. Eng.* 22, 231–236.
- Lamm, M., Singer, R.F., 2007. The Effect of Casting Conditions on the High-Cycle Fatigue Properties of the Single-Crystal Nickel-Base Superalloy PWA 1483. *Metall. Mater. Trans. A* 38, 1177–1183.
- Lavigne, O., Ramusat, C., Drawin, S., Caron, P., Boivin, D., Pouchou, J.L., 2004. Relationships between microstructural instabilities and mechanical behaviour in new generation nickel-based single crystal superalloys, in: Green, K.A., Pollock, T.M., Harada, H., Howson, T.E., Reed, R.C., Schirra, J.J., Walston, S. (Eds.), *Proceedings of International Symposium on Superalloys 2004*. Springer US, Seven Springs, PA, USA, pp. 667–675.
- le Graverend, J.B., Adrien, J., Cormier, J., 2017. Ex-situ X-ray tomography characterization of porosity during high-temperature creep in a Ni-based single-crystal superalloy: Toward understanding what is damage. *Mater. Sci. Eng. A* 695, 367–378.
- le Graverend, J.B., Cormier, J., Gallerneau, F., Kruch, S., Mendez, J., 2016. Strengthening behavior in non-isothermal monotonic and cyclic loading in a Ni-based single crystal superalloy. *Int. J. Fatigue* 91, 257–263.
- le Graverend, J.B., Cormier, J., Kruch, S., Gallerneau, F., Mendez, J., 2012. Microstructural parameters controlling high-temperature creep life of the nickel-base single-crystal superalloy MC2. *Metall. Mater. Trans. A Phys. Metall. Mater. Sci.* 43, 3988–3997.
- Lerch, B.A., Antolovich, S.D., 1990. Fatigue crack propagation behavior of a single crystalline superalloy. *Metall. Trans. A* 21, 2169–2177.
- Lerch, B.A., Jayaraman, N., Antolovich, S.D., 1984. A study of fatigue damage mechanisms in Waspaloy from 25 to 800°C. *Mater. Sci. Eng.* 66, 151–166.
- Lindblad, N.R., 1969. A Review of the Behavior of Aluminide-Coated Superalloys. *Oxid. Met.* 1,

143–170.

- Link, T., Zabler, S., Epishin, A., Haibel, A., Bansal, M., Thibault, X., 2006. Synchrotron tomography of porosity in single-crystal nickel-base superalloys. *Mater. Sci. Eng. A* 425, 47–54.
- Liu, C.T., Sun, X.F., Guan, H.R., Hu, Z.Q., 2005. Effect of rhenium addition to a nickel-base single crystal superalloy on isothermal oxidation of the aluminide coating. *Surf. Coatings Technol.* 194, 111–118.
- Liu, L., Husseini, N.S., Torbet, C.J., Kumah, D.P., Clarke, R., Pollock, T.M., Wayne Jones, J., 2008. In situ imaging of high cycle fatigue crack growth in single crystal nickel-base superalloys by synchrotron X-radiation. *J. Eng. Mater. Technol. Trans. ASME* 130, 0210081–0210086.
- Liu, Y., Yu, J.J., Xu, Y., Sun, X.F., Guan, H.R., Hu, Z.Q., 2007. High cycle fatigue behavior of a single crystal superalloy at elevated temperatures. *Mater. Sci. Eng. A* 454–455, 357–366.
- Loh, N.L., Sia, K.Y., 1992. An overview of hot isostatic pressing. *J. Mater. Process. Tech.* 30, 45–65.
- Long, H., Mao, S., Liu, Y., Zhang, Z., Han, X., 2018. Microstructural and compositional design of Ni-based single crystalline superalloys — A review. *J. Alloys Compd.* 743, 203–220.
- Lopez-Galilea, I., Koßmann, J., Kostka, A., Drautz, R., Mujica Roncery, L., Hammerschmidt, T., Huth, S., Theisen, W., 2016. The thermal stability of topologically close-packed phases in the single-crystal Ni-base superalloy ERBO/1. *J. Mater. Sci.* 51, 2653–2664.
- Lopez-Galilea, I., Rutttert, B., He, J., Hammerschmidt, T., Drautz, R., Gault, B., Theisen, W., 2019. Additive manufacturing of CMSX-4 Ni-base superalloy by selective laser melting: Influence of processing parameters and heat treatment. *Addit. Manuf.* 30, 100874.
- Ma, J., Jiang, W., Wang, J., Zhang, Y., Zhang, Z., 2020. Initial oxidation behavior of a single crystal superalloy during stress at 1150 °C. *Sci. Rep.* 10, 1–9.
- Ma, X., Jiang, J., Zhang, W., Shi, H.J., Gu, J., 2019. Effect of local recrystallized grains on the low cycle fatigue behavior of a nickel-based single crystal superalloy. *Crystals* 9, 312.
- Ma, X., Shi, H.J., Gu, J., Yang, Z., Chen, G., Luesebrink, O., Harders, H., 2015. Influence of surface recrystallization on the low cycle fatigue behaviour of a single crystal superalloy. *Fatigue Fract. Eng. Mater. Struct.* 38, 340–351.
- Mackay, R.A., Maier, R.D., 1982. Influence of Orientation on the Stress Rupture Properties of

- Nickel-Base Superalloy Single Crystals. *Metall. Trans. A* 13, 1747–1754.
- MacLachlan, D.W., Knowles, D.M., 2001. Fatigue behaviour and lifing of two single crystal superalloys. *Fatigue Fract. Eng. Mater. Struct.* 24, 503–521.
- Marines-Garcia, I., Paris, P.C., Tada, H., Bathias, C., 2007. Fatigue crack growth from small to long cracks in VHCF with surface initiations. *Int. J. Fatigue* 29, 2072–2078.
- Mataveli Suave, L., 2017. High temperature durability of DS200+Hf alloy. PhD Thesis - Ecole Nationale Supérieure de Mécanique et d'Aérotechnique (ISAE-ENSMA), Poitiers, France. <https://theses.fr/2017ESMA0032>.
- Mataveli Suave, L., Cormier, J., Villechaise, P., Bertheau, D., Benoit, G., Mauget, F., Cailletaud, G., Marcin, L., 2016. High Temperature Creep Damage Mechanisms in a Directionally Solidified Alloy: Impact of Crystallography and Environment, in: Hardy, M.C., Huron, E., Glatzel, U., Griffin, B., Lewis, B., Rae, C.M.F., Seetharaman, V., Tin, S. (Eds.), *Proceedings of the International Symposium on Superalloys 2016*. Springer US, Seven Springs, PA, USA, pp. 747–756.
- Mataveli Suave, L., Serrano Munoz, A., Gaubert, A., Benoit, G., Marcin, L., Kontis, P., Villechaise, P., Cormier, J., 2018. Thin-Wall Debit in Creep of DS200 + Hf Alloy. *Metall. Mater. Trans. A* 49, 4021–4028.
- Mattiello, A., 2018. Visco-plasticity and damage modeling of single crystal superalloys at high temperatures: a tensorial microstructure-sensitive approach. PhD Thesis - Ecole Normale Supérieure Paris-Saclay, Paris, France.
- Matuszewski, K., Rettig, R., Matysiak, H., Peng, Z., Povstugar, I., Choi, P., Müller, J., Raabe, D., Spiecker, E., Kurzydłowski, K.J., Singer, R.F., 2015. Effect of ruthenium on the precipitation of topologically close packed phases in Ni-based superalloys of 3rd and 4th generation. *Acta Mater.* 95, 274–283.
- Mauget, F., Hamon, F., Morisset, M., Cormier, J., Riallant, F., Mendez, J., 2017. Damage mechanisms in an EB-PVD thermal barrier coating system during TMF and TGMF testing conditions under combustion environment. *Int. J. Fatigue* 99, 225–234.
- Mauget, F., Marchan, D., Morisset, M., Bertheau, D., Cormier, J., Mendez, J., 2012. Nouveau moyen de caractérisation des matériaux Conditions extrêmes et sollicitations thermomécaniques proches des conditions d'usages. *Matériaux Tech.* 100, 541–545.
- Mauget, F., Marchand, D., Benoit, G., Morisset, M., Bertheau, D., Cormier, J., Mendez, J.,

- Hervier, Z., Ostoja-Kuczynski, E., Moriconi, C., 2014. Development and use of a new burner rig facility to mimic service loading conditions of Ni-based single crystal superalloys. *MATEC Web Conf.* 14.
- Maurel, V., Bartsch, M., Vidal-Setif, M.H., Vaben, R., Guipont, V., 2021. Coated single crystal superalloys: processing, characterization, and modeling of protective coatings, in: Cailletaud, G., Cormier, J., Eggeler, G., Maurel, V., Naze, L. (Eds.), *Nickel Base Single Crystals across Length Scales*. Elsevier, Amsterdam, pp. 283–338.
- Mayer, H., 1999. Fatigue crack growth and threshold measurements at very high frequencies. *Int. Mater. Rev.* 44, 1–34.
- Mazot, P., de Fouquet, J., 1962. Détermination par la méthode de résonance du module de monocristaux de superalliage base nickel AM1 entre l'ambiante et 1100°C. *Mem. Etudes Sci. Met.* 165–170.
- Mazur, Z., Garcia-Illescas, R., Aguirre-Romano, J., Perez-Rodriguez, N., 2008. Steam turbine blade failure analysis. *Eng. Fail. Anal.* 15, 129–141.
- McCartney, D.G., Hunt, J.D., 1981. Measurements of cell and primary dendrite arm spacings in directionally solidified aluminium alloys. *Acta Metall.* 29, 1851–1863.
- McLean, M., Webster, G.A., Nabarro, F.R.N., Cottrell, A., 1995. Nickel-base superalloys: Current status and potential. *Philos. Trans. R. Soc. A Math. Phys. Eng. Sci.* 351, 419–433.
- McVay, R.V., Williams, P., Meier, G.H., Pettit, F.S., 1992. Oxidation of Low Sulfur Single Crystal Nickel-Base Superalloys, in: Antolovich, S.D., Stusrud, R.W., Mackay, R.A., Anton, D.L., Khan, T., Kissinger, R.D., Klarstrom, D.L. (Eds.), *Proceedings of the International Symposium on Superalloys 1992*. Springer US, Seven Springs, PA, USA, pp. 807–816.
- Meid, C., Dennstedt, A., Ramsperger, M., Pistor, J., Rutttert, B., Lopez-Galilea, I., Theisen, W., Körner, C., Bartsch, M., 2019a. Effect of heat treatment on the high temperature fatigue life of single crystalline nickel base superalloy additively manufactured by means of selective electron beam melting. *Scr. Mater.* 168, 124–128.
- Meid, C., Eggeler, M., Watermeyer, P., Kostka, A., Hammerschmidt, T., Drautz, R., Eggeler, G., Bartsch, M., 2019b. Stress-induced formation of TCP phases during high temperature low cycle fatigue loading of the single-crystal Ni-base superalloy ERBO/1. *Acta Mater.* 168, 343–352.
- Miao, J., Pollock, T.M., Wayne Jones, J., 2009. Crystallographic fatigue crack initiation in nickel-

- based superalloy René 88DT at elevated temperature. *Acta Mater.* 57, 5964–5974.
- Milligan, W.W., Antolovich, S.D., 1987. Yielding and deformation behavior of the single crystal superalloy PWA 1480. *Metall. Trans. A* 18, 85–95.
- Miracle, D.B., 1993. The physical and mechanical properties of NiAl. *Acta Metall. Mater.* 41, 649–684.
- Morrissey, R.J., Golden, P.J., 2007. Fatigue strength of a single crystal in the gigacycle regime. *Int. J. Fatigue* 29, 2079–2084.
- Mottura, A., Finnis, M.W., Reed, R.C., 2012. On the possibility of rhenium clustering in nickel-based superalloys. *Acta Mater.* 60, 2866–2872.
- Mughrabi, H., 2015. Microstructural mechanisms of cyclic deformation, fatigue crack initiation and early crack growth. *Philos. Trans. R. Soc. A Math. Phys. Eng. Sci.* 373, 1–21.
- Mujica Roncery, L., Lopez-Galilea, I., Rutttert, B., Huth, S., Theisen, W., 2016. Influence of temperature, pressure, and cooling rate during hot isostatic pressing on the microstructure of an SX Ni-base superalloy. *Mater. Des.* 97, 544–552.
- Munier, R., Doudard, C., Calloch, S., Weber, B., 2017. Identification of the micro-plasticity mechanisms at the origin of self-heating under cyclic loading with low stress amplitude. *Int. J. Fatigue* 103, 122–135.
- Murakami, Y., Endo, M., 1994. Effects of defects, inclusions and inhomogeneities on fatigue strength. *Int. J. Fatigue* 16, 163–182.
- Murakumo, T., Kobayashi, T., Koizumi, Y., Harada, H., 2004. Creep behaviour of Ni-base single-crystal superalloys with various gamma prime volume fraction. *Acta Mater.* 52, 3737–3744.
- Nembach, E., Neite, G., 1985. Precipitation hardening of superalloys by ordered gamma prime particles. *Prog. Mater. Sci.* 29, 177–319.
- Nicholson, R.B., 1976. Nickel Base Materials Developments for High Temperatures. *Philos. Trans. R. Soc. A Math. Phys. Eng. Sci.* 282, 389–399.
- Nie, B., Zhao, Z., Liu, S., Chen, D., Ouyang, Y., Hu, Z., Fan, T., Sun, H., 2018. Very high cycle fatigue behavior of a directionally solidified Ni-base superalloy DZ4. *Materials (Basel)*. 11, 1–12.
- Nishijima, S., Kanazawa, K., 1999. Stepwise S-N curve and fish-eye failure in gigacycle fatigue. *Fatigue Fract. Eng. Mater. Struct.* 22, 601–607.
- Nowak, W.J., Ochał, K., Wierzba, P., Gancarczyk, K., Wierzba, B., 2019. Effect of substrate

- roughness on oxidation resistance of an aluminized ni-base superalloy. *Metals (Basel)*. 9, 1–14.
- Ohtani, R., Tada, N., Shibata, M., Taniyama, S., 2001. High temperature fatigue of the nickel-base single-crystal superalloy CMSX-10. *Fatigue Fract. Eng. Mater. Struct.* 24, 867–876.
- Okazaki, M., 2001. High-temperature strength of Ni-base superalloy coatings. *Sci. Technol. Adv. Mater.* 2, 357–366.
- Ott, M., Tetzlaff, U., Mughrabi, H., 1999. Influence of directional coarsening on the isothermal high-temperature fatigue behaviour of the monocrystalline nickel-base superalloys CMSX-6 and CMSX-4. *Mater. Sci. Eng. A* 272, 24–30.
- Parsa, A.B., Ramsperger, M., Kostka, A., Somsen, C., Körner, C., Eggeler, G., 2016. Transmission electron microscopy of a CMSX-4 Ni-base superalloy produced by selective electron beam melting. *Metals (Basel)*. 6, 1–17.
- Paul, S.K., 2019. A critical review of experimental aspects in ratcheting fatigue: Microstructure to specimen to component. *J. Mater. Res. Technol.* 8, 4894–4914.
- Pedraza, F., Mollard, M., Rannou, B., Balmain, J., Bouchaud, B., Bonnet, G., 2012. Potential thermal barrier coating systems from Al microparticles. Mechanisms of coating formation on pure nickel. *Mater. Chem. Phys.* 134, 700–705.
- Pedraza, F., Troncy, R., Pasquet, A., Delautre, J., Hamadi, S., 2020. Critical Hafnium Content for Extended Lifetime of AM1 Single Crystal Superalloy, in: Tin, S., Hardy, M.C., Clews, J., Cormier, J., Feng, Q., Marcin, J., O'brien, C., Suzuki, A. (Eds.), *Proceedings of the International Symposium on Superalloys 2020*. Springer US, Seven Springs, PA, USA, pp. 781–788.
- Perruchaut, P., 1997. Étude des interactions fatigue-fluage-oxydation sur l'endommagement du superalliage monocristallin AM1. PhD Thesis - Ecole Nationale Supérieure de Mécanique et d'Aérotechnique (ISAE-ENSMA), Poitiers, France.
- Perrut, M., Caron, P., Thomas, M., Couret, A., 2018. High temperature materials for aerospace applications: Ni-based superalloys and  $\gamma$ -TiAl alloys. *Comptes Rendus Phys.* 19, 657–671.
- Pessah, M., Caron, P., Khan, T., 1992. Effect of  $\mu$  phase on the mechanical properties of a nickel-base single crystal superalloy, in: Antolovich, S.D., Stusrud, R.W., MacKay, R.A., Anton, D.L., Khan, T., Kissinger, R.D., Klarstrom, D.L. (Eds.), *Proceedings of International Symposium on Superalloys 1992*. Springer US, Seven Springs, PA, USA, pp. 567–576.

- Pettinari-Sturmel, F., Nazé, L., 2021. Microstructure and chemical characterization, in: Naze, L., Morel, V., Eggeler, G., Cormier, J., Cailletaud, G. (Eds.), *Nickel Base Single Crystals across Length Scales*. Elsevier Ltd, pp. 69–105.
- Pearcey, B.J., Kear, B.H., Smashey, R.W., 1967. Correlation of structure with properties in a directionally solidified nickel-base superalloy. *Trans. Am. Soc. Met.* 60, 634–643.
- Pineau, A., Antolovich, S.D., 2015. High temperature fatigue: Behaviour of three typical classes of structural materials. *Mater. High Temp.* 32, 298–317.
- Pineau, A., Antolovich, S.D., 2009. High temperature fatigue of nickel-base superalloys – A review with special emphasis on deformation modes and oxidation. *Eng. Fail. Anal.* 16, 2668–2697.
- Pineau, A., McDowell, D.L., Busso, E.P., Antolovich, S.D., 2016. Failure of metals II: Fatigue. *Acta Mater.* 107, 484–507.
- Pistor, J., Körner, C., 2021. A novel mechanism to generate metallic single crystals. *Sci. Rep.* 11, 1–8.
- Pistor, J., Körner, C., 2019. Formation of topologically closed packed phases within CMSX-4 single crystals produced by additive manufacturing. *Mater. Lett. X* 1, 1–4.
- Plancher, E., Gravier, P., Chauvet, E., Blandin, J.J., Boller, E., Martin, G., Salvo, L., Lhuissier, P., 2019. Tracking pores during solidification of a Ni-based superalloy using 4D synchrotron microtomography. *Acta Mater.* 181, 1–9.
- Plekhov, O., Naimark, O., Narykova, M., Kadomtsev, A., Betehtin, V., 2016. Study of Dissipation Properties and Structure Evolution in Metals with Different Grain Size under HCF and VHCF Loadings. *Procedia Struct. Integr.* 2, 2084–2090.
- Pollock, T.M., Argon, A.S., 1992. Creep resistance of CMSX-3 nickel base superalloy single crystals. *Acta Metall. Mater.* 40, 1–30.
- Pollock, T.M., Laux, B., Brundidge, C.L., Suzuki, A., He, M.Y., 2011. Oxide-assisted degradation of Ni-base single crystals during cyclic loading: The role of coatings. *J. Am. Ceram. Soc.* 94, 136–145.
- Pollock, T.M., Tin, S., 2008. Nickel-Based Superalloys for Advanced Turbine Engines: Chemistry, Microstructure and Properties. *J. Propuls. Power* 22, 361–374.
- Prasad, M.R.G., Gao, S., Vajragupta, N., Hartmaier, A., 2020. Influence of trapped gas on pore healing under hot isostatic pressing in nickel-base superalloys. *Crystals* 10, 1–15.

- Pyttel, B., Schwerdt, D., Berger, C., 2011. Very high cycle fatigue - Is there a fatigue limit? *Int. J. Fatigue* 33, 49–58.
- Rae, C.M.F., Reed, R.C., 2001. The precipitation of topologically close-packed phases in rhenium-containing superalloys. *Acta Mater.* 49, 4113–4125.
- Rame, J., Cormier, J., 2019. Ni-based superalloy for single crystalline turbine blade. US20210214822A1.
- Rame, J., Utada, S., Bortoluci Ormastroni, L.M., Mataveli Suave, L., Despres, L., Kontis, P., Cormier, J., 2020. Platinum containing new generation nickel-based superalloys for single crystalline applications, in: Tin, S., Hardy, M., Clews, J., Cormier, J., Feng, Q., Marcin, J., O'Brien, C., Suzuki, A. (Eds.), *Proceedings of the International Symposium on Superalloys 2020*. Springer US, Seven Springs, PA, USA, pp. 71–81.
- Ramsperger, M., Mújica Roncery, L., Lopez-Galilea, I., Singer, R.F., Theisen, W., Körner, C., 2015. Solution Heat Treatment of the Single Crystal Nickel-Base Superalloy CMSX-4 Fabricated by Selective Electron Beam Melting. *Adv. Eng. Mater.* 17, 1486–1493.
- Ramsperger, M., Singer, R.F., Körner, C., 2016. Microstructure of the Nickel-Base Superalloy CMSX-4 Fabricated by Selective Electron Beam Melting. *Metall. Mater. Trans. A Phys. Metall. Mater. Sci.* 47, 1469–1480.
- Rannou, B., Bouchaud, B., Balmain, J., Bonnet, G., Pedraza, F., 2014. Comparative isothermal oxidation behavior of new aluminide coatings from slurries containing Al particles and conventional out-of-pack aluminide coatings. *Oxid. Met.* 81, 139–149.
- Rannou, B., Velasco, F., Guzmán, S., Kolarik, V., Pedraza, F., 2012. Aging and thermal behavior of a PVA/Al microspheres slurry for aluminizing purposes. *Mater. Chem. Phys.* 134, 360–365.
- Reed, R.C., 2006. *The superalloys - Fundamentals and applications*, First edit. ed. Cambridge University Press, Cambridge.
- Reger, M., Rémy, L., 1988a. Fatigue oxidation interaction in IN 100 superalloy. *Metall. Trans. A, Phys. Metall. Mater. Sci.* 19 A, 2259–2268.
- Reger, M., Rémy, L., 1988b. High temperature, low cycle fatigue of IN-100 superalloy I: Influence of temperature on the low cycle fatigue behaviour. *Mater. Sci. Eng. A* 101, 47–54.
- Rémy, L., Alam, A., Haddar, N., Köster, A., Marchal, N., 2007. Growth of small cracks and prediction of lifetime in high-temperature alloys. *Mater. Sci. Eng. A* 468–470, 40–50.

- Reppich, B., Schepp, P., Wehner, G., 1982. Some new aspects concerning particle hardening mechanisms in  $\gamma'$  precipitating nickel-base alloys—II. Experiments. *Acta Metall.* 30, 95–104.
- Reuchet, J., Rémy, L., 1983. Fatigue Oxidation Interaction in a Superalloy - Application To Life Prediction in High Temperature Low Cycle Fatigue. *Metall. Trans. A* 14 A, 141–149.
- Rezaei, M., Kermanpur, A., Sadeghi, F., 2018. Effects of withdrawal rate and starter block size on crystal orientation of a single crystal Ni-based superalloy. *J. Cryst. Growth* 485, 19–27.
- Riallant, F., 2014. Modes d'endommagement à chaud du système AM1/NiAl/Pt EBPVD: impact de la plasticité et interactions revêtement - substrat. PhD Thesis - Ecole Nationale Supérieure de Mécanique et d'Aérotechnique (ISAE-ENSMA), Poitiers, France. <https://theses.fr/2014ESMA0008>.
- Ritchie, R.O., Boyce, B.L., Campbell, J.P., Roder, O., Thompson, A.W., Milligan, W.W., 1999. Thresholds for high-cycle fatigue in a turbine engine Ti-6Al-4V alloy. *Int. J. Fatigue* 21, 653–662.
- Roué, V., 2020. Détermination rapide des propriétés en fatigue à grand nombre de cycles à partir de mesures d'auto-échauffement sous sollicitations cycliques: applications aux alliages métalliques pour turboréacteurs aéronautiques. PhD Thesis - Université Bretagne Sciences Loire pour l'Ingénieur (ENSTA-Bretagne), Brest, France. <https://tel.archives-ouvertes.fr/tel-03364460>.
- Ruttert, B., Ramsperger, M., Mujica Roncery, L., Lopez-Galilea, I., Körner, C., Theisen, W., 2016. Impact of hot isostatic pressing on microstructures of CMSX-4 Ni-base superalloy fabricated by selective electron beam melting. *Mater. Des.* 110, 720–727.
- Saboundji, A., Jaquet, V., Mataveli, L., Rame, J., 2020. Development of a new coating compatible with third-generation Nickel-based superalloys and thermal barrier coatings, in: Tin, S., Hardy, M., Clews, J., Cormier, J., Feng, Q., Marcin, J., O'Brien, C., Suzuki, A. (Eds.), *Proceedings of International Symposium on Superalloys 2020*. Springer US, Seven Springs, PA, USA, pp. 804–812.
- Sato, A., Chiu, Y.L., Reed, R.C., 2011. Oxidation of nickel-based single-crystal superalloys for industrial gas turbine applications. *Acta Mater.* 59, 225–240.
- Sato, A., Yeh, A.-C., Kobayashi, T., Yokokawa, T., Harada, H., Murakumo, T., Zhang, J.X., 2007. Fifth generation Ni based single crystal superalloy with superior elevated temperature

- properties. *Energy Mater.* 2, 19–25.
- Seo, S.M., Lee, J.H., Yoo, Y.S., Jo, C.Y., Miyahara, H., Ogi, K., 2011. A comparative study of the  $\gamma/\gamma'$  eutectic evolution during the solidification of Ni-base superalloys. *Metall. Mater. Trans. A Phys. Metall. Mater. Sci.* 42, 3150–3159.
- Shao, S., Khonsari, M.M., Guo, S., Meng, W.J., Li, N., 2019. Overview: Additive Manufacturing Enabled Accelerated Design of Ni-based Alloys for Improved Fatigue Life. *Addit. Manuf.* 29, 100779.
- Shida, Y., Wood, G.C., Stott, F.H., Whittle, D.P., Bastow, B.D., 1981. Intergranular oxidation and internal void formation in Ni-40% Cr alloys. *Corros. Sci.* 21, 581–597.
- Shyam, A., Padula, S.A., Marras, S.I., Milligan, W.W., 2002. Fatigue-crack-propagation thresholds in a nickel-base superalloy at high frequencies and temperatures. *Metall. Mater. Trans. A Phys. Metall. Mater. Sci.* 33, 1949–1962.
- Simonetti, M., Caron, P., 1998. Role and behaviour of  $\mu$  phase during deformation of a nickel-based single crystal superalloy. *Mater. Sci. Eng. A* 254, 1–12.
- Sims, C.T., Stoloff, N.S., Hagel, W.C., 1986. *Superalloys II*. Wiley, New York.
- Sinha, A.K., 1969. Close-Packed Ordered  $Ab_3$  Structures in Ternary Alloys of Certain Transition Metals. *Transit. Met. Alloy.* 245, 911–917.
- Siredey, N., Boufoussi, M., Denis, S., Lacaze, J., 1993. Dendritic growth and crystalline quality of nickel-base single grains. *J. Cryst. Growth* 130, 132–146.
- Smialek, J.L., Meier, G.H., 1987. *Superalloys II*. John Wiley & Sons, New York.
- Stanzl-Tschegg, S., 2014. Fatigue testing at ultrasonic frequencies. *Int. J. Fatigue* 60, 2–17.
- Steuer, S., Hervier, Z., Thabart, S., Castaing, C., Pollock, T.M., Cormier, J., 2014. Creep behavior under isothermal and non-isothermal conditions of AM3 single crystal superalloy for different solutioning cooling rates. *Mater. Sci. Eng. A* 601, 145–152.
- Steuer, S., Villechaise, P., Pollock, T.M., Cormier, J., 2015. Benefits of high gradient solidification for creep and low cycle fatigue of AM1 single crystal superalloy. *Mater. Sci. Eng. A* 645, 109–115.
- Stoloff, N.S., 1972. *The superalloys*. Wiley, New York.
- Swinkels, F.B., Wilkinson, D.S., Arzt, E., Ashby, M.F., 1983. Mechanisms of hot-isostatic pressing. *Acta Metall.* 31, 1829–1840.
- Szczotok, A., Rodak, K., 2012. Microstructural studies of carbides in MAR-M247 nickel-based

- superalloy. IOP Conf. Ser. Mater. Sci. Eng. 35.
- Telesman, J., Ghosn, L.J., 1996. Fatigue crack growth behavior of PWA 1484 single crystal superalloy at elevated temperatures. Proc. ASME Turbo Expo 5, 399–405.
- Tetzlaff, U., Mughrabi, H., 2000. Enhancement of the High-Temperature Tensile Creep Strength of Monocrystalline Nickel-Base Superalloys by Pre-rafting in Compression, in: Pollock, T.M., Kissinger, R.D., Bowman, R.R., Green, K.A., McLean, M., Olson, S., Schirra, J.J. (Eds.), Proceedings of the International Symposium on Superalloys 2000. Springer US, Seven Springs, PA, USA, pp. 273–282.
- Texier, D., Cormier, J., Villechaise, P., Stinville, J.C., Torbet, C.J., Pierret, S., Pollock, T.M., 2016a. Crack initiation sensitivity of wrought direct aged alloy 718 in the very high cycle fatigue regime: the role of non-metallic inclusions. Mater. Sci. Eng. A 678, 122–136.
- Texier, D., Gómez, A.C., Pierret, S., Franchet, J.M., Pollock, T.M., Villechaise, P., Cormier, J., 2016b. Microstructural Features Controlling the Variability in Low-Cycle Fatigue Properties of Alloy Inconel 718DA at Intermediate Temperature. Metall. Mater. Trans. A Phys. Metall. Mater. Sci. 47, 1096–1109.
- Texier, D., Monceau, D., Crabos, F., Andrieu, E., 2017. Tensile properties of a non-line-of-sight processed  $\beta$  -  $\gamma$  -  $\gamma'$  MCrAlY coating at high temperature. Surf. Coat. Technol. 326, 28–36.
- Texier, D., Monceau, D., Hervier, Z., Andrieu, E., 2016c. Effect of interdiffusion on mechanical and thermal expansion properties at high temperature of a MCrAlY coated Ni-based superalloy. Surf. Coat. Technol. 307, 81–90.
- Texier, D., Monceau, D., Selezneff, S., Longuet, A., Andrieu, E., 2020. High temperature micromechanical behavior of a Pt-modified Nickel aluminide bond-coating and its interdiffusion zone with the superalloy substrate. Metall. Mater. Trans. A 51, 1475–1480.
- Tin, S., Zhang, L., Ofori, A.P., Miller, M.K., 2007. Atomic partitioning of platinum and ruthenium in advanced single crystal Ni-based superalloys. Mater. Sci. Forum 546–549, 1187–1194.
- Totemeier, T.C., Gale, W.F., King, J.E., 1996. Isothermal fatigue of an aluminide-coated single-crystal superalloy: Part II. Effects of brittle precracking. Metall. Mater. Trans. A Phys. Metall. Mater. Sci. 27, 363–369.
- Totemeier, T.C., Gale, W.F., King, J.E., 1993. Fracture behaviour of an aluminide coating on a single crystal nickel base superalloy. Mater. Sci. Eng. A 169, 19–26.

- Totemeier, T.C., King, J.E., 1996. Isothermal fatigue of an aluminide-coated single-crystal superalloy: Part I. *Metall. Mater. Trans. A Phys. Metall. Mater. Sci.* 27, 353–361.
- Tucho, W.M., Cuvillier, P., Sjolyst-Kverneland, A., Hansen, V., 2017. Microstructure and hardness studies of Inconel 718 manufactured by selective laser melting before and after solution heat treatment. *Mater. Sci. Eng. A* 689, 220–232.
- Utada, S., Bortoluci Ormastroni, L.M., Rame, J., Villechaise, P., Cormier, J., 2021. VHCF life of AM1 Ni-based single crystal superalloy after pre-deformation. *Int. J. Fatigue* 148, 106224.
- Utada, S., Rame, J., Hamadi, S., Delautre, J., Villechaise, P., Cormier, J., 2020. Kinetics of creep damage accumulation induced by a room-temperature plastic deformation introduced during processing of AM1 Ni-based single crystal superalloy. *Mater. Sci. Eng. A* 789, 139571.
- Van Sluytman, J.S., 2010. Microstructure and high temperature creep of platinum group metal modified nickel base superalloys. PhD Thesis - University of Michigan, Michigan, USA. <https://deepblue.lib.umich.edu/handle/2027.42/77722>.
- Vattré, A., Devincre, B., Roos, A., 2009. Dislocation dynamics simulations of precipitation hardening in Ni-based superalloys with high  $\gamma'$  volume fraction. *Intermetallics* 17, 988–994.
- Volek, A., Pyczak, F., Singer, R.F., Mughrabi, H., 2005. Partitioning of Re between  $\gamma$  and  $\gamma'$  phase in nickel-base superalloys. *Scr. Mater.* 52, 141–145.
- Wahl, J.B., Harris, K., 2016. CMSX-4 Plus Single Crystal Alloy Development, Characterization and Application Development, in: Hardy, M.C., Huron, E., Glatzel, U., Griffin, B., Lewis, B., Rae, C., Seetharaman, V., Tin, S. (Eds.), *Proceedings of International Symposium on Superalloys 2016*. Springer US, Seven Springs, PA, USA, pp. 25–33.
- Walston, S., Cetel, A., MacKay, R., O'Hara, K., Duhl, D., Dreshfield, R., 2004. Joint development of a fourth generation single crystal superalloy, in: Green, K.A., Pollock, T.M., Harada, H., Howson, T.E., Reed, R.C., Schirra, J.J., Walston, S. (Eds.), *Proceedings of the International Symposium on Superalloys 2004*. Springer US, Seven Springs, PA, USA, pp. 15–24.
- Walston, W.S., Bernstein, I.M., Thompson, A.W., 1991. The Role of the  $\gamma/\gamma'$  eutectic and porosity on the tensile behavior of a single-crystal nickel-base superalloy. *Metall. Trans. A* 22, 1443–1451.
- Walston, W. S., O'Hara, K.S., Ross, E.W., Pollock, T.M., Murphy, W.H., 1996. René N6: Third generation single crystal superalloy. *Miner. Met. Mater. Soc.* 27–34.
- Walston, W.S., Schaeffer, J.C., Murphy, W.H., 1996. A New Type of Microstructural Instability

- in Superalloys - SRZ, in: Kissinger, R.D., Deye, D.J., Anton, D.L., Cetel, A.D., Nathal, M. V., Pollock, T.M., Woodford, D.A. (Eds.), Proceedings of International Symposium on Superalloys 1996. Springer US, Seven Springs, PA, USA, pp. 9–18.
- Wang, L., Pyczak, F., Zhang, J., Lou, L.H., Singer, R.F., 2012. Effect of eutectics on plastic deformation and subsequent recrystallization in the single crystal nickel base superalloy CMSX-4. *Mater. Sci. Eng. A* 532, 487–492.
- Wang, Y.L., Yu, X., Richards, N.L., Chaturvedi, M.C., 2004. Weldability of Directionally Solidified TMS-75 and TMD-103 Superalloys, in: Green, K.A., Pollock, T.M., Harada, H., Howson, T.E., Reed, R.C., Schirra, J.J., Walston, S. (Eds.), Proceedings of International Symposium on Superalloys 2004. Springer US, Seven Springs, PA, USA, pp. 529–535.
- Warnken, N., Ma, D., Drevermann, A., Reed, R.C., Fries, S.G., Steinbach, I., 2009. Phase-field modelling of as-cast microstructure evolution in nickel-based superalloys. *Acta Mater.* 57, 5862–5875.
- Whitesell, H.S., Li, L., Overfelt, R.A., 1999. Influence of solidification variables on the dendrite arm spacings of Ni-based superalloys. *Mettallurgical Mater. Trans. B* 31B, 546–551.
- Willertz, L.E., 1980. Ultrasonic fatigue. *Int. Met. Rev.* 25, 65–77.
- Wilson, B.C., Cutler, E.R., Fuchs, G.E., 2008. Effect of solidification parameters on the microstructures and properties of CMSX-10. *Mater. Sci. Eng. A* 479, 356–364.
- Wilson, B.C., Hickman, J.A., Fuchs, G.E., 2003. The effect of solution heat treatment on a single-crystal Ni-based superalloy. *JOM - Res. Summ.* 55, 35–40.
- Wukusick, C.S., Buchakjian Jr., L., 1991. U.K. Patent. 2 235 597 A.
- Yang, W., Hu, S., Huo, M., Sun, D., Zhang, J., Liu, L., 2019. Orientation controlling of Ni-based single-crystal superalloy by a novel method: Grain selection assisted by un-melted reused seed. *J. Mater. Res. Technol.* 8, 1347–1352.
- Yi, J.Z., Torbet, C.J., Feng, Q., Pollock, T.M., Jones, J.W., 2007. Ultrasonic fatigue of a single crystal Ni-base superalloy at 1000 °C. *Mater. Sci. Eng. A* 443, 142–149.
- Zhang, J.X., Murakumo, T., Koizumi, Y., Kobayashi, T., Harada, H., Masaki, S., 2002. Interfacial dislocation networks strengthening a fourth-generation single-crystal TMS-138 superalloy. *Metall. Mater. Trans. A Phys. Metall. Mater. Sci.* 33, 3741–3746.
- Zhang, W.J., 2016. Thermal mechanical fatigue of single crystal superalloys: Achievements and challenges. *Mater. Sci. Eng. A* 650, 389–395.

- Zhang, Y., Liu, L., Huang, T., Yue, Q., Sun, D., Zhang, J., Yang, W., Su, H., Fu, H., 2017. Investigation on a ramp solution heat treatment for a third generation nickel-based single crystal superalloy. *J. Alloys Compd.* 723, 922–929.
- Zhao, M., Wu, T., Zhao, Z., Liu, L., Luo, G., Chen, W., 2020. Ultrasonic fatigue device and behavior of high-temperature superalloy inconel 718 with self-heating phenomenon. *Appl. Sci.* 10, 1–14.
- Zhao, Z., Li, Q., Zhang, F., Xu, W., Chen, B., 2021a. Transition from internal to surface crack initiation of a single-crystal superalloys in the very-high-cycle fatigue regime at 1100 °C. *Int. J. Fatigue* 150, 106343.
- Zhao, Z., Li, Q., Zhang, F., Xu, W., Chen, B., 2021b. Transition from internal to surface crack initiation of a single-crystal superalloy in the very-high-cycle fatigue regime at 1100 °C. *Int. J. Fatigue* 150.
- Zhao, Z., Liang, Z., Li, Q., Zhang, F., Chen, B., 2022. Crack initiation and propagation behaviour under high-temperature very-high-cycle fatigue: Directionally solidified columnar-grained vs. single-crystal superalloys. *Mater. Sci. Eng. A* In Press, 142711.
- Zitara, M., Cetel, A., Czyska-Filemonowicz, A., 2011. Microstructure Stability of 4th Generation Single Crystal Superalloy, PWA 1497, during High Temperature Creep Deformation. *Mater. Trans.* 52, 336–339.



## **Mécanismes d'amorçage de fissures en fatigue gigacyclique à haute températures des superalliages base-Ni monogranulaires : transition cœur/surface**

La transition cœur/surface de l'amorçage de fissure par fatigue des superalliages base Ni monocristallins à haute température a été au centre de cette étude. Les nouveaux défis résultant de l'augmentation de la température des moteurs aéronautiques, et donc, le besoin des superalliages base Ni monocristallins de plus en plus résistants à la température ont conduit au développement de nouvelles générations, de procédés de traitement plus avancés (LMC, Fabrication additive, CIC), et le développement de revêtements. Cependant, des mécanismes d'endommagement supplémentaires à ceux rencontrés à basses températures apparaissent. Ainsi, pour analyser ces nouveaux mécanismes, des caractérisations mécaniques et microstructurales ont été réalisées pour dix superalliages base-Ni monocristallins en fatigue gigacyclique ( $R_r=-1$ , 20 kHz, et 1,000 °C) ou oligocyclique ( $R_r=0.5$ , 0.05 Hz, et 900/950 °C). Dans un premier temps, les effets des méthodes de solidification et des traitements CIC de neuf superalliages en régime gigacyclique ont été étudiés. Cette étude a permis de développer une base de données riche, présentant non seulement des résultats de superalliages de différentes générations, mais aussi, présentant pour la première fois dans la littérature, la caractérisation mécanique d'un superalliage base Ni monocristallin solidifié par une technique de fabrication additive. Un nouveau mécanisme d'amorçage piloté par l'oxydation à très grande durée de vie a été mis en évidence. L'analyse a aussi été menée sur l'impact des conditions de surface telles que la présence d'un revêtement sur trois superalliages dans des conditions de fatigue oligocyclique et gigacyclique. Il a été étudié l'influence de la couche NiAl déposée non seulement par un procédé industriel (APVS), mais aussi par un procédé de type Slurry. L'interaction entre pore de fonderie et la zone d'interdiffusion semble contrôler la durabilité en fatigue gigacyclique d'échantillons revêtus.

Mots clés : Fatigue, Alliages réfractaires, Hautes températures, Revêtements, Solidification, Fatigue gigacyclique, Fatigue oligocyclique, Amorçage de fissure par fatigue.

## **Crack initiation mechanisms in Very High Cycle Fatigue at high temperatures of Ni-based single crystal superalloys: transition from internal sites to the surface**

The fatigue crack initiation transition from internal defects to the surface at high temperatures has been the focus of this study. The new challenges resulting from the increase in temperature of aero-engines, and thus, the need for Ni-based SX superalloys more and more resistant to temperature led to the development of new generations, improved processing methods (LMC, additive manufacturing, HIP), and coating solutions. However, additional damage mechanisms to those encountered at lower temperature are arising. Thus, to identify new damage mechanisms scenarios, mechanical and microstructure characterizations were carried out for ten Ni-based SX superalloys in VHCF ( $R_r=-1$ , 20 kHz, and 1,000 °C) or LCF ( $R_r=0.5$ , 0.05 Hz, and 900/950 °C) conditions. At first, it was investigated the benefits and the consequences of the solidification methods and HIP treatments of nine Ni-based SX superalloys in the VHCF regime. This study enabled the development of a rich database, not only presenting results from superalloys from different generations, but also, presenting for the first time in the literature, the mechanical characterization of a Ni-based SX superalloy processed by an additive manufacturing route. A new failure mechanism assisted by oxidation at ultra-high lives has been uncovered. Later, the analysis was carried out to investigate the impact of the surface conditions such as the presence of the bond coat on three Ni-based SX superalloys under LCF and VHCF conditions. It was investigated the influence of the NiAl bond coat not only deposited by an industrial (APVS) deposition process, but also by a slurry-type process. The interaction between casting pores and the interdiffusion zone has been shown to control VHCF life of coated specimens.

Keywords: Fatigue, Heat resistant alloys, High temperatures, Coatings, Solidification, VHCF, LCF, Fatigue crack initiation.